Journal of Experimental and Theoretical Physics, Vol. 94, No. 1, 2002, pp. 1–7.
Translated from Zhurnal Éksperimental'noĭ i Teoreticheskoĭ Fiziki, Vol. 121, No. 1, 2002, pp. 5–13.

GRAVITATION, ASTROPHYSICS

A Common Origin of Neutralino Stars and Supermassive Black Holes

V. I. Dokuchaev* and Yu. N. Eroshenko**

Institute for Nuclear Research, Russian Academy of Sciences, pr. Shestidesyatiletiya Oktyabrya 7a, Moscow, 117312 Russia

**e-mail: dokuchaev@inr.npd.ac.ru*

***e-mail: erosh@ns.ufn.ru*

Received July 20, 2001

Abstract—To account for the microlensing events observed in the Galactic halo, Gurevich, Zybin, and Sirota have proposed a model of gravitationally bound, noncompact objects with masses of $\sim(0.01–1)M_\odot$. These objects are formed in the expanding Universe from adiabatic density perturbations and consist of weakly interacting particles of dark matter, for example, neutralinos. They assumed the perturbation spectrum on some small scale to have a distinct peak. We show that the existence of this peak would inevitably give rise to a large number of primordial black holes (PBHs) with masses of $\sim 10^5 M_\odot$ at the radiation-dominated evolutionary stage of the Universe. Constraints on the coefficient of nonlinear contraction and on the compactness parameter of noncompact objects were derived from constraints on the PBH number density. We show that noncompact objects can serve as gravitational lenses only at a large PBH formation threshold, $\delta_c > 0.5$, or if noncompact objects are formed from entropic density perturbations. © *2002 MAIK "Nauka/Interperiodica".*

1. INTRODUCTION

Dark objects with masses of $\sim(0.01–1)M_\odot$ were detected in the Galactic halo when the microlensing of stars from the Large Magellanic Cloud was observed. Brown and white dwarfs and Jupiter-like planets were proposed as possible baryonic candidates. According to the latest data [1], dark objects must account for about 20% of the hidden mass in the Galactic halo. However, the theory of primordial nucleosynthesis imposes much more stringent constraints on the number of such baryonic objects. Gravitationally bound, noncompact objects, which are also called neutralino stars, were considered among nonbaryonic candidates; these objects can explain some microlensing events with evidence of gravitational lenses being noncompact [2, 3]. The hypothetical noncompact objects are the lightest objects in the hierarchical large-scale structure of the Universe. In the model of Gurevich, Zybin, and Sirota [3], these are formed immediately after the passage of the Universe to the dust stage.

To reconcile the parameters of noncompact objects with data for the observed microlensing events, Gurevich *et al.* [3] assumed the cosmological density perturbation spectrum on some small scale to increase sharply with an rms fluctuation of the order of 1 at the peak. For adiabatic perturbations, rms fluctuations of the order of 0.05 correspond to these fluctuations at the radiation-dominated stage on the cosmological horizon scale. As was shown in [4, 5], fluctuations with such an rms value give rise to primordial black holes (PBHs) at the radiation-dominated evolutionary stage of the Universe. As we will see below, the mass of the forming PBHs exceeds the mass of noncompact objects by several orders of magnitude. The large difference between the masses of noncompact objects and PBHs stems from the fact that the mass of the radiation contained in a fixed comoving volume at the radiation-dominated stage is much larger than the mass of cold dark matter (CDM) in the same volume at the dust stage.

If the power spectrum of primordial cosmological perturbations is a power law with an index $n \geq 1$, then PBHs are formed in a wide range of masses. If, however, the spectrum has a peak on some scale, then PBHs are formed mostly in a narrow range of masses, near the mass that corresponds to this peak. A sharp peak emerges in the fluctuation spectrum if the inflationary potential $V(\phi)$ has a flat segment [6, 7]. Indeed, if the derivative at some value of the scalar field is

$$V' = dV(\phi)/d\phi \longrightarrow 0,$$

then a peak emerges in the perturbation spectrum on the corresponding scale, because the mean density perturbation on the horizon scale is

$$\delta_H \sim M_{\rm Pl}^{-3} V^{3/2}/V',$$

where $M_{\rm Pl}$ is the Planck mass. A similar effect is achieved in inflationary models with several scalar fields [8, 9]. In this case, the spectrum outside the peak can have an ordinary shape (for example, it can be a Harrison–Zel'dovich spectrum) and can give rise to galaxies, their clusters, and superclusters according to standard scenarios.

Certain evidence for a deviation of the initial perturbation spectrum from a simple power-law shape, more specifically, for a spectral break near large scales, $k \approx (0.06–0.6)h$ Mpc^{-1}, was obtained in the counting of APM galaxies and in the Boomerang and Maxima cosmic microwave background (CMB) anisotropy measurements [10]. Therefore, there is reason to suggest that the spectrum may also exhibit features on small scales.

Here, we show that, if the perturbation spectrum has a peak, then there is a clear relationship between the masses of noncompact objects and PBHs; a PBH mass of the order of $10^5 M_\odot$ corresponds to a noncompact object mass of the order of $0.1M_\odot$. For noncompact objects to be able to serve as gravitational lenses, they must originate from sufficiently large dark matter density fluctuations. At the radiation-dominated stage, these fluctuations logarithmically increase with time and become nonlinear even at this stage. To study the evolution of the fluctuations at the radiation-dominated stage, we use the nonlinear model proposed by Kolb and Tkachev [11] and specify the initial data for this model according to the linear theory.

Based on standard astrophysical constraints on the PBH number density in the Universe, we obtained constraints on the rms fluctuations at the peak. In turn, the constraints on the fluctuations give constraints on the radius of a noncompact object. As was shown in [3], a noncompact object can serve as a gravitational lens and can produce observable microlensing events only if its radius exceeds the Einstein radius for this object by no more than a factor of 10. Stringent constraints on the coefficient of nonlinear contraction for noncompact objects follow from this condition.

The inferred relationship between noncompact objects and PBHs holds only for adiabatic cosmological density perturbations. If the density perturbations are entropic, then even if there are large fluctuations in the dust component, the radiation density on the horizon scale is almost uniform and no PBHs are formed.

It should be emphasized that when talking about a common origin of noncompact objects and PBHs, we have in mind not the relationship between individual noncompact objects and PBHs but the fact that the fluctuations from which the entire collection of noncompact objects and the entire collection of PBHs originate have a common spectrum. If a PBH emerged at some point in space, then a noncompact object can no longer emerge at this point. Conversely, if there is a noncompact object, then no PBH was previously (at the radiation-dominated stage) formed at this point.

2. THE FORMATION OF PBHS

The PBH formation criterion was analytically derived by Carr [5] and confirmed by numerical calculations [12, 13]. The region of space with a density

$$\rho > \rho_c = \frac{3H^2}{8\pi G}$$

can be roughly considered to be part of the closed Universe. Gravitational collapse of this region and the formation of a PBH take place if the relative radiation density fluctuation

$$\delta_H = \frac{\rho - \rho_c}{\rho_c}$$

at the time the PBH goes under the horizon satisfies the conditions

$$\delta_c \le \delta_H \le 1, \tag{1}$$

where $\delta_c = 1/3$. The left-hand inequality implies that the radius of the perturbed region at the time t that its expansion stops exceeds the Jeans radius $ct/\sqrt{3}$, while the right-hand inequality corresponds to the formation of a PBH rather than an isolated universe. The mass of the forming PBH in this model is

$$M_{BH} = \frac{M_H}{3^{3/2}}, \tag{2}$$

where M_H is the mass within the horizon.

In recent years, numerical experiments have revealed the so-called critical gravitational collapse, during which the mass of the forming PBH is [14, 15]

$$M_{BH} = AM_H(\delta_H - \delta_c)^\gamma, \tag{3}$$

where $A \sim 3$, $\gamma \approx 0.36$, and $\delta_c \approx 0.65–0.7$. The mass (3) can be much smaller than M_H. However, as shown in [16], the PBH mass distribution for critical gravitational collapse is concentrated near $M_{BH} \sim M_H$, and the contribution of low masses to the cosmological PBH density is modest. Here, we consider various cases where δ_c lies within the range $1/3 \le \delta_c \le 0.7$.

Following [6–8], we assume that there is a sharp peak in the fluctuation spectrum on some fixed (in comoving coordinates) scale $\xi = r/a(t)$. Since the PBH formation threshold is large, $\delta_H > 1/3$, most ξ-scale fluctuations do not collapse into a PBH but are preserved until the passage to the dust stage if the dark matter particle free streaming length is moderately large [3]. The mass M_H within the horizon as a function of the mass M_x of the dust component in fluctuations of the same comoving scale can be calculated by using the standard Friedmann equations. Noncompact objects are formed on time scales $t \le t_{eq}$, where t_{eq} is the time of equality between the matter and radiation densities. At this epoch, a flat cosmological model serves as a good approximation:

$$\begin{aligned} a(\eta) &= a_{eq}\left[2\frac{\eta}{\eta_*} + \left(\frac{\eta}{\eta_*}\right)^2\right], \\ ct &= a_{eq}\eta_*\left[\left(\frac{\eta}{\eta_*}\right)^2 + \frac{1}{3}\left(\frac{\eta}{\eta_*}\right)^3\right], \end{aligned} \tag{4}$$

where

$$\eta_*^{-2} = 2\pi G\rho_{eq}a_{eq}^2/3c^2,$$

a_{eq} is the scale factor at time t_{eq},

$$\begin{aligned}\rho_{eq} &= \rho_0(1+z_{eq})^3\\ &= 3.2\times10^{-20}\left(\frac{h}{0.6}\right)^8\left(\frac{\Omega_m}{0.3}\right)^4 \text{ g cm}^{-3},\\ 1+z_{eq} &= 2.32\times10^4\Omega_m h^2,\\ \rho_0 &= 1.9\times10^{-29}\Omega_m h^2 \text{ g cm}^{-3}\end{aligned} \quad (5)$$

is the present cosmological matter density, and h is the Hubble constant (in units of 100 km s^{-1} Mpc^{-1}). We perform our calculations for two cosmological models: the model with the present matter density parameter $\Omega_m = 0.3$ and the cosmological term $\Omega_\Lambda = 1 - \Omega_m \approx 0.7$ and the model without the Λ term and with $\Omega_m = 1$. The presence of the Λ term reduces only to a change in ρ_{eq}; it does not affect the formation of noncompact objects, because the Λ term contributes negligibly to the total cosmological density on time scales $t \le t_{eq}$.

For M_H and M_x, we have the expressions

$$M_H = \frac{4\pi}{3}\rho_H(a(\eta_H)\xi)^3, \quad M_x = \frac{4\pi}{3}\rho_0(a(\eta_0)\xi)^3. \quad (6)$$

On the horizon scale,

$$a(\eta_H)\xi = 2ct_H,$$

with $\eta_H \ll \eta_*$ and $\rho_H = 3/32\pi G t_H^2$. The present density is

$$\rho_0 = \rho_{eq}(a_{eq}/a_0)^3.$$

Using (4), we obtain

$$\begin{aligned}M_H &= \frac{1}{2^{2/3}}\left(\frac{3}{2\pi}\right)^{1/6}\frac{M_x^{2/3}c}{G^{1/2}\rho_{eq}^{1/6}} = 1.96\times10^5\\ &\times\left(\frac{M_x}{0.1M_\odot}\right)^{2/3}\left(\frac{\Omega_m}{0.3}\right)^{-2/3}\left(\frac{h}{0.6}\right)^{-4/3}M_\odot,\end{aligned} \quad (7)$$

$$t_H = \frac{GM_H}{c^3} = 0.5\left(\frac{M_H}{10^5M_\odot}\right)\text{s}. \quad (8)$$

Denote the rms density fluctuation δ_H by

$$\Delta_H \equiv \langle\delta_H^2\rangle^{1/2}.$$

The fraction of the radiation mass that transformed into PBHs at time t_H is then [5, 8]

$$\begin{aligned}\beta &= \int_{\delta_c}^{1}\frac{d\delta_H}{\sqrt{2\pi}\Delta_H}\exp\left(-\frac{\delta_H^2}{2\Delta_H^2}\right)\\ &= \frac{1}{2}\left[\text{erf}\left(\frac{1}{\sqrt{2}\Delta_H}\right) - \text{erf}\left(\frac{\delta_c}{\sqrt{2}\Delta_H}\right)\right] \approx \frac{\Delta_H}{\delta_c\sqrt{2\pi}}\exp\left(-\frac{\delta_c^2}{2\Delta_H^2}\right),\end{aligned} \quad (9)$$

where erf(x) is the error integral. Since, according to [16], the fraction of the collapsing mass of the Universe for critical gravitational collapse is 0.8β, Eq. (9) for critical collapse is also a good approximation.

Using (7) and (9), we can calculate the cosmological PBH density parameter Ω_{BH} at the present time t_0:

$$\begin{aligned}\Omega_{BH} &= \frac{\beta}{2^{2/3}}\left(\frac{3}{2\pi}\right)^{1/6}\frac{c}{M_x^{1/3}G^{1/2}\rho_{eq}^{1/6}} = 3.45\times10^5\\ &\times\left(\frac{M_x}{0.1M_\odot}\right)^{-1/3}\left(\frac{\Omega_m}{0.3}\right)^{-2/3}\left(\frac{h}{0.6}\right)^{-4/3}\frac{\Delta_H}{\delta_c}\exp\left\{-\frac{\delta_c^2}{2\Delta_H^2}\right\}.\end{aligned} \quad (10)$$

To within a factor of order unity, expression (7) can be derived from a simple estimate

$$M_H \approx M_x a(t_{eq})/a(t_H) \approx M_x(t_{eq}/t_H)^{1/2},$$

where $t_H = GM_H/c^3$ and $t_{eq} \sim 6\times10^{10}$ s is the completion time of the radiation-dominated stage. In the same way, we can derive (10) from the estimate

$$\Omega_{BH} \approx \beta a(t_{eq})/a(t_H).$$

PBHs are formed in the tail of the Gaussian fluctuation distribution, while most noncompact objects are formed from rms fluctuations. Therefore, we repeat that not every fluctuation, by any means, from which a noncompact object formed could collapse into a PBH at time t_H.

3. THE EVOLUTION OF PERTURBATIONS

The evolution of a radiation density perturbation at the radiation-dominated stage follows the law [17]

$$\delta_r = xf(x) + \frac{3x^2}{x^2+6}\frac{d}{dx}f(x), \quad (11)$$

where for the growing mode

$$f(x) = A_{in}j_1(x/\sqrt{3}),$$

j_1 is the spherical Bessel function, A_{in} is the normalization constant, $x = k\eta$, and k is the comoving perturba-

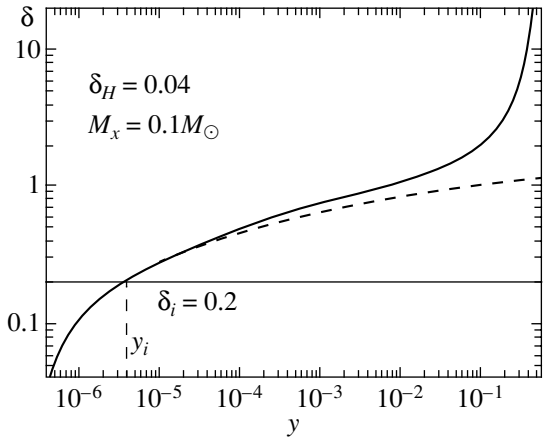

Fig. 1. The evolution of a CDM density perturbation δ. The plot corresponds to the parameters $\delta_H = 0.04$, $M_x = 0.1M_\odot$, and $\Omega_m = 0.3$. The curve was obtained from formula (13) before the point ($y_i = 3.96 \times 10^{-6}$, $\delta_i = 0.2$), and a numerical solution to Eq. (14) was used at $y > y_i$. The cosmological expansion of a noncompact object stops at the radiation-dominated stage at $y = a/a_{\rm eq} \approx 0.49$. The dashed line indicates the evolution of δ according to the linear theory (13).

tion wave vector. The physical perturbation wavelength $\lambda_{\rm ph}$ satisfies the relations

$$\lambda_{\rm ph}(\eta) = a(\eta)\left(\frac{2\pi}{k}\right), \qquad M_x = \frac{4\pi}{3}\rho_0\left(\frac{\lambda_{\rm ph}(t_0)}{2}\right)^3. \tag{12}$$

On the horizon scale, $\lambda_{\rm ph}/2 \approx 2ct$, $x_H \approx \pi$, and we obtain from (11)

$$\delta_r = \delta_H = A_{\rm in}\phi,$$

where $\phi \approx 0.817$.

For adiabatic perturbations, the perturbation in nonrelativistic matter at $x \ll 1$ is $\delta = 3\delta_r/4$. In [17], an analytic solution was found for $\delta(x)$ in the entire interval from $x \ll 1$ to $x \gg 1$ at the radiation-dominated stage. At $x \gg 1$, this solution is

$$\delta = \frac{3A_{\rm in}}{2}\left[\ln\left(\frac{x}{\sqrt{3}}\right) + \gamma_E - \frac{1}{2}\right], \tag{13}$$

where $\gamma_E - 1/2 \approx 0.077$ and $A_{\rm in} = \delta_H/\phi$ is the same as in (11).

The applicability of (13) is limited to a linear stage, $\delta \ll 1$. When passing to a nonlinear stage, we will use the spherical model from [11]. In this model, the evolution of adiabatic perturbations is described by the equation

$$y(y+1)\frac{d^2b}{dy^2} + \left[1 + \frac{3}{2}y\right]\frac{db}{dy} + \frac{1}{2}\left[\frac{1}{b^2} - b\right] = 0, \tag{14}$$

where $y = a(\eta)/a_{\rm eq}$ and the following parametrization was introduced for the radius of the perturbed region:

$$r = a(\eta)b(\eta)\xi. \tag{15}$$

Here, ξ is the comoving coordinate, and $b(\eta)$ allows for the deceleration of cosmological expansion in the region of enhanced density. The quantity b in (15) can be expressed in terms of δ as

$$b = (1 + \delta)^{-1/3}. \tag{16}$$

This relation means the passage from the Eulerian description of the perturbation evolution (13) to its Lagrangian description (14).

To solve (14) requires specifying δ_i at some initial y_i, $b_i = (1 + \delta_i)^{-1/3}$ according to (16), and the expansion rate db/dy. In [11], Eq. (14) was solved for entropic perturbations when the initial velocity may be disregarded, $db/dy \approx 0$. In our case of adiabatic perturbations, the initial velocity is large; we specify it according to the solution (13). At $x \gg 1$ and $y \ll 1$, we have

$$x = \frac{\pi}{2^{2/3}}\left(\frac{3}{2\pi}\right)^{1/6}\frac{yc}{M_x^{1/3}G^{1/2}\rho_{\rm eq}^{1/6}} = 2.86 \times 10^6 y \times \left(\frac{\Omega_m}{0.3}\right)^{-2/3}\left(\frac{h}{0.6}\right)^{-4/3}\left(\frac{M_x}{M_\odot}\right)^{-1/3}. \tag{17}$$

We obtain from (13), (16), and (17)

$$\left.\frac{db}{dy}\right|_{y_i} = -\frac{\delta_H b_i^4}{2y_i\phi}. \tag{18}$$

We solve Eq. (14) numerically. The time y_i must be chosen in such a way that (13) and (14) are simultaneously valid. An optimum choice is the time when $\delta_i = 0.2$. A test shows that the results of our calculations change by no more than 15% for a different choice of δ_i in the range 0.1–0.3. Having specified δ_i, we obtain x_i and y_i from (13) and (17). The evolution of $\delta = b^{-3} - 1$ is illustrated in Fig. 1.

The cosmological expansion of noncompact objects stops when $dr/dt = 0$. According to [11], this is equivalent to

$$\frac{db}{dy} = -\frac{b}{y}. \tag{19}$$

Denote b and y at the time the expansion stops by $b_{\rm max}$ and $y_{\rm max}$, respectively. The CDM density in noncompact objects at the same time is

$$\rho_{\rm max} = \rho_{eq}y_{\rm max}^{-3}b_{\rm max}^{-3}, \tag{20}$$

and, consequently, the radius of the noncompact object at the stoppage time is

$$R_{\rm max} = \left(\frac{3M_x}{4\pi\rho_{\rm max}}\right)^{1/3}. \tag{21}$$

The numerically calculated dependence of $R_{\rm max}$ on δ_H is shown in Fig. 2.

Thus, we have shown how the radius of a noncompact object at the time its cosmological expansion stops can be determined for the specified perturbation δ_H on the horizon scale.

4. THE PARAMETERS OF GRAVITATIONAL LENSES

After its cosmological expansion stops, a noncompact object begins to contract, with its final radius being

$$R_x = \kappa R_{\max}, \tag{22}$$

where κ is the coefficient of nonlinear contraction. It is generally believed [18] that, after the cosmological expansion of a noncompact object stops, it is virialized, radially contracting by a factor of 2, i.e., $\kappa = 0.5$. According to the theory of gravitational instability, $\kappa \approx 0.3$ in a multiflow region [3]. At present, the physical processes that could cause a noncompact object to contract to $\kappa < 0.3$ are unknown. Therefore, we take $\kappa \approx 0.3$ as the lower limit.

For a noncompact object to be able to serve as a gravitational lens producing observable microlensing events in the Galactic halo, its radius should not significantly exceed the Einstein radius

$$R_E = 2\sqrt{GM_x d/c^2}, \tag{23}$$

where $d \sim 20$ kpc for microlensing in the halo. We define ε as

$$\varepsilon \equiv 10\frac{R_E}{R_x}. \tag{24}$$

According to calculations [3], the inequality $\varepsilon \geq 1$ must hold. If $\varepsilon < 1$, then the theory comes into conflict with observational data on the light curves [3]. One of the microlensing events with a lens mass $M_x \approx 0.02M_\odot$ was studied in detail in [19]. A comparison of the observed and calculated light curves showed that, if a noncompact object has no baryonic core at its center, then it must have the size $R_x = 1.6 \times 10^{13}$ cm and a compactness parameter (in our notation) $\varepsilon \approx 19$. In the presence of a baryonic core with a mass of $0.05M_x$, $R_x = 5.7 \times 10^{13}$ cm and $\varepsilon \approx 4.8$. It was noted in [19] that the model of a pointlike lens for this event is also acceptable because of the large observational errors.

We obtain from (21), (23), and (24)

$$\kappa\varepsilon = 10\frac{R_E}{R_{\max}} = \frac{1.9\times 10^{15}\ \text{cm}}{R_{\max}}\left(\frac{M_x}{M_\odot}\right)^{1/2}\left(\frac{d}{20\ \text{kpc}}\right)^{1/2}. \tag{25}$$

On the other hand, using our calculations (see the preceding section), we derived a relationship between $R_{\max}$ and δ_H; the quantity δ_H defines the present cosmological PBH density according to Eq. (10). It should be noted that noncompact objects are formed from rms fluctuations. Therefore, δ_H from the preceding section should be set equal to the rms fluctuation $\delta_H = \Delta_H$. Using our numerical calculations, we derive the dependence of Ω_{BH} on the product $\kappa\varepsilon$ (see Figs. 3 and 4).

There are several astrophysical constraints on the mass and number of PBHs. It follows from a constraint

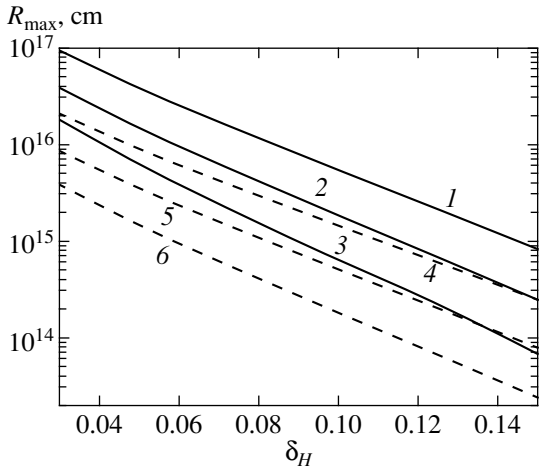

Fig. 2. Radius $R_{\max}$ of noncompact objects at the time their expansion stops versus perturbation magnitude δ_H on the horizon scale. Solid curves *1*, *2*, and *3* correspond to the masses of noncompact objects $M_x = 1M_\odot$, $0.1M_\odot$, and $0.01M_\odot$ in the cosmological model with $\Omega_m = 0.3$. Dashed lines *4*, *5*, and *6* were constructed for $\Omega_m = 1$ at the same masses.

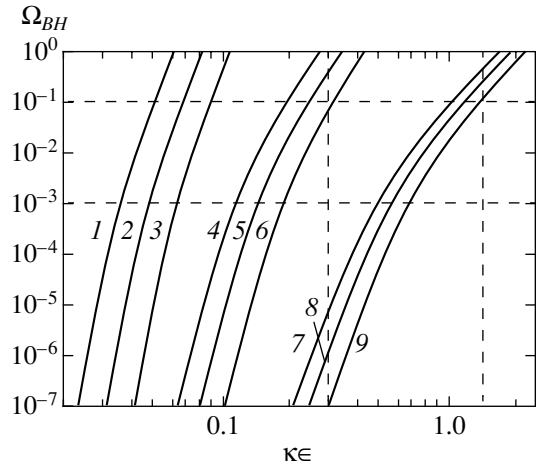

Fig. 3. PBH density parameter Ω_{BH} versus nonlinear contraction coefficient and compactness parameter for noncompact objects $\kappa\varepsilon$ in the model with $\Omega_m = 0.3$. Curves *1*, *2*, and *3* correspond to the masses of noncompact objects $M_x = (0.01, 0.1, 1)M_\odot$ at $\delta_c = 1/3$. Curves *4*, *5*, and *6* correspond to $\delta_c = 1/2$; curves *7–9* correspond to $\delta_c = 0.7$ for the same masses. The horizontal and vertical lines correspond to the upper observational limits $\Omega_{BH} = 0.1$, 10^{-3} and to $\kappa\varepsilon = 0.3$, 1.44, respectively. The admissible regions lie below the horizontal lines and to the right of the vertical lines.

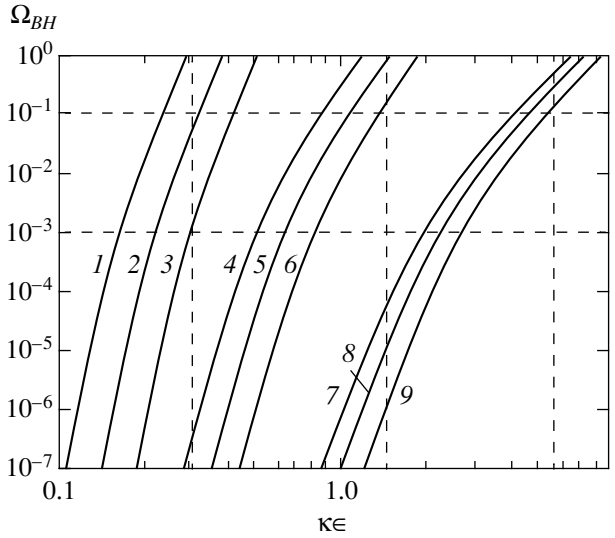

Fig. 4. Same as Fig. 3 for the cosmological model with $\Omega_m = 1$. The vertical lines correspond to $\kappa\varepsilon = 0.3$, 1.44, and 5.7.

on the age of the Universe that $\Omega_{BH} \le 1$. If PBHs provide the dominant part of dark matter in the Galaxy, then they must tidally interact with globular clusters by disrupting them. The PBH mass was constrained for this case in [20], $M_{BH} \le 10^4 M_\odot$. At $\Omega_{BH} \sim 1$, PBHs are capable of distorting the CMB spectrum if they are formed about 1 s after the annihilation of e^+e^- pairs [5]. Mass accretion by black holes at the pregalactic and present epochs contributes to the background radiation in different wavelength ranges [21]. However, calculations strongly depend on the model and yield $\Omega_{BH} \le 10^{-3}$–10^{-1} for $M_{BH} \sim 10^5 M_\odot$. In [22], the constraint $\Omega_{BH} < 0.1$ on intergalactic PBHs was obtained from the condition for the absence of reliable gamma-ray-burst lensing events for $10^5 M_\odot < M_{BH} < 10^9 M_\odot$. A more stringent lensing constraint, $\Omega_{BH} < 0.01$ for the mass range $10^6 M_\odot < M_{BH} < 10^8 M_\odot$, was obtained from VLBI observations of compact radio sources [23].

Let us first consider the microlensing event studied in [19] by assuming that $\varepsilon = 0.3$. If the noncompact object has no baryonic core (the vertical line $\kappa\varepsilon \approx 5.7$ in Figs. 3 and 4 corresponds to this case), then the constraint $\Omega_{BH} < 0.1$ rules out the interpretation of this event as microlensing by noncompact objects for all $\delta_c = 1/3$–0.7 in the two cosmological models under consideration. In the presence of a baryonic core (the vertical line $\kappa\varepsilon \approx 1.44$), the case with $\delta_c = 0.7$ remains admissible in the cosmological model without the Λ term (Fig. 4).

Consider the less stringent condition $\kappa\varepsilon > 0.3$, which is satisfied at $\varepsilon > 1$ and $\kappa > 0.3$. At $\Omega_\Lambda \approx 0.7$ (Fig. 3), the constraint $\Omega_{BH} < 0.1$ rules out all models with $\delta_c < 0.5$. At $\Omega_{BH} > 10^{-6}$, the case with $\delta_c \approx 0.7$ remains possible. If $\Omega_\Lambda = 0$, then the constraint $\Omega_{BH} < 0.1$ leaves a narrow region (see Fig. 4) with $M_x > 0.1 M_\odot$ and $\delta_c = 1/3$. The constraint $\Omega_{BH} < 10^{-3}$ completely rules out the models with $\delta_c = 1/3$, but allows the cases with $\delta_c > 1/3$.

5. CONCLUSIONS

We have shown that the formation of noncompact dark-matter objects (neutralino stars) proposed in [2, 3] to account for the observed microlensing events in the Galactic halo must be preceded by the formation of PBHs with masses on the order of $10^5 M_\odot$. These PBHs and neutralino stars are formed from the same peak in the primordial fluctuation spectrum.

Astrophysical constraints on the number of PBHs in the Universe allowed us to constrain the coefficient of nonlinear contraction and compactness parameter for a noncompact object; our constraints are shown in Figs. 3 and 4. The most stringent constraints are obtained in the presence of a cosmological term $\Omega_\Lambda \approx 0.7$. In this case, noncompact objects can serve as gravitational lenses only at a large PBH formation threshold, $\delta_c > 0.5$, which was calculated in the model of critical gravitational collapse. At smaller δ_c, the model of noncompact objects as microlensing objects is ruled out. The constraint on $\kappa\varepsilon$ is significantly relaxed if the Λ term is small (Fig. 4). However, this possibility is currently considered to be unlikely.

It is important to note that to avoid the situation where $\ln(\Omega_{BH}) \ll 0$ requires an accurate adjustment of the parameters for the inflationary model that ensures that Δ_H is in a narrow interval, ≈0.05–0.12. Therefore, if the observed microlensing events are actually produced by noncompact objects, then these objects most likely originate from entropic density perturbations. In this case, our constraints are removed, as discussed in the Introduction.

The constraints can also be significantly relaxed if, for some reason, PBHs are formed in smaller quantities than that given by expression (9). This is possible, for example, in the case of great importance of the nonlinear effects that accompany the generation of metric perturbations at the inflationary stage if these effects suppress the appearance of large fluctuations [24]. Note, however, that the role of nonlinear effects is presently not completely understood, and the results of calculations depend on the specific inflationary model. For example, it was found in [25] that nonlinear effects cause the PBH formation probability to increase, which is directly opposite to the result from [24].

Conversely, if the noncompact nature of lenses is proven in the future, then for adiabatic density perturbations this will lead us to conclude that a large number of PBHs with masses of the order of $10^5 M_\odot$ can be formed at the radiation-dominated sage of the Universe. These PBHs must affect the evolution of galaxies and their nuclei. It may well be that one of such PBHs was found by the Chandra space X-ray observatory in the

galaxy M 82 [26]. In a separate paper [27], we develop a model for the formation of galaxies through multiple mergers of protogalaxies with condensation centers in the form of massive PBHs. The mergers of galaxies and the growth of central massive black holes at the galactic nuclei take place simultaneously with the formation of galaxies. The recently found correlations between the masses of central black holes and the bulge velocity dispersion have been shown to arise naturally in this scenario.

Since noncompact objects and PBHs originate from a common perturbation spectrum, we can in principle reconstruct the shape of the perturbation spectrum and determine the PBH mass function from the distribution of noncompact objects in mass and radius using a Press–Schechter-type theory [28]. Unfortunately, only a few objects were detected by microlensing, and such a calculation will become possible only in the future when the statistics improve.

We may consider a situation that, in a sense, is reverse to the situation described previously. According to the hypothesis [7], the dark halo objects responsible for microlensing are PBHs with masses of the order of $(0.01–1)M_\odot$. If elementary particles with a free streaming length $\ll\xi$ compose the remaining part of the dark matter, then miniclusters will be formed from these particles at the dust stage. Using formula (7), we can immediately estimate the minicluster mass as $(10^{-11}–10^{-8})M_\odot$. Such masses are possible if the mass of the dark-matter particles exceeds 1 GeV [3]. The formation of PBHs with $\Omega_{BH} \sim 1$ requires rms fluctuations $\Delta_H \approx 0.06$. At time t_{eq}, fluctuations in the dust component $\delta \sim 1$, which give rise to miniclusters, correspond to them.

ACKNOWLEDGMENTS

We thank K.P. Zybin and V.N. Lukash for helpful discussions. This study was supported by the INTAS (grant no. 99-1065) and the Russian Foundation for Basic Research (project nos. 01-02-17829, 00-15-96697, and 00-15-96632).

REFERENCES

1. C. Alcock, R. A. Allsman, D. R. Alves, *et al.*, Astrophys. J. **542**, 281 (2000).
2. A. V. Gurevich and K. P. Zybin, Phys. Lett. A **208**, 276 (1995).
3. A. V. Gurevich, K. P. Zybin, and V. A. Sirota, Usp. Fiz. Nauk **167**, 913 (1997) [Phys. Usp. **40**, 869 (1997)].
4. Ya. B. Zel'dovich and I. D. Novikov, Astron. Zh. **43**, 758 (1966) [Sov. Astron. **10**, 602 (1967)].
5. B. J. Carr, Astrophys. J. **201**, 1 (1975).
6. A. A. Starobinsky, Pis'ma Zh. Éksp. Teor. Fiz. **55**, 477 (1992) [JETP Lett. **55**, 489 (1992)].
7. P. Ivanov, P. Naselsky, and I. Novicov, Phys. Rev. D **50**, 7173 (1994).
8. J. Yokoyama, astro-ph/9509027.
9. J. Garcia-Bellido, A. Linde, and D. Wands, Phys. Rev. D **54**, 6040 (1996).
10. J. Barriga, E. Gaztanaga, M. G. Santos, and S. Sarkar, astro-ph/0011398.
11. E. W. Kolb and I. I. Tkachev, Phys. Rev. D **50**, 769 (1994).
12. D. K. Nadezhin, I. D. Novikov, and A. G. Polnarev, Astron. Zh. **55**, 216 (1978) [Sov. Astron. **22**, 129 (1978)].
13. I. D. Novikov, A. G. Polnarev, A. A. Starobinsky, and Ya. B. Zeldovich, Astron. Astrophys. **80**, 104 (1979).
14. M. W. Choptuik, Phys. Rev. Lett. **70**, 9 (1993).
15. J. C. Niemeyer, astro-ph/9806043.
16. J. Yokoyama, astro-ph/9804041.
17. C. Schmid, D. J. Schwarz, and P. Widerin, Phys. Rev. D **59**, 043517 (1999).
18. W. C. Saslaw, *Gravitational Physics of Stellar and Galactic Systems* (Cambridge Univ. Press, Cambridge, 1985; Mir, Moscowt 1989).
19. V. A. Sirota, Zh. Éksp. Teor. Fiz. **117**, 261 (2000) [JETP **90**, 227 (2000)].
20. B. Moore, Astrophys. J. Lett. **413**, L93 (1993).
21. B. J. Carr, Mon. Not. R. Astron. Soc. **189**, 123 (1979).
22. R. J. Nemiroff, G. F. Marani, J. P. Norris, and J. T. Bonnel, Phys. Rev. Lett. **86**, 580 (2001).
23. P. N. Wilkinson, D. R. Henstock, I. W. A. Browne, *et al.*, Phys. Rev. Lett. **86**, 584 (2001).
24. J. S. Bullock and J. B. Primack, astro-ph/9806301.
25. P. Ivanov, astro-ph/9708224.
26. P. Kaaret, A. H. Prestwich, A. Zezas, *et al.*, astro-ph/0009211.
27. V. I. Dokuchaev and Yu. N. Eroshenko, Pis'ma Astron. Zh. **27** (12), 883 (2001) [Astron. Lett. **27** (12), 759 (2001)].
28. E. V. Bugaev and K. V. Konishchev, astro-ph/0103265.

Translated by V. Astakhov

Journal of Experimental and Theoretical Physics, Vol. 94, No. 1, 2002, pp. 108–118.
Translated from Zhurnal Éksperimental'noĭ i Teoreticheskoĭ Fiziki, Vol. 121, No. 1, 2002, pp. 129–141.

SOLIDS
Structure

Dynamics of Kinks on Dislocations in SiGe Single Crystals

Yu. L. Iunin[a, *], V. I. Nikitenko[a], V. I. Orlov[a], D. V. D'yachenko-Dekov[a], B. V. Petukhov[b], N. V. Abrosimov[a, c], S. N. Rossolenko[a], and W. Schröder[c]

[a]*Institute of Solid-State Physics, Russian Academy of Sciences, Chernogolovka, Moscow oblast, 142432 Russia*
[b]*Institute of Crystallography, Russian Academy of Sciences, Moscow, 117333 Russia*
[c]*Institut für Kristallzüchtung, Max-Born-Str. 2, 12489 Berlin, Germany*
** e-mail: iunin@issp.ac.ru*
Received June 25, 2001

Abstract—The method of intermittent pulse loading is used for obtaining the dependences of the mean free path of individual dislocations in SiGe single crystals with various concentration of Ge (0–5.5 at. %) on the duration of loading pulses and time intervals between them. It is found that these dependences change qualitatively upon an increase in the Ge concentration. It is shown that the motion of dislocations in SiGe crystals under small shear stresses is characterized by a nonlinear drift of kinks and the formation of superkinks. A theory of the motion of dislocations under the action of intermittent pulse loading under the conditions of heterogeneous kink dynamics is developed. Extended quasi-one-dimensional defects repeating the shape of a part of a segment of a moving dislocation are discovered in SiGe crystals containing 0.96 at. % Ge. The mechanism of formation of such defects as the result of the shedding of a part of the impurity atmosphere by a dislocation segment during overcoming of a local obstacle is proposed. © *2002 MAIK "Nauka/Interperiodica".*

1. INTRODUCTION

The Peierls relief, i.e., a periodic dependence of the energy of a dislocation on its position in the slip plane, is a direct consequence of the translational symmetry of the crystal lattice. It is manifested most clearly in crystals with covalent bonds (diamond, Si, Ge, and their alloys). It is generally assumed that the motion of dislocations in the Peierls relief occurs through thermal-fluctuation-induced formation of pairs of kinks and their subsequent expansion to the ends of a dislocation segment or until annihilation with opposite-polarity kinks from adjacent pairs on a dislocation line [1, 2]. Kinks are short segments of a dislocation, connecting dislocation segments in adjacent valleys of the relief. The Peierls mechanism of the motion of dislocations has been generally accepted for crystals with a deep relief. Moreover, the existence of kinks has been confirmed recently by direct observations in a high-resolution electron microscope [3–5].

An analysis of experimental results on the dynamics of dislocations and kinks in silicon and germanium [6, 7] having identical crystalline structures proved that a number of serious discrepancies with the predictions of the theory of motion of dislocations in an ideal Peierls relief [1, 2] are observed even in high-purity semiconducting crystals. It was found that the discrepancies observed in Si crystals in the region of small shear stresses are due to the entraining of mobile point defects and impurities by a dislocation [6, 8]. As the concentration of point defects in the vicinity of a dislocation attains a certain critical value, the dislocation mobility decreases abruptly down to its complete arrest (starting stresses for the motion of the dislocation). In weakly doped Ge crystals for which the starting stresses for the motion of a dislocation are not revealed, the discrepancies with the theory of motion of a dislocation in an ideal Peierls relief are due to the interaction between the dislocation and the surrounding point defects and impurities which determine the barriers for the motion of a kink, which are distributed at random along the dislocation [7, 9].

Thus, the nucleation and motion of dislocation kinks determine the mobility of dislocations in semiconducting materials. However, the dynamics of these topological excitations in systems with a random disorder has not been adequately investigated experimentally. Such investigations are especially important in view of the possibility of the emergence of anomalous modes in the motion of kinks in such systems. It was proved earlier [10, 11] (see also the review in [12]) that, in the presence of a considerable amount of impurities, an excitation of the crystal lattice may result in the change from the conventional kink dynamics to the so-called heterogeneous mode. This phenomenon is of a general nature and must be manifested not only for dislocation kinks, but also for other topological defects (twin and domain boundaries, interfaces, etc.). The change of the mode occurs when the driving force F for a kink becomes smaller than a certain critical value F_c determined by the extent of disorder created by defects. The new type of the dynamics is characterized by a nonlinear drift, in which the displacement of a kink with time satisfies the equation

$$x \approx x_0\left(\frac{t}{t_0}\right)^{\delta}, \quad \delta = \frac{F}{F_c} \leq 1, \tag{1}$$

where $x_0 = kT/F_c$, $t_0 = x_0^2/2D_k$, D_k is the diffusion coefficient for the kink, k is Boltzmann's constant, and T is the temperature.

In SiGe crystals, Ge atoms are distributed at random and can be regarded as a low-mobility neutral substitutional impurity in a Si crystal, which, together with mobile impurities, is responsible for a random modulation of the Peierls relief. This work is devoted to the experimental investigation of the effect of this modulation on the formation and motion of dislocation kinks.

2. EXPERIMENTAL TECHNIQUE

Single crystals of the $Si_{1-y}Ge_y$ ($0 \le y \le 0.15$) alloy having a diameter up to 42 mm were grown by the Czochralski method at the Institut für Kristallzüchtung in Berlin (Germany) [13]. The ingots were characterized by a small Ge concentration gradient in the direction of the growth axis [111], were weakly doped with phosphorus or boron with a concentration of the order of 10^{15} cm^{-3}, and contained oxygen with an approximate concentration of 6×10^{17} cm^{-3}.

The samples of SiGe in the form of right-angle prisms with edges oriented along the $[1\bar{1}0]$, $[11\bar{2}]$, and [111] axes, having a size of $35 \times 4 \times 1.5$ mm and a Ge concentration up to 5.5 at. %, were cut from a part of the ingots free of dislocations and subjected to mechanical and chemical polishing. The Ge concentration was determined from the position of the *TO* phonon line [14].

Individual dislocation half-loops were introduced by indentation of the broad (111) sides of the sample with a diamond pyramid at room temperature, followed by loading at 873 K through four-point bending about the $[11\bar{2}]$ axis. The dislocations introduced in this way were "dispersed" to a diameter of 200–220 μm by a reduced shear stress of 30 MPa. It should be noted that in the given geometry, dislocation half-loops are generated and slide in the $(1\bar{1}1)$ and $(\bar{1}11)$ planes, while the segments emerging at the (111) surface can have only the 60° orientation (a priori 60° side) on one side of the indents and both 60° and screw orientation (hybrid side) on the other side [15].

Considerable starting stresses σ_s for the motion of dislocations in SiGe samples were detected earlier [16]; the magnitude of these stresses depends on the state of the dislocation atmosphere of point defects [17, 18]. The reproducibility of the results requires that similar conditions of the atmosphere state be created. For this purpose, before each loading, dislocations were "dispersed" for 10–15 min under the action of shear stresses $\sigma = 30$ MPa at temperature $T = 873$ K. Then the sample was slowly cooled with the furnace and the positions of dislocations were revealed by selective chemical etching in the Sirtl etchant $1CrO_3 + 2H_2O + 3HF$ [19]. Immediately before the main loading, a short-term (120 s) preliminary loading by a shear stress of 50 MPa was carried out, which made it possible to reduce the starting stresses considerably and to study the kink dynamics under small stresses. The geometry of traces behind dislocations was determined and studied by removing the material layer by layer in the polishing solution $7HNO_3 + 1HF$ and by selective chemical etching.

The dynamics of kinks on 60° dislocations was studied by the method of intermittent pulse loading (IPL) [6, 7], which is based on the loading of a sample containing individual dislocations by a sequence of stress pulses σ_i. The duration t_i of an individual pulse is comparable with the mean time of the displacement of a dislocation through a crystal lattice parameter, $t_a = a/V_{st}$, where V_{st} is the velocity of the steady motion of the dislocation under conventional static loading. Pulses are separated by pauses of duration t_p, during which no stress is applied ($\sigma_p = 0$). During a loading pulse, new pairs of kinks are formed on the dislocation and propagate in addition to equilibrium kinks. During a pause, when the pulse load is removed, these kinks become nonequilibrium and collapse to the nucleation centers under the action of the applied stress, mutual attraction of pairs, and due to the interaction of the dislocation and the kink with point defects. It will be shown in Subsection 3.2 that information on the kinetics of the formation of kink pairs and their expansion and relaxation can be obtained by varying the duration of pulses and pauses and by measuring the characteristics of the path length distribution of dislocations.

The samples were deformed through four-point bending by a series of load pulses produced by an electromagnetic transducer with a shear stress amplitude $\sigma_i = 15$ MPa. The total duration $\sum t_i$ of active loading was maintained at a constant level and was chosen equal to the time of static loading under which dislocations were displaced over distances of 40–50 μm. The duration of the loading pulse leading edge was kept unchanged (4 ms). The temperature was measured by a thermocouple and maintained constant to within ±1 K. In order to determine the temporal characteristics of the formation of a pair of kinks and their drift, we measured the dependences of the mean paths of 60° dislocations both on the pulse duration, $l(t_i)$ (for $t_i = t_p$), and on the pause duration, $l(t_p)$, for a fixed duration of load pulses.

3. RESULTS AND DISCUSSION

3.1. Mobility of Individual Dislocations and Kink Dynamics

Figure 1 shows the dependences of the velocity of individual 60° dislocations on shear stresses in SiGe single crystals with various Ge concentrations. It can be seen that the three dependences differ insignificantly in the range of high stresses. On the contrary, the difference between the curves corresponding to different Ge

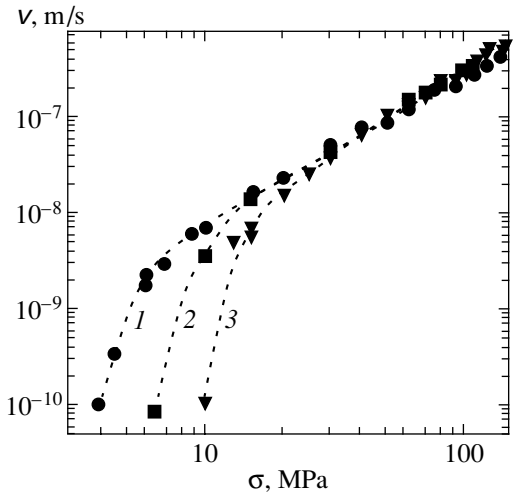

Fig. 1. Dependence of the velocity of individual 60° dislocations in $Si_{1-y}Ge_y$ crystals on the shear stress; $y = 0.02$ (*1*), 0.033 (*2*), and 0.055 (*3*); $T = 873$ K.

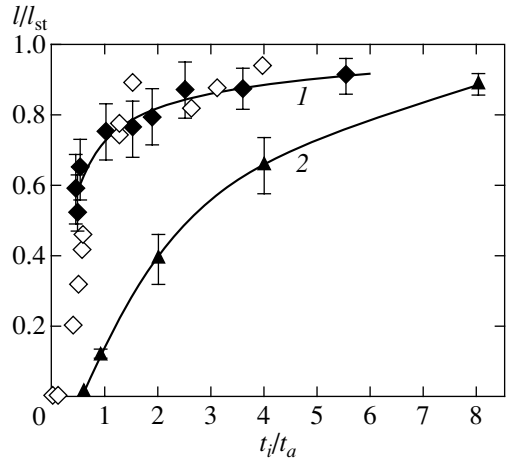

Fig. 2. Mean free paths of individual 60° dislocations under the IPL in Si (*1*) and $Si_{1-y}Ge_y$ ($y = 0.048$) (*2*) as functions of the duration of load pulses ($t_p = t_i$). The paths are normalized to the mean free path value under static loading, $\sigma_i = 15$ MPa, $T = 873$ K. Light rhombi correspond to the results obtained on Si samples grown by float zone technique for $\sigma_i = 7$ MPa, $T = 873$ K [6].

concentrations in the region of small shear stresses becomes considerable (dashed curves in Fig. 1).

In order to study the kinetics of kinks on the dislocation line by the method of intermittent pulse loading, we measured the dependence of the mean path of dislocations on the duration of loading pulses for Si and SiGe samples (Fig. 2). It can be seen that with increasing pulse duration, the dislocation path lengths increase both in Si and in SiGe. However, the rates of this increase differ considerably. In silicon, path lengths of dislocations increase sharply for $t_i/t_a \approx 0.5$ in analogy with the situation observed in silicon samples grown by the float zone technique [6] (light rhombi). The curve obtained for SiGe samples slopes more gently; i.e., the mean path lengths of dislocations in SiGe samples attain values on the order of the steady-state path length for much larger relative durations of a pulse ($\sim 10t_a$) than in Si samples ($\sim t_a$).

It was proved by us earlier [6] that such a long time of attainment of saturation for the dislocation velocity is associated with the accumulation of kinks on the dislocation line and the formation of superkinks. Superkinks are formed in the presence of sufficiently high barriers for the motion of kinks, when the time required by a kink to move over an obstacle is longer than the time of formation of a new pair of kinks. In the theory, two types of obstacles for the motion of a kink were considered. The first type is formed by structural defects of the dislocation core or defects located in the immediate vicinity of the core: dislocation jogs, clusters of impurity atoms, etc. [20, 21]. The second type is associated with fluctuations in the density of point defects along the dislocation line, which determine the localization of a kink in the random force field [10].

The kink dynamics is determined to a considerable extent by the dominating type of obstacles. We analyzed the kink dynamics with the help of experiments in which the mean path length of dislocations in SiGe samples with different Ge concentrations was studied as a function of the duration of pauses between loading pulses (Fig. 3). It can be seen that the curves differ qualitatively. The samples with Si concentration of 2 at. % (curve *1*) are characterized by an *S*-shaped curve with a point of inflection. Similar curves were observed for Si crystals grown by zone melting [6]. A model providing a qualitative explanation of such dependences as the result of entrainment and redistribution of mobile point defects by a moving dislocation completely immobilized during long "pauses" was proposed in [8].

The crystals with Ge concentrations of 3.3 and 5.5 at. % (curves *2* and *3* in Fig. 3) display a monotonic decrease in dislocation path lengths upon an increase in the duration of "pauses" in analogy with the behavior of Ge crystals [9]. However, a stress of the opposite polarity had to be applied during pauses for a similar decrease in Ge samples.

Let us compare these dependences with the model taking into account only the change in the kink energy in the field of a point defect [20, 21]. This model determines the linear drift of a kink under the action of the applied force.

In accordance with the theory, there exists a thermodynamically equilibrium density of kinks on a dislocation even in the absence of shear stresses. The application of a load causes a drift of kinks, which must result in the motion of the dislocation even for an indefinitely large duration of pauses. Such thermal kinks determine a certain minimum (but not zero) value of the disloca-

tion velocity under the IPL conditions in the absence of additional loading during pauses [22]:

$$V_{\min} \approx \exp\left[-\frac{(\alpha a b \sigma_i)^{1/2}}{kT}\right] V_{st},$$

where α is the elastic interaction constant for kinks and b is the Burgers vector for the dislocation. Under the experimental conditions, $V_{\min}$ was approximately equal to $V_{st}/2$. However, its value obtained in our experiments was smaller by more than an order of magnitude.

In accordance with the theory [23], the nonequilibrium kinks generated during stress pulses lead to the following contribution to the path lengths of dislocations, which decrease linearly upon an increase in the duration of pauses under the IPL conditions:

$$\frac{l}{l_{st}} = 1 - \frac{|v_p|}{v_i}\frac{t_p}{t_i}, \quad (2)$$

where $v_{i,p}$ are the velocities of kinks during an pulse and during a pause. This prediction does not match the obtained experimental results. Curve *3* in Fig. 3 is obviously nonlinear and contradicts Eq. (2) even qualitatively. At first glance, curve *2* can be described approximately by a linear equation. It can be seen from the behavior of curve *2* that complete relaxation of kinks occurs during the time $t_p \approx t_i$. The agreement with the experimental results could be reached only for

$$\frac{|v_p|}{v_i} \approx 1.$$

To this end, it is necessary that the virtually identical forces act on kinks during load pulses and pauses. However, in the experiment under investigation, no external forces were applied during pauses, while internal stresses associated with the long-range elastic interaction of kinks in a pair [1] are too small according to simple estimates.

Thus, our experimental results on the motion of dislocations under the action of intermittent pulse loading in SiGe crystals cannot be described in the model for the motion of kinks in a random potential. We must take into account the nonuniformity in the distribution of impurities between adjacent grooves of the Peierls relief. This nonuniformity is determined by the redistribution and accumulation of point defects in the vicinity of the dislocation core, which are responsible for an additional decrease in the dislocation energy. This creates a force returning kinks to their nucleation centers and determines the emergence of starting stresses for the motion of dislocations [24]:

$$\sigma_s = (c_1 - c_2)\frac{u}{ab}. \quad (3)$$

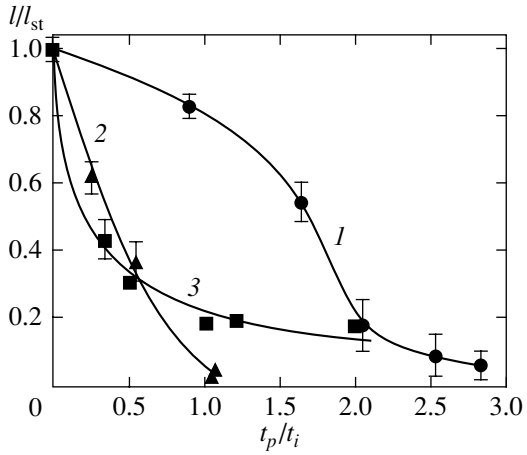

Fig. 3. Mean free paths of individual 60° dislocations in $Si_{1-y}Ge_y$ under the IPL as functions of the relative duration of "pauses" between pulses: y = 0.02 (*1*), 0.033 (*2*), and 0.055 (*3*); $t_i = 0.8t_a$, σ_i = 15 MPa; T = 873 K.

Here, $c_{1,2}$ are the concentrations of point defects in adjacent grooves of the potential relief, and u is the energy of the short-range interaction of the dislocation with a point defect.

It was mentioned above that in this approximation, the perturbation of the potential relief by point defects (including randomly distributed Ge atoms) changes the kink dynamics. Under certain conditions, the motion of kinks can be characterized by a qualitatively different type of kinetic mechanisms, viz., the so-called heterogeneous dynamics with the nonlinear drift (1) for $\sigma < \sigma_c$,

$$\sigma_c \approx \sigma_0 + \sigma_s, \quad (4)$$

$$\sigma_0 = (c_1 + c_2)\frac{u^2}{2kTab}. \quad (5)$$

For stresses $\sigma > \sigma_c$ not very close to the threshold, the velocity of a kink in the field of a random force can be described by the formula [11, 12, 25]

$$v_k = \frac{D_k}{kT}(\sigma - \sigma_c)ab, \quad (6)$$

where σ assumes the values of σ_s during "pauses" and $\sigma_i - \sigma_s$ during load pulses. If, however, we estimate the parameter $\delta = \sigma/\sigma_c$ (see Eq. (1)), it follows from Eq. (4) that, in our experiments, δ is always smaller than unity during "pauses" and, hence, the model of linear drift (2) is also inapplicable in the approximation of the modified kink velocity (6). Thus, we must consider the mode of nonlinear drift of kinks. The model dealing with this mode will be described in the next subsection.

3.2. Motion of a Dislocation under the Action of Intermittent Pulse Loading under the Conditions of Heterogeneous Kink Dynamics: Model and Comparison with Experiment

Let us briefly describe some concepts of the heterogeneous kink dynamics that are required for describing the experimental results considered above. A transition to the heterogeneous dynamics is connected with the existence of a broad spectrum $P(\tau)$ of the kink delay τ at the obstacles created by the density fluctuations of defects. The transition takes place when the kink drag at a single most intense barrier within the mean free path becomes dominating over the kink retardation by many typical average-intensity barriers. This can be illustrated by the following simple consideration [10].

Let $P(\tau)$ (the probability of encountering a barrier with a delay time longer than τ),

$$P(\tau) = \int_{\tau}^{\infty} p(t)dt,$$

where $p(t)$ is the probability density, decrease for large values of time as $1/\tau^{\delta}$. In this case, the mean time of overcoming the barrier,

$$\langle \tau \rangle = \int_{0}^{\infty} \tau p(\tau)d\tau = \int_{0}^{\infty} P(\tau)d\tau,$$

is finite for $\delta > 1$ and diverges for $\delta \le 1$. Thus, for $F \le F_c$, where F_c corresponds to the value of δ equal to unity in Eq. (1), $\langle \tau \rangle \longrightarrow \infty$ and the mean velocity of kinks becomes zero.

Under these conditions, the time required for traversing a certain segment of the path is determined by the most intense barrier in it. The probability of encountering a barrier with a delay longer than t over the path length x can be estimated as $(x/\Delta l)P(t)$, where Δl is the average barrier width and $x/\Delta l$ is the number of independent positions. As a rule, the highest and, hence, the most uncommon barrier existing over the length l satisfies the following condition:

$$\frac{x}{\Delta l}P(x) \approx 1.$$

This relation leads to the following nonlinear dependence of displacement x on time t (cf. formula (1)):

$$x \approx \frac{\Delta l}{P(t)} \propto t^{\delta}.$$

It should be emphasized that this kinetic law is not determinate and it is more appropriate to use its probabilistic interpretation in which x is generally a random quantity with a mean value equal to the average distance $\langle x \rangle \approx \Delta l/P(t)$ between the corresponding barriers.

Although the motion of a kink under the heterogeneous conditions cannot be described by the average velocity (which is equal to zero), the dislocation preserves, a finite mobility and its velocity can be estimated on the basis of the following considerations. We denote by J_0 the rate of formation of kink pairs per unit time per unit dislocation length under the action of a constant stress. The number density of kinks generated by the instant t is $J_0 t$ and the mean distance between the kinks is $1/J_0 t$. The average displacement of kinks over this time interval is

$$x \approx x_0\left(\frac{t}{t_0}\right)^{\delta}.$$

When this displacement becomes equal to the mean distance between the kinks, the process of their coalescence begins, and the dislocation passes to the next valley of the Peierls relief. Thus, the duration t_a of the transition is determined by the equation

$$\frac{1}{J_0 t} = x_0\left(\frac{t}{t_0}\right)^{\delta}, \tag{7}$$

leading to the following expression:

$$t_a = \frac{t_0}{(J_0 t_0 x_0)^{1/(1+\delta)}}.$$

Hence, the velocity of the steady motion of the dislocation is given by

$$V = \frac{a}{t_a} = \frac{a}{t_0}(J_0 t_0 x_0)^{1/(1+\delta)}. \tag{8}$$

The intermittent pulse loading is the most suitable method for experimental investigation of nonlinear modes of motion of a kink. It was proved in [16] that the motion of dislocation kinks in SiGe in the stress range under investigation has the form of a nonlinear drift both in the "forward" direction under pulse loading and in the "backward" direction during "pauses." In both cases, the displacements of a kink are described by the kinetic law (1), but with different exponents δ_i and δ_p due to different magnitudes of the forces acting on the kink: $F_{i,p} = \sigma_{i,p} ab$. It should be noted that the barriers for the forward and backward movements of the kink are formed by fluctuations of different polarities. For this reason, these barriers are not correlated with one another (the barrier for the forward motion does not play any significant role in the backward motion, and vice versa).

In contrast to the steady-state mode of motion, a new possibility to return during the "pause" to the nucleation center and to annihilate with its "partner" appears for a newly born kink in the case of intermittent loading. Consequently, we must take into account only the kinks remaining after the complete loading cycle "loading pulse + pause." At the stage of kink movement, we must take into account the possibility of returning to the initial position in front of a barrier during the pause for kinks which surmounted the barrier during the preceding pulse, as well as a decrease in the

effective frequency of attempts to overcome the barrier due to the backward motion of a kink from the barrier during the preceding "pause." The inclusion of these corrections (see the Appendix) makes it possible to derive the following expression for the dislocation path lengths under intermittent pulse loading:

$$\frac{l}{l_{st}} = (I_1 I_2^{\delta_i})^{1/(1+\delta_i)}, \quad (9)$$

where

$$I_1 = \int_0^1 dt \frac{t^{2\delta_i}(t^{\delta_i} + 3x_p/x_i)}{(t^{\delta_i} + x_p/x_i)^3}, \quad (10)$$

$$I_2 = \int_0^1 dt \frac{t^{\delta_i}(1-t)^{\delta_i}}{(x_p/x_i + t^{\delta_i})[x_p/x_i + (1-t)^{\delta_i}]}, \quad (11)$$

$x_i \equiv x_i(t_i)$, and x_p is the mean distance between the barriers for backward motion with the surmounting time longer than the duration t_p of the pause ($x_{i,p}(t) \equiv x_0(t/t_0)^{\delta_{i,p}}$).

Let us now compare the experimental results (curve *3* in Fig. 3) with the theory. According to the theory developed by Hirth and Lothe [1], the velocity of the steady motion of a dislocation with a linear drift of kinks can be expressed as follows in terms of the kink concentration c_k and the kink velocity v_k (6): $V = ac_k v_k$. It was proved in [1] that the kink concentration in the region of low stresses is independent of the stress. Thus, the dependence of the velocity of the dislocation on the stress for $\sigma > \sigma_c$ has the form

$$V = c_k \frac{D_k}{kT}(\sigma - \sigma_c)a^2 b. \quad (12)$$

In the region below the threshold ($\sigma < \sigma_c$), the stress dependence of V is nonlinear and is defined by formula (8).

In order to estimate the critical shear stress $\sigma_c = F_c/ab$, for which the mean velocity of a kink vanishes, we plot the dependence of the mean velocity of a dislocation on the shear stress. Figure 4 shows the $V(\sigma)$ dependence for SiGe samples with the Ge concentration of 5.5 at. % in linear coordinates. It can be seen that for stresses 30–70 MPa, the experimental results are correctly described by a linear dependence of the form (12) with $\sigma_c = 17.68$ MPa. Using this value and choosing t_0 and x_0 as fitting parameters, we calculated dependence (9). The solid curve in Fig. 5 presents the results of fitting. It can be seen that the results of calculations are in good agreement with the experimental data obtained for the following values of the parameters: $t_0 = 8.25$ ms and $x_0 = 22b$.

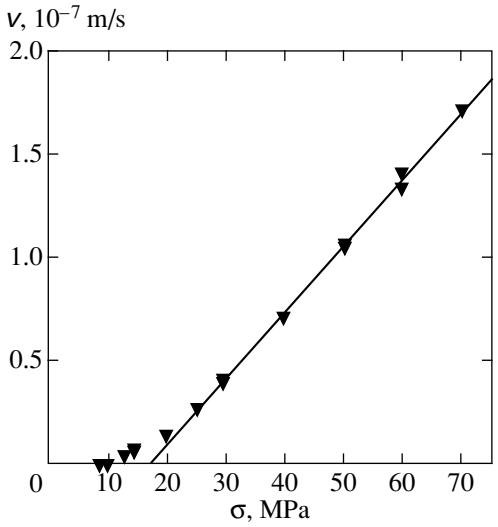

Fig. 4. Velocity of 60° dislocations as a function of stress in $Si_{1-y}Ge_y$ ($y = 0.055$) (curve *3* in Fig. 1) plotted in linear coordinates.

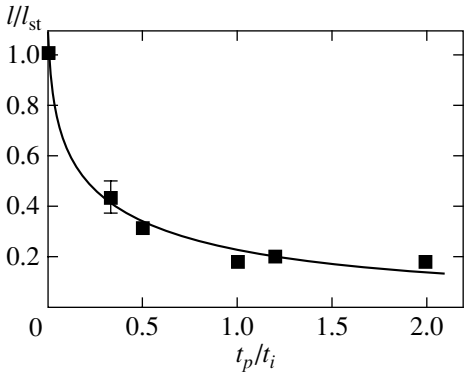

Fig. 5. Comparison of the experimental data presented in Fig. 3 (curve *3*) with the results of calculations based on the model (9)–(11) (solid curve).

Using these values, we can estimate the diffusion coefficient for a kink from the relation

$$D_k \approx \frac{x_0^2}{2t_0} = 2.29 \times 10^{-15} \text{ m}^2/\text{s} \quad (13)$$

and the activation energy from

$$W_m = kT \ln\left(\frac{\nu_D b^2}{D_k}\right) \approx 1.55 \text{ eV}. \quad (14)$$

This value is quite close to the estimate obtained for the energy of kink migration on dislocations in pure silicon [6].

An analysis of the results obtained for a SiGe sample with an intermediate Ge concentration of 3.3 at. % (curve *2* in Fig. 3) revealed that, in the framework of model (9), a satisfactory description of experimental results cannot be obtained. Apparently, a more complex

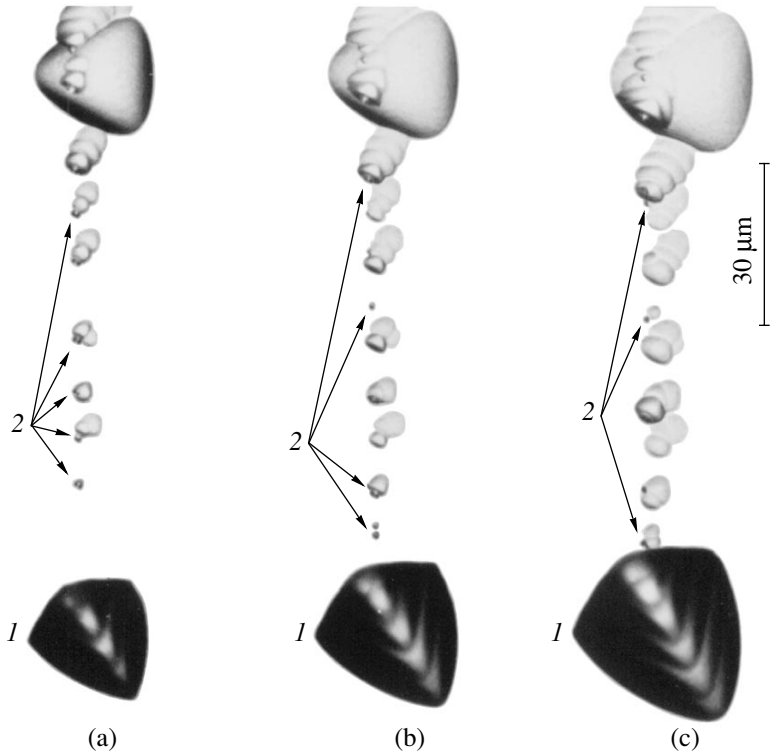

Fig. 6. The (111) surface of a $Si_{1-y}Ge_y$ sample (y = 0.0096) upon gradual removal of material layers by chemical polishing and selective chemical etching: removed layer thickness is 7.5 (a), 10.7 (b), and 13.5 μm (c); dislocation etch pits (*1*) and traces behind dislocations (*2*).

model taking into account the nonuniformity of the point defect distribution along the dislocation line (retardation of kinks in the field of a random force) as well as the defect concentration gradient across the dislocation (entrainment of mobile impurities by the moving dislocation) is required for describing this dependence. The development of such a model requires a separate analysis.

Thus, the qualitative change in the shape of the curves in Fig. 3 upon an increase in the Ge concentration indicates a gradual change in the mechanism controlling the kink dynamics from the avalanche-like entrainment of impurities with the immobilization of dislocations (in the case of pure Si) to the quasi-static effect of impurities with a clearly manifested nonlinear drift of kinks in the case of Ge.

3.3. Traces of Dislocations in SiGe Crystals

One of numerous manifestations of the interaction between a dislocation and point defects is the revelation of various types of traces left by moving dislocations on the etched surfaces of various materials [26–30]. In this work, we observed traces in the form of randomly distributed flat-bottomed etch pits on the line of intersection of the swept part of the dislocation slip plane and the surface of observation, which are left by individual dislocations moving under the action of stresses varying from 20 to 35 MPa in SiGe samples containing 0.96 at. % Ge at 873 K after selective etching. The size of pit traces was noticeably smaller than the size of dislocation etch pits (Fig. 6).

It should be noted that, in contrast to the traces observed earlier [28– 30], the traces in our samples were revealed only after the removal of the surface layer of thickness 3–4 μm. The layer-by-layer removal of the material and etching showed that the traces located closer to the initial position of a dislocation are revealed first (Fig. 6a). The subsequent removal of layers revealed new traces located closer to the final position of the dislocation in addition to the traces observed earlier (Fig. 6b). Some of the latter traces remained noncorroded. The maximum number of pits in a chain was revealed after the removal of a layer 10–15 μm thick. The number of etching pits decreased upon subsequent polishing (Fig. 6c). After the complete removal of the dislocation half-loop, traces were not etched either.

It was also found that traces are revealed only behind definite types of dislocations. On the sample surface where compressive stresses were acting, chains of traces were etched only on the mixed side (both behind screw dislocations and 60° dislocations), while, on the stretched surface, traces appeared only on the 60° side.

An analysis of the change in the position of etch pits upon the removal of layers shows that they have the form of extended quasi-one-dimensional defects similar to those observed in [28]. These defects lie in the dislocation slip plane, but are oriented parallel to the dislocation segment located at the opposite end of the half-loop rather than to the segment generating them.

After the repeated movement of dislocations under the same conditions, it was found that the position of the traces revealed after the first loading remained unchanged. It should be noted that etching of the freshly swept part of the slip plane revealed traces only after the removal of a surface layer of thickness 10–12 μm as in the case of the first loading. In this case also, the pits located closer to the initial position of the dislocation are revealed first. The maximum number of traces in a chain was now revealed after the removal of a layer 20–25 μm thick.

Subsequent loading showed that, in each next loading, the depth at which traces start being revealed increases, while the number of etch pits in the chain decreases. When the overall time of sample deformation exceeds 1.5 h, no traces are revealed. In this case, the time during which the samples are kept in the furnace at temperatures of 723–873 K (including the time of extraction, temperature stabilization, and cooling with the surface) amounts approximately to 5.5 h. No traces behind dislocations introduced into a sample annealed preliminarily for 3 h at 873 K were revealed either.

What is the origin of the traces revealed in SiGe crystals? The traces in the form of etch pits [27] observed earlier in alkali-halide crystals were interpreted as the result of etching of dislocation dipoles appearing upon cross slip. However, dipoles are formed in silicon (in fact, the samples under investigation were made of strongly alloyed silicon) only as a result of a considerable plastic deformation at temperatures 200–300 degrees higher than the temperature used in our experiments [26].

Another possible reason for the emergence of a chain of etch pits is the multiplication of dislocations upon overcoming local obstacles. However, the stresses and temperature used in our experiments are too low for the multiplication of dislocations. In addition, the size of etch pits in the traces was considerably smaller than for the dislocation etch pits, and their position remained unchanged after repeated loading.

In this connection, it was proposed that the reason for the emergence of traces behind dislocations lies in the shedding of a part of the point defect atmosphere by a dislocation. It was shown in [28] that, under certain conditions (upon a change in the direction of motion or a sharp increase in the velocity), a dislocation may shed a part of its impurity atmosphere. In the regions of such a shedding, flat-bottomed triangular pits were revealed using selective chemical etching.

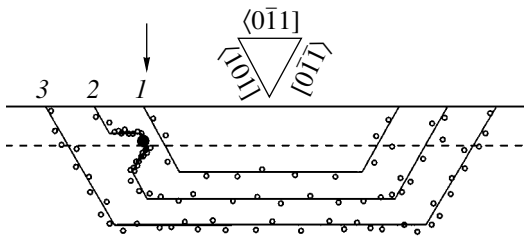

Fig. 7. Diagram of the formation of one-dimensional defects in the course of the formation of superkinks on a dislocation segment (broken line) while overcoming a local obstacle (filled circle). Numbers *1, 2,* and *3* mark successive positions of the dislocation loop; light circles are point defects; the horizontal dashed line indicates the depth at which a trace starts being revealed; the arrow marks the position of the trace.

The nonuniform distribution of pits suggests that atmosphere shedding occurs as a result of overcoming of randomly distributed obstacles by a dislocation. Figure 7 shows the possible scheme of such a process. When a dislocation encounters a local barrier, its parts located at large distances from the obstacle continue their motion, leading to the accumulation of kinks in the obstacle region and to the formation of superkinks. After the surmounting of the barrier, superkinks that were formerly at rest start moving, shedding a part of the point defect atmosphere. Since one of the superkinks is parallel to the surface of observation, the trace left behind it can hardly be revealed by selective chemical etching. However, another superkink directed along $[0\bar{1}\bar{1}]$ leaves the trace sought. The emergence of traces only in a certain range of shear stresses confirms this hypothesis: the formation of superkinks becomes disadvantageous from the energy point of view for low shear stresses, while, for high stresses, the dislocation overcomes the local barrier in a forced manner without the formation of superkinks.

The fact that no traces are revealed after the annealing of crystals shows that the obstacles for the motion of a dislocation are readily annealed. This is indirect proof of the fact that local barriers are clusters of point defects. A gradual increase in the depth starting from which traces start being revealed can be explained by the annealing of clusters and by the emergence of point defects at the sample surface. SiGe samples with 0.96 at. % Ge were cut from the initial part of the ingot in the vicinity of the seed. Since no traces were revealed in the samples with a higher Ge concentration, which were cut from parts of the ingot separated from the seed by longer distances, we can assume that the reason for the emergence of point defect clusters is supersaturation of the initial part of the ingot with point defects in the process of crystal growth.

4. CONCLUSIONS

It has been established that the disorder introduced by Ge atoms leads to the formation of superkinks on the dislocation line during the motion of the dislocation under the action of stresses ≤30 MPa. It is shown that an increase in the Ge concentration in SiGe leads to a gradual change of the mechanism controlling the kink dynamics from the avalanche-like entrainment of impurities accompanied by immobilization of dislocations to the quasistatic effect of impurities with a clearly manifested nonlinear drift of kinks. Traces in the form of chains of etch pits revealed in SiGe samples containing 0.96 at. % Ge are probably associated with the formation of superkinks at point defect clusters.

ACKNOWLEDGMENTS

This work was supported financially by the INTAS (grant no. 96-363).

APPENDIX

Let us describe the expected regularities in the motion of dislocations with a nonlinear drift of kinks under loading by pulses of amplitude σ_i separated by "pauses" during which a stress σ_p of the opposite sign (or equal to zero) is applied. Two main stages can be singled out in this process: the formation of kink pairs and their propagation until the recombination with kinks from neighboring pairs. Let us first consider the stage of formation of a kink pair. It was mentioned above that the number of kinks generated per unit length of a dislocation during any time interval dt under the action of a constant stress is equal to $J_0 dt$. In the case of intermittent loading, a new possibility appears to return to the nucleation center and to annihilate with its "partner" during a "pause." Consequently, we must take into account only the kinks remaining after a complete loading cycle. Let us calculate the number of such kinks.

Assuming the independence of fluctuations in the density of defects creating various solitary barriers, we will describe their spatial separation with the help of the Poisson distribution with the mean density $n = P(t)/\Delta l$. Although such an interpretation is not quite accurate and a more correct description can be obtained on the basis of Levi's laws (see, for example, [12, 31, 32]), we will use this interpretation owing to its simplicity and evidence. Among other things, it provides a simple description of the distribution of separations between the barriers. For example, the probability that a kink does not encounter a barrier over a distance x is $\exp(-nx)$, while the probability that a next barrier is encountered at a distance from the previous barrier in the interval between x and $x + dx$ is $\exp(-nx)ndx$.

The probability that a kink generated at instant t' after the beginning of a loading pulse is separated from the site of its birth by a distance in the interval from x_1 to $x_1 + dx_1$ by the end of an pulse of duration t_i is given by

$$\exp\left[-\frac{x_1}{x_i(t_i - t')}\right]\frac{dx_1}{x_i(t_i - t')}.$$

Here, $x_i(t)$ is the mean distance between the barriers with a surmounting time longer than t,

$$x_i(t) \approx x_0\left(\frac{t}{t_0}\right)^{\delta_i}.$$

Similarly, the probability that the second kink in the pair moves through a distance in the interval from x_2 to $x_2 + dx_2$ is

$$\exp\left[-\frac{x_2}{x_i(t_i - t')}\right]\frac{dx_2}{x_i(t_i - t')}.$$

The probability density $p_r(x)$ for the kink of a pair to be separated from each other by a distance x is given by

$$\begin{aligned} p_r(x) &= \int_0^\infty\int_0^\infty \frac{dx_1}{x_i(t_i - t')}\exp\left[-\frac{x_1}{x_i(t_i - t')}\right] \\ &\times \frac{dx_2}{x_i(t_i - t')}\exp\left[-\frac{x_2}{x_i(t_i - t')}\right]\delta(x_1 + x_2 - x) \\ &= \frac{x}{x_i^2(t_i - t')}\exp\left[-\frac{x}{x_i(t_i - t')}\right]. \end{aligned} \tag{15}$$

Then, the probability $P_r(x)$ that a pair of kinks does not annihilate during a pause is equal to the probability that the total path length traversed by the kinks during the "pause" is smaller than x. Since the probability density that the kinks in the pair are characterized by the relative path length x' during a "pause" is equal to $(x'/x_p^2)\exp(-x'/x_p)$ (in analogy with formula (15), where x_i is replaced by x_p), we have

$$\begin{aligned} P_r(x) &= \int_0^x \frac{x'}{x_p^2}\exp\left(-\frac{x'}{x_p}\right)dx' \\ &= 1 - \left(\frac{x}{x_p} + 1\right)\exp\left(-\frac{x}{x_p}\right). \end{aligned} \tag{16}$$

Integrating the product of probabilities (15) and (16) with respect to all possible values of x from 0 to ∞, we obtain the fraction of kinks that survived after the "pause":

$$\begin{aligned} \nu(t') &= \int_0^\infty \frac{x\,dx}{x_i^2(t_i - t')}\exp\left[-\frac{x}{x_i(t_i - t')}\right]P_r(x) \\ &= \frac{x_i^2(t_i - t')[x_i(t_i - t') + 3x_p]}{[x_p + x_i(t_i - t')]^3}. \end{aligned}$$

Consequently, the total number ΔN of kinks generated during a loading cycle is

$$\Delta N = J_0 \int_0^{t_i} dt' \nu(t') = J_0 t_i I_1, \quad (17)$$

where I_1 is defined by formula (10).

Thus, the "pauses" between pulses lead to the transformation of the frequency J_0 of generation of kink pairs under static loading into the "effective" frequency $J_0 I_1$.

Let us now consider the stage of propagation of a kink during a loading pulse. It should be recalled that, in the approximation we are dealing with, the displacement of a kink during a loading pulse is mainly determined by the distance to a strong barrier (which is referred to as the principal barrier) with a given surmounting time τ. If, however, the fraction of kinks surmounting the barrier during the time dt' is equal to dt'/τ, the presence of "pauses" in pulse loading introduces two corrections.

The first correction is the possibility for the kinks that have surmounted a barrier during an pulse to return to their initial position in front of the barrier during the next "pause." The probability that a kink surmounting a barrier at instant t' is found at a distance x from the barrier (in the interval from x and $x + dx$) is

$$\exp\left(-\frac{x}{x_i(t_i - t')}\right)\frac{dx}{x_i(t_i - t')}.$$

The probability that the kink does not return to the initial position is equal to the probability of the presence on the length x of a barrier with the surmounting time longer than t_p, i.e., $1 - \exp(-x/x_0)$. Integrating the product of these two probabilities over all possible values of x, we obtain the fraction of kinks surmounting the barrier during a complete cycle,

$$\frac{x_i(t_i - t')}{x_p + x_i(t_i - t')},$$

which renormalizes dt'/τ.

The second correction is due to a decrease in the effective frequency of attempts at surmounting a barrier due to the backward motion of a kink from the barrier during the previous "pause." Under the action of a constant stress, a kink is permanently pressed against the barrier, while, under the conditions of intermittent loading, a kink regresses during "pauses." Its return to the barrier takes a certain time after the beginning of a loading pulse, and a shorter time is left for surmounting the barrier.

The probability of the regress to a distance lying in the interval between x' and $x' + dx'$ is

$$\exp\left(-\frac{x'}{x_p}\right)\frac{dx'}{x_p}.$$

The probability that a kink returns to the barrier by instant t' after the beginning of an pulse is $\exp(-x'/x_i(t'))$. The integration of the product of these two probabilities over all possible values of x' gives the additional factor

$$\frac{x_i(t')}{x_p + x_i(t')}$$

to dt'/τ. Thus, the fraction of kinks surmounting the barrier during a cycle is

$$\int_0^{t_i} \frac{dt'}{\tau} \frac{x_i(t')x_i(t_i - t')}{[x_p + x_i(t')][x_p + x_i(t_i - t')]} = \frac{t_i}{\tau} I_2,$$

where I_2 is defined by formula (11).

We now have all what is required for generalizing Eq. (8) and calculating the modified velocity of dislocations under intermittent pulse loading. Let the transition of a dislocation to the next valley of the minimum take n cycles. This means that the barrier controlling the propagation of a kink and preventing its annihilation with an antikink is surmounted over n cycles with a probability close to unity:

$$nI_2 \frac{t_i}{\tau} \approx 1.$$

The mean free path for a kink equal to the mean distance between such barriers determining the annihilation of kinks is $x_i(\tau) \approx x_i(nI_2 t_i)$.

We also know that the number of kinks generated per unit dislocation length during n cycles is $n\Delta N$ and the mean distance between them is $1/n\Delta N$. Equating the mean distance between kinks to the mean free path of kinks, we obtain the condition for the passage of the dislocation to the next valley:

$$\frac{1}{n\Delta N} = x_i(nI_2 t_i). \quad (18)$$

Solving this equation for n, we obtain the renormalization of the duration t_a of a dislocation transition under the static loading conditions to the effective duration nt_i under intermittent loading. Assuming that the displacement l of the dislocation is inversely proportional to the duration of the transition process, we arrive at formula (9).

REFERENCES

1. J. P. Hirth and J. Lothe, *Theory of Dislocations* (McGraw-Hill, New York, 1967; Atomizdat, Moscow, 1972).
2. A. Seeger, J. Phys. (Paris) **42**, C5-201 (1981).
3. H. R. Kolar, J. C. H. Spence, and H. Alexander, Phys. Rev. Lett. **77**, 4031 (1996).
4. K. Maeda, M. Inoue, K. Suzuki, *et al.*, J. Phys. III **7**, 1451 (1997).

5. C. Koch, J. C. H. Spence, C. Zorman, *et al.*, J. Phys.: Condens. Matter **12**, 10175 (2000).
6. Yu. L. Iunin, V. I. Nikitenko, V. I. Orlov, and B. Ya. Farber, Zh. Éksp. Teor. Fiz. **100**, 1951 (1991) [Sov. Phys. JETP **73**, 1079 (1991)].
7. Yu. L. Iunin, V. I. Nikitenko, V. I. Orlov, and B. Ya. Farber, Fiz. Tverd. Tela (Leningrad) **33**, 1262 (1991) [Sov. Phys. Solid State **33**, 715 (1991)].
8. Yu. L. Iunin, V. I. Nikitenko, V. I. Orlov, and B. V. Petukhov, in *Proceedings of 10th International Conference on the Strength of Metals and Alloys, ICSMA-10, Sendai, Japan, 1994*, p. 101.
9. Yu. L. Iunin, V. I. Nikitenko, V. I. Orlov, and B. V. Petukhov, Phys. Rev. Lett. **78**, 3137 (1997).
10. B. V. Petukhov, Fiz. Tverd. Tela (Leningrad) **13**, 1445 (1971) [Sov. Phys. Solid State **13**, 1204 (1971)].
11. M. V. Feigel'man and V. M. Vinocur, J. Phys. (Paris) **49**, 1731 (1988).
12. J.-P. Bouchaud and A. Georges, Phys. Rep. **195**, 127 (1990).
13. N. V. Abrosimov, S. N. Rossolenko, V. Alex, *et al.*, J. Cryst. Growth **166**, 657 (1996).
14. J. Donecker, A. Gerhardt, and J. Wollweber, Mater. Sci. Eng. B **B28**, 18 (1994).
15. V. N. Erofeev, V. I. Nikitenko, V. I. Polovinkina, and É. V. Suvorov, Kristallografiya **16**, 190 (1971) [Sov. Phys. Crystallogr. **16**, 151 (1971)].
16. Yu. L. Iunin, V. I. Orlov, D. V. Dyachenko-Dekov, *et al.*, Solid State Phenom. **57**, 419 (1997).
17. I. E. Bondarenko, V. G. Eremenko, V. I. Nikitenko, and E. B. Yakimov, Phys. Status Solidi A **60**, 341 (1980).
18. B. V. Petukhov, Zh. Tekh. Fiz. **60** (10), 64 (1990) [Sov. Phys. Tech. Phys. **35**, 1150 (1990)].
19. E. Sirtl and A. Adler, Z. Metallkd. **52**, 529 (1961).
20. V. Celli, M. Kabler, T. Ninomiya, and R. Thomson, Phys. Rev. **131**, 58 (1963).
21. V. V. Rybin and A. N. Orlov, Fiz. Tverd. Tela (Leningrad) **11**, 3251 (1969) [Sov. Phys. Solid State **11**, 2635 (1969)].
22. V. I. Nikitenko, B. Ya. Farber, and Yu. L. Iunin, Zh. Éksp. Teor. Fiz. **93**, 1304 (1987) [Sov. Phys. JETP **66**, 738 (1987)].
23. B. V. Petukhov and Yu. I. Polyakov, Kristallografiya **37**, 291 (1992) [Sov. Phys. Crystallogr. **37**, 144 (1992)].
24. B. V. Petukhov, Fiz. Tverd. Tela (Leningrad) **24**, 439 (1982) [Sov. Phys. Solid State **24**, 248 (1982)].
25. B. V. Petukhov, Fiz. Tverd. Tela (St. Petersburg) **41**, 1988 (1999) [Phys. Solid State **41**, 1824 (1999)].
26. W. C. Dash, J. Appl. Phys. **29**, 705 (1958).
27. W. G. Johnston and J. J. Gilman, J. Appl. Phys. **31**, 632 (1960).
28. V. I. Nikitenko, B. Ya. Farber, and I. E. Bondarenko, Zh. Éksp. Teor. Fiz. **82**, 1539 (1982) [Sov. Phys. JETP **55**, 891 (1982)].
29. I. E. Bondarenko and E. B. Yakimov, Izv. Akad. Nauk SSSR, Ser. Fiz. **51**, 703 (1987).
30. V. Eremenko, N. Abrosimov, and A. Fedorov, Phys. Status Solidi A **171**, 383 (1999).
31. B. V. Gnedenko and A. N. Kolmogorov, *Limit Distributions for Sums of Independent Random Variables* (Gostekhizdat, Moscow–Leningrad, 1949; Addison-Wesley, Reading, 1954).
32. V. M. Zolotarev, V. V. Uchaikin, and V. V. Saenko, Zh. Éksp. Teor. Fiz. **115**, 1411 (1999) [JETP **88**, 780 (1999)].

Translated by N. Wadhwa

Journal of Experimental and Theoretical Physics, Vol. 94, No. 1, 2002, pp. 119–122.
Translated from Zhurnal Éksperimental'noĭ i Teoreticheskoĭ Fiziki, Vol. 121, No. 1, 2002, pp. 142–145.

SOLIDS
Structure

Magnetic Resonance in Dilute Quasi-One-Dimensional Antiferromagnet $CsNi_{1-x}Mg_xBr_3$

L. A. Prozorova*, G. V. Pupkov, S. S. Sosin, and S. V. Petrov
Kapitza Institute of Physical Problems, Russian Academy of Sciences, Moscow, 117334 Russia
**e-mail: prozorov@kapitza.ras.ru*
Received September 5, 2001

Abstract—The effect of alloying with nonmagnetic Mg^{2+} ions on the low-frequency branch of resonance of a noncollinear quasi-one-dimensional $CsNiBr_3$ antiferromagnet is investigated experimentally. It is found that a weak dilution ($x = 2$ to 4%) leads to a considerable (up to 15%) reduction of the resonant gap and of the spin-flop field. The results agree with the theory of Korenblit and Schender, according to which the small parameter of perturbation of the initial system is $x\sqrt{J/J'}$ rather than the impurity concentration x; i.e., a quasi-one-dimensional amplification coefficient exists, which is equal in this case to approximately six. *© 2002 MAIK "Nauka/Interperiodica".*

1. INTRODUCTION

The introduction of nonmagnetic impurities into a magnetic material brings about considerable changes in its properties. These changes are especially pronounced in magnetic structures of reduced dimensions, in particular, in quasi-one-dimensional antiferromagnets. The problem on the properties of dilute antiferromagnetic chains was treated theoretically by Bulaevskiĭ [1]. He has demonstrated that the rupture of antiferromagnetic chains due to nonmagnetic inclusions is accompanied by the emergence of magnetic defects (additional degrees of freedom) associated with the fact that half of the chain segments will exhibit uncompensated spin. The emerging defects behave as a paramagnetic impurity.

Real quasi-one-dimensional antiferromagnets at $T < T_N \sim \sqrt{JJ'}$ (J is the constant of exchange interaction along the chain and J' is the interchain interaction constant) are characterized by three-dimensional magnetic order. At low temperatures, the magnetic defects due to alloying cease to be independent and come to be associated with other spins. This fact must influence the process of ordering and all of the magnetic properties of the system. The effect of impurity on the properties of a quasi-one-dimensional antiferromagnet was treated theoretically within the classical approximation of the spin-wave theory at $T = 0$ by Korenblit and Schender [2]. The corrections to the values of the susceptibility $\chi_\perp$ and of the gap in the spin wave spectrum $\omega(q = 0)$, calculated in the first order of perturbation theory, are defined by the following expressions, depending on the impurity concentration x:

$$\begin{aligned}\chi &= \chi(x = 0)\left(1 + \alpha x\sqrt{\frac{J}{J'}}\right),\\ \omega &= \omega(x = 0)\left(1 - \frac{\alpha x}{2}\sqrt{\frac{J}{J'}}\right),\end{aligned} \qquad (1)$$

where α is a numerical coefficient of the order of unity, dependent on the configuration of spins and on the number of nearest neighbors. Therefore, the small parameter of perturbation is $x\sqrt{J/J'}$ rather than the impurity concentration x; i.e., a "quasi-one-dimensional amplification" of the impurity effect exists.

Considerable variations of the ordering temperature T_N and magnetic susceptibility in the case of alloying were observed in a number of experimental studies (see, for example, [3–5]). It was further found [6] that the introduction of Mg^{2+} ions into a quasi-one-dimensional antiferromagnet with a noncollinear ("triangular") structure, $CsNiCl_3$, caused a reduction of the energy gap in the spectrum $\nu_1(H = 0)$ (at $x = 0.07$, the frequency of antiferromagnetic resonance in zero field decreased almost by half) in accordance with theoretical predictions [2]. However, the introduction of a 2–3% Mg impurity into single crystals of $RbNiCl_3$ isomorphic to $CsNiCl_3$ brought about qualitatively different results [7]: an insignificant increase in the gap $\nu_1(H = 0)$ was accompanied by the emergence of additional resonance absorption in the range from 3 to 20 GHz. The field dependence of the frequency of this additional line resembles the acoustic branch of resonance $\nu_3(H)$ characteristic of triangular structures of strong easy-axis anisotropy. Note that no resonance absorption is present in this frequency range for pure $RbNiCl_3$, and the frequency $\nu_3(H = 0)$ is estimated at only 0.5 GHz. In order to interpret this strange phenomenon, it was assumed that the Mg^{2+} ions introduced into $RbNiCl_3$ did not get to the lattice sites, this resulting in strong distortions and in the emergence of additional anisotropy causing an increase in the oscillation frequencies ν_1 and ν_3. This assumption is supported by the fact that it is impossible to grow single crystals of

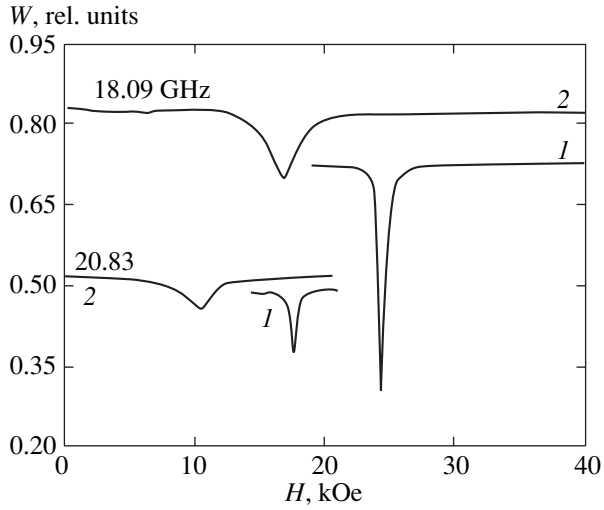

Fig. 1. Lines of absorption of a microwave signal in (*1*) pure and (*2*) dilute $CsNiBr_3$ at different frequencies. The impurity concentration in dilute substance $x = 0.04$, $T = 1.3$ K.

$RbNi_{1-x}Mg_xCl_3$ with an Mg concentration of more than 3%. Therefore, there is no doubt interest in investigating the effect of substitutional impurity on resonance frequencies in other triangular quasi-one-dimensional antiferromagnets, in which the oscillation branch ν_3 is known to be in the microwave-frequency range, and to find out how it varies when an impurity is introduced.

We investigated $CsNiBr_3$ whose magnetic properties were experimentally studied by a number of researchers (see, for example, [8–10]). According to the results of those studies, three-dimensional magnetic ordering occurs at $T < T_N \sim 12$ K, and, as in the case of $CsNiCl_3$ and $RbNiCl_3$, a plane "triangular" magnetic structure arises, with the spin plane being perpendicular to the basal plane of the crystal. The acoustic branches of oscillation at $H \parallel C_6$, $H < H_c$ are described by the following formulas (see [11, 12]):

$$\nu_1^2 = \gamma^2(\eta H_c^2 + H^2), \quad \nu_2^2 = 0,$$
$$\nu_3^2 = \eta\Delta_3^2\frac{H_c^2 - H^2}{\eta H_c^2 + H^2}\left[1 - \left(\frac{H}{H_c}\right)^2\right]^3, \tag{2}$$

where

$$\eta = (\chi_\parallel - \chi_\perp)/\chi_\perp, \quad \Delta_3 \sim \nu_1(H = 0)\frac{D}{J},$$

H_c is the spin-flop field, $H_c^2 = D/(\chi_\parallel - \chi_\perp)$, and D is the easy-axis anisotropy constant.

At $H \perp C_6$, the first two branches are the roots of the biquadratic equation

$$\nu^4 - \nu^2(H^2 + \eta H_c^2 + \eta^2 H^2) + \gamma^2\eta^2 H^2(H_c^2 + H^2) = 0, \tag{3}$$

and the third branch is independent of the field.

2. EXPERIMENTAL PROCEDURE AND SAMPLES

Microwave spectrometers with direct amplification were used to investigate the antiferromagnetic resonance. The measurements were performed at helium temperatures in the frequency range from 9 to 36 GHz and in fields of up to 65 kOe.

Single crystals of $CsNiBr_3$ were grown similarly to single crystals of $CsMnBr_3$ [13]. The method used to prepare single crystals of solid solutions of $CsNi_{1-x}Mg_xBr_3$ was as follows. Single crystals of $CsNiBr_3$ and metallic magnesium in the form of shavings (1–2% by weight) were placed in a quartz ampoule. The ampoule was evacuated and sealed. It was then cautiously heated by a burner to initiate the $CsNiBr_3 + Mg = CsMgBr_3 + Ni$ reaction. After that, the ampoule contents were melted and stirred. The ampoule was placed into a furnace for growing a single crystal. According to our observations, $CsMgBr_3$ melts at a lower temperature than $CsNiBr_3$; therefore, the top portion of the obtained single crystal is richer in magnesium than its bottom portion. The impurity of metallic nickel formed does not interfere with the crystal growth. The Mg content in the samples selected for measurements was determined by γ-activation analysis [6].

3. EXPERIMENTAL RESULTS

Figure 1 gives examples of recordings of resonance lines for pure and doped $CsNiBr_3$ at $T = 1.3$ K in a field directed parallel to the C_6 axis. One can clearly see that, in the case of alloying, the resonance line corresponding to the ν_3 mode broadens severalfold and shifts towards lower fields. No absorption in fields higher than H_c was observed in the region of the ν_2 branch at any one of the measuring frequencies. No respective recordings at $H \perp C_6$ are given, because the ν_3 branch cannot be observed in this orientation due to the absence of dispersion over the field, and the impurity had almost no effect on the ν_2 branch. Figure 2 gives the results of our measurements of the $\nu_2(H)$ and $\nu_3(H)$ curves for pure single crystals and single crystals with an impurity of Mg^{2+} ions with the concentrations $x = 0.02$ and 0.04 and field directions $H \parallel C_6$ and $H \perp C_6$. The solid curves indicate the results of calculations by formulas (2) and (3) with the parameters $\eta = 0.75$, $H_c = 75.3$, 64.0, and 53.4 kOe, and $\Delta_3 = 25.3$, 23.9, and 22.1 GHz for $x = 0$, 0.02, and 0.04, respectively. The inset gives the dependences of the relative variation of Δ_3 and H_c on the impurity concentration, as well as their linear fits with the coefficients three and seven, the first

of which defines, according to formula (1), the value of quasi-one-dimensional amplification of the impurity effect. In our case, this parameter is equal to approximately six,

$$Q = \frac{2}{x}\left(\frac{\Delta_3(0)}{\Delta_3(x)} - 1\right) = \alpha\sqrt{\frac{J}{J'}} \approx 6. \quad (4)$$

Note that the values of H_c, determined from our fits for all samples, prove to be less than the real field of spin plane flop H_{sf}. For example, the spin-flop field determined by the results of magnetostatic measurements for $CsNiBr_3$ [8] is approximately 90 kOe. This is apparently due to the existence in the samples of two successive spin-reorientation transitions, as was observed in another quasi-one-dimensional easy-axis triangular $CsMnJ_3$ antiferromagnet [14]. In this case, the field dependence $\nu_3(H)$ at $H < H_c$ differs rather little from that derived from formula (2); however, the ν_3 branch relaxes at both points. The field of first transition is determined by fitting. Also indicative of this is the absence of resonance absorption in fields $H > H_c$ in a sample with $x = 0.04$, in spite of the fact that the calculated values of the resonance fields corresponding to the ν_1 andν_2 branches lie within the accessible experimental range. Our results indicate that the effect of impurity on the field H_c proves to be twice as strong as its effect on the gap Δ_3; this is possibly the result of broadening of the intermediate range $H_c < H < H_{sf}$ due to alloying. The dependences $\nu_3(H)$ in the case of deviation of the magnetic field from rational directions are also well described by the theoretical formulas of [12]. Therefore, one can conclude that, in the case of light alloying, a type of magnetic ordering persists, and the observed reduction of the resonance gap and critical field with increasing impurity concentration is in qualitative agreement with theory [2].

In order to perform a qualitative comparison, one must determine the ratio J/J' from other experiments. The value of J may be calculated from the results of magnetostatic measurements (according to [8], $J = 17$ K) or from the excitation spectrum obtained using the inelastic neutron scattering (it follows from [9] that $J = 22$ K). The difference in the values of J obtained from different experiments is 20% (we assumed in calculations that $J = 20$ K). The constant J' may be calculated using the experimentally obtained value of $\nu_3(H)$. It follows from our data, in view of the results of Kambe *et al.* [10], that $J' = 1.3$ K.

Therefore, the experimentally observed quasi-one-dimensional amplification coefficient for $CsNiBr_3$ is close to the estimate that may be derived from the data given above for J and J'. The observed discrepancy may be attributed both to the difference of the coefficient α from unity and to the errors in determining the parameters J and J', which are inevitable in the case of describing quasi-one-dimensional magnetic systems within the classical approximation of the spin wave theory. Note that the inclusion of the contribution by zero oscillation to the magnetization and to the spin wave spectrum would bring about excess accuracy as compared with the theoretical results [2].

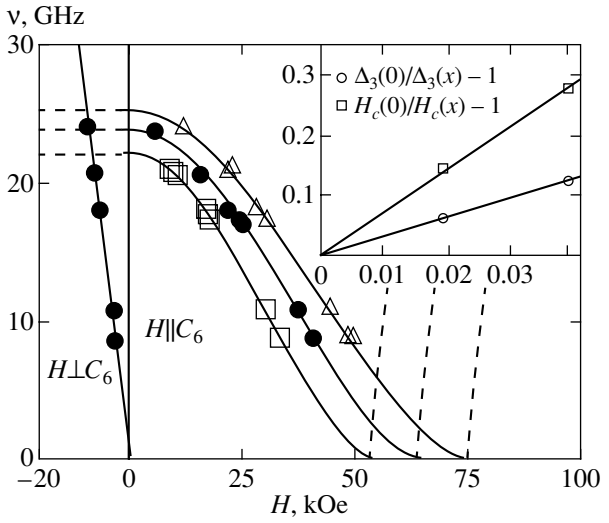

Fig. 2. The resonance frequencies $\nu_{2,3}$ as functions of magnetic field for $CsNi_{1-x}Mg_xBr_3$ at $T = 1.3$ K: △, $x = 0$; ●, $x = 0.02$; □, $x = 0.04$; solid curves, calculation by formulas (2) and (3) (dashed curves, not observed experimentally). The inset gives the relative variation of the parameters Δ_3 and H_c with the impurity concentration in view of linear fits.

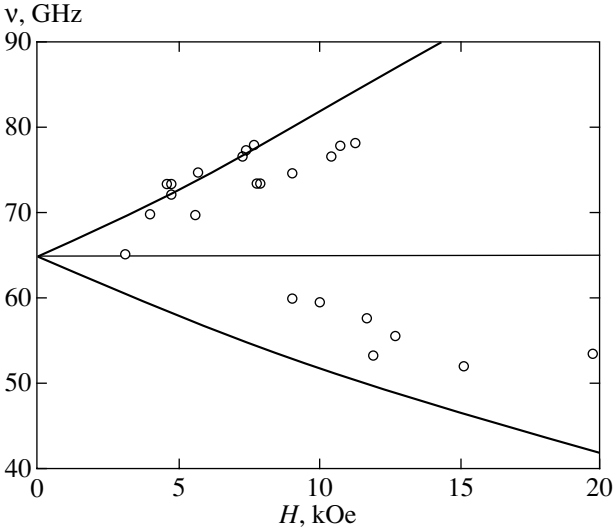

Fig. 3. The resonance absorption frequency as a function of magnetic field at $T = 1.3$ K for $CsNi_{0.74}Mg_{0.26}Br_3$. The curves indicate the theoretically obtained dependence for spin glass, calculated by formula (5).

In the case of strong dilution, the form of the spectrum changes. Figure 3 gives the experimental data for $CsNi_{0.74}Mg_{0.26}Br_3$. This spectrum is close to that char-

acteristic of transversely polarized resonant modes of spin glass [15],

$$\nu_{1,2} = \sqrt{\Delta^2 + \left(\frac{\gamma H}{2}\right)^2} \pm \frac{\gamma H}{2}. \quad (5)$$

The theoretically obtained dependence $\nu_{1,2}(H)$ for spin glass with $\Delta = 65$ GHz and $\gamma = 3$ GHz/kOe is shown in the same graph by solid curves. However, additional investigations are required before making a conclusive statement to the effect that spin glass is formed in this case.

ACKNOWLEDGMENTS

We are grateful to Yu.M. Tsipenyuk for performing the γ-activation analysis of samples. This study was supported in part by the Russian Foundation for Basic Research (project no. 00-02-170317), as well as by INTAS (grant no. 99-0155) and CRDF (grant no. RP1-2097).

REFERENCES

1. L. N. Bulaevskiĭ, Fiz. Tverd. Tela (Leningrad) **11**, 1132 (1969) [Sov. Phys. Solid State **11**, 921 (1969)].
2. I. Ya. Korenblit and E. F. Schender, Phys. Rev. B **48**, 9478 (1993).
3. C. Dupas and J. P. Renard, Phys. Rev. B **18**, 401 (1978).
4. D. Visser, A. Harrison, and D. J. McIntyre, J. Phys. (Paris) **49**, C8-1255 (1988).
5. J. Chadwick, D. H. Jones, J. A. Johnson, *et al.*, J. Phys.: Condens. Matter **1**, 6731 (1989).
6. S. S. Sosin, I. A. Zaliznyak, L. A. Prozorova, *et al.*, Zh. Éksp. Teor. Fiz. **112**, 209 (1997) [JETP **85**, 114 (1997)].
7. M. E. Zhitomirskiĭ, O. A. Petrenko, S. V. Petrov, *et al.*, Zh. Éksp. Teor. Fiz. **108**, 343 (1995) [JETP **81**, 185 (1995)].
8. R. Brenner, E. Ehrenfreund, H. Shechter, *et al.*, J. Phys. Chem. Solids **38**, 1023 (1977).
9. K. Kakurai, Physica B (Amsterdam) **180–181**, 153 (1992).
10. T. Kambe, H. Tanaka, Sh. Kimura, *et al.*, J. Phys. Soc. Jpn. **65**, 1799 (1996).
11. I. A. Zaliznyak, V. I. Marchenko, S. V. Petrov, *et al.*, Pis'ma Zh. Éksp. Teor. Fiz. **47**, 172 (1988) [JETP Lett. **47**, 211 (1988)].
12. S. I. Abarzhi, M. E. Zhitomirskiĭ, O. A. Petrenko, *et al.*, Zh. Éksp. Teor. Fiz. **104**, 3232 (1993) [JETP **77**, 521 (1993)].
13. I. A. Zaliznyak, L. A. Prozorova, and S. V. Petrov, Zh. Éksp. Teor. Fiz. **97**, 359 (1990) [Sov. Phys. JETP **70**, 203 (1990)].
14. V. I. Marchenko and A. M. Tikhonov, Pis'ma Zh. Éksp. Teor. Fiz. **68**, 844 (1998) [JETP Lett. **68**, 887 (1998)].
15. A. F. Andreev and V. I. Marchenko, Usp. Fiz. Nauk **130**, 39 (1980) [Sov. Phys. Usp. **23**, 21 (1980)].

Translated by H. Bronstein

Journal of Experimental and Theoretical Physics, Vol. 94, No. 1, 2002, pp. 12–21.
Translated from Zhurnal Éksperimental'noĭ i Teoreticheskoĭ Fiziki, Vol. 121, No. 1, 2002, pp. 19–30.

NUCLEI, PARTICLES, AND THEIR INTERACTION

Radiation Loss of Electrons under Scattering by a Thomas–Fermi Atom

V. A. Astapenko[a, *], L. A. Bureeva[b], and V. S. Lisitsa[c]

[a]*Moscow Institute of Physics and Technology, Dolgoprudnyĭ, Moscow oblast, 141700 Russia*
[b]*Research Council on Spectroscopy, Russian Academy of Sciences, Moscow, 117924 Russia*
[c]*Russian Research Centre Kurchatov Institute, Moscow, 123481 Russia*
e-mail: astval@hotmail.com

Received July 5, 2001

Abstract—A universal theory and calculation results for the bremsstrahlung of electrons on complex atoms are presented. The theory accounts for the dynamic polarization of the core in the energy range from 0.5 to 10 keV, which is characteristic of radiation energy losses in a hot plasma with heavy ions. The treatment is based on the statistical atom model and the quasi-classical approximation of the incident electron. The model accounts for the penetration of the incident electron into the atomic core, which affects the relationship between the polarization and static radiation channels. The contribution of the polarization channel in both the spectral and the total radiation loss of electrons at various frequencies, nucleus charges, and energies of the incident particle is analyzed. It is shown that the contribution of the polarization channel is comparable with that of the static channel (which was calculated elsewhere) in a wide range of parameters. The results obtained are in a reasonable quantitative agreement with the detailed quantum-mechanical calculation carried out for individual atoms.

1. INTRODUCTION

Radiation loss of electrons in a continuous spectrum under scattering by heavy atoms is due to their bremsstrahlung in the atomic potential field (we do not consider the loss due to the excitation of atomic electrons, which correspond to a discrete radiation spectrum). A specific feature of these processes is the penetration of the incident electron into the atomic core, which results in the increase of the effective charge interacting with the electron. As a result, the dependence of the bremsstrahlung spectrum on frequency increases, while it decreases for the purely Coulomb field (see survey [1]). This phenomenon plays an important role in the diagnostics and radiation loss in plasma with heavy ions, which possess a substantial electron core. In fact, we face here the interaction of electrons with energies between 0.5 and 10 keV with atoms with the nucleus charge greater than 20.

Calculations of the bremsstrahlung in a static atomic potential were performed by various methods—in [2] in the framework of Born's approximation, in [3] on the basis of the semiclassical approach, in [4, 5] on the basis of a numerical solution of the Schrödinger equation in the Thomas–Fermi potential, in [6] by the self-consistent field method, and in [7] by the quasi-classical method. In the latter case, it was shown that the classical approximation is exact for atomic potentials in the case of moderate electron energies, which is characteristic of plasma. Moreover, the so-called "rotational approximation" can be used for the calculation of spectra in the range of high frequencies, which are responsible for the greater part of electron energy loss. This approximation accounts for the radiation at the most curved part of the electron's trajectory in the atomic potential. In the framework of this approximation, the spectrum of the bremsstrahlung is entirely determined by the dynamics of the electron's scattering and is expressed in terms of a functional of this potential (for details, see [1, 7] and below). A detailed comparison of the results of classical and quantum-mechanical calculations confirmed a high accuracy of the classical method. It is about 5% for the purely Coulomb potential and varies within 20% for complex ions depending on the structure of the ion core.

Despite a good agreement on the whole between the theories based on the static potential of the electron–atom interaction, the comparison of the calculated data [6] with those found by experiment [8] shows a systematic discrepancy for atoms with a large nucleus charge ($Z > 60$), which is especially significant in the low-frequency range.

This disagreement between the theory and experiment can be caused by a number of factors including the contribution of the polarization channel associated with the dynamic polarization of the atomic core, which is not taken into account in the consideration of the ordinary (static) bremsstrahlung. Numerous calculations of the polarization bremsstrahlung show that the contribution of this process can be comparable to (or even exceed) the static channel contribution. A detailed quantum-mechanical calculation of the polarization

bremsstrahlung on a multielectron atom was carried out in [10] for krypton by the chaotic phase approximation method with exchange. Calculation of the polarization bremsstrahlung spectra similar to that for the static potential [7] is carried out in the present paper. The statistical atom model and quasi-classical approximation similar to that used in [7] for the static bremsstrahlung is used as the working theoretical model. Thus, it becomes possible to directly compare the polarization bremsstrahlung and static bremsstrahlung for all types of atoms in a wide range of frequencies of emitted quanta and energy of the incident particles.

2. ROTATIONAL APPROXIMATION IN THE THEORY OF THE POLARIZATION BREMSSTRAHLUNG

It was mentioned in the Introduction that the rotational approximation was successfully used for the calculation of the static radiation of quasi-classical electrons in the atomic potential [7]. In addition to being very accurate, this method is characterized by simple computations. The expression for the effective spectral radiation over the static channel, which was first obtained in [7], has the form (in this paper we use atomic units)

$$\left(\frac{d\kappa}{d\omega}\right)_{\rm st}^{\rm rot} = \frac{8\pi A}{3c^3\sqrt{2T}}\int_0^\infty (f_{\rm st}(r))^2 \times \sqrt{1+\frac{|U(r)|}{T}}\,\delta(\omega-\omega_{\rm rot}(r))r^2dr. \quad (1)$$

Here A is the normalizing factor, $U(r)$ is the atomic potential,

$$f_{\rm st}(r) = -\frac{dU}{dr} = \frac{Z_{\rm eff}(r)}{r^2} \quad (2)$$

is the conventional "static" force acting on the incident electron, $Z_{\rm eff}(r)$ is the effective atomic charge at the distance r from the nucleus, T is the initial kinetic energy of the incident particle, and $\omega_{\rm rot}(r)$ is the rotational frequency determined by the equation

$$\omega_{\rm rot}(r, T) = \frac{\sqrt{2(T+|U(r)|)}}{r}. \quad (3)$$

The quantity $\omega_{\rm rot}(r, T)$ naturally arises in the quasi-classical limit of matrix elements that determine the spectrum of bremsstrahlung in the atomic potential. The delta function in Eq. (1) accounts for the dominance of the matrix elements with the difference of frequencies $\omega - \omega_{\rm rot}$ over the corresponding matrix elements with their sum (see [7]). Since the same quasi-classical wave functions of the incident electron are also involved in the calculation of the polarization bremsstrahlung, it is natural to use the rotational approximation for the polarization channel as well.

The simplest variant of the rotational approximation in the polarization bremsstrahlung theory consists in replacing the "static" force by the "polarization" one [11]. The polarization force, which depends on frequency, is determined by the equation

$$f_{\rm pol}(r, \omega) = \frac{N_{\rm pol}(r, \omega)}{r^2}, \quad (4)$$

where $N_{\rm pol}(r, \omega)$ is the effective charge of the atomic core that causes radiation at the frequency ω over the polarization channel. In the local electron density model [11], this charge can be represented in the form

$$N_{\rm pol}(r, \omega) = \omega^2\left|\int_0^r \beta(r', \omega)4\pi r'^2 dr'\right|. \quad (5)$$

Here $\beta(r, \omega)$ is the space density of dynamic polarizability of the target for which we will use the Brandt–Lundqvist approximation [12], which corresponds to the statistical plasma model of the atom,

$$\beta(r, \omega) = \frac{n(r)}{4\pi n(r) - \omega^2 - i0}, \quad (6)$$

where $n(r)$ is the local electron density of the atomic core. The presence of the current radius (distance from the nucleus) in the upper integral limit in (5) accounts for the penetration of the incident electron into the target's core and related effects (see below).

It must be noted that introduction of the polarization force (4)–(6) is rather conventional, since it is determined by both the real and the imaginary part of polarizability (6). The possible interference of the static and polarization radiation channels can be related only to the real part. The relative smallness of interference effects, which is confirmed by numerical calculation [10], is associated with the fact that polarization effects, in accordance with (5), are proportional to the square of the emitted frequency ω^2; hence, the contribution of the real part of polarization can be noticeable only at sufficiently large values of ω. However, the effective core charge (5) decreases due to the penetration of the incident electron into the core, while the effective charge $Z_{\rm eff}$ increases; hence, the interference terms are small. Thus, the smallness of the interference contribution is caused by the penetration of the incident electron into the target's core, which is essential in the frequency and energy ranges under consideration. It must be noted that the interference of the static and polarization radiation channels can play an important role in the cases when the penetration can be neglected [13] or is insignificant [14].

The approach based on Eqs. (5) and (6) can be called the local plasma frequency approximation. It can be used to study polarization effects in the framework of statistical atom models.

Substituting (4) into (1), we obtain the following expression for the spectral loss of energy on radiation

over the polarization channel in the framework of the rotational approximation:

$$\left(\frac{d\kappa}{d\omega}\right)_{\rm pol}^{\rm rot} = \frac{8\pi A}{3c^3\sqrt{2T}}\int_0^\infty N_{\rm pol}^2(r,\omega) \times\sqrt{1+\frac{|U(r)|}{T}}\delta(\omega-\omega_{\rm rot}(r))r^{-2}dr. \quad (7)$$

It is pertinent to note that the electrostatic interaction of electrons with each other is small compared with their interaction with the nucleus, which is known to exceed the former interaction by a factor of seven in the Thomas–Fermi model (see the problem in [15, Section 70]). This fact enables us to use in the treatment of the polarization bremsstrahlung the same trajectory of the incident electron as in static bremsstrahlung.

The presence of the delta function in (1) and (7) makes it possible to find the integrals in an explicit form. Then, with regard for (3), we find for the static channel (cf. [7]) that

$$\left(\frac{d\kappa}{d\omega}\right)_{\rm st}^{\rm rot} = \frac{8\sqrt{3}\pi\omega}{3c^3\sqrt{2T}} \times\frac{Z_{\rm eff}^2(r_{\rm eff}(\omega,T))\sqrt{1+\dfrac{|U(r_{\rm eff}(\omega,T))|}{T}}r_{\rm eff}^2(\omega,T)}{\omega^2 r_{\rm eff}^3(\omega,T)+Z_{\rm eff}(r_{\rm eff}(\omega,T))}. \quad (8)$$

Similarly, we have for the polarization channel

$$\left(\frac{d\kappa}{d\omega}\right)_{\rm pol}^{\rm rot} = \frac{8\sqrt{3}\pi\omega}{3c^3\sqrt{2T}} \times\frac{N_{\rm pol}^2(r_{\rm eff}(\omega,T),\omega)\sqrt{1+\dfrac{|U(r_{\rm eff}(\omega,T))|}{T}}r_{\rm eff}^2(\omega,T)}{\omega^2 r_{\rm eff}^3(\omega,T)+Z_{\rm eff}(r_{\rm eff}(\omega,T))}. \quad (9)$$

In formulas (8) and (9), we introduced the characteristic radiation radius in the rotational approximation $r_{\rm eff}$ [1, 7]. It is determined from the equation

$$2(T+|U(r)|) = \omega^2 r^2. \quad (10)$$

The physical meaning of (10) is that the radiation under our approach is determined by the distance from the target's nucleus at which the radiation frequency coincides with the angular rotation velocity of the classical electron in the atomic field at the point of the closest approach.

Formulas (8) and (9) imply the following expression for the spectral R factor in the rotational approximation:

$$R^{\rm (rot)}(\omega,T) = \left\{\frac{d\kappa_{\rm pol}(\omega,T)}{d\kappa_{\rm st}(\omega,T)}\right\}^{\rm (rot)} = \left[\frac{N_{\rm pol}(r,\omega)}{Z_{\rm eff}(r)}\right]^2_{r=r_{\rm eff}(\omega,T)}. \quad (11)$$

An expression for the total energy loss due to the bremsstrahlung over the static and polarization channels can be obtained by integrating (8) and (9) with respect to the frequency up to the initial kinetic energy T. On the other hand, the integration can be carried out in formulas (1) and (7), which include the delta function. Then, we obtain the following expressions for the total effective radiation over each of the channels:

$$\kappa_{\rm st} = \frac{8\sqrt{3}\pi}{3c^3\sqrt{2T}} \times\int_{r_{\rm eff}(T,T)}^\infty Z_{\rm eff}^2(r)\sqrt{1+\frac{|U(r)|}{T}}r^{-2}dr, \quad (12)$$

$$\kappa_{\rm pol}^{\rm rot} = \frac{8\sqrt{3}\pi}{3c^3\sqrt{2T}} \times\int_{r_{\rm eff}(T,T)}^\infty N_{\rm pol}^2(r,\omega_{\rm rot}(r,T))\sqrt{1+\frac{|U(r)|}{T}}r^{-2}dr. \quad (13)$$

Thus, formulas (8), (9) and (12), (13) with regard for (3), (5), and (6) yield a general solution of the problem for quasi-classical electrons if the target potential and the electron density of its core are known. Below, we use this approach to calculate the spectral and total energy loss in the framework of the statistical atom model.

3. POLARIZATION CHARGE IN THE FRAMEWORK OF THE STATISTICAL ATOM MODEL

It is seen from (9) and (13) that the key quantity that determines radiation over the polarization channel is the effective polarization charge $N_{\rm pol}(r,\omega)$, which depends on frequency. Properties of this quantity are investigated in this section.

First, we write general relations for the polarization charge using the local electron density approximation based on formulas (5) and (6). It is readily seen that $N_{\rm pol}$ satisfies the regular high-frequency asymptotics

$$N_{\rm pol}^\infty(r) = N_{\rm pol}(r,\omega\longrightarrow\infty) = N_e(r) = \int_0^r 4\pi n(r)r^2dr, \quad (14)$$

which can also be derived from the quantum-mechanical expression for polarizability. Here $N_e(r)$ is the number of electrons in the atomic sphere of radius r. Naturally, for $r > R_0$ (where R_0 is the atom size), $N_e(r)$ equals the total number of electrons in the target core N_{0e}.

In the low-frequency limit, we obtain from (5) and (6)

$$N_{\rm pol}^{(0)}(r, \omega) = \omega^2\left[\theta(r - R_0)\frac{R_0^3}{3} + \theta(R_0 - r)\frac{r^3}{3}\right]. \quad (15)$$

Note that (15) entails the following relation for the static dipole polarizability of the target:

$$\alpha_0 = \omega^{-2}N_{\rm pol}^{(0)}(r > R_0, \omega) = \frac{R_0^3}{3}$$

for atoms and ions with closed shells and a sufficiently large number of bound electrons ($N_{0e} \geq 30$); this formula has a reasonable accuracy if the atom (ion) size is calculated according to the Thomas–Fermi–Dirac model [11].

In static models, the electron density of the neutral atom core, which determines the polarization charge (see (5), (6)), can be represented in the form (see [15])

$$n(r) = Z^2 f\left(\frac{r}{r_{TF}}\right). \quad (16)$$

Here $r_{TF} = b/Z^{1/3}$ is the Thomas–Fermi radius, Z is the nucleus charge, and

$$b = \left(\frac{9\pi^2}{128}\right)^{1/3} \approx 0.8853.$$

The form of the function $f(x)$ depends on the underlying statistical model. In the Thomas–Fermi model, we have (see [15])

$$f_{TF} = \frac{1}{4\pi b^3}\left(\frac{\chi(x)}{x}\right)^{3/2}, \quad (17)$$

where $\chi(x)$ is the Thomas–Fermi function. The following expression for $f(x)$ obtained in the framework of the Lenz–Jensen statistical model provides a better description for the behavior of the electron density at large distances from the nucleus (see [16]):

$$f_{LJ}(x) \approx 3.7e^{-\sqrt{9.7x}}\frac{(1 + 0.26\sqrt{9.7x})^3}{(9.7x)^{3/2}}. \quad (18)$$

Note that for $x \leq 1$ functions (17) and (18) give practically the same result.

Substituting (16) and (17) into (5) and (6), we obtain the following expression for the polarization charge in the Thomas–Fermi model:

$$N_{\rm pol}(r, \omega, Z) = Zg\left(\frac{r}{r_{TF}}, \frac{\omega}{Z}\right). \quad (19)$$

Here, we use the universal function

$$g(x, \nu) = \nu^2\left|\int_0^x \frac{\chi^{3/2}(x')\sqrt{x'}dx'}{b^{-3}(\chi(x')/x')^{3/2} - \nu^2 - i0}\right|, \quad (20)$$

which is the polarization charge normalized to the total number of the atomic electrons as a function of dimensionless distance $x = r/r_{TF}$ and the reduced frequency $\nu = \omega/Z$. Formulas (19) and (20) provide a universal representation of the polarization charge in the Thomas–Fermi model.

Note that (19), (20) extend the one-parameter similarity law for dipole polarization of the Thomas–Fermi atom, which was first obtained in [17], to the case of two variables. The dipole limit for $N_{\rm pol}$ is obtained from (19), (20) by replacing the upper integration limit in (20) by infinity; i.e., $g^{\rm dip}(\nu) = g(x \longrightarrow \infty, \nu)$.

We compared the calculation results for the real and imaginary parts of the dipole polarization of a krypton atom (multiplied by the frequency squared) obtained in the framework of the approach under consideration with the results of quantum-mechanical calculations on the basis of the chaotic phase approximation with exchange [10]. It was discovered that, in the case of the Thomas–Fermi atom, the local plasma frequency method gives an averaged description of the exact spectral dependence of the shell atom structure. For the Slater electron density, our method results in the appearance of maxima and minima associated with ionization of electron subshells; however, the universal character of the description, which is characteristic of the Thomas–Fermi atom, is lost. Thus, we conclude that the approximation under consideration yields a rather accurate value for the atom's dipole polarizability without going into quantum-mechanical details of the atomic electron distribution.

In what follows, we use the polarization charge calculated under the rotational approximation, $N_{\rm pol}^{(\rm rot)}(\omega, T)$, since it takes into account the penetration effect of incident particles into the target's core, which is essential for quasi-classical electrons. The corresponding expression is obtained from formula (5) and the relation

$$N_{\rm pol}^{(\rm rot)}(\omega, T) = N_{\rm pol}(r_{\rm eff}(\omega, T), \omega). \quad (21)$$

Here $r_{\rm eff}(\omega, T)$ is a solution to Eq. (10). Hence, we have, for the normalized polarization charge in the rotational approximation,

$$g^{(\rm rot)}(\nu, t) = g(x_{\rm eff}(\nu, t), \nu), \quad (22)$$

where $t = bT/Z^{4/3}$ is the reduced energy and $x_{\rm eff}(n, t)$ is the solution to Eq. (10) written in terms of the parameters ν and t.

4. SPECTRAL BREMSSTRAHLUNG LOSS OF ELECTRON ENERGY UNDER SCATTERING FROM A THOMAS–FERMI ATOM

Spectral loss of energy of quasi-classical electrons over the static channel under scattering from the Thomas–Fermi atom was calculated in [7] on the basis of the rotational approximation (within its scope $\nu > 3t$)

and in the low-frequency range ($\nu < 3t$) on the basis of the linear interpolation to the "transport" limit. The comparison of these results with the results obtained by the quantum-mechanical calculation [6] carried out in [7] demonstrated a high accuracy of those approximations. The rotational approximation yields a universal expression for the spectral bremsstrahlung loss over the polarization channel under scattering from the Thomas–Fermi atom. This is conveniently done in terms of the R factor (11), which is the ratio of contributions of the polarization and static radiation mechanisms. Changing to reduced variables in (4) and (11), it is easy to obtain the following expression:

$$\tilde{R}_{TF}^{(\mathrm{rot})}(\nu, t) = \left[\frac{g(x, \nu)}{\chi(x) + x|\chi'(x)|}\right]_{x = x_{\mathrm{eff}}(\nu, t)}^2, \qquad 3t < \nu < \nu_{hf} \le 10. \tag{23}$$

Here, the prime means differentiation with respect to the argument, and $g(x, \nu)$ is the normalized polarization charge determined by formula (20). The maximal reduced frequency ν_{hf} is determined from the energy conservation law and is a function of the reduced initial energy and the nucleus charge

$$\nu_{hf} = \frac{Z^{1/3}}{b} t.$$

The following relation allows us to pass to the conventional frequency and energy:

$$R_{TF}^{(\mathrm{rot})}(\omega, T) = \tilde{R}_{TF}^{(\mathrm{rot})}\left(\frac{\omega}{Z}, \frac{Tb}{Z^{4/3}}\right), \qquad \frac{b}{Z^{1/3}} T < \omega < T. \tag{24}$$

Thus, relations (23), (24), (20), and the definition of $x_{\mathrm{eff}}(\nu, t)$ yield a universal (i.e., valid for all values of the nucleus charge) representation for the R factor on the basis of our approach. These formulas must be supplemented with the expression for the spectral loss over the static channel (8), which, for the Thomas–Fermi atom, is expressed in terms of the reduced variables as

$$\left(\frac{d\kappa}{d\omega}\right)_{\mathrm{st}}^{\mathrm{rot}} = \frac{8\sqrt{3}\pi Z^{2/3} b^{5/2} \nu}{3c^3\sqrt{2t}} \times \left\{\frac{x^4[(\chi/x)']^2\sqrt{1 + \chi/xt}}{b^3 x\nu^2 + |(\chi/x)'|}\right\}_{x = x_{\mathrm{eff}}(\nu, t)}. \tag{25}$$

An equation equivalent to (25) was first obtained in [7] in terms of the Gaunt factor for the rotational approximation. In the Coulomb ($\chi(x) = 1$) and Kramers ($x_{\mathrm{eff}}^{-1} > t$) limits, we obtain from (25)

$$\left(\frac{d\kappa}{d\omega}\right)_{\mathrm{st}}^{\mathrm{rot, Coul}} = \left(\frac{d\kappa}{d\omega}\right)^{\mathrm{Kramers}} = \frac{8\pi}{3\sqrt{3}c^3}\frac{Z^2}{T}. \tag{26}$$

A relation for the spectral radiation over the polarization channel is obtained from (25) by the change of variables

$$x^2(\chi/x)' \longrightarrow g(x, \nu),$$

which follows from (23):

$$\left(\frac{d\kappa}{d\omega}\right)_{\mathrm{pol}}^{\mathrm{rot}} = \frac{8\sqrt{3}\pi Z^{2/3} b^{5/2} \nu}{3c^3\sqrt{2t}} \times \left\{\frac{g(x, \nu)^2\sqrt{1 + \chi/xt}}{b^3 x\nu^2 + |(\chi/x)'|}\right\}_{x = x_{\mathrm{eff}}(\nu, t)}. \tag{27}$$

We also write the corresponding expression obtained in [17] in the Born–Bethe approximation, which has the following form in terms of the reduced variables:

$$\left(\frac{d\kappa}{d\omega}\right)_{\mathrm{pol}}^{B-B} = \frac{8}{3c^3}\frac{Z^{2/3}}{t}|g_{\mathrm{dip}}(\nu)|^2 \ln\left(\frac{1}{\nu}\sqrt{\frac{2t}{b^3}}\right), \qquad t > \frac{1}{8bZ^{2/3}}. \tag{28}$$

Here, $g_{\mathrm{dip}}(\nu) = g(x \longrightarrow \infty, \nu)$ is the normalized polarization charge (20) in the dipole approximation. It follows from (28) that there is an upper limitation of frequency for the Born–Bethe approximation in contrast to the rotational approximation: $\nu < 1.7\sqrt{t}$.

Figure 1 presents the dependence of the effective radiation of an electron on the Thomas–Fermi atom on reduced frequency over the polarization and static channels for two values of the initial energy of incident particles calculated in the framework of various approximations. Curves *1* and *3* describe the polarization channel calculated within the rotational and the Born–Bethe approximation (28), respectively. In the calculation of curve *2* for the static channel, the Gaunt factor $g_0(t)$ was used in the low-frequency range for the Thomas–Fermi atom in the transport limit. The corresponding interpolation for $g_0(t)$ was obtained with the use of the data presented in [18]. It is seen from Fig. 1 that the rotational approximation in the range $\nu < t$ yields, for the polarization radiation, an almost identical result to that obtained within the Born–Bethe approximation. Note that the inequality $\nu < t$ can be written in the form $\omega < bT/Z^{1/3}$. Therefore, for large Z it corresponds to the applicability condition of the low-frequency approximation in the theory of bremsstrahlung. In this case, an electron scattered from a neutral atom is weakly perturbed by the radiation process, and we can assume in the calculation of the polarization bremsstrahlung that its motion is uniform and rectilinear even for slow electrons [13]. This fact justifies the validity of using the Born–Bethe approximation for the polarization channel in the low-frequency range. Thus, in view of a good conjugation of curves *1* and *3*, we will use the rotational approximation to calculate the polar-

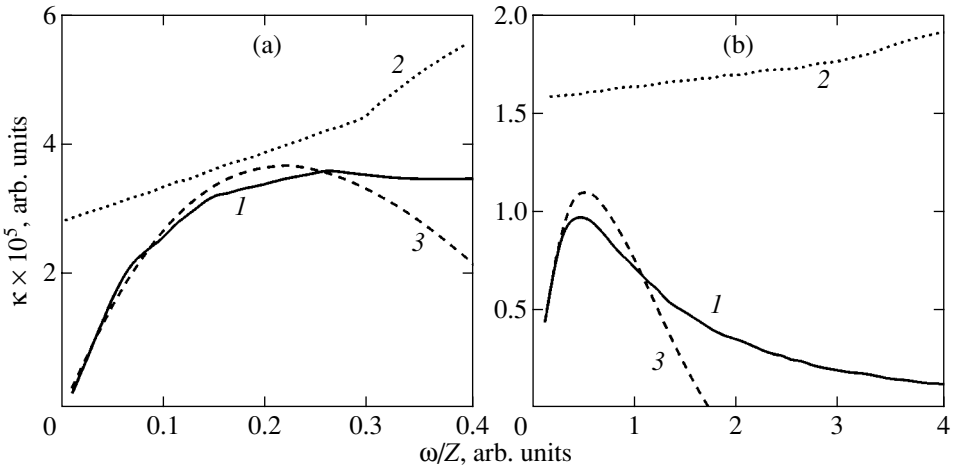

Fig. 1. The effective spectral radiation of an electron on the Thomas–Fermi atom ($Z = 60$) as a function of reduced frequency $\nu = \omega/Z$ for various values of reduced energy of the incident electron $t = 0.1$ (a) and 1 (b). *1* corresponds to the polarization channel (in the rotational approximation), *2* to the static channel, and *3* to the polarization channel (in the Born–Bethe approximation).

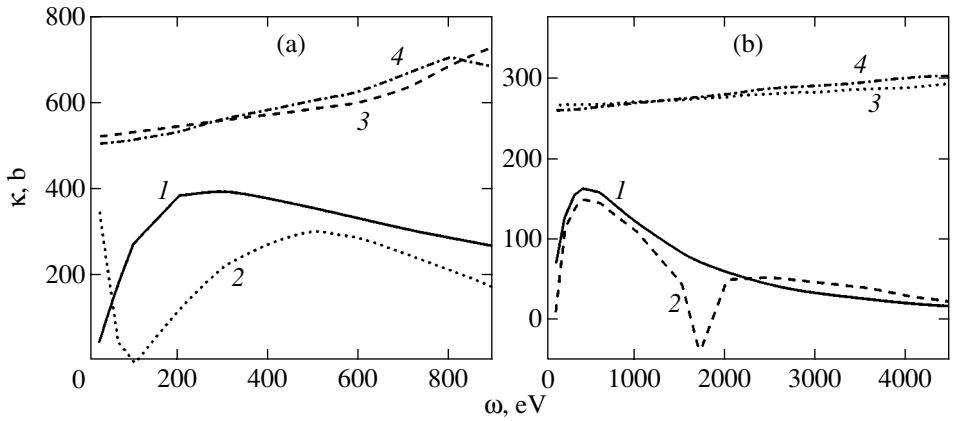

Fig. 2. Spectral intensity of the bremsstrahlung of electrons with the energy of 1 keV (a) and 5 keV (b) on the krypton atom over different channels. *1* corresponds to the polarization channel (the calculation carried out in this paper); *2* corresponds to the polarization channel with account for the interference contribution (calculation in the chaotic phases approximation with exchange [10]); *3* shows the contribution of the static channel (the calculation carried out in this paper); and *4* shows the contribution of the static channel according to [10].

ization radiation in the entire spectral domain under consideration. The decrease in $(d\kappa/d\omega)_{\text{pol}}^{\text{rot}}$ with increasing frequency shown in Fig. 1 is a consequence of the penetration of incident particles into the target's core; however, it is not so large as it follows from the Born–Bethe approximation. The initial increase in $(d\kappa/d\omega)_{\text{pol}}$ with increasing frequency, which is well known in the theory of polarization bremsstrahlung [9], is caused by the factor ν^2 involved in formula (20) for the polarization charge. Thus, the spectral dependence of the polarization bremsstrahlung intensity has a maximum with the central frequency shifted to the region of high frequencies as the initial energy of the incident particles increases. This is in agreement with the conclusion made in [17] in which the relation $\omega_{\max} \approx 0.8T$ was obtained on the basis of the Born approximation. It is also seen from Fig. 1 that in the range of parameters under consideration the contribution of the polarization channel is less than that of the static channel, and the difference increases with the energy of the incident particles.

Figure 2 presents the spectral effective radiation over the static and polarization channels for electrons with the energy of 1 keV and 5 keV scattered from a krypton atom. The radiation was calculated on the basis of the approach suggested in this paper (curves *1* and *3*) and by quantum-mechanical methods in [10] (curves *2* and *4*). The calculation for the static channel was carried out on the basis of formula (23) and the linear interpolation procedure to the domain of low frequencies $\nu < 3t$ [7], which was mentioned above. Note that the static bremsstrahlung was calculated in [10] in the framework of the distorted plane wave approximation

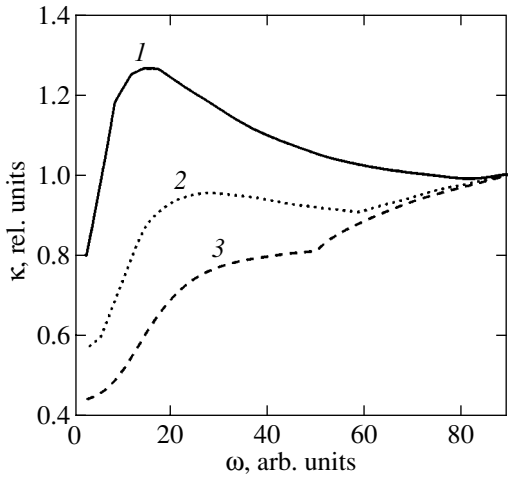

Fig. 3. Spectra of the bremsstrahlung of a 100-a.u.-energy electron scattered from the Thomas–Fermi atom with account for the polarization channel normalized to their values at ω = 90 a.u. The nucleus charge is $Z = 30$ (*1*), 60 (*2*), and 90 (*3*).

by summing partial contributions of various angular momenta with the use of the exact potential of the krypton atom. It is seen the results of both approaches are very close for the static channel. A small difference of curves *3* and *4* in the high-frequency domain is due to an arbitrary choice of the upper frequency boundary for linear interpolation. For the polarization channel, the difference of our result from that in [10] is greater. The latter result was obtained in the framework of the chaotic phase approximation with exchange, which takes into account not only individual quantum-mechanical features of the atomic electron motion, but also interparticle correlation effects. This difference is most significant in the vicinity of ionization potentials of electron subshells, where the real and imaginary parts of the atomic polarizability possess resonance structures. For electrons with the energy of 1 keV, the wide dip in the spectral dependence of the polarization bremsstrahlung intensity is due to the ionization of the 3*d* subshell of the krypton atom. In the case of electrons with the energy of 5 keV, which is shown in Fig. 2b, the dip on curve *2* is caused by the ionization of the 2*p* subshell. Its relative width is noticeably less; hence, the agreement between the results of our approach with those of the quantum-mechanical calculation is better. It must be noted that in [10], in contrast to this study, the interchannel interference was additionally taken into account, and it was shown that the influence of this interference on the total intensity of the bremsstrahlung is small. Interference effects are most significant in the vicinity of ionization potentials of electron subshells and in the high-frequency domain of the spectrum. It seems that they cause the difference of curves *1* and *2* in Fig. 2b for photons with energy greater than 2200 eV. On the whole, Fig. 2 demonstrates a reasonable accuracy of our method for the calculation of the polarization bremsstrahlung on a multielectron atom.

Note that the relative contribution of the polarization channel for a given reduced frequency increases with the initial energy of the electron, although the maximal value of the *R* factor decreases as the energy of the incident particles increases. This is due to the fact that the effective radiation radius in the framework of the rotational approximation increases with the energy of the incident particles if the radiation frequency is fixed. The spectral *R* factor attains its maximum at $\nu_{max} \approx 0.15$–0.45; moreover, ν_{max} increases with the energy of the incident particles, whereas $\nu_{max} \approx 1$ for fast electrons [20]. It is interesting that for slow electrons ($T < I$, where I is the atom's ionization potential) the maximum of the polarization bremsstrahlung contribution is shifted to high frequencies [13, 19]. This is explained by the fact that, in this case, the incident particles do not penetrate the target's core.

Formula (24) for the *R* factor makes it possible to investigate its dependence on the charge of the Thomas–Fermi atom nucleus under fixed values of the radiation frequency and energy of incident particles. Calculations for various values of the frequency and identical initial energy in the kiloelectronvolt range show that the relative contribution of the polarization channel increases with the nucleus charge. For the same initial energy, the *R* factor is larger for lower radiation frequencies.

The polarization bremsstrahlung theory elaborated in this paper predicts an increase in the relative contribution of the polarization mechanism with increasing nucleus charge, which is in qualitative agreement with the experimental result obtained in [8]. In that paper, it was discovered that the intensity of the bremsstrahlung in the low-frequency range for a large nucleus charge ($Z \approx 90$) is larger by approximately a factor of two than the static bremsstrahlung predicted by the quantum-mechanical calculation (without account for the polarization channel) [6]. At the same time, for small and moderate values of Z, there was good agreement between the experiment and the exact theory of ordinary (static) bremsstrahlung. It must be noted that the polarization bremsstrahlung theory fails to give a quantitative description of this phenomenon; it is possible that it is caused by the contribution of other radiation processes, such as two-photon bremsstrahlung, which was noted in [8].

Figure 3 shows the total (summed over the static and polarization channels) effective radiation for three values of the nucleus charge of the Thomas–Fermi atom as a function of photon energy. It is seen that the contribution of the polarization bremsstrahlung modifies the shape of the spectrum as compared with the static case (see curves *3* and *4* in Fig. 2).

5. TOTAL LOSS OF ENERGY FOR QUASI-CLASSICAL ELECTRONS UNDER SCATTERING FROM THE THOMAS–FERMI ATOM

The general expression (12) for the total energy loss over the static channel was first obtained in [3] in the framework of the semiclassical approach; for the Thomas–Fermi atom, it can be written in terms of the reduced variables as

$$\kappa_{st}\left(T = \frac{Z^{4/3}}{b}t\right) = \frac{8\sqrt{3}\pi\sqrt{b}}{3c^3}\frac{Z^{5/3}}{\sqrt{2t}} \times \int\limits_{x_{eff}(\nu_{hf}, t)}^{\infty}\left[\left(\frac{\chi(x)}{x}\right)'\right]^2\sqrt{1+\frac{\chi(x)}{tx}}x^2dx. \quad (29)$$

Here, as in (23), $\nu_{hf} = (Z^{1/3}/b)t$ is the reduced frequency corresponding to the high-frequency limit of the bremsstrahlung. It is essential that, for relation (29) to be valid, it is not necessary that the rotational approximation condition $\nu > \nu_{min}^{(rot)}(t) \approx 3t$ be satisfied; it is sufficient that the motion of the electron being scattered be quasi-classical, $t \le 1$. On the other hand, the correct normalizing factor can be obtained only by comparing the semiclassical result obtained in [3] with the quasi-classical limit of the exact quantum-mechanical relation for the spectral cross section (see [7]).

In a similar way, we rewrite formula (13) for the total loss of energy over the polarization channel to obtain

$$\kappa_{pol}\left(T = \frac{Z^{4/3}}{b}t\right) \approx \kappa_{pol}^{rot}(t) = \frac{8\sqrt{3}\pi\sqrt{b}}{3c^3}\frac{Z^{5/3}}{\sqrt{2t}} \times \int\limits_{x_{eff}(\nu_{hf}, t)}^{\infty} g^2(x, \nu_{rot}(x, t))\sqrt{1+\frac{\chi(x)}{tx}}x^{-2}dx. \quad (30)$$

Here, the function $g(x, \nu)$ is the normalized polarization charge (20), and $\nu_{rot}(x, t)$ is the reduced rotational frequency, which depends on reduced distance and energy; an expression for it can be obtained from (3):

$$\nu_{rot}(x, t) = \sqrt{\frac{2}{b^3}\frac{t+\chi(x)/x}{x^2}}. \quad (31)$$

Relation (30) for the total loss of energy over the polarization channel is obtained on the basis of the rotational approximation, which yields an adequate description of the polarization bremsstrahlung (in contrast to static bremsstrahlung, see the preceding section) in the low frequency range as well.

Note that formulas (29) and (30), in contrast to the corresponding relations for the spectral loss (25) and (27), involve (in addition to the factor $Z^{5/3}$) an explicit dependence on the nucleus charge. This is due to the fact that Z depends on the lower limit of the integral with respect to the dimensionless distance x. Indeed, the lower limit of the integral is given by the solution to the equation

$$t + \frac{\chi(x)}{x} = \frac{bZ^{2/3}}{2}x^2t^2, \quad (32)$$

which involves the parameter Z. Thus, the total loss of energy of the quasi-classical electron scattered from the Thomas–Fermi atom does not obey the exact similarity law with respect to reduced frequency and energy, which is characteristic of the spectral energy loss. However, calculations show that the dependence on the lower integral limit on Z in (30) is very weak; more precisely, as the nucleus charge varies by a factor of two, the quantity $x_{eff}(\nu_{hf}, t)$ changes only by 10–15%. Therefore, we conclude that there exists an approximate law of similarity for the total radiation loss of energy on the Thomas–Fermi atom.

From the viewpoint of unifying radiation processes, it is interesting to note that (29) can be represented in a form similar to (30) if we introduce an effective (normalized) radiation charge over the static channel:

$$g_{st}(x) = x^2\left(\frac{\chi(x)}{x}\right)'.$$

In the rotational approximation, the effective polarization channel at small distances from the nucleus increases, while remaining almost independent of the energy of the incident particles, and coincides with the radial distribution of the electron charge of the core. At large distances, the polarization charge becomes a decreasing function of distance, and its magnitude is greater for larger energies of the incident particles. If we take into account the dependence of the rotational frequency $\nu_{rot}(x, t)$ on the distance to the nucleus and the energy of the incident particles, these facts can be explained as follows. According to (3), $\nu_{rot}(x, t)$ is large at small distances (independently of the parameter t), and the high-frequency approximation (12) is valid for the polarization charge; in this approximation, the distribution of the polarization charge coincides with the radial distribution of the core's electron charge. At large distances from the nucleus, the rotational frequency decreases the faster the less the initial energy, and the polarization charge begins to decrease, as is implied by its definition (see formula (20)).

Figure 4 presents the dependence of the Gaunt factor, i.e., the ratio of the total energy lost by a quasi-classical electron scattered from the Thomas–Fermi atom ($Z = 60$) to its Kramers analog, on reduced energy of the incident particles over the static and polarization channels. It is seen that there exists a very small region in the low-frequency range ($t < 0.05$) where the polarization channel dominates the static one; in terms of the conventional units for the given charge, this corresponds to $T < 360$ eV. Note that for such energy of the incident particles, the characteristic radiation frequencies lie at

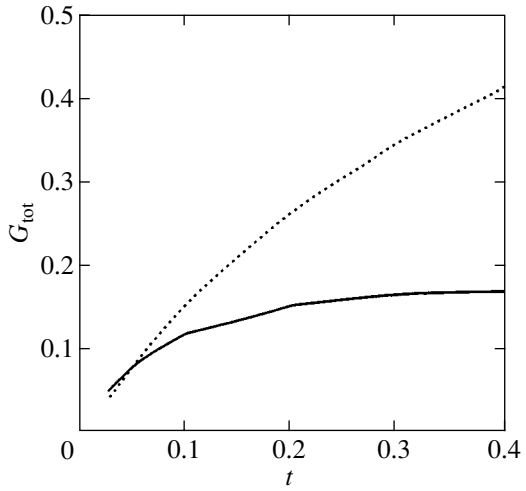

Fig. 4. The Gaunt factor for the total energy loss of a quasi-classical electron scattered from the Thomas–Fermi atom ($Z = 60$) over the static (dotted curve) and polarization (solid curve) channels as a function of reduced energy $t = bT/Z^{4/3}$ (T is the initial energy of the electron in atomic units).

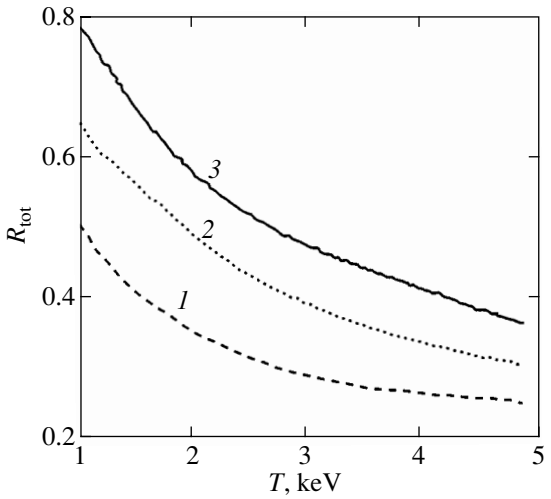

Fig. 5. Dependence of the R factor characterizing the relative contribution of the polarization channel to the total loss of energy on initial energy under scattering of a quasi-classical electron from Thomas–Fermi atoms with various nucleus charges: $Z = 30$ (*1*), 60 (*2*), and 90 (*3*).

the boundary of the domain where the Brandt–Lundqvist approximation for the target polarizability is applicable. It is also seen from Fig. 4 that the total loss of energy over the polarization channel quickly reaches a saturation value as the electron's energy increases, in contrast to the loss over the static channel, which increases up to the Coulomb limit. A fast saturation of the energy loss over the polarization channel is explained by the increase in the penetration effect of the electron into the target core with the energy of the incident particles and the associated decrease in the polarization charge. As a result, the scattered electron chiefly emits relatively low frequencies over the polarization channel, so that the increase in its energy does not result in the increase in the total energy loss over the polarization channel.

By analogy with the spectral R factor (23), (24), one can introduce an R factor for the total loss of energy, which has the following form in terms of the reduced units:

$$\tilde{R}_{tot}(t, Z) = \frac{\kappa_{pol}(t, Z)}{\kappa_{st}(t, Z)}. \quad (33)$$

In terms of the dimensional energy units, we have

$$R_{tot}(T, Z) = \tilde{R}_{tot}\left(\frac{Tb}{Z^{4/3}}, Z\right). \quad (34)$$

The dependence of R_{tot} on the initial energy of the electron (in terms of the conventional units) for various values of the atom's nucleus charge is shown in Fig. 5. It is seen that, in the range $T > 1$ keV, the contribution of the polarization effects to the total bremsstrahlung loss monotonically decreases with an increase in energy of the incident particles. For a fixed initial energy, the relative contribution of the polarization channel increases with the charge of the target nucleus; this is also the case for the spectral radiation losses (see the preceding section).

6. CONCLUSIONS

In this paper, we studied the role of the target's core polarization in the spectral and total radiation loss of quasi-classical electrons with the energy of 1–10 keV when they are scattered from the Thomas–Fermi atom. A universal relation for the effective spectral radiation over the polarization channel in terms of the reduced frequency and energy was obtained on the basis of the rotational approximation. This relation gives a unified description for this process for any nucleus charge. It was shown that, in contrast to the static bremsstrahlung, the rotational approximation in the theory of polarization bremsstrahlung admits a correct passage to the limit to the low-frequency domain and thus can be used to calculate the total energy loss.

The statistical model of the atom provides highly accurate results for the static bremsstrahlung channel. In the case of the polarization channel, the model is accurate only on the average, while its discrepancy with the quantum-mechanical calculation [10] is rather high in the vicinity of the ionization potentials of electronic shells.

On the basis of an analysis of frequency and energy dependences of the R factor, it was established that the contribution of the polarization mechanism is maximal in the low-frequency range $\nu \approx 0.15$–0.45, where the R factor is about unity, and the central frequency of the maximum increases with the energy of the incident par-

ticles. At a fixed frequency, the magnitude of the R factor increases in the high-frequency range as the energy of the scattered electron decreases; in the low-frequency range, the R factor decreases.

It was shown that the relative magnitude of the polarization radiation at a fixed frequency and energy of the incident particles increases with the charge of the atom's nucleus; this fact is in qualitative agreement with the available experimental data [8].

An analysis of the total energy loss over the polarization channel showed that its part is comparable with the loss over the static channel. The domain where the polarization channel dominates is determined by the inequality

$$T < 0.05\frac{Z^{4/3}}{b} \text{ a.u.},$$

and the characteristic radiation frequencies lie at the boundary of the region where the underlying model is applicable. As the energy of incident particles increases, the polarization bremsstrahlung loss under scattering of a quasi-classical electron from the Thomas–Fermi atom quickly reaches a saturation level, while the static bremsstrahlung loss continues to grow (for $t \le 1$). The saturation over the polarization channel is achieved due to the penetration of electrons into the target's core. The characteristic magnitude of the relative contribution of the polarization channel to the total loss of energy in the energy range of 1–5 keV varies in the range from 80 to 25%; it decreases with the increase in energy and increases with the charge of the atom's nucleus.

Thus, we conclude that the role of polarization effects in the bremsstrahlung of electrons with a moderate energy increases with the charge of the nucleus and with a decrease in the frequency and energy of the incident particles.

ACKNOWLEDGMENTS

We are grateful to V.I. Kogan and A.B.Kukushkin for useful discussions of the method for the calculation of the static bremsstrahlung channel.

The work was supported by the Russian Foundation for Basic Research (project no. 01-02-16305) and by the Ministry for Science under the *Fundamental Spectroscopy* project.

REFERENCES

1. V. I. Kogan, A. B. Kukushkin, and V. S. Lisitsa, Phys. Rep. **213**, 1 (1992).
2. V. D. Kirillov, B. A. Trubnikov, and S. A. Trushin, Fiz. Plazmy **1**, 218 (1975) [Sov. J. Plasma Phys. **1**, 117 (1975)].
3. V. I. Gervids and V. I. Kogan, Pis'ma Zh. Éksp. Teor. Fiz. **22**, 308 (1975) [JETP Lett. **22**, 142 (1975)].
4. V. P. Zhdanov and M. I. Chibisov, Zh. Tekh. Fiz. **47**, 1804 (1977) [Sov. Phys. Tech. Phys. **22**, 1045 (1977)].
5. V. P. Zhdanov, Fiz. Plazmy **4**, 128 (1978) [Sov. J. Plasma Phys. **4**, 71 (1978)].
6. C. M. Lee, L. Kissel, R. H. Pratt, and H. K. Tseng, Phys. Rev. A **13**, 1714 (1976).
7. V. I. Kogan and A. B. Kukushkin, Zh. Éksp. Teor. Fiz. **87**, 1164 (1984) [Sov. Phys. JETP **60**, 665 (1984)].
8. R. Hippler, K. Saeed, I. McGregor, and H. Kleinpoppen, Phys. Rev. Lett. **46**, 1622 (1981).
9. *Polarized Bremsstrahlung from Particles and Atoms*, Ed. by V. N. Tsytovich and I. M. Oiringel' (Nauka, Moscow, 1987).
10. A. V. Korol', A. G. Lyalin, O. I. Obolenskiĭ, and A. V. Solov'ev, Zh. Éksp. Teor. Fiz. **114**, 458 (1998) [JETP **87**, 251 (1998)].
11. V. A. Astapenko, L. A. Bureeva, and V. S. Lisitsa, Zh. Éksp. Teor. Fiz. **117**, 496 (2000) [JETP **90**, 434 (2000)].
12. W. Brandt and S. Lundqvist, Phys. Rev. A **139**, 612 (1965).
13. B. A. Zon, Zh. Éksp. Teor. Fiz. **77**, 44 (1979) [Sov. Phys. JETP **50**, 21 (1979)].
14. V. A. Astapenko, Zh. Éksp. Teor. Fiz. **115**, 1619 (1999) [JETP **88**, 889 (1999)].
15. L. D. Landau and E. M. Lifshitz, *Course of Theoretical Physics*, Vol. 3: *Quantum Mechanics: Non-Relativistic Theory* (Nauka, Moscow, 1989, 4th ed.; Pergamon, New York, 1977, 3rd ed.).
16. P. Gombas, *Die statistische Theorie des Atoms und ihre Anwendungen* (Springer-Verlag, Vienna, 1949; Inostrannaya Literatura, Moscow, 1951).
17. V. A. Astapenko, L. A. Bureeva, and V. S. Lisitsa, Zh. Éksp. Teor. Fiz. **117**, 906 (2000) [JETP **90**, 788 (2000)].
18. V. V. Ivanov, A. B. Kukushkin, and V. I. Kogan, Fiz. Plazmy **15**, 1531 (1989) [Sov. J. Plasma Phys. **15**, 892 (1989)].
19. V. Kas'yanov and A. Starostin, Zh. Éksp. Teor. Fiz. **48**, 295 (1965) [Sov. Phys. JETP **21**, 193 (1965)].
20. V. A. Astapenko, Laser Phys. **11**, 1042 (2001).

Translated by A. Klimontovich

Journal of Experimental and Theoretical Physics, Vol. 94, No. 1, 2002, pp. 123–134.
Translated from Zhurnal Éksperimental'noĭ i Teoreticheskoĭ Fiziki, Vol. 121, No. 1, 2002, pp. 146–159.

SOLIDS
Electronic Properties

Band Splitting and Relative Spin Alignment in Bilayer Systems

A. A. Ovchinnikov[a, b, *] and M. Ya. Ovchinnikova[a]

[a] *Joint Institute of Chemical Physics, Russian Academy of Sciences, Moscow, 117977 Russia*
[b] *Max-Planck-Institut für Physik Komplexer Systeme, 01187 Dresden, Germany*
**e-mail: aovchin@mpipks-dresden.mpg.de*

Received May 31, 2001

Abstract—It is shown that one-particle spectra of the lower Hubbard band of bilayer correlated 2D systems with different relative alignments of the spin systems in the layers differ significantly. In particular, the bilayer band splitting differs from zero for identically directed alternating spins of different layers (F_z configuration), but tends to zero for antiparallel alignment (AF_z configuration). It is found that the type of the alignment of the ground state changes upon an increase in the doping δ from the lower AF_z configuration to the F_z configuration of the alignment observed for large values of δ. The behavior of bilayer splitting in $Bi_2Sr_2CaCu_2O_{8+\delta}$ suggests that the configuration of the alignment may change from $F_z \longrightarrow AF_z$ simultaneously with the superconducting transition. The effects associated with the influence of spin alignment on the magnetic excitation spectrum as a method of studying the spin structure of bilayer systems are considered for homogeneous solutions of effective spin models. *© 2002 MAIK "Nauka/Interperiodica".*

1. INTRODUCTION

One of the features of HTSC materials, viz., the dependence of their properties on the number of CuO_2 planes, indicates the importance of the interaction between adjacent layers. The bilayer splitting of energy bands and Fermi surfaces in $Bi_2Sr_2CaCu_2O_{8+\delta}$ (BSCCO) was discovered recently in photoemission experiments (ARPES) [1–3]. It was precisely the absence of bilayer splitting in earlier photoemission experiments that led Anderson *et al.* [4] to a hypothesis concerning the mechanism of superconductivity assuming the simultaneous coherent transport of two particles between layers with suppressed one-particle transport [4]. New experiments change the point of view on this problem. The peculiarity of new results [2] is a considerable decrease in the bilayer splitting in the region $k \sim (\pi, 0)$ upon a transition to the superconducting state [2]. The topology of the Fermi surface in this range of k values is not completely clear. It has not been determined unambiguously whether the Fermi surface near $k \sim (\pi, 0)$ is of the electron [5–7] or hole [8–10] type, while the hole nature of the main segments on the Fermi surface around directions $k_x = k_y$ is generally accepted. Another phenomenon observed only in double-layer (and not in single-layer) cuprates is the emergence of magnetic resonance in inelastic scattering of neutrons in the superconducting state [11–16].

The interpretation of these differences is important for understanding the electron structure of cuprates possessing many properties of a doped Mott insulator. The main feature of this material is the Hubbard band splitting associated with antiferromagnetic correlations. Although the long-range antiferromagnetic 2D order vanishes for a low doping, $\delta_c = 1 - n_c \sim 0.05$, the local spin 2D order is apparently preserved in a fairly wide doping range including the superconductivity region. This conclusion is confirmed by the results on μ-MR, NMR, and NQR [17, 18] as well as by the large length of spin correlations with $Q = (\pi, \pi)$ and the smooth evolution of collective magnetic excitations in the course of doping (see the review in [11]), the observation of shadow Fermi boundaries, etc. Finally, direct proof of the antiferromagnetic order has been obtained recently (from Bragg reflections) [19, 20] even for the superconducting state of $YBa_2Cu_3O_{6.5}$ in the nanosecond range.

A detailed analysis of antiferromagnetic zones and interactions on the basis of the Hubbard model was carried out in the classical work by Schrieffer *et al.* [21]. A simple mean field method gives overestimated values of the alternating spin d_0 and the boundary $\delta_c \sim 0.45$ of the antiferromagnetic spin order region. Band renormalization on the basis of the zeroth antiferromagnetic approximation [21] and calculations based on the t–t'–U Hubbard model using the slave boson technique [22] or on the states with correlations of the valence bond type [23] reduce the value of d_0 and give the boundary $\delta_c \sim 0.3$ of local magnetization vanishing. According to the results of our previous investigations [23], the region $\delta < \delta_c$ includes the superconductivity region also. The conservation of Hubbard's band splitting for $\delta < \delta_c$ [23] in the t–t'–U as well as in the t–t'–J model [24–26] is responsible for a change in the topology of the Fermi surface under optimal doping with a transi-

tion from hole pockets to a large Fermi surface with segments of the electron and hole types.

If this pattern is correct, the interaction between the layers in bilayer systems and the magnon excitation spectrum may be determined to a considerable extent by the relative orientation (alignment) of local alternating spins of the two layers even if this orientation is not stationary in the rigorous sense and is preserved only in a characteristic time scale. In the case of a small difference in the energies of configurations with different spin alignments, one can expect a strong effect of doping and temperature on the properties of magnetic excitations. The search for this kind of effects could explain the origin of magnetic resonance in neutron scattering in YBCO and BSCCO.

In the present work, a variational analysis of bands, total energies, phase curves $T_c(\delta)$, and splitting is carried out using the bilayer t–t'–U Hubbard model. The analysis is carried out on the basis of correlated states with the valence bond type correlations, i.e., a band analogue of the Anderson RVB states. It was proved by us earlier [23] that the so-called correlated hopping interaction emerging in the effective Hamiltonian upon the formation of valence bonds provides the attraction between holes in the d channel and the corresponding d-type superconductivity compatible with the antiferromagnetic spin order. Here, we use the same method for studying the effect of interaction between two layers. In other words, we assume that the intralayer pairing mechanism operates and do not augment it by an artificial coherent transfer of pairs between the layers in contrast to the mechanism proposed by Anderson *et al.* [4]. We are interested in whether or not the large (in doping) region of antiferromagnetic spin order is preserved and what the relative alignment of the spin systems of the two layers and the bilayer band splitting are for various dopings. In the method used by us, the Hubbard splitting is preserved up to the optimal doping.

It should be emphasized that the approach used by us here differs from the fluctuation exchange (FLEX) method employed in [27] for investigating the bilayer Hubbard model. According to FLEX, the attraction between holes and band renormalization (in particular, bilayer splitting) are due to the exchange of spin fluctuations. The latter are described by the average isotropic susceptibility $\chi''(q, \omega)$ with a peak at $k \longrightarrow (\pi, \pi)$. However, the RPA analysis [21, 28, 29] on the basis of the antiferromagnetically split band makes it possible to observe the low-frequency mode only for spin excitations transverse to the vector $\mathbf{d}_0$ of the local alternating spin. The contribution of such fluctuations to the interaction of particles from the lower Hubbard band is suppressed by vanishing of the corresponding matrix elements at nesting lines [21, 30]. This means that the attraction between holes is determined by close ($\sim a$) antiferromagnetic correlations (in contrast to long-wave fluctuations in the FLEX method). In the simplest version, such fluctuations correspond to the formation of valence bonds, i.e., singlets of bonds between nearest sites. In the subsequent analysis, we will use precisely this model, although the inclusion of only one type of valence bonds may introduce an error.

In contrast to the averaged analysis based on the FLEX method, we calculate two specific configurations of a bilayer system with the parallel or antiparallel (opposite) alignment of alternating spins of the two layers. We will denote these configurations as the F_z and AF_z (ferro- and antiferromagnetic in z) alignment, although both cases correspond to a local antiferromagnetic spin order in each layer. Leaving aside other possible configurations (spiral or stripe phases), we cannot expect that our results can be unequivocally used for cuprates for which neutron measurements indicate the presence of incommensurate structures. Nevertheless, the effects observed in model calculations for the structures under investigation may be useful in an analysis of bilayer splitting and magnetic properties of bilayer cuprates.

2. COMPUTATIONAL METHOD

We begin with the Hubbard Hamiltonian of a bilayer system:

$$H = \sum_{\gamma} H_{\gamma}(U, t) + \Delta H(t', t_z)$$

$$= \sum_{n, m} \sum_{\gamma, \gamma', \sigma} t_{\gamma n, \gamma' m}(c^{\dagger}_{\gamma, n, \sigma} c_{\gamma', m, \sigma} + \text{H.c.}) \qquad (1)$$

$$+ U \sum_{n, \gamma} n_{\gamma, n, \uparrow} n_{\gamma, n, \downarrow}.$$

Here, n and m are 2D indices of a plane; $\gamma, \gamma' = 0, 1$ are the layer indices; and $t_{\gamma n, \gamma' m}$ are the hopping integrals. The main interactions $H_{\gamma}(U, t)$ within each layer γ are determined by the standard parameters t and U of the Hubbard model. The additional term $\Delta H(t', t_z)$ includes hopping interactions t' and t_z between the next neighboring centers in a layer and between the centers of different layers. The signs of the standard strong coupling parameters t, t', and t_z are defined in such a way that the zeroth bands (corresponding to $U = 0$) have the form

$$\epsilon^{(0)}_{\pm} = -2t(\cos k_x + \cos k_y)$$

$$+ 4t' \cos k_x \cos k_y \mp \frac{1}{4} t_z (\cos k_x - \cos k_y)^2. \qquad (2)$$

The dependence of the splitting $\Delta\epsilon(k) = \epsilon_+ - \epsilon_-$ of the bonding and antibonding (in z) zeroth bands on k is derived in [27, 31, 32].

A variational correlated state Ψ with the valence bond type correlations is constructed [23] with the help of the unitary transformation of an uncorrelated state Φ:

$$\Psi = \hat{W}(\alpha)\Phi, \quad \hat{W}(\alpha) = \exp\left[\alpha \sum_{\gamma} Z_{\gamma}\right], \qquad (3)$$

$$Z_\gamma = \frac{1}{2}\sum_{\sigma,\langle nm\rangle}(c^\dagger_{\gamma,n,\sigma}c_{\gamma,m,\sigma} - \text{H.c.})(n_{\gamma,n,-\sigma} - n_{\gamma,m,-\sigma}). \quad (4)$$

The choice of the unitary operator $W(\alpha)$ with the variational parameter α is explained in [23]. The variational analysis of the problem with the initial Hamiltonian H in the basis of correlated states Ψ is equivalent to an analysis of the effective Hamiltonian

$$H_{\text{eff}}(\alpha) = W^\dagger(\alpha)HW(\alpha) \approx \sum_\gamma\left\{H_\gamma(t,U) + \alpha[H_\gamma, Z_\gamma] + \frac{\alpha^2}{2}[[H_\gamma, Z_\gamma], z_\gamma]\right\} + \Delta H(t', t_z) \quad (5)$$

based on the mean field method. For the effective Hamiltonian, we use its approximate expression, confining our analysis to the second-order terms in the variational parameter α ($\alpha \sim 0.22$ for $U/t \sim 8$) for the main interactions $H_\gamma(U, t)$ and to the zeroth order in α for the contribution $H_\gamma(t', t_z)$ from additional interactions removing degeneracy along nesting lines.

For the uncorrelated function $\{\Phi\}$, we will use the BCS-model function with anomalous means of the d symmetry and with the antiferromagnetic spin order. The energy averaged over such a state for Hamiltonian (1),

$$\langle H\rangle_\Psi = \langle H_{\text{eff}}\rangle_\Phi = \bar{H}(y_{\gamma\nu}, z), \quad (6)$$

is obtained as an explicit function of the set of one-electron means $y_\nu = \langle\hat{y}_\nu\rangle_\Phi$ and $z = \langle T_z\rangle_\Phi$ over the uncorrelated state Φ (for the sake of brevity, subscript Φ in the means $\langle\ \rangle_\Phi$ will henceforth be omitted). The set of these means includes the density components $r_{\gamma l}$ ($|l| = 0, 1, \sqrt{2}, 2\sqrt{5}, 3$), analogous alternating spin components $d_{\gamma l}$ ($|l| = 0, \sqrt{2}, 2$), anomalous means $w_{\gamma l}$ of the d symmetry ($|l| = 1, 2, \sqrt{5}, 3$) for each layer $\gamma = 0, 1$, and the quantity z determining the mean $\langle T_z\rangle = -t_z z$ of the one-electron hopping interaction between the layers:

$$r_{\gamma l} = \frac{1}{2N}\sum_{n,\sigma}\langle c^\dagger_{\gamma,n,\sigma}c_{\gamma,n+l,\sigma}\rangle,$$

$$d_{\gamma l} = \frac{1}{2N}\sum_{n,\sigma}(-1)^n\frac{\sigma}{|\sigma|}\langle c^\dagger_{\gamma,n,\sigma}c_{\gamma,n+l,\sigma}\rangle,$$

$$w_{\gamma l} = \frac{1}{2N}\sum_n \text{sgn}(l_x^2 - l_y^2)\langle c^\dagger_{\gamma,n,\uparrow}c^\dagger_{\gamma,n+l,\downarrow} + \text{H.c.}\rangle, \quad (7)$$

$$z = \frac{1}{N}\sum_k\frac{1}{2}\langle[c^\dagger_{1,k,\sigma}c_{2,k,\sigma} + \text{H.c.}]\rangle\frac{(\cos k_x - \cos k_y)^2}{4}.$$

In view of symmetry, all quantities in relations (5) depend only on the modulus $l = |\mathbf{l}|$ and not on the direction of vector $\mathbf{l}$, and the components of density r_l are the same for the two layers (independent of γ). We will analyze the following four versions of relative alignment for spin and anomalous components:

$$d_{\gamma=1,l} = \zeta_d d_{y=0,l}, \quad \zeta_d = \pm 1;$$
$$w_{\gamma=1,l} = \zeta_w w_{\gamma=0,l} = w_l, \quad \zeta_w = \pm 1. \quad (8)$$

The self-consistent minimization of the mean energy $\bar{H}$ in Φ for a fixed variational parameter α and subsequent minimization in α are standard procedures [23]. The sought solution Φ is determined by the filling of lower one-electron states of the linearized Hamiltonian

$$H_{\text{lin}} = \sum_{\nu,\gamma}^{h}\frac{\partial\bar{H}}{\partial y_{\gamma\nu}}(\hat{y}_{\gamma\nu} - y_{\gamma\nu}) + t_z(\hat{z} - z) + \bar{H}(y_{\gamma\nu}, z) = \sum_k^F\hat{h}_k + \text{const}. \quad (9)$$

In turn, the value of Φ determines the order parameters $\{y_{\gamma\nu}, z\}$, thus closing the self-consistent procedure. Operators $\hat{y}_{\gamma\nu}$, $\hat{z}$ correspond to means (7), respectively. Vector $\mathbf{k}$ in Eq. (9) runs through values within the magnetic Brillouin zone F ($|k_x + k_y| \le \pi$), and operator $\hat{h}_k$ in Eq. (9) has the form

$$\hat{h}_k = h_{ij}(k)b^\dagger_{ik}b_{jk} \quad (10)$$

in the basis of the following operators of the Nambu representation:

$$b^\dagger_{ik} = \{c^\dagger_{0,k,\uparrow}, c^\dagger_{0,\tilde{k},\uparrow}, c_{0,-k,\downarrow}, c_{0,-\tilde{k},\downarrow}, c^\dagger_{1,k,\uparrow}, c^\dagger_{1,\tilde{k},\uparrow}, c_{1,-k,\downarrow}, c_{1,-\tilde{k},\downarrow}\}_i, \quad (11)$$
$$i = 1, \ldots, 8; \quad \tilde{k} = k + (\pi, \pi).$$

The difference between our calculations carried out here and in [23] lies in the doubling of the basis of Fermi operators in the bilayer system. The structure of the $h_{ij}(k)$ matrix appearing in Eq. (10) is explained in the Appendix.

The calculation of the $T_c(\delta)$ phase curves describing the superconducting transition for two versions of the symmetry of anomalous means ($w_{1l} = \pm w_{2l}$) was carried out on the basis of formulas (A.9)–(A.11). In this case, only the principal harmonic with $l = 1$ was preserved in Eqs. (7). The sufficiently high accuracy of this approximation used for calculating $T_c(\delta)$ was demonstrated by us earlier. It should be recalled that, in such an approach, the *e–e* pairing itself is due to the formation of valence bonds, viz., singlets of particles from adjacent sites [23]. The transformation $W(\alpha)$ in formulas (3) describing these correlations supplements H_{eff} with

the correlated hopping interaction (index γ is omitted below):

$$V \sim \alpha U \sum_{\langle mn\rangle,\sigma} (c^{\dagger}_{n,\sigma} c_{m,\sigma} + \text{H.c.}) \times (n_{n,-\sigma} + n_{m,-\sigma} - 2n_{n,-\sigma} n_{m,-\sigma}). \quad (12)$$

Hirsh [33] was the first to demonstrate that interactions of this type may provide for the attraction between particles. For each $\langle nm\rangle$ bond, interaction (12) contains a six-fermion contribution $V^{(6)}_{nm} \sim \alpha U c^{\dagger}_{n,\sigma} c_{m,\sigma} n_{n,-\sigma} n_{m,-\sigma}$ providing the attraction of holes in the *d* channel. This term was omitted in the truncated correlated hopping interaction of the form $V_{nm} \sim c^{\dagger}_{n,\sigma} c_{m,\sigma}(n_{n,-\sigma} + n_{m,-\sigma})$, which was used by Hirsh. He applied this interaction to extra holes with a low concentration in the oxygen subsystem. Such an interaction gives attraction only in the *s* channel. However, the one-band Hubbard model (2) corresponds to a hybridized *p–d* band with a high (of the order of unity) total concentration of holes, and the *s*-type superconductivity is suppressed by the strong repulsion *U*. At the same time, a term of the $V^{(6)}$ type, which is significant for a high concentration, gives attraction in the *d* channel. The mean value of this term contains a contribution proportional to $r_1 w_1^2$ with anomalous means of the *d* symmetry. Ultimately, for the mean energy of each layer, we obtain the expression

$$\bar{H}_{1L} = \bar{H}_{1L}(r_l, d_l) + \kappa_{ll'} w_l w_{l'}, \quad \kappa = \kappa_{11} = -8\alpha U r_1 + O(\alpha^2) < 0 \quad (13)$$

with a negative principal superconducting pairing constant k_{11}.

3. DISCUSSION

Let us first consider qualitatively the effect of the superconducting transition on the band splitting in a bilayer system $\{a_k, b_k\}$ without antiferromagnetic order. According to [27], the band splitting (2) in the normal state is given by

$$\Delta\epsilon^N_k = 2t_z \varphi_z(k), \quad \varphi_z(k) = (\cos k_x - \cos k_y)^2/4. \quad (14)$$

In the limit of a strong attraction of particles in the layers and a large superconducting gap ($\Delta_{sc} > \Delta\epsilon^N$), the wave function of the superconducting state in the zeroth approximation in V_{ab} is equal to the product of the BCS-type wave functions of each layer ($\Phi_0 = \Phi^a\Phi^b$). The splitting of excited states emerging during photoemission from such a ground state can be written in the form

$$\Delta\epsilon^{sc} = -2\langle \Phi_0 \beta_{k\uparrow} | V_{ab} | \alpha^{\dagger}_{k\uparrow} \Phi_0\rangle = (v^a_k v^b_k - u^a_k u^b_k)\Delta\epsilon^N. \quad (15)$$

Here, $\alpha^{\dagger}$ and $\beta^{\dagger}$ are the creation operators of quasiparticles, $\alpha^{\dagger} = u^a_k a^{\dagger}_{k\uparrow} - v^a_k a_{-k\downarrow}$, and a similar expression can be written for $\beta^{\dagger}$ with corresponding coefficients *u* and *v*. This leads to the following expression for the ratio of bilayer splittings in the normal and superconducting states:

$$\Delta\epsilon^{sc}/\Delta\epsilon^N = \frac{1}{2}(1 - \zeta_w) + \frac{1}{2}(1 + \zeta_w)\frac{\xi_k}{(\xi^2_k + \Delta^2_{sc})^{1/2}}, \quad (16)$$

where $\xi_k = \epsilon_k - \mu$, Δ_{sc} is the superconducting gap, and $\zeta_w = w^a_1/w^b_1 = \pm 1$ is determined by the symmetry of anomalous means of layers *a* and *b* in accordance with Eqs. (8). Thus, the first-order estimate in the interlayer interaction predicts that the bilayer splitting in the region of the Fermi boundary ($\xi_k = 0$) either vanishes or remains unchanged depending on the relative sign of anomalous means for the two layers.

Similar estimates for a system with an antiferromagnetic spin order show that the two-band splitting of states of the lower Hubbard band depends on the relative orientation ($\zeta_d = \pm 1$) of the alternating spins of the layers in Eqs. (8). In the normal state, it is given by

$$\Delta\epsilon^N_k = -t_z \varphi_z(k) \times \left\{\frac{1}{2}(1 + \zeta_d) + \frac{1}{2}(1 - \zeta_d)\frac{\epsilon_k - \epsilon_{\tilde{k}}}{2G_k}\right\}, \quad (17)$$

where $\tilde{k} = k - (\pi, \pi)$, $G_k = [(\epsilon_k - \epsilon_{\tilde{k}})^2/4 + \Delta^2_{AF}]^{1/2}$, and $\Delta_{AF} \sim Ud_0$ is the Hubbard band splitting. On nesting lines and, in particular, at point $(\pi, 0)$, the bilayer splitting (17) vanishes for the AF_z configuration ($\zeta_d = -1$) and coincides with an unperturbed interaction for the F_z configuration ($\zeta_d = 1$). In the latter case, the superconducting transition lowers the bilayer splitting in the case when anomalous means have the same sign ($\zeta_w = 1$).

Thus, the antiferromagnetic spin order blocks the bilayer splitting in the case of the AF_z (and not F_z) configuration and can be affected by the superconducting transition. This is confirmed by numerical calculations.

Let us make several preliminary remarks concerning the choice of parameters of the model (1), (2). For the ratio of the main parameters, we used the value $U/t = 8$, following from the cluster derivation of the one-band model [34, 35]. Another parameter t' controls the position of the Van Hove singularity (VHS) in the density of states $E_{VHS} = E(\pi, 0)$ relative to the edge of the lower Hubbard band owing to its contribution $\delta\epsilon^{(0)} = 4t'\cos k_x \cos k_y$ to the band dispersion. In single-layer *t–t'–U* or *t–t'–J* models, the value of t' determining the optimal doping δ_{opt} since the T_c peak corresponds to the coincidence of the chemical potential μ with E_{VHS}. According to calculations [23–27], the reasonable values of $\delta_{\text{opt}} \sim 0.2$–$0.25$ led to $t'/t \sim 0.05$–0.1.

These values differ from the estimates $t'/t \sim 0.2$–0.4 obtained from the processing of photoemission data and quantum-chemical bands on the basis of the strong-coupling approximation. The two approaches differ fundamentally. In the former case, the Hubbard band splitting is preserved in a considerable doping range ($\delta \le 0.3$), while in the second approach it is assumed that a single unsplit band exists everywhere except the region $\delta \le 0.05$ of antiferromagnetic dielectric state $t' = 0.05$–0.3. We varied parameter t' from 0.05 to 0.3 in order to find arguments supporting either of these approaches.

The parameter of the interaction between the layers was also varied in the limit $t_z/t = 0.07$–0.3. Previous calculations [27, 31, 32] led to the unrenormalized value $t_z/t \sim 1/3$. Recent (ARPES) measurements of bilayer splitting $\Delta = 2t_z = \delta\epsilon_k(\pi, 0)$ [1, 2] resulted in a value of $t_z/t \le 0.1$. The determination of the signs of t_z in Eq. (2) and of $t_\perp$ in [1, 2] corresponds to the relation $t_z = -t_\perp$.

We begin with models corresponding to small values of t' and t_z, to a higher density of states at the Fermi boundary, and a higher value of T_c.

Figure 1 shows the dependence of the difference $\Delta H = \overline{H}(AF_z) - \overline{H}(F_z)$ between the mean energies of a bilayer system on the doping for two types of the relative alignment of the spins in the layers. The following features of this dependence are worth noting.

(1) The quantity $\Delta H(\delta)$ changes its sign for a certain δ. In an undoped system ($\delta = 0$), the AF_z state with the antiparallel alignment of alternating spins in the layers is lower than the F_z state with parallel alignment (in Eqs. (8), $\zeta_d = -1$ or $+1$, respectively). For large values of δ, the situation is opposite up to the boundary value δ_c for which local magnetization vanishes and the solution becomes paramagnetic. The negative sign of $\Delta H(\delta = 0)$ can be explained by the positive exchange coupling $J_z \sim 2t_z^2/U > 0$. The sign reversal of ΔH is the result of the bilayer splitting of bonding and antibonding (in z) bands, in particular, the splitting of the Van Hove singularity and, accordingly, different populations of these bands for the two cases of spin alignment.

(2) The peak of $\Delta H(\delta)$ corresponds to the doping optimal for the 1L model with a single layer. At such a doping, $E_{VHS}^{1L} - \mu = 0$. An increase in t' simultaneously shifts δ_{opt} and the position of the peak on the $\Delta H(\delta)$ curve. Such a relationship is not accidental. According to [27, 31], the bilayer splitting $\delta\epsilon_z^{(0)} = 2t_z(\cos k_x - \cos k_y)^2/4$ of zeroth bands is maximum in the region $k \sim (\pi, 0)$ forming a Van Hove singularity in the density of states. However, the splitting can contribute to the mean energy only if the bonding and antibonding bands in the given region of k are populated and empty, respectively. The latter takes place only for the relation $E^{1L}(\pi, 0) = E_{VHS}^{1L} = \mu$ for unsplit band energies of the single layer.

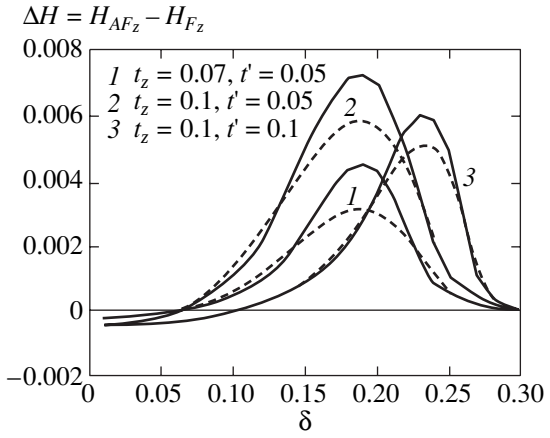

Fig. 1. Dependence of the energy difference for the two configurations of spin alignment in a bilayer system on the doping. Solid curves correspond to the normal state, and dashed curves, to the superconducting state, of a model with $U/t = 8$. The values of parameters t_z and t' in units of t are indicated in the figure.

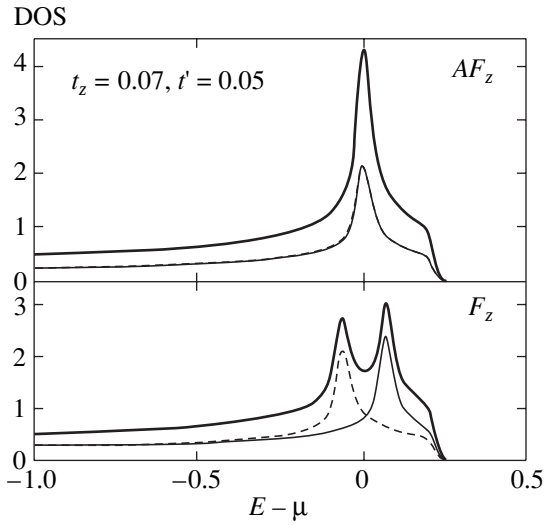

Fig. 2. Density of states for two types (AF_z and F_z) of spin alignment in a model with small t_z and t'. Thin solid and dashed curves correspond to the contributions to the DOS from the bonding and antibonding bands. The energy counted from the chemical potential is given in units of t.

It remains for us to explain why the contributions of bilayer splitting in the mean energies of different configurations do not coincide and are preserved in the difference $\Delta H = \overline{H}(AF_z) - \overline{H}(F_z)$. The reason lies in different two-band splittings for different alignments.

Figure 2 shows the density of states (DOS) of the lower Hubbard band for two configurations of spin alignment for a system with small values of t' and t_z for $\delta \sim 0.2$. The DOS(E) curve is smoothed with the help of a Gaussian function with dispersion $\delta E = 0.02t$. The

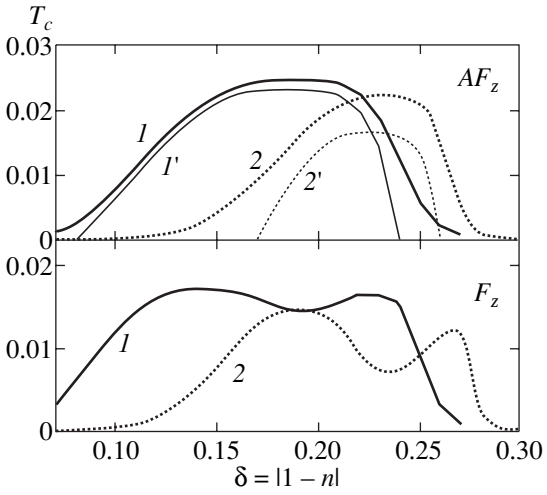

Fig. 3. Superconducting transition temperature as a function of the doping for models with parameters $U = 8$ and $t' = 0.05$, $t_z = 0.07$ (curves *1*) or $t' = 0.1$, $t_z = 0.1$ (curves *2*, *2'*) for the F_z and AF_z configurations of spin alignment. Curves *1*, *2* or *1'*, *2'* correspond to solutions with different symmetries ($\zeta_w = \pm 1$ in Eqs. (8)) of anomalous means for the two layers (only one type of symmetry survives for the F_z configuration). All quantities T_c, t', and t_z are given in units of t.

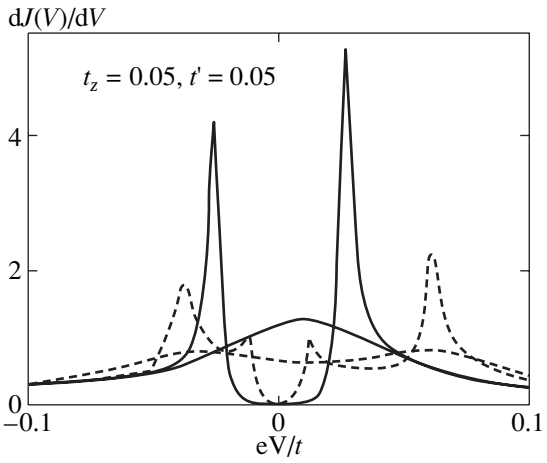

Fig. 4. Differential tunnel spectra (Eq. (A.10) for $n = 0.8$ in two configurations of spin alignment: AF_z corresponds to solid curves and F_z to dashed curves. The curves with sharp and smoothed peaks correspond to temperatures $T = 0.002t$ and $T = 0.023t$ below and above T_c, respectively.

bilayer splitting is absent for the AF_z alignment, but can be clearly observed for the F_z configurations. This is in complete accord with the splitting (17) following from the structure of the states in the lower Hubbard band.

The different behaviors of the density of states are directly reflected in the shape of the phase curves $T_c(\delta)$ of the superconducting transition. Figure 3 shows the examples of $T_c(\delta)$ calculated by formula (42) for the two models. For the AF_z configuration, we have a curve with a single peak in contrast to the case of the F_z alignment for which two peaks on the $T_c(\delta)$ curve correspond to two peaks in the density of states. For the F_z configuration, we have only a solution with symmetry $\zeta_w = 1$ of an anomalous order in Eqs. (8). The solutions of Eq. (A.9) for the AF_z alignment exist for two symmetries $\zeta_w = \pm 1$ in Eqs. (8). However, solutions with $\zeta_w = -1$ give smaller values of $T_c^{\max}$ and vanish upon an increase in parameters t' and t_z. For this reason, we will consider below only superconducting states with the symmetry $\zeta_w = 1$ of anomalous means (8).

The following characteristic properties of models with small t', $t_z \lesssim 0.1$ are worth noting.

(1) Relatively large values of $T_c^{\max} \approx 0.02t \approx 116$ K for $t = 0.5$ eV (in contrast to [23], the interaction $V > 0$ between adjacent sites, which suppresses T_c, is neglected here).

(2) Very small difference in the energies for two configurations of alignment, $|\Delta H| < kT_c^{\max}$.

(3) In the normal state for $\delta \sim \delta_{\text{opt}}$, the F_z configuration of spin alignment corresponds to a lower energy.

(4) The condensation energy in our models is low (its order can be seen in Fig. 1).

(5) Bilayer band splitting takes place for the F_z alignment but is absent or suppressed for the AF_z configuration.

The last properties is close from the physical point of view to the blocking of interlayer tunneling as a result of intralayer scattering [36, 37]. As applied to the two specific configurations of spin alignment, this property must be manifested in the tunneling spectra of the system. Figure 4 shows the differential tunnel current as a function of the applied voltage, calculated for two temperatures on the basis of formula (A.13) in the one-particle approximation for the model with $t_z = t' = 0.05t$ at a nearly optimal doping of a single-layer system. In addition to the peaks at the superconducting gap boundaries for $eV = \pm\Delta_{sc}$, the spectrum also reflects the Van Hove singularity of the normal state. In particular, two peaks can be seen for the F_z alignment at low temperatures, which correspond to the bilayer splitting of the Van Hove singularity. For $T > T_c$, the peaks are preserved on the curves in a smoothed form. For $\delta \sim \delta_{\text{opt}}^{1L}$, the peaks corresponding to the Van Hove singularity are symmetric relative to $V = 0$ and resemble the manifestation of a pseudogap in tunnel spectra. However, the symmetry is broken when δ deviates from δ_{opt}^{1L}. The results of our calculations do not allow us to attribute the pseudogap of the normal state of cuprates to bilayer splitting in view of their different doping dependences.

In contrast to the normal state, the prediction of the lower spin configuration in the superconducting state for $\delta \sim \delta_{opt}$ on the basis our analysis can hardly be regarded as unambiguous. As a matter of fact, the estimates for the condensation energy $\sim\kappa_{11} w_1^2$ and the heat capacity jump give values reduced approximately by a factor of five as compared to those observed for YBCO [38]. For this reason, we will consider the spin configuration in the superconducting state on the basis of the behavior of the bilayer splitting observed for the superconducting transition in BSCCO [1, 2]. The bilayer splitting in BSCCO observed in [2] for $k \sim (0, \pi)$ decreases from $\Delta\epsilon(0, \pi) = 80$ meV in the normal state to the value $\delta\epsilon \sim 20$ meV in the superconducting state. In light of the effects considered above for homogeneous solutions, two different explanations can be proposed for such a behavior. If we assume that the F_z configuration corresponding to a lower energy is preserved in the normal as well as superconducting states, the decrease in the value of $\Delta\epsilon$ upon the superconducting transition corresponds to the decrease predicted on the basis of formula (16). However, the decrease in the density of states due to the band splitting with such an alignment leads to relatively small values of T_c and to two peaks on the phase curve. In the other version, the behavior of $\Delta\epsilon$ during the superconducting transition could be explained by the change in spin alignment upon the superconducting transition. It cannot be ruled out that the superconducting transition itself is induced by the change in the configuration $F_z \longrightarrow AF_z$ since such a transition is accompanied by an increase in the density of states at the Fermi boundary.

For models with large values of t' and t_z, the form of the dependence of the energy difference $\Delta H(\delta)$ for the two types of alignment on the doping is preserved. It can be seen from Fig. 5 that the value of $|\Delta H|$ increases with t_z. An increase in t' shifts the position of the F_z–AF_z crossover towards higher dopings. The calculations confirm that the local magnetization $d_{\gamma 0} \neq 0$ for each layer is preserved in solutions in a considerable doping region $\delta \lesssim 0.3$ for models with large values of t_z, $t' \approx 0.1$–0.3 also. The value of d_0 is an order of magnitude higher than the antiferromagnetic spin density measured in the superconducting state of YBCO with the help of elastic neutron scattering. This difference is probably due to the spread in directions (or signs) of the spin moments for different biplanes of the crystal. The noticeable decrease in the value of $T_c^{\max}$ and the deformation of phase curves upon an increase in the values of t' and t_z are associated with a decrease in the density of states at the Fermi boundary for these models. For large values of t_z, a more intricate profile of the band energy at the boundary of the magnetic Brillouin zone leads to bilayer splitting of the Van Hove singularity, not only for the F_z, but also for the AF_z configuration, although this splitting is smaller in the latter case (see Fig. 6).

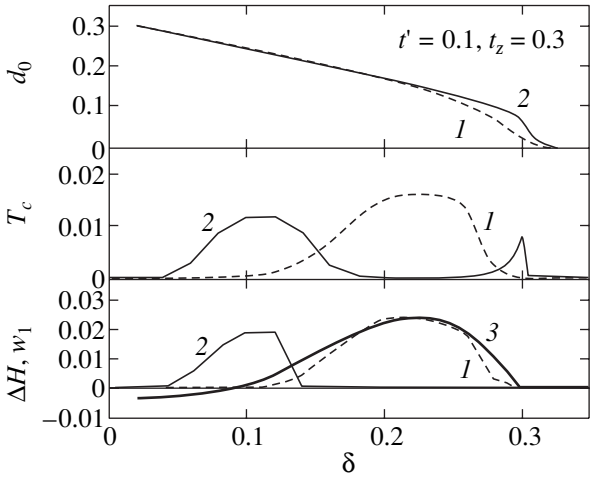

Fig. 5. Doping-level dependences of the local magnetization $d_0(\delta)$ (top), $T_c(\delta)$ (middle), and the value of anomalous order parameter $w_1(\delta)$ (bottom) for the AF_z and F_z configurations (curves *1* and *2*, respectively). Curve *3* at the bottom corresponds to the energy difference for these configurations. The values of the quantities T_c, t', t_z, and ΔH are indicated in units of t.

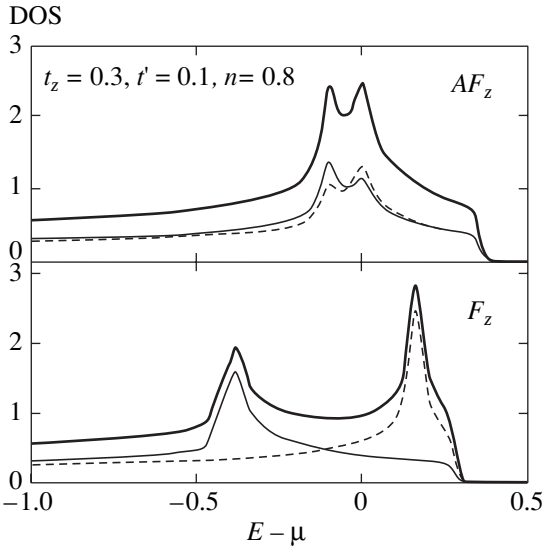

Fig. 6. Density of states for the two configurations in models with a large ratio $t_z/t = 0.3$ for $n = 0.8$. Thin solid and dashed curves correspond to contributions to the DOS from the bonding and antibonding bands of a bilayer system.

4. POSSIBLE EFFECT OF SPIN ALIGNMENT ON THE MAGNETIC EXCITATION SPECTRUM

It would be interesting to find the relation between spin alignment and the magnetic excitation spectrum in connection with the discovery of resonance in the neu-

tron scattering of bilayer cuprates in the superconducting state and with its peculiar dispersion [11–16].

According to one of the widely discussed hypotheses [39, 40], the origin of this resonance is associated with the so-called π resonance, i.e., the excitation of an *e*–*e* pair with $q \sim Q = (\pi, \pi)$ in the triplet state,

$$O^{\dagger}_{Q,\mu=1} = \sum_{p} (\cos k_x - \cos k_y) c^{\dagger}_{k+Q,\uparrow} c^{\dagger}_{-k,\uparrow}.$$

The simplest arguments supporting this hypothesis follow from the relation connecting such an excitation with spin excitations and with the *d*-wave anomalous mean *w*:

$$\langle [O^{\dagger}_{Q,\mu}, S_{Q,-\mu}] \rangle \sim w_1.$$

However, in this case, the integral (in ω) weight of the resonance, which is of the order of w_1^2/d_0, must differ from the integral intensity

$$I_q \sim \langle [S_{q+Q,\mu}, S_{-q,-\mu}] \rangle \sim d_0$$

of transverse spin waves by more than an order of magnitude since the ratio w/d_0 of the anomalous and spin order parameters is approximately equal to 0.1–0.2. The explanation of spin excitations and incommensurate peaks in the susceptibility $\chi''(q, \omega)$ by the properties of the Fermi surface (see, for example, [41]) also contradicts the high integrated intensity. In addition, in doped systems, it varies only slightly as compared to the same characteristic of an undoped insulator. The most feasible hypothesis is that of the general magnetic origin of incommensurate anomalies in $\chi''(q, \omega)$ and of the resonance [42]. This origin is associated with the presence of antiferromagnetic domains, i.e., incommensurate modulation of the local alternating spin [42]. The existence of the stripe structure was confirmed for LaSrCuO [43] and is also possible for double-layer cuprates. However, when this hypothesis is applied for bilayer cuprates, the fact that the resonance appears only in the superconducting state and only in the odd channel cannot be explained. For double-layer cuprates, the effect of relative spin alignment on the magnetic excitation spectrum is significant and must be taken into consideration apart from the effect of incommensurate configurations.

This section is devoted to an analysis of the effects of the influence of spin alignment on the magnetic excitation spectrum for the simplest homogeneous states of a bilayer system.

Let us consider the phenomenological spin Hamiltonian describing the bilayer model $\{S_a, S_b\}$:

$$H = \sum_{\gamma=0,1} J_0 \sum_{\langle nm \rangle} \mathbf{S}^{\gamma}_n \mathbf{S}^{\gamma}_m + V_{ab}, \tag{18}$$

$$V_{ab} = J_{ab} \sum_{n\gamma} \mathbf{S}^{\gamma}_n \mathbf{S}^{1-\gamma}_n. \tag{19}$$

Index $\gamma = 0, 1$ corresponds to layers *a* and *b*. We assume that the homogeneous ground state is characterized by the spin density

$$\langle \mathbf{S}^{\gamma}_n \rangle = (\zeta_d)^{\gamma} \mathbf{e}_z (-1)^n d_0, \quad \gamma = 0, 1, \tag{20}$$

with a certain alignment ($\zeta_d = 1$ or $\zeta_d = -1$) stabilized by spinless interactions. We calculate the transverse susceptibilities in the even and odd channels,

$$\chi^{\text{even(odd)}}_{\mu}(q, \omega) = i \int_0^{\infty} e^{i\omega t} \sum_{\gamma\gamma'} (\pm 1)^{\gamma+\gamma'} \times \langle \langle S^{\gamma}_{\mu q}(t) | (S^{\gamma'}_{\mu q})^{\dagger} \rangle \rangle dt, \tag{21}$$

in the RPA approximation on the basis of the linear theory of spin waves [44]. In this relation, $S_{\mu} = S_x + \mu i S_y$, $\mu = \pm 1$, $\langle \langle A|B \rangle \rangle = \langle [A, B] \rangle$, and the signs ± correspond to the even and odd components, respectively. The parity (even/odd ratio) is determined relative to the transposition of the layers.

Linearizing the equations of motion for the spin components $S^{\gamma}_{\mu q}(t)$, we obtain

$$\text{Im}[\chi^{\nu}(q, \omega)] = I^{\nu}(q)[\delta(\omega - \omega^{\nu}_q) - \delta(\omega + \omega^{\nu}_q)], \tag{22}$$

where ν = even, odd. For the frequencies of transverse spin excitations for the F_z (AF_z) alignment ($\zeta_d = \pm 1$), we obtain

$$F_z: \omega^{\text{even}}(q) = \Omega \sqrt{\varphi \tilde{\varphi}}, \quad \omega^{\text{odd}}(q) = \Omega \sqrt{(\varphi - g)(\tilde{\varphi} - g)}, \tag{23}$$

$$AF_z: \omega^{\text{even}}(q) = \Omega \sqrt{(\varphi + g)\tilde{\varphi}}, \quad \omega^{\text{odd}}(q) = \Omega \sqrt{\varphi(\tilde{\varphi} + g)}. \tag{24}$$

Here,

$$\varphi = 2 + \cos q_x + \cos q_y, \quad \tilde{\varphi} = 2 - \cos q_x - \cos q_y, \quad g = J_{ab}/J_0, \quad \Omega = 2 J_0 d_0, \tag{25}$$

q corresponds to the complete Brillouin zone, so that the most intense excitation peaks in $\chi''(q, \omega)$ for $q \longrightarrow Q = (\pi, \pi)$ correspond to the gapless excitation branches $\omega_q = c|q - Q|$.

Expression (25) coincides (except for a multiplier) with the results obtained in [45] for a bilayer system from the spin-wave theory. In contrast to [45], here, as well as in the linear theory [43] and in the band RPA calculations of $\chi(q, \omega)$ [21, 28, 29], the frequencies and intensities of spin fluctuations are proportional to the alternating spin density d_0.

The dispersions of frequencies (23) and (24) are presented in Fig. 7. For $J_{ab} > 0$, the spin gap $\Delta = 4d_0\sqrt{J_0 J_{ab}}$ for undoped systems with the AF_z alignment is open in

the even (optical) excitation branch. For the opposite sign ($J_{ab} < 0$), the excitation frequencies for the F_z and AF_z configurations change place simultaneously with the even $\longleftrightarrow$ odd transposition of the excitation channels.

In the case of the AF_z configuration, the doping of the system leads to a decrease in the value of d_0, in the spin wave velocity, and in the spin gap for the even channel. Such a behavior completely corresponds to the observed decrease in the spin gap in weakly doped $YBa_2Cu_3O_{6.25}$. Homogeneous systems with a high doping and with the lower F_z configuration have gapless excitations for $|q - Q| = \sqrt{2g}$, but not for discrete incommensurate values of quasimomentum as in the case of YBCO and BSCCO [13, 14].

The lower value of energy in the F_z configuration implies a negative contribution to the effective exchange interaction constant J_{ab}. For this reason, we consider a more general spin interaction V_{ab} between the layers by introducing, for example, anisotropy, i.e., different constants of the interaction between the layers for the longitudinal and transverse components:

$$V_{ab} = \sum_n \{ J_{z,ab} S^a_{zn} S^b_{zn} + J_{\perp,ab} (S^a_{xn} S^b_{xn} + S^a_{yn} S^b_{yn}) \}. \quad (26)$$

The z direction in the "spin" system of coordinates is determined by the vector of alternating spin $\langle \mathbf{S}^\gamma_n \rangle = \mathbf{e}_z (\zeta_d)^\gamma d_0$, $\gamma = 0, 1$, for each layer a or b.

In the case of the F_z alignment, the frequencies $\omega(q)$ and intensities $I(q)$ of susceptibility (22) are given by

$$\omega^{\text{even}}(q) = \Omega \sqrt{(\varphi - g_1)(\tilde{\varphi} - g_1)},$$
$$I^{\text{even}}(q) = I_0 \sqrt{(\tilde{\varphi} - g_1)/(\varphi - g_1)}, \quad (27)$$

$$\omega^{\text{odd}}(q) = \Omega \sqrt{(\varphi - g_2)(\tilde{\varphi} - g_2)},$$
$$I^{\text{odd}}(q) = I_0 \sqrt{(\tilde{\varphi} - g_2)/(\varphi - g_2)}. \quad (28)$$

In the case of the AF_z alignment, the corresponding quantities have the form

$$\omega^{\text{even}}(q) = \Omega \sqrt{(\varphi + g_2)(\tilde{\varphi} + g_1)},$$
$$I^{\text{even}}(q) = I_0 \sqrt{(\tilde{\varphi} + g_1)/(\varphi + g_2)}, \quad (29)$$

$$\omega^{\text{odd}}(q) = \Omega \sqrt{(\varphi + g_1)(\tilde{\varphi} + g_2)},$$
$$I^{\text{odd}}(q) = I_0 \sqrt{(\tilde{\varphi} + g_2)/(\varphi + g_1)}. \quad (30)$$

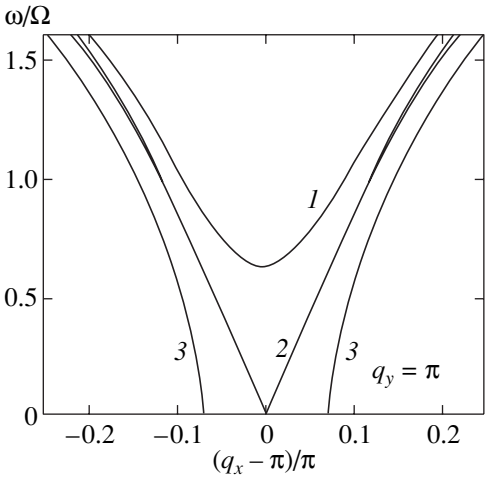

Fig. 7. Magnetic excitation branches $\omega(q)$ of a bilayer system for two spin configurations in a model with $g = J_{ab}/J_0 = 0.1$. Curves *1* and *2* correspond to $\omega^{\text{even(odd)}}$ for the AF_z configuration, while curves *2* and *3* correspond to $\omega^{\text{even(odd)}}$ for the F_z alignment. For $g = -0.1 < 0$, the same curves *1*, *2* or *2*, *3* correspond to the $\omega^{\text{odd(even)}}$ channels.

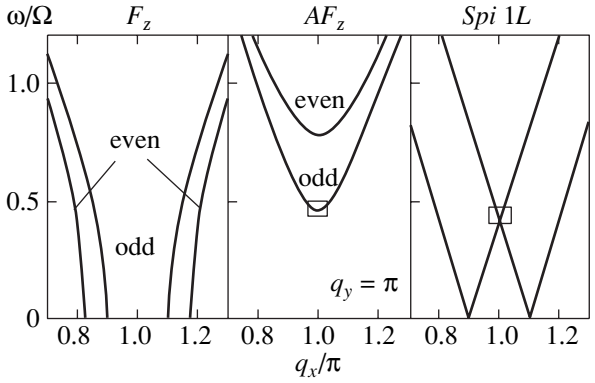

Fig. 8. The curves for F_z and AF_z demonstrate the change in the magnetic excitation spectra upon the change $F_z \longrightarrow AF_z$ in the spin configuration for a model with anisotropic interlayer interaction (22) for the values of parameters $g_1 = 0.05$ and $g_2 = 0.15$. The right figure shows schematically the excitation branches in the case of a spiral (Sp) or modulated incommensurate spin structure of the ground state with $Q_\eta = (\pi(1 - \eta), \pi)$ and $\eta = 0.1$. The square marks the predicted resonance frequencies in the interpretation based on homogeneous solutions in the bilayer model (center) or the interpretation [42] based on a modulated structure in the single-layer model.

Here, Ω and the functions $\varphi = \varphi(q)$ and $\tilde{\varphi} = \varphi(q + Q)$ are defined by Eqs. (25), while the quantities $g_{1(2)}$ and I_0 are given by

$$g_{1(2)} = \frac{J_{z,ab} \mp J_{\perp,ab}}{2J_0}, \quad I_0 = 2\pi d_0. \quad (31)$$

For $g_2 > g_1 > 0$ and for the AF_z alignment, spin gaps open in the even and odd channels:

$$\Delta^{\text{even(odd)}} = 2\Omega\sqrt{g_{2(1)}}. \quad (32)$$

Thus, the low-frequency spin excitations with $\omega < \Delta^{\text{odd}} < \Delta^{\text{even}}$ are absent for the AF_z configuration. At the same time, the excitation spectrum for the F_z configuration is gapless for the same relation $g_2 > g_1 > 0$. However, the low-frequency peaks are characterized by a relatively low intensity and are observed beginning from the incommensurate quasimomenta

$$|\mathbf{q} - \mathbf{Q}| > \delta q^{\text{v}}, \quad \delta q^{\text{even(odd)}} = \sqrt{2g_{1(2)}}. \quad (33)$$

Figure 8 shows the dispersion of spin excitations in the even and odd channels for the two types of alignment for a model with $g_1 = 0.05$ and $g_2 = 0.15$. If the superconducting transition occurs simultaneously with the spin configuration rearrangement $F_z \longrightarrow AF_z$ in accordance with the above hypothesis, an intense peak appears in the odd channel (χ^{odd}) for $q \sim (\pi, \pi)$ at a frequency $\omega = \Delta^{\text{odd}} = 2\Omega\sqrt{g_1}$. This peak was absent in the F_z configuration, which, in accordance with our assumption, is the main configuration for $T > T_c$. This homogeneous model fails to describe the susceptibility peaks $\chi''(q, \omega \longrightarrow 0)$ for incommensurate discrete values of quasimomenta $Q_\eta = (\pi)(1 + \eta), \pi)$ observed for YBCO and BSCCO [12, 14] and indicating the presence of incommensurate structures. A generalization of such kind of structures is essential. The right part of Fig. 8 shows schematically the spin excitation branches for spiral states [28, 29] or states with a modulation of the local spin $\langle S_{zn}\rangle = d_0 \cos \mathbf{Q}_\eta \mathbf{n}$ [42] in single-layer (1L) models. The resonance frequency in [42] was identified with the frequency $\omega(Q)$ corresponding to the intersection of the branches for $Q = (\pi, \pi)$. With such a pattern, it is unclear, however, how the emergence of the resonance is connected with the superconducting transition and why the resonance is observed only in the odd channel.

5. CONCLUSIONS

1. In the models with the interlayer mechanism of superconducting pairing, the maximum superconducting transition temperature $T_c^{\max}$ for homogeneous solutions obtained for a bilayer system does not exceed the corresponding value for a single-layer system. This disagrees with the observed difference in the values of $T_c^{\max}$ for cuprates. Probably, T_c in single-layer cuprates is suppressed by inhomogeneities of the stripe type structure.

2. The local magnetization d_0 is preserved in a broad doping region for a wide range of parameters t' and t_z. The value of d_0 is an order of magnitude larger than the antiferromagnetic spin density measured in the superconducting state of YBCO by the elastic neutron scattering. The difference is probably associated with the spread in the directions (or signs) of spin moments in different bilayer planes of the crystal.

3. A crossover of the two configurations of the spin system upon a change in the doping is revealed. The lower state for small values of δ with the AF_z alignment is replaced by the lower state with the F_z alignment of alternating local spins of the layers for large values of δ. The peak of the energy difference between these configurations corresponds to the optimum doping of a single-layer system and is connected with the splitting of Van Hove singularities, which is the strongest in this case. The small energy difference for these configurations indicates the possibility of a strong effect of temperature (and, probably, condensation of pairs) on the spin alignment.

4. The bilayer band splitting $\delta\epsilon(k)$ and, in particular, the splitting of a Van Hove singularity in the density of states are absent for the AF_z alignment, but are clearly manifested for the F_z alignment of local spins in the layers.

5. According to our models, the large bilayer splitting observed in $Bi_2Sr_2CaCu_2O_{8+\delta}$ in the normal state and the small splitting in the superconducting state [2] may indicate a transformation of the spin alignment configuration ($F_z \longrightarrow AF_z$) in the course of or simultaneously with the superconducting transition. Further investigations are required in order to find out whether a transformation of this type or a rearrangement of more complex spin structures of the stripe type can explain the emergence of magnetic resonance in neutron scattering in the superconducting state of double-layer cuprates.

6. It is shown that the magnetic excitation spectrum strongly depends on the type of spin alignment. An example of a spin model in which the configuration change from F_z to AF_z leads to the emergence of resonance (spin excitation gap) in χ^{odd} in the odd channel for $q = (\pi, \pi)$ is considered.

One of the urgent problems is an extension of the study to inhomogeneous stripe-type spin structures of bilayer systems.

ACKNOWLEDGMENTS

The authors are grateful to V.Ya. Krivnov for stimulating discussions of the problem and to P. Fülde for the opportunity to work at the Max Planck Institute of the Physics of Complex Systems.

This work was supported by the Russian Foundation for Basic Research (project nos. 00-03-32981 and 00-15-97334).

APPENDIX

The mean energy (6) for Hamiltonian (1) after transformation (5) can be presented in the form

$$\overline{H}(y_\nu, z) = \sum_\gamma \overline{H}_\gamma(r_{\gamma l}, d_{\gamma l}, w_\gamma) + t_z z. \tag{A.1}$$

Here, $H_\gamma(y_{\gamma\nu})$ are the contributions from each layer $\gamma = 0, 1$, and the last term is the contribution from hopping between the layers. The quantities z, $y_{\gamma\nu} = \{r_{\gamma l}, d_{\gamma l}, w_\gamma\}$ are defined by Eqs. (7). The expressions for $\overline{H}_\gamma(y_{\gamma\nu})$ in the single-layer Hubbard model were derived earlier [1, 2].

The eighth-order matrices $h_{ij}(k)$ determining the linearized Hamiltonian (9) in the basis of operators (11) are given by

$$h_{ij} = \begin{pmatrix} A_1 & h_z \\ h_z^\dagger & A_2 \end{pmatrix}, \tag{A.2}$$

$$(h_z)_{ll'} = t_z\varphi^2(k)\delta_{l,l'}\{1, 1, -1, -1\}_l, \quad l, l' = 1, \ldots, 4. \tag{A.3}$$

Blocks A_γ of the fourth order correspond to each layer $\gamma = 0, 1$. The expressions for these blocks in terms of the derivatives $\partial\overline{H}_\gamma/\partial y_{\gamma\nu}$ were given earlier [23].

The diagonalization of matrix (A.2),

$$h_{ij}U_{j,\lambda} = U_{j,\lambda}E_{k\lambda}, \quad i, j, \lambda = 1, \ldots, 8, \tag{A.4}$$

for each k gives energies $E_{k\lambda}$ and eigenoperators in the basis of operators (11):

$$\chi^\dagger_{k\lambda} = \sum_j b^\dagger_{kj}U_{j,\lambda}. \tag{A.5}$$

Their knowledge makes it possible to calculate the set of mean values $\{y_{\gamma\nu}, z\}$ in accordance with the equations

$$y_{\gamma\nu} = \frac{1}{N}\sum_k^F g_\nu[\theta_{\gamma\nu}]_{ij}U^*_{i\lambda}U_{j\lambda}f_\lambda,$$
$$z = \frac{1}{N}\sum_k^F g_z[\theta_z]_{ij}U^*_{i\lambda}U_{j\lambda}f_\lambda, \tag{A.6}$$

$$\theta_{\gamma\nu} = \begin{pmatrix} \theta^{00}_\nu & 0 \\ 0 & \theta^{11}_\nu \end{pmatrix}, \quad \theta_z = \begin{pmatrix} 0 & \theta^{01}_z \\ \theta^{10}_z & 0 \end{pmatrix}. \tag{A.7}$$

In Eqs. (A.6), $f_\lambda = f(E_{k\lambda})$ are the Fermi functions. The weight functions $g_\nu(k)$ and the structure of the matrices follow from definition (7) of quantities $y_{\gamma\nu}$. The functions $r_{\gamma\nu}$ for $d_{\gamma\nu}$ and the 4×4 blocks θ^{ii}_ν in Eqs. (A.6) and (A.7) are the same as those presented earlier for a single-layer system. The quantity z is defined in accordance with Eqs. (A.6) and (A.7), in which

$$g_z(k) = \frac{1}{4}(\cos k_x - \cos k_y)^2,$$
$$(\theta^{01}_z)_{ll'} = (\theta^{10}_z)_{ll'} = \delta_{ll'}\{1, 1, -1, -1\}_l. \tag{A.8}$$

The equation for T_c used for computing phase curves is derived by expanding the right- and left-hand sides of the equations for w_γ from Eqs. (A.6) for $w_\gamma \longrightarrow 0$. Thus, $w_{\gamma=1} = \zeta_w w_{\gamma=0}$ and $\zeta_w = \pm 1$ for both types of symmetry of the superconducting order of a bilayer system. As a result, we obtain the following equations for T_c:

$$1 = \kappa(r_{\gamma l}d_{\gamma l}) \times \frac{1}{N}\sum_k^F \sum_{\lambda,\lambda'} \left|U^*_{i\lambda}\theta^w_{ij}U_{j\lambda}\right|^2 \frac{f_\lambda - f_{\lambda'}}{E_\lambda - E_{\lambda'}}\varphi_1^2(k). \tag{A.9}$$

Here, $f_\lambda = f(E_{k\lambda})$ are the Fermi functions; E_λ and $U_{i\lambda}$ are determined by the solution of the linear problem (A.4) for a given k; and $\varphi_1(k) = \cos k_x - \cos k_y$. The eighth-order matrix θ^w depends on the superconducting order symmetry ($\zeta_w = \pm 1$ in Eqs. (8)) and is given by

$$\theta^w_{ij} = \begin{pmatrix} a & 0 \\ 0 & a \end{pmatrix}, \quad a = \begin{pmatrix} 0 & \sigma_3 \\ \zeta_w\sigma_3 & 0 \end{pmatrix}. \tag{A.10}$$

The pairing constant κ in Eq. (A.9) for the effective Hamiltonian (5) is given by

$$\kappa = \frac{1}{4}\sum_\gamma \frac{\partial^2\overline{H}_\gamma}{\partial w_\gamma^2}. \tag{A.11}$$

The main negative contribution to κ comes from the quantity appearing in Eqs. (13). Tunnel current in the so-called *S–I–N* contact typical of STM is calculated in the one-particle approximation. The total tunnel current $J(V) = e(W_\mathrm{I} - W_\mathrm{II})$ is determined by the probabilities $W_{\mathrm{I(II)}}$ of the electron transition from the superconductor to the metal and back. We simulate the tunnel interaction between the metal states ($d_{\epsilon\sigma}$) and the external layer (say, through the layer $\gamma = 1$) of the bilayer superconductor by the expression

$$V_\mathrm{tun} = \sum_{\sigma,n} F(k)(c^\dagger_{1,k,\sigma}d_{\epsilon,\sigma} + \mathrm{H.c.}). \tag{A.12}$$

In this case, the differential tunnel current as a function of the applied potential difference eV is given by

$$\frac{dI(V)}{dV} = -\frac{1}{N}\sum_k^F \{[U^2_{1\lambda}R + U^2_{2\lambda}\tilde{R}]f'(E_{k\lambda} - eV) + [U^2_{3\lambda}R + U^2_{4\lambda}\tilde{R}]f'(E_{k\lambda} + eV)\}. \tag{A.13}$$

Here, $R = F^2(k)$, $\tilde{R} = F^2(\tilde{k})$; $f'(E) = df/dE$ is the derivative of the Fermi function; and $U_{i\lambda}$ and $E_{k\lambda}$ determine the solutions of the linear problem (A.4) in the basis of operators (11). The form factor $F(k) = \varphi_1^2(k)$ is taken in the same form as for the bilayer splitting in Eq. (2).

REFERENCES

1. Y.-D. Chuan, A. D. Gromko, A. Fedorov, *et al.*, cond-mat/0102386.
2. D. L. Feng, N. P. Armitage, D. H. Lu, *et al.*, cond-mat/0102385.
3. J. Mesot, M. Boehm, M. R. Norman, *et al.*, cond-mat/0102339.
4. S. Chakravarty, S. Sudbo, P. W. Anderson, and S. Strong, Science **261**, 337 (1993); P. W. Anderson, *The Theory of Superconductivity in High-T_c Cuprates* (Princeton Univ. Press, Princeton, New-Jersey, 1997).
5. H. M. Fretwell, A. Kaminski, J. Mesot, *et al.*, Phys. Rev. Lett. **84**, 4449 (2000).
6. S. V. Borisenko, M. S. Golden, S. Legner, *et al.*, Phys. Rev. Lett. **84**, 4453 (2000).
7. J. Mesot, M. Randeria, M. R. Norman, *et al.*, Phys. Rev. B **63**, 224516 (2001); cond-mat/9910430.
8. N. L. Saini, J. Avila, A. Bioconi, *et al.*, Phys. Rev. Lett. **79**, 3467 (1997).
9. Y.-D. Chuang, A. D. Gromko, D. S. Dessau, *et al.*, Phys. Rev. Lett. **83**, 3717 (1999).
10. P. V. Bogdanov, A. Lanzara, X. J. Zhou, *et al.*, cond-mat/0005394.
11. J. N. Tranquada, G. Shirane, B. Keimer, *et al.*, Phys. Rev. B **40**, 4503 (1989).
12. P. Bourges, in *The Gap Symmetry and Fluctuations in High Temperature Superconductors*, Ed. by J. Bok, G. Deutscher, D. Pavuna, and S. A. Wolf (Plenum, New York, 1998), p. 349.
13. P. Bourges, Y. Sidis, H. F. Fong, *et al.*, Science **288**, 1234 (2000).
14. H. A. Mook, P. Dai, F. Dogan, *et al.*, Nature **404**, 729 (2000).
15. P. Dai, H. A. Mook, R. D. Hunt, *et al.*, Phys. Rev. B **63**, 54525 (2001).
16. P. Dai, H. A. Mook, S. M. Hayden, *et al.*, cond-mat/0001249.
17. A. Rigamonti, F. Borza, and P. Carett, Rep. Prog. Phys. **61**, 1367 (1998).
18. Ch. Niedermayer, C. Bernhard, T. Blasius, *et al.*, Phys. Rev. Lett. **80**, 3843 (1998).
19. H. A. Mook, P. Dai, F. Dogan, *et al.*, cond-mat/0102047.
20. Y. Sidis, C. Ulrich, P. Bourges, *et al.*, cond-mat/0101095; Phys. Rev. Lett. **86**, 4100 (2001).
21. J. R. Schrieffer, X. G. Wen, and F. C. Zhang, Phys. Rev. B **39**, 11663 (1989).
22. U. Trapper, D. Ihle, and H. Fenke, Phys. Rev. B **52**, 11553 (1995).
23. A. A. Ovchinnikov and M. Ya. Ovchinnikova, Phys. Lett. A **249**, 531 (1998); A. A. Ovchinnikov, M. Ya. Ovchinnikova, and E. A. Plekhanov, Pis'ma Zh. Éksp. Teor. Fiz. **67**, 350 (1998) [JETP Lett. **67**, 369 (1998)]; Zh. Éksp. Teor. Fiz. **114**, 985 (1998) [JETP **87**, 534 (1998)]; Zh. Éksp. Teor. Fiz. **115**, 649 (1999) [JETP **88**, 356 (1999)]; A. A. Ovchinnikov and M. Ya. Ovchinnikova, Zh. Éksp. Teor. Fiz. **120**, 175 (2001) [JETP **93**, 153 (2001)].
24. N. M. Plakida, V. S. Oudovenko, P. Horsch, and A. J. Liechtenstein, Phys. Rev. B **55**, 11997 (1997).
25. R. O. Kuzian, R. Hayn, A. F. Barabanov, and L. A. Maksimov, Phys. Rev. B **58**, 6194 (1998).
26. F. Onufrieva, P. Pfeuty, and M. Kiselev, Phys. Rev. Lett. **82**, 2370 (1999).
27. A. I. Liechtenstein, O. Gunnarsson, O. K. Andersen, and R. M. Martin, Phys. Rev. B **54**, 12505 (1996).
28. A. V. Chubukov and K. A. Mussaelian, Phys. Rev. B **51**, 12605 (1995).
29. A. A. Ovchinnikov and M. Ya. Ovchinnikova, Zh. Éksp. Teor. Fiz. **116**, 1058 (1999) [JETP **89**, 564 (1999)].
30. B. I. Schraiman and E. D. Siggia, Phys. Rev. B **40**, 9162 (1989).
31. O. K. Andersen, O. Jepsen, A. I. Liechtenstein, and I. I. Mazin, Phys. Rev. B **49**, 4145 (1994).
32. D. L. Novikov and A. J. Freeman, Physica C (Amsterdam) **212**, 273 (1993).
33. J. E. Hirsh, Phys. Rev. B **39**, 11515 (1989); cond-mat/0106310.
34. J. H. Jefferson, H. Eskes, and L. F. Feiner, Phys. Rev. B **45**, 7959 (1992).
35. H. B. Schuttler and A. J. Fedro, Phys. Rev. B **45**, 7588 (1992).
36. N. Kumar, T. P. Pareek, and A. M. Jayannavar, Phys. Rev. B **57**, 13399 (1998).
37. S. Chakravarty and P. Anderson, Phys. Rev. Lett. **72**, 3859 (1994).
38. D. M. Ginsberg, in *Physical Properties of High Temperature Superconductors*, Ed. by D. M. Ginsberg (World Sci., Singapore, 1989; Mir, Moscow, 1990).
39. E. Demler and S. C. Zhang, Phys. Rev. Lett. **75**, 4126 (1995).
40. O. Tchernyshyov, M. R. Norman, and A. V. Chubukov, cond-mat/0009072.
41. A. A. Abrikosov, Phys. Rev. B **62**, 15156 (2000).
42. C. D. Batista, G. Ortiz, and A. V. Balatsky, cond-mat/0008345.
43. R. J. McQueeney, J. L. Sarrao, P. G. Pagliouso, *et al.*, cond-mat/0104118.
44. T. Ziman and P.-A. Lindgard, Phys. Rev. B **33**, 1976 (1986).
45. D. Reznik, P. Bourges, L. P. Regnault, *et al.*, Phys. Rev. B **53**, 14741 (1996).

Translated by N. Wadhwa

Journal of Experimental and Theoretical Physics, Vol. 94, No. 1, 2002, pp. 135–148.
Translated from Zhurnal Éksperimental'noĭ i Teoreticheskoĭ Fiziki, Vol. 121, No. 1, 2002, pp. 160–174.

SOLIDS
Electronic Properties

The Effect of Quasinesting and a Magnon Mode on the Antiferromagnetic Vector for the Optical Conductivity of a Doped Two-Dimensional Antiferromagnet

S. A. Gordyunin[a], A. M. Belemouk[b], A. E. Karakozov[b], and A. F. Barabanov[b, *]

[a]*Moscow Institute of Physics and Technology, Dolgoprudnyĭ, Moscow oblast, 141700 Russia*
[b]*Vereshchagin Institute of High-Pressure Physics, Russian Academy of Sciences, Troitsk, Moscow oblast, 142190 Russia*
**e-mail: abarabanov@mtu-net.ru*

Received June 19, 2001

Abstract—The optical spectrum of the normal state of a doped two-dimensional antiferromagnet is analyzed in a Kondo lattice model with regard to the complex structure of a spin polaron. The optical properties are determined by sharply anisotropic scattering of spin–polaron excitations by antiferromagnetic fluctuations of a system of localized spins. It is shown that the relaxation of carriers in the infrared range is mainly attributed to the strong coupling between these carriers and the mode of low-frequency spin excitations with the quasimomentum close to the antiferromagnetic vector $\mathbf{Q} = (\pi, \pi)$. The latter coupling is associated with the fact that the regions of the Fermi surface of the lower polaron band are close to the boundary of the antiferromagnetic Brillouin zone. The calculated optical characteristics are in qualitative agreement with experimental data for the normal state of high-temperature superconductors (HTSCs). *© 2002 MAIK "Nauka/Interperiodica".*

1. INTRODUCTION

At present, the optical properties of the CuO_2 plane are being intensively studied in view of the fact that this plane represents the basic structural element of high-temperature superconductors (HTSCs) (see, for example, [1–7] and survey [8]). Investigations in the field of infrared radiation give valuable information about the scattering of charge carriers. In particular, the theoretical analysis of optical data about HTSCs, combined with photoemission data on quasiparticle excitations and neutron data on a boson subsystem, can give information about the relative amplitude of scattering of charge carriers by phonons and spin fluctuations. Such an analysis is carried out both on the basis of the traditional electron–phonon scenario of coupling (within the Eliashberg formalism) [8] and within the models of strongly correlated electrons that are based on various modifications of the Hubbard model (which takes into account a strong coupling between electron and spin subsystems) [9].

The experimental data obtained in [10] exhibit strong anisotropy in the optical properties in the directions parallel and normal to the CuO_2 planes as well as the high sensitivity of these properties to the carrier density in these planes. Below, we will restrict the analysis to the optical properties of the normal state in the *ab* plane.

Experiments carried out in the infrared range in the *ab* plane for various cuprates (for example, those based on lanthanum, $La_{2-x}Sr_xCuO_4$ [2]; yttrium, $YBa_2Cu_3O_{6+x}$ (YBCO) [1]; bismuth, $Bi_2Sr_2CaCu_2O_8$ (Bi2212) [3, 5] and $Bi_2Sr_2CuO_6$ (Bi2201) [4–6]; and certain other HTSCs [7]) show that these substances exhibit the same properties near the optimal doping level: a sharp peak at zero frequency and a non-Drude tail of optical conductivity $\sigma(\omega)$ in the range of higher infrared frequencies, the spectral weights of this peak and the tail being strongly dependent on the doping level; linear temperature dependence of the electric conductivity ρ; strong frequency dependence of the relaxation time and effective mass; and nearly linear frequency dependence of the reflectivity $R(\omega)$.

A number of models have been proposed to give a theoretical explanation for the optical properties of the normal state of cuprates. Here, we mention the models based on the electron–phonon coupling [11, 12], on the theory of almost antiferromagnetic Fermi liquid [13], and on the electron–electron scattering in a nested Fermi liquid [14], as well as the studies within the *t–J* model based on the method of Hubbard operators [15] and the method in which fermion operators are represented by products of holons and spinons [16]. A number of approaches, including computational methods, were presented in survey [9].

Usually, the optical conductivity $\sigma(\omega)$ is considered in terms of the generalized Drude formula

$$\sigma(\omega) = \frac{\omega_{pl}^2}{4\pi}\frac{m}{m^*(\omega)}\frac{1}{1/\tau^*(\omega) - i\omega}, \qquad (1)$$

where the functions $m^*(\omega)$ and $1/\tau^*(\omega)$ are interpreted as the optical (or transport) effective mass and the relaxation rate, respectively.

In the traditional approach, the square of the plasma frequency, ω_{pl}^2, is related to the Fermi velocity through the formula ($h = 1$)

$$\frac{\omega_{pl}^2}{4\pi} = 2e^2\frac{1}{N}\sum_{\mathbf{k}} v_x^2(\mathbf{k})\delta(\varepsilon_{\mathbf{k}}), \quad (2)$$

where $v_x(\mathbf{k})$ is the velocity and $\varepsilon_{\mathbf{k}}$ is the energy of a quasiparticle with quasimomentum $\mathbf{k}$. In the simplest, isotropic, case, we have

$$\frac{\omega_{pl}^2}{4\pi} = \frac{e^2 n}{m}, \quad (3)$$

where n and m are the density of quasiparticles and their mass, respectively.

The theoretical analysis of the optical data on HTSCs within the Eliashberg formalism shows [8] that the optical properties of the normal state of HTSC compounds are primarily determined by a relatively strong coupling (with a coupling constant of $\lambda \sim 2$) of charge carriers to phonon excitations with energies of at least 500 K. An appropriate choice of $\omega_{pl} \sim 2.5$–3 eV allows one to correctly describe the infrared behavior of the reflectivity $R(\omega)$ [11] and the temperature dependence of the resistivity; the result weakly depends on a particular form of the Eliashberg transport function $\alpha_{tr}^2(\omega)F(\omega)$.

At the same time, it is known from the data on inelastic scattering of spin-polarized neutrons that spin excitations in the normal state of an HTSC have a resonant structure at energies of 300 K, i.e., at energies comparable with the aforementioned phonon energies. The spin excitations responsible for this resonance are determined by the quasimomenta of magnons close to the antiferromagnetic vector $\mathbf{Q} = (\pi, \pi)$ [17]. Actually, the coupling constant λ of these excitations to carriers is unknown. In a number of papers [18, 19], this constant is used as a fitting parameter for describing an experimental situation under the assumption that the coupling is of d character. The coupling to a spin subsystem is also introduced purely phenomenologically [13] with the use of various model forms of the spin susceptibility $\chi(\mathbf{q} + \mathbf{Q}, \omega)$ near the antiferromagnetic vector $\mathbf{Q}$; for example,

$$\chi(\mathbf{q} + \mathbf{Q}, \omega) = \frac{\chi_Q(T)}{1 + \xi^2 q^2}\frac{1}{1 - i\tanh(\omega/\omega_{SF})},$$

$$\omega_{SF}(q) = \frac{\Gamma}{\pi\sqrt{\beta}}\left(\frac{a}{\xi}\right)^2(1 + \xi^2 q^2),$$

where $\chi_Q(T)$ is the static spin susceptibility for the vector $\mathbf{Q}$, ξ is the antiferromagnetic correlation length, Γ is the energy parameter of the spin subsystem, β is the fitting parameter, and a is the lattice constant.

Note that the majority of the aforementioned theoretical approaches do not take into account the real spectrum of carriers, which is obtained by angle-resolved photoemission experiments (ARPES); for example, one applies models with the carrier bandwidth W, which is much greater than the experimental bandwidth.

In the present paper, we investigate the optical conductivity within the Kondo lattice model. We do not use any fitting parameters except for the energy parameters of the Hamiltonian. The problem is solved within the theory of a spin polaron [20], which reproduces all the basic features of the lower hole band of elementary excitations observed in the recent ARPES experiments [21–23]: a large Fermi surface with comparatively small number of carriers, small bandwidth (~0.5 eV), the presence of regions of the Fermi surface situated near the boundary of the antiferromagnetic Brillouin zone (quasinesting), and a small distance between the Fermi level and the bottom of the conduction band (~0.05 eV).

We consider an antiferromagnetic subsystem of localized spins in a spherically symmetric approximation with allowance for the spin frustration. This approach predicts the existence of low-energy (~500 K) spin excitations with the momenta close to the antiferromagnetic vector $\mathbf{Q}$. This fact, together with the quasinesting character of the lower band, is of special interest.

To calculate the optical conductivity, we applied the formalism of memory functions [15, 24]. In this formalism, the conductivity $\sigma(\omega)$ is given by the generalized Drude formula

$$\sigma(\omega) = \frac{1}{V}\frac{i\chi_0}{\omega + M(\omega)}. \quad (4)$$

The complex memory function $M(\omega) = M'(\omega) + i\Gamma(\omega)$ determines $m^*(\omega)$ and $1/\tau^*(\omega)$ in (1). The quantity $\tilde{\omega}_{pl}^2 = 4\pi\chi_0 V^{-1}$ is an analogue of ω_{pl}^2 in (1). Our basic concern will be the study of $\Gamma(\omega)$ and χ_0. We will show that the calculated value of $\tilde{\omega}_{pl}$ is close to the values for copper oxide systems, $\omega_{pl} \sim 1$ eV [25], and is not anomalously small despite the strong polaron narrowing of the band and low density n of carriers (as should be expected from (2) and (3)).

We will demonstrate that the behavior of the function $\Gamma(\omega)$ is really determined by the spin excitations with the momenta close to $\mathbf{Q}$ and energies of about 500 K. The calculated values of the electric conductivity are in agreement with experimental data.

2. THE MODEL AND THE SPIN–POLARON DESCRIPTION OF THE CARRIER SPECTRUM

As for the spectrum of a hole in the normal state of cuprates, it is well known that the condition of an intermediate doping level corresponds to a Fermi surface in the form of four hole pockets near the points $N = (\pm\pi/2, \pm\pi/2)$. Optimally doped compounds exhibit a large Fermi surface centered at the point $M = (\pm\pi, \pm\pi)$; the shape of this surface is close to the Fermi surface calculated using a tight-binding model with the filling $1 + n_h$. The observed quasiparticle band is very narrow (a band width of ~0.5 eV). These facts (and a number of other ones) cannot be explained on the basis of the conventional one-electron band model.

Essential details of the hole spectrum in cuprates are well described within the frustrated effective three-band model in a spin–polaron approximation [26]. This model is rather complicated; however, its basic features are reproduced by the generalized Kondo lattice model if one chooses the on-site exchange parameter J as the greatest energy parameter [27–29].

The Hamiltonian of a square Kondo lattice is given by

$$\hat{H} = \hat{T} + \hat{J} + \hat{I}, \tag{5}$$

where

$$\hat{T} = \sum_{\mathbf{r},\mathbf{g},\sigma} t_g a^\dagger_{\mathbf{r}+\mathbf{g},\sigma} a_{\mathbf{r},\sigma} + \sum_{\mathbf{r},\mathbf{d},\sigma} t_d a^\dagger_{\mathbf{r}+\mathbf{d},\sigma} a_{\mathbf{r},\sigma} + \sum_{\mathbf{r},2\mathbf{g},\sigma} t_{2g} a^\dagger_{\mathbf{r}+2\mathbf{g},\sigma} a_{\mathbf{r},\sigma},$$

$$\hat{J} = J \sum_{\mathbf{r},\sigma_1,\sigma_2} a^\dagger_{\mathbf{r},\sigma_1} S^\alpha_{\mathbf{r}} \hat{\sigma}^\alpha_{\sigma_1\sigma_2} a_{\mathbf{r},\sigma_2},$$

$$\hat{I} = \frac{1}{2} I_1 \sum_{\mathbf{r},\mathbf{g}} S^\alpha_{\mathbf{r}+\mathbf{g}} S^\alpha_{\mathbf{r}} + \frac{1}{2} I_2 \sum_{\mathbf{r},\mathbf{d}} S^\alpha_{\mathbf{r}+\mathbf{d}} S^\alpha_{\mathbf{r}}.$$

Here, $\mathbf{g} = \pm\mathbf{g}_x \pm \mathbf{g}_y$ are the nearest-neighbor vectors, $\mathbf{d}$ and $2\mathbf{g}$ are the second- and third-nearest-neighbor vectors, and $\hat{\sigma}^\alpha$ are the Pauli matrices (summation is assumed over repeated Cartesian indices α). The Fermi operator $a^+_{\mathbf{r}\sigma}$ generates a hole with the spin $S = 1/2$ at node $\mathbf{r}$ with the spin projection $\sigma/2$.

The Hamiltonian $\hat{T}$ describes the hopping of a hole between the nearest, second nearest, and the third nearest neighbors with the respective amplitudes t_g, t_d, and t_{2g}. The on-site Kondo coupling is described by the Hamiltonian $\hat{J}$. The exchange Hamiltonian $\hat{I}$ describes a frustrated antiferromagnetic coupling between localized spins, p $(0 \le p \le 1)$ is the frustration parameter, and $I_1 = (1 - p)I$ and $I_2 = pI$ are the exchange constants for the nearest and next nearest neighbors.

In the momentum representation, the Hamiltonian $\hat{T}$ is expressed as

$$\hat{T} = \sum_{\mathbf{k},\sigma} \varepsilon_{\mathbf{k}} a^\dagger_{\mathbf{k},\sigma} a_{\mathbf{k},\sigma},$$

where

$$\begin{aligned}
\varepsilon_{\mathbf{k}} &= \sum_{\mathbf{r}=\mathbf{g},2\mathbf{g},\mathbf{d}} r_{\mathbf{r}} e^{-i\mathbf{k}\mathbf{r}} = 4t_g\gamma_g(\mathbf{k}) \\
&\quad + 4t_{2g}\gamma_{2g}(\mathbf{k}) + 4t_d\gamma_d(\mathbf{k}), \\
\gamma_g(\mathbf{k}) &= \frac{1}{2}(\cos k_x g + \cos k_y g), \\
\gamma_{2g}(\mathbf{k}) &= \frac{1}{2}(\cos 2k_x g + \cos 2k_y g), \\
\gamma_d(\mathbf{k}) &= \cos k_x g \cos k_y g.
\end{aligned} \tag{6}$$

The Hamiltonian $\hat{J}$ is responsible for the strong coupling between a bare hole and the local spin subsystem. This means that the elementary excitations represent a spin polaron—the superposition of the operator $a_{\mathbf{k},\sigma}$ of a bare hole and the operators describing the dressing of $a_{\mathbf{k},\sigma}$ in the operators of the spin subsystem. The problem is solved within the standard Mori–Zwanzig projection method with the use of retarded two-time Green's functions. As is known, the Mori–Zwanzig method suggests a choice of a finite set of basis operators, which, in the case under consideration, should take into account the pairing of a bare hole with localized spins from the very beginning.

It is known [30, 31] that the following set of basis operators serves as the minimal "good" nodal set:

$$\varphi^{(1)}_{\mathbf{r}\sigma} = a_{\mathbf{r},\sigma}, \quad \varphi^{(2)}_{\mathbf{r}\sigma} = S^\alpha_{\mathbf{r}} \hat{\sigma}^\alpha_{\sigma\sigma_1} a_{\mathbf{r},\sigma_1}, \tag{7}$$

$$\begin{aligned}
\varphi^{(3)}_{\mathbf{r}\sigma} &= \frac{1}{N} \sum_{\rho,\mathbf{q}\in\Omega} e^{i\mathbf{q}\rho} S^\alpha_{\mathbf{r}+\rho} \hat{\sigma}^\alpha_{\sigma\sigma_1} a_{\mathbf{r},\sigma_1}, \\
\varphi^{(4)}_{\mathbf{r}\sigma} &= \frac{1}{N} \sum_{\rho,\mathbf{q}\in\Omega} e^{i\mathbf{q}\rho} S^\alpha_{\mathbf{r}+\rho} S^\beta_{\mathbf{r}} \hat{\sigma}^\beta_{\sigma_1\sigma_2} a_{\mathbf{r},\sigma_2}, \\
\Omega &= \{\mathbf{q}: |\pm(\pi/g) - q_{x,y}| < L\}.
\end{aligned} \tag{8}$$

The first two operators $\varphi^{(1)}_{\mathbf{r}\sigma}$ and $\varphi^{(2)}_{\mathbf{r}\sigma}$ can be interpreted as local spin–polaron operators, and the next two operators $\varphi^{(3)}_{\mathbf{r}\sigma}$ and $\varphi^{(4)}_{\mathbf{r}\sigma}$ correspond to a spin polaron of intermediate radius and describe the pairing of the local polaron operators $\varphi^{(1)}_{\mathbf{r}\sigma}$ and $\varphi^{(2)}_{\mathbf{r}\sigma}$ with the spin-wave operators

$$S^\alpha_{\mathbf{q}} = \frac{1}{\sqrt{N}} \sum_{\rho} e^{i\mathbf{q}(\mathbf{r}+\rho)} S^\alpha_{\mathbf{r}+\rho}.$$

A characteristic feature of operators (8) is the fact that they describe the pairing of spin waves with momenta $\mathbf{q}$ close to the antiferromagnetic vector $\mathbf{Q} = (\pi, \pi)$: the momenta $\mathbf{q}$ occupy a domain Ω consisting of four

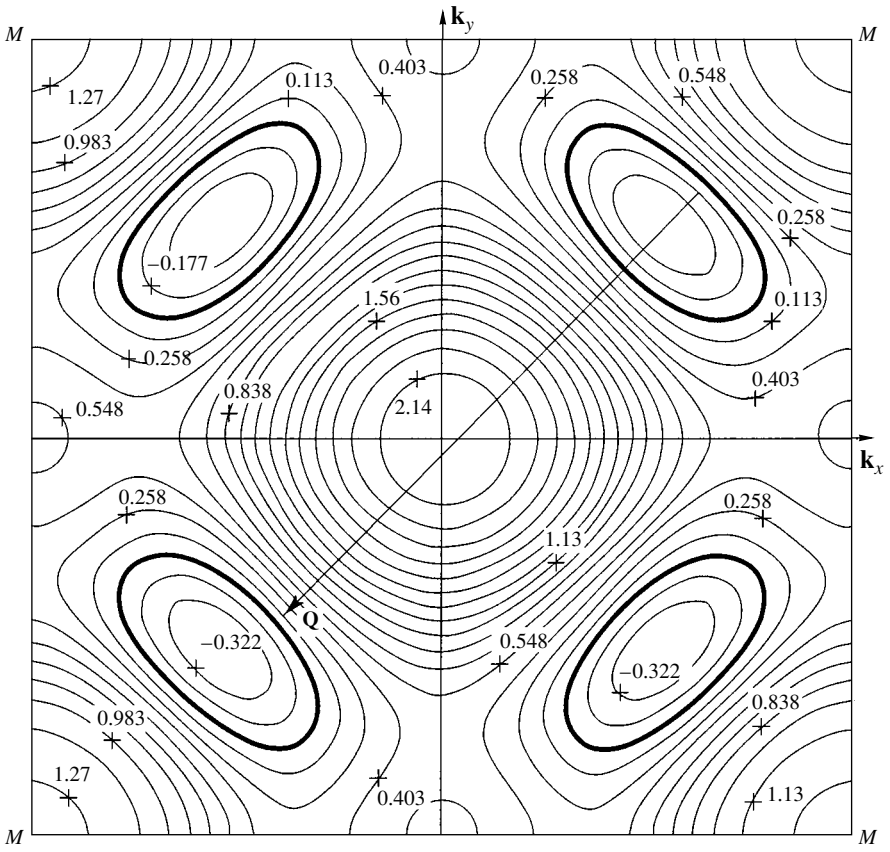

Fig. 1. The spectrum of the lower polaron band (for $T = 0.04\tau \approx 200$ K, $p = 0.15$, $I = 0.4\tau$, $J = 1.5\tau$, $t_g = 0.3\tau$, $t_d = 0.25\tau$, $t_{2g} = 0.2\tau$, and $\tau = 0.4$ eV) represented by the equal-energy lines $E_{\mathbf{k}}^{(1)} - \mu = \text{const}$; the heavily drawn solid curve $E_{\mathbf{k}}^{(1)} - \mu = 0$ corresponds to the Fermi surface for a doping level of $n_h = 0.15$. The energies are given in units of 0.1 eV. The arrow indicates the antiferromagnetic vector $\mathbf{Q} = (\pi, \pi)$

squares $L \times L$ at the corners of the first Brillouin zone (below, we set $\Omega = L \times L = 0.25(\pi/g)^2$). The pairing with such $S_{\mathbf{q}}^2$ takes into account a sharp peak of the spin–spin structural factor in the domain close to the vector $\mathbf{Q}$ and leads to the splitting of the lower quasiparticle band that arises in the local-polaron approximation [30, 31]. Moreover, taking into account the finite domain Ω is necessary for describing a correct passage to the limit as $T \longrightarrow 0$ [30].

The standard projection procedure for solving equations for the Green's functions in the momentum representation for operators (7) and (8) yields four bands for a spin polaron $E_{\mathbf{k}}^{(i)}$, an explicit expression for the Green's function of a bare hole $G_h(\mathbf{k}, \omega)$, and the number of bare holes n_h (see Appendix A):

$$G_h(\mathbf{k}, \omega) = \langle\langle a_{\mathbf{k},\sigma} | a_{\mathbf{k},\sigma}^{\dagger} \rangle\rangle_{\omega} = \sum_{l=1}^{4} \frac{Z_{\mathbf{k}}^{(l)}}{\omega - E_{\mathbf{k}}^{(l)}},$$
$$n_h = \sum_{\mathbf{k},\sigma} \sum_{l=1}^{4} Z_{\mathbf{k}}^{(l)} n_F(E_{\mathbf{k}}^{(l)}), \tag{9}$$

where $n_F(E_{\mathbf{k}}) = (e^{(E_{\mathbf{k}} - \mu)/T} + 1)^{-1}$ and μ is the chemical potential.

The comparison of the present method of a complex spin polaron [30] with calculations within the framework of the self-consistent Born approximation (SCBA) (at $T = 0$) [32] makes it clear that the lower band $E_{\mathbf{k}}^{(1)}$ and the residues $Z_{\mathbf{k}}^{(1)}$ describe well the quasiparticle SCBA peak and its intensity. The three upper bands $E_{\mathbf{k}}^{(2,3,4)}$ effectively describe the incoherent part $A_{\text{incoh}}(\mathbf{k}, \omega)$ of the total hole spectral SCBA function

$$A_{\text{SCBA}}(\mathbf{k}, \omega) = Z_{\mathbf{k}}^{(1)} \delta(\omega - E_{\mathbf{k}}^{(1)}) + A_{\text{incoh}}(\mathbf{k}, \omega).$$

We chose the following set of parameters in our calculations: $p = 0.15$, $T = 0.1I = 0.04\tau$, $I = 0.4\tau$, $J = 1.5\tau$, $t_g = 0.3\tau$, $t_d = 0.25\tau$, and $\tau_{2g} = 0.2\tau$. All energy parameters are given in units of τ. The value of τ was chosen equal to 0.4 eV. This choice corresponds to a bandwidth of $W = 0.7\tau \approx 0.3$ eV, which agrees with the data of ARPES experiments. In addition, this choice of τ gives a reasonable value of the exchange coupling between copper ions, $I \sim 2000$ K. The matrix elements arising in the projection method depend on the spin–spin correlation functions and are given in Appendix A.

Figure 1 represents the lower polaron band by equal-energy lines and the Fermi surface for a doping level of $n_h = 0.15$. One can see that the translation of the parts of the Fermi surface by the vector **Q** approximately leads to the superimposition of the parts situated in different squares, i.e., leads to the quasinesting.

Figure 2 illustrates the evolution of the Fermi surface as the doping level increases. One can see that conditions for quasinesting are preserved in the range of doping levels up to $n_h = 0.3$, which are of interest for superconductivity. The characteristic values of the residues below the Fermi surface amount to $Z_{\mathbf{k}}^{(1)} \approx 0.3$. According to the data of ARPES experiments, up to an optimal doping level of $n_h \sim 0.3$, the regions of the Fermi surface are situated in the close vicinity of the antiferromagnetic Brillouin zone.

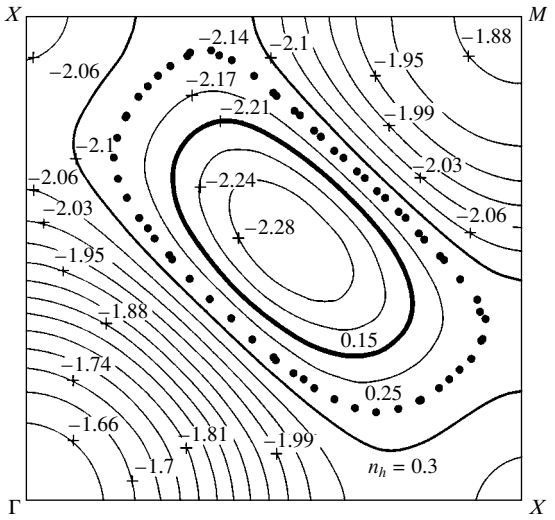

Fig. 2. The spectrum of the lower polaron band in the first quadrant of the Brillouin zone with the distinguished Fermi surfaces corresponding to $n_h = 0.15$, 0.25, and 0.3. The energy $E_{\mathbf{k}}^{(1)}$ is given in units of τ (parameters are the same as in Fig. 1).

3. CHARACTERISTIC FEATURES OF THE SPIN SUBSYSTEM

It is known that the antiferromagnetic long-range order vanishes in the entire temperature range even for comparatively low doping level of the CuO_2 plane. It is usually assumed that the doping leads to the antiferromagnetic coupling between the next nearest neighbors in the Cu^{2+} subsystem, i.e., to the frustration [33]. Cluster calculations give a sufficiently large value of the frustration parameter, $J_2/J_1 \sim 0.1$, even for undoped La_2CuO_4 [34]. As the doping level increases, the spin–spin correlation length decreases; an increase in the frustration yields a similar result.

The frustration parameter p can be regarded as an analogue of the number of holes x per one copper atom. An estimate based on the single-band Hubbard model for $U/t \sim 5$ yields a value of $p \sim 0.1$ for $x = 0.1$. Note that, for $La_{2-x}Sr_xCuO_4$, the spin subsystem of the CuO_2 plane loses the long-range order for $x > 0.02$.

Therefore, the interpretation of a frustrated spin within a spherically symmetric theory [35] that we adopted here is essential. In particular, this implies that the average spin at a node is $\langle S_{\mathbf{r}}^{\alpha} \rangle = 0$; however, antiferromagnetic spin–spin correlation functions $\langle S_0^{\alpha} S_{\mathbf{r}}^{\alpha} \rangle$ (α is fixed) are different from zero and independent of the Cartesian index α. Spin-wave excitations are described by the Green's function

$$G(\mathbf{q}, \omega) = \langle\langle S_{-\mathbf{q}}^{\alpha} | S_{\mathbf{q}}^{\alpha} \rangle\rangle_{\omega} = \frac{F_{\mathbf{q}}}{\omega^2 - \omega_{\mathbf{q}}^2}, \qquad (10)$$

where

$$F_{\mathbf{q}} = -8(I_1(1-\gamma_g(\mathbf{q}))C_g + I_2(1-\gamma_d(\mathbf{q}))C_d),$$

$$\omega_{\mathbf{q}} = \frac{8}{3} I \{ (1-\gamma_g)(A_1 + (1+\gamma_g)A_2) \qquad (11)$$

$$+ (1-\gamma_d)(A_3 + (1+\gamma_d)A_4) + \gamma_g(1-\gamma_d)A_5 \}^{1/2}.$$

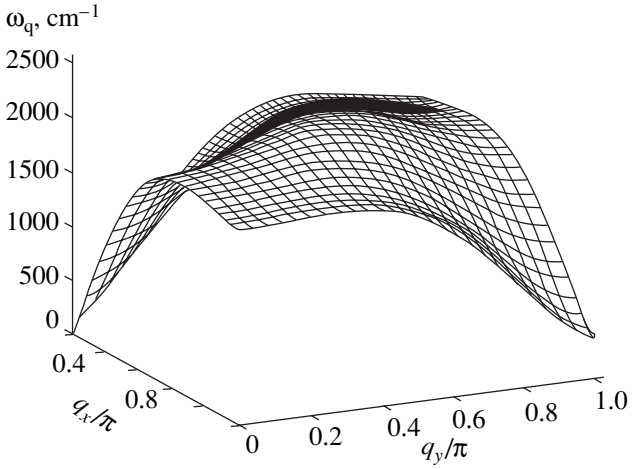

Fig. 3. The spectrum of spin excitations $\omega_{\mathbf{q}}$.

The parameters A_1, A_2, A_3, A_4, and A_5 are represented in a self-consistent manner in terms of the frustration parameter p and the spin–spin correlation functions $C_{\mathbf{r}} = \langle \mathbf{S}_{\mathbf{r}_0} \mathbf{S}_{\mathbf{r}_0+\mathbf{r}} \rangle$.

Note that $G(\mathbf{q}, \omega)$ in (10) strongly differs from the appropriate Green's function within the two-sublattice approximation: the numerator $F_{\mathbf{q}}$ and the spectrum $\omega_{\mathbf{q}}$ tend to zero as $\mathbf{q} \longrightarrow 0$ by analogy with an ordinary phonon pattern as $\mathbf{q} \longrightarrow 0$; however, as $\mathbf{q} \longrightarrow \mathbf{Q}$, the numerator $F_{\mathbf{q}}$ tends to a finite quantity and has a gap of $\Delta = \omega_{\mathbf{Q}}$ for finite temperatures and frustrations $\omega_{\mathbf{q}}$. Thus, the spin excitations (10) are periodic only with

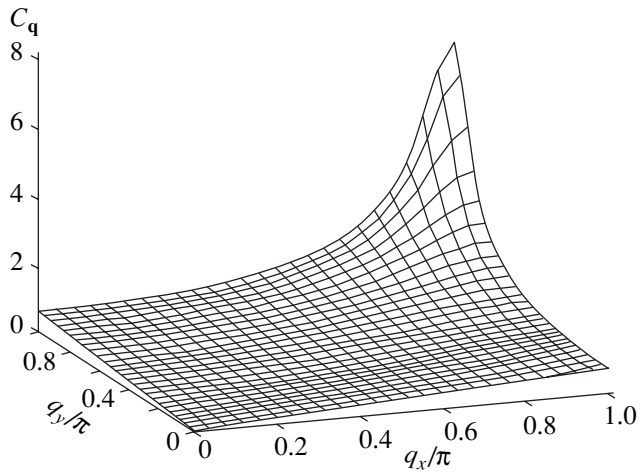

Fig. 4. The spin–spin structural factor $C_{\mathbf{q}}$.

respect to the total, rather than the antiferromagnetic, Brillouin zone, and the points (0, 0) and **Q** are not equivalent.

As we pointed out above, we choose a realistic value for the frustration parameter of $p = 0.15$. Figure 3 represents the spectrum $\omega_{\mathbf{q}}$ for $T \approx 200$ K ($T = 0.1I$, $I = 0.4\tau$). The gap Δ proves to be equal to ~500 K. These excitations lie in that domain of boson energies that was discussed in the Introduction.

Figure 4 shows the spin–spin correlation function $C_{\mathbf{q}}$ entering in the expression for the optical conductivity,

$$C_{\mathbf{q}} = \langle \mathbf{S}_{-\mathbf{q}}\mathbf{S}_{\mathbf{q}}\rangle = \frac{F_{\mathbf{q}}}{2\omega_{\mathbf{q}}}(1 + 2n_B(\omega_{\mathbf{q}})),$$
$$n_B(\omega) = (e^{\omega/T} - 1)^{-1}. \quad (12)$$

One can see that $C_{\mathbf{q}}$ has a sharp peak at $\mathbf{q} = \mathbf{Q}$, while $\omega_{\mathbf{q}}$ attains a local minimum. This is a direct consequence of the fact that the mode with $\mathbf{q} = \mathbf{Q}$ is a macroscopic mode for $T = 0$ and small frustration [35]. We will demonstrate that, with regard to the quasinesting, strong scattering occurs exactly on the mode with **q** close to **Q**. For calculating the optical damping $\Gamma(\omega)$, the combination $J^2F_{\mathbf{q}}\omega_{\mathbf{q}}^{-1}$ serves as an effective coupling in the problem of scattering of carriers. Note that this scattering is sharply anisotropic in a wide range of **q**.

To analyze a coupling, one usually introduces the Eliashberg function $\alpha^2(\omega)F(\omega)$[8, 36]. In our strongly anisotropic case, to characterize the coupling on average, we present in Fig. 5 the density of states of spin waves $\nu_m(\omega)$ and the spectral density $\Phi(\omega)$, which is an analogue of the Eliashberg function $\alpha^2(\omega)F(\omega)$; in Fig. 6, we present the spectral function of the coupling

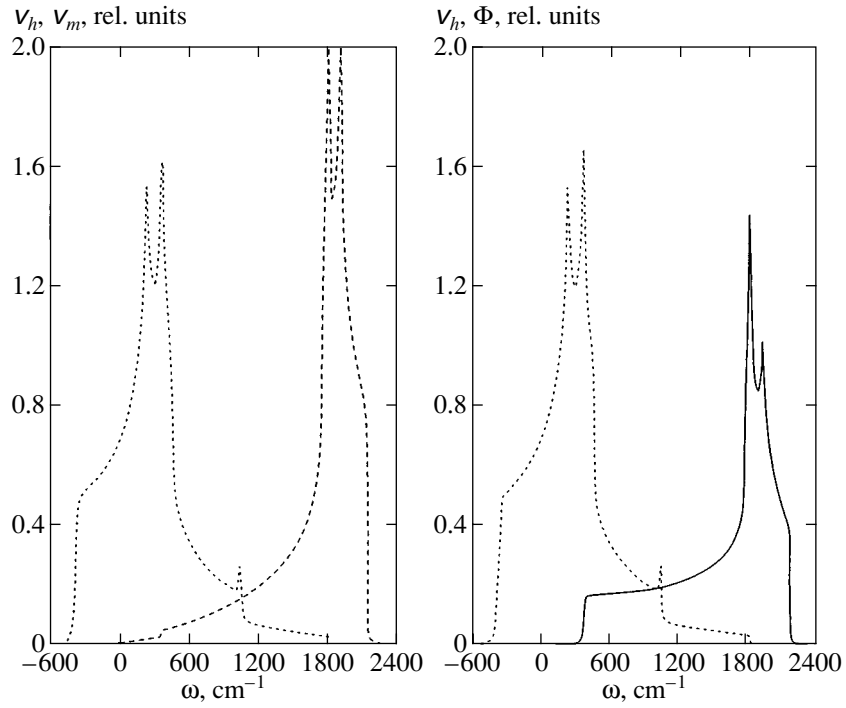

Fig. 5. The density of states of (dotted curve) a bare hole $\nu_h(\omega - \mu)$, (dashed curve) spin excitations $\nu_m(\omega - \mu)$, and (solid curve) the function $\Phi(\omega)$ (an analogue of the Eliashberg function (see [13])) in relative units. The parameters are the same as in Fig. 1; $\omega = 0$ corresponds to the chemical potential for $n_h = 0.15$.

with thermal magnons, $\Phi_{\text{th}}(\omega)$:

$$\nu_m(\omega) = \int \frac{d^2q}{(2\pi)^2}\delta(\omega - \omega_{\mathbf{q}}),$$
$$\Phi(\omega) = J^2\int \frac{d^2q}{(2\pi)^2}\delta(\omega - \omega_{\mathbf{q}})\frac{F_{\mathbf{q}}}{\omega_{\mathbf{q}}}, \quad (13)$$

$$\Phi_{\text{th}}(\omega) = J^2\int \frac{d^2q}{(2\pi)^2}\delta(\omega - \omega_{\mathbf{q}})\frac{F_{\mathbf{q}}}{\omega_{\mathbf{q}}}n_B(\omega_{\mathbf{q}}). \quad (14)$$

These figures also represent the hole density of states (the energy is measured from the chemical potential for a doping level of $n_h = 0.15$; see Fig. 2),

$$\nu_h(\omega) = \int \frac{d^2k}{(2\pi)^2}\delta(\omega - E^{(1)}_{\mathbf{k}})Z^{(1)}_{\mathbf{k}}. \quad (15)$$

Figure 5 shows that the function $\nu_m(\omega)$ has a small step at $\omega = \omega_{\mathbf{Q}} \sim 400$ cm$^{-1} \approx 500$ K, which is attributed to the contribution of spin waves with the momenta close to **Q**. However, for the function $\Phi(\omega)$, this feature is manifested much more clearly due to the large value of $C_{\mathbf{Q}}$ (see Fig. 4).

As for the spectral function $\Phi_{\text{th}}(\omega$ (Fig. 6), it has a sharp peak at the same frequency. This peak and the position of the maximum of the density of states of carriers will be discussed in greater detail in Section 5 when analyzing $\sigma(\omega)$.

4. CONDUCTIVITY IN THE INFRARED RANGE

The expression for the conductivity in the theory of linear response is given by [37]

$$\sigma(\omega) = \frac{1}{V}\langle\langle P_x|j_x\rangle\rangle_\omega,$$

where $\hat{\mathbf{P}}$ and $\hat{\mathbf{j}}$ are the operators of polarization and current, respectively, and V is the volume of the system. The polarization ($e = 1$)

$$\hat{\mathbf{P}} = \sum_{n,\sigma}\mathbf{r}_n a^\dagger_{n\sigma}a_{n_\sigma}$$

and the current are related by the standard formula $\hat{\mathbf{j}} = \dot{\hat{\mathbf{P}}} = i[\hat{H}, \hat{\mathbf{P}}]$. For Hamiltonian (5), the operator of current is given by

$$\hat{\mathbf{j}} = -i\sum_{\mathbf{r},\rho,\sigma} t_\rho \rho a^\dagger_{\mathbf{r}+\rho,\sigma}a_{\mathbf{r},\sigma} = \sum_{\mathbf{k},\sigma}\mathbf{v}(\mathbf{k})a^\dagger_{\mathbf{k},\sigma}a_{\mathbf{k},\sigma},$$
$$\mathbf{v}(\mathbf{k}) = \frac{\partial\varepsilon_{\mathbf{k}}}{\partial\mathbf{k}},$$

where $\mathbf{v}(\mathbf{k})$ is the velocity of a bare hole.

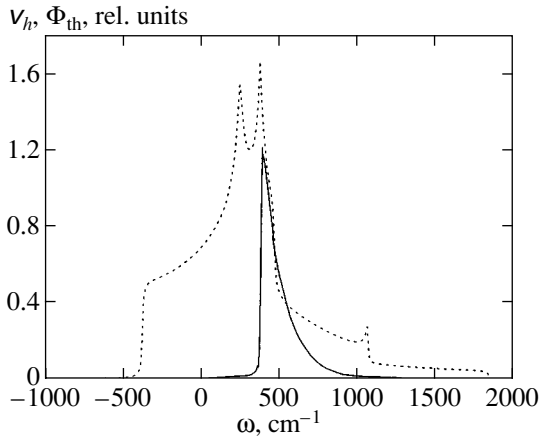

Fig. 6. The density of states of (dashed curve) a bare hole $\nu_h(\omega - \mu)$ and (solid curve) the thermal spectral function $\Phi_{\text{th}}(\omega)$ (see [14]) in relative units. The parameters are the same as in Fig. 1; $\omega = 0$ corresponds to the chemical potential for $n_h = 0.15$.

To calculate the conductivity $\sigma(\omega)$, it is convenient to apply the apparatus of memory functions $M(\omega)$ [24]:

$$\sigma(\omega) = \frac{1}{V}\frac{i\chi_0}{\omega + M(\omega)}, \quad M(\omega) = M'(\omega) + i\Gamma(\omega), \quad (16)$$

where $\Gamma(\omega)$ determines the inverse of the relaxation time and $M'(\omega)$ is related to the renormalization of mass.

The parameter χ_0 is expressed in terms of the operators of polarization and current,

$$\chi_0 = i\langle[\hat{j}_x, \hat{P}_x]\rangle, \quad (17)$$

and is given by

$$\chi_0 = \sum_{\mathbf{k},\sigma}\frac{\partial^2\varepsilon_{\mathbf{k}}}{\partial k_x^2}\langle a^\dagger_{\mathbf{k},\sigma}a_{\mathbf{k},\sigma}\rangle$$
$$= 2\sum_{\mathbf{k},\,i=1}^{4}\frac{\partial^2\varepsilon_{\mathbf{k}}}{\partial k_x^2}n_F(E^{(i)}_{\mathbf{k}})Z^{(i)}_{\mathbf{k}}. \quad (18)$$

Here, the mean value $\langle a^\dagger_{\mathbf{k},\sigma}a_{\mathbf{k},\sigma}\rangle$ is expressed in terms of the Green's function (9).

To obtain an explicit expression for $M(\omega)$, one should avail oneself of a chain of Green's functions with differentiation with respect to the first and second variables:

$$\omega\langle\langle P_x|j_x\rangle\rangle_\omega = i\chi_0 + i\langle\langle j_x|j_x\rangle\rangle_\omega, \quad (19)$$

$$\omega\langle\langle P_x|j_x\rangle\rangle_\omega = i\chi_0 + \langle\langle P_x|F^\dagger_x\rangle\rangle_\omega, \quad (20)$$

$$\omega\langle\langle j_x|j_x\rangle\rangle_\omega = \langle\langle j_x|F^\dagger_x\rangle\rangle_\omega. \quad (21)$$

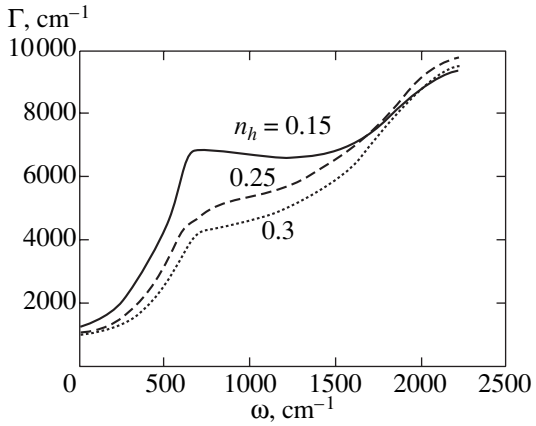

Fig. 7. Optical damping Γ(ω) for three values of the doping level: n_h = 0.15, 0.25, and 0.3.

Here, the force operator $\hat{\mathbf{F}}$ arises:

$$\hat{\mathbf{F}} = [\hat{\mathbf{j}}, \hat{H}],$$

$$\mathbf{F} = -iJ \sum_{\substack{\mathbf{r},\ \rho = \mathbf{g}, 2\mathbf{g}, \mathbf{d} \\ \sigma_1, \sigma_2}} t_\rho \rho a^\dagger_{\mathbf{r}+\rho, \sigma_1} (S^\alpha_{\mathbf{r}} - S^\alpha_{\mathbf{r}+\boldsymbol{\rho}}) \hat{\sigma}^\alpha_{\sigma_1\sigma_2} a_{\mathbf{r}, \sigma_2}.$$

As a result, $M(\omega)$ is expressed in terms of the force–force-type irreducible Green's function

$$M(\omega) = -(\chi_0\omega)^{-1}[K + \langle\langle F_x | F_x^\dagger \rangle\rangle^{\text{irred}}_\omega],$$

where $K = \langle [j_x, F_x^\dagger] \rangle$ is a real quantity.

One can calculate $\langle\langle F_x | F_x^\dagger \rangle\rangle^{\text{irred}}_\omega$ in the mode-coupling approximation. The detailed procedure of deriving expressions for Γ(ω) and $M'(\omega)$ is described in Appendix B. Here, we give the final form of Γ(ω):

$$\Gamma(\omega) = \frac{1 - e^{-\omega/T}}{\omega} \frac{\pi J^2}{\chi_0} \frac{1}{N} \sum_{\mathbf{k}, \mathbf{q}} (v_x(\mathbf{k}) - v_x(\mathbf{k}+\mathbf{q}))^2$$
$$\times \frac{F_\mathbf{q}}{\omega_\mathbf{q}} \sum_{i, j = 1}^{4} Z^{(i)}_\mathbf{k} Z^{(j)}_{\mathbf{k}+\mathbf{q}} n_F(E^{(j)}_\mathbf{k})(1 - n_F(E_{\mathbf{k}+\mathbf{q}}))$$
$$\times [(1 + n_B(\boldsymbol{\omega}_\mathbf{q}))\delta(E^{(j)}_{\mathbf{k}+\mathbf{q}} - E^{(i)}_\mathbf{k} + \omega_\mathbf{q} - \omega)$$
$$+ n_B(\omega_\mathbf{q})\delta(E^{(j)}_{\mathbf{k}+\mathbf{q}} - E^{(i)}_\mathbf{k} - \omega_\mathbf{q} - \omega)]. \quad (22)$$

The structure of Γ(ω) has a clear physical meaning. The terms proportional to $(1 + n_B(\omega_\mathbf{q}))$ and $n_B(\omega_\mathbf{q})$ describe, respectively, the processes with the creation and annihilation of a magnon with energy $\omega_\mathbf{q}$. The combination of Fermi distributions $n_F(E^{(i)}_\mathbf{k})(1 - n_F(E^{(j)}_{\mathbf{k}+\mathbf{q}}))$ takes into account the filling probabilities of the initial, **k**, and final, **k** + **q**, states. The coupling to the spin subsystem is described by the factor $J^2 F_\mathbf{q} \omega_\mathbf{q}^{-1}$.

Expression (16) is usually represented in the form of the generalized Drude formula:

$$\sigma(\omega) = \frac{\tilde{\omega}^2_{pl}}{4\pi} \frac{m}{m^*(\omega)} \frac{1}{1/\tau^*(\omega) - i\omega}, \quad (23)$$

where

$$\frac{m^*}{m} = 1 + \frac{M'(\omega)}{\omega}, \quad \frac{1}{\tau^*} = \frac{\Gamma(\omega)}{1 + M'(\omega)/\omega},$$
$$\tilde{\omega}^2_{pl} = 4\pi\chi_0 V^{-1}. \quad (24)$$

It follows from expression (22) that the damping in our model is associated with the scattering of a spin polaron by spin waves and is described by the Hamiltonian $\hat{J}$ in (5).

5. RESULTS AND DISCUSSION

To calculate σ(ω), ρ, and $\tilde{\omega}_{\text{pl}}$ in practical units, we have to specify the average distance a_z between CuO_2 planes; we assumed that a_z = 6.6 Å, which corresponds to lanthanum compounds [2]. We present the results of calculations in the frequency range up to ω ≈ 2000 cm^{-1} (~0.25 eV). In this frequency interval, a contribution to M' and the optical damping Γ(ω) is made only by the hole scattering within the lower band $E^{(1)}_\mathbf{k}$, which is shown in Fig. 2 (i.e., the terms with $i = j = 1$ in (22)). This is associated with the fact that, within our method, the incoherent part of the hole spectral function is simulated by three upper bands. These bands are located at an energy greater than 0.3 eV ~ 2400 cm^{-1} from the Fermi level, which (for a reasonable doping level) lies in the lower band. In principle, the scattering to the incoherent part can be taken into account by smearing the upper bands over energies for every fixed **k**.

Figure 7 represents the optical damping Γ(ω) at temperature $T = 0.1I \approx 200$ K for three values of the doping level: n_h = 0.15, n_h = 0.25, and n_h = 0.3. A sharp increase in Γ(ω) up to frequencies of 750 cm^{-1} represents an interesting feature against the background of generally increasing Γ(ω); this feature is most clearly displayed in the case of n_h = 0.15.

Let us dwell in greater detail on the doping level n_h = 0.15. In the low-frequency range, Γ(ω) is mainly determined by the scattering on the spin excitations with the momenta **q** close to **Q**. This fact becomes obvious if we consider, in the low-frequency domain, the contribution to Γ(ω) due to the scattering to vectors **q** satisfying the inequalities $0.9Q_{x,y} < |q_{x,y}| < Q_{x,y}$ (i.e., the vectors **q** lie in small domains near the four points *M* of the Brillouin zone). This contribution is shown in Fig. 8 by a dot-and-dash curve together with the total Γ(ω) value (solid curve). To find out why these scatter-

ing processes prove to be dominant, we consider expression (22) with $\omega = 0$. In this case, both summands involving the delta functions of energies coincide, and $\Gamma(0)$ takes the form

$$\Gamma(0) = 2\frac{1}{T}\frac{\pi J^2}{\chi_0}\frac{1}{N}\sum_{\mathbf{k},\mathbf{q}}((v_x(\mathbf{k}) - v_x)(\mathbf{k}+\mathbf{q}))^2 \times Z_{\mathbf{k}}^{(1)} Z_{\mathbf{k}+\mathbf{q}}^{(1)} n_F(E_{\mathbf{k}}^{(i)})(1 - n_F(E_{\mathbf{k}+\mathbf{q}}^{(j)})) \times \frac{F_{\mathbf{q}}}{\omega_{\mathbf{q}}} n_B(\omega_{\mathbf{q}})\delta(E_{\mathbf{k}+\mathbf{q}}^{(1)} - E_{\mathbf{k}}^{(1)} - \omega_{\mathbf{q}}). \quad (25)$$

The spectral function $\Phi_{\text{th}}(\omega)$ contains a multiplier $F_{\mathbf{q}}\omega_{\mathbf{q}}^{-1} n_B(\omega_{\mathbf{q}})$ and attains a maximum, associated with close values of the vectors $\mathbf{q}$ and $\mathbf{Q}$, at $\omega_{\mathbf{q}} \approx 500$ K (see Fig. 6). This is the first factor that determines a large contribution made by the scattering processes with $\mathbf{q} \sim \mathbf{Q}$ to (25).

The second important factor is the quasinesting of the Fermi surface, which allows us to satisfy the energy conservation law in (25) under scattering on $\mathbf{q} \sim \mathbf{Q}$. In this case, we have a large phase volume of scattered states.

Suppose, for example, that a state $\mathbf{k}$ is in the first quadrant below the Fermi surface and $\mathbf{k} \approx (0.6\pi, 0.6\pi)$; then, the scattered state $\mathbf{k} + \mathbf{Q}$ turns out to be in the third quadrant near the relevant sheet of the Fermi surface (see Fig. 1). According to (25), in this case, a magnon $\omega_{\mathbf{Q}}$ is absorbed. If we had a nesting situation, i.e., if each sheet of the Fermi surface was symmetric with respect to the boundary of the appropriate Brillouin zone ($(\pm\pi, 0)$, $(0, \pm\pi)$), then such scattering would not contribute to (25) because of the violation of the energy conservation law (since $E_{\mathbf{k}+\mathbf{Q}} \approx E_{\mathbf{k}}$) and, in addition, both states would lie below the Fermi surface. In the case of quasinesting, the bottom of the hole band lying below the ellipsoidal Fermi surface in each quadrant of the Brillouin zone is shifted toward points M relative to the points $(\pm\pi/2, \pm\pi/2)$, as is the case in doped HTSCs. Due to the quasinesting, the state $\mathbf{k} + \mathbf{Q}$ turns out to be in the third quadrant over the appropriate sheet of the Fermi surface with the factor $(1 - n_F(E_{\mathbf{k}+\mathbf{Q}}^{(1)})) \sim 1$. Simultaneously, it becomes possible to satisfy the energy conservation law $E_{\mathbf{k}+\mathbf{Q}}^{(1)} - E_{\mathbf{k}}^{(1)} - \omega_{\mathbf{Q}} = 0$. To illustrate the latter statement, in the inset of Fig. 8 (curve *1*), we show the states $\mathbf{k}$ such that the energy conservation law $E_{\mathbf{k}+\mathbf{Q}}^{(1)} - E_{\mathbf{k}}^{(1)} - \omega_{\mathbf{Q}} = 0$ is satisfied. Curve *2* represents the points $\mathbf{k} + \mathbf{Q}$ from the third quadrant that are obtained by reflection with respect to the diagonal connecting the points $(-\pi, \pi)$ and $(\pi, -\pi)$.

The juxtaposition of curve *1* and the Fermi surface for $n_h = 0.15$ (Fig. 2) shows that a substantial part of this curve lies rather deep below the Fermi surface. For the parameters of our model ($p = 0.15$, $I = 0.4\tau$, $J = 1.5\tau$, $t_g = 0.3\tau$, $t_d = 0.25\tau$, $t_{2g} = 0.2\tau$, and $\tau = 0.4$ eV) when

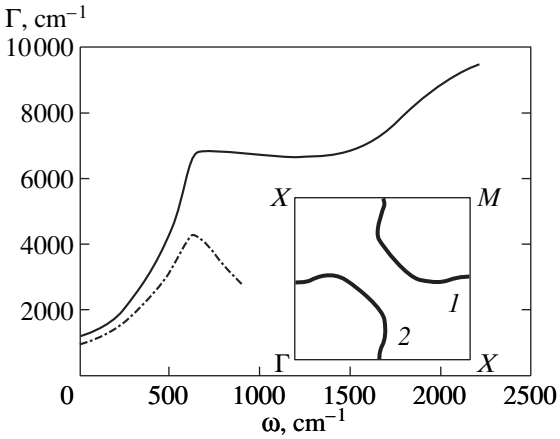

Fig. 8. (solid curve) Optical damping $\Gamma(\omega)$ and (dot-and-dash curve) contribution to the low-frequency part of $\Gamma(\omega)$ associated with the scattering into vectors $\mathbf{q}$ close to the antiferromagnetic vector $\mathbf{Q}$; $0.9Q_{x,y} < |q_{x,y}| < Q_{x,y}$ (the doping level is $n_h = 0.15$). The inset represents curves *1* and *2* (see the text).

$n_h = 0.15$, the distance W_μ between the chemical potential and the bottom of the band is $W_\mu \approx 0.04$ eV (see Fig. 2). The energy of spin excitations for $\mathbf{q} \sim \mathbf{Q}$ is of the same order of magnitude (Fig. 3). This means that a contribution to the scattering is made by the $\boldsymbol{k}$ states that lie rather deep below the Fermi surface. This fact, in particular, makes our model different from electron–phonon scattering in ordinary metals, where phonon frequencies are small as compared with the Fermi energy.

The scattered states $\mathbf{k} + \mathbf{q}$, $\mathbf{q} \sim \mathbf{Q}$, have energy of $\sim\omega_{\mathbf{Q}}$ with respect to the chemical potential. Figure 6 shows that not only the peak of the spectral function $\Phi_{\text{th}}(\omega)$ but also the peak of the density of states $\nu_h(\omega)$ of carriers corresponds to these energies.

Thus, by an example of the case $\omega = 0$, $n_h = 0.15$, one can explain the decisive role of the quasinesting and the boson mode with $\omega_{\mathbf{Q}} \sim 500$ K for the low-frequency domain of $\Gamma(\omega)$.

Figure 9 represents the diagrams of $\sigma(\omega)$ for three values of the doping level: $n_h = 0.15$, $n_h = 0.25$, and $n_h = 0.3$. These diagrams exhibit conventional behavior for doped compounds: a sharp peak at a frequency of $\omega = 0$ and non-Drude behavior at larger frequencies, $\omega > 500$ cm^{-1}. They also exhibit nonmonotonic behavior at $\omega \approx 800$ cm^{-1}.

The table shows the temperature dependence of the gap in the spectrum of spin excitations $\omega_{\mathbf{Q}}$, the electric conductivity ρ, and the plasma frequency $\tilde{\omega}_{\text{pl}}$. One can see that $\omega_{\mathbf{Q}}$ is primarily determined by the frustration parameter $p = 0.15$ and slowly increases with temperature.

The calculated values of conductivity ρ are comparable with experimental results. Recall that we consider

Energy $\omega_{\mathbf{Q}}$ of spin excitations for $\mathbf{Q} = (\pi, \pi)$, the temperature dependence of electric conductivity ρ, and the plasma frequency $\tilde{\omega}_{\mathrm{pl}}$ for $n_h = 0.15$

T	$0.05I$ (90 K)	$0.075I$ (140 K)	$0.1I$ (190 K)	$0.15I$ (280K)	$0.2I$ (370 K)	$0.25I$ (460 K)	$0.3I$ (560 K)
$\omega_{\mathbf{Q}}$	0.114τ	0.115τ	0.119τ	0.132τ	0.149τ	0.171τ	0.194τ
$\omega_{\mathbf{Q}}/T$	5.7	3.8	3.0	2.2	1.9	1.7	1.6
ρ, $\mu\,\Omega$ cm	50	280	620	1290	1710	1920	2100
$\tilde{\omega}_{\mathrm{pl}}$, eV	1.37	1.35	1.31	1.24	1.19	1.14	1.10

the doping level $n_h = 0.15$ as intermediate, while the optimal doping level is $n_h = 0.3$. At a temperature of $T \approx 300$ K, the optimal doping level corresponds to $\rho \approx 700\ \mu\Omega$ cm. This value is of the same order of magnitude but is greater than the experimental value $\rho \approx 300\ \mu\Omega$ cm [3] by approximately a factor of 2. The table shows that the conductivity exhibits an almost linear dependence on temperature.

The characteristic value $\tilde{\omega}_{\mathrm{pl}} \approx 1.3$ eV (see table) is close to the experimental value, $\omega_{\mathrm{pl}} \approx 1$ eV, which is obtained from the measurement of energy losses of fast electrons [25, 38, 39]. Despite the low concentration of carriers and a relatively small width of the lower polaron band, we obtain a reasonable value for $\tilde{\omega}_{\mathrm{pl}}$ since the quantity χ_0 (18) essentially depends on the velocity $\mathbf{v}(\mathbf{k})$ of bare carriers. Introducing the effective mass according to (24), we obtain $m^* \approx 8$ for the low-frequency region.

Thus, our analysis of a strongly correlated Kondo lattice model within a spin–polaron approach shows that the spin-excitation mode with $\omega_{\mathbf{Q}} \sim 500$ K and the strong coupling of this mode to the subsystem of carriers due to the quasinesting character of the structure of the lower band allow one to qualitatively describe the low-frequency part of the optical conductivity in the CuO_2 plane.

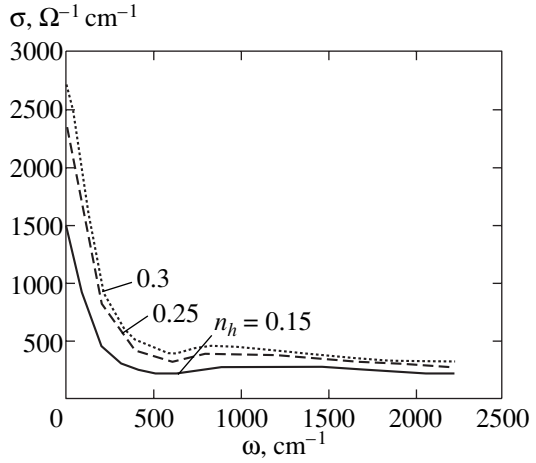

Fig. 9. Conductivity $\sigma(\omega)$ for three values of the doping level: $n_h = 0.15$, 0.25, and 0.3.

In conclusion, we point out several disadvantages of the approach proposed, which, in our opinion, lead to certain discrepancies with experiment. These discrepancies result from the calculation of the reflectivity $R(\omega)$, which demonstrates a correct quasilinear decrease in a wide range of frequencies; however, the slope of the decrease is substantially greater than the experimental value.

The Kondo lattice model does not reflect the following important feature of the plane CuO_2: the residues $Z_{\mathbf{k}}^{(1)}$ in the lower band are strongly suppressed for the vectors $\mathbf{k}$ close to the points $\Gamma = (0, 0)$ and M. Such a decrease in $Z_{\mathbf{k}}^{(1)}$ is described by a three-band model, and taking into consideration this decrease may significantly reduce the value of $\Gamma(\omega)$ and eliminate the discrepancy with experimental data in the behavior of $R(\omega)$. Next, our approach simulates the incoherent part of the spectral function of a polaron in the form of upper coherent polaron bands. Our analysis shows that such a description is not quite adequate and leads to an artificial decrease in $\Gamma(\omega)$ for $\omega \geq 2500$ cm^{-1}. Finally, we should have taken into account that the frustration parameter p increases with the doping level n_h.

ACKNOWLEDGMENTS

This work was supported by the INTAS (grant no. 97-11066), the Russian Foundation for Basic Research (project no. 01-02-16719), and the NATO Collaborative Linkage Grant (PST.CLG.976416).

We are grateful to R. Kuzian and R. Hayn for useful discussions. We also thank E.G. Maksimov for remarks and suggestions.

APPENDIX

Appendix A

Here, we present a method for determining the spin–polaron bands $E_{\mathbf{k}}^{(l)}$ and residues $Z_{\mathbf{k}}^{(l)}$ (see (9)) and an explicit expression for the matrix elements arising in the projection method.

For the given basis of spin–polaron operators (7), (8), we introduce retarded two-time Green's functions

$G_{ij}(t, \mathbf{k})$ for the Fourier components $\varphi_{\mathbf{k}}^{(j)}$ of the operators $\varphi_{\mathbf{r}}^{(j)}$ (for short, we omit the spin indices):

$$\begin{aligned} G_{ij}(t, \mathbf{k}) &\equiv \langle\langle \varphi_{\mathbf{k}}^{(i)}(t) | \varphi_{\mathbf{k}}^{(j)\dagger}(0) \rangle\rangle \\ &= -i\Theta(t)\langle\{\varphi_{\mathbf{k}}^{(i)}(t), \varphi_{\mathbf{k}}^{(j)\dagger}(0)\}\rangle, \\ \varphi_{\mathbf{k}}^{(j)} &= \frac{1}{\sqrt{N}}\sum_{\mathbf{r}} e^{-i\mathbf{kr}}\varphi_{\mathbf{r}}^{(j)}, \quad i, j = 1\text{–}4. \end{aligned} \tag{26}$$

The equation of motion for the Fourier components of the Green's functions is given by

$$\begin{aligned} \omega\langle\langle \varphi_{\mathbf{k}}^{(i)} | \varphi_{\mathbf{k}}^{(j)\dagger} \rangle\rangle_\omega &= K_{ij} + \langle\langle \psi_{\mathbf{k}}^{(i)} | \varphi_{\mathbf{k}}^{(j)\dagger} \rangle\rangle_\omega, \\ K_{ij}(\mathbf{k}) &= \langle\{\varphi_{\mathbf{k}}^{(i)}, \varphi_{\mathbf{k}}^{(j)\dagger}\}\rangle, \quad \psi_{\mathbf{k}}^{(i)} = [\varphi_{\mathbf{k}}^{(i)}, \hat{H}]. \end{aligned} \tag{27}$$

In the projection method, the new operators $\psi_{\mathbf{k}}^{(i)}$ are approximated by the projections of the basis operators (7), (8) onto the space $\{\varphi_{\mathbf{k}}^{(i)}\}$:

$$\begin{aligned} \psi_{\mathbf{k}}^{(i)} &\approx \sum_l L_{il}(\mathbf{k})\varphi_{\mathbf{k}}^{(l)}, \quad L(\mathbf{k}) = D(\mathbf{k})K^{-1}, \\ D_{ij}(\mathbf{k}) &= \langle\{\psi_{\mathbf{k}}^{(i)}, \varphi_{\mathbf{k}}^{(j)\dagger}\}\rangle. \end{aligned} \tag{28}$$

After the substitution of the approximate expressions for the operators $\{\varphi_{\mathbf{k}}^{(i)}\}$ (28) into the equation of motion (27), the system of equations (27) for the Green's functions $\langle\langle \varphi_{\mathbf{k}}^{(i)} | \varphi_{\mathbf{k}}^{(j)\dagger} \rangle\rangle_\omega$ becomes closed, and it can be represented in the following matrix form:

$$(\omega E - DK^{-1})G = K, \tag{29}$$

where E is the identity matrix. The solution of the system allows one to determine the Green's function (9) of a bare hole.

In particular, the spectrum $E_{\mathbf{k}}$ of quasiparticles is defined by the poles of the Green's function G and is determined from the equation

$$\det|KE_{\mathbf{k}} - D| = 0.$$

Let us give explicit expressions for the matrix elements of K and D.

Below, we adopted the following notation: $D_{ij}(\mathbf{k}) = \langle\{[\varphi_{\mathbf{k}}^{(i)}, (\hat{T} + \hat{J} + \hat{I})], \varphi_{\mathbf{k}}^{(j)\dagger}\}\rangle = \tilde{T}_{ij} + \tilde{J}_{ij} + \tilde{I}_{ij}$; K_{ij}, $\tilde{T}_{ij}$, $\tilde{J}_{ij}$, and $\tilde{I}_{ij}$ are symmetric matrices; $\gamma_g = 0.5(\cos k_x + \cos k_y)$; $\gamma_d = \cos k_x \cos k_y$; $\gamma_{2g} = 0.5(\cos 2k_x + \cos 2k_y)$. Below, we give the nonzero matrix elements.

***K* matrix**

$$\begin{aligned} K_{11} &= 1, \quad K_{14} = u, \\ K_{22} &= 0.75, \quad K_{23} = u, \quad K_{24} = -u, \\ K_{33} &= u, \quad K_{34} = w - 2uv, \\ K_{44} &= 0.75u - w + 2uv. \end{aligned}$$

***$\tilde{T}$* matrix**

$$\begin{aligned} T_{11} &= 4t_g\gamma_g + 4t_d\gamma_d + 4t_{2g}\gamma_{2g}, \\ T_{14} &= u(4t_g\gamma_g + 4t_d\gamma_d + 4t_{2g}\gamma_{2g}), \\ T_{22} &= 4t_g\gamma_g C_g + 4t_d\gamma_d C_d + 4t_{2g}\gamma_{2g}C_{2g}, \\ T_{23} &= 4t_g\gamma_g u_g + 4t_d\gamma_d u_d + 4t_{2g}\gamma_{2g}u_{2g}, \\ T_{24} &= 4t_g\gamma_g C_g(v_g - v) \\ &+ 4t_d\gamma_d C_d(v_d - v) + 4t_{2g}\gamma_{2g}C_{2g}(v_{2g} - v), \\ T_{33} &= T_{23}, \\ T_{34} &= 4t_g\gamma_g(w_g - uv_g - u_g v) + 4t_d\gamma_d(w_d - uv_d - u_d v) \\ &+ 4t_{2g}\gamma_{2g}(w_{2g} - uv_{2g} - u_{2g}v), \\ T_{44} &= 4t_g\gamma_g\Big(C_g u_g + C_g(v^2 + 2v_g v) + \frac{2}{3}C_g^2(v^2 + 3v_g^2) \\ &- 4C_g\Big(\frac{1}{3}u_g v + uv_g\Big) + u^2 - \frac{1}{3}u^2 - \frac{2}{3}W_g^{(1)}\Big) \\ &+ 4t_d\gamma_d\Big(C_d u_d + C_d(v^2 + 2v_d v) + \frac{2}{3}C_d^2(v^2 + 3v_d^2) \\ &- 4C_d\Big(\frac{1}{3}u_d v + uv_d\Big) + u^2 - \frac{1}{3}u_d^2 - \frac{2}{3}W_d^{(1)}\Big) \\ &+ 4t_{2g}\gamma_{2g}\Big(C_{2g}u_{2g} + C_{2g}(v^2 + 2v_{2g}v) + \frac{2}{3}C_{2g}^2(v^2 + 3v_{2g}^2) \\ &- 4C_{2g}\Big(\frac{1}{3}u_{2g}v + uv_{2g} + u^2 - \frac{1}{3}u_{2g}^2 - \frac{2}{3}W_{2g}^{(1)}\Big). \end{aligned}$$

***$\tilde{J}$* matrix**

$$\begin{aligned} J_{1j} &= JK_{2j}, \quad j = 1, 2, 3, 4, \\ J_{2j} &= J(0.75K_{1j} - K_{2j}), \quad j = 2, 3, 4 \\ J_{33} &= JK_{34}, \\ J_{34} &= J(0.75u - w + 2uv), \\ J_{44} &= J\Big(\frac{7}{4}w - 3.5uv - 0.75u\Big). \end{aligned}$$

***$\tilde{I}$* matrix**

$$\begin{aligned} I_{22} &= -4I_1C_g - 4I_2C_d, \\ I_{23} &= 4I_1C_g(v_g - v) + 4I_2C_d(v_d - v), \\ I_{24} &= 2I_1(C_g(v - v_g) + u_g) + 2I_2(C_d(v - v_d) + u_d), \\ I_{33} &= 4I_1C_g(v_g - v) + 4I_2C_d(v_d - v), \end{aligned}$$

$$I_{34} = 4I_1\left(\frac{2}{3}W_g^{(3)} + \frac{2}{3}C_g(uv - w - uv_g + w_g)\right.$$
$$\left. + C_g(v^2 - 1.5vv_g + 0.5v_g^2) + \frac{2}{3}C_g^2(v_g^2 - vv_g)\right)$$
$$+ 4I_2\left(\frac{2}{3}W_d^{(3)} + \frac{2}{3}C_d(uv - w - uv_d + w_d)\right.$$
$$\left. + C_d(v^2 - 1.5vv_d + 0.5v_d^2) + \frac{2}{3}C_d^2(v_d^2 - vv_d)\right),$$
$$I_{44} = 4I_1\left(0.5w_g^{(1)} - u_gv_g - vv_g\left(C_g + \frac{8}{3}C_g^2\right)\right.$$
$$- v_g^2C_g + \frac{8}{3}C_gu_gv_g + \frac{8}{3}C_guv - C_gv^2 - C_gu$$
$$\left. - \frac{2}{3}u_gu + \frac{2}{3}W_g^{(2)} + 0.75C_g(v_g - v)\right)$$
$$+ 4I_2\left(0.5w_d^{(1)} - u_dv_d - vv_d\left(C_d + \frac{8}{3}C_d^2\right)\right.$$
$$- v_d^2C_d + \frac{8}{3}C_du_dv_d + \frac{8}{3}C_duv - C_dv^2$$
$$\left. - C_du - \frac{2}{3}u_du + \frac{2}{3}W_d^{(2)} + 0.75C_d(v_d - v)\right) - I_{34}.$$

Here, we used the following notation:

$$v = \frac{1}{N}\sum_{\kappa}1, \quad \frac{1}{N}\sum_{\kappa} \equiv \frac{1}{N}\sum_{\kappa\in\Omega},$$
$$v_l = \frac{1}{N}\sum_{\kappa}e^{i\kappa l}; \quad l = g, d, 2g,$$
$$u = \frac{1}{N}\sum_{\kappa}C_\kappa,$$
$$u_l = \frac{1}{N}\sum_{\kappa}e^{i\kappa l}C_\kappa, \quad l = g, d, 2g;$$
$$w = \frac{1}{N^2}\sum_{\kappa_1,\kappa_2}C_{\kappa_1-\kappa_2},$$
$$w_l = \frac{1}{N^2}\sum_{\kappa_1,\kappa_2}e^{-i\kappa_1 l}C_{\kappa_1-\kappa_2}, \quad l = g, d, 2g,$$
$$w_l^{(1)} = \frac{1}{N^2}\sum_{\kappa_1,\kappa_2}e^{-i(\kappa_1-\kappa_2)l}C_{\kappa_1-\kappa_2}, \quad l = g, d,$$
$$W_l^{(1)} = \frac{1}{N^2}\sum_{\kappa_1,\kappa_2,\rho}e^{-i(\kappa_1-\kappa_2)\rho}e^{-i\kappa_2 l}C_\rho C_{\rho-l}, \quad l = g, d, 2g,$$
$$W_l^{(2)} = \frac{1}{N^2}\sum_{\kappa_1,\kappa_2,\rho}e^{-i(\kappa_1-\kappa_2)\rho}C_\rho C_{\rho-g}, \quad l = g, d,$$
$$W_l^{(3)} = \frac{1}{N^2}\sum_{\kappa_1,\kappa_2}(e^{i\kappa_2 l} - e^{-i(\kappa_1-\kappa_2)l})C_{\kappa_1-\kappa_2}C_{\kappa_2}, \quad l = g, d.$$

Appendix B

To represent $\sigma(\omega)$ in the form (16), we apply Eqs. (19), (20), and (21). Let us rewrite (21) in the following identical form:

$$\omega\langle\langle j_x|j_x\rangle\rangle_\omega\langle\langle P_x|j_x\rangle\rangle_\omega^{-1}\langle\langle P_x|j_x\rangle\rangle_\omega = \langle\langle j_x|F_x^\dagger\rangle\rangle_\omega.$$

Next, we apply Eq. (20) to obtain

$$\langle\langle j_x|j_x\rangle\rangle_\omega\langle\langle P_x|j_x\rangle\rangle_\omega^{-1}(i\chi_0 + \langle\langle P_x|F_x^\dagger\rangle\rangle_\omega) = \langle\langle j_x|F_x^\dagger\rangle\rangle_\omega.$$

It is convenient to rewrite this equation as

$$\langle\langle j_x|j_x\rangle\rangle_\omega = (i\chi_0)^{-1}[\langle\langle j_x|F_x^\dagger\rangle\rangle_\omega$$
$$- \langle\langle j_x|j_x\rangle\rangle_\omega\langle\langle P_x|j_x\rangle\rangle_\omega^{-1}\langle\langle P_x|F_x^\dagger\rangle\rangle_\omega]\langle\langle P_x|j_x\rangle\rangle_\omega.$$

Now, we substitute the last equation into (19). As a result, we have

$$\langle\langle P_x|j_x\rangle\rangle_\omega = i\chi_0\{\omega - \chi_0^{-1}[\langle\langle j_x|F_x^\dagger\rangle\rangle_\omega$$
$$- \langle\langle j_x|j_x\rangle\rangle_\omega\langle\langle P_x|j_x\rangle\rangle_\omega^{-1}\langle\langle P_x|F_x^\dagger\rangle\rangle_\omega]\}^{-1}.$$

Thus, we obtain an explicit expression for $M(\omega)$ in terms of the current–force-type irreducible Green's function [40]:

$$M(\omega) = -\frac{1}{\chi_0}[\langle\langle j_x|F_x^\dagger\rangle\rangle_\omega$$
$$- \langle\langle j_x|j_x\rangle\rangle_\omega\langle\langle P_x|j_x\rangle\rangle_\omega^{-1}\langle\langle P_x|F_x^\dagger\rangle\rangle_\omega]$$

or

$$M(\omega) = -\frac{1}{\chi_0}\langle\langle j_x|F_x^\dagger\rangle\rangle_\omega^{\text{irred}}.$$

Next, we have to express $M(\omega)$ in terms of the force–force-type irreducible function $\langle\langle F_x|F_x^\dagger\rangle\rangle_\omega^{\text{irred}}$. Differentiating the function $\langle\langle j_x|F_x^\dagger\rangle\rangle_\omega^{\text{irred}}$ with respect to the first variable, we obtain

$$M(\omega) = -(\chi_0\omega)^{-1}[K + \langle\langle F_x|F_x^\dagger\rangle\rangle_\omega^{\text{irred}}],$$

where the irreducibility implies the following combination:

$$\langle\langle F_x|F_x^\dagger\rangle\rangle_\omega^{\text{irred}} = \langle\langle F_x|F_x^\dagger\rangle\rangle_\omega$$
$$- \langle\langle F_x|j_x^\dagger\rangle\rangle_\omega\langle\langle P_x|j_x^\dagger\rangle\rangle_\omega^{-1}\langle\langle P_x|F_x^\dagger\rangle\rangle_\omega.$$

Since K is purely real, it is convenient to calculate first the imaginary part of $M(\omega)$. Then,

$$\Gamma(\omega) = -(\chi_0\omega)^{-1}\mathrm{Im}\langle\langle F_x|F_x^\dagger\rangle\rangle_\omega^{\mathrm{irred}}$$
$$= (2\chi_0\omega)^{-1}(e^{\omega/T}-1)\mathcal{T}^{\mathrm{irred}}_{F_x^\dagger F_x}(\omega),$$

where $\mathcal{T}^{\mathrm{irred}}_{F_x^\dagger F_x}(\omega)$ is the spectral intensity of the function $\langle F_x^\dagger F_x(t)\rangle^{\mathrm{irred}}$.

Taking into account that $F_x^\dagger = -F_x$, we obtain the function $\Gamma(\omega)$ expressed in terms of the force–force-type irreducible correlation function [15]:

$$\Gamma(\omega) = \frac{1-e^{\omega/T}}{2\chi_0\omega}\int_{-\infty}^{+\infty}\langle F_xF_x(t)\rangle^{\mathrm{irred}}e^{i\omega t}dt.$$

Within the framework of the mode-coupling approximation, we retain in the correlation function $\langle F_xF_x(t)\rangle^{\mathrm{irred}}$ only the first term corresponding to the correlation function $\langle F_xF_x(t)\rangle$ and untangle it as follows:

$$\langle a^\dagger_{\mathbf{k}_1,\sigma_1}S^\alpha_{\mathbf{k}_1-\mathbf{k}_2}\hat\sigma^\alpha_{\sigma_1\sigma_2}a_{\mathbf{k}_2,\sigma_2}a^\dagger_{\mathbf{k}_1',\sigma_1'}(t)S^\beta_{\mathbf{k}_1'-\mathbf{k}_2'}(t)\hat\sigma^\beta_{\sigma_1'\sigma_2'}a_{\mathbf{k}_2',\sigma_2'}(t)\rangle$$
$$\approx 2\langle a_{\mathbf{k}_2,\sigma_2}a^\dagger_{\mathbf{k}_2,\sigma_2}(t)\rangle\langle S^\alpha_{\mathbf{k}_1-\mathbf{k}_2}S^\alpha_{\mathbf{k}_2-\mathbf{k}_1}(t)\rangle$$
$$\times\langle a^\dagger_{\mathbf{k}_1,\sigma_1}a_{\mathbf{k}_1,\sigma_1}(t)\rangle\delta_{\mathbf{k}_1\mathbf{k}_2'}\delta_{\mathbf{k}_2\mathbf{k}_1'}\delta_{\sigma_1\sigma_2'}.$$

Then, we express the correlation functions $\langle S^\alpha_{\mathbf{q}}S^\alpha_{-\mathbf{q}}(t)\rangle$, $\langle a_{\mathbf{k},\sigma}a^\dagger_{\mathbf{k},\sigma}(t)\rangle$, and $\langle a^\dagger_{\mathbf{k},\sigma}a_{\mathbf{k},\sigma}(t)\rangle$ in terms of the Fourier components of the hole and spin Green's functions presented in Sections 2 and 3. As a result, we arrive at expression (22) for $\Gamma(\omega)$. The expression for the real part $M'(\omega)$ is obtained from the Kramers–Kronig relation:

$$M'(\omega) = \frac{1}{\pi}\int_{-\infty}^{+\infty}\frac{\Gamma(\zeta)}{\zeta-\omega}d\zeta.$$

Thus, in the approximation of coupled modes, the complex memory function $M(\omega)$ can be represented as

$$M(\omega) = \frac{J^2}{\chi_0}\frac{1}{N^2}\sum_{\mathbf{k},\mathbf{q}}(v_x(\mathbf{k})-v_x(\mathbf{k}+\mathbf{q}))^2$$
$$\times\sum_{i,j=1}^{4}Z^{(i)}_{\mathbf{k}}Z^{(j)}_{\mathbf{k}+\mathbf{q}}(1-n_F(E^{(i)}_{\mathbf{k}}))n_F(E^{(j)}_{\mathbf{k}+\mathbf{q}})$$
$$\times\frac{F_{\mathbf{q}}}{\omega_{\mathbf{q}}}(1+n_B(\omega_{\mathbf{q}}))\frac{e^{E/T}-1}{E}\left[\frac{1}{E-\omega-i\delta}-\frac{1}{E+\omega+i\delta}\right],$$

where $E = E^{(j)}_{\mathbf{k}+\mathbf{q}} - E^{(i)}_{\mathbf{k}} - \omega_{\mathbf{q}}$, $\delta > 0$.

REFERENCES

1. J. Orenstein, G. A. Thomas, A. J. Millis, *et al.*, Phys. Rev. B **42**, 6342 (1990).
2. S. Uchida, T. Ido, H. Takagi, *et al.*, Phys. Rev. B **43**, 7942 (1991).
3. H. L. Liu, D. B. Tanner, H. Berger, and G. Margaritondo, Phys. Rev. B **59**, 8962 (1999); M. A. Quijada, D. B. Tanner, R. J. Kelley, *et al.*, Phys. Rev. B **60**, 14917 (1999).
4. N. L. Wang, A. W. McConnell, B. P. Clayman, and G. D. Gu, Phys. Rev. B **59**, 576 (1999); N. L. Wang, A. W. McConnell, and B. P. Clayman, Phys. Rev. B **60**, 14883 (1999); M. E. Ziaei, N. L. Wang, B. P. Clayman, and G. D. Gu, Phys. Rev. B **62**, 9818 (2000).
5. D. B. Romero, C. D. Porter, D. B. Tanner, *et al.*, Phys. Rev. Lett. **68**, 1590 (1992).
6. S. Lupi, P. Calvani, M. Capizzi, and P. Roy, Phys. Rev. B **62**, 12418 (2000).
7. J. J. McGuire, M. Windt, T. Startseva, *et al.*, Phys. Rev. B **62**, 8711 (2000).
8. E. G. Maksimov, Usp. Fiz. Nauk **170**, 1033 (2000).
9. E. Dagotto, Rev. Mod. Phys. **66**, 763 (1994).
10. S. Uchida, K. Tamasaku, and S. Tajima, Phys. Rev. B **53**, 14558 (1996).
11. E. G. Maksimov, H. J. Kaufmann, E. K. H. Salje, *et al.*, Solid State Commun. **112**, 449 (1999).
12. S. V. Shulga, O. V. Dolgov, and E. G. Maksimov, Physica C (Amsterdam) **178**, 266 (1991).
13. B. Arfi, Phys. Rev. B **45**, 2352 (1992).
14. J. Ruvalds and A. Virosztek, Phys. Rev. B **43**, 5498 (1991).
15. N. Plakida, Z. Phys. B **103**, 383 (1997).
16. R. B. Laughlin, J. Low Temp. Phys. **99**, 443 (1995).
17. P. Bourges, in *The Gap Symmetry and Fluctuations in High Temperature Superconductors*, Ed. by J. Bok, G. Deutscher, D. Pavuna, and S. A. Wolf (Plenum, New York, 1998), p. 349.
18. F. Marsiglio, J. P. Carbotte, A. Puchkov, and T. Timusk, Phys. Rev. B **53**, 9433 (1996).
19. J. P. Carbotte, E. Schachinger, and D. N. Basov, Nature **401**, 354 (1999); E. Schachinger and J. P. Carbotte, Phys. Rev. B **62**, 9054 (2000).
20. A. F. Barabanov, L. A. Maksimov, and A. V. Mikheyenkov, in *Lectures on the Physics of Highly Correlated Electron Systems IV: Fourth Training Course in the Physics of Correlated Electron Systems and High-T_c Superconductors, Salerno, 1999*, Ed. by F. Mancini (American Inst. of Physics, Melville, 2000), AIP Conf. Proc. **527**.
21. V. Borisenko, M. S. Golden, S. Legner, *et al.*, Phys. Rev. Lett. **84**, 4453 (2000).
22. A. G. Loeser, Z. X. Shen, D. S. Dessau, *et al.*, Science **273**, 325 (1996).
23. M. R. Norman, H. Ding, M. Randeria, *et al.*, Nature **392**, 157 (1998).
24. W. Götze and P. Wölfle, Phys. Rev. B **6**, 1226 (1972).
25. V. G. Grigoryan, G. Paasch, and S.-L. Drechsler, Phys. Rev. B **60**, 1340 (1999).
26. A. F. Barabanov, R. Hayn, A. A. Kovalev, *et al.*, Zh. Éksp. Teor. Fiz. **119**, 777 (2001) [JETP **92**, 677 (2001)].

27. P. Prelovshek, Phys. Lett. A **126**, 287 (1988).
28. A. Ramsak and P. Prelovshek, Phys. Rev. B **40**, 2239 (1989); **42**, 10415 (1990).
29. A. F. Barabanov, A. A. Kovalev, O. V. Urazaev, and A. M. Belemouk, Phys. Lett. A **265**, 221 (2000).
30. A. F. Barabanov, E. Zasinas, O. V. Urazaev, and L. A. Maksimov, Pis'ma Zh. Éksp. Teor. Fiz. **66**, 173 (1997) [JETP Lett. **66**, 182 (1997)].
31. A. F. Barabanov, O. V. Urazaev, A. A. Kovalev, and L. A. Maksimov, Pis'ma Zh. Éksp. Teor. Fiz. **68**, 386 (1998) [JETP Lett. **68**, 412 (1998)]; A. F. Barabanov, O. V. Urazaev, A. A. Kovalev, and L. A. Maksimov, Dokl. Akad. Nauk **366** (2), 188 (1999) [Dokl. Phys. **44**, 286 (1999)].
32. R. O. Kuzian, R. Hayn, A. F. Barabanov, and L. A. Maksimov, Phys. Rev. B **58**, 6194 (1998).
33. M. Inui, S. Doniach, and M. Gabay, Phys. Rev. B **38**, 6631 (1988).
34. J. F. Annet, R. M. Martin, A. K. McMahan, and S. Satpathy, Phys. Rev. B **40**, 2620 (1989).
35. A. F. Barabanov and V. M. Berezovsky, Phys. Lett. A **186**, 175 (1994); Zh. Éksp. Teor. Fiz. **106**, 1156 (1994) [JETP **79**, 627 (1994)].
36. E. G. Maksimov, D. Yu. Savrasov, and S. Yu. Savrasov, Usp. Fiz. Nauk **167**, 353 (1997) [Phys. Usp. **40**, 337 (1997)].
37. D. N. Zubarev, Usp. Fiz. Nauk **71**, 71 (1960) [Sov. Phys. Usp. **3**, 320 (1960)].
38. N. Nucker, U. Eckern, J. Fink, and P. Muller, Phys. Rev. B **44**, 7155 (1991).
39. Y.-Y. Wang, G. Feng, and A. L. Ritter, Phys. Rev. B **42**, 420 (1990).
40. Yu. A. Tserkovnikov, Teor. Mat. Fiz. **49**, 219 (1981).

Translated by I. Nikitin

Journal of Experimental and Theoretical Physics, Vol. 94, No. 1, 2002, pp. 149–161.
Translated from Zhurnal Éksperimental'noĭ i Teoreticheskoĭ Fiziki, Vol. 121, No. 1, 2002, pp. 175–190.

SOLIDS
Electronic Properties

The "Pair" Fermi Contour and High-Temperature Superconductivity

V. I. Belyavsky[a, *] and Yu. V. Kopaev[b, **]

[a]*Voronezh State Pedagogical University, Voronezh, 394043 Russia*
[b]*Lebedev Physical Institute, Russian Academy of Sciences, Leninskiĭ pr. 53, Moscow, 117924 Russia*
**e-mail: vib@vspu.ac.ru*
***e-mail: kopaev@lebedev.sci.ru*
Received June 28, 2001

Abstract—Superconducting pairing of holes with a large (on the order of doubled Fermi) total pair momentum and small relative motion momenta is considered taking into account the quasi-two-dimensional electronic structure of high-T_c cuprates with clearly defined nesting of the Fermi contour situated in an extended neighborhood of the saddle point of the electronic dispersion law (the momentum space region with a hyperbolic metric) and the arising of a spatially inhomogeneous (stripe) structure as a result of the redistribution of current carriers (holes) that restores regions with antiferromagnetic ordering. The superconducting energy gap and condensation energy were determined, and their dependences on the doping level were qualitatively studied. The energy gap was shown to exist in some hole concentration region limited on both sides. The superconducting state with a positive condensation energy appears in a narrower range of doping within this region. The reason for the arising of the superconducting state at a repulsive screened Coulomb interaction between holes is largely the redistribution of hole pairs in the momentum space related to the special features of the hyperbolic metric, which is responsible for the formation of the "pair" Fermi contour, and the renormalization of the kinetic energy of holes when the chemical potential changes because of the condensation of pairs. Hole pairs of the type under consideration exist not only in the condensate but also in the form of quasi-stationary states with very weak decay at temperatures substantially exceeding the superconducting transition temperature. The pseudogap region of the phase diagram of high-T_c cuprates is related to such states. The pairing mechanism under consideration allows not only the principal characteristics of the phase diagram but also key experimental data on high-T_c cuprate materials to be qualitatively explained. © *2002 MAIK "Nauka/Interperiodica".*

1. INTRODUCTION

The special properties of the quasi-two-dimensional (2D) electronic structure of the compounds that exhibit high-temperature superconductivity (the presence of long almost rectilinear Fermi contour portions, which are situated in an extended neighborhood of the saddle point of the electronic dispersion law) result, because of screened Coulomb repulsion, in the arising of quasi-stationary states of hole pairs with a large total momentum $K \approx 2k_F$ (k_F is the Fermi momentum in the direction of vector **K**) and a small relative motion momentum [1]. Such quasi-stationary states are characterized by very weak decay [1] and can therefore be treated as peculiar elementary excitations of the electronic subsystem of crystals. The appearance of bound states of hole pairs under repulsive interaction conditions and virtual absence of their decay (although the levels of the quasi-stationary states lie in the region of the continuous spectrum of one-particle excitations) is explained by different signs of the principal values of the tensor of effective masses which determines the kinetic energy of the relative motion of a pair in the vicinity of the saddle point (the momentum space in an extended neighborhood of the saddle point has a pseudo-Euclidean or hyperbolic metric). The qualitative description of the pseudogap state of underdoped high-T_c materials suggested in [1] was based on the concept of quasi-stationary states of hole pairs. It was, in particular, shown how characteristic temperature T^* of the appearance of a pseudogap depended on the doping level [1].

The scattering amplitude of the relative motion of hole pairs considered in [1] contains one more complex pole [2], possibly, responsible for superconducting instability. The imaginary part of the corresponding pole should be related to the superconducting gap Δ value and the T_c superconducting transition temperature. The disappearance of the complex pole and, conversely, a monotonic increase in the energy of quasi-stationary states with increasing repulsive Coulomb interaction between holes explain the substantial difference between T^* and T_c in the strongly underdoped region and qualitatively describe the observed phase diagram of high-T_c cuprates (in the temperature–doping level coordinates).

The absence of a quasi-particle peak [3] in the angular-resolved photoemission spectra (ARPES) at $T_c < T < T^*$ is also explained by the presence of hole-pair quasi-stationary states in this temperature interval. Indeed, each state of such a pair with a given total momentum is represented by the sum of Bloch one-par-

ticle (hole) states, all of which are present in quasi-stationary states with small weights $g \ll 1$ [1]. In ARPES experiments, an inner-shell electron is excited into one of the Bloch states near the Fermi contour and, therefore, has $g = 1$. This state strongly decays because of excitation redistribution between quasi-stationary states with different total momenta. In the scheme under consideration, the observation of a quasi-particle peak at $T < T_c$ [3] is explained by the presence of a complex scattering amplitude pole and Bose condensation of a macroscopic number of hole pairs, when the weight of Bloch states in the condensate of pairs with a given momentum **K** is close to one ($g \sim 1$).

If the concentration of holes p becomes smaller than a certain p_N value as $T \longrightarrow 0$, the high-T_c compound becomes insulator and acquires a long-range antiferromagnetic order. At $p > p_N$, short-range antiferromagnetic order is retained, and a spatially inhomogeneous quasi-one-dimensional (1D) state arises in the conducting planes of high-T_c compounds in the form of static or dynamic stripes, that is, regions with restored antiferromagnetic order depleted of holes and separated by layers with metallic conductivity, which are enriched in holes [3]. It follows that antiferromagnetic and superconducting orderings in high-T_c compounds are closely and nontrivially related to each other. In particular, short-range antiferromagnetic order may play a stabilizing role in the arising and superconducting condensation of hole pairs with large total momenta considered in [1]. Indeed, the real part of the complex scattering amplitude pole is positive [2]. Energy loss caused by depopulating some hole states in the region with a hyperbolic metric within the Fermi contour can therefore be balanced by the redistribution of hole pairs in the **r** space, which results in the coexistence of regions of the metallic and antiferromagnetic types. Such a phase stratification [4] accompanied by changes in hole state populations in the momentum space may correspond to an energy minimum.

The superconducting state with a large ($K \approx 2k_F$) total pair momentum studied below has formally been considered in [5] in terms of microscopic models of the coexistence of superconductivity and antiferromagnetism or charge density waves (structural phase transition; the $\approx 2k_F$ momentum then transforms into a new reciprocal lattice vector). States with large pair momenta then arise as a result of the coexistence of antiferromagnetic ordering and Cooper pairs with a zero total momentum. Phenomenologically, such transformations are described as breaking of certain symmetries, for instance, by the $SO(5)$ or $SU(4)$ models [6, 7].

As is known [8, 9], increased doping of the antiferromagnetic phase related to the spin density wave may result in that simultaneous appearance of a charge density wave will be also energetically favorable. This leads to a weak ferromagnetism observed in some compounds [10]. Existence of the charge ordering was also reported in superconducting bismuth cuprates [11]. The formation of a one-dimensional stripe structure naturally leads to modulation of the spin and charge density, which may result in the appearance of weak ferromagnetism.

In this work, we show that, for pairs predominantly formed from states within the Fermi hole contour and from states outside the Fermi contour, the total pair momenta (**K** and **K**', respectively) are not equal (this should result in actually observed asymmetry of tunnel volt–ampere characteristics with respect to changing the sign of bias voltage.) These momenta are equal neither to the antiferromagnetic vector nor to the doubled Fermi vector, and Cooper pairs with a zero total momentum can therefore not appear, as is assumed in what follows. The hyperbolic metric of the kinetic energy of the relative motion of such pairs results in the redistribution of particles in the momentum space, that is, in the appearance of a pair Fermi contour which does not coincide with the Fermi contour defined as a zero-energy line of one-particle excitations. Such a nonuniformity of the distribution of particle pairs in the momentum space against the background of doping-dependent antiferromagnetic ordering corresponds to the nonuniform (stripe) electronic structure of conducting planes in high-T_c compounds.

2. THE HAMILTONIAN OF HOLE PAIRS

Relative motion momentum **k** of a hole pair with total momentum **K** ($K \approx 2k_F$, where k_F is the Fermi momentum in direction **K**) belongs to some **K**-dependent region Ξ_K within the 2D Brillouin zone [1]. Because the Fermi contour is situated in an extended neighborhood of the saddle point of the electronic dispersion law, this region is naturally separated into two parts, in one of which the energy of pair relative motion is positive ($\Xi_K^{(+)}$), and, in the other, negative ($\Xi_K^{(-)}$). The Ξ_K region corresponding to pair momentum **K** (**K** pair) which is smaller than twice the Fermi momentum in direction **K** ($K < 2k_F$) is schematically shown in Fig. 1. In Fig. 1, direction **K** coincides with the direction of the Cu–O bond in the conducting plane (antinodal direction). The shape of the Fermi contour (a square with rounded angles; a part of the Fermi contour is shown in Fig. 1 as a line labeled by the corresponding hole energy value, which equals the Fermi energy E_F) is typical of high-T_c cuprates with p-type doping [16]. The Ξ_K region for the selected direction **K** therefore consists of two parts. One part is situated inside the Fermi contour, and the other, outside it. The energy of the pair along the a–a' and b–b' lines, which separate the $\Xi_K^{(+)}$ and $\Xi_K^{(-)}$ regions, equals the energy of the center of mass $2\varepsilon(K/2)$. Clearly, there are many hole pairs with momentum **K** and the same energy in which the $\mathbf{k}_\pm = \mathbf{K}/2 \pm \mathbf{k}$ momenta of the holes constituting these pairs belong to some line in the **k** space region bounded by

the Fermi contour. In addition, there exist pairs with the same momentum **K** of the center of mass and the same energy but hole momenta $\mathbf{k}'_{\pm}$ outside the region bounded by the Fermi contour. It follows that, because of the hyperbolic **k** space metric, the removal of a pair of holes with momenta $\mathbf{k}_{\pm}$ (the creation of two electrons inside the Fermi hole contour) and the creation of a pair of holes with momenta $\mathbf{k}'_{\pm}$ outside the Fermi contour can occur without a change in energy. If the pair momentum **K**' value (**K**' pair) is larger than twice the Fermi momentum ($K' > 2k_F$), the corresponding $\Xi_{K'}$ region fully lies outside the Fermi contour. The transfer of a pair of holes from Ξ_K to $\Xi_{K'}$ is definitely related to an increase in energy (the energy of the center of mass then increases). However, note that such a transfer can involve the removal of pairs with a positive relative motion energy from Ξ_K and the appearance of pairs with a negative relative motion energy in $\Xi_{K'}$.

The transfer of hole pairs from the $\Xi_K^{(+)}$ part of the Ξ_K region to the **k** space region outside the Fermi contour can be related to the formation of a spatially inhomogeneous (stripe) structure in which regions with decreased and increased (with respect to the mean value) hole concentrations alternate. The region to which hole pairs can be transferred can be the $\tilde{\Xi}_K$ part of the Ξ_K region that is situated outside the Fermi contour and corresponds to the same $K < 2k_F$ pair momentum value or the $\Xi_{K'}^{(-)}$ part of the $\Xi_{K'}$ region that corresponds to the $K' > 2k_F$ pair momentum (Fig. 1). The density of states of the relative pair motion is substantially higher in $\Xi_{K'}^{(-)}$ than in $\tilde{\Xi}_K$, which allows us to consider $\Xi_K^{(+)} \longrightarrow \Xi_{K'}^{(-)}$ transitions only. The pairs that come from Ξ_K have positive relative motion energies, whereas relative pair motion energies in $\Xi_{K'}$ are negative. A peculiar band diagram for pairs with momenta **K** and **K**' is shown in Fig. 2. There is some energy gap $\delta\varepsilon_{KK'}$ between the highest pair energy $2E_F$ in $\Xi_K^{(+)}$ and the lowest pair energy in $\Xi_{K'}^{(-)}$. As mentioned above, hole transfer from $\Xi_K^{(+)}$ to $\Xi_{K'}^{(-)}$ therefore results in kinetic energy loss. To estimate this loss, suppose that a certain δN number of pairs from $\Xi_K^{(+)}$ are transferred to $\Xi_{K'}^{(-)}$. In the $\Xi_K^{(+)}$ region (when $T \longrightarrow 0$ and there is no interaction between holes), free pair states appear in some energy interval near $2E_F$, which is small compared with $\delta\varepsilon_{KK'}$. The same number of pairs fill a narrow energy interval (determined from the condition of the conservation of the number of pairs) at the lower boundary of the zone corresponding to the $\Xi_{K'}^{(-)}$ region,

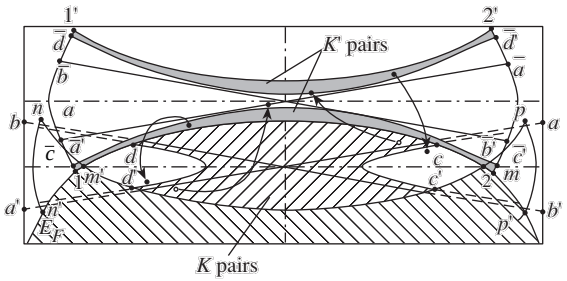

Fig. 1. Regions of admissible relative motion momenta of **K** pairs (region Ξ_K bounded by the *m*'*dcmc*'*d*'*m*' line and region $\tilde{\Xi}_K$ bounded by the *nm*'*n*'*n* and *pmp*'*p* lines) and **K**' pairs (region $\Xi_{K'}$ bounded by the 1'2'21 line). The straight lines aa' and bb' ($\bar{a}\bar{a}'$ and $\bar{b}\bar{b}'$) correspond to **K** (**K**') pair energy equal to the center-of-mass energy $2\varepsilon(K/2)$ ($2\varepsilon(K'/2)$). The region of negative relative pair motion energies lies above and below these lines, and the region of positive energies, to the left and to the right of them. The $\Xi_K^{(-)}$ region corresponding to negative **K**-pair relative motion energies counted from the chemical potential level is bounded by the *m*'*dcmc*'*d*'*m*' line, and the $\Xi_K^{(+)}$ region of positive energies, by the *m*'*dd*'*m* and *mcc*'m lines. For **K**' pairs, the 1'2'$\bar{d}'$ $\bar{d}$ 1' and 12$\bar{c}\bar{c}'$1 lines bound the $\Xi_{K'}^{(-)}$ region, and the $\bar{d}\bar{d}'\bar{c}\bar{c}'\bar{d}$ line bounds the $\Xi_{K'}^{(+)}$ region. The *nn*' and *pp*' lines are portions of the boundary of the momentum space region with a hyperbolic metric for **K** pairs, and the 11' and 22' lines are similar boundaries for **K**' pairs. The Fermi contour labeled by E_F (the Fermi energy) is the line passing through the *n*'1*m*'*dcm*2*p*' points. The pair Fermi contour is shown by lines *dd*' and *cc*' for **K** pairs and by lines $\bar{c}\bar{c}'$ and $\bar{d}\bar{d}'$ for **K**' pairs.

and energy loss caused by the transfer of holes from $\Xi_K^{(+)}$ to $\Xi_K^{(-)}$ can therefore be estimated as $\delta N\delta\varepsilon_{KK'}$.

The $\Xi_K^{(+)} \longrightarrow \Xi_{K'}^{(-)}$ transition in the **k** space corresponds to the transfer of holes from antiferromagnetic to metallic part of the stripe region in the **r** space (Fig. 3). The accompanying strengthening of antiferromagnetic correlations in $\Xi_K^{(+)}$ somewhat decreases energy, which should balance energy loss caused by the excitation of hole pairs from $\Xi_K^{(+)}$ to $\Xi_K^{(-)}$. Energy gain in the removal of a hole pair from $\Xi_K^{(+)}$ (that is, from the antiferromagnetic part of the stripe region) can be taken into account phenomenologically, by the introduction of an $I = I(x)$ parameter depending on the $p - p_N \equiv x$ difference. Let each hole pair removed from the $\Xi_K^{(+)}$ region give energy gain I. The hole energy gain of removing δN pairs then equals $-\delta NI$. It follows that the stripe structure is energetically favorable if

$$I > \delta\varepsilon_{KK'}. \qquad (2.1)$$

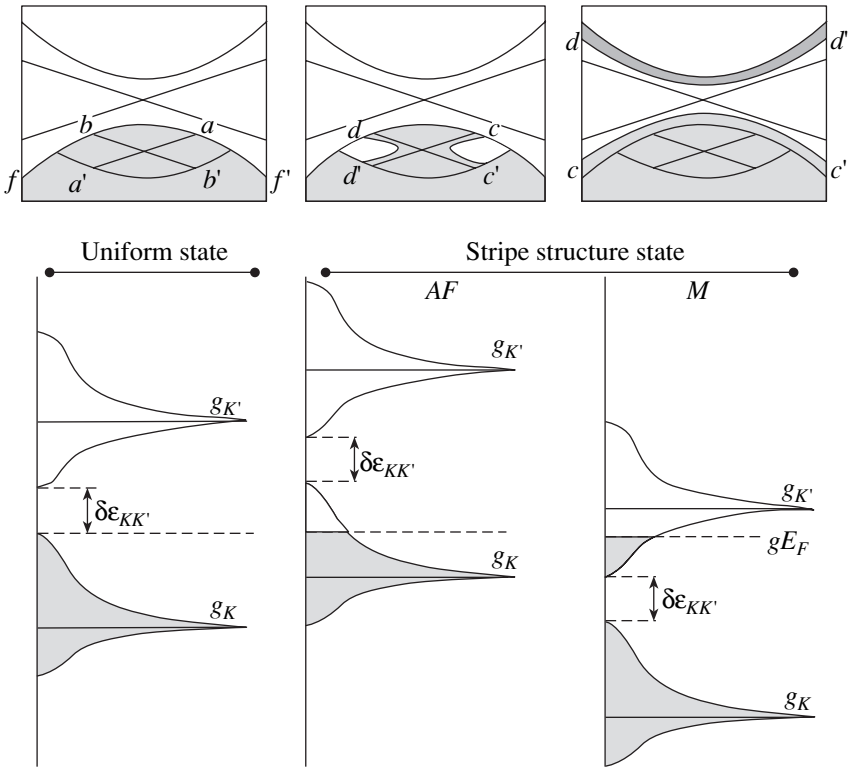

Fig. 2. Given at the top are the Ξ_K and $\Xi_{K'}$ regions. Along the straight lines within Ξ_K and $\Xi_{K'}$, relative motion energies of **K** and **K**' pairs, respectively, equal zero. The *ff*' line is a portion of the Fermi contour corresponding to the homogeneous state of the electronic system (left diagram, top part). The *cc*' and *dd*' lines are pair Fermi contour portions for antiferromagnetic (AF) stripe region (diagram in the middle, top part) and stripe region with metallic conductivity (M) (right diagram, top part). Occupied states are shaded. The bottom band schemes of relative motion energy show the uniform electronic system state (left diagram), AF stripe part (middle diagram), and M stripe part (right diagram). The lower band corresponds to **K** pairs, and the upper one, to **K**' pairs.

Note that the arising of the stripe structure within the approach that we use is not at all related to a possible transition of the electronic subsystem into the superconducting state.

Note also that, whereas, in this work, the transfer of holes from the $\Xi_K^{(+)}$ to the $\Xi_{K'}^{(-)}$ region sustained by the restoration of antiferromagnetic order in the formation of stripes that is considered, in [12], the redistribution of holes between the Ξ_K region and some acceptor reservoir level was implicitly assumed to occur. The degree of transfer (and the chemical potential value in the absence of superconducting pairing) is then determined by the energy position of the acceptor level. For instance, if the acceptor level of an E_A energy (this energy may be due to the presence of the corresponding doping admixtures in layers-reservoirs) is situated below the Fermi level, the depopulation of hole states in the energy layer of width $\delta E = E_F - E_A$ near the Fermi contour should occur at $T = 0$. If the hole dispersion law is isotropic and the momentum space has the usual Euclidean metric, then the Fermi contour congruently shrinks precisely by δE. Holes that leave the initially populated region become bound with impurity atoms uniformly distributed in the **r** space. If the Fermi contour with long almost rectilinear portions is strongly anisotropic, then it follows from the aforesaid that, because of the hyperbolic metric of the momentum space in the vicinity of the Fermi contour, the corresponding change in the population of states near the Fermi contour will be nonuniform, which should result

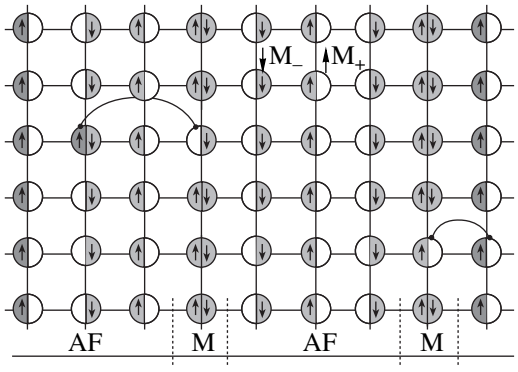

Fig. 3. A schematic diagram of the stripe ordering. Arrows indicate the hole transitions from metallic to antiferromagnetic stripe region corresponding to the transitions in the momentum space indicated by arrows in Fig. 1.

in a spatially inhomogeneous population of acceptor states [3].

The presence of a hole-populated part in the $\Xi_K = \Xi_K^{(-)} + \Xi_K^{(+)}$ region (for this part, we will use the $\Xi_K^{(-)}$ notation introduced above), where the relative hole motion energy counted from the chemical potential level is by definition negative, and of a depopulated part (denoted by $\Xi_K^{(+)}$) with a positive relative motion energy (and a similar distribution of holes in the **k** space in the $\Xi_{K'}$ region) makes hole pairing possible near the lines that separate Ξ_K and $\Xi_{K'}$ region parts depopulated and populated as a result of stripe formation. It follows that these lines (Fig. 1) play the role of a peculiar "pair" Fermi contour on which a superconducting gap can arise. If the $\mathbf{K}' - \mathbf{K}$ vector value that determines the scale of the stripe structure is substantially larger than the $\delta k_c \sim \Delta$ characteristic size of the **k** space region near the Fermi contour in which the superconducting order parameter is nonzero (as is assumed in what follows), the problems of pairing in Ξ_K and $\Xi_{K'}$ can in a first approximation be considered independently of each other.

It should be taken into account in writing the Hamiltonian of hole pairs with momentum **K** that each hole virtually transferred from $\Xi_K^{(-)}$ to $\Xi_K^{(+)}$ in the **k** space as a result of superconducting pairing (as shown by arrows in Fig. 1) goes into the antiferromagnetic part of the stripe in the **r** space which, as noted above, may feature weak ferromagnetic ordering caused by the simultaneous existence of spin and charge density waves. It is natural to suggest that the resulting average magnetization is proportional to the phenomenological parameter $I(x)$ introduced above and the hole energy can be expressed as

$$\varepsilon_\sigma(\mathbf{k}) = \varepsilon(\mathbf{k}) + \chi I(x)\sigma\theta_k, \tag{2.2}$$

where $\varepsilon(\mathbf{k})$ is the dispersion law of holes with momenta **k** and σ is the projection of the hole spin. The characteristic function θ_k equals 1 for the relative hole motion momentum $\mathbf{k} \in \Xi_K$ and $\theta_k = 0$ for $\mathbf{k} \in \Xi_{K'}$. The coefficient of proportionality between the weak magnetization (arising in the antiferromagnetic part of the stripe) and the Weiss antiferromagnetic field $I(x)$ is sufficiently small ($\chi \ll 1$); in particular, assuming $\chi \longrightarrow 0$ in (2.2), it is possible to consider the superconducting pairing in the absence of weak ferromagnetism. It follows that the Hamiltonian of hole pairs with momentum **K** has the form

$$\hat{H}_K = \sum_k \{[\varepsilon_\uparrow(\mathbf{k}_+) - \mu]\hat{a}^+_{k_+\uparrow}\hat{a}_{k_+\uparrow} + [\varepsilon_\downarrow(\mathbf{k}_-) - \mu]\hat{a}^+_{k_-\downarrow}\hat{a}_{k_-\downarrow}\} + \sum_{k,k'} \tilde{U}(\mathbf{k} - \mathbf{k}')\hat{a}^+_{k_+\uparrow}\hat{a}^+_{k_-\downarrow}\hat{a}_{k'_-\downarrow}\hat{a}_{k'_+\uparrow}, \tag{2.3}$$

where $\mathbf{k}'_\pm = \mathbf{K}/2 \pm \mathbf{k}'$, $\hat{a}^+_{k_\pm\sigma}$ ($\hat{a}_{k_\pm\sigma}$) are the operators of creation (annihilation) of a hole with momentum $\mathbf{k}_\pm$ and spin projection σ, symbol $\uparrow$ ($\downarrow$) corresponds to $\sigma = 1/2$ ($-1/2$), μ is the chemical potential of holes, and the summation with respect to **k**, **k**' is performed over the whole domain of definition of the relative motion momentum of the **K** and **K**' pairs.

The Fourier transform of the energy of screened Coulomb repulsion of holes $\tilde{U}(\mathbf{k} - \mathbf{k}')$ depends on the **k** space region within which scattering in interactions between holes is allowed [1]. Because of the limitations imposed by the Pauli principle, the whole region of allowed scattering for the **K** pair components ($\mathbf{k}_+$ and $\mathbf{k}_-$ momenta) is Ξ_K. However, if **K** pairs with negative relative motion energies are considered, that is, if $\mathbf{k}, \mathbf{k}' \in \Xi_K^{(-)}$, then, clearly, $\tilde{U}(\mathbf{k} - \mathbf{k}') = U_0\Xi_K^{(-)}$. Similarly, if $\mathbf{k}, \mathbf{k}' \in \Xi_K^{(+)}$, that is, **K** pairs with positive relative motion energies are considered, then $\tilde{U}(\mathbf{k} - \mathbf{k}') = U_0\Xi_K^{(+)}$. If scattering involves the transfer of pairs from $\Xi_K^{(-)}$ to $\Xi_K^{(+)}$, that is, if $\mathbf{k} \in \Xi_K^{(-)}$ and $\mathbf{k}' \in \Xi_K^{(+)}$ (and vice versa), then the region allowed for scattering is the whole Ξ_K region, and we must then assume that $\tilde{U}(\mathbf{k} - \mathbf{k}') = U_0\Xi_K$. In the case when the momenta **k** and **k**' belong to the regions Ξ_K and $\Xi_{K'}$ corresponding to different total momenta **K** and **K**', the energy $\tilde{U}(\mathbf{k} - \mathbf{k}')$ is determined in a similar way. Here [1], $U_0 = 4\pi e^2 r_0^2 a^2/cS$; r_0 is the screening radius; a and c are the interatomic distances in the conducting plane and between neighboring planes, respectively; and S is the normalization area. The area of the Ξ_K region or the related dimensionless $\Xi_K a^2/(2\pi)^2$ value, which is the ratio between this area and the 2D Brillouin zone area determining the statistical weight of the **K** pair [1], takes into account statistical correlations in the system of holes and thereby plays the role of the correlation attenuation factor [17].

3. ENERGY GAP

Approximate diagonalization of Hamiltonian (2.3) can, as usual [18], be performed with the use of the Bogoliubov transformation, which introduces new one-particle creation and annihilation operators,

$$\hat{a}_{k_+\uparrow} = u_k b_{k,+1} + \nu_k \hat{b}^+_{k,-1}, \qquad \hat{a}_{k_-\downarrow} = u_k \hat{b}_{k,-1} - \nu_k \hat{b}^+_{k,+1}. \tag{3.1}$$

The subscripts K and K', indicating domains of the particle creation and annihilation operators for the operators and amplitudes u_k and ν_k in Eq. (3.1), will be omitted below. Hamiltonian (2.3) can be written [18] accurate to $\hat{b}^2$

as $\hat{H} = E_0 + \hat{H}^{(0)} + \hat{H}^{(1)}$, where the ground state energy is

$$E_0 = -2\sum_k \xi_k v_k^2 + \sum_k \Delta_k u_k v_k, \tag{3.2}$$

$2\xi_k \equiv \varepsilon(k_+) + \varepsilon(k_-) - 2\mu$ is the hole pair energy counted from the chemical potential level, and $\hat{H}^{(0)}$ and $\hat{H}^{(1)}$ are, respectively, the transformed Hamiltonian diagonal and off-diagonal parts, which have the form

$$\hat{H}^{(0)} = \sum_{k;\ \beta = \pm 1} \eta_\beta(k)\hat{b}^+_{k\beta}\hat{b}_{k\beta}, \tag{3.3}$$

$$\begin{aligned}\hat{H}^{(1)} &= \sum_k \{2\xi_k u_k v_k - (v_k^2 - u_k^2)\Delta_k\} \\ &\times (\hat{b}^+_{k,+1}\hat{b}^+_{k,-1} + \hat{b}_{k,-1}\hat{b}_{k,+1}).\end{aligned} \tag{3.4}$$

Let us define the order parameter as

$$\Delta_k = \sum_{k'} \tilde{U}(k-k')u_{k'}v_{k'}(1 - n_{k',1} - n_{k',-1}), \tag{3.5}$$

where $n_{k,\beta} \equiv \langle \hat{b}^+_{k\beta}\hat{b}_{k\beta}\rangle = [\exp(\eta_\beta(k)/T) + 1]^{-1}$ are the mean occupation numbers determined by the energies

$$\eta_\beta(k) = \sqrt{\xi_k^2 + \Delta_k^2} + \frac{\beta}{2}I\theta_k \tag{3.6}$$

that correspond to two $\beta = \pm 1$ branches of the spectrum of one-particle excitations. The population of the region where the hole pair energy $2\xi_k < 0$ and the condition of off-diagonal Hamiltonian part $\hat{H}^{(1)}$ vanishing determine the selection of the amplitudes in the Bogoliubov transformation,

$$\begin{aligned}v_k^2 &= \frac{1}{2}\left(1 - \frac{\xi_k}{\sqrt{\xi_k^2 + \Delta_k^2}}\right), \\ u_k v_k &= -\frac{1}{2}\frac{\Delta_k}{\sqrt{\xi_k^2 + \Delta_k^2}}.\end{aligned} \tag{3.7}$$

The equation for the order parameter takes the form

$$\Delta_k = -\frac{1}{2}\sum_{k'} \frac{\tilde{U}(k-k')\Delta_{k'}}{\sqrt{\xi_{k'}^2 + \Delta_{k'}^2}}(1 - n_{k',1} - n_{k',-1}). \tag{3.8}$$

It follows from (3.8) that, at $\tilde{U}(k-k') > 0$, a constant-sign solution is absent in Ξ_K. Let us therefore assume, for finding an approximate solution, that the dependence of the order parameter on the relative motion momentum is determined by a discontinuous function, which abruptly changes sign in passing across the Fermi contour. We restrict our consideration to the simplest case when the order parameter takes on constant (independent of k) values on both sides of the Fermi contour. Namely, we assume that $\Delta_k \equiv \Delta_- > 0$ in $\Xi_K^{(-)}$ and $\Delta_k \equiv -\Delta_+ < 0$ in $\Xi_K^{(+)}$. This selection of the solution (as well as of the simplest solution in the BCS theory [19, 20]) most probably does not correspond to an exact minimum of the ground state energy. However, this solution leads (as will be shown below) to an energy gain in the superconducting pair condensation. It should be noted that the superconducting pairing considered independently on the pair Fermi contour in each of the Ξ_K and $\Xi_{K'}$ domains may lead only to the trivial solution $\Delta_+ = \Delta_- = 0$ because (as noted above) Eq. (3.8) has no nontrivial constant-sign solutions. Thus, the transitions of particles between states close to the pair Fermi contour parts inside (Ξ_K domain) and outside ($\Xi_{K'}$ domain) of the Fermi contour account for the main contribution to the superconducting pairing. In the **r** space, these transitions correspond to the transitions between metallic and antiferromagnetic parts of the stripe. For this reason, the mean field approximation used in writing Eq. (2.2) is valid, strictly speaking, only provided that the spatial scale of the stripe structure does not exceed the coherence length.

Equation (3.8) can be rewritten in the form

$$\begin{aligned}(1-\alpha)\Delta_- + \Delta_+ &= \frac{1}{2}U_0\Xi_K(1 - \alpha + \alpha^2)\Delta_- \\ &\times \sum_{k\in\Xi_{K'}^{(-)}} \frac{1 - n_{k,1} - n_{k,-1}}{\sqrt{\xi_k^2 + \Delta_-^2}}, \\ \Delta_- + \alpha\Delta_+ &= \frac{1}{2}U_0\Xi_K(1 - \alpha + \alpha^2)\Delta_+ \\ &\times \sum_{k\in\Xi_{K'}^{(+)}} \frac{1 - n_{k,1} - n_{k,-1}}{\sqrt{\xi_k^2 + \Delta_+^2}}.\end{aligned} \tag{3.9}$$

Here, $\alpha = \Xi_{K'}^{(-)}/(\Xi_{K'}^{(+)} + \Xi_{K'}^{(-)})$. Note that the $(1 - \alpha + \alpha^2) > 0$ multiplier is positive at arbitrary α in the range $0 < \alpha < 1$. This multiplier, which is proportional to $\Xi_{K'}^2 - \Xi_K^{(-)}\Xi_{K'}^{(+)}$, appears as the difference between the square of the matrix element of the interaction energy between holes "off-diagonal" with respect to the ($\pm$) indices and the product of the matrix elements "diagonal" with respect to these indices; it takes into account the population of states within the pair Fermi contour, that is, statistical (determined by the Pauli principle) correlations in the electronic system. The inequality specified above is met irrespective of the above suggestion that the matrix element of screened Coulomb repulsion $U_0 = \text{const}$ in the whole Ξ_K region.

As excitation energy (3.6) is positive by definition in the whole $\Xi_K^{(-)}$ region, that is, $\eta_{\pm 1}(k) = \sqrt{\xi_k^2 + \Delta_k^2} > 0$, the $2\xi_k$ energy of the pair in this region lies in the range $-2\varepsilon_{K-} \le 2\xi_k \le 0$, where ε_{K-} is the energy width of the

$\Xi_{K'}^{(-)}$ region (Fig. 2). According to (3.6), we have $\eta_{\pm 1}(k) = \sqrt{\xi_k^2 + \Delta_k^2} \pm \chi I/2$ in the $\Xi_K^{(+)}$ region. Clearly, $\eta_{+1}(k) > 0$ always, whereas the $\eta_{-1}(k) > 0$ condition, which is necessary in order that the multiplier containing occupation numbers be equal to one on the right-hand side of the second equation in (3.9) when $T \longrightarrow 0$, is met if $\chi I\sqrt{1 - (2\Delta_k/\chi I)^2} \le 2\xi_k \le 2\varepsilon_{K+}$, where ε_{K+} is the energy width of the $\Xi_K^{(+)}$ region (Fig. 2). Indeed, if $0 \le 2\xi_k \le \chi I\sqrt{1 - (2\Delta_k/\chi I)^2}$, we have $n_{k,1} = 0$ and $n_{k,-1} = 1$ for $T \longrightarrow 0$ in this region of pair energy variations (and in the corresponding momentum space region within $\Xi_K^{(+)}$). It follows that the $(1 - n_{k,1} - n_{k,-1})$ multiplier excludes some part of the $\Xi_K^{(+)}$ region from the sum in the second equation in (3.9).

Assuming that $\Delta_+ \ll I < 2\varepsilon_{K+}$ (the hole pair energy can then be counted from the chemical potential level established as a result of the stratification of holes in the formation of the stripe structure; at this stage, we can therefore ignore the chemical potential shift caused by the formation of the condensate of pairs in calculating the $\Delta_\pm$ order parameter, because this shift is small as $\Delta_\pm$) and passing from the summation to the integration,

$$\sum_{k \in \Xi_{K'}^{(-)}} 1 \longrightarrow Sg^{(-)} \int_{-\varepsilon_{K-}}^{0} d\xi,$$
$$\sum_{k \in \Xi_K^{(+)}} 1 \longrightarrow Sg^{(+)} \int_{\chi I/2}^{\varepsilon_{K+}} d\xi, \tag{3.10}$$

where $g^{(+)}$ ($g^{(-)}$) is the mean density of states in $\Xi_K^{(+)}$ ($\Xi_{K'}^{(-)}$), let us rewrite (3.9) for $T \longrightarrow 0$ as

$$(1 - \alpha)\Delta_- + \Delta_+ = \alpha w_-(\alpha)\Delta_- \ln\frac{2\varepsilon_-}{\Delta_-},$$
$$\Delta_- + \alpha\Delta_+ = (1 - \alpha)w_+(\alpha)\Delta_+ \ln\frac{2\varepsilon_+}{\chi I}, \tag{3.11}$$

where the notation $w_\pm(\alpha) = (e^2 r_0^2 a^2/2\pi c\varepsilon_\pm)\Xi_K^2(1 - \alpha + \alpha^2)$ is used. The second equation in (3.11) is linear, whence it immediately follows that $\Delta_+ = \gamma\Delta_-$, where the coefficient relating order parameter values in the $\Xi_{K'}^{(-)}$ and $\Xi_K^{(+)}$ regions has the form

$$\gamma = [(1 - \alpha)w_+(\alpha)\ln(2\varepsilon_+/\chi I) - \alpha]^{-1}. \tag{3.12}$$

By definition, $\gamma > 0$. Taking (2.1) into account, we therefore arrive at the conclusion that a solution to (3.8) exists if

$$\delta\varepsilon_{KK'} < I < \frac{2\varepsilon_{K+}}{\chi}\exp\left(-\frac{\alpha}{(1 - \alpha)w_{K+}(\alpha)}\right). \tag{3.13}$$

As the $I = I(x)$ antiferromagnetic energy value depends on the doping level, inequalities (3.13) actually determine the region of doping in which the order parameter is nonzero.

The first equation in (3.11) yields the order parameter value, which also depends on the doping level,

$$\Delta_- = 2\varepsilon_-\left(\frac{\chi I}{2\varepsilon_+}\right)^\nu \exp\left(-\frac{\gamma}{\alpha w_+}\right). \tag{3.14}$$

Here, $w_\pm(\alpha) = w_\pm(1 - \alpha + \alpha^2)$ and $\nu = \gamma(1 - \alpha)^2 w_+/\alpha w_-$. Although the obtained expression is formally similar to that for the energy gap in the BCS theory [19, 20], (3.14) exhibits a dependence on the U_0 effective coupling constant which is substantially more complex than and different from that in the BCS theory, because this constant is present in the definitions of the γ and ν parameters. The preexponential factor is determined by the kinetic energy of the pair in the $\Xi_{K'}^{(-)}$ region; on the other hand, this energy itself depends on how large the $\Xi_K^{(+)}$ region depleted of holes as a result of stripe structure formation and determined by the I antiferromagnetic energy value is. Of course, parameter (3.14) also depends on pair momentum **K**. This momentum should in principle be determined by comparing the ground state energies of the system in the superconducting and normal phases.

In calculating superconducting order parameter (3.14), we only considered the situation when the pair Fermi contour opens as a result of the redistribution of holes between the Ξ_K and $\Xi_{K'}$ regions and ignored possible influence of the $\tilde{\Xi}_K$ region (corresponding to the same pair total momentum as the Ξ_K region) on superconducting pairing. For this influence, there is no $I > \delta\varepsilon_{KK'}$ restriction on the antiferromagnetic energy, and a minimum hole transfer energy from Ξ_K to $\tilde{\Xi}_K$ is zero (points m and m' in Fig. 1; in the situation that we are considering, the pair Fermi contour degenerates into these two points). The formation of such a contour of a finite length requires energy expenditure related to the redistribution of holes between Ξ_K and $\tilde{\Xi}_K$. It is likely that a stripe structure does not form in this case, and such an energy loss can be balanced by restoring partial antiferromagnetic order in such a redistribution of holes over energies. As mentioned, the density of states vanishes at m and m', which means that superconducting transition temperatures, even moderately high, can hardly be attained in this case.

As a consequence of crystallographic symmetry, all wave functions of the pair that correspond to the set of vectors that form the star of vector **K** are equivalent. The wave function of the pair having the symmetry properties of the crystal should therefore be represented as some linear combination with coefficients selected according to the irreducible representations of the symmetry group of the crystal. In tetragonal crystals, the

momentum space region comprising four, generally nonoverlapping in the vicinity of nodal directions, Ξ_K regions (Fig. 1) corresponds to this linear combination. For this reason, in this neighborhood corresponding to some finite Fermi contour region, the superconducting order parameter should vanish irrespective of the irreducible representation (A_{1g} or B_{1g}) under which the wave function of the pair transforms. Transformations under the A_{1g} representation formally correspond to anisotropic *s*-wave order parameter symmetry (which also exists when Ξ_K regions pairwise overlap each other). In the case of B_{1g} transformations, we have *d*-wave symmetry irrespective of whether the Ξ_K regions do or do not overlap; rotation through $\pi/4$ then corresponds to the transformation $\Delta_- \longleftrightarrow \Delta_+$.

4. THE SHIFT OF THE CHEMICAL POTENTIAL

The $2E_F$ chemical potential value of hole pairs in a spatially uniform system means that the whole Ξ_K region is filled, whereas states in the $\Xi_{K'}$ region are vacant. The appearance of an inhomogeneous stripe structure results in the redistribution of holes between Ξ_K and $\Xi_{K'}$ and the formation of a pair Fermi contour, which is the line that, at $T = 0$, separates occupied and unoccupied states in Ξ_K and $\Xi_{K'}$. Precisely as a result of such a redistribution sustained by partial restoration of antiferromagnetic order, the very possibility of pairing of holes arises. This pairing may result in the formation of an energy gap on the pair Fermi contour. The degree of depletion of the Ξ_K region and population of $\Xi_{K'}$ is determined by the *I* antiferromagnetic energy value, which is responsible for the position of the 2μ chemical potential of hole pairs with respect to energy band boundaries with the $g_K(\varepsilon)$ and $g_{K'}(\varepsilon)$ densities of states corresponding to the Ξ_K and $\Xi_{K'}$ regions, as is shown in Fig. 2.

To determine the shift of chemical potential μ' directly caused by the condensation of hole pairs, we must take into account that the formal definition of the mean number of holes in Ξ_K,

$$\langle N_K \rangle = 2\sum_{k \in \Xi_K} \nu_k^2 + \sum_{k \in \Xi_K} (u_k^2 - \nu_k^2)(n_{k,1} + n_{k,-1}), \quad (4.1)$$

takes into account holes experiencing transfer from $\Xi_K^{(+)}$ to $\Xi_{K'}^{(-)}$; at equilibrium, this transfer is balanced by holes supplied to $\Xi_K^{(+)}$ from $\Xi_{K'}^{(-)}$. The conserved value is therefore the sum $\langle N_K \rangle + \langle N_{K'} \rangle$, where the second term is the mean number of holes in the Ξ_K' region. When a condensate of pairs with momenta **K** and **K'** is formed, hole fluxes between Ξ_K and $\Xi_{K'}$ change. However, if $|\mathbf{K}' - \mathbf{K}| \gg \delta k_c$ (as was assumed above), condensations in Ξ_K and $\Xi_{K'}$ can be considered independent of each other. As the contribution to $\langle N_K \rangle$ of transitions from Ξ_K to $\Xi_{K'}$ is nonzero, only transitions related to the condensation of **K** pairs can be taken into account if the position of the pair Fermi contour determined by the *I* phenomenological parameter is set and transitions of hole pairs caused by interaction (2.3) across this contour are considered. Precisely these transitions are responsible for the shift of the pair Fermi contour as a result of pairing interaction of holes in hole pair Hamiltonian (2.3). Strictly speaking, the inclusion of pairing interaction (when $\Delta_- \equiv \Delta \neq 0$) also causes a small (against Δ) change in hole pair fluxes between Ξ_K and $\Xi_{K'}$. On the other hand, the shift of chemical potential μ' caused by the condensation is itself small as Δ, and taking into account changes in fluxes between Ξ_K and $\Xi_{K'}$ can only slightly change the values of the λ and τ coefficients introduced below without giving qualitatively new results. It follows that $\langle N_K \rangle$ has the meaning of an approximately conserved number of holes in the $\Xi_K^{(-)}$ region; this number is determined by the *I* parameter. As in [12], (4.1) can, at $T = 0$, be rewritten as

$$\sum_{k \in \Xi_K^{(+)}} 1 - \sum_{k \in \Xi_K^{(-)}} 1 = \sum_{k \in \Xi_K} \frac{\xi_k}{\sqrt{\xi_k^2 + \Delta_k^2}}. \quad (4.2)$$

Passing from summation to integration yields

$$\begin{aligned} \delta\Xi &= g_-\{\sqrt{\mu'^2 + \Delta^2} - \sqrt{(\varepsilon_- + \mu')^2 + \Delta^2}\} \\ &+ g_+\{\sqrt{(\varepsilon_+ - \mu')^2 + \gamma^2\Delta^2} - \sqrt{\mu'^2 + \gamma^2\Delta^2}\}. \end{aligned} \quad (4.3)$$

Here, $\delta\Xi \equiv \Xi_K^{(+)} - \Xi_K^{(-)}$. The index labeling **K** pairs and the $(2\pi)^{-2}$ common factor of the mean densities of states $g_\pm = \Xi_K^{(\pm)}/\varepsilon_\pm$ in the $\Xi_K^{(\pm)}$ regions are omitted. As the shift of chemical potential μ' counted from the pair Fermi contour determined for $\Delta \longrightarrow 0$ is small in Δ, we assume that $\mu' = \lambda|\Delta| + \tau\Delta^2$ (here, we select $\Delta > 0$ and will therefore omit the modulus sign; note also that the shift of the chemical potential is identical for all crystallographically equivalent directions of the total pair momentum). Further, assuming that $\varepsilon_\pm \gg \Delta$, we can rewrite (4.3) with accuracy to terms of the order of Δ^2 inclusive. The equality corresponding to (4.3) should be fulfilled at arbitrary $\Delta \neq 0$. The λ and τ values can therefore be found by equating the coefficients of Δ and Δ^2 to zero in the expansion. The equation for λ has the form

$$g_-\sqrt{\lambda^2 + 1} - g_+\sqrt{\lambda^2 + \gamma^2} - (g_- + g_+)\lambda = 0, \quad (4.4)$$

whence

$$\lambda = \frac{g_-^2 - g_+^2\gamma^2}{2\sqrt{g_-g_+(g_- + g_+)(g_- + g_+\gamma^2)}}. \quad (4.5)$$

Using λ allows the τ coefficient to be found,

$$\tau = -\left[\frac{1}{2}\left(\frac{g_-}{\varepsilon_-} - \gamma^2\frac{g_+}{\gamma_+}\right) + \frac{1}{4}\left(\frac{g_-}{\varepsilon_-} - \frac{g_+}{\varepsilon_+}\right)\lambda^2\right] + \left[(g_- + g_+) - \left(\frac{g_-\lambda}{\sqrt{\lambda^2+1}} - \frac{g_+\lambda}{\sqrt{\lambda^2+\gamma^2}}\right)\right]^{-1}. \quad (4.6)$$

Coefficients (4.5) and (4.6) that determine the shift of the chemical potential caused by the condensation depend on expression (3.12) for the γ parameter relating the superconducting order parameter values Δ_- and Δ_+, which are constant within the $\Xi_{K'}^{(-)}$ and $\Xi_K^{(+)}$ regions, respectively. According to (3.12), the γ parameter depends on the shape and size of the $\Xi_{K'}^{(-)}$ and $\Xi_K^{(+)}$ regions (which determine the α, $\varepsilon_\pm$, and $w_\pm$ values) and on antiferromagnetic energy I. This energy, like effective coupling constants $w_\pm$, depends on doping level x. As has been mentioned above, $I(x)$ is a monotonically decreasing function of its argument (Fig. 4). If we initially assume that $\chi I_0 \equiv \chi I(0) > 2\varepsilon_+$, then $\ln[2\varepsilon_+/\chi I(x)]$ in the definition of γ is a slowly increasing function of x, which passes zero at some point $x_a > 0$ (this is shown in Fig. 4). In contrast, $w_\pm(x) \sim r_0^2$ is a decreasing function of x (for simplicity, below the assume $w_+ = w_- = w$); the plot of $w(x)$ is also presented in Fig. 4. The $w(x)\ln[2\varepsilon_+/\chi I(x)]$ product is therefore a function with a maximum and passes through x_a (Fig. 4). The $\gamma \geq 0$ condition can be written as

$$w(x)\ln\frac{2\varepsilon_+}{\chi I(x)} \geq \frac{\alpha}{(1-\alpha)(1-\alpha+\alpha^2)} \equiv \kappa. \quad (4.7)$$

This condition can be used to find the doping level interval, $x_1 \leq x \leq x_2$, within which there exists a solution to (3.11) for the superconducting order parameter (Fig. 4). The denominator in (3.12) vanishes at $x = x_{1,2}$; therefore, $\gamma \longrightarrow +\infty$ if $x \longrightarrow x_1 + 0$ or $x \longrightarrow x_2 - 0$. The $x = x_{1,2}$ points are the simple poles of the $\gamma = \gamma(x)$ function; this function is schematically plotted in Fig. 4.

It is believed [3] that antiferromagnetic correlations are essentially suppressed at the doping level that approximately corresponds to the optimal doping level, $x = x_c$ (at $x = x_c$, the temperature of the superconducting transition is a maximum; clearly, $x_1 < x_c < x_2$). Set $I(x) = I_0\exp(-x/x_c)$. We will only use the linear term of the expansion of $w(x)$ in powers of x; that is, $w(x) = w(1 - x/x_b)$, where $x_b > x_c$. The left-hand side of (4.7) can then be written in the form

$$w(x)\ln\frac{2\varepsilon_+}{\chi I(x)} \approx \frac{w}{x_b x_c}(x - x_a)(x_b - x) \quad (4.8)$$

[the right-hand side of (4.7) is determined by the special features of the electronic spectrum at $x_1 < x < x_2$ and, in this doping level interval, can be considered independent of x]. The plot of function (4.8) is a parabola passing through points x_b and $x_a \equiv x_c\ln(\chi I_0/2\varepsilon_+)$. The maximum value of this function, $(w/4x_b x_c)(x_b - x_a)^2$, is attained at $\bar{x} = (x_b + x_a)/2$ and can exceed κ in (4.7) only if the w coupling constant is fairly large. It follows that inequality (4.7) imposes restrictions on the minimum coupling constant value. As $w \sim \Xi_K^2$, condition (4.7) can only be satisfied if the Ξ_K region exceeds some definite value. The Ξ_K region may be large for an appropriate value of the antiferromagnetic energy ensuring (due to the Fermi contour nesting) a sufficiently large length of the pair Fermi contour, whereby the vectors **K** and **K'** are aligned with the nesting vector (antinodal direction). On the contrary, the Ξ_K region is fairly small for the **K** and **K'** vectors rotated through $\pi/4$ with respect to the nesting vector (nodal directions). For this reason, condition (4.7) actually establishes the direction of the pair momentum at which the condensation of pairs occurs.

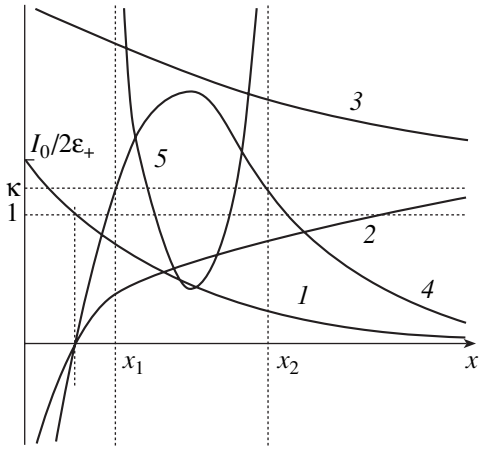

Fig. 4. Doping dependences (drawn schematically, not to scale) of the functions (*1*) $I(x)$, (*2*) $\ln[2\varepsilon_+/\chi I(x)]$, (*3*) $w(x)$, (*4*) $w(x)\ln[2\varepsilon_+/\chi I(x)]$, and (*5*) $\gamma(x)$.

By definition, $x_a > 0$ if $\chi I_0 > 2\varepsilon_+$. As follows from Fig. 4, we then have $x_1 > 0$. The long-range antiferromagnetic order region is therefore separated from the $x_1 < x < x_2$ region, where the superconducting order parameter is nonzero, by a finite doping level interval, as, for instance, in the $La_{2-x}Sr_xCuO_4$system [21]. At $x_a < 0$, that is, if $\chi I_0 < 2\varepsilon_+$, situations with $x_1 \leq 0$ are possible; that is, the region with a nonzero superconducting order parameter (when $T \longrightarrow 0$) borders upon the antiferromagnetic phase as the doping level increases, as, for instance, in the $YBa_2Cu_3O_{6+x}$ phase [21].

5. CONDENSATION ENERGY

The existence of solution (3.14) for the superconducting order parameter in the $x_1 < x < x_2$ doping interval does not mean that the superconducting state arises in all of this interval or at least in some part of it, that is, that the electronic system should experience the transi-

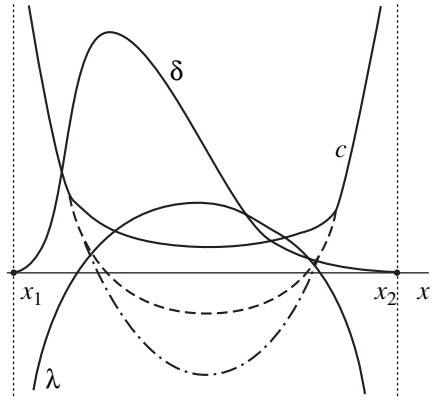

Fig. 5. Doping dependences (drawn schematically, not to scale) of dimensionless order parameter $\delta(x)$ and the $\lambda(x)$ and $c(x)$ parameters determining the condensation energy; $c(x)$ function behaviors discussed in the text are shown by the dashed and dot-and-dash lines.

tion from the nonsuperfluid normal phase to the superfluid superconducting phase as temperature decreases. For such a transition to occur, it is necessary that the condensation energy determined as the difference of the ground state energies of the system in the normal and superconducting phases be positive.

The ground state energy $T = 0$ can, according to (3.2), be written as

$$E_{0S} = \sum_k \xi_k - \sum_k \left\{ \frac{\xi_k^2}{\sqrt{\xi_k^2 + \Delta_k^2}} + \frac{1}{2} \frac{\Delta_k}{\sqrt{\xi_k^2 + \Delta_k^2}} \right\}. \quad (5.1)$$

Using the chemical potential shift caused by the condensation found above, $\mu' = \lambda\Delta + \tau\Delta^2$, we can write (5.1) in the form

$$E_{0S} = E_{0N} - 4g_-\varepsilon_-^2 S\delta(\lambda + c\delta), \quad (5.2)$$

where the dimensionless order parameter $\delta \equiv \Delta/2\varepsilon_-$ is introduced and the ground state energy of the normal state,

$$E_{0N} = -Sg_-\varepsilon_-^2, \quad (5.3)$$

is defined as the limit to which (5.1) tends as $\delta \longrightarrow 0$. The parameter c determined in (5.2) is related to the coefficient τ in (4.6) as

$$c = 2\tau\varepsilon_- + \frac{g_- + g_+\gamma^2}{4g_-}. \quad (5.4)$$

The second term in (5.4), which is not related to the condensation-induced chemical potential shift, formally originates from the direct contribution of the potential energy of pairing interaction in Hamiltonian (2.3) to the condensation energy, whereas the contributions related to the λ and τ coefficients can be explained by the renormalization of the kinetic energy of relative pair motion caused by the condensation of pairs. Although such an artificial separation [15, 16] of the condensation energy into kinetic and potential energy contributions [both these contributions, naturally, disappear as the coupling constant in (2.3) tends to zero] is quite conventional, applying it to (5.2) allows us to get a clearer idea of the role played by the hyperbolic metric of the momentum space and the resulting spatially inhomogeneous spin and charge density distributions in the formation of the ground state of the system.

As follows from (5.2), energy gain as a result of the condensation of pairs is possible if

$$\lambda + c\delta > 0. \quad (5.5)$$

This gain is largely caused by the renormalization of the kinetic energy of pairs. Indeed, the chemical potential change accompanying the arising of a condensate of hole pairs changes the position of the pair Fermi contour. Under condition (5.5), the contour shifts in such a way that the part of the Ξ_K region in which the relative pair motion energy is negative expands. Filling this region during condensation decreases the ground state energy.

In this context, the important experimental result obtained in [24] should be mentioned. In conventional superconductors, the sum rule holds fairly well. According to this rule, the density of the Bose condensate approximately equals the integral of the $\sigma_{1N} - \sigma_{1S}$ difference of the conductivities of the normal and superconducting phases with respect to frequency taken from zero to ~Δ. It was found in [24] that the Bose condensate density in the known high-T_c compounds exceeded this integral several fold. Measurements showed [24] that the $\sigma_{1N} - \sigma_{1S}$ difference was nonzero in a frequency range much broader than Δ. As follows from the BCS theory, the condensation of each Cooper pair in conventional superconductors yields energy gain Δ, and the condensation region itself in the momentum space in the neighborhood of the Fermi surface has an energy width also of the order of Δ. Precisely for these reasons, the condensation energy is of the order of Δ^2. The presence of the term linear in Δ in ground state energy (5.2) is evidence that each **K** pair also gives an energy gain of the order of Δ, but the condensation region in the momentum space (in this case, related to the pair Fermi contour rather than the Fermi surface and determined precisely by the kinetic energy of holes of the order of ε_-) is substantially broader, which substantiates the conclusion drawn in [24].

Let us define the condensation energy per unit area as

$$\varepsilon_c \equiv \frac{E_{0N} - E_{0S}}{S} = 4g_-\varepsilon_-^2\delta(\lambda + c\delta) \quad (5.6)$$

and qualitatively study its dependence on the level of doping. Note that (5.6) determines the contribution to

the energy of condensation only of one Ξ_K region corresponding to the total pair momentum **K**. We must therefore multiply (5.6) by the number of vectors in the star of vector **K**. The $\gamma(x)$ function determines the doping level dependence of order parameter (3.14) and coefficients (4.5) and (4.6) that determine the chemical potential shift caused by the condensation of pairs. According to (3.14), the dimensionless order parameter has the form

$$\delta(x) = \left(\frac{\chi I(x)}{2\varepsilon_+}\right)^{\nu} \exp\left(-\frac{\gamma}{\alpha w(x)}\right). \qquad (5.7)$$

As $\nu \sim \gamma$ and $\chi I(x) < 2\varepsilon_+$ in the $x_1 < x < x_2$ doping interval, it is easy to see that $\delta(x)$ exponentially tends to zero as either $x \longrightarrow x_1 + 0$ or $x \longrightarrow x_2 - 0$. Function (5.7) has a maximum at $x_1 < x < x_2$ and is sharply asymmetric (Fig. 5) because $I(x)$ and $w(x)$ are both decreasing functions of x. Condition (5.5) allows the doping level interval ($x_* < x < x^*$) within which the condensation of pairs results in energy gain to be found.

Equation (5.7) with the found λ and τ coefficients that determine the condensation-induced chemical potential shift is a very complex function of the doping level, which also depends on several parameters specific to a given high-T_c superconductor. For instance, the α parameter is directly determined by the structure of the lines of equal energy in the vicinity of the Fermi contour, the $\varepsilon_\pm$ parameters characterize the energy width of the momentum space domain of definition of **K** pairs, and $w_\pm$ and I_0 are the Coulomb and antiferromagnetic interactions in the system of holes. Depending on the ratio between these parameters, a complex and diversified behavior of the condensation energy as a function of doping can be expected. Below, this behavior is characterized only in general.

The $\gamma(x)$ function, which actually determines the (also doping-dependent) $\lambda(x)$ and $c(x)$ coefficients in expression (5.6) for the energy of condensation, is schematically plotted in Fig. 4. As directly follows from (4.5), the $\lambda(x)$ function definitely changes sign twice within the $x_1 < x < x_2$ interval (Fig. 5), and, if condition (3.13) is fulfilled, the character of this dependence does not change. The other function, $c(x)$, exhibits a more diversified behavior when the $\varepsilon_\pm$ parameters change. For instance, it can be positive everywhere in the $x_1 < x < x_2$ interval or twice change its sign within this interval if the parameters are properly selected; in addition, it can be negative everywhere within the whole $x_1 < x < x_2$ interval. The first two possibilities are also shown in Fig. 5.

Precisely the combination of functions shown in Fig. 5 determines the dependence of the condensation energy on doping (Fig. 6). If $c(x) > 0$ everywhere in the $x_1 < x < x_2$ interval, the condensation energy is positive in some $x_* < x < x^*$ interval (within $x_1 < x < x_2$) and negative at $x_1 < x < x^*$ and $x^* < x < x_2$. Possible changes in the behavior of the $c(x)$ dependence, that is, the existence of concentration regions within which $c(x) < 0$, can cause the appearance of two clearly discernible maxima of the $\varepsilon_c(x)$ curve instead of one (the dashed line in Fig. 6). What is more, we can in principle select such **K**-pair parameters that cause the appearance of two separated regions in which $\varepsilon_c(x) > 0$, as is also shown in Fig. 6 by the dash and dot-and-dash curves. Such a nonmonotonic doping dependence of the superconducting transition temperature, clearly, directly related to the condensation energy, is well known for many high-T_c cuprates [21].

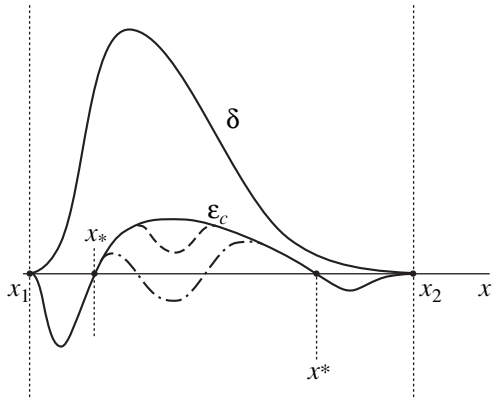

Fig. 6. Doping dependences (drawn schematically, not to scale) of condensation energy $\varepsilon_c(x)$ and dimensionless parameter $\delta(x)$ also shown in Fig. 5; the dashed and dot-and-dash $\varepsilon_c(x)$ curves correspond to $c(x)$ function behaviors discussed in the text and shown in Fig. 5.

Figure 6, in which the dependence of the order parameter on doping, $\delta(x)$, shown in Fig. 5 is reproduced, allows certain qualitative conclusions to be drawn regarding the $2\Delta/T_c$ ratio, which is a universal quantity in the BCS theory, $(2\Delta/T_c)_{BCS} \approx 3.5$. This is definitely not so with high-T_c compounds; especially strong deviations toward increasing this ratio are observed in extremely underdoped cuprates. According to Fig. 6, the condensation energy (and, accordingly, T_c) is very low in the superconducting region [where $\varepsilon_c(x) > 0$] close to its left edge $x = x^*$, whereas the order parameter, which approximately equals $\delta(x_*)$, is, conversely, fairly large. It is therefore natural to expect that, in this doping region, we will have $2\Delta/T_C \gg 3.5$, as is often observed in experiments. Figure 6 also shows that the $\delta(x)$ and $\varepsilon_c(x)$ curves approach each other in the overdoped region, which should correspond to smaller $2\Delta/T_c$ ratio values.

6. CONCLUSION

The special features of the crystal chemical structure of high-T_c compounds lead to a peculiar quasi-two-dimensional electronic structure responsible for the existence of an extended momentum space region with a hyperbolic metric. At the concentration of carriers

close to half-filling, the hole Fermi contour with a clearly defined nesting along the sides of the square 2D Brillouin zone (antinodal directions) is situated precisely in this **k** space region. This opens up a possibility of the arising of hole pairs with a large total momentum (of the order of twice the Fermi momentum) and comparatively small relative motion momenta [1]. There is no need to consider some attractive interaction between holes constituting a pair because the hyperbolic metric causes the appearance of bound states in the form of hole pairs under screened Coulomb repulsion conditions [1, 2]. What is more, precisely under repulsive interaction conditions, the dependence of the scattering amplitude on the energy of relative motion of two holes allows certain conclusions to be drawn [2] that qualitatively agree with the known phase diagram for high-T_c cuprates, especially in the underdoped region. In the energy region corresponding to repulsion, the scattering amplitude has two poles. One pole with a high positive energy and very weak decay is related to the quasi-stationary hole pair state [1]. The density of one-particle excitations then substantially decreases, which can be related to the pseudogap state in the phase diagram. The second scattering amplitude pole [2] is related to the development of superconducting instability (the imaginary part of this pole corresponds to the superconducting gap).

The positive sign of the real part of the second pole is likely to correspond to some energy loss. This energy loss appears because, for pairs to arise, at least some part of the domain of definition of the relative motion momentum of a pair with a given total momentum should be free of holes. Depopulating this region requires a certain number of hole pairs to be transferred to states outside the Fermi contour. The resulting inhomogeneity of state populations in the momentum space should cause a nonuniform distribution of holes in the conventional space, which is generally energetically unfavorable. However, if partial restoration of antiferromagnetic ordering (inherent in an undoped compound but violated by doping) occurs in real space regions depleted of holes (as is likely to be the case with high-T_c compounds), there arises some energy gain capable of balancing energy loss caused by the transfer of hole pairs outside the Fermi contour. Such a transfer is related to the special features of the hyperbolic momentum space metric near the Fermi contour: hole pairs that have positive relative motion energies within the Fermi contour go outside it to the **k** space region where the energy of their relative motion is negative. In this way, regions inside and outside the Fermi contour are formed in which the relative motion momenta of pairs with given total momenta can vary. The occupied and free parts of these regions are separated by lines that are a peculiar Fermi contour for relative pair motions, or the pair Fermi contour.

The presence of long almost rectilinear Fermi contour portions determines the structure of the pair Fermi contour for the pair momentum directed along the boundary of the 2D Brillouin zone; namely, the distribution of populated and depopulated regions is one-dimensional in character. A consequence of this may be quasi-one-dimensional spatially inhomogeneous spin and charge density distributions in the form of a stripe structure, whose characteristic period should be determined by the $|\mathbf{K}' - \mathbf{K}|$ value. The arising of the superconducting order parameter requires that the antiferromagnetic energy, which determines the stripe structure, be limited by inequalities (3.13). Increasing doping decreases $I(x)$ and, through this, the Ξ_K region part free of holes (accordingly, the length of the pair Fermi contour decreases). Increasing doping also decreases $w(x)$, which results in an increase in the exponential multiplier in (3.13). When Ξ_K becomes fully occupied, the superconducting order parameter vanishes at some $x = x_2$ value. A virtually depopulated Ξ_K region with a small pair Fermi contour length corresponds to large $I(x)$ values. The right inequality in (3.13) therefore results in the existence of some I value corresponding to the $x = x_1$ doping level at which the superconducting order parameter reduces to zero. It follows that the order parameter passes a maximum at some point within the $x_1 < x < x_2$ interval.

The static picture of stripe ordering that we consider persists even when the τ_{AF} characteristic antiferromagnetic fluctuation lifetime exceeds the τ_{SC} characteristic time of attaining the superconducting state, $\tau_{AF} > \tau_{SC}$. Elementary estimates based on the uncertainty relation show that $\tau_{AF} \sim I^{-1}$, whereas, as follows from (3.14), τ_{SC} is inversely proportional to the right-hand side of (3.13). It follows that the quasi-static stripe structure picture (dynamic stripes) conforms with condition (3.13), which determines the existence of the superconducting order parameter.

When we cross the optimal doping level in passing from underdoped to overdoped conditions, the amplitude of stripes (dynamic or static) can become rather small; this is a possible reason why we do not have experimental proof of the existence of stripes in the overdoped region. It follows from (3.13) that an increase in the amplitude of stripes eventually suppresses superconducting ordering. The possibility of the existence of a nontrivial solution for the superconducting order parameter persists while inequalities (3.13) can be satisfied.

The spectacular result obtained in [26], which leads to an unexpected conclusion if a traditional (based on the picture of independent one-particle excitations) interpretation is used [26], is easy to bring into conformity with the concept of the pair Fermi contour. If the electronic spectra of some high-T_c cuprates are studied by the ARPES method when the energy of an electron excited from inner atomic shells differs from the Fermi level energy by 100 meV or less, the ARPES data quite unambiguously show that the states near the Fermi

level have a 2D character [26] and lead to the well-known Fermi contour shape, which is a square with rounded corners [16]. However, if the energy "window" of ARPES measurements is broadened (that is, an electron is excited into a state separated from the Fermi level by approximately 500 meV), the results imply that the electronic structure is one-rather than two-dimensional. Note, however, that the simple crosslike shape of the Fermi contour suggested in [26] was obtained not directly from experiment but from some plausible reasoning based on the concept of ideal quasi-one-dimensional stripes.

The conclusion of the 2D $\longrightarrow$ 1D "transformation" of the electronic spectrum made in [26] is in conformity with the pair Fermi contour concept. Indeed, for the pair Fermi contour, which lies within the Fermi contour as is shown at the top of the scheme in the middle of Fig. 2, to manifest itself in ARPES experiments, electrons should be excited to energies substantially different from the Fermi energy (for instance, to energies substantially lower than E_F).

The observation of so-called "dip-hump" structure in ARPES spectra can be considered one more piece of evidence in favor of the pair Fermi contour. The maximum (hump) that appears precisely in the situation that we are considering (antinodal direction), when the area of the Ξ_K region is a maximum, is observed at energies substantially higher than that corresponding to the quasi-particle peak and can be related to excitations in the form of pairs near the pair Fermi contour.

The phenomenological approach that we use to take into account the influence of antiferromagnetic fluctuations on hole pairing allows the key experimental data on high-T_c cuprates to be given a sound and consistent interpretation. Note that the principal conclusions concerning a hyperbolic metric and the arising of a pair Fermi contour remain valid in approaches alternative to the band description and based, for instance, on the t–J model [27] taking into account next-nearest-neighbor interactions (the t–t'–J model [28]).

ACKNOWLEDGMENTS

The authors thank Yu.M. Kagan, L.V. Keldysh, and Yu.E. Lozovik for useful discussions. This work was financially supported by the Russian Scientific-Educational "Integratsiya" Program (projects AO133 and AO155).

REFERENCES

1. V. I. Belyavsky, V. V. Kapaev, and Yu. V. Kopaev, Zh. Éksp. Teor. Fiz. **118**, 941 (2000) [JETP **91**, 817 (2000)].
2. V. I. Belyavsky and Yu. V. Kopaev, Pis'ma Zh. Éksp. Teor. Fiz. **72**, 734 (2000) [JETP Lett. **72**, 511 (2000)].
3. J. Orenstein and A. J. Millis, Science **288**, 468 (2000).
4. A. A. Gorbatsevich, Yu. V. Kopaev, and I. V. Tokatly, Zh. Éksp. Teor. Fiz. **101**, 971 (1992) [Sov. Phys. JETP **74**, 521 (1992)].
5. Yu. V. Kopaev, in *Problems of High-Temperature Superconductivity*, Ed. by V. L. Ginzburg and D. A. Kirzhnits (Nauka, Moscow, 1977), pp. 205–239.
6. S.-C. Zhang, Science **275**, 1089 (1997).
7. M. Guidry, L.-A. Wu, Y. Sun, and C.-L. Wu, Phys. Rev. B **63**, 134516 (2001).
8. B. A. Volkov, Yu. V. Kopaev, and A. I. Rusinov, Zh. Éksp. Teor. Fiz. **68**, 1899 (1975) [JETP **41**, 952 (1975)].
9. V. B. Barzykin and L. P. Gor'kov, Phys. Rev. Lett. **84**, 2207 (2000).
10. D. P. Young, D. Hall, M. E. Tarelli, *et al.*, Nature (London) **397**, 412 (1999).
11. G. Seibold and M. Grilli, Phys. Rev. B **63**, 224505 (2001).
12. V. I. Belyavsky and Yu. V. Kopaev, Pis'ma Zh. Éksp. Teor. Fiz. **73**, 87 (2001) [JETP Lett. **73**, 82 (2001)].
13. B. A. Volkov, A. A. Gorbatsevich, Yu. V. Kopaev, and V. V. Tugushev, Zh. Éksp. Teor. Fiz. **81**, 726 (1981) [Sov. Phys. JETP **54**, 391 (1981)].
14. V. L. Ginzburg, A. A. Gorbatsevich, Yu. V. Kopaev, and B. A. Volkov, Solid State Commun. **50**, 339 (1984).
15. S. Chakravarty, R. B. Laughlin, D. K. Morr, and C. Nayak, Phys. Rev. B **62**, 094503 (2001).
16. Z.-X. Shen, W. E. Spicer, D. M. King, *et al.*, Science **267**, 343 (1995).
17. M. Schafroth, S. Butler, and J. Blatt, Helv. Phys. Acta **30**, 93 (1957).
18. E. M. Lifshitz and L. P. Pitaevskii, *Course of Theoretical Physics*, Vol. 5: *Statistical Physics* (Nauka, Moscow, 1978; Pergamon, New York, 1980), Part 2.
19. J. Bardeen, L. Cooper, and J. Schrieffer, Phys. Rev. **108**, 1175 (1957).
20. J. R. Schrieffer, *Theory of Superconductivity* (Benjamin, New York, 1964; Nauka, Moscow, 1970).
21. E. Dagotto, Rev. Mod. Phys. **66**, 763 (1994).
22. M. R. Norman, M. Randeria, B. Janko, and J. C. Campuzano, Phys. Rev. B **61**, 14742 (2000).
23. J. E. Hirsch, Phys. Rev. B **62**, 14487 (2000).
24. D. N. Basov, S. I. Woods, A. S. Katz, *et al.*, Science **283**, 49 (1999).
25. M. Oda, T. Matsuzaki, N. Momono, and M. Ido, Physica C **341**–**348**, 847 (2000).
26. X. J. Zhou, P. Bogdanov, S. A. Kellar, *et al.*, Science **286**, 268 (1999).
27. F. C. Zhang and T. M. Rice, Phys. Rev. B **37**, 3759 (1988).
28. T. Tohyama and S. Maekawa, Phys. Rev. B **49**, 3596 (1994).

Translated by V. Sipachev

Journal of Experimental and Theoretical Physics, Vol. 94, No. 1, 2002, pp. 162–171.
Translated from Zhurnal Éksperimental'noĭ i Teoreticheskoĭ Fiziki, Vol. 121, No. 1, 2002, pp. 191–202.

SOLIDS
Electronic Properties

Diamagnetic Domains and Magnetostriction in Beryllium

V. S. Egorov* and Ph. V. Lykov
Russian Research Centre Kurchatov Institute, Moscow, 123182 Russia
**e-mail: egorov@isssph.kiae.ru*
Received July 3, 2001

Abstract—Magnetostriction was for the first time studied under the conditions of formation of diamagnetic domains (Condon domains). Transverse magnetostriction oscillations on a beryllium single crystalline plate oriented normally to magnetic field were measured in magnetic fields up to 7 T at temperatures down to 1.5 K. The relative amplitude of oscillations increased almost as the square of magnetic field and reached 10^{-5}. The signal had a sawtoothed shape corresponding to alternation of homogeneous and inhomogeneous (domain) states in the region of the existence of magnetic domains. The arising of domains was accompanied by singularities in the observed signals which is explained by an anomalous increase in the compressibility coefficient of the domain state: coefficient oscillations were more than 100 times larger than the value predicted by the standard theory. The observed relation between magnetization current and deformation led us to conclude that the compressibility of the metal was fully determined by conduction electrons. Magnetostriction then exactly compensated Fermi level oscillations. The position of the Fermi level therefore remained constant under magnetic field variations. In addition, the domain wall thickness had to increase as the plate grew thicker. © *2002 MAIK "Nauka/Interperiodica".*

1. INTRODUCTION

Landau was the first to introduce the quantization of free electron orbital motion in a magnetic field for explaining diamagnetism of metals [1]. The formation of Landau levels doubtless plays the key role in all aspects of the low-temperature physics of metals. In the same work [1], Landau predicted the appearance of a periodic magnetic field dependence of magnetization in strong magnetic fields at fairly low temperatures. This was in essence a prediction of the de Haas–van Alphen effect discovered later, which was the first one in a large series of oscillation effects in metals described by Schönberg [2] fairly fully and in detail. The de Haas–van Alphen effect had in due time played the decisive part in studying and interpreting the shape and size of the Fermi surfaces of most metals. Its role cannot, however, be reduced to the possibility of obtaining information about the Fermi surfaces. The de Haas–van Alphen effect is central to a very interesting phenomenon, namely, the phase transition of metals from the state with homogeneous magnetization to the inhomogeneous state with a diamagnetic domain structure. The formation of such diamagnetic domains, or Condon domains (Condon was the first to observe this effect for a plate oriented normally to magnetic field [3]), is a macroscopic quantum effect, which is of obvious interest of its own. Nevertheless, works that have ever since been concerned with this phenomenon are exceedingly few, in all probability because of the extreme complexity of creating conditions necessary for the formation of domains. This domain structure is certainly alternation of phases with opposite magnetizations; that is, it is both diamagnetic and paramagnetic with respect to an external magnetic field. The term "diamagnetic" is traditionally used in relation to diamagnetic orbital motion of electrons with expressly differentiating the corresponding phenomena from spin magnetism.

Diamagnetic domains were for the first time described by Condon and Walstedt [4]. A nuclear magnetic resonance (NMR) signal was observed in a single crystalline silver plate oriented normally to the magnetic field. The arising of a domain structure was established from the beat signal corresponding to NMR line splitting. The splitting equaled $\Delta B = 12$ Oe in a 9-T magnetic field. In addition, the authors made an attempt, unfortunately unsuccessful, to observe a similar effect in beryllium at $H = 1.9$ T. Only some thirty years later were the authors of [5, 6] able to observe diamagnetic domains in beryllium directly from splitting of the resonance peak of free muon precession (μSR). The μSR method for locally measuring magnetic fields in substances [7] has been exceedingly successful and has allowed diamagnetic domains to be observed in several other metals (primarily, tin [8]) in recent years. Note also that Bozhko and Vol'skii [9] claimed the formation of domains in aluminum based on helicon resonance measurements.

In this work, we studied the problem of direct interrelation between the formation of domains and metal deformation and elastic properties caused by the magnetostriction effect. Chandrasekhar [10] (1963) was the first to note that magnetization oscillations should always be accompanied by simultaneous magnetostriction oscillations. In a short period of time, magnetostriction oscillations in Ag, As, Bi, Cd, Cu, Ga, Sb, Sn, and Zn [11] were studied experimentally. Experiments

were also performed for differently oriented beryllium samples [12]. In [12] and, as a rule, in the other works, experiments were performed for samples whose demagnetization factors were much smaller than one, as is natural for measuring the de Haas–van Alphen effect. For this reason, diamagnetic domains did not form in these experiments. The purpose of this work was to study magnetostriction under the conditions of formation of diamagnetic domains [2], that is, when, first, the inequality

$$-\frac{\partial^2\tilde{\Omega}}{\partial B^2} = \frac{\partial M}{\partial B} > \frac{1}{4\pi} \quad (1)$$

(here, $\tilde{\Omega}$ is the oscillating part of electron gas energy, B is the magnetic field induction in the sample, and M is the magnetization) was fulfilled and, secondly, the demagnetization factor in the external magnetic field direction was close to one.

As the period of δB oscillations is proportional to B^2 and therefore increases more rapidly than the $M(B)$ amplitude, condition (1) bounds from above the interval of magnetic fields in which domains are formed. On the other hand, the distance between Landau levels should be substantially larger than temperature ($\hbar\omega_c \gg kT$), which requires using fairly low temperatures. In addition, the magnetic field should be strong enough for this distance to exceed the Landau level width $\hbar/\tau$; that is, the inequality $\omega_c\tau > 1$ should be met. Here, ω_c is the cyclotron frequency of conduction electrons in the field, and τ is the mean free time of electrons in the sample. It follows that the lower bound of the interval of fields for observing domains is determined not only by temperature but also by the quality of the sample. In addition, this interval is also bounded from below by solenoid magnetic field inhomogeneity in the sample: the inhomogeneity value should be substantially smaller than one-quarter of the oscillation period. In this interval of magnetic fields, domains periodically arise in samples. The magnetization vector in each domain is either collinear or anticollinear with respect to the external magnetic field. The absolute M values are equal in all domains.

We used the beryllium single crystal in which the arising of domains was observed in the earlier experiments, first, in μSR measurements at fields H up to 3 T [5, 6]. In these measurements, a diamagnetic domain structure was shown to arise in the sample up to $T \leq 3$ K. For instance, the μSR spectrum experienced splitting at $T \sim 0.8$ K and external field $H = 27.38$ kOe. The splitting value, $\Delta B = 30$ Oe, remained constant up to external field $H = 27.41$ kOe. The same sample was also used by us earlier [13] to establish the formation of a domain structure by studying magnetic breakdown oscillations of thermoelectromotive force and resistance under the conditions identical to those studied in this experiment. The results described below were briefly reported in [14].

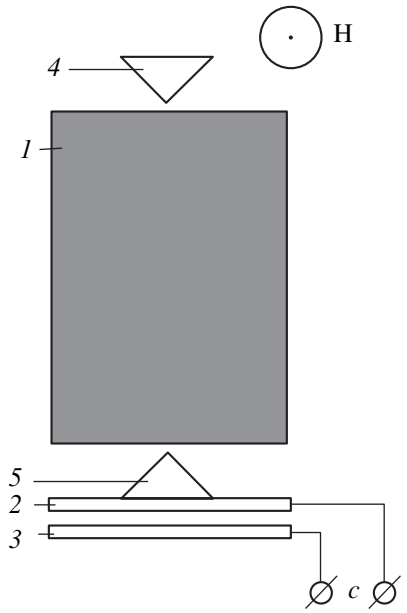

Fig. 1. A schematic of the dilatometer with the sample: (*1*) beryllium single crystal, (*2*) mobile capacitor plate (spring is not shown), (*3*) static capacitor plate, (*4*) adjustment screw, (*5*) mobile plate protuberance, and (*c*) measuring bridge input.

2. EXPERIMENTAL

The beryllium single crystal was an $11 \times 9 \times 1.8$ mm^3 plate cut in such a way that its hexagonal crystallographic axis was directed along the shortest edge. The ratio between the specific resistances at room and liquid helium temperatures was $\rho_{300\,K}/\rho_{4.2\,K} \approx 300$. We measured magnetostriction ε, that is, sample size oscillations $\delta l = \varepsilon l$, along its longer edge ($l = 1.1$ cm). For this purpose, the sample was placed into a dilatometer (Fig. 1) operating by the principle of measuring the capacitance of a plane capacitor. The corresponding face of the sample was fairly small (9×1.8 mm^2), and it would be difficult to use it as a mobile capacitor plate, as is usually done (e.g., see [15]). The mobile plate was therefore made as a separate spring-supported plate with a protuberance against which the sample rested by its face in the first variant of measurements (see Fig. 1). An adjusting screw, which rested against the opposite face, could be used to slightly shift the sample and thereby change the distance between measuring capacitor plates and the initial capacitance. The adjustment could only be performed at room temperature. The capacitance increased as temperature decreased because of the difference in the expansion coefficients of the sample and holder. This allowed us to establish the final capacitance at a level slightly below 100 pF, which corresponded to the highest resolving power of the bridge.

The sample in the dilatometer was in the center of a superconducting solenoid. Solenoid magnetic field uniformity within the sample was ±0.015% or better, which equaled ±4.5 Oe at a 30 kOe field. The period of

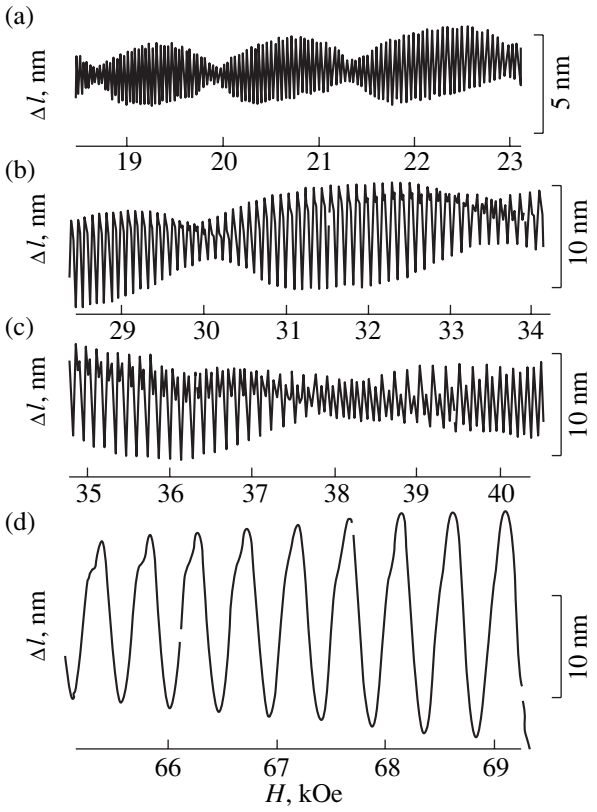

Fig. 2. Magnetostriction shape variations in a wide range of magnetic fields at $T = 1.5$ K; scheme of measurements is shown in Fig. 1. Scales of linear size changes are shown to the right of each record. Anomalous behavior caused by the arising of diamagnetic domains is quite noticeable in records (b) and (c) (see text).

de Haas–van Alphen oscillations in such a field was approximately ~93 Oe. The magnetic field was parallel to the hexagonal axis of the sample and, accordingly, perpendicular to the plate. Recall that, earlier [13], magnetic breakdown oscillations of resistance and thermoelectromotive force were observed for the same sample at the same temperatures in the same solenoid and that the magnetic field dependences of these oscillations corresponded to the arising of magnetic domains. This led us to believe that diamagnetic domains were also formed in the same interval of magnetic fields and temperatures in magnetostriction measurements, although no additional control was exercised.

Measurements were performed both in liquid helium (normal or superfluid) and in helium vapor. The results were substantially different in the level and character of noise. In normal liquid helium, noise was caused by helium boiling and equaled about 2×10^{-3} pF. At a capacitance of about 100 pF and, accordingly, an approximately 10^{-3} cm gap, this corresponded to $\delta\varepsilon \approx 2 \times 10^{-8}$. In superfluid helium, noise decreased to about 10^{-3} pF, but occasional signal spikes were observed, which might be caused by incidental appearance of gas bubbles between measuring capacitor plates. In addition, when the surface of liquid helium passed through the capacitor, we observed a substantial change in capacitance, which virtually prevented us from taking measurements. The most favorable conditions were created in helium vapor: noise equaled ~0.5×10^{-3} pF at 1.5 K, which corresponded to the relative deformation of the sample equal to $\varepsilon \equiv \delta l/l \approx 5 \times 10^{-9}$.

Temperature was controlled by monitoring vapor pressure. Measurements were taken with the use of a TESLA BM484 semiautomatic bridge. The measuring capacitance was connected to the bridge by shielded wires, which allowed us to exclude the capacitance of the leads. The magnetic field dependences of capacitance were recorded on a two-coordinate recorder.

3. RESULTS

Magnetostriction measurements were performed in magnetic fields of 10 to 70 kOe at helium temperatures; the results are shown in Fig. 2. The external magnetic field dependences of magnetostriction at 4.2 K closely agree with the results obtained earlier [12]. These dependences are almost identical in shape to magnetic moment oscillations with beats characteristic of beryllium (Fig. 2a). The beat frequency is approximately 33 times lower than the frequency of oscillations. (This is explained by the presence of two closely spaced extremal cross sections of the Fermi surface of beryllium; the corresponding frequencies are $F_1 = 9.42 \times 10^6$ Oe, $F_2 = 9.71 \times 10^6$ Oe, and $F_2 - F_1 = 0.29 \times 10^6$ Oe [16].) A much more complex pattern is, however, observed at 1.5 K and fields of 2 to 6 T, that is, under the conditions of the formation of diamagnetic domains in the sample. Starting with fields of about 2 T, small amplitude dips appear close to size maxima (Fig. 2b), and double maxima are actually observed. The depth of these dips increases as the magnetic field grows. The dips become comparable with the amplitude of oscillations in the field range 39–42 kOe, and the frequency of oscillations as though doubles (Fig. 2c). A further field increase causes changes in the opposite direction, and, starting with fields of $H \sim 6$ T, oscillations take on the usual form of magnetic moment oscillations (Fig. 2d).

It would certainly be natural to explain this unusual behavior by the arising of diamagnetic domains. In addition, the suggestion was made that the formation of a domain structure, that is, a peculiar state in which two phases, generally, of different densities coexist, could be accompanied by a noticeable decrease in the compressibility coefficient. As a result, the pointed tips (the protuberance of the mobile capacitor plate and the end of the adjusting screw) against which the sample rests periodically "dip" into the sample. (Note that beryllium is one of the hardest metals, inferior only to iridium and tungsten.) Copper spacers ~0.5 mm thick put under the copper tips fully excluded these anomalies. The results

of measurements performed with and without copper spacers at equal magnetic fields under identical conditions are compared in Fig. 3. With spacers, we observe a well-defined sawtooth signal whose amplitude is noticeably larger. Ascending and descending sawtooth portions alternatively correspond to a uniform sample state with smoothly changing deformation and magnetization and to a nonuniform state, or a domain structure, consisting of oppositely deformed diamagnetic and paramagnetic domains.

The results of measurements in the whole range of magnetic fields are shown in Fig. 4. Amplitude measurements were accompanied by beats, and the dependences were constructed based only on the points that corresponded to oscillation antinodes. The amplitude of the signal measured with the use of spacers falls within the region situated noticeably higher than the region of domain formation; this amplitude was approximately 2 times larger close to $H \sim 4$ T. The dotted line was obtained by treating the obtained dependence according to the quadratic law. To the left and to the right of the domain region, that is, in low and high fields in which the state of the crystal is everywhere homogeneous, this curve passes noticeably lower than that measured without the spacers. It is likely that this result can be explained by a much more rigid kinematic connection between the sample and the measuring capacitor through screw and protuberance tips compared with the connection through copper spacers.

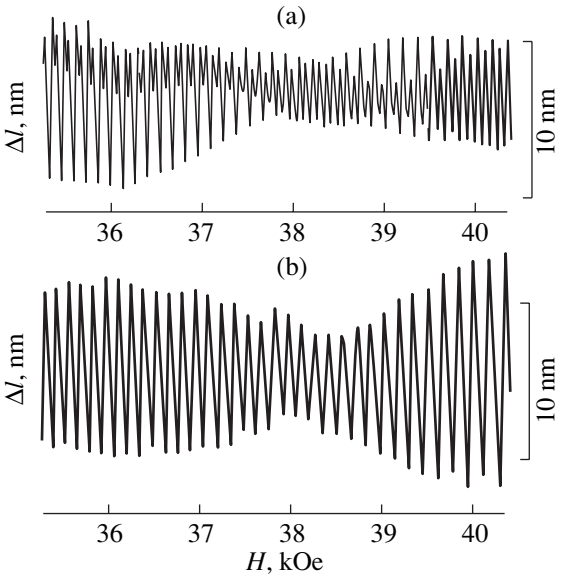

Fig. 3. A comparison of the results obtained in magnetostriction measurements (b) with and (a) without spacers in the same range of magnetic field variations under identical conditions.

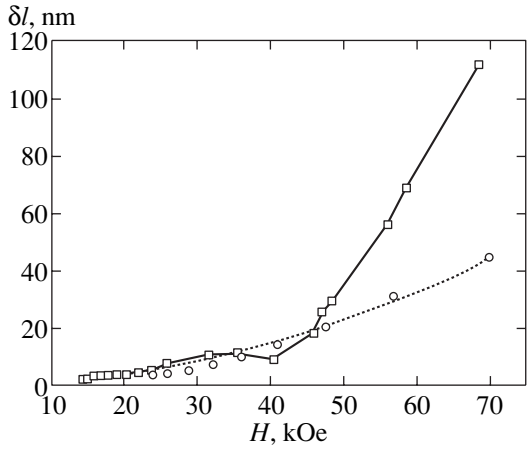

Fig. 4. Field dependence of magnetostriction amplitude (from peak to peak) in experiments (○) with and (□, solid line) without spacers. Symbols are placed at field values corresponding to oscillation antinodes. The dotted line corresponds to the quadratic law.

4. DISCUSSION

1. The hypothesis formulated above allows a quantitative estimate of elasticity modulus oscillations to be obtained. To do this, we must take into account that, in addition to the usual magnetostriction signal $\delta l = \varepsilon l$ present in the absence of a load, loadings, even insignificant, should cause additional oscillating deformation and elasticity modulus oscillations

$$\delta l' = \tilde{h}_0 + \tilde{h}. \tag{2}$$

Here, h_0 is the homogeneous static deformation under an evenly distributed load, h is the depth of sample surface deflection ("pit") under the pointed copper tip (see Fig. 5), and $\tilde{h}_0 + \tilde{h}$ is the oscillating contribution of these deformations proportional to the amplitude of elasticity modulus oscillations, that is,

$$\tilde{h}_0 + \tilde{h} = (h_0 + h)\tilde{E}/E. \tag{3}$$

First, let us find $\tilde{E}/E$ using the simple approximation for the oscillation contribution to the energy,

$$\tilde{\Omega} = a\cos\varphi. \tag{4}$$

Here, a is some amplitude, and $\varphi = 2\pi F/B$ is the phase, where F is the magnetic frequency corresponding to the cross section of the Fermi surface and B is the induction in the sample. The change in energy in a magnetic field including the elastic contribution then can be written as

$$\delta\Omega = a\cos\varphi + \frac{1}{2}E(\varepsilon_x^2 + \varepsilon_y^2 + \varepsilon_z^2). \tag{5}$$

For beryllium, this is a good approximation, because the anisotropy of its compressibility coefficient is very small (±5%) [17], its Poisson coefficient virtually equals zero, and all deformations can therefore be considered independent. Beryllium is indeed a unique metal in this respect: its Young's modulus is $E = 300$ GPa,

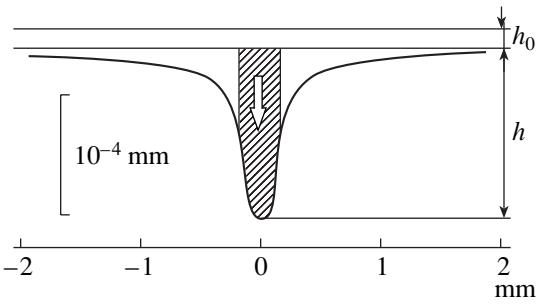

Fig. 5. Calculated deflection profile $u_z(R)$ [see Eq. (12)] of sample surface under a point load. The vertical and horizontal scales differ by a factor of 10^4. The hatched region with an arrow schematically depicts a pointed tip. Deflection h equals 0.14 μm at E = 300 GPa, $\sigma = 0$, F = 10 N, and R_0 = 0.15 mm. Deformation h_0 under the action of the same load evenly distributed over a sample face equals 0.022 μm for an $11 \times 9 \times 1.8$ mm^3 sample.

and the compressibility coefficient $K = -(V^{-1})(\partial V/\partial P) = 9.97 \times 10^{-12}$ Pa^{-1} [18]. The Poisson coefficient value calculated from the well-known equation $K^{-1} = E/3(1 - 2\sigma)$ equals $\sigma = 5 \times 10^{-3} \approx 0$, which closely agrees with the tabulated data [18]. Under thermodynamic equilibrium conditions, we must have

$$\frac{\partial \Omega}{\partial \varepsilon_i} = 0, \quad i = x, y, z. \tag{6}$$

The first derivative of oscillating contribution (4) is therefore given by

$$\frac{\partial \tilde{\Omega}}{\partial \varepsilon_i} = -a \sin\varphi \frac{\partial \varphi}{\partial \varepsilon_i} = -a\varphi \sin\varphi \frac{\partial \ln F}{\partial \varepsilon_i} = -\varepsilon_i E, \tag{7}$$

and the equation for magnetostriction takes the form

$$\varepsilon_i = \frac{a\varphi}{E} \frac{\partial \ln F}{\partial \varepsilon_i} \sin\varphi. \tag{8}$$

Differentiating the rapidly oscillating contribution yields the oscillating part of Young's modulus

$$\tilde{E} = \frac{\partial^2 \tilde{\Omega}}{\partial \varepsilon_i^2} \approx a\varphi^2 \left(\frac{\partial \ln F}{\partial \varepsilon_i}\right)^2 \cos\varphi. \tag{9}$$

Let us denote the amplitude of magnetostriction oscillations (from peak to peak) by

$$|\varepsilon_i|_{\max} = \frac{a\varphi}{E} \frac{\partial \ln F}{\partial \varepsilon_i}. \tag{10}$$

The relative Young's modulus oscillations in the harmonic approximation that we use can then be written as

$$\frac{\tilde{E}}{E} = |\varepsilon_i|_{\max} \varphi \frac{\partial \ln F}{\partial \varepsilon_i} \cos\varphi. \tag{11}$$

Applying (11) to the problem under consideration yields $\tilde{E}/E \approx 10^{-3}$. This estimate is based on the following values: the "cigar" cross section is described by $F = 10^7$ G, and the phase value in magnetic field $H = 4 \times 10^4$ Oe is therefore $\varphi \approx 1500$; $\partial \ln F/\partial \varepsilon \sim 1$ [see below, Eq. (22)]; and $|\varepsilon|_{\max} \approx 10^{-6}$ (experimental value).

Let us also find h and h_0. The problem of the shape of the deflection of an elastic medium surface under the action of a force concentrated in some surface portion can be solved using the results obtained by Landau and Lifshitz [19, §8]. For this purpose, it suffices to integrate the equation given in [19] with the weight function describing the distribution of pressure over the surface of the medium. Displacements u_z of surface points along the z axis normal to the surface are given by

$$u_z(R) = \frac{1 - \sigma^2}{\pi E} \int_0^{2\pi} d\varphi \times \int_0^{R_0} r dr \frac{f(r, \varphi)}{\sqrt{R^2 + r^2 - 2Rr\cos\varphi}}, \tag{12}$$

where E and σ are Young's modulus and the Poisson coefficient of the medium, respectively; R is the distance from the origin (along the surface) to the point whose displacement u_z is to be calculated; $f(r, \varphi)$ is the distribution density of the external force over the surface; and R_0 is the radius of the surface within which $f(r, \varphi)$ does not identically equal zero. We will restrict our consideration to the simplest distribution function, namely, $f = F/\pi R_0^2$ for $r \le R_0$ and $f = 0$ for $r > R_0$ (here, F is the force applied to a tip). Numerically integrating (12) then gives the deflection profile shown in Fig. 5. The calculations were performed for E = 300 GPa [18], $\sigma = 0$, force F = 10 N (experimental), and R_0 = 0.15 mm (copper tip). The last value was determined both experimentally (visual microscopic examination) and from the yield point of copper; the two methods gave closely similar results. The calculated deflection value was $h = 1.4 \times 10^{-5}$ cm. The same force evenly distributed over the face of the sample (such a distribution was attained in experiments by putting copper plates under the tips) gave an $h_0 = 2.2 \times 10^{-6}$ cm deformation (calculated).

The expected additional oscillating deformation value caused by loading can easily be calculated. According to (2) and (3), $\delta l' \approx (1.4 \times 10^{-5} + 2.2 \times 10^{-6}) \times 10^{-3} \approx 1.6 \times 10^{-8}$ cm. In other words, we should have $\delta l' \sim 10^{-2} \delta l$ in the approximation that we use. In addition, these oscillations should be shifted in phase by $\pi/2$ with respect to the magnetostriction signal. Clearly, this contribution is then absolutely unobservable, although h is almost an order of magnitude larger than h_0.

In our experiments, in which the crystal was in contact with a copper tip, $\delta l'$ oscillations were, however, approximately equal to δl (see Figs. 2c, 3). It can, therefore, be assumed that the $\tilde{h}$ amplitude approximately

equals δl, that is, approximately 1.5×10^{-6} instead of 1.6×10^{-8} cm. Therefore, $\tilde{E}/E \sim 10^{-1}$, which is approximately 100 times larger that the value calculated in the harmonic approximation, $\tilde{E}/E \sim 10^{-3}$. When copper spacers are used, we only have an evenly distributed load, and $\delta l' \sim 10^{-1}\delta l$ oscillations are then also shifted by $\pi/2$ with respect to ε. This contribution might in principle be observed under a sufficiently larger load but is virtually unnoticeable under the conditions of our experiments.

It follows that the results obtained in this work should be interpreted as a giant increase in compressibility caused by the formation of diamagnetic domains. As the domain structure is in essence a mixture of two phases having different densities, such an increase in compressibility is not very surprising. Diamagnetic and paramagnetic domains are deformed "oppositely" and noticeably differ in density and, accordingly, in the density of charge carriers (electrons and holes). Note anticipatively that precisely the charge carrier density gradient in a magnetic field determines the magnetization current density in domain walls [20].

2. Next, consider the role played by deformation in the formation of domains in more detail. Let us return to (5) taking into account magnetization energy. We then have

$$\delta\Omega = a\cos\varphi + \frac{1}{8\pi}(B-H)^2 + \frac{1}{2}E(\varepsilon_x^2+\varepsilon_y^2+\varepsilon_z^2). \quad (13)$$

In addition to the equation for magnetostriction given above [Eq. (8)], we obtain

$$-M = \frac{\partial\tilde{\Omega}}{\partial B} = a\varphi\sin\varphi\frac{1}{B} \quad (14)$$

by differentiating $\tilde{\Omega}$ with respect to B. Comparing (14) with (8), we obtain the well-known [2] proportionality relation between magnetostriction and magnetization,

$$\varepsilon_i = -\frac{MH}{E}\frac{\partial\ln F}{\partial\varepsilon_i}. \quad (15)$$

Here, we used the inequality $B - H = 4\pi M \ll H$, according to which $B \sim H$ in equations of this kind. (The difference of B and H should only be taken into account for phase changes within a period. Here, by the magnetization M we imply the magnetic moment of a sample with a zero demagnetization factor.) Equations for magnetostriction in the other directions are obtained similarly. As a result, crystal magnetization (along the z axis in the problem under consideration) is accompanied by the total deformation in all directions. The total deformation is generally anisotropic and ensures the required δF change. All deformations are very small. It can therefore be thought that all these values including

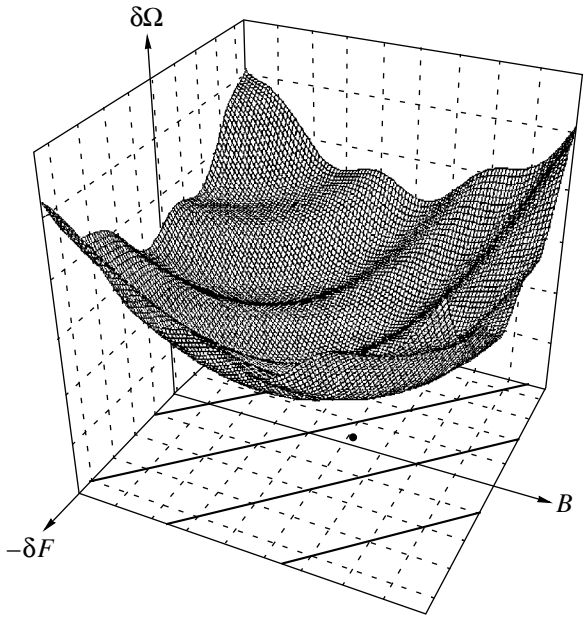

Fig. 6. Schematic drawing of $\delta\Omega$ energy changes depending on induction B and sample deformation proportional to δF at given external field H. Slant lines in the (B, δF) plane correspond to constant phase φ values. The dot on this plane is the projection of the global energy minimum slightly displaced to the left and upward with respect to the (H, 0) paraboloid vertex. This point traces the phase trajectory as external field H changes (more details are given in Fig. 7).

δF are linearly related to each other. This means that energy changes (13) in a magnetic field can be described as functions of H (external magnetic field) and two variables, namely, $B - H$ (magnetization) and δF (the magnetostriction effect). The "three-dimensional" plot shown in Fig. 6 is a paraboloid with a vertex at (H, 0). Superimposed crimping is caused by the $\tilde{\Omega} = a\cos\varphi$ oscillating contribution; the larger the a value, the greater the degree of crimping. [Recall that the a amplitude is determined by experimental conditions such as temperature, the quality of the sample (the Dingle temperature), and magnetic field uniformity.]

Clearly, the crimping shifts the projection of the minimum onto the (B, δF) plane with respect to the (H, 0) vertex; this shift is shown separately in Fig. 7. The displacement to the left and upward corresponds to the diamagnetic state with sample deformation toward increasing the Fermi surface volume, that is, toward larger charge density N and cross section F. The displacement to the right and downward during the second half-period corresponds to the paramagnetic state with a lower density, that is, with negative δF. According to (15), the ratio between these displacements, that is, the ratio between deformation and magnetization (more exactly, magnetization current) within one period, is to a high accuracy constant. In other words, the phase shift slope angle is proportional to the magnetic field and inversely proportional to Young's modulus, and, if the

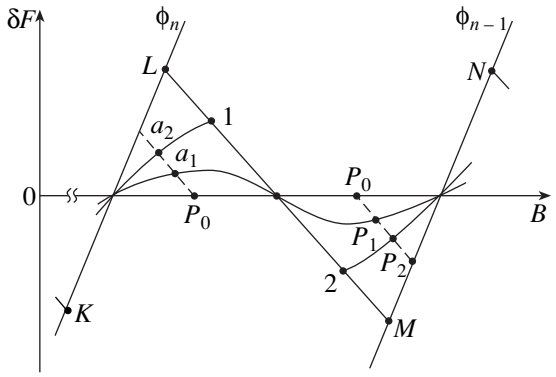

Fig. 7. Metal state phase trajectories. Slant lines correspond to constant phases of the oscillating contribution to energy, $\phi = 2\pi n$ and $\phi = 2\pi(n - 1)$. Curves a_1 and a_2 are the phase trajectories at different amplitudes ($a_1 < a_2$). Trajectory a_1 is continuous, whereas the transition from 1 to 2 along a_2 occurs in a jump. The P_1 and P_2 points show state changes with respect to the $P_0(H, 0)$ point. *KLMN* is the phase trajectory of a two-dimensional electron gas.

scale is selected properly, this displacement is everywhere virtually perpendicular to the corresponding constant phase lines, which are shown by slanting lines in Figs. 6 and 7 for the $\varphi = 2\pi$ and $\varphi = 2\pi(n - 1)$ phase values. Such a trace of the minimum position is the phase trajectory of the simultaneously magnetized and deformed state of the metal under external field H variations. Naturally, the phase trajectory of a sample with arbitrary demagnetization factor also remains the same, although the displacement angle changes. For example, in a plate with $B = H$ this displacement is vertical.

This trajectory is everywhere continuous if the crimping a value is small (see curve a_1 in Fig. 7). The displacement of the state from the $P_0(H, 0)$ point to P_1 then occurs to the left and upward (diamagnetism and a density increase) during the first half-period and, accordingly, to the right and downward (paramagnetism and a density decrease) during the second half-period. However, if the a amplitude is fairly large (curve a_2 in Fig. 7), which virtually coincides with condition (1), and if H is situated precisely at the center of the period, when the Landau level is half-filled, the $\delta\Omega$ value at minimum 1 equals that at minimum 2. This means that, if the demagnetization factor of the sample approximately equals zero (a thin rod along the field), the whole metal experiences a jump transition from state 1 to state 2, and both deformation and magnetization change their signs. If the demagnetization factor approximately equals one (that is, as in our experiments) and the plate is oriented normally to the field, then this plate is divided into phases 1 and 2 in the range $B_1 \le H \le B_2$, and these phases differ in both deformation and magnetization. Naturally, magnetization and deformation and therefore electron densities N_1 and N_2 are constant within each phase. Close to the boundary between the phases, or domains, a smooth transition from state 1 to 2 should occur; that is, both deformation and, accordingly, electron density change across interdomain walls. The difference of the electron densities to the left and to the right of the domain wall creates a magnetization current in a magnetic field. This current flows in the wall and causes the $\delta B = 4\pi\delta M$ difference between neighboring domains. Precisely the same mechanism is doubtless responsible for the arising of magnetization currents when magnetization is uniform, that is, when domains are absent. This means that magnetostriction should be uniform in the whole sample except a region near its boundary (where this deformation vanishes), whose thickness is of the same order as that of domain boundaries. Indeed, closed Larmor motion of electrons cannot occur at distances from the boundary smaller than the Larmor diameter, and the corresponding oscillating contribution to energy is zero. Earlier [21, 22], precisely the Larmor orbit diameter has been suggested as the domain wall thickness. This is hard to argue with, but the problem of deformation has not been tackled in [21, 22], and the situation should therefore be considered in more detail.

Deformation is doubtless isotropic in the basal plane in a homogeneous phase, either diamagnetic or paramagnetic. Deformation can also be considered isotropic when domains of the "new" phase are formed as long as the amount of the new phase is so small that it is likely to consist of separate inclusions. However generally, the transition to the laminar structure, which is much more favorable energetically, should occur very rapidly as the volume of the new phase increases. This unambiguously follows from the behavior of "domains" in the transition state of superconductors of the first kind [23], in which separate filamentary inclusions only exist close to the transition to the normal state.

Each phase of a laminar structure cannot be considered locally isotropic. Indeed, the difference of deformations in neighboring domains should then "accumulate" along the interphase boundary, which would cause the arising of shear stress and increase the energy. Of course, it would be much more favorable energetically if the necessary difference of deformations (more exactly, electron densities) only existed in the direction normal to the boundary. (Exactly the same reasoning applies to the boundary layer of a sample in the usual situation with homogeneous magnetization, when inhomogeneous deformation in this layer should be anisotropic with respect to the side boundary because of such a peculiar "surface tension.") For this reason, anisotropic deformation in separate domains should exist in laminar domain structures, although, on average over the whole crystal, the situation in the absence of a preferential direction should, we believe, remain isotropic because of mosaic orientations of laminar regions, as is observed in a similar situation in the transition state of superconductors of the first kind [23]. This scenario appears to be quite plausible, which

allows such a giant increase in the compressibility coefficient caused by the formation of a domain structure to be partly explained. Indeed, local anomalous deformation under a point load can only occur as a result of reorientation and redistribution of closely lying anisotropic domains.

In any event, there is a difference of deformations in neighboring domains along the magnetic field direction. This leads us to conclude that the domain wall thickness cannot but increase as the thickness of the crystal increases. This is at variance with the above suggestion that the interdomain wall thickness is always of the order of the Larmor diameter. This value (the Larmor diameter) may play the role of the lower domain wall thickness limit in thin samples.

Figure 7 can be used to examine the role played by magnetostriction in the behavior of a metal in the model of two-dimensional (or quasi-two-dimensional) electron gas, that is, a metal whose Fermi surface is a cylinder. Let us, for definiteness, assume that the magnetic field increases. The phase trajectory is then the …*KLMN*…, etc., polygonal line. The metal is homogeneous in the *KL* and *MN* regions and smoothly contracts while experiencing the transition from the paramagnetic to the diamagnetic state. The corresponding Landau level is then always filled, and the next level is absolutely empty. If (1) is satisfied, we have an instability along the whole *LM* portion, and the transition from point *L* to *M* occurs either in a jump if the sample is a long rod aligned with the magnetic field or with the formation of domains if the sample is a plate oriented normally to the field. Homogeneous and inhomogeneous state portions then alternate along the phase trajectory. Note that taking magnetostriction into account makes the region of the existence of domains, $B_L - B_M$, smaller than the period value. If (1) is not satisfied (this is inevitable in fairly high magnetic fields, where the Landau level number becomes smaller than the critical number), the volume and magnetization smoothly change along the whole polygonal line. Clearly, if magnetostriction is forbidden and the volume cannot change, the picture radically changes, and the Fermi level should oscillate at a constant electron density [24]. As a result, magnetization current oscillations should arise under certain conditions. The magnetization current is then related to the contact potential difference rather then magnetostriction. Such a current is in antiphase with the "classic" de Haas–van Alphen effect and is especially important in superhigh magnetic fields [25]. In particular, precisely this current is responsible for the quantum Hall effect.

3. It is easy to see that the difference in magnetization between neighboring domains is indeed caused by deformation accompanied by electron density changes. The magnetization current density in a domain wall can be described by the formula [20]

$$\mathbf{j}_m = c\,\mathrm{curl}\sum_k n_k(\mathbf{r})\boldsymbol{\mu}_k. \tag{16}$$

Here, $n_k(\mathbf{r})$ is the number of Larmor orbits corresponding to the $\boldsymbol{\mu}_k$ magnetic moment of a unit volume. Let us integrate (16) over the domain wall thickness from one domain to another taking into account that the orbital magnetic moments of all electrons are parallel to the external field. This gives the magnetization current in the wall related to a unit length of this wall along the field,

$$J = c\sum_k (N_2 - N_1)_k \mu_k, \tag{17}$$

where $(N_{1,2})_k$ are the volume densities of charges with magnetic moment μ_k in neighboring domains. Because the δN difference is small, all orbits can be considered to be situated on the Fermi surface. The characteristic values can be estimated as follows. The magnetic moment of the Larmor orbit is

$$\mu = \frac{J_0 S}{c}, \tag{18}$$

where

$$J_0 = \frac{e\omega_c}{2\pi}, \quad S = \pi R_H^2, \quad R_H = \frac{v_\perp}{\omega_c}. \tag{19}$$

Here, ω_c is the cyclotron frequency, e is the charge of the electron, R_H is the Larmor radius, and $v_\perp$ is the velocity of the electron on the Fermi surface in the direction normal to the field. Complete current J in the domain wall per unit wall length in the magnetic field direction is

$$J = \frac{\delta N e}{2}\overline{\omega_c}\,\overline{R_H^2}, \tag{20}$$

where δN is the total difference of the numbers of charge carriers (electrons and holes) in neighboring domains, that is, the difference of the Fermi surface volumes in these domains, and $\overline{\omega_c}$ and $\overline{R_H^2}$ are the corresponding values averaged over the Fermi surface. Beryllium is a compensated metal, and the volume of electrons (two cigars) always strictly equals the volume of holes (crown). It follows that determining δN only requires volume changes to be calculated for the cigar, which is much simpler, because the cigar is close in shape to a cylinder. The total difference of Fermi surface volumes in neighboring domains can therefore be written as

$$\begin{aligned}\delta N &\approx N_0\left(\frac{\Delta F}{F} + \frac{\Delta L}{L}\right)\\ &= N_0\sum_i\left(\frac{\partial \ln F}{\partial \varepsilon_i} + \frac{\partial \ln L}{\partial \varepsilon_i}\right)\varepsilon_i.\end{aligned} \tag{21}$$

Here, N_0 is the total number (Fermi surface volume) of charge carriers in beryllium, and the value in parentheses is the relative change in the volume of the cigar in

opposite domains caused by the total deformation (F and L are the cigar cross section area and length, respectively). The $\partial \ln F/\partial \varepsilon_i$ and $\partial \ln L/\partial \varepsilon_i$ values can be determined from the well-known relation between the Fermi surface of beryllium and the Brillouin zone size [26–29]. This is especially simple to do precisely for beryllium, because its Poisson coefficient $\sigma \approx 0$, and, as mentioned above, all deformations can be considered mutually independent. Such calculations closely agree with the experimental results [12], and it can be assumed that

$$\frac{\partial \ln F}{\partial \varepsilon_{x,y}} = -1, \quad \frac{\partial \ln F}{\partial \varepsilon_z} = 6,$$
$$\frac{\partial \ln L}{\partial \varepsilon_{x,y}} = -1, \quad \frac{\partial \ln L}{\partial \varepsilon_z} = 1.6 \tag{22}$$

Substituting the $\varepsilon_x = \varepsilon_y = \varepsilon$ and $\varepsilon_z = -6\varepsilon$ deformation values yields $\delta N \approx -50\varepsilon N_0$, where ε is understood to be $\delta l/l$ from peak to peak. Clearly, we have such a large coefficient (50) because the Fermi surface of beryllium is formed close to Brillouin zone vertices and edges and constitutes a very small part of the Harrison sphere. (Clearly, this coefficient equals 3 in the model of free electrons.) The ω_c and R_H values in the basal cigar plane are well known, $\omega_c = eH/m^*c = 4.17 \times 10^{12}$ s^{-1} ($m^* = 0.16m_e$ and $H = 4 \times 10^4$ G), $R_H = v_F/\omega_c = 0.24 \times 10^{-4}$ cm ($v_F \approx 10^8$ cm/s), and the total number of charge carriers $N_0 = 0.43 \times 10^{22}$ cm^{-3} can be obtained from the data reported in [29], according to which we have 0.01573 electrons per atom and two atoms per unit cell, the volume of the cell being 109.0758 (rel. units)^3. Note that this amounts to 1.6% of the Harrison sphere volume. We believe that estimating the mean orbit area πR_H^2 at half the area of the central orbit of the cigar cannot introduce a large error. Combining these estimates and substituting the value $\varepsilon \approx 1.37 \times 10^{-6}$ (Fig. 3) in field $H = 4 \times 10^4$ G gives $J \approx 29$ A/cm. Considering the roughness of the estimates made above, this value more than satisfactorily agrees with the value $\Delta B = 4\pi\Delta M \approx 30$ G observed in [6], although the conditions of experiments performed in [6] and this work do not completely coincide.

It is easy to see that Eq. (20) for current can be rewritten as

$$J = \delta N c_1 \varepsilon_F \frac{c}{H}, \tag{23}$$

where coefficient c_1 takes into account averaging over the Fermi surface. As the induction jump between neighboring domains is $\Delta B \equiv 4\pi\Delta M \approx (4\pi/c)J$, we have

$$\Delta MH = \delta N c_1 \varepsilon_F, \tag{24}$$

where δN can always be considered equal to $N_0 \varepsilon c_2$ and c_2 is the coefficient unambiguously determined by the Fermi surface shape. In the problem under consideration, it equals 50. Representing (24) in the form $\varepsilon = (\Delta MH/E)c_3$ and comparing it with the equation for magnetostriction [Eq. (8)], we obtain the equation for Young's modulus

$$E = \varepsilon_F N_0 c_1 c_2 c_3, \tag{25}$$

where all coefficients, c_1, c_2, and c_3, are fully determined by the structure of the Fermi surface. Here, ε_F is the kinetic energy of the electron on the Fermi surface, that is, $\varepsilon_F = \hbar^2 k_F^2/2m$. For instance, for beryllium, $k_F \approx 1.03$ (a.u.)$^{-1}$, and $N_0 = 0.43 \times 10^{22}$ cm^{-3} [29]. The correct Young's modulus value for beryllium is obtained at a quite plausible coefficient c_1 value, $c_1 \approx 0.6$. In other words, we arrive at the conclusion that the Fermi surface determines not only the electronic properties of metals but also their elastic properties. Note that this assertion is correct accurate to the assumption that the magnetization current is fully determined by the charge density gradient in the magnetic field.

The above conclusion deserves a more detailed discussion. The problem of the contribution of conduction electrons to metal compressibility is of obvious interest, and different views on this problem have been expressed. For instance, the estimates made in [30] lead the authors to conclude that the electronic contribution to compressibility amounted to 60–80%. On the other hand, the ionic contribution to compressibility was fully ignored in [31], where it was actually assumed that the elastic properties of metals, niobium in particular, were fully determined by conduction electrons. This problem was central to explaining numerous experiments [2] performed to determine Fermi level oscillations in magnetic fields predicted earlier [24]. For the first time, in a similar and very accurate experiment and precisely for beryllium [32], these oscillations were shown to be absent with an accuracy of 10% of the theoretically expected value [24]. To explain this result, it was shown in [32] that, if metal compressibility was fully determined by conduction electrons, Fermi level oscillations in a magnetic field should exactly be compensated by magnetostriction effects. Generally, this is not at all at variance with the result obtained in [24], where magnetostriction was not taken into account and, in essence, a model with a given and constant volume density of electrons in a metal was considered. It follows from the results obtained in [32] that the electronic contribution to the compressibility of beryllium was at least 90%. The suggestion that the compressibility coefficients of the other metals are also determined almost entirely by conduction electrons is substantiated by very accurate theoretical calculations by Brovman and Kagan performed for magnesium [33]. The summation of all electronic and ionic contributions to compressibility (see Table 3 in [33]) with an accuracy of 3% or higher only leaves the contribution of conduction electrons, which, equally accurately, agrees with the tabulated Young's modulus of magnesium.

To summarize, our calculations on beryllium described above show that conduction electrons should fully determine its compressibility coefficient. At the same time, the character of our reasoning leads us to believe that this conclusion applies to all metals. Indeed, the formation of diamagnetic domains is doubtless characteristic of all metals; the only problem is the extreme difficulty of creating the necessary conditions for most of them. As mentioned, such domains were observed in silver, beryllium, tin, and aluminum. On the other hand, if and only if compressibility is fully determined by the electronic contribution, volume and magnetization only oscillate when the magnetic field varies, whereas the Fermi level remains constant. This means that the Fermi levels of neighboring domains are equal, and there is no contact potential difference between domains; the existence of such a difference would be both fairly unexpected and energetically unfavorable. In other words, the very possibility of the existence of diamagnetic domains lends support to the point of view according to which conduction electrons should fully determine the compressibility of metals. Of course, we do not know to what extent this conclusion is quantitatively accurate.

ACKNOWLEDGMENTS

The authors thank L. Maksimov, E. Krasnoperov, and G. Sholt for discussions. This work was financially supported by the Russian Foundation for Basic Research (project no. 98-02-17142).

REFERENCES

1. L. Landau, Z. Phys. **64**, 629 (1930).
2. D. Shoenberg, *Magnetic Oscillations in Metals* (Cambridge Univ. Press, Cambridge, 1984; Mir, Moscow, 1986).
3. J. H. Condon, Phys. Rev. **145**, 526 (1966).
4. J. H. Condon and R. E. Walstedt, Phys. Rev. Lett. **21**, 612 (1968).
5. G. Solt, C. Baines, V. S. Egorov, *et al.*, Phys. Rev. Lett. **76**, 2575 (1996).
6. G. Solt, C. Baines, V. S. Egorov, *et al.*, Phys. Rev. B **59**, 6834 (1999).
7. A. Schenck, *Muon Spin Rotation Spectroscopy* (Hilger, Bristol, 1986).
8. G. Solt, V. S. Egorov, C. Baines, *et al.*, Phys. Rev. B **62**, R11933 (2000).
9. V. I. Bozhko and E. P. Vol'skiĭ, Pis'ma Zh. Éksp. Teor. Fiz. **26**, 337 (1977) [JETP Lett. **26**, 223 (1977)].
10. B. S. Chandrasekhar, Phys. Lett. **6**, 27 (1963).
11. T. E. Thomson, P. R. Aron, B. S. Chandrasekhar, *et al.*, Phys. Rev. B **4**, 518 (1971).
12. B. S. Chandrasekhar, E. Fawcett, D. M. Sparlin, and G. K. White, in *Proceedings of the 10th Conference on Low Temperature Physics, LT-10* (VINITI, Moscow, 1967), Vol. 3, p. 328.
13. V. S. Egorov, E. P. Krasnoperov, Ph. V. Lykov, *et al.*, Fiz. Tverd. Tela (St. Petersburg) **40**, 524 (1998) [Phys. Solid State **40**, 482 (1998)].
14. V. S. Egorov, F. V. Lykov, and O. A. Repina, Pis'ma Zh. Éksp. Teor. Fiz. **72**, 28 (2000) [JETP Lett. **72**, 18 (2000)].
15. G. K. White, Cryogenics **1**, 151 (1961).
16. V. S. Egorov, Zh. Éksp. Teor. Fiz. **69**, 2231 (1975) [Sov. Phys. JETP **42**, 1135 (1975)].
17. J. F. Smith and C. L. Arbogast, J. Appl. Phys. **31**, 99 (1960).
18. *Handbook of Physical Quantities*, Ed. by I. S. Grigoriev and E. Z. Meilikhov (Énergoizdat, Moscow, 1991; CRC Press, Boca Raton, 1997).
19. L. D. Landau and E. M. Lifshitz, *Course of Theoretical Physics*, Vol. 7: *Theory of Elasticity* (Nauka, Moscow, 1965; Pergamon, New York, 1986).
20. D. A. Frank-Kamenetskii, *Lectures on Plasma Physics* (Atomizdat, Moscow, 1968).
21. I. A. Privorotskiĭ, Zh. Éksp. Teor. Fiz. **52**, 1755 (1967) [Sov. Phys. JETP **25**, 1167 (1967)].
22. A. A. Abrikosov, *Fundamentals of the Theory of Metals* (Nauka, Moscow, 1987; North-Holland, Amsterdam, 1988).
23. T. E. Faber, Proc. R. Soc. London, Ser. A **248**, 460 (1958).
24. M. I. Kaganov, I. M. Lifshits, and K. D. Sinel'nikov, Zh. Éksp. Teor. Fiz. **32**, 605 (1957) [Sov. Phys. JETP **5**, 500 (1957)].
25. V. S. Egorov, Physica B (Amsterdam) **301**, 212 (2001).
26. T. L. Loucks and P. H. Cutler, Phys. Rev. **133**, A819 (1964).
27. J. H. Terrel, Phys. Rev. **149**, 526 (1966).
28. B. R. Watts, Proc. R. Soc. London, Ser. A **282**, 521 (1964).
29. J. H. Tripp, P. M. Everett, W. L. Gordon, and R. W. Stark, Phys. Rev. **180**, 669 (1969).
30. B. G. Lazarev, É. A. Kaner, and L. V. Chebotarev, Fiz. Nizk. Temp. **3**, 808 (1977) [Sov. J. Low Temp. Phys. **3**, 394 (1977)].
31. J. Ashkenasi, M. Dacorogna, M. Peter, *et al.*, Phys. Rev. B **18**, 4120 (1978).
32. N. E. Alekseevskii and V. I. Nizhankovskii, Zh. Éksp. Teor. Fiz. **88**, 1771 (1985) [Sov. Phys. JETP **61**, 1051 (1985)].
33. E. G. Brovman and Yu. M. Kagan, Usp. Fiz. Nauk **112**, 369 (1974) [Sov. Phys. Usp. **17**, 125 (1974)].

Translated by V. Sipachev

Journal of Experimental and Theoretical Physics, Vol. 94, No. 1, 2002, pp. 172–177.
From Zhurnal Éksperimental'noĭ i Teoreticheskoĭ Fiziki, Vol. 121, No. 1, 2002, pp. 203–209.

SOLIDS
Electronic Properties

Electronic Transport in Quasicrystals¶

Yu. Kh. Vekilov*, E. I. Isaev, and D. V. Livanov**

Theoretical Physics Department, Moscow Steel and Alloys Institute, Moscow, 117936 Russia
**e-mail: vekilov@linux.trf.misa.ac.ru*
***e-mail: isaev@linux.trf.misa.ac.ru*

Received July 10, 2001

Abstract—Mobility of electrons in quasicrystals is considered in the framework of the fractional Fermi surface (FS) model, i.e., a multiconnected FS with many electron–hole pockets. The Mott law for the variable range hopping conductivity is obtained when intervalley scattering processes with small momentum transfer are taken into account. The transition to the power-law temperature dependence is discussed. © *2002 MAIK "Nauka/Interperiodica".*

1. INTRODUCTION

Quasicrystals (QCs) are materials that have a long-range aperiodic atomic order and rotational symmetries which are crystallographically forbidden for periodic structures (e.g., five-, eight-, ten-, and twelvefold rotational axes). Quasicrystals usually are intermetallic alloys, but their physical properties differ from those of the crystalline and amorphous metallic phases. Like metals, quasicrystals have a nonzero electronic contribution to the specific heat, although it is smaller than the value calculated within the free-electron model. At the same time, the electronic resistivity of quasicrystals at low temperature is anomalously high and increases with increasing the structural order and annealing the defects. The highest resistivity of all the known quasicrystals occurs in icosahedral (*i*) Al–Pd–Re quasicrystal, where the value of resistivity at 4.2 K exceeds 1 Ω cm. Large values of the resistivity ratio $\mathcal{R} = \rho(4.2\text{ K})/\rho(295\text{ K})$, up to 200, are also observed for this material (the values of $\mathcal{R}$ are 1.1 for *i*-Al–Li–Cu, up to 2 for *i*-Al–Cu–Fe, and about 4 for Al–Cu–Ru), which shows how perfect the sample is [1–5]. In contrast to the Matissen rule, where the resistivities are additive, the conductivity of quasicrystals behaves as $\sigma = \sigma(0) + \Delta\sigma(T)$ over a wide range of temperatures, where $\sigma(0)$ is the residual conductivity at zero temperature, and $\Delta\sigma(T)$ represents the T-dependent part. Usually, $\sigma(0)$ increases with the structural disorder and $\Delta\sigma(T)$ increases with the temperature as $\Delta\sigma(T) \propto T^{\beta}$ [1–3]. In a series of *i*-Al–Pd–Re samples with different $\mathcal{R}$, Gignoux *et al.* [3] obtained $1 < \beta < 1.5$ in the temperature range from 7 to 700 K. Pierce *et al.* [4] measured $\sigma(T)$ in several *i*-Al–Pd–Re samples (with various $\mathcal{R}$ ratios) and found the power-law temperature dependence with β in the range 0.5 to 1 for temperatures from 0.45 to 3 K.

Different explanations of the transport properties of quasicrystals have been proposed. Much attention has been given to the power-law temperature dependence of $\sigma(T)$. The role of the pseudogap in the density of states (DOS) at the Fermi level, the role of quantum interference effects (weak localization and electron–electron interactions), proximity to the metal–insulator transition, the spiky structure of the electronic spectrum, and the criticality of wave functions have been discussed in connection with this problem (see the review articles by Poon [1] and Rapp [2]). Fujiwara *et al.* [6, 7] tried to obtain the $\sigma(T)$ dependence on the basis of the band structure and Fermi surface (FS) calculations for crystalline approximants. Macia [8] gave a phenomenological description of $\sigma(T)$ based on the DOS model that takes the pertinent experimental results into account. The problem was analyzed by Burkov *et al.* [9], who used the fractional Fermi surface model, i.e., a multiconnected FS with many electron-hole pockets. They considered the intravalley and intervalley scattering processes in order to explain the power-law dependence of $\sigma(T)$. They also predicted a zero value of σ at $T = 0$ K for the perfect QC (with no scattering centers) and a small residual conductivity for "dirty" QC.

Currently, the physical origin of the high resistivity of intermetallic quasicrystalline alloys compared to other systems composed only of metals is not well understood, and this has challenged the experimenters to examine the possibility of a metal–insulator transition (MIT) in quasicrystalline systems and to investigate whether these materials are metallic. Recent experiments on the perfect icosahedral $Al_{70.5}Pd_{21}Re_{3.5}$ quasicrystals have shown that, at low temperatures, their conductivity follows the Mott law for the variable range hopping (VRH) conductivity,

$$\sigma = \sigma_0 \exp[-(T_0/T)^p], \qquad (1)$$

¶This article was submitted by the authors in English.

where $p = 1/4$ [10–13]. The temperature range where the Mott law is fulfilled was found to be 0.45–10, 0.02–0.6, and 0.5–7 K according to Guo and Poon [10], Delahaye *et al.* [12], and Wang *et al.* [13], respectively. In *i*-$Al_{70.5}Pd_{21}Re_{8.5-x}Mn_x$, it was found that the VRH including the Coloumb interaction ($p = 1/2$) can describe the experimental data for $2 < x < 4$ [10]. The experimental data on bulk *i*-Al–Pd–Re samples are rather contradictory. Different authors quote different values of T_0. According to [10, 11, 13], T_0 reaches 100 K and is higher for samples with higher $\mathcal{R}$. On the other hand, in [12], the very low value of $T_0 \sim 1$ mK was given. However, the lowest temperature reached in this experiment was 20 mK, and the value of T_0 was determined by extrapolation. Moreover, in [10], a small but finite value of $\sigma(0)$ was obtained, although it decreased upon increasing the perfectness of the sample [11]. At the same time, in [12, 13], the conductivity was fitted to Eq. (1) without including any extra $\sigma(0)$ term, while it was used by Guo and Poon [10] in order to analyze their experimental data on conductivity. We note that the presence of a residual conductivity is quite possible, because the different conductivity channels in QC are parallel, and a nearly vanishing conductivity $\sigma(0)$ cannot hide the VRH conductivity.

The occurrence of the Mott law (Eq. (1)) shows that electronic states in QC are localized and the sample is on the insulating side of the MIT. Qualitatively, the possible role of the hopping conduction between localized states in QC at low temperatures has been previously discussed by several authors on experimental grounds [1, 3, 5, 14]. Poon [1], Pierce *et al.* [14], and Mayou *et al.* [5] discussed the possibility of explaining the power-law dependence of σ by a hopping mechanism taking the criticality of the wave functions into account. Janot [15] considered this problem in the framework of the hierarchical cluster model and predicted the conductivity that scales roughly as $T^{3/2}$. But the localization lengths ξ obtained experimentally (we recall that $T_0 \propto \xi^{-3}$ in accordance with the Mott theory) are much larger than the separation, ~20 Å, of the ideal clusters that are assumed to be structure units between which the electrons hop in the Janot model. In addition, in the subsequent paper [16], Janot proposed that "the power law T^{β} may be lost experimentally because of extrinsic effects due to structural defects, boundaries, and periodic approximant distortion which may restore the $T^{-1/4}$ law of the Mott model." That is, the existence of the Mott law was related to the presence of disorder in QC, which contradicts the experimental data. A rather interesting but unrealistic idea was put forward by Rivier and Durand [17] based on the results obtained for the one-dimensional model. In order to obtain the VRH conductivity, they suggested that the electronic structure of a quasicrystal looks somewhat similar to highly doped, *p*-type semiconductors, but no reliable explanation of the Mott law, Eq. (1), for quasicrystals was given.

In this paper, we proceed on the ground of the band structure theory to explain the VRH conductivity in QC. Although the Bloch theorem does not apply to a quasicrystal, the ideas of the band structure theory can be used to describe the transport properties of QC, with the quasicrystalline state considered as a structural limit of a sequence of rational periodic approximants with increasing periods. Therefore, we take the band structure effects into account that are specific for the quasicrystalline symmetry and use the fractional Fermi surface model [9] to explain the origin of the VRH conductivity in QC. However, the hopping mechanism of conductivity involves hops between localized states, and we therefore begin with the discussion of the nature of localization in the regular and perfect QC without phasons and other distortions.

The paper is organized as follows. In Section 2, the localization of electrons in quasicrystals is discussed. The VRH conductivity is discussed in Section 3. In Section 4, the crossover to the power-law temperature dependence of conductivity is considered.

2. LOCALIZATION OF ELECTRONS IN QUASICRYSTALS

For amorphous alloys, granular metal films, and doped semiconductors, the electronic localization plays an important role in the low-temperature electron transport. For the above systems, the localization of electrons is known to arise from disorder. But the object of our discussion is the origin of localization in QC. The Al–Pd–Re QC is a highly ordered material with very sharp X-ray diffraction spots, and as mentioned above, improving the perfection of the quasilattice order has been found to lead to increasing of the resistivity.

The experimental results for *i*-Al–Pd–Re show that, at low temperatures, the regular and perfect quasicrystal behaves as a material in the Fermi glass state, that is, the DOS is finite at the Fermi level, but the electrons are localized. This localization in a QC is a consequence of the coherent interference of the electronic states caused by the specific symmetry and the structure of the material, and the more perfect the material is, the more localized the electrons are. Whereas in a disordered metal or a heavily doped semiconductor the origin of the localization is the destruction of the phase coherency of the wave functions due to disorder (the Anderson localization), in the QC, the phase coherency of the wave functions is the main source of localization. The following simple observations can justify this conclusion.

First, within the six-dimensional periodic description of the icosahedral structure, it is obvious that each scattering wave vector in the quasicrystal corresponds to a reciprocal wave vector in the periodic structure of a higher dimension. Thus, the set of the reciprocal lattice vectors densely fills the reciprocal space of the quasicrystal, and all the electron states at the Fermi level

have zero group velocity (standing waves) due to the Bragg reflections (evidently, with different intensities), i.e., due to the constructive interference of the electron states at the Fermi level.

Second, it is convenient to elucidate this picture by considering the quasicrystal as a structural limit of a sequence of rational approximants (crystal analogs) with an increasing lattice period. The Brillouin zone (BZ) volume is diminished upon increasing the order of the approximant because the lattice period increases, and the BZ volume becomes infinitely small ($\sim h^3$) in the quasicrystalline limit. Therefore, employing the usual approach to the construction of the FS [18], one can see that, in the hierarchy of higher order approximants, the energy bands are folded down and the FS becomes fractional in the quasicrystalline limit, namely, it is multiconnected with a large number of electron and hole "pockets," and for atomically ordered perfect QC as was pointed out by Poon [1], the electron states must be localized at zero temperature, because the strong localization condition $k_F^i l \sim 1$ (where l is the mean free path and k_F^i is Fermi momentum) is satisfied for the electrons in each valley i. Therefore, each valley plays a role similar to that of a localization center in a disordered object. Hence, there is a formal analogy between a well-ordered quasiperiodic object with a fractional FS and a disordered metal or a heavily doped semiconductor. This analogy helps one to explain the occurrence of the Mott law in perfect quasicrystals at very low temperatures, because the electrons in localized states can participate in conductivity only via hopping between localization sites.

3. VRH CONDUCTIVITY IN QC

Mott was the first to point out that, at low temperatures, the most frequent hopping process would not be the hopping to a nearest neighbor [19]. To explain the conduction with an activation energy monotonically decreasing with decreasing temperature, Mott proposed a model where, in strongly localized systems with a sufficiently high density of states $N(E_F)$ near the Fermi level, the states that are optimal for conduction accumulate closer and closer to the Fermi level as T decreases. Thus, the activation energy decreases, while the hop length grows with decreasing temperature. The simplest arguments were as follows. Within a radius R around a given site, the total number of electron states near the Fermi energy is

$$\frac{4\pi}{3}R^3N(E_F), \tag{2}$$

and the lowest activation energy ΔE for a hopping process at the distance R is reciprocal to Eq. (2),

$$\Delta E = \frac{3}{4\pi}\frac{1}{R^3N(E_F)}. \tag{3}$$

Therefore, ΔE decreases upon increasing the hopping range. But hopping by a large distance involves tunneling with the probability proportional to $\exp(-2\alpha R)$, where $1/\alpha = \xi$ is the decay length of the localized wave function. Therefore, there exists an optimum hopping distance R_{opt}, for which the expression

$$\exp(-2\alpha R)\exp(-\Delta E/k_BT) \tag{4}$$

has a maximum. This maximum occurs at the minimum value of the exponent

$$2\alpha R + \frac{3}{4\pi R^3}\frac{1}{N(E_F)k_BT}, \tag{5}$$

which gives

$$R_{\text{opt}} = \left(\frac{9}{8\pi N(E_F)\alpha k_BT}\right)^{1/4}. \tag{6}$$

Inserting R_{opt} in (4), we find that the hopping probability, and hence the conductivity, is given by Eq. (1) with $p = 1/4$ and

$$T_0 \sim \frac{1}{\xi^3 N(E_F)}. \tag{7}$$

We now consider the quasicrystalline state. In the fractional FS model with a practically infinite number of valleys, all the electrons in the atomically ordered quasicrystal are localized at zero temperature. At a finite temperature, the scattering of an electron from a particular valley to the state in a neighboring valley can occur not only due to thermal excitation but also due to tunneling via the gap formed by Bragg reflections. At very low temperatures, the process with a higher probability is the scattering with a small momentum transfer; in the real space, this corresponds to a hopping by a large distance. But the tunneling and, correspondingly, the large-distance hopping are a necessary process for the VRH mechanism. Thus, following the Mott procedure [19] and using expression (5), we immediately obtain Eq. (1). The Mott formalism usually fails when $R < \xi$ or $T_0 < T$. But in the case of a quasicrystal, it is always possible to find a state for which $T_0 < T$, even though $R > \xi$. As a matter of fact, the material with a fractional FS has a hierarchy of localization lengths. Therefore, the characteristic temperature T_0 can change from sample to sample in an arbitrary way.

This mesoscopical situation is typical of QC and conventional disordered systems in the vicinity of MIT [20]. It is known that, in amorphous alloys and heavily doped semiconductors, the electron wave functions show a characteristic change from localized to extended behavior because of this transition. This corresponds to a change from the states that do not enable transport in the limit of vanishing temperature to the states that do, thereby distinguishing the insulating and metallic character. In the localized regime, the spatial behavior of the wave functions is usually described by an exponential decay length reflecting the spatial extent

of the wave function, whereas, on the metallic side, the wave functions are extended. As the MIT is approached, the localization length diverges. Close to the MIT, the localization length is already much greater than the numerically accessible system size, and therefore, there can be no direct reflection of the localization in the calculated eigenstates. Exactly at the MIT, where the characteristic length scale is absent, the eigenstates show fractal characteristics and the wave functions are critical. However, characterizing the eigenstates and wave functions at the transition point requires a more general concept of multifractality. This implies that different parts of the same eigenstate must scale with different exponents, thus extending the simple fractal picture that comprised only one scaling exponent. Schriber and Grussbach found that, at the critical point of the 3D Anderson model, strong fluctuations of the wave function amplitudes display the multifractal character on all length scales and the singularity spectrum of the critical wave function does not depend on the system size [21]. The same state is typical of QC [11]. As shown in [22], most of the wave functions in a three-dimensional icosahedral QC are critical and their electronic spectrum contains a singular part. The situation is mesoscopic, and it is possible to experimentally obtain different values of T_0 for different samples (see [10–13]). We also note that the fractional FS model implies that the VRH mechanism ceases to work beginning with some ξ_{min}, when tunneling probability becomes negligibly small.

The VRH mechanism in the fractional FS model depends on the structure of the FS; for a perfect material, the VRH conductivity must always exist in bulk samples and in films. Recently, it was shown by Rosenbaum *et al.* [23] that some thin (2200 Å) icosahedral films of $Al_{72}Pd_{20}Re_8$ prepared by magnetron sputtering exhibit insulating transport properties down to 0.07 K, where their resistivity follows an activated Mott VRH law. Although we did not consider the role of electron–electron interactions, it is possible to assume that, with decreasing temperature, the Mott law ($T^{-1/4}$) is followed by the Efros–Shklovskii law ($T^{-1/2}$). Although it is difficult to distinguish between $T^{-1/4}$ and $T^{-1/2}$ dependences experimentally, one could observe this crossover on the high-quality *i*–Al–Pd–Re samples with a high resistance ratio $\mathcal{R}$.

In contrast to the Anderson localization, the localization of electrons in quasicrystals is due to constructive interference (phase coherence) of the wave functions and is unstable with respect to small perturbations [22]. The system can therefore be driven to the metallic side of MIT by increasing the temperature or the number of imperfections. Moreover, in a "dirty" object at temperatures larger than approximately 10 K, the electronic states are smeared by the inelastic scattering processes that wash out the fine details of the FS with a large number of pockets and lead to the FS with an effectively finite number of pockets, depending on the perturbations [13]. When the number of FS pockets is finite, the VRH mechanism does not work, and the crossover to another temperature dependence must occur.

4. HIGH-TEMPERATURE CONDUCTIVITY

In a real quasicrystal, one must take the smearing of electron states in the momentum space into account. Because the energy of a quasiparticle is defined with the uncertainty $\delta\varepsilon \sim \max(T, \hbar/\tau)$, where T is the temperature and τ is the electron relaxation time, the splitting of the FS within the procedure described above makes sense as long as the characteristic size of the pockets is larger than $\delta\varepsilon$. This leads to the FS with a finite number of electron–hole pockets with the size of the pocket defined by the uncertainty of the electron energy. This also leads to a nonmetallic regime of the conductivity caused by an intravalley scattering. At these conditions, the VRH mechanism does not work, because the intervalley scattering with small momentum transfer is ineffective. On the contrary, the momentum transfer that is now required for the intervalley scattering is large (of the order $1/a$, where a is the quasilattice constant). In the FS model with a finite number of valleys, the temperature-dependent conductivity is governed by the intravalley and intervalley processes. As shown in [9], σ is inversely proportional to the scattering relaxation time and should increase with increasing temperature according to a power-law dependence. However, the high-temperature region ($T > u/a \sim \Theta_D$, where u is the sound velocity and Θ_D is the Debye temperature) has not been considered previously, and we now appropriately analyze this regime. In this region, the temperature dependence of σ is governed by the electron–phonon intervalley scattering processes and a sharp decrease of the electron–phonon scattering time should be observed, accompanied by the corresponding change in the character of conductivity.

We consider the probability for an electron with the momentum $\mathbf{k}$ in a tiny pocket of the Fermi surface to be scattered by a phonon to the free electron state with the momentum $\mathbf{k}'$. This probability is given by

$$w(\mathbf{k}, \mathbf{k}') = g^2(\mathbf{K})[\delta(\epsilon_{\mathbf{k}'} - \epsilon_{\mathbf{k}} - \hbar\omega_{\mathbf{q}})n^0_{\mathbf{q}} f^0_{\mathbf{k}}(1 - f^0_{\mathbf{k}'}) + \delta(\epsilon_{\mathbf{k}'} - \epsilon_{\mathbf{k}} + \hbar\omega_{\mathbf{q}})(n^0_{\mathbf{q}} + 1) f^0_{\mathbf{k}'}(1 - f^0_{\mathbf{k}})]. \quad (8)$$

Here, $\mathbf{K} = \mathbf{k}' - \mathbf{k}$, $\mathbf{q} + \mathbf{g} = \mathbf{k}' - \mathbf{k}$ (where $\mathbf{g}$ is a reciprocal lattice vector), $\omega_{\mathbf{q}}$ is the phonon energy, $n_{\mathbf{q}}$ is the Bose–Einstein distribution, $f_{\mathbf{k}}$ is the Fermi–Dirac distribution, and $g(\mathbf{K}) = \pi(n_e/E_F)(\mathbf{Ke})/\sqrt{N_i M_i \omega_{\mathbf{q}}}$ is the matrix element of the electron–phonon interaction, where n_e is the electron density at the Fermi level, e is the phonon polarization vector, and N_i and M_i are the ion density and mass, respectively (in the case where the Fermi surface pocket is considered as a sphere of the diameter μ_0, we have $n_e/E_F = 2\mu/3$). To obtain the electron–phonon

relaxation time τ_0, we must integrate Eq. (8) over **k** and **k'**. This integration procedure is similar to those for the electron–phonon relaxation time calculation in usual metals: the integration over the modulus of **k'** eliminates the delta function; the intergration of the Fermi distribution function over the modulus of **k** gives the so-called structural factor. The remaining angular integrations can then be easily reduced to an integral over the angle Θ between the vectors **k** and **k'**. After the final integration over Θ, we find the equation for τ_0 for the hypothetical metal with one tiny valley,

$$\tau_0^{-1} = \frac{k_0 q_D^6}{\pi^2 m N_i M_i \Theta_D}\left(\frac{T}{\Theta_D}\right)^5 \times \int_0^{\Theta_D/T} \frac{z^5}{(1-e^{-z})(e^z-1)}, \quad (9)$$

where q_D and Θ_D are the Debye wave vector and temperature, respectively. For the object with the *N*-component Fermi surface under the conditions of valley uniformity, we obtain $\tau_{e-ph}^{-1} = N\tau_0^{-1}$, where *N* is a parameter of the model. The effective number *N* of the FS electron–hole pockets can be estimated using X-ray or electron diffraction experiments, from the amount of main strong Bragg reflections that satisfy the condition $\mathbf{G} = 2\mathbf{k}_F$ (**G** is a vector of the six-dimensional reciprocal lattice) [1], including the multiplicity factor.

In discussing the application of these relations to quasicrystals, one should remember that the electron–phonon interaction can change the electron momentum only by a small amount, of the order T/u. We again note that a large momentum transfer is necessary for the intervalley scattering to occur. Hence, there exists a characteristic temperature $T^* \sim u/a \sim \Theta_D$, below which the phonons are unable to scatter the electrons from one pocket to another, thereby permitting only the intravalley processes. Accordingly, the electron–phonon scattering mechanism is ineffective for the temperatures $T < T^*$ because Eq. (9) does not contain the factor $N \gg 1$. Hence, we can neglect the electron–phonon scattering in the low-temperature region and consider the high-temperature limit of Eq. (9) only. The integral in Eq. (9) is then proportional to $(\Theta/T)^4$ and we find that the electron–phonon relaxation time at high temperatures is given by

$$\tau_{e-ph}^{-1} \approx Nq^4 k_0 (N_i M_i u^2 m)^{-1} T.$$

Because the probability of the electron scattering by phonons is linear in *T*, it is easy to show, using the results of [9], that the temperature dependence of the conductivity at high temperatures must be linear. We note that according to some experimental data, the $\sigma(T)$ dependence at high temperatures for some *i*-quasicrystals is indeed nearly linear [2, 24, 25].

We finally estimate the conductivity at zero temperature. The relaxation of the electronic momentum on the structural imperfections results in a finite value of σ, in analogy with metallic systems. On the other hand, it was found that $\sigma(0)$ is proportional to the concentration of the structural imperfections, in contrast to the usual metallic Drude-like conductivity [9],

$$\sigma(0) \approx e^2 \hbar^{-1} N^2 m^2 n_{\text{imp}} |U_0|^2,$$

where $|U_0|$ is the amplitude of the Born scattering of an electron by the structural defects, *m* is the electron mass, and n_{imp} is the concentration of defects. To check the agreement of the predicted data with the experimental data, we numerically estimate the magnitude of $\sigma(0)$. With the rough assumptions $|U_0| \sim 10^{-8}$ cm (atomic radius) and $n_{\text{imp}} \sim 10^{22}$ cm^{-3}, we immediately obtain $\sigma(0) \sim 10N^2$ [Ω^{-1} cm^{-1}]. For *N*, we can assume a reasonable value of about one hundred [1], which gives the reasonable estimation for $\sigma(0)$. For the imperfection concentration $n_{\text{imp}} \sim 10^{-5}$, $\sigma(0)$ is about 1 Ω^{-1} cm^{-1}, which approximately corresponds to the experimental values for the perfect Al–Pd–Re alloys with the high resistance ratio $\mathcal{R}$ [2].

5. CONCLUSION

We have considered a "scenario" in which the band structure effects, namely, the constructive interference of wave functions due to Bragg reflections, are responsible for the localization of the electrons and, consequently, for the electron transport in quasicrystals. The Fermi surface of an atomically ordered perfect icosahedral quasicrystal (such as *i*-Al–Pd–Re) at zero temperature contains an infinite number of electron–hole pockets where the electrons are localized. In this case, the VRH mechanism of conductivity should be operative, because the intervalley scattering processes with small momentum transfer are available. The Mott law is obtained for the low-temperature region taking the intervalley tunneling transitions into account. We note that the importance of interband tunneling transitions was previously pointed out in [26]; recently, Krajčí and Hafner [27] emphasized the significance of these transitions for the electron transport in QC. With increasing temperature and QC imperfections, the FS effectively contains a finite number of pockets due to smearing, and the conductivity becomes power-law temperature dependent. The estimate made in the framework of the fractional FS model predicts that, at high temperatures ($T > \Theta_D$), the conductivity should linearly depend on the temperature. Finally, it is worth noting that we have considered only the role of the band structure effects and did not discuss either the influence of the quantum interference effects, which can be important for a material with a low value of the resistance ratio $\mathcal{R}$, or other possible mechanisms of the conductivity in QC. In addition, we based our consideration only on the experiments carried out for the *i*-Al–Pd–Re quasicrystal.

Although the scattering mechanisms in different types of QC may be different, we believe that our conclusions about the mechanism of conductivity in QC in the framework of the fractional FS model are quite general.

ACKNOWLEDGMENTS

We would like to thank I. A. Abrikosov and P. A. Korzhavyĭ for discussions and help during the work. We also are grateful to J. S. Poon for fruitful discussions.

This work was supported by the Netherlands Organization for Scientific Research (NWO project 047-008-016), the Russian Foundation for Basic Research (project no. 00-02-17668), the Royal Swedish Academy of Science, the Russian Ministry of Education, and the Department of Science and Technology of the Moscow Government (grant 1.1.240).

REFERENCES

1. S. J. Poon, Adv. Phys. **41**, 303 (1992).
2. O. Rapp, in *Physical Properties of Quasicrystals*, Ed. by Z. M. Stadnik (Springer-Verlag, Berlin, 1999), p. 127.
3. C. Gignoux, C. Berger, G. Fourcaudot, *et al.*, Europhys. Lett. **39**, 171 (1997).
4. F. S. Pierce, Q. Guo, and S. J. Poon, Phys. Rev. Lett. **73**, 2220 (1994).
5. D. Mayou, C. Berger, F. Cirot-Lackmann, *et al.*, Phys. Rev. Lett. **70**, 3915 (1993).
6. T. Fujiwara, S. Yamamoto, and G. T. de Loussardiere, Phys. Rev. Lett. **71**, 4166 (1993); S. Roche and T. Fujiwara, Phys. Rev. B **58**, 11338 (1998).
7. T. Fujiwara, in *Physical Properties of Quasicrystals*, Ed. by Z. M. Stadnik (Springer-Verlag, Berlin, 1999), p. 169.
8. E. Macia, Phys. Rev. B **61**, 8771 (2000).
9. S. E. Burkov, A. A. Varlamov, and D. V. Livanov, Phys. Rev. B **53**, 11504 (1996).
10. Q. Guo and S. J. Poon, Phys. Rev. B **54**, 12793 (1996).
11. M. Rodmar, F. Zavaliche, S. J. Poon, and O. Rapp, Phys. Rev. B **60**, 10807 (1999).
12. J. Delahaye, J. Brison, and C. Berger, Phys. Rev. Lett. **81**, 4204 (1998).
13. C. R. Wang, H. S. Kuan, S. T. Lin, and Y. Y. Chen, J. Phys. Soc. Jpn. **67**, 2383 (1998).
14. F. S. Pierce, S. J. Poon, and Q. Guo, Science **261**, 737 (1993).
15. C. Janot, Phys. Rev. B **53**, 181 (1996).
16. C. Janot, J. Phys.: Condens. Matter **9**, 1493 (1997).
17. N. Rivier and M. Durand, Mater. Sci. Eng. A **294–296**, 534 (2000).
18. W. Harrison, *Pseudopotentials in the Theory of Metals* (Benjamin, New York, 1966; Mir, Moscow, 1968).
19. N. Mott, *Conduction in Noncrystalline Materials* (Clarendon, Oxford, 1993).
20. A. D. Mirlin and F. Evers, Phys. Rev. B **62**, 7920 (2000).
21. M. Schriber and M. Grussbach, Phys. Rev. Lett. **67**, 607 (1991).
22. Yu. Kh. Vekilov, E. I. Isaev, and S. F. Arslanov, Phys. Rev. B **62**, 14040 (2000).
23. R. Rosenbaum, R. Haberkern, P. Mäussler, *et al.*, J. Phys.: Condens. Matter **12**, 9735 (2000).
24. A. Bianchi, F. Bommedi, M. A. Chernikov, *et al.*, Phys. Rev. B **55**, 5730 (1997).
25. A. Perrot and J. Dubois, Ann. Chim. (Paris) **18**, 501 (1993).
26. Yu. Kh. Vekilov, P. A. Korzhavyĭ, and D. V. Olenev, Pis'ma Zh. Éksp. Teor. Fiz. **62**, 349 (1995) [JETP Lett. **62**, 372 (1995)].
27. M. Krajčí and J. Hafner, J. Phys.: Condens. Matter **13**, 3817 (2001).

Journal of Experimental and Theoretical Physics, Vol. 94, No. 1, 2002, pp. 178–190.
From Zhurnal Éksperimental'noĭ i Teoreticheskoĭ Fiziki, Vol. 121, No. 1, 2002, pp. 210–224.

SOLIDS
Electronic Properties

Lattice Relaxation and Charge-Transfer Optical Transitions Due to Self-Trapped Holes in Nonstoichiometric $LaMnO_3$ Crystal¶

N. N. Kovaleva[a, b, *], J. L. Gavartin[b], A. L. Shluger[b], A. V. Boris[a, c], and A. M. Stoneham[b]

[a] *Institute of Solid State Physics, Russian Academy of Sciences, Chernogolovka, Moscow oblast, 142432 Russia*
[b] *University College London, London WC1E 6BT, United Kingdom*
[c] *Max-Planck-Institut für Festkörperforschung, 70569, Stuttgart, Germany*
**e-mail: nkovalev@issp.ac.ru*

Received April 12, 2001

We explore the role of electronic and ionic polarization energies in the physics of "colossal" magnetoresistive (CMR) materials. We use the Mott–Littleton approach to evaluate polarization energies in the $LaMnO_3$ lattice associated with holes localized on both the Mn^{3+} cation and the O^{2-} anion. The full (electronic and ionic) lattice relaxation energy for a hole localized at the O site is estimated at 2.4 eV, which is appreciably greater than that of 0.8 eV for a hole localized at the Mn site, indicating a strong electron–phonon interaction in the former case. The ionic relaxation around the localized holes differs for anion and cation holes. The relaxation associated with Mn^{4+} is approximately isotropic, whereas ionic displacements around O^- holes show axial symmetry with the axis directed towards the apical oxygens. Using the Born–Haber cycle, we examine thermal and optical energies of the hole formation associated with the electron ionization from Mn^{3+}, O^{2-}, and La^{3+} ions in the $LaMnO_3$ lattice. For these calculations, we derive a phenomenological value for the second electron affinity of oxygen in the $LaMnO_3$ lattice by matching the optical energies of the La^{4+} and O^- hole formation with maxima of binding energies in the experimental photoemission spectra. The calculated thermal energies predict that the electronic hole is marginally more stable in the Mn^{4+} state in the $LaMnO_3$ host lattice, but the energy of a hole in the O^- state is only higher by a small amount, 0.75 eV, suggesting that both possibilities should be treated seriously. We examine the energies of a number of fundamental optical transitions, as well as those involving self-trapped holes of Mn^{4+} and O^- in the $LaMnO_3$ lattice. The reasonable agreement of our predicted energies, linewidths, and oscillator strengths with experimental data leads us to plausible assignments of the optical bands observed. We deduce that the optical band near 5 eV is associated with the O(2*p*)–Mn(3*d*) transition of a charge-transfer character, whereas the band near 2.3 eV is rather associated with the presence of Mn^{4+} and/or O^- self-trapped holes in the nonstoichiometric $LaMnO_3$ compound. © *2002 MAIK "Nauka/Interperiodica".*

1. INTRODUCTION

The striking behavior of the "colossal" magnetoresistive (CMR) oxides of $R_{1-x}A_xMnO_3$ (where R stands for trivalent rare-earth ions and A for divalent alkaline-earth ions, and $0.2 \le x \le 0.5$) arises from the interplay of several distinct energy terms: magnetic interactions, electronic band structure energies, crystal field splittings, vibrational energies, and the electron–lattice coupling, including small polaron ideas and the Jahn–Teller (JT) effect. Understanding this behavior has been helped very greatly by the use of models to map the various regimes of behavior [1]. The experimental evidence [2] suggests that manganites are doped charge-transfer insulators having O(2*p*) holes rather than Mn^{3+}(3*d*) electrons as the current carriers. However, whether holes reside at O and/or Mn sites is still a subject of controversy. Some of the models of polarization and vibration in CMR systems make major approximations, such as a single vibrational frequency (Einstein model) or rigid, unpolarizable ions. These simplifications are known to give seriously inadequate results, both quantitatively and qualitatively. For example, for the charge transfer transitions of the zinc vacancy center V^- in ZnSe, optical spectroscopy [3] allows one to obtain the key relaxation and tunneling energies. But in the simple one-frequency rigid-ion model, these values are inconsistent with the observed charge localization on a single Se neighbor to the vacancy [4]. However, the consistency and good agreement with experiment are restored in the general model at the harmonic and dipole approximation level, namely, the shell model. Important properties of the shell model [5, 6] consist, first, in properly separating the ionic and electronic polarizations, such that phonons are well predicted and polarization at the atomic scale is well reproduced, and, second, in recognizing that the local environment affects the polarizability of ions through short-range repulsive forces. As a result, the shell model provides an adequate framework for understanding energies dominated by polarization and distortion. Such energies include those describing small polarons [3–5] and optical charge

¶This article was submitted by the authors in English.

transfer transitions (as considered for MgO [7] and V^- centers in ZnSe [4]). The shell model has also been extensively used in studies of defect energetics and nonstoichiometry in oxides [8]. Its considerable quantitative success arises largely because it provides such an accurate description of the large polarization energies.

It is helpful to recognize the orders of magnitude of the several energy terms for CMR oxides. Obviously, a small energy does not mean that the particular energy is unimportant, but a small value often means that very simple ideas for those terms are sufficient in examining phenomena dominated by large energies. Typical magnitudes are as follows:

CMR instability energy of an electron in an external field of 10 T, 0.001 eV ($\sim\mu_B gH$);

Magnetic exchange (from kT_N, with T_N being the Néel temperature), 0.01 eV;

Energy of the noncubic structural deformation of the $LaMnO_3$ cell, ≤0.4 eV;

JT energy (from the largest known JT energies), ≤0.4 eV;

Crystal-field splitting energies (from data on many systems), 1 eV typical;

Polarization energies (net charge $\pm e$), 5 to 10 eV;

Free-ion ionization potentials, tens of eV;

Madelung energies (fully ionic models), tens of eV.

In this paper, we mainly consider the polarization energies, for which the large energy terms are dominant. We only discuss the JT and crystal field energies in simple terms, although we remark that one-frequency models of the JT effect also lead to inconsistencies.

We apply the shell model calculations to look specifically at energies associated with the localized holes of Mn^{4+} and O^- in a nonstoichiometric or slightly doped "parent" $LaMnO_3$ compound. Using this model, we address some of the issues in the physics of CMR systems for which the polarization energies are crucial. First, we calculate the electronic and ionic polarization energies due to holes localized on Mn^{3+} and O^{2-} ions in order to estimate the key polaron energies and examine the controversial question of whether holes reside at Mn or O sites in the $LaMnO_3$ lattice. Second, we estimate the energies of the main charge transfer transitions including Mn^{4+} and O^- species, which determine specific transport properties of doped CMR materials. We analyze their contribution to the optical conductivity in the nonstoichiometric $LaMnO_3$ crystal and make the assignment of bands in the optical conductivity spectrum more clear-cut.

2. DESCRIPTION OF THE $LaMnO_3$ SYSTEM AND THE SHELL MODEL APPROXIMATION

Many of the CMR materials are hole-doped systems of perovskite manganites of the form $La_{1-x}A_xMnO_3$. Their properties are intimately related to those of the "parent" compound ($x = 0$). Below $T_N \approx 140$ K, $LaMnO_3$ is an A-type antiferromagnet in which the MnO_2 ferromagnetic layers are stacked along the c axis with alternating spin directions. The structure of the perovskite manganites can be clearly understood starting from the simple cubic perovskite structure ($Pm3m$). The idealized cubic structure of $LaMnO_3$ featuring a chain of the corner-sharing MnO_6 octahedra is presented in Fig. 1. The Mn^{3+} ion with the $3d^4$ electronic configuration is known to exhibit a large JT effect in other systems [9]. Therefore, it is natural to assume that the JT instability of the Mn^{3+} ion can contribute to an orthorhombic distortion of the perovskite structure of the *Pnma* symmetry in the $LaMnO_3$ crystal. The orthorhombic structure can be obtained from the cubic perovskite structure by two consequent and coordinated rotations of the MnO_6 octahedra around the [010] and [101] directions, as shown in Fig. 1. Another possible contribution to the observed distortion from the cubic symmetry in $LaMnO_3$ could be attributed to an atomic size mismatch: the sum of the Mn–O layer ionic radii, $r_{Mn} + r_O$, does not match that of the La–O layer, $(r_{Mn} + r_O)/\sqrt{2}$, in the right way for a stable cubic structure. The size mismatch effect is known to be a common reason for distortions in different perovskite oxides. Our shell model calculations performed for the $LaMnO_3$ *Pnma* structure indicate that the orthorhombic distortions experimentally observed at low temperatures could not simply be caused by the lattice mismatch effect (which, in principle, must be properly described in the framework of the shell model approximation),

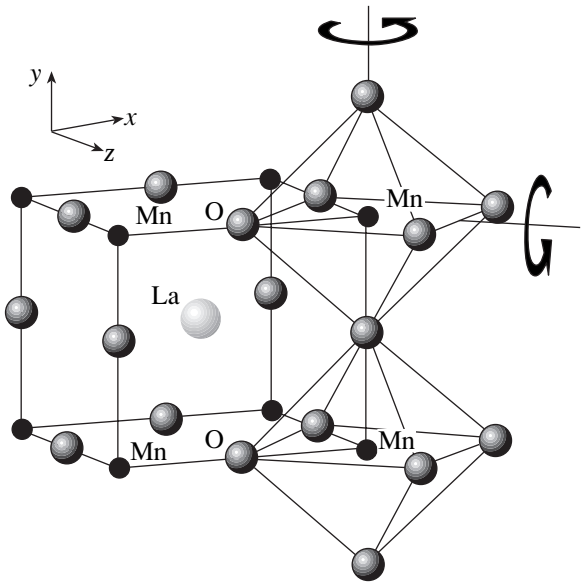

Fig. 1. The idealized cubic perovskite structure (*Pm*3*m*) of the $LaMnO_3$ crystal. The orthorhombic *Pnma* structure can be obtained by two consequent rotations of the MnO_6 octahedra around the [010] and [101] directions.

Table 1. Potential parameters for short-range interactions in $LaMnO_3$ (*Pm*3*m*): (a) elaborated in the present work; (b) from Islam *et al*. [17]; (c) from Grimes [20] for Mn^{3+} and Mn^{4+} different valence states; r_{cutoff} = 20 Å

		A, eV	ρ, Å	*C*, eV Å^{-6}	*Y*, $\|e\|$	*k*, eV Å^{-2})
(a)	La^{3+}–O^{2-}	1516.3	0.3639	0.00		
	Mn^{3+}–O^{2-}	1235.9	0.31525	0.00		
	O^{2-}–O^{2-}	22764.3	0.1490	20.37	−2.48	16.8
(b)	La^{3+}–O^{2-}	1516.3	0.3525	0.00		
	Mn^{3+}–O^{2-}	1235.9	0.3281	0.00		
	O^{2-}–O^{2-}	22764.3	0.1490	43.00		
(c)	La^{3+}–O^{2-}	2088.79	0.3460	23.25		
	Mn^{3+}–O^{2-}	922.83	0.3389	0.00		
	Mn^{4+}–O^{2-}	1386.14	0.3140	0.00		
	O^{2-}–O^{2-}	9547.96	0.2192	32.00	−2.04	6.3

but are caused by both effects, with a comparative contribution of the JT effect. Some special efforts should be undertaken to empirically account for the JT effect in the framework of the shell model. We perform the shell model calculations for the cubic perovskite structure (Fig. 1). This approximation seems to be mostly relevant to the nonmagnetic quasi-cubic perovskite structure of the $LaMnO_3$ crystal experimentally observed at high temperatures $T \geq 400$ K > $T_N \approx 140$ K. We suggest that our modeling of the cubic perovskite structure provides a reasonable model because we are mainly interested in estimating the key polarization energies associated with polaron-type charge carriers in the high-temperature insulating quasi-cubic phase of the CMR lattices.

We model the $LaMnO_3$ system using methods based on the shell model and the Mott–Littleton approach that have been successfully applied to studying the properties of a wide range of oxides (including transition metal oxides), halides, and other systems [10, 11]. The calculations are performed using the GULP code [12]. In the shell model [5], the lattice is considered as an assembly of polarizable ions, represented by massive point cores and massless shells coupled by isotropic harmonic forces. The interaction potential includes contributions of the Coulomb, polarization, and short-range interactions. We adopt a fully ionic model (with the formal charges of ions in the $LaMnO_3$ lattice, La^{3+}, Mn^{3+}, and O^{2-}). This is less restrictive than one might think because a parallel covalent description is possible [13]. The sum of the core and shell charges is equal to the formal charge of the ion in the lattice. The core and shell charges and the spring constant of each ion are parameters of the model. The electronic polarization of the ions is represented by the displacement of their shells relative to the cores in the dipole approximation. The lattice distortion is simulated by the core displacements from their lattice site positions.

In our model, cations are treated as unpolarizable and the short-range interactions between relatively small cations (core–core interactions) are ignored. The short-range potentials used for the shell–shell (oxygen–oxygen) and core–shell (metal–oxygen) interactions are of the Buckingham form,

$$V_{ij} = A_{ij}\exp\left(-\frac{r}{\rho_{ij}}\right) - \frac{C_{ij}}{r^6}. \quad (1)$$

The parameters of both repulsive and attractive components of the Buckingham potential for the shell–shell (O^{2-}–O^{2-}) interactions used in this work are obtained in [14] and presented in Table 1, part a. The Buckingham parameters for the core–shell Mn^{3+}–O^{2-} and La^{3+}–O^{2-} interactions were fitted in this work using the experimental data including the lattice parameter, the static and high-frequency dielectric constants, and the frequencies of the transverse optical (TO) phonons in the $LaMnO_3$ crystal [15]. The dielectric constants are especially important if one wishes to predict polarization energies accurately. We have not found an experimental value of the static dielectric constant of $LaMnO_3$ in the literature. We are grateful to T. Arima and Y. Tokura [16] for sending us the experimental data on the reflectivity spectra of $LaMnO_3$ measured at room temperature and reported in [15]. In the present work, the experimental value of the static dielectric constant $\epsilon_0 \approx 18 \pm 2$ was derived from these data by Kramers–Kronig analysis and was further used in the fitting procedure. The parameters fitted for $LaMnO_3$ (*Pm*3*m*) in [17] (see Table 1, part b) were used as the starting values for the core–shell La^{3+}–O^{2-} and Mn^{3+}–O^{2-} short-range interaction potentials. The oxygen shell charge was taken as $-2.48|e|$, and the shell–core spring constant *k* was chosen to give the correct value of the static dielectric constant ϵ_0.

The final values of our shell model parameters are presented in Table 1, part a. The calculated and experimental properties of $LaMnO_3$ (*Pm*3*m*) are summarized in Table 2. One can see that both sets of parameters (Table 1, parts a, b) give close values for the lattice parameter and cohesive energy; however, at the same time, our parameters give results that are close to the static and high-frequency dielectric constants. The value of the static dielectric constant calculated with the parameters given in [17] is much higher than that derived from the experimental reflectivity spectra. Our model also agrees well with the experimental values of the transverse optical phonon energies [15]. The phonon bands obtained in our calculations correlate well with those observed with higher oscillator strengths. In particular, the predicted phonon energies agree well for the La external mode (ω_{TO_1}), Mn–O–Mn

Table 2. Crystal properties of $LaMnO_3$ ($Pm3m$) calculated using the shell model potentials (Table 1) and compared with experimental data

	Lattice const. a_0, Å	Cohesive energy E_{lat}, eV	ϵ_0	ϵ_∞	ω_{TO_1}, cm^{-1}	ω_{TO_2}, cm^{-1}	ω_{TO_3}, cm^{-1}
Experiment	3.889		18 ± 2 [15]	4.9 [15]	172 [15]	360 [15]	560 [15]
Calcd. (a)	3.889	–140.52	15.6	4.9	172	308	513
Calcd. (b)	3.904	–139.12	56.17	–	–	–	–
Calcd. (c)	3.906	–139.58	14.1	4.6	156	252	368

bending mode (ω_{TO_2}), and Mn–O stretching mode (ω_{TO_3}) for the quasi-cubic perovskite structure of the strongly doped perovskite manganite system $La_{0.67}Ca_{0.33}MnO_3$ [18, 19].

We have also tested another set of short-range pair potentials that are different for the Mn ion in different valence states Mn^{2+}, Mn^{3+}, and Mn^{4+}. The potentials were obtained by fitting the equilibrium structures of several oxide compounds, such as MnO, $LaMnO_3$, and Ca_2MnO_4 [20]. We tested pair potentials for Mn^{4+} and Mn^{3+} from this set, presented in Table 1, part c. These parameters also give good results (see the set of values (c) in Table 2) for the lattice parameter and dielectric constants, but are less successful in predicting the optical phonon frequencies. As we show below, both these and our parameters give similar values for the calculated properties of polarons in these crystals, thereby validating the correctness of the shell model approach.

We then apply the shell model parameters to estimate key defect energies using the well-known Mott–Littleton method (see [11] for a more detailed description). It is based on the concept that the total energy of the crystal lattice containing a defect is minimized by relaxation of the ions surrounding the defect, and this relaxation fairly rapidly decreases at distances away from the defect. In these calculations, the crystal is divided into three regions: an inner spherical region I, containing the defect and its immediate surroundings; an intermediate finite region II, which is created to properly link region I; and an outer infinite region III, which responds as a dielectric continuum. Finite regions I and II are embedded in infinite region III. The typical radii of regions I and II used in our calculations were 10 and 25 Å, respectively. We considered an electronic hole located in the center of region I, which is the most perturbed. The displacements of cores and shells in this region are calculated explicitly. In intermediate region II, the ions are also treated within the shell model, but their displacements and polarizations are derived from the dielectric continuum approximation. The system total energy is minimized (the preset accuracy was 0.01 eV) with respect to the positions of all cores and shells in regions I and II in the potential produced by polarized region III.

The Mott–Littleton method is especially valuable to estimate key polaron energies because the long-range polarization fields are treated properly; many other methods (such as cluster methods or periodic cell methods) treat these significant terms badly.

3. ELECTRONIC HOLES IN $LaMnO_3$

3.1. Relaxation Energies of the Localized Holes in $LaMnO_3$

We study possible hole localization (self-trapping) on Mn^{3+} and O^{2-} ions in a slightly hole-doped or nonstoichiometric $LaMnO_3$ crystal. Theoretical predictions of the electron charge carrier self-trapping in the ideal lattice are based on calculations of the so-called self-trapping energy [10], which is the difference between the localization and relaxation energies. The first of these terms is basically an increase in the hole (electron) kinetic energy due to its localization on a finite number of lattice sites from a completely delocalized state. The second is the energy gain due to the lattice polarization by the localized charge. They represent a very delicate balance of large terms that in many cases differ by 0.1 eV only. The calculation of the localization energy, especially in complex crystals, is the most difficult part of the study of the electron charge carrier self-trapping [10] and requires accurate electronic structure calculations beyond the scope of this work. Our aim is rather to compare the relaxation energies for the hole localization in two different sublattices of the same crystal. These energies are indicative of the strength of the electron–phonon interaction, and their difference can suggest whether there are major differences in hole trapping in one of the sublattices.

The hole formation process can generally be seen as the ionization of the in-crystal ion with an electron being taken out of the crystal and put on the vacuum level. The energy required in this process (the hole formation energy E_h^α for α = Mn, O, La) is the work done against the in-crystal ionic core potential, I^α, and the crystalline electrostatic potential, U_M^α, less than the energy gain due to the lattice polarization effects, R^α:

$$E_h^\alpha = I^\alpha + U_M^\alpha + R^\alpha. \quad (2)$$

Table 3. Formation and polarization energies for localized holes in $LaMnO_3$: (a) for the pair potentials explored in this work; (c) for the pair potentials from Grimes [20] (Table 1) for Mn^{3+} and Mn^{4+} different valence states

	α-hole	$E^{\alpha}_{h,\,\mathrm{opt}}$	$E^{\alpha}_{h,\,\mathrm{th}}$	I^{α} (E^{α}_{IV})	$S^{\alpha}_{\mathrm{opt}}$	S^{α}_{th}	U^{α}_{M}	$R^{\alpha}_{\mathrm{opt}}$	$\Delta R^{\alpha}_{\mathrm{th}}$	$E^{\alpha}_{\mathrm{PES}}$
(a)	Mn^{4+}	2.56	1.73	47.41 (51.20)	−44.85	−45.68	−38.3	−6.55	−0.83	1.2
	O^{-}	4.86	2.48	−13.91	18.77	16.39	22.1	−3.33	−2.38	3.5
	La^{4+}	18.36	17.63	49.45 (49.45)	−31.09	−31.82	−27.4	−3.68	−0.73	17.0
(c)	Mn^{4+}	2.62	1.95	46.83 (51.20)	−44.27	−44.94	−38.1	−6.17	−0.67	1.2
	O^{-}	4.92	2.52	−13.82	18.74	16.34	22.0	−3.26	−2.40	3.5
	La^{4+}	18.42	17.84	49.45 (49.45)	−31.03	−31.61	−27.4	−3.63	−0.58	17.0

To assess the extent of the lattice perturbation by the hole localization and calculate the hole relaxation energy, it is useful to distinguish the "electronic" and "ionic" terms in the polarization energy. The first term, which we call $R^{\alpha}_{\mathrm{opt}}$, is due to the "electronic" polarization of ions by the momentarily localized hole, which in our method is represented by the displacements of shells with respect to the cores that are fixed at their perfect crystal positions. This term takes the lattice response on, e.g., the Franck–Condon photoionization into account. The lattice distortion term due to displacements of cores and related adjustment of shells after the complete lattice relaxation, denoted as $\Delta R^{\alpha}_{\mathrm{th}}$, is the difference between the full polarization energy R^{α} and $R^{\alpha}_{\mathrm{opt}}$,

$$\Delta R^{\alpha}_{\mathrm{th}} = R^{\alpha} - R^{\alpha}_{\mathrm{opt}}. \qquad (3)$$

It represents the hole relaxation energy. If this energy exceeds the localization energy, i.e., the kinetic energy rise due to the complete hole localization on this site, then one can talk about the hole being self-trapped on this site. Given this assumption, Eq. (2) takes the form

$$E^{\alpha}_{h} = I^{\alpha} + U^{\alpha}_{M} + R^{\alpha}_{\mathrm{opt}} + \Delta R^{\alpha}_{\mathrm{th}}. \qquad (4)$$

The shell model Mott–Littleton calculations give the cumulative energy of the second and third terms, $S^{\alpha}_{\mathrm{opt}}$, or of the last three terms, S^{α}_{th}, in Eq. (4) depending on whether both shells and cores or shells only were allowed to relax. It is sensible, however, to evaluate these terms separately. This can be rigorously done by independently calculating the on-site electrostatic potential U^{α}_{M} within the periodic model and using the definition introduced by Eq. (3). The values of $R^{\alpha}_{\mathrm{opt}}$ and S^{α}_{th} and the calculated terms U^{α}_{M}, $R^{\alpha}_{\mathrm{opt}}$, and $\Delta R^{\alpha}_{\mathrm{th}}$ are summarized in Table 3.

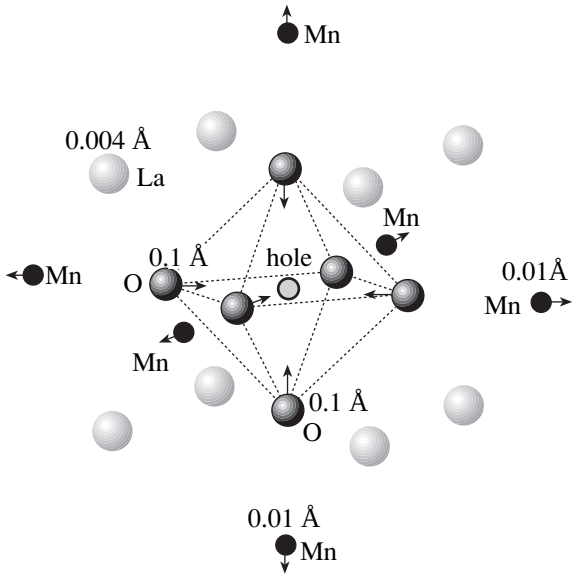

Fig. 2. The core displacements (≥0.004 Å) of the ions surrounding the Mn^{4+} electronic hole defect after the complete relaxation of cores and shells in the $LaMnO_3$ lattice.

It follows from the calculations that there is a large difference in the lattice relaxation energies for the O^{-} and Mn^{4+} holes. The lattice relaxation energy $-\Delta R^{\alpha}_{\mathrm{th}}$ caused by the hole localization at the O site (2.38 eV) appears to be significantly larger than that for the hole localized at the Mn site (0.83 eV), as shown in Table 3a. This indicates a strong electron–phonon interaction in the case of the hole localized at the O site and could suggest that the hole trapping is more preferential in the oxygen sublattice. However, the width of the Mn(3*d*) subband in the density of states, which determines the hole localization energy, is much narrower than that of the O(2*p*) related subband [21]. Without a much fuller electronic structure calculation of the localization energy, it is therefore impossible to draw any final conclusion as to in which sublattice the holes could be localized.

One experimental test could involve the analysis of local vibrations due to the hole localization. It can be facilitated by the qualitative difference in the lattice relaxation around the two centers that is clearly seen in Figs. 2 and 3. The completely relaxed configuration of the ions surrounding the Mn^{4+} electronic hole defect

(see Fig. 2) corresponds to the positions of cores in region I that have appreciable displacements (more than or equal to 0.004 Å) from their perfect lattice sites. The cores of the six nearest neighbor oxygen ions are symmetrically displaced by about 0.1 Å towards the Mn^{4+} ion carrying the hole. The rest of the lattice relaxation comprises small displacements of the Mn and La ions (about 0.01 and 0.004 Å, respectively) out from the Mn^{4+} hole center.

By contrast, the ionic relaxation around the O^- hole center has axial symmetry, with the largest lattice displacements of the nearby Mn ions (about 0.21 Å) along the axis away from the O^- hole center (see Fig. 3). These displacements cause the next two apical oxygen ions along the axis to move away from the O^- hole center by about 0.1 Å. The equatorial oxygen ions in the octahedron relax towards the hole center by about 0.03 Å. In-plane La ions also show appreciable displacements away from the O^- hole center. The qualitative difference in the symmetry of the lattice relaxation around the two centers implies the difference in the local vibrational modes, which can be used for experimentally probing the hole localization in $LaMnO_3$.

3.2. Photoemission Spectra and In-Crystal Ionization Potentials in $LaMnO_3$: Formation Energies of the Localized Holes in the $LaMnO_3$ Crystal

To evaluate the hole formation energy, we need to estimate the values of the unknown in-crystal ionization energies I^α. We suggest estimating the ionization potentials from the experimental photoemission spectroscopy (PES) data, which can be directly related to our calculations. In principle, PES at different excitation energies probes bonding states as well as nonbonding states. The latter, being ion-in-crystal-like, can be related to the Franck–Condon energies obtained in our calculations. In order to juxtapose experimental and calculated values, we must also take into account that the PES binding energy E_{PES} is measured with respect to the Fermi energy level E_F of the sample. Therefore, we write

$$I^\alpha + U_M^\alpha + R_{\text{opt}}^\alpha = E_{PES}^\alpha + E_F. \quad (5)$$

In the PES spectra of $LaMnO_3$, there are two main photoemission bands around 3.5- and 6-eV binding energies at T = 100, 200 K for the HeI ($h\nu$ = 21.2 eV) and HeII ($h\nu$ = 40.8 eV) photon energies for which the O(2p) photoionization cross section is dominant [22]. The main maximum at 3.5 eV has been primarily assigned to the O(2p) nonbonding states, whereas the second maximum is assigned to the Mn(3d)–O(2p) bonding states and the decrease of the O(2p) character correlates with the decrease of the Mn(3d)–O(2p) hybridization strength. For higher energies with the HeII PES study, the $\sigma_{Mn(3d)}/\sigma_{O(2p)}$ cross-section ratio increases and a feature near 2.7 eV appears [22]. At high photon energies of 500 eV and T = 280 K, the band at 3.5 eV is not clearly evident, but the band at 2.7 eV becomes dominant over the band at 6 eV, which stands for the maximum contribution of Mn(3d) $3t_{2g}$ states at the binding energy of 2.7 eV [23]. The crystal field splitting between the Mn(3d) $3t_{2g}$ and e_g states in $LaMnO_3$ has been estimated from the PES study to be about $\Delta_{CF} \approx 1.5$ eV [23]. The peak at 17 eV has been assigned to the La(5p) states [23].

Thus, in accordance with the dominant contributions to the PES spectra of $LaMnO_3$ [22, 23], we assign the values $E_{PES}^{O} \approx 3.5$ eV, $E_{PES}^{La} \approx 17.0$ eV, and $E_{PES}^{Mn} \approx 1.2$ eV, suggesting that the Mn hole formation process is associated with the electron photoionization from the e_g level. These maxima in the PES spectra correlate well with the maxima in the density of states for the O(2p) and Mn(3d) e_g valence bands in $LaMnO_3$ calculated within the local spin density approximation (LSDA) [21]. The corresponding schematic representation of the band structure in accordance with the assigned maxima of binding energies in the PES spectra [22, 23] in the scale of energies related to the crystal Fermi level E_F is shown in Fig. 4. The gap in the e_g elec-

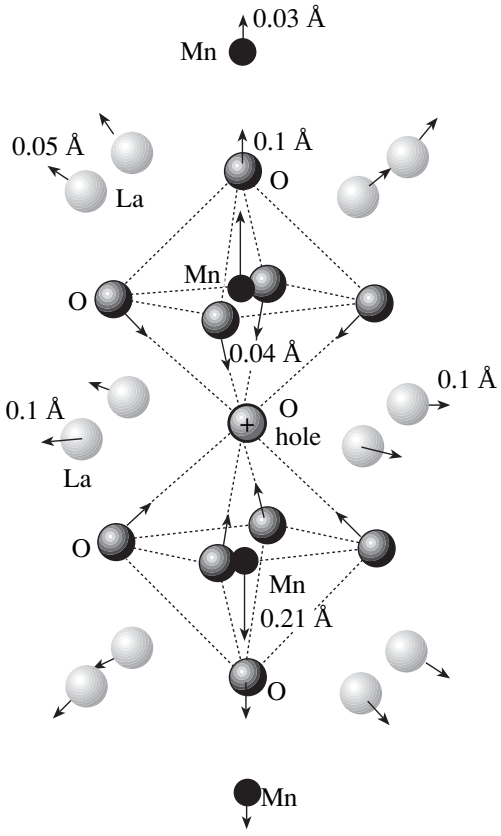

Fig. 3. The core displacements (≥0.03 Å) of the ions surrounding the O^- electronic hole defect after the complete relaxation of cores and shells in the $LaMnO_3$ lattice.

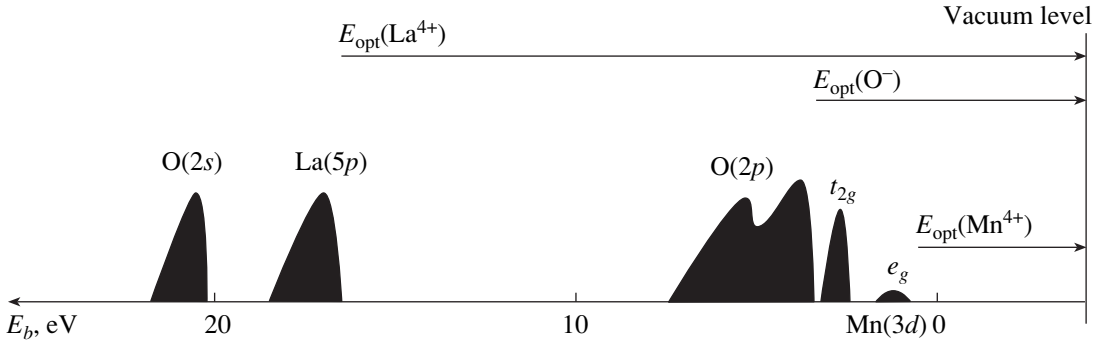

Fig. 4. A schematic representation of the valence band structure of the $LaMnO_3$ crystal, showing binding energies [22, 23] with respect to the crystal Fermi level E_F. The processes of the optical electron excitation from the Mn(3*d*) e_g, O(2*p*), and La(5*p*) valence bands to the vacuum level are shown by arrows. These optical excitation energies can be compared with experimental PES data [22, 23] and with the calculated values of optical energies E_{opt}, for the Mn^{4+}, O^{-}, and La^{4+} hole formation (Table 3).

tron band opened at E_F due to the lattice distortion (the JT effect and/or lattice mismatch effect) is shown in accordance with the PES crystal field splitting data [23]. The relevant electron excitations from the Mn(3*d*) e_g, O(2*p*), and La(5*p*) valence band levels are schematically shown by arrows. The corresponding PES energies E^{α}_{PES} are summarized in Table 3.

Having assigned the E^{α}_{PES} energies, we now proceed with the evaluation of the hole formation energies E^{α}_{h}. We first obtain the crystal Fermi energy using Eq. (5) and data for the La ion. We assume that the electronic density of the closed-shell La^{3+} ion is not significantly deformed by the crystalline field, and the in-crystal ionization energy I^{La} can therefore be plausibly estimated by the fourth standard ionization potential E_{IV} of a free La atom [24], presented in Table 3. This approximation is consistent with the full ionic charges adopted in our shell model parametrization. We note that the above approximation of a free cation is shown to be reliable only for closed-shell cations. This gives $E_F \approx 1.36$ eV for the Fermi energy of the $LaMnO_3$ crystal.

The situation is more complicated for manganese and oxygen. The Mn^{3+} ion has a nonclosed 3*d* shell with four electrons in it, and we therefore expect the in-crystal ionization energy I^{Mn} to be different from the fourth ionization potential of a free Mn atom. Because the O^{2-} ion is only stabilized by the crystalline field, it has a negative ionization potential that cannot be defined in a nonspeculative way. Using the Mn(3*d*) and O(2*p*) related maxima in the PES spectra, E^{α}_{PES}, and the obtained value $E_F \approx 1.36$ eV, we can now estimate the effective ionization energies I^{α} for manganese and oxygen in the $LaMnO_3$ crystal from Eq. (5). These values are presented in Table 3, with the free metal ionization potentials [24] given in brackets for comparison. The O^{2-} in-crystal ionization potential I^{O} (negative electron affinity of O^{-}) is then estimated to be –13.91 eV. The absolute value of this potential is within the limits of O^{-} electron affinities calculated for many oxide compounds in [25] using the embedded cluster *ab initio* method. Those calculations predicted 10.6 eV for MgO and 12.9 eV for ThO_2. Taking the semiempirical nature of our calculations into account, we find this agreement quite good.

The optical and thermal energies of the hole formation, $E^{\alpha}_{h,\,opt}$ and $E^{\alpha}_{h,\,th}$, are calculated using these effective values of the in-crystal ionization energies in accordance with Eq. (4) and presented in Table 3. Taking the crystal field splitting effect into account, we have found that the electronic hole is marginally more stable at the Mn site than at the O site in the $LaMnO_3$ lattice, but the energy difference between the thermal energies of the hole formation, $E^{\alpha}_{h,\,th}$, is too small (0.75 eV). This result rather suggests that both possibilities should be treated seriously. That is, providing the balance between the localization and relaxation energies favors the possibilities for hole self-trapping at the Mn and O sites, the electronic hole in $LaMnO_3$ is likely to be localized on the manganese, or on both the oxygen anion and the transition metal cation, rather than on the oxygen ion alone.

To assess the accuracy of the calculated energies of the hole formation and lattice relaxation, we need to discuss the following issue related to the pair potentials used in these calculations. The energies presented in Table 3a were obtained using the pair potentials listed in Table 1a. To verify the robustness of our results, we repeated the same calculations using the potentials in [20], which give close values for the dielectric constants in $LaMnO_3$ (see Table 2, part c), but were specially optimized to treat different Mn^{3+} and Mn^{4+} charge states. The calculated values of formation and polarization energies for the localized holes Mn^{4+}, O^{-},

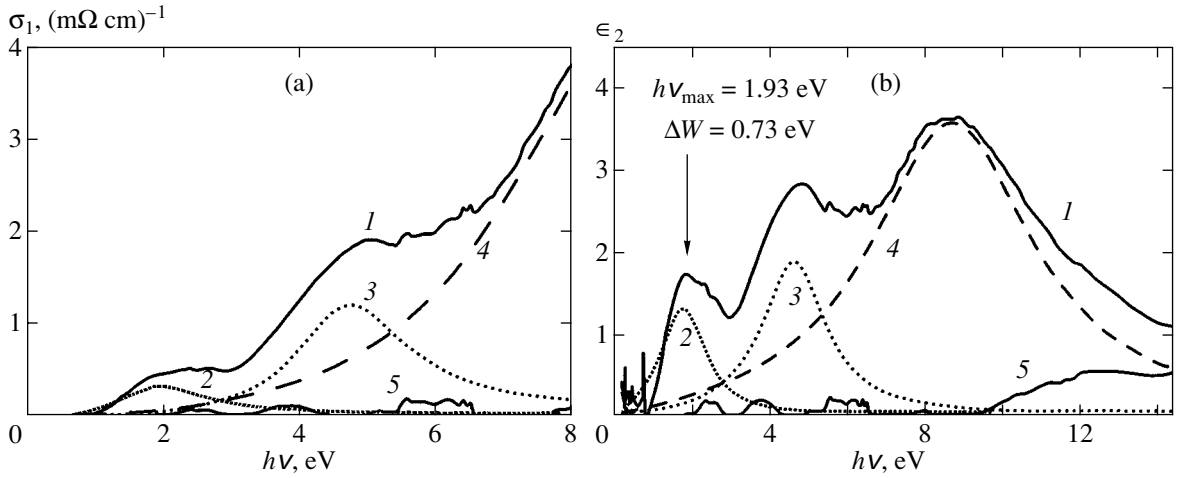

Fig. 5. (a) The experimental optical conductivity spectrum of the $LaMnO_3$ crystal [15] (curve *1*, $T = 300$ K) represented by the contributions from the three Lorentz oscillators in accordance with the dispersion analysis of the imaginary part of the dielectric function ϵ_2 shown in Fig. 5b. (b) The experimental ϵ_2 spectrum of $LaMnO_3$ (curve *1*, $T = 300$ K) represented by a sum of three main Lorentzian-shaped bands: 1.93, 4.75, and 9.07 eV (drawn by curves *2*, *3*, and *4*, respectively). The rest of the ϵ_2 spectrum after subtraction of the Lorentzian bands is shown by line *5*. The Lorentzian band parameters are given in Table 4 together with the estimated oscillator strengths f_i.

and La^{4+} and the energies deduced in Eq. (4) using these pair potentials are presented in Table 3, part c. These calculations demonstrate that the hole relaxation energy of Mn^{4+} is decreased by 0.16 eV if we account for the change in the short-range potentials caused by the change in the Mn charge state. Comparing these with our results, we can see good coincidence for the similar values and for the thermal and optical energies of hole formation.

4. OPTICAL CHARGE TRANSFER TRANSITIONS IN $LaMnO_3$

Polaronic-type electron charge carriers mostly determine specific transport properties of CMR materials in their high-temperature insulating paramagnetic phase, which are always associated with photoinduced charge transfer transitions. In hole-doped systems of perovskite manganites $R_{1-x}A_xMnO_3$, the most important charge transfer transitions associated with localized charge carriers are apparently those involving Mn^{4+} and O^- self-trapped holes. In this section, using the derived values of the in-crystal ionization energies, we calculate energies of the main charge transfer transitions, suggesting that holes could be localized at the Mn or O sites. We analyze the contribution of these charge transfer transitions to the experimental optical conductivity in nonstoichiometric or slightly hole-doped $LaMnO_3$ crystals to make the assignment of the bands in the optical conductivity spectrum more clear-cut and to verify our shell model approach. We now proceed with a brief analysis of the optical conductivity.

4.1. Analysis of the Optical Conductivity Spectra in $LaMnO_3$

The room-temperature optical conductivity spectrum of $LaMnO_3$ measured in [15] is shown by solid curve *1* in Fig. 5a in the spectral region 0 to 8 eV (reproduced from the original data with permission of Arima and Tokura [15, 16]). This spectrum is very similar to that measured by Okimoto *et al.* at $T = 9$ K [26]. It reveals the optical gap near 1.3 eV and includes several broad absorption bands with maxima near 2.3, 5, and 9 eV. The gap is assumed to be of the charge transfer type [15]. The first transition around 2.3 eV has been suggested to be of O(2*p*)–Mn(3*d*) character. The band near 5 eV is thought to be due to excitations to a higher lying Mn 3*d* e_g antiparallel spin configuration, separated by a Hund rule coupling energy. The wide band observed around 9 eV in the optical conductivity spectrum is assigned to the O(2*p*)–La(5*d*) interband optical transition [15].

The optical spectra measured in hole-doped manganese oxides show striking changes over a wide photon region (0 to 6 eV) as the temperature and doping concentration change. In the $La_{1-x}Sr_xMnO_3$ system, with increasing doping concentration ($x = 0$ to 0.3, $T = 9$ K [26]), the excitations around 2.3 and 5 eV shift appreciably to lower energies. However, the principal changes occur in the low-energy mid-infrared spectral region stemming from the filling of the gap because of the hole doping. In the insulating paramagnetic phase of hole-doped manganites, there are two features clearly observed in the experimental mid-infrared optical conductivity, around 0.6 eV [18, 26] and around 1.2–1.5 eV [27, 28]. The optical band around 0.6 eV

Table 4. Parameters of the imaginary part ϵ_2 of the dielectric function [15, 16] represented by the sum of Lorentzian shaped bands

E_i, eV	γ_i, eV	ν_{pi}^2, eV^2	f_i
1.93	1.46	1.895	0.51
4.75	2.0	4.22	0.187
9.07	5.1	12.75	0.155

seems to be associated with polaronic-type charge carriers in doped CMR manganites, and the consistent value of the activation energy of about 0.15 eV was measured for the hopping conductivity in the adiabatic temperature limit [29, 30]. The origin of these features is still a subject of many controversial discussions. It is well known that the $LaMnO_3$ crystal has a strongly distorted orthorhombic structure at low temperatures, which in many works is ascribed due to a strong electron–phonon interaction stemming from the JT effect inherent for Mn^{3+} ion in the octahedral oxygen configuration. In this case, the e_g bands split into two subbands separated by the JT energy E_{JT}. Because the on-site *d–d* transitions are dipole-forbidden, these mid-infrared peaks around 0.6 and 1.2–1.5 eV were qualitatively explained as occurring because of an electron transition from an occupied site Mn^{3+} to an unoccupied site Mn^{4+} and an adjacent occupied site Mn^{3+}, respectively [1].

In a recent theoretical study of the optical conductivity spectra of 3*d* transition metal perovskites $LaMO_3$ (M = Ti–Cu) [31] using the local spin density approximation method (LSDA + U), the authors estimated the role of lattice distortions in the band structure calculations and concluded that the JT structural distortions play a crucial role in opening the optical gap in the $LaMnO_3$ Mn(3*d*) e_g valence band. Considering the experimentally observed distorted structure of the $LaMnO_3$ crystal, the direct gap in the LSDA study has been estimated at approximately 0.7 eV, which is less than the observed optical gap (about 1.3 eV [15, 26]). There are also some discrepancies observed at higher energies between the experimental optical conductivity in 3*d* transition metal perovskites $LaMO_3$ and the calculated optical conductivity considering contributions from the interband and intraband transitions for the perfect lattice [31], which complicates the assignment of the optical bands. In addition, the contribution from the charge transfer transitions to the optical conductivity in the nonstoichiometric lattice must be taken into account to describe the optical conductivity at low energies satisfactorily and to clarify the assignment of the optical bands in the $LaMnO_3$ crystal.

To estimate the contribution of the charge transfer transitions to the experimental optical conductivity of the $LaMnO_3$ crystal, shown by curve *1* in Fig. 5a, we have analyzed the imaginary part $\epsilon_2(\nu)$ of the dielectric function [15, 16]. For this purpose, we represented the $\epsilon_2(\nu)$ spectrum, shown by curve *1* in Fig. 5b, as the sum of the first three main bands with Lorentzian line shapes,

$$\epsilon_2(\nu) = \sum_i \frac{\nu_{pi}^2 \gamma_i \nu}{(E_i^2 - \nu^2)^2 + \gamma_i^2 \nu^2}, \qquad (6)$$

where $(\nu_{pi}/E_i)^2 = f_i$ is the oscillator strength, ν_{pi} is the plasma frequency, γ_i is the bandwidth, and E_i is the resonance frequency of the *i*th oscillator. The three Lorentzian bands with the maxima E_i at 1.93, 4.75, and 9.07 eV and the respective widths γ_i of 1.46, 2.0, and 5.1 eV are represented by curves *2*, *3*, and *4* in Fig. 5b. The rest of the imaginary part of the dielectric function after subtraction of the Lorentzian bands is shown by curve *5*. The Lorentzian band parameters together with the estimated oscillator strengths are given in Table 4. These Lorentzian bands contribute to the experimental optical conductivity spectrum, as shown by the corresponding lines in Fig. 5a, with more details at low energies.

4.2. Calculation of Charge Transfer Transition Energies

Using the Born–Haber cycle and the shell model, we can consider both thermally assisted and optical charge transfer processes. This can be illustrated for a hypothetical transformation of two ions $X^{(m+1)+}$ and $Y^{(n-1)+}$ into X^{m+} and Y^{n+} with an electron transferred from Y to X (or a hole from X to Y),

$$X^{(m+1)+} + Y^{(n-1)+} \longrightarrow X^{m+} + Y^{n+}. \qquad (7)$$

There are two basic steps: (1) removing an electron from the in-crystal $Y^{(n-1)+}$ ion to infinity, outside the crystal; (2) adding an electron from infinity, outside the crystal, to the in-crystal $X^{(m+1)+}$ ion. The steps are standard within the shell model. Whether shells alone or shells and cores are relaxed depends on which transition is being calculated. In the case of a thermally assisted hopping, the shell and core positions are considered to be fully relaxed in both charge states and the transition energy is denoted by E_{th}. Comparison of the two charge states gives an additional indication which species are more stable. For optical transitions, the Franck–Condon approximation is used and the transition energies E_{opt} are calculated on the assumption that only shells can relax (corresponding to full electronic polarization), whereas the cores remain in the positions corresponding to the initial state. The major contributions into these energies come from ionization energies I_n^Y, $I_{(m+1)}^X$; the Madelung and polarization terms, whose cumulative energies for the defect configuration corresponding to the charge transfer transition considered, $S[X^{m+}, Y^{n+}]_{opt, th}$, result from the Mott–Littleton

Table 5. Calculated optical (E_{opt}) and thermal (E_{th}) energies for the main charge transfer transitions in $LaMnO_3$; S_{opt} and S_{th} are resultant calculated values of the sum of defect energies for the corresponding charge transfer process

No.	Charge transfer transition	E_{opt}, eV	Exp., eV	E_{th}, eV	S_{opt}, eV	S_{th}, eV
1	$Mn^{4+} + Mn^{3+} \longrightarrow Mn^{3+} + Mn^{4+}$	1.33	–	0.00	–44.35	–45.68
2	$O^- + Mn^{3+} \longrightarrow O^{2-} + Mn^{4+}$	1.43 (2.29)	1.93	–0.75 (0.12)	–43.50	–45.66
3	$Mn^{4+} + O^{2-} \longrightarrow Mn^{3+} + O^-$	2.98 (2.12)	1.93	0.75 (–0.12)	18.62	16.39
4	$2Mn^{3+} \longrightarrow Mn^{4+} + Mn^{2+}$	3.72	3.5 [27], 3.2 [32]	2.68	–13.06	–14.10
5	$Mn^{3+} + O^{2-} \longrightarrow Mn^{2+} + O^-$	5.61 (4.75)	4.75	3.50	50.15	48.04
6	$La^{3+} + O^{2-} \longrightarrow La^{2+} + O^-$	8.93	9.07	6.47	42.02	39.56

Note: Transitions nos. 4, 5, and 6 are associated with the Mn(3*d*) gap, O(2*p*)–Mn(3*d*), and O(2*p*)–La(5*d*) transitions, respectively.

calculations (as in Eq. (4)). If the charge transfer includes a localized hole in thermal equilibrium in the initial state (the related values in the $LaMnO_3$ lattice are presented as S_{th}^{α} in Table 3), the corresponding thermal energy $S[X^{(m+1)+}, Y^{(n-1)+}]_{th}$ of the initial defect configuration must be subtracted. Thus, the thermal and optical energies of the charge transfer transitions can be calculated using the formulas

$$E_{opt} = I_n^Y - I_{m+1}^X + S[X^{m+}, Y^{n+}]_{opt} - S[X^{(m+1)+}, Y^{(n-1)+}]_{th}, \quad (8)$$

$$E_{th} = I_n^Y - I_{m+1}^X + S[X^{m+}, Y^{n+}]_{th} - S[X^{(m+1)+}, Y^{(n-1)+}]_{th}. \quad (9)$$

Evidently, there is some dependence on the separation of X and Y. The charge transfer optical transitions for nearest neighbors are likely to dominate, and the relevant key cases have been calculated. If X and Y are the same (symmetric), the ionization terms cancel each other, as for the intervalence charge transfer transition

$$Mn^{4+} + Mn^{3+} \longrightarrow Mn^{3+} + Mn^{4+}.$$

Here, we emphasize that the calculations of charge transfer transitions between the metal Mn sublattice ions are more reliable because they do not depend on the difference between the Madelung potentials of the two sublattices nor on the phenomenologically deduced parameter of the O^{2-} in-crystal ionization potential.

The cumulative thermal S_{th} and optical S_{opt} energies following from the Mott–Littleton calculations for the charge transfer transitions involving Mn^{4+} and O^- species and those characterizing fundamental electronic transitions in the $LaMnO_3$ lattice (e.g., the Mn(3*d*) gap transition O(2*p*)–Mn(3*d*) and O(2*p*)–La(5*d*)) are presented in Table 5 by transitions 1–3 and 4–6, respectively. To calculate the optical and thermal energies of the charge transfer transitions, we used a self-consistent set of the ionization potentials (see Table 3, part a) derived by matching the calculated optical energies of the hole formation with the photoemission experimental energies and the standard ionization potentials for a free La atom. We must also estimate the third in-crystal ionization potential of Mn, I_{III}^{Mn}. We suggest that it should be shifted in-crystal from the standard value for a free Mn atom (33.67 eV [24]) by the same value as the fourth potential of Mn (from the standard value 51.2 eV), by subtracting the crystal field splitting effect ($\Delta_{CF} \approx 1.5$ eV); we thus calculate in-crystal

$$I_{III}^{Mn} = 33.67 - (51.2 - (47.41 + \Delta_{CF}/2)) = 30.63 \text{ eV}.$$

Taking the standard value $I_{III}^{La} = 19.18$ eV, the calculated optical energy of the fundamental transition of the charge transfer character O(2*p*)–La(5*d*),

$$E_{opt} = I^O - I_{III}^{La} + S[La^{3+}, O^{2-}]_{opt} = 8.93 \text{ eV}$$

(see Table 5, transition 6), correlates well with the maximum of the broad band in the ϵ_2 function near 9.07 eV (curve *4* in Fig. 5b). This encouraging consistency between the experimental and calculated energies allows us to suggest that the earlier estimated in-crystal value $I^O = -13.91$ eV provides a reasonable value in this shell model calculation. We also calculated the optical energy of the fundamental transition of the charge transfer character O(2*p*)–Mn(3*d*),

$$E_{opt} = I^O - I_{III}^{Mn} + S[Mn^{3+}, O^{2-}]_{opt} = 5.61 \text{ eV}$$

(see Table 5, transition 5). We suggest that the relevant transition should correlate with the broad optical band observed in the ϵ_2 function near 4.75 eV (curve *3* in Fig. 5b). Our calculations therefore predict transitions which appear to correlate with the maxima of the major broadband features in the optical conductivity spectrum. The calculated optical energy for the transition between the Mn(3*d*) valence band and the upper Hubbard Mn(3*d*) band is estimated to be

$$E_{opt} = I_{IV}^{Mn} - I_{III}^{Mn} + S[Mn^{3+}, Mn^{3+}]_{opt} = 3.72 \text{ eV}$$

(see Table 5, transition 4), predicting a band gap of the Mott–Hubbard type in the $LaMnO_3$ crystal. This value agrees well with the assigned transition experimentally observed near 3.5 eV in $Nd_{0.7}Sr_{0.3}MnO_3$ [27] and near 3.2 eV in $La_{0.825}Sr_{0.175}MnO_3$ [32]. A small contribution

to the experimental optical conductivity can be observed around 3.7 eV in the $LaMnO_3$ crystal, as shown by curve *5* in Fig. 5b, resulting from our dispersion analysis.

Having assigned the fundamental electronic transitions in the $LaMnO_3$ crystal in accordance with the results of our calculations, which are also consistent with the consideration in [27], we note that the assignment of the optical conductivity band around 2.3 eV still remains controversial. In the earlier study [15], this band was associated with the fundamental charge transfer transition of the O(2*p*)–Mn(3*d*) e_g character, whereas the band at about 5 eV was associated by the authors with the excitations to a higher lying Mn 3*d* e_g antiparallel spin configuration, separated by the Hund rule coupling energy. However, our results allow us to argue that an alternative interpretation of this transition obtained in this work can be correct. We suggest that the band at about 2.3 eV is rather associated with the presence of Mn^{4+} and/or O^- localized holes in the $LaMnO_3$ crystal, which is known to exhibit a strongly nonstoichiometric behavior with respect to the oxygen content, up to 0.1 in as-grown crystal.

Indeed, if an optical band is associated with a charge transfer transition in a crystal lattice, its maximum position $h\nu_{max}$ and the half-width ΔW are known to be related by a simple formula in the high-temperature limit [33],

$$h\nu_{max} = \frac{\Delta W^2}{16kT\ln 2}. \quad (10)$$

We can invoke this expression to verify the charge transfer transition character of the bands associated with the photoinduced hopping conductivity of the localized charge carriers. Using this expression, the estimates for $T = 300$ K show a very encouraging consistency between the half-width and the maximum energy of the first Lorentzian band (curve *2* in Fig. 5b, with the parameters given in Table 4): from $\Delta W \approx 0.73$ eV, we obtain $h\nu_{max} \approx 1.92$ eV, which matches well the maximum position estimated to be near 1.93 eV from the dispersion analysis of the ϵ_2 function. This is consistent with the view that this transitions could be of the charge transfer type, associated with the presence of localized electronic charge carriers in the $LaMnO_3$ crystal lattice.

The main contributions to the optical conductivity are then expected from the following charge transfer transitions:

(1) the intervalence Mn^{3+}/Mn^{4+} charge transfer transition,

$$Mn^{4+} + Mn^{3+} \longrightarrow Mn^{3+} + Mn^{4+},$$

$$E_{opt} = S[Mn^{3+}, Mn^{4+}]_{opt} - S_{th}^{Mn} = 1.33 \text{ eV};$$

(2) the transition of the O^- self-trapped hole to a neighboring manganese ion,

$$O^- + Mn^{3+} \longrightarrow O^{2-} + Mn^{4+},$$

$$E_{opt} = I_{IV}^{Mn} - I^O + S[O^-, Mn^{3+}]_{opt} - S_{th}^O = 1.43 \text{ eV};$$

(3) the transition of the Mn^{4+} self-trapped hole to a neighboring oxygen ion,

$$Mn^{4+} + O^{2-} \longrightarrow Mn^{3+} + O^-,$$

$$E_{opt} = I^O - I_{IV}^{Mn} + S[O^{2-}, Mn^{4+}]_{opt} + S_{th}^{Mn} = 2.98 \text{ eV}$$

(see transitions nos. 1–3, respectively, in Table 5).

Analyzing all calculated and experimental optical energies given in Table 5, we can conclude that the agreement is much better for the calculations not involving the in-crystal ionization potentials of manganese, I_{III}^{Mn} and I_{IV}^{Mn}, or in the case where their difference enters and the inaccuracy due to these terms cancels out. Relying on the correlation between the calculated and experimental optical energies, we can try to refine the values of I_{III}^{Mn} and I_{IV}^{Mn}, whose in-crystal determination presents difficulties due to a nonclosed 3*d* shell of the Mn^{3+} ion. Indeed, expecting the calculated optical energy of the fundamental transition of the charge transfer character O(2*p*)–Mn(3*d*),

$$E_{opt} = I^O - I_{III}^{Mn} + S[Mn^{3+}, O^{2-}]_{opt}$$
$$= -13.91 - 30.63 + 50.15 = 5.61 \text{ eV}$$

(see Table 5, transition no. 5) to be correlated with the broad optical band observed in the ϵ_2 function near 4.75 eV (curve *3* in Fig. 5b), we can refine the third in-crystal ionization potential of manganese as $(I_{III}^{Mn})^* = 31.49$ eV and, correspondingly, $(I_{IV}^{Mn})^* = 48.27$ eV. Using these corrected values, we recalculated the energies of transitions nos. 2 and 3 in Table 5 associated with the charge transfer transitions of O^- and Mn^{4+} self-trapped holes and obtained close values of optical energies, $E_{opt} = 2.29$ eV and $E_{opt} = 2.12$ eV, respectively. These corrected values for the optical charge transfer transition energies are presented in brackets in Table 5 for transitions nos. 2 and 3. We suggest that these transitions, $Mn^{4+} + O^{2-} \longrightarrow Mn^{3+} + O^-$ and $O^- + Mn^{3+} \longrightarrow O^{2-} + Mn^{4+}$, associated with the hole transfer along the chain Mn^{4+}–O^{2-}–Mn^{3+}, could be responsible for the band around 2.3 eV in the optical conductivity spectrum (the related band in the ϵ_2 spectrum has the maximum energy 1.93 eV) of the as-grown nonstoichiometric $LaMnO_3$ crystal. If the band is thus assigned, the net oscillator strength of this band, $f_i = 0.51$ (see Table 4), must depend on the concentration of the localized holes as $f_i = f_{CT}/x$, thereby providing an estimate of the oscillator strength for the charge transfer transition, f_{CT}. The typical value $x \approx 0.1$ for an as-grown $LaMnO_3$ crystal

gives an estimate for the oscillator strength consistent with the transition of the charge transfer type.

The negative value of the thermal energy, E_{th} = –0.75 eV, for transition no. 2 in Table 5 indicates a more thermally stable state of the Mn^{4+} hole compared to the O^- hole state, in accordance with our results for the thermal energies E_{th}^{α} of the formation of holes (Table 3a) based on preliminary estimates for the fourth in-crystal ionization potential of the manganese ion. Using the refined value I_{IV}^{Mn} = 48.27 eV deduced from the comparison between the calculated and experimental optical energies, we now derive the respective thermal energies 0.12 and –0.12 eV for transitions nos. 2 and 3. This result reinforces our arguments made above that the electronic hole can be thermally stable on both the transition metal cation and the oxygen anion in the $LaMnO_3$ crystal.

In accordance with our shell model calculations, the intervalence charge transfer transition $Mn^{4+} + Mn^{3+} \longrightarrow Mn^{3+} + Mn^{4+}$ is predicted to have the optical energy E_{opt} = 1.33 eV (Table 5, transition no. 1); compared with the energy of the optical gap in $LaMnO_3$, it is not observable in an as-grown pure crystal.

Because of the doping effect, the optical spectra in CMR manganese oxides show striking changes over a wide photon region (0 to 6 eV). In the $La_{1-x}Sr_xMnO_3$ system, with increasing the doping concentration from x = 0 to 0.3 at T = 9 K [26], the optical conductivity bands around 2.3 and 5 eV shift to lower energies by more than 0.5 eV. We have analyzed the low-energy ϵ_2 function in a slightly doped $La_{7/8}Sr_{1/8}MnO_3$ compound [28] and found it to be well described by the Lorentzian curve with the maximum at 1.32 eV and the half-width of 0.61 eV, as presented in Fig. 6. We emphasize that the maximum position of this band and its half-width are also in a good correlation with the formula describing a transition of the charge transfer character (see Eq. (10)): from $\Delta W \approx 0.61$ eV, we obtain $h\nu_{max} \approx 1.34$ eV, which matches well the maximum position observed experimentally. It is reasonable to suggest that this band is of the same origin as the band at ϵ_2 = 1.93 eV in the pure $LaMnO_3$ compound, assigned to transitions nos. 2 and 3 in Table 5 and shifted by about 0.5 eV to lower energies because of the hole interaction effect in CMR systems. Using this line of reasoning, we can also suggest that the 0.6-eV band [18, 26] in the optical conductivity of CMR compounds is due to the intervalence charge transfer transition $Mn^{4+} + Mn^{3+} \longrightarrow Mn^{3+} + Mn^{4+}$ and is associated with the photoinduced hopping conductivity of Mn^{4+} localized holes, with the consistent value of hopping conductivity activation energy of approximately 0.15 eV measured in the adiabatic temperature limit [29, 30].

The results given are based on the shell model parameters (Table 1, part a), which were fitted to give good values for both the dielectric constants and the TO modes. When we use the second set of the shell model parameters, determined primarily using the oxide structures MnO, $LaMnO_3$, and Ca_2MnO_4 [20] (Table 1, part c), the resulting energies are very similar for the low-energy optical charge transfer transition band near 2.3 eV, but the predicted energies are about 1.5 eV higher for the 5-eV optical band.

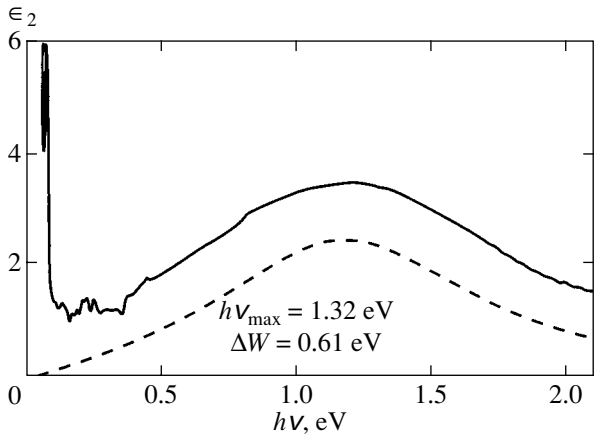

Fig. 6. The experimental ϵ_2 spectrum (solid line) of $La_{7/8}Sr_{1/8}MnO_3$ [28] (T = 300 K) approximated by the Lorentzian-shaped band (dashed line).

5. CONCLUSIONS

In this paper, we explore the role of electronic and ionic polarization energies in the physics of CMR materials. In particular, we examine energies associated with the localized Mn^{4+} and O^- holes in the lattice of the "parent" $LaMnO_3$ compound. Our calculations are done for the idealized cubic perovskite $LaMnO_3$ structure, which is relevant to the nonmagnetic quasi-cubic perovskite structure experimentally observed at high temperatures $T \geq 400$ K > $T_N \approx 140$ K. To estimate the polarization energy terms, we use a fully ionic shell model. The shell model parameters that we derive satisfy the equilibrium conditions for the quasi-cubic perovskite structure $LaMnO_3$ and agree well with experimental values of the static and high-frequency dielectric constants as well as the TO phonons.

As a result of our shell model calculations, we find that, on one hand, there is a huge difference between the hole relaxation energies on the oxygen and manganese sites, which indicates a strong electron–phonon interaction in the case of a hole localized at the O site. On the other hand, the difference that we find between the thermal energies of the Mn^{4+} and O^- holes is too small. This means that we must seriously consider the possibility that the electronic hole in $LaMnO_3$ is localized on the manganese, or on both the oxygen anion and the transition metal cation, rather than on the oxygen ion alone.

If so, this system would be similar to many other transition metal oxides.

Assuming that holes in the $LaMnO_3$ crystal can localize in either or in both of the Mn and O sublattices, we estimate the main associated optical charge transfer transition energies, which we relate to the experimentally observed optical conductivity spectra. Applying the Mott–Littleton approach, we estimate the charge transfer transition energies within the Born–Haber cycle using the in-crystal ionization potentials for ions in the $LaMnO_3$ crystal obtained in our study of the experimental photoemission spectra.

Our analysis allows us to suggest a new interpretation of the main bands in the optical conductivity spectrum near 2.3 and 5 eV. We suggest that the band around 5 eV is associated with the fundamental O(2p)–Mn(3*d*) transition of the charge transfer character, whereas the band near 2.3 eV is rather associated with the presence of Mn^{4+} and/or O^- self-trapped holes in the nonstoichiometric $LaMnO_3$ compound.

To summarize, we believe that the results of this work demonstrate the applicability and usefulness of the shell model approach to preliminary modeling of polaron-related features in complex oxides such as CMR materials, and we hope that they will stimulate further theoretical and experimental studies of the character and properties of hole states in these materials.

ACKNOWLEDGMENTS

The authors thank J. Gale for making available the General Utility Lattice Program (GULP) used in the present calculations. We greatly appreciate Y. Tokura and T. Arima for providing us with the original reflectivity spectra in $LaMnO_3$. We thank F. Mayr and coauthors for the permission to reproduce their experimental data. We would also like to thank W.C. Mackrodt and A. Ionov for useful information. We are grateful to R.W. Grimes and D.J. Bradfield for fruitful discussions and for making available to us one set of interatomic potentials. We are also grateful for the Royal Society/NATO support of the visit to the University College London of one of us (N. N. K.).

REFERENCES

1. A. J. Millis, R. Mueller, and B. I. Shraiman, Phys. Rev. B **54**, 5405 (1996).
2. H. L. Ju, H. C. Sohn, and Kannan M. Krishnan, Phys. Rev. Lett. **79**, 3230 (1997).
3. G. D. Watkins, Inst. Phys. Conf. Ser. **31**, 95 (1977); K. M. Lee, Le Si Dang, and G. D. Watkins, Solid State Commun. **35**, 527 (1980); D. Jeon, H. P. Gislason, and G. D. Watkins, Mater. Sci. Forum **10–12**, 851 (1986).
4. J. H. Harding and A. M. Stoneham, J. Phys. C **15**, 4649 (1982).
5. B. G. Dick and A. W. Overhauser, Phys. Rev. **112**, 90 (1958).
6. W. Cochran, CRC Crit. Rev. Solid State Sci. **2**, 1 (1971).
7. A. M. Stoneham, M. J. L. Sangster, and P. W. Tasker, Philos. Mag. B **44**, 603 (1981).
8. D. G. Muxworthy and C. R. A. Catlow, Philos. Mag. B **37**, 63 (1978).
9. R. Englman, *The Jahn–Teller Effect in Molecules and Crystals* (Wiley-Interscience, London, 1972).
10. A. L. Shluger and A. M. Stoneham, J. Phys.: Condens. Matter **5**, 3049 (1993).
11. N. F. Mott and M. J. Littleton, Trans. Faraday Soc. **34**, 485 (1938); C. R. A. Catlow and W. C. Mackrodt, *Computer Simulations of Solids* (Springer-Verlag, Berlin, 1982); C. R. A. Catlow and A. M. Stoneham, J. Chem. Soc., Faraday Trans. 2, 85 (1989).
12. J. D. Gale, Philos. Mag. B **73**, 3 (1996); J. Chem. Soc., Faraday Trans. **93**, 629 (1997).
13. C. R. A. Catlow and A. M. Stoneham, J. Phys. C **16**, 4321 (1983).
14. C. R. A. Catlow, W. C. Mackrodt, M. J. Norgett, and A. M. Stoneham, Philos. Mag. **35**, 177 (1977).
15. T. Arima and Y. Tokura, J. Phys. Soc. Jpn. **64**, 2488 (1995).
16. T. Arima and Y. Tokura, private communication.
17. M. S. Islam, M. Cherry, and C. R. A. Catlow, J. Solid State Chem. **124**, 230 (1996).
18. A. V. Boris, N. N. Kovaleva, A. V. Bazhenov, *et al.*, Phys. Rev. B **59**, R697 (1999).
19. A. V. Boris, N. N. Kovaleva, A. V. Bazhenov, *et al.*, J. Appl. Phys. **81**, 5756 (1997).
20. R. Grimes and D. Bradfield, private communication.
21. W. E. Pickett and D. J. Singh, Phys. Rev. B **53**, 1146 (1996).
22. T. Saitoh, Phys. Rev. B **56**, 8836 (1997).
23. J. H. Park, C. T. Chen, S.-W. Cheong, *et al.*, Phys. Rev. Lett. **76**, 4215 (1996).
24. D. R. Lide, in: *Handbook of Chemistry and Physics* (CRC Press, Boca Raton, 1993).
25. J. H. Harding and N. C. Pyper, Philos. Mag. Lett. **71**, 113 (1995).
26. Y. Okimoto, T. Katsufuji, T. Ishikawa, *et al.*, Phys. Rev. B **55**, 4206 (1997).
27. H. J. Lee, J. H. Jung, Y. S. Lee, *et al.*, Phys. Rev. B **60**, 5251 (1999).
28. F. Mayr, C. Hartinger, M. Paraskevopoulos, *et al.*, Phys. Rev. B **62**, 15673 (2000).
29. M. Jaime, M. B. Salamon, M. Rubinstein, *et al.*, Phys. Rev. B **54**, 11914 (1996).
30. A. Machida, Y. Morimoto, and A. Nakamura, Phys. Rev. B **58**, 12540, R4281 (1998).
31. I. Solovyev, N. Hamada, and K. Terakura, Phys. Rev. B **53**, 7158 (1996).
32. K. Takenaka, Y. Sawaki, R. Shiozaki, and S. Sugai, Phys. Rev. B **62**, 13864 (2000).
33. N. S. Hush, Prog. Inorg. Chem. **8**, 391 (1967).

Journal of Experimental and Theoretical Physics, Vol. 94, No. 1, 2002, pp. 191–199.
From Zhurnal Éksperimental'noĭ i Teoreticheskoĭ Fiziki, Vol. 121, No. 1, 2002, pp. 225–234.

SOLIDS
Electronic Properties

Nonequilibrium Tunneling Effects of Interacting Hubbard–Anderson Impurities¶

P. I. Arseev[a], N. S. Maslova[b], V. I. Panov[b], and S. V. Savinov[b]
[a]*Lebedev Institute of Physics, Russian Academy of Sciences, Moscow, 119991 Russia*
e-mail: ars.@pli.ac.ru
[b]*Moscow State University, Moscow, 119899 Russia*
Received April 20, 2001

Nonequilibrium interaction effects of two Hubbard–Anderson impurities have been experimentally studied by means of STM/STS methods and theoretically analyzed using a self-consistent approach based on the Keldysh formalism. *© 2002 MAIK "Nauka/Interperiodica".*

Impurity states at surfaces and interfaces of semiconductors can strongly modify the local electronic structure. As the system size decreases, the correct understanding of localized state properties becomes more and more important. The interaction between impurities must also be taken into account as the impurity concentration increases. If the distance between impurities is of the order of the localization radius, sufficiently strong correlation effects arise that modify the tunneling conductivity. The electronic structure of such complexes can be tuned by an external electric field. These effects are believed to determine electronic properties of semiconductor nanostructures in the future. However, local effects caused by the interaction of two impurity states near the surface are not well examined at present. A powerful tool for studying the local electronic structure is scanning tunneling spectroscopy (STS) combined with scanning tunneling microscopy (STM) imaging. In the present work, the electronic structure of localized impurity states formed by a pair of impurity Si atoms separated by 3 nm at the (110) GaAs surface is studied by STM/STS methods.

The samples under investigation are GaAs single crystals doped with compensating impurities Si and Zn with the respective concentrations of 5×10^{18} cm^{-3} and 2×10^{19} cm^{-3}. All measurements were carried out at 4.2 K with a home-built low-temperature STM equipped with an *in situ* cleavage mechanism [1]. After the crystal was cleaved along the (110) plane, two Si atoms with a spatial separation of about 3 nm were chosen as the object of investigation. The separation distance is comparable to the visible localization radius of the Si impurity states, which is about 1–1.5 nm (Fig. 1a). A high doping level accounts for a nonuniform Coulomb potential in the sample. This is one of the reasons why the initial electronic states of the observed atoms are not equivalent. The scanned area was 10 nm × 10 nm, and within this area, the tunneling conductivity $(dI/dV)/(I/V)$ was measured with a spatial step of 0.25 nm.

In the experimentally observed spatial distribution of the local tunneling conductivity, one can distinguish a twofold switching on and off for each of the atomic *a* and *b* states upon changing the tunneling bias within the semiconductor band gap (visible as the dark stripe in Fig. 1). After switching on, the excess tunneling conductivity occurs in the vicinity of each of these atoms in a bias range of about 0.65 eV, which is much greater than the level width of the localized state. At the same time, the transition from the dark state to the light one occurs within the bias change range of ≈0.15 eV, which is comparable to the energy level width of the localized state.

The map view of the tunneling conductivity allows the evolution of the local density of states (LDOS) near each impurity atom to be analyzed. At zero applied bias, atom *a* forms a bright area of the enhanced tunneling conductivity and remains switched on in a bias range from –0.2 to +0.4 V. Atom *b* is invisible at $V \approx 0$. In the bias range from +0.4 to +0.7 V, the tunneling conductivity decreases in the vicinity of atom *a* (dark area). The next switching on of this atom occurs at +0.7 V, and a bright spot of the enhanced tunneling conductivity is observed up to +1.3 V.

The enhanced tunneling conductivity near atom *b* is also observed in two separated bias ranges: from +0.1 to +0.5 V and at the same polarity from +0.6 to +1.2 V. In Fig. 2, two experimentally obtained $(dI/dV)/(I/V)$ curves are shown for two different positions of the STM tip: above atom *a* and above atom *b*.

Because such effects have not been observed for an isolated impurity, a natural question is to what extent the interaction between the two impurities modifies the kinetic processes. To answer this question, we suggest a self-consistent theoretical analysis of the local tunneling conductivity behavior in the vicinity of two inter-

¶This article was submitted by the authors in English.

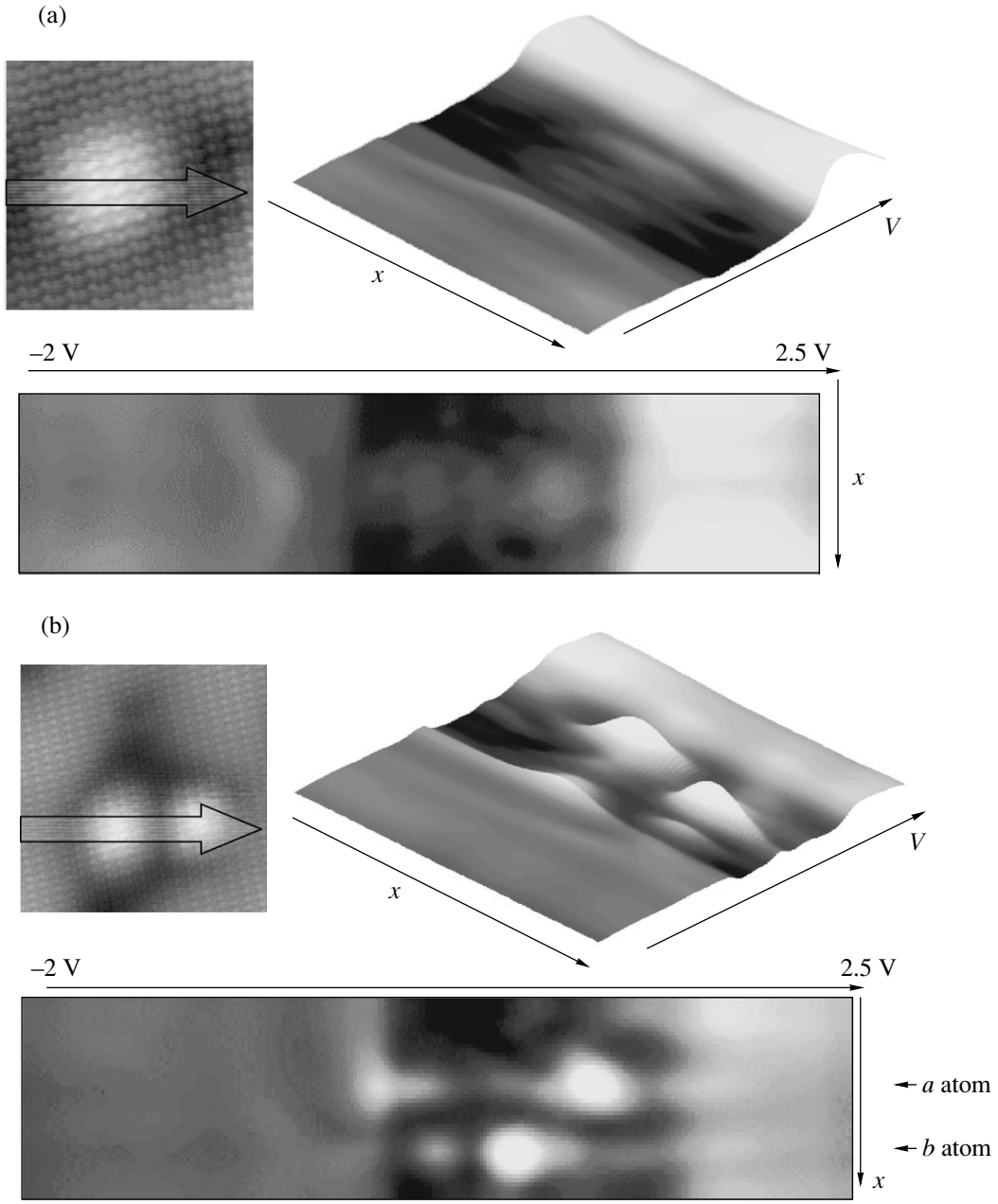

Fig. 1. STM images (right panel) and the map view of the normalized tunneling conductivity measured along the direction *x* depicted on the STM topography images (left panel). (a) An isolated Si impurity, scan area 5.8 nm, bias range from +2.5 to –2 V; (b) two interacting Si impurities, scan area 10 nm, bias range from +2.5 to –2 V.

acting Anderson impurities on a semiconductor surface [2]. In the Anderson model [3], an individual impurity state is characterized by the following parameters: the bare impurity electron level ε_0, the on-site Coulomb repulsion of localized electrons U, and the level broadening Γ caused by the hybridization with continuum states. It is known that nontrivial effects occur in the Anderson model if the on-site Coulomb repulsion is sufficiently strong. Because the experimentally observed localization radius of Si impurity states at the GaAs surface is on the order of 1 nm, the estimated value of the Hubbard energy is about 0.5–1 eV. It must be mentioned that, although the Si atoms in the bulk GaAs are known to form a shallow impurity state with binding energies of about 6 meV at low doping levels, the situation is different near the surface in the presence of the STM tip. It was experimentally observed by many authors (see, e.g., [4–6]) that the band bending induced by the surface and by the STM tip can considerably change the position of the Si impurity level rela-

tive to the conduction band edge. Numerous STM images (see references above) show that the localization radius of the Si atom state is about 1–1.5 nm. In addition, in highly doped crystals, the electronic state of any particular atom can be strongly modified by the presence of neighboring dopant atoms.

The electron transport through a single Anderson impurity in the Coulomb blockade and the Kondo regime has been studied experimentally and is still under theoretical investigation [7–13]. However, most of the authors concentrated on the weak tunneling coupling, when the tunnel junction is used only as a probe without affecting the impurity states [9]. Therefore, the tunneling conductivity through the Anderson impurity is usually supposed to be determined by the equilibrium impurity density of states. In the Coulomb blockade regime of tunneling through an impurity or a quantum dot, the influence of the tunneling current on the impurity (dot) spectrum is neglected [11]. The impurity charge therefore takes discrete values; n_σ and $n_{-\sigma}$ can be equal only to 0 or 1. The width of the tunneling conductivity peak in the Coulomb blockade regime is determined by the sum of relaxation rates and cannot achieve (without destroying this regime) the experimentally observed anomalously large values ≈0.65 eV even at room temperatures. As the tunneling coupling increases, the impurity charge is no longer a discrete value and one must consider impurity electron filling numbers (which now become continuous variables) determined from the kinetic equations.

We note that the coupling to the leads in the Kondo regime modifies the impurity spectrum, but charge fluctuations are suppressed because the initial impurity level lies deep below the Fermi level [14]. In the equilibrium case, the electron filling numbers n_σ and $n_{-\sigma}$ satisfy the relation

$$n_\sigma + n_{-\sigma} = 1.$$

Spin fluctuations dominate in this case because the impurity state is always single occupied. This requires the following relations between the parameters of the Anderson model: $-\varepsilon_0 \gg \Gamma$ and $\varepsilon_0 + U \gg \Gamma$. The Kondo resonance then contributes to the zero-bias anomaly of the tunneling conductivity. But the contribution of the Kondo effect to the tunneling conductivity dependence on the applied voltage becomes almost negligible when the applied bias exceeds a typical energy value determined by the Kondo temperature (small compared to ε_0 and Γ) (see [15, 16]). When the applied bias increases (decreases) to the impurity energy level, the Kondo resonance is destroyed.

In the present work, we are interested in the tunneling conductivity behavior in a wide bias range from +2.5 to –2 V (while the typical value of the Kondo temperature is less than 1 meV). The adopted parameters of the model correspond to the mixed-valence regime, $\varepsilon \approx \Gamma$ or $\varepsilon + U \approx \Gamma$ (although $U \gg \Gamma$). This choice of the set of parameters is more adequate for our analysis of the anomalies in the tunneling conductivity behavior observed experimentally in a wide bias range V comparable to U and $V \geq \varepsilon_0$. Under all these conditions, the Kondo effect does not reveal itself in the tunneling characteristics, although spin asymmetry of the electron filling numbers occurs in particular bias ranges.

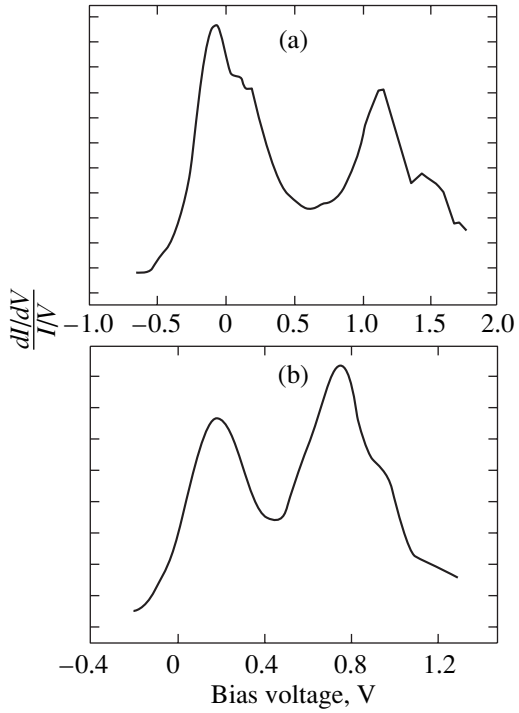

Fig. 2. The normalized conductance $(dI/dV)/(I/V)$ measured within the semiconductor band gap in the vicinity of impurity atoms: (a) the STM tip is placed over the *a* atom in Fig. 1b; (b) the STM tip is placed over the *b* atom in Fig. 1b.

As the applied bias is increased, nonequilibrium processes start playing a significant role, especially at low temperatures. Nonequilibrium effects in the tunneling conductivity spectra of metallic nanoparticles have been considered by Agam and coauthors [17]. In this work, changes in the energy of an excited single electron state are caused at large applied bias by different nonequilibrium occupancy configurations of other single electron states. It was assumed that the electron spectrum of a nanoparticle consists of many levels and the level spacing is smaller than the applied bias. But the filling numbers of each level are equal to either 0 or 1. Different random configurations of the electron occupation result in fluctuations of the Coulomb interaction energy. However, continuous changes in nonequilibrium electron filling numbers caused by kinetic processes were not taken into account.

In the present work, the nonequilibrium charge distribution due to tunneling processes and the effect of the tunneling bias voltage on the impurity state energy values are taken into account. Nonequilibrium electron filling numbers on the Hubbard–Anderson impurities

are calculated from a self-consistent system of kinetic equations based on the Keldysh diagram technique [18]. At the final stage of calculations, the Coulomb interaction of localized electrons is treated self-consistently in the mean-field approximation. It is shown that, with an increase in the tunneling bias, two states with different energies for opposite-spin electrons can appear at each impurity: the transition from the paramagnetic regime to the magnetic one can occur. The inverse transition from the magnetic to the paramagnetic state can also occur with a further increase in the tunneling bias. We have also determined the conditions under which the transition to the magnetic state is enhanced by the interaction between two Anderson impurities. We found that the impurity interaction results in a redistribution of localized nonequilibrium charges and can lead to pinning of the impurity levels near the Fermi level of each electrode and to the mutual attraction of the energy levels of different impurities in particular ranges of the applied bias.

We consider a theoretical model with two interacting Anderson impurities. The STM tip is assumed to be positioned above one of the impurity atoms (atom a). The Hamiltonian of the model is given by

$$\hat{H} = \hat{H}_0 + \hat{H}_{\text{tun}} + \hat{H}_{\text{int}} + \hat{H}_{\text{imp}}, \tag{1}$$

where

$$\hat{H}_0 = \sum_{\mathbf{k},\sigma}(\varepsilon_{\mathbf{k}} - \mu)c^+_{\mathbf{k},\sigma}c_{\mathbf{k},\sigma} + \sum_{\mathbf{p},\sigma}(\varepsilon_{\mathbf{p}} - \mu - eV)c^+_{\mathbf{p},\sigma}c_{\mathbf{p},\sigma} \tag{2}$$

describes noninteracting electrons in the two electrodes, ($\mathbf{k}$, σ) for the tip and ($\mathbf{p}$, σ) for the example.

The part $\hat{H}_{\text{imp}}$ corresponds to the impurity states and takes the Hubbard repulsion into account,

$$\hat{H}_{\text{imp}} = \varepsilon_a\sum_\sigma a^+_\sigma a_\sigma + \frac{U_a}{2}\sum_\sigma n^a_\sigma n^a_{-\sigma} + \varepsilon_b\sum_\sigma b^+_\sigma b_\sigma + \frac{U_b}{2}\sum_\sigma n^b_\sigma n^b_{-\sigma}. \tag{3}$$

Here, $n^a_\sigma = a^+_\sigma a_\sigma$, a_σ destroys an impurity a electron with the spin σ, $n^b_\sigma = b^+_\sigma b_\sigma$, b_σ destroys an impurity b electron with the spin σ; and ε_a and ε_b are the energy levels of impurities a and b (they depend on the bias V in general).

The part $\hat{H}_{\text{int}}$ describes the interaction between the impurity states,

$$\hat{H}_{\text{int}} = T\sum_\sigma (a^+_\sigma b_\sigma + \text{h.c.}), \tag{4}$$

and $\hat{H}_{\text{tun}}$ is responsible for tunneling transitions from the impurity states to each electrode (tip or substrate),

$$\hat{H}_{\text{tun}} = T_{\mathbf{p},a}\sum_{\mathbf{p},\sigma}(c^+_{\mathbf{p},\sigma}a_\sigma + \text{h.c.}) + T_{\mathbf{p},b}\sum_{\mathbf{p},\sigma}(c^+_{\mathbf{p},\sigma}b_\sigma + \text{h.c}) + T_{\mathbf{k},a}\sum_{\mathbf{k},\sigma}(c^+_{\mathbf{k},\sigma}a_\sigma + \text{h.c.}). \tag{5}$$

Nonequilibrium effects in the tunneling current and conductivity are naturally described by the Keldysh diagram technique ([19]; see also the recent paper [16]).

The tunneling current is determined as [19]

$$I(V) = \sum_{\mathbf{k},\sigma}\int d\omega\ T_{\mathbf{k}a}(G^{\sigma<}_{a\mathbf{k}} - G^{\sigma<}_{\mathbf{k}a}). \tag{6}$$

The functions $G^{\sigma<}_{a\mathbf{k}}$ can be obtained from the kinetic equations, which in the Keldysh formalism are of the general form

$$(\hat{G}_0^{-1} - \hat{G}_0^{*-1})\hat{G}^< = (\hat{\Sigma}\hat{G})^< - (\hat{G}\hat{\Sigma})^<, \tag{7}$$

where $\hat{\Sigma}$ usually includes all the interactions; in our case, however, $\hat{\Sigma}$ is determined only by the tunneling coupling to the leads and by the interaction between the impurities. Therefore, the elements of $\hat{\Sigma}$ simply reduce to the corresponding nonzero parameters $T_{\alpha,\beta}$ ($\alpha, \beta = a, b, \mathbf{k}, \mathbf{p}$). It is reasonable to use the approximation in which the strongest interaction of the considered model—the on-site Coulomb repulsion U—is included in G_0. At this stage, it is not necessary to consider the details of any particular approximation for treating U.

With the help of the kinetic equations, tunneling current (6) can be transformed to the form

$$I_\sigma(V) = -4\gamma_{\mathbf{k}} \times \int \text{Im}G^{R\sigma}_{a,a}(\omega)(n^\sigma_a(\omega) - n^0_{\mathbf{k}}(\omega - eV))\,d\omega, \tag{8}$$

where $n^0_k(\omega)$ is the equilibrium filling number for the metallic tip, $G^R_{a,a}(\omega, V)$ is the exact retarded Green's function of the impurity a state, $n^\sigma_a(\omega)$ is the exact impurity filling number, and the tunneling rate $\gamma_{\mathbf{k}}$ is one of the set of kinetic coefficients determined by

$$\gamma_{\mathbf{k}}(\omega) = |T_{\mathbf{k}a}|^2\nu_{\mathbf{k}}(\omega), \quad \gamma_b(\omega) = |T_{\mathbf{p}b}|^2\nu_{\mathbf{p}}(\omega), \quad \gamma_a(\omega) = |T_{\mathbf{p}a}|^2\nu_{\mathbf{p}}(\omega), \quad \Gamma = \gamma_a + \gamma_a + \gamma_{\mathbf{k}}, \tag{9}$$

where

$$\nu_{\mathbf{k}}(\omega) = -\frac{1}{\pi}\sum_{\mathbf{k}}\text{Im}G^R(\mathbf{k},\omega)$$

is the density of states in the metallic tip and

$$\nu_{\mathbf{p}}(\omega) = -\frac{1}{\pi}\sum_{\mathbf{p}} \mathrm{Im}G^R(\mathbf{p}, \omega)$$

is the substrate density of states.

In Eq. (8) and in what follows, we use the standard approximation with the filling numbers $n^0_{\mathbf{k}}(\omega)$ and $n^0_{\mathbf{p}}(\omega)$ for the continuum states of the banks unperturbed by the tunneling processes, which yields

$$\begin{aligned} G^<_{\mathbf{k},\mathbf{k}}(\omega) &= -2in^0_{\mathbf{k}}(\omega)\mathrm{Im}G^R_{\mathbf{k},\mathbf{k}}, \\ G^<_{\mathbf{p},\mathbf{p}}(\omega) &= -2in^0_{\mathbf{p}}(\omega)\mathrm{Im}G^R_{\mathbf{p},\mathbf{p}}. \end{aligned} \tag{10}$$

Equation (8) shows that the problem is reduced to finding the exact nonequilibrium filling number n^σ_a. This problem can be solved using Eqs. (7) for $G^<_{aa}$, $G^<_{bb}$, and $G^<_{ab}$ in the stationary case,

$$\begin{aligned} 0 = \frac{\partial}{\partial t}G^<_{aa} &= T(G^<_{ba} - G^<_{ab}) + 2\gamma_a\mathrm{Im}G^{\sigma R}_{aa}(n^a - n^0_{\mathbf{p}}) \\ &+ 2\gamma_{\mathbf{k}}\mathrm{Im}G^{\sigma R}_{aa}(n^a - n^0_{\mathbf{k}}), \end{aligned} \tag{11}$$

$$\begin{aligned} 0 = \frac{\partial}{\partial t}G^<_{bb} &= T(G^<_{ab} - G^<_{ba}) \\ &+ 2\gamma_b\mathrm{Im}G^{\sigma R}_{bb}(n^b - n^0_{\mathbf{p}}), \end{aligned} \tag{12}$$

$$\begin{aligned} 0 = \frac{\partial}{\partial t}G^<_{ab} &= -R^{-1}_{ab}G^<_{ab} + T(G^<_{bb} - G^<_{aa}) \\ &+ 2(\gamma_a G^{\sigma A}_{ab} - \gamma_b G^{\sigma R}_{ab})n^0_{\mathbf{p}} + 2\gamma_{\mathbf{k}}G^{\sigma A}_{ab}n^0_{\mathbf{k}}, \end{aligned} \tag{13}$$

$$\begin{aligned} 0 = \frac{\partial}{\partial t}G^<_{ba} &= R^{-1}_{ab}G^<_{ba} + T(G^<_{aa} - G^<_{bb}) \\ &+ 2(\gamma_b G^{\sigma A}_{ba} - \gamma_a G^{\sigma R}_{ba})n^0_{\mathbf{p}} - 2\gamma_{\mathbf{k}}G^{\sigma R}_{ba}n^0_{\mathbf{k}}, \end{aligned} \tag{14}$$

where we use the notation

$$R^{-1}_{ab} = G^{R-1}_{0a} - G^{A-1}_{0b} - i\Gamma. \tag{15}$$

For $n^\sigma_a(\omega)$ and $n^\sigma_b(\omega)$, we then have

$$\begin{aligned} &\gamma_{\mathbf{k}}\mathrm{Im}G^{\sigma R}_{aa}(\omega)(n^\sigma_a(\omega) - n^0_{\mathbf{k}}(\omega)) \\ &= -[\gamma_a\mathrm{Im}G^{\sigma R}_{aa}(\omega)(n^\sigma_a(\omega) - n^0_{\mathbf{p}}(\omega)) \\ &+ \gamma_b\mathrm{Im}G^{\sigma R}_{bb}(\omega)(n^\sigma_b(\omega) - n^0_{\mathbf{p}}(\omega))], \\ &\eta^\sigma\mathrm{Im}G^{\sigma R}_{aa}(\omega)n^\sigma_a(\omega) - \mathrm{Im}G^{\sigma R}_{bb}(\omega)n^\sigma_b(\omega) \\ &= \gamma_b\mathrm{Im}G^{\sigma R}_{bb}(\omega)(n^\sigma_b(\omega) - n^0_{\mathbf{p}}(\omega)) \\ &+ n^0_{\mathbf{p}}(\omega)T(\gamma_a\mathrm{Im}(R^\sigma_{ab}G^{\sigma A}_{ab}) - \gamma_b\mathrm{Im}(R^\sigma_{ab}G^{\sigma R}_{ab})) \\ &+ n^0_{\mathbf{k}}(\omega)T\gamma_{\mathbf{k}}\mathrm{Im}(R^\sigma_{ab}G^{\sigma A}_{ab}), \end{aligned} \tag{16}$$

where

$$\eta^\sigma = T^2\mathrm{Im}R^\sigma_{ab}$$

and where $n^0_{\mathbf{p}}(\omega)$ and $n^0_{\mathbf{k}}(\omega - eV)$ are the respective equilibrium filling numbers of the substrate and the metallic tip states.

It must be noted that no particular approximation for treating the Coulomb interaction has been used until now. If we use the mean-field approximation, which is suitable for the mixed-valence regime, for decoupling the on-site Coulomb interaction, we obtain

$$\begin{aligned} R^\sigma_{ab} &= \frac{1}{(\tilde{\varepsilon}^\sigma_a - \tilde{\varepsilon}^\sigma_b) - i(\gamma_{\mathbf{k}} + \gamma_a + \gamma_b)}, \\ G^{\sigma R}_{aa}(\omega) &= \frac{\omega - \tilde{\varepsilon}^\sigma_b + i\gamma_b}{(\omega - \tilde{\varepsilon}^\sigma_b + i\gamma_b)(\omega - \tilde{\varepsilon}^\sigma_a + i(\gamma_a + \gamma_{\mathbf{k}})) - T^2}, \\ G^{\sigma R}_{bb}(\omega) &= \frac{\omega - \tilde{\varepsilon}^\sigma_a + i(\gamma_a + \gamma_{\mathbf{k}})}{(\omega - \tilde{\varepsilon}^\sigma_b + i\gamma_b)(\omega - \tilde{\varepsilon}^\sigma_a + i(\gamma_a + \gamma_{\mathbf{k}})) - T^2}, \\ G^{\sigma R}_{ab}(\omega) &= \frac{T}{(\omega - \tilde{\varepsilon}^\sigma_b + i\gamma_b)(\omega - \tilde{\varepsilon}^\sigma_a + i(\gamma_a + \gamma_{\mathbf{k}})) - T^2}. \end{aligned} \tag{17}$$

In the mean-field approximation, the impurity energies depend on the applied bias V both directly through the external field in the contact area (which changes the "bare" impurity level) and indirectly through the Coulomb interaction of the nonequilibrium electron density,

$$\begin{aligned} \tilde{\varepsilon}^\sigma_a &= \varepsilon_a + \alpha V + U_a\langle n^{-\sigma}_a\rangle, \\ \tilde{\varepsilon}^\sigma_b &= \varepsilon_b + \beta V + U_b\langle n^{-\sigma}_b\rangle. \end{aligned} \tag{18}$$

The coefficients α and β (α, $\beta < 1$) approximately describe the potential drop between the semiconductor substrate and the impurity. (If one deals with the Coulomb blockade regime, the electron filling numbers $\langle n^\sigma\rangle$ are set equal to 0 or 1, because the hybridization with the lead states is neglected.)

For simplicity, the indirect interaction between the impurities through the semiconductor band states is not included in the results presented. This interaction can easily be taken into account, but it does not lead to any new qualitative changes in the tunneling conductivity behavior.

Now, the main point is that the nonequilibrium electron filling numbers for impurity atoms *a* and *b* must satisfy the self-consistency condition

$$\begin{aligned} n^\sigma_a &= \int d\omega\, n^\sigma_a(\omega)\mathrm{Im}G^R_{aa}(\omega), \\ n^\sigma_b &= \int d\omega\, n^\sigma_b(\omega)\mathrm{Im}G^R_{bb}(\omega), \end{aligned} \tag{19}$$

where $n_a^\sigma(\omega)$ and $n_b^\sigma(\omega)$ are determined by stationary equations (16). Equations (19) can be rewritten as

$$n_a^\sigma = n_{\mathbf{p}}^\sigma(a) + \frac{\gamma_{\mathbf{k}}(\gamma_b + \eta_\sigma)(n_{\mathbf{k}}^\sigma(a) - n_{\mathbf{p}}^\sigma(a)) + \gamma_b\Gamma_{ab}}{(\gamma_{\mathbf{k}} + \gamma_a)(\gamma_b + \eta_\sigma) + \gamma_b\eta_\sigma}, \quad (20)$$

$$n_b^\sigma = n_{\mathbf{p}}^\sigma(b) + \frac{\gamma_{\mathbf{k}}\eta_\sigma(n_k^\sigma(a) - n_{\mathbf{p}}^\sigma(a)) - (\gamma_a + \gamma_{\mathbf{k}})\Gamma_{ab}}{(\gamma_{\mathbf{k}} + \gamma_a)(\gamma_b + \eta_\sigma) + \gamma_b\eta_\sigma}, \quad (21)$$

where

$$\Gamma_{ab} = T\gamma_{\mathbf{k}}\int \mathrm{Im}(R_{ab}G_{ab}^{R\sigma}(\omega))(n_{\mathbf{k}}(\omega) - n_{\mathbf{p}}(\omega))d\omega, \quad (22)$$

$$n_{\mathbf{p}(\mathbf{k})}^\sigma(a) = \int d\omega n_{\mathbf{p}(\mathbf{k})}^0(\omega)\mathrm{Im}G_{aa}^R(\omega) \quad (23)$$

(with the Fermi level for $n_{\mathbf{k}}$ shifted by eV from the Fermi level for $n_{\mathbf{p}}$). For the equilibrium case, $V = 0$ and $n_a^\sigma = n_{\mathbf{p}}^\sigma(a) = n_{\mathbf{k}}^\sigma(a)$.

Solving Eqs. (16) for $n_a^\sigma(\omega)$, we can rewrite the tunneling current in Eq. (8) in the final form

$$I_\sigma(V) = \frac{\gamma_{\mathbf{k}}(\gamma_b + \eta_\sigma)}{(\gamma_a + \gamma_{\mathbf{k}})(\gamma_b + \eta_\sigma) + \gamma_b\eta_\sigma} \times \int\left[\left(\gamma_a + \frac{\gamma_b\eta_\sigma}{\gamma_b + \eta_\sigma}\right)\mathrm{Im}G_{aa}^{R\sigma}(\omega, V) + T\frac{\gamma_b\gamma_{\mathbf{k}}}{\gamma_b + \eta_\sigma}\mathrm{Im}(R_{ab}G_{ab}^{A\sigma}(\omega, V))\right] \times (n_{\mathbf{p}}^0(\omega) - n_{\mathbf{k}}^0(\omega - eV))d\omega, \quad (24)$$

where the self-consistent values for n_a^σ and n_b^σ are inserted in G_{aa}^R, G_{ab}^R, and R_{ab} for each value of the bias V. As expected, the tunneling current depends only on the difference of the electron distribution functions of the electrodes. The first term of the above expression for the tunneling current describes the renormalization of the relaxation rate by the interaction with the neighboring impurity atom b,

$$\gamma_a \longrightarrow \gamma_a + \frac{\gamma_b\eta_\sigma}{\gamma_b + \eta_\sigma}. \quad (25)$$

If the interaction is absent, $T = 0$, then $\eta = 0$ and the usual form of the tunneling current through the impurity localized state is restored. The second term is responsible for the charge redistribution between the interacting impurity atoms. As a consequence of this charge redistribution, we find that the tunneling conductivity (see (24)) is no longer simply proportional to the impurity density of states. These complications make the investigation of the tunneling current through a multichannel system with the interaction between different channels much more difficult (see, e.g., [20]).

In what follows, the interaction between the impurities is chosen (in accordance with the experimental situation) to be no greater than the tunneling rates. This implies that the equilibrium level splitting (see Eqs. (17)) is not resolved via level broadening. In kinetic processes, however, the interaction considerably modifies the charge distribution. The opposite situation, with the zero-bias conductivity determined by the exact equilibrium spectrum of the two-site complex, was recently analyzed in [13].

We emphasize that Eq. (6) is exact and is valid in any case, irrespective of the approximations used in calculating $\mathrm{Im}G_a^R$ and n_a. Equations (19)–(24) can be applied to any regime, including the Coulomb blockade regime, with the proper choice of the retarded Green's function and the R_{ab} function. However, as noted in the introduction, in the present paper, we are mainly interested in the mixed valence regime $\varepsilon \approx \gamma$ or $\varepsilon + U \approx \gamma$ and $U \gg \gamma$, and we therefore use mean-field equations (17) for numerical calculations of the tunneling conductivity.

The tunneling conductivity enhancement can usually be observed at the tunneling bias voltage such that

$$\left|\varepsilon_a^{\pm\sigma}(V) - E_F^t\right| < \Gamma$$

or

$$\left|\varepsilon_a^{\pm\sigma}(V) - E_F^s\right| < \Gamma.$$

However, it is very important to note that any increase in the LDOS in the energy interval

$$E_F - eV < \varepsilon < E_F$$

with changes in the applied bias V leads to an enhancement of the tunneling conductivity at eV. This increase in the LDOS for an interacting system is not necessarily related to crossing a single electron level ε by the shifted Fermi level $E_F - eV$.

The analysis of the proposed model allows one to describe different possible regimes of the tunneling conductivity behavior in the vicinity of impurity atoms in a wide range of tunneling bias changes. In numerical calculations, we adopt $\alpha \approx 0.3$ and $\beta \approx 0.1$ in Eq. (18).

(1) If $\gamma_{\mathbf{k}} \ll \gamma_a, \gamma_b$, one of the impurity atoms (atom a) can be in the magnetic state in a certain tunneling bias range. The transition from the paramagnetic regime to the magnetic one and vice versa can occur with a change in the applied voltage (Fig. 3a). This behavior leads to switching the a atom "on" and "off" twice on spatially resolved local tunneling conductivity spectra (Fig. 3b), which are very similar to the STS experimental data shown in Fig. 2.

In addition, the energy levels are pinned in the vicinity of the Fermi level of one of the electrodes (tip or

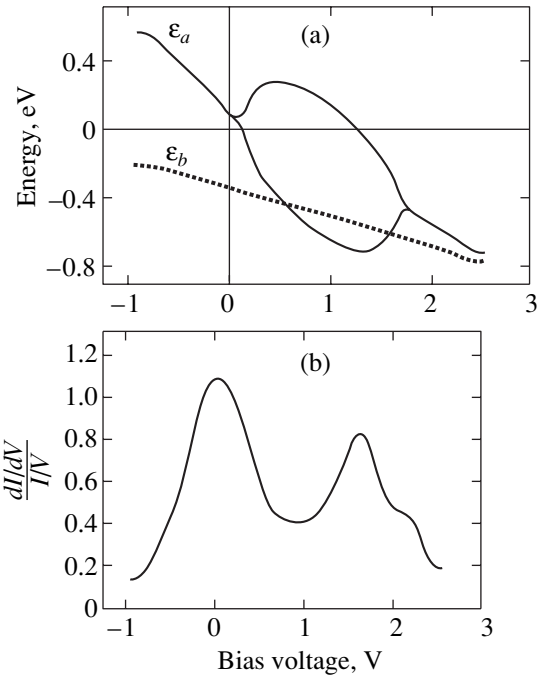

Fig. 3. A well-pronounced twofold structure of the tunneling conductivity with an increased peak width, very similar to the one observed in STS experiments. (a) The dependence of the *a* and *b* atom energies on the applied bias *V*; the parameter values are (in eV) $\varepsilon_a^0 = -0.25$, $\varepsilon_b^0 = -0.5$, $U_a = 1.6$, $U_b = 0.5$, $\gamma_a = 0.2$, $\gamma_b = 0.2$, $\gamma_{\mathbf{k}} = 0.05$, $\varepsilon_a = \varepsilon_a^0 - 0.3$ V, $\varepsilon_b = \varepsilon_b^0 - 0.1$ V; $T = 0.2$; solid curves correspond to ε_a^σ and $\varepsilon_a^{-\sigma}$; dotted curve shows the mean value of $\varepsilon_b = (1/2)(\varepsilon_b^\sigma + \varepsilon_b^{-\sigma})$ because atom *b* is close to the paramagnetic state for this set of parameters. (b) The normalized tunneling conductivity vs. the applied bias voltage.

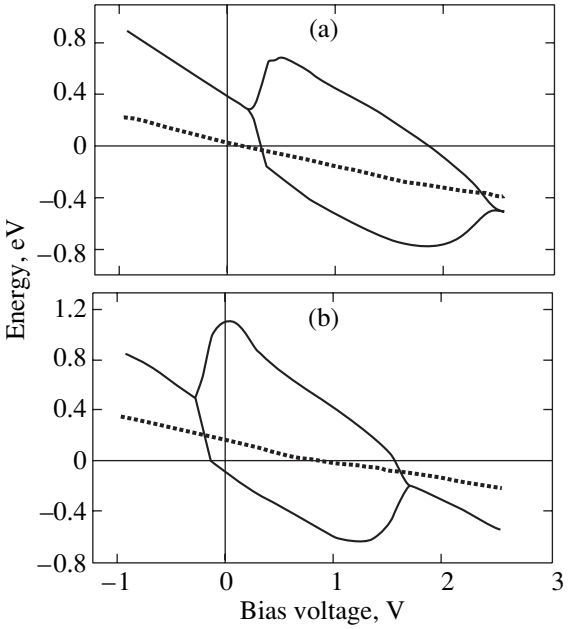

Fig. 4. The dependence of the *a* and *b* atom energies on the applied bias *V*. The parameter values are (in eV) $\varepsilon_a^0 = -0.25$, $\varepsilon_b^0 = -0.1$, $U_a = 1.8$, $U_b = 0\ 5$, $\gamma_a = 0.15$, $\gamma_b = 0.2$, $\gamma_{\mathbf{k}} = 0.05$, $\varepsilon_a = \varepsilon_a^0 - 0.3$ V, $\varepsilon_b = \varepsilon_b^0 - 0.1$ V; $T = 0.2$ (a), 0 (b). Solid curves correspond to ε_a^σ and $\varepsilon_a^{-\sigma}$. The dotted curve shows the mean value of $\varepsilon_b = (1/2)(\varepsilon_b^\sigma + \varepsilon_b^{-\sigma})$ because atom *b* is close to the paramagnetic state for this set of parameters.

sample) while the bias voltage changes within an order *U* range.

In the nonequilibrium case, where the tunneling bias is not zero, the interaction between atoms *a* and *b* can enhance the magnetic state and increase the difference between the energy values ε_σ and $\varepsilon_{-\sigma}$ of the opposite-spin electrons localized on atom *a*.

A detailed analysis of the tunneling bias range for which

$$\left|\varepsilon_a^{-\sigma}(V, n_a^\sigma) - E_F^s\right| < \Gamma$$

leads to the following conclusions.

If there is no interaction between the atoms (the bias range is such that $|\varepsilon_a^{-\sigma}(V, n_a^\sigma) - E_F^s| < \Gamma$), the occupancy of the state $\varepsilon_a^{-\sigma}(V, n_a^\sigma)$ grows and $n_a^{-\sigma}(V)$ and $\varepsilon_a^\sigma(V)$ increase; consequently, $n_a^\sigma(V)$ and $\varepsilon_a^{-\sigma}(V)$ decrease. The levels $\varepsilon_a^{-\sigma}(V, n_a^\sigma)$ and $\varepsilon_a^\sigma(V, n_a^{-\sigma})$ become closer, and a sharp transition from the magnetic to the paramagnetic state occurs (Fig. 4b).

In the presence of interaction, the $\varepsilon_a^{-\sigma}(V, n_a^\sigma)$ state filling is suppressed because of a charge redistribution between the two interacting atoms *a* and *b*. Correspondingly, the increase in $\varepsilon_a^\sigma(V, n_a^{-\sigma})$ and the decrease in $\varepsilon_a^{-\sigma}(V, n_a^\sigma)$ also are not as fast as in the noninteracting case. Therefore, when atom *a* is in the magnetic state, the range of the applied bias becomes wider because of the interatomic interaction (compare Figs. 4a and 4b). We stress that this enhancement of the magnetic regime is possible only in the nonequilibrium case, i.e., for a nonzero tunneling bias and energy levels $\varepsilon_{a(b)}^{\pm\sigma}(V, n_{a(b)}^{\mp\sigma})$ close to the Fermi level of one of the electrodes.

In the equilibrium case, the interaction with paramagnetic atom *b* results in the suppression of the magnetic state on atom *a* (compare Figs. 4a and 4b).

Figures 5a and 5b depict the dependence of the tunneling conductivity on the applied bias in the vicinity of

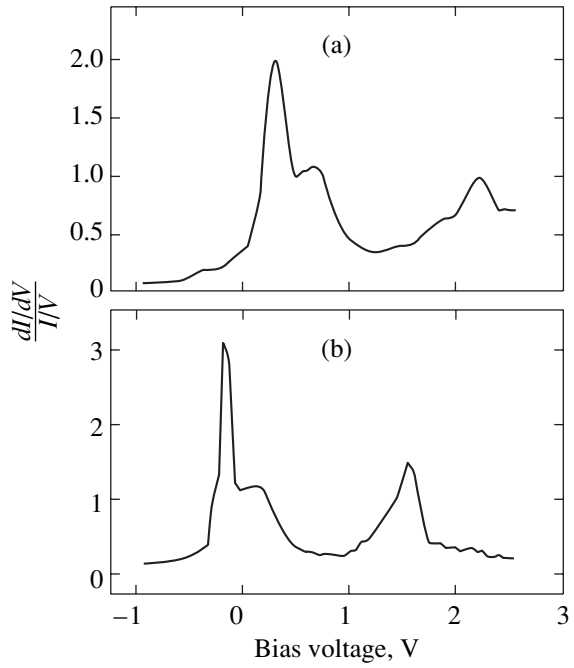

Fig. 5. The dependence of the normalized tunneling conductivity on the applied bias voltage for the same sets of parameters as in Figs. 4a and 4b.

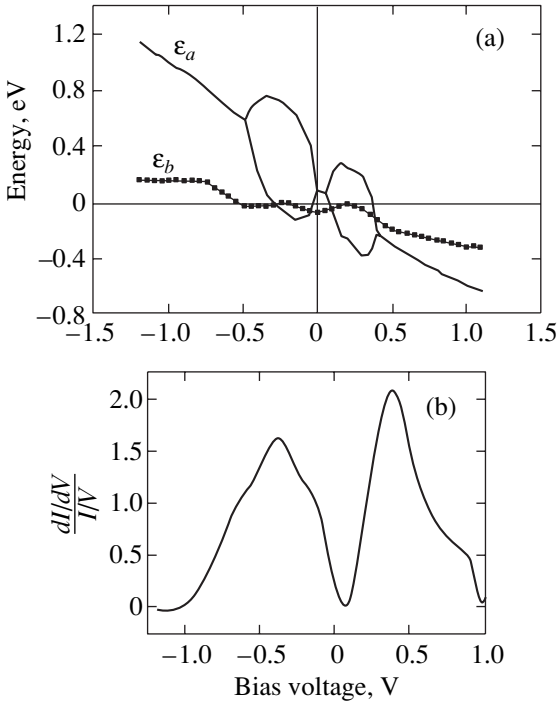

Fig. 6. Double switching "on–off" of the magnetic regime of atom *a* for a strong coupling to the STM tip. (a) The dependence of the *a* and *b* atom energies on the applied bias *V*; the parameters values are (in eV) $\varepsilon_a^0 = -0.7$, $\varepsilon_b^0 = -0.5$, $U_a = 2.0$, $U_b = 0.5$, $\gamma_a = 0.05$, $\gamma_b = 0.05$, $\gamma_{\mathbf{k}} = 0.35$, $\varepsilon_a = \varepsilon_a^0 - 0.3$ V, $\varepsilon_b = \varepsilon_b^0 - 0.1$ V; $T = 0.2$; solid curves correspond to ε_a^σ and $\varepsilon_a^{-\sigma}$; dotted curve shows the mean value of ε_b^σ. (b) The normalized tunneling conductivity vs. the applied bias voltage.

the *a* atom. Two broad peaks in the tunneling conductivity spectra correspond to switching "on" the *a* atom at

$$\varepsilon_a^\sigma(V, n_a^{-\sigma}) = E_F^t$$

and

$$\varepsilon_a^{-\sigma}(V, n_a^\sigma) = E_F^s.$$

(2) For $\gamma_{\mathbf{k}} \gg \gamma_a, \gamma_b$ (i.e., for a sufficiently strong coupling to the STM tip), the magnetic state on the *a* atom can appear twice for the opposite polarity. In Fig. 6a, the dependence of $\varepsilon_{a(b)}^{\pm\sigma}(V, n_{a(b)}^{\mp\sigma})$ on the applied bias is shown. In the applied bias range

$$\left|\varepsilon_a^\sigma(V, n_a^{-\sigma}) - E_F^s\right| < \Gamma,$$

atom *a* is in the magnetic state. But as the tunneling bias increases, the filling numbers rapidly decrease and the magnetic regime is suppressed, and atom *a* can be found in the paramagnetic state. However, for the opposite polarity of the applied bias, atom *a* can again be found in the magnetic state when $|\varepsilon_a^\sigma(V, n_a^{-\sigma})|$ is close to the Fermi level of the tip,

$$\left|\varepsilon_a^\sigma(V, n_a^{-\sigma}) - E_F^t\right| < \Gamma.$$

The interaction between the *a* and *b* atoms can enhance this transition. Tunneling conductivity versus bias voltage is shown in Fig. 6b.

(3) Finally, when the coupling to the STM tip is comparable to the coupling of the impurity atom to the substrate, i.e., $\gamma_{\mathbf{k}} \geq \gamma_a, \gamma_b$, increasing the tunneling bias usually leads to the suppression of the magnetic state (Fig. 7a) because filling numbers decrease due to the tunneling processes. Figure 7b depicts the suppression of the second maximum of the tunneling conductivity in this case.

Thus, a significant role of the nonequilibrium electron distribution in tunneling processes through coupled Anderson impurities is demonstrated. Tunneling conductivity resonances are sensitive to changes of the electron filling numbers, which are not discrete at a nonzero applied bias. We have shown that an impurity atom can be found in the magnetic state for the applied bias within a certain range. Transitions from the paramagnetic regime to the magnetic one and vice versa can occur with changes in the bias voltage. In the presence of such transitions, impurity levels can be pinned near the Fermi levels of each electrode, thereby leading to the twofold structure of spatially resolved tunneling conductivity spectra with enormously broad peaks in the vicinity of each impurity. The theoretical approach proposed here allows us to explain the experimentally

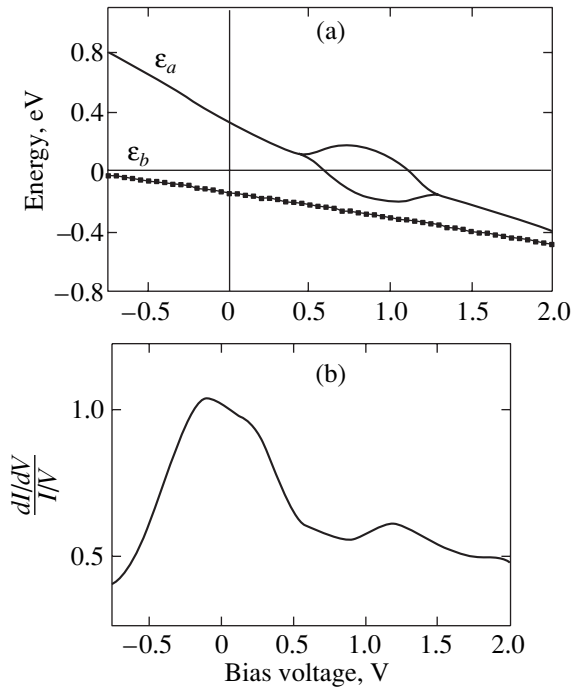

Fig. 7. Suppression of the twofold structure of the tunneling conductivity with the increase of $\gamma_{\mathbf{k}}$. (a) The dependence of the *a* and *b* atom energies on the applied bias *V*; the parameters values are the same as in Fig. 3 except $\gamma_{\mathbf{k}} = 0.1$. (b) The normalized tunneling conductivity vs. the applied bias voltage.

obtained STS results and predicts some new interesting possible switching regimes. An interesting theoretical prediction is that the interaction between impurities with different values of the Coulomb repulsion can unexpectedly enhance the magnetic regime of a single atom in the nonequilibrium case at a large applied bias. At the same time, the interaction with a more paramagnetic neighbor always leads to the suppression of the magnetic state in the equilibrium.

ACKNOWLEDGMENTS

This work was supported in part by the Russian Foundation for Basic Research, project nos. 00-15-96558, 00-15-96555, and 00-02-17759.

REFERENCES

1. A. Depuydt, C. van Haesendonck, N. S. Maslova, *et al.*, Phys. Rev. B **60**, 2619 (1999).
2. P. I. Arseev, N. S. Maslova, S. I. Oreshkin, *et al.*, Pis'ma Zh. Éksp. Teor. Fiz. **72**, 819 (2000) [JETP Lett. **72**, 565 (2000)].
3. P. W. Anderson, Phys. Rev. **124**, 41 (1961).
4. M. B. Johnson, O. A. Albrektsen, R. M. Feenstra, and H. W. M. Salemnik, Appl. Phys. Lett. **63**, 2923 (1993).
5. J. F. Zheng, X. Liu, N. Newman, *et al.*, Phys. Rev. Lett. **72**, 1490 (1994).
6. M. C. M. M. van der Wielen, A. J. A. van Roij, and H. van Kempen, Phys. Rev. Lett. **76**, 1075 (1996).
7. Y. Goldin and Y. Avishai, Phys. Rev. B **61**, 16750 (2000).
8. A.-P. Jauho, N. S. Wingreen, and Y. Meir, Phys. Rev. B **50**, 5528 (1994).
9. J. Konig, T. Pohjola, H. Schoeller, and G. Schon, Physica E (Amsterdam) **6**, 371 (2000).
10. Y. Meir, N. S. Wingreen, and P. A. Lee, Phys. Rev. Lett. **66**, 3048 (1991).
11. D. V. Averin, A. N. Korotkov, and K. K. Likharev, Phys. Rev. B **44**, 6191 (1991).
12. I. M. Ruzin, V. Chandrasekhar, E. I. Levin, and L. I. Glazman, Phys. Rev. B **45**, 13469 (1992).
13. K. Kikoin and Y. Avishai, Phys. Rev. Lett. **86**, 2090 (2001).
14. G. D. Mahan, *Many-Particle Physics* (Plenum, New York, 1990).
15. Y. Goldin and Y. Avishai, Phys. Rev. Lett. **81**, 5394 (1998).
16. M. Plihal and J. W. Gadzuk, Phys. Rev. B **63**, 85404 (2001).
17. Oded Agam, N. S. Wingreen, and B. L. Altshuler, Phys. Rev. Lett. **78**, 1956 (1997).
18. P. I. Arseev, N. S. Maslova, and S. V. Savinov, Pis'ma Zh. Éksp. Teor. Fiz. **68**, 299 (1998) [JETP Lett. **68**, 320 (1998)].
19. P. I. Arseev and N. S. Maslova, Zh. Éksp. Teor. Fiz. **102**, 1056 (1992) [Sov. Phys. JETP **75**, 575 (1992)].
20. F. Hofmann, T. Heinzel, D. A. Wharam, *et al.*, Phys. Rev. B **51**, 13872 (1995).

Journal of Experimental and Theoretical Physics, Vol. 94, No. 1, 2002, pp. 200–202.
Translated from Zhurnal Éksperimental'noĭ i Teoreticheskoĭ Fiziki, Vol. 121, No. 1, 2002, pp. 235–238.

On *n*-Quantum Vortices in Superconductors

V. I. Marchenko* and E. R. Podolyak

Kapitza Institute for Physical Problems, Russian Academy of Sciences, ul. Kosygina 2, Moscow, 117334 Russia
**e-mail: mar@kapitza.ras.ru*

Received June 18, 2001

Abstract—Taking into account terms of a higher order than those usually included in the expansion of free energy close to $\kappa = 1/\sqrt{2}$ in the Ginzburg–Landau theory can lead either to the transition from the mixed to the intermediate state, as is commonly supposed, or to a chain of sequential transitions from one- to *n*-quantum vortices ($n = 2, 3, \ldots$). © *2002 MAIK "Nauka/Interperiodica".*

The transition from type I to type II superconductors occurs at the critical Ginzburg–Landau parameter value $\kappa = 1/\sqrt{2}$ [1]. In the presence of a magnetic flux, this is, clearly, a first-order transition because the intermediate state cannot continuously transform into an Abrikosov vortex lattice. The commonly employed approximation, however, involves random degeneracy, namely, both intermediate state and vortex lattice lose stability at the transition point. On the one hand, the surface energy of the *NS* boundary vanishes [1], and, on the other, repulsion of vortices changes into their attraction at the transition point [2]. What is more, according to Kramer [2], the energy of an *n*-quantum vortex at $\kappa = 1/\sqrt{2}$ equals $\varepsilon_n = n$ (we use units natural for the Ginzburg–Landau theory [1]); that is, for each flux quantum, there is the same fraction of energy as in the normal state in the critical field. This degeneracy is quite familiar to specialists thanks to Bogomol'nyi [3].

As there is no physical reason for such a degeneracy, taking into account next terms in the expansion in order parameter Ψ and gradients should remove it. For an isotropic system, we have four such invariants of equal order with respect to closeness to the transition temperature, namely,

$$\Psi\Psi^*(-i\sqrt{2}\nabla + \kappa\mathbf{A})\Psi(i\sqrt{2}\nabla + \kappa\mathbf{A})\Psi^*,$$

$$\nabla(\Psi\Psi^*)\nabla(\Psi\Psi^*),$$

$$(-i\sqrt{2}\nabla + \kappa\mathbf{A})^2\Psi(i\sqrt{2}\nabla + \kappa\mathbf{A})^2\Psi^*, \quad (\Psi\Psi^*)^3.$$

Our goal is to show the possibility in principle of substantial changes in the character of the transition. For this purpose, we include the simplest correction $|\Psi|^6$. The Ginzburg–Landau functional then takes the form

$$F = a|\Psi|^2 + \frac{b}{2}|\Psi|^4 + c|\Psi|^6 + g\left|\nabla\Psi - i\frac{2e}{c\hbar}\mathbf{A}\Psi\right|^2 + \frac{B^2}{8\pi} - \frac{BH_0}{4\pi}, \tag{1}$$

where H_0 is the external field and $\mathbf{B} = \mathrm{rot}\,\mathbf{A}$. In the equilibrium state and in the absence of a magnetic field, this functional reaches a minimum at $|\Psi|^2 = |\Psi_0|^2$,

$$|\Psi_0|^2 = -\frac{a}{b}\left(1 - \frac{3}{2}\gamma\right), \tag{2}$$

where $\gamma = -2ac/b^2$ (note that, at the phase transition point, $a = 0$ and γ vanishes). This energy gain reduces to zero in critical field H_c,

$$H_c^2 = 4\pi\frac{a^2}{b}(1 - \gamma). \tag{3}$$

The ratio between correlation length ξ and penetration depth δ,

$$\xi^2 = 4\pi\frac{|\Psi_0|^2 g}{H_c^2}, \quad \delta = \frac{\hbar^2 c^2}{32\pi e^2}\frac{1}{|\Psi_0|^2 g}, \tag{4}$$

determines the Ginzburg–Landau κ parameter,

$$\kappa = \frac{\hbar c}{8\pi\sqrt{2}|e|}\frac{H_c}{|\Psi_0|^2 g} = \kappa_0(1 + \gamma). \tag{5}$$

Let us introduce the dimensionless variables

$$r = \frac{R}{\delta}, \quad \psi = \frac{\Psi}{\Psi_0}, \quad b = \frac{B}{H_c}, \quad h_0 = \frac{H_0}{H_c}, \quad \mathbf{a} = \frac{\mathbf{A}}{H_c}, \quad f = \frac{F}{H_c^2\delta^2}. \tag{6}$$

Functional (1) then takes the form

$$f = \frac{1}{8\pi}\left\{b^2 + \left|\left(\frac{\sqrt{2}}{\kappa}\nabla - i\mathbf{a}\right)\psi\right|^2 + (1 - |\psi|^2)^2(1 + \gamma|\psi|^2) - 1 - 2bh_0\right\}. \tag{7}$$

1063-7761/02/9401-0200$22.00 © 2002 MAIK "Nauka/Interperiodica"

We will not consider field penetration into a superconductor and will therefore assume that the magnetic flux is constant; accordingly, we will omit the $2bh_0$ term. In addition, the κ parameter will be considered independent, because its variations are not fully described by (5) in real superconductors.

Consider a separate *n*-quantum vortex. We select the calibration at which the order parameter phase equals $n\phi$, where ϕ is the azimuthal angle, and the vector-potential only has the $a(r)$ azimuthal component. The energy of an axially symmetrical vortex in the cylindrical coordinate system is then given by the equation

$$\varepsilon_n = \frac{1}{4}\int_0^\infty \left[\left(a' + \frac{a}{r}\right)^2 + \frac{2}{\kappa^2}(\psi_n')^2 + \left(\frac{\sqrt{2}n}{\kappa r} - a\right)^2 \psi_n^2 + (1-\psi_n^2)^2(1+\gamma\psi_n^2)\right] r\,dr; \quad (8)$$

here, $\psi_n(r)$ is the order parameter modulus. The Ginzburg–Landau equations with the boundary conditions $\psi_n(0)= 0$, $r\psi_n'|_{r=0} = 0$, $a(0) = 0$, and $\psi_n(\infty) = 1$ correspond to the lowest energy. We solved this problem numerically at arbitrary κ values and γ of –0.1 to 0.1. The *n*-quantum vortex energy fraction per flux quantum at $\gamma = -0.1$ is shown in Fig. 1.

If $\gamma > 0$, we obtain the commonly expected picture of the transition from type II to type I superconductors with one-quantum vortices, into which magnetic flux penetrates in the form of macroscopic normal regions. At $\gamma < 0$, sequential transitions from one- to *n*-quantum vortices ($n = 2, 3, \ldots$) should occur as κ decreases in the region close to the $1/\sqrt{2}$ critical value; clearly, the width of this region is proportional to γ (Fig. 2). The chain of such transitions becomes denser (the *n* value infinitely increases) in approaching some critical $\kappa^* = \kappa^*(\gamma)$ value. At $\kappa = \kappa^*$, the surface energy of the *NS* boundary changes sign. Indeed, at large *n*, a vortex is a macroscopic cylinder in the normal state with the magnetic field virtually equal to the critical field. The volume contribution to vortex energy divided by *n* is an *n*-independent value (the fraction of the normal state energy per flux quantum). The dependence on *n* arises if the energy of the boundary between the normal and superconducting states, σ_{NS}, is taken into account. The ε_n/n function then acquires a capillary correction proportional to $\sigma_{NS}/\sqrt{n}$. It follows that transitions can only condense at the point of σ_{NS} vanishing.

According to Luk'yanchuk [4], widely spaced vortices attract each other at $\kappa\sqrt{2} - 1 < -\gamma/2$. Therefore, in the region of parameters of interest to us ($\kappa < 1/\sqrt{2}, \gamma < 0$), the necessary condition of the existence of an *n*-quantum vortex is its stability with respect to the decomposition into a bound state of several vortices carrying the same total flux. An analysis of the stability of vortices will be performed using perturbation theory. The Ginzburg–Landau equations for degenerate unperturbed solutions (at $\kappa = 1/\sqrt{2}$, $\gamma = 0$) can be replaced by the Bogomol'nyi equations

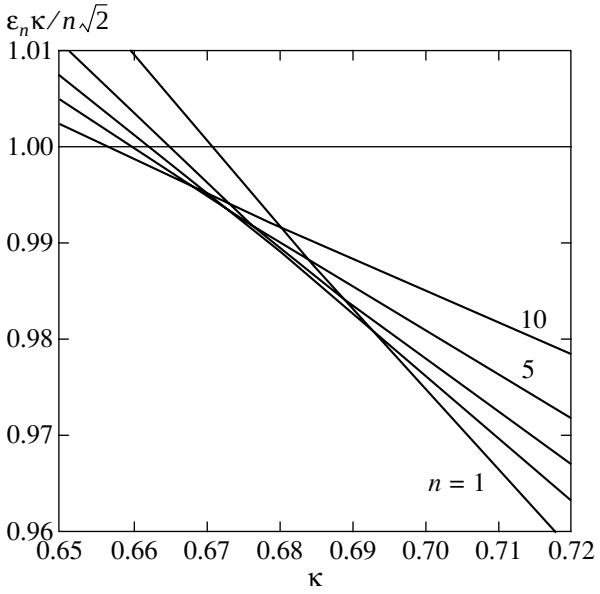

Fig. 1. *n*-Quantum vortex energy fraction $\varepsilon_n\kappa/n\sqrt{2}$ per flux quantum at $\gamma = -0.1$.

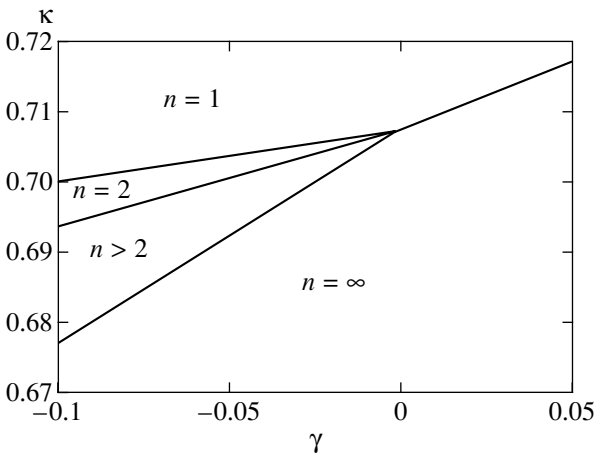

Fig. 2. Regions in which vortices with different parameter *n* values correspond to energy minimum.

$$\nabla^2 \ln|\psi| = -\frac{1}{2}(1-|\psi|^2) + 2\pi\sum_i n_i\delta(\mathbf{r}-\mathbf{r}_i), \quad (9)$$

$$b = 1 - |\psi|^2, \quad (10)$$

and the potential for perturbation theory can be written as

$$\delta f = \frac{1}{8\pi}|\psi|(1-|\psi|^2)\{\gamma(1-|\psi|^2) - 2\alpha\sqrt{2}\}, \quad (11)$$

where $\alpha = \kappa - 1/\sqrt{2}$. The unperturbed solution in the form of an axially symmetrical *n*-quantum vortex is described by the equation $\psi(\mathbf{r}) = v_n(r)e^{in\phi}$, and the

amplitude of the order parameter satisfies the equation

$$\nabla^2 \ln v_n = -\frac{1}{2}(1 - v_n^2) \tag{12}$$

with the asymptotic behavior $v_n(r) \propto r^n$ as $r \longrightarrow 0$ and $v_n(r) \longrightarrow 1$ as $r \longrightarrow \infty$.

The energy of a separate n-quantum vortex per flux quantum can be written in the form

$$\frac{\varepsilon}{n} = 1 + \frac{1}{4}\{\gamma Q_n - 2\alpha\sqrt{2}P_n\}, \tag{13}$$

where the quantities

$$Q_n = n^{-1}\int r dr\, v_n^2(1 - v_n^2)^2$$

and

$$P_n = n^{-1}\int r dr\, v_N^2(1 - v_N^2)$$

are found by numerically integrating solutions (12). The condition under which $(n + 1)$-quantum vortices become more energetically favorable than n-quantum vortices is as follows:

$$\frac{\alpha}{\gamma} > \frac{Q_n - Q_{n+1}}{2\sqrt{2}(P_n - P_{n+1})}, \quad \gamma < 0. \tag{14}$$

This conclusion corresponds with direct numerical calculations (Fig. 1) and the result obtained in [4] for $n = 1$; according to this result, two-quantum vortices become more favorable than one-quantum vortices at $\alpha/\gamma > 0.034$, $\gamma < 0$. Upon the attainment of the lower critical field $H_0 = H_{c1}$, the magnetic flux penetrates into a superconductor in the form of the most favorable n-quantum vortices. Two-quantum vortices are the most favorable at $0.034 < \alpha/\gamma < 0.066$, three-quantum vortices are the most favorable at $0.066 < \alpha/\gamma < 0.081$, etc. In the limit $n \longrightarrow \infty$, Eq. (14) also yields the condition under which the *NS* boundary energy vanishes, namely, $\alpha/\gamma = 0.155$. Note that separate vortices and even vortex lattices can be observed as metastable states at a positive *NS* boundary energy, that is, in usual type I superconductors.

A separate most favorable n-quantum vortex can decompose into bound one-quantum vortices or other combinations of m-quantum vortices with the conservation of the total flux. To study the stability of an n-quantum vortex toward decomposition, consider the perturbed solution as a combination of vortices with the coordinates $|\mathbf{r}_i| \ll 1$. The order parameter can then be expanded into a series in powers of $\mathbf{r}_i$. Truncating this series after the second-order term yields [4]

$$|\psi(\mathbf{r})| = v_n(r) + \frac{1}{2n}\sum_i (\mathbf{r}_i, \nabla)^2 v_n(r). \tag{15}$$

Substituting (15) into potential (11) and integrating the result, we obtain

$$\delta\varepsilon = \frac{1}{16n}\sum_i |\mathbf{r}_i|^2 \left\{\gamma\int r dr\, v_n^2(1 - v_n^2)^2(3v_n^2 - 1) - 2\alpha\sqrt{2}\int r dr\, v_n^2(1 - v_n^2)(2v_n^2 - 1)\right\}. \tag{16}$$

This yields the condition of the stability of an n-quantum vortex in the form

$$\frac{\alpha}{\gamma} > \frac{1}{2\sqrt{2}}\frac{\int r dr\, v_n^2(1 - v_n^2)^2(3v_n^2 - 1)}{\int r dr\, v_n^2(1 - v_n^2)(2v_n^2 - 1)}, \quad \gamma < 0. \tag{17}$$

A two-quantum vortex is stable with respect to the decomposition into two one-quantum vortices at $\alpha/\gamma > 0.14$.

To summarize, we do not agree with the assertion [4] that the structures with one-quantum vortices can only be stable. We consider this conclusion erroneous. Indeed, in [4], the interaction energy between narrowly spaced vortices was analyzed without taking into account terms proportional to $|\psi|^2$.

Calculations of the coefficient of $|\psi|^6$ in the Ginzburg–Landau theory for the standard BCS model [5] showed that the sign of this coefficient was negative. According to the results obtained in this work, this circumstance is favorable to the observation of n-quantum vortices. Candidates for observing n-quantum vortices are superconductors in which vortex lattices with attraction are formed. The existence of attraction manifests itself through a finite magnetization jump in field $H_0 = H_{c1}$. If temperature variations cause changes in the behavior of a superconductor such that its magnetization in field $H_0 = H_c$ vanishes jumpwise, as is characteristic of type I superconductors, observing n-quantum vortices near this transition is feasible.

ACKNOWLEDGMENTS

The authors thank M.Yu. Kagan and I.A. Fomin for useful discussions. This work was financially supported by the Russian Foundation for Basic Research (project no. 00-02-16250).

REFERENCES

1. E. M. Lifshitz and L. P. Pitaevskii, *Course of Theoretical Physics*, Vol. 5: *Statistical Physics* (Nauka, Moscow, 1978; Pergamon, New York, 1980).
2. L. Kramer, Phys. Rev. B **3**, 3821 (1971).
3. E. B. Bogomol'nyĭ, Yad. Fiz. **24**, 861 (1976) [Sov. J. Nucl. Phys. **24**, 449 (1976)].
4. I. Luk'yanchuk, Phys. Rev. B **63**, 174504 (2001).
5. Yu. A. Ovchinnikov, Zh. Éksp. Teor. Fiz. **115**, 726 (1999) [JETP **88**, 398 (1999)].

Translated by V. Sipachev

Journal of Experimental and Theoretical Physics, Vol. 94, No. 1, 2002, pp. 203–215.
Translated from Zhurnal Éksperimental'noĭ i Teoreticheskoĭ Fiziki, Vol. 121, No. 1, 2002, pp. 239–252.

SOLIDS
Electronic Properties

Conductivity and Field and Current Distributions in a Two-Component System Composed of Regular Triangles

Yu. N. Ovchinnikov[a, b] and I. A. Luk'yanchuk[b, c]

[a]*Max-Planck-Institut für Physik Komplexer Systeme, 01187, Dresden, Germany*

[b]*Landau Institute for Theoretical Physics, Russian Academy of Sciences, Chernogolovka, Moscow oblast, 117940 Russia*

[c]*LPMC, Université de Picardie Jules Verne, F-80039, Amiens, France*

Received August 31, 2001

Abstract—The problem of the effective conductivity and the distributions of a field and currents is analyzed in a regular two-component system composed of regular triangles. An efficient solution method is developed that admits a generalization to multicomponent systems. *© 2002 MAIK "Nauka/Interperiodica".*

1. INTRODUCTION

In 1970, Dykhne [1] put forward a hypothesis about a universal dependence of the effective conductivity σ_{eff} of a two-component system on the conductivities $\sigma_{1,2}$ of its constituents:

$$\sigma_{\text{eff}} = \sqrt{\sigma_1\sigma_2}. \quad (1)$$

The hypothesis is that relation (1) is always valid, provided that the following two conditions are satisfied: the conductivity of each component is isotropic, and the distributions of the components are symmetric with respect to the interchange $1 \longleftrightarrow 2$. A proof is based on the analysis of the equation for a current, $\mathbf{j} = \sigma(r)\mathbf{E}$, and the equation obtained from it by the vector multiplication by $\mathbf{n}$ ($\mathbf{n}$ is a normal vector to the surface), $\mathbf{n} \times \mathbf{j} = \sigma(r)\mathbf{n} \times \mathbf{E}$. The quantity $\mathbf{n} \times \mathbf{j}$ can be represented as $\mathbf{n} \times \mathbf{j} = \nabla\mathbf{H} = \mathbf{E}'$, where $\mathbf{j} = \text{curl}(0, 0, H)$ and H is a magnetic field. The vector $\mathbf{E}'$ can be interpreted as an electric field in a medium with the same structure and the conductivity $\sigma' = \sigma_0^2/\sigma(\mathbf{r})$, where σ_0 is an arbitrary constant. The current density $\mathbf{j}'$ is defined by the equation $\mathbf{j}' = \sigma_0^2\,\mathbf{n} \times \mathbf{E}$. One can readily verify that the quantities $\mathbf{j}'$, $\mathbf{E}'$, and $\sigma_0^2/\sigma(\mathbf{r})$ satisfy both the equation and the boundary conditions for the field and current. Averaging the equations for $\mathbf{j}$ and $\mathbf{j}'$ over the sample area and taking into account that the effective conductivity is isotropic in both media, we obtain the Dykhne relation [1, 2]

$$\sigma_{\text{eff}}(\sigma_1, \sigma_2)\sigma_{\text{eff}}(\sigma_0^2/\sigma_1, \sigma_0^2/\sigma_2) = \sigma_0^2. \quad (2)$$

Relation (1) is a particular case of Eq. (2) for $\sigma_0 = \sqrt{\sigma_1\sigma_2}$. Relation (2) is also valid for multicomponent systems and admits a generalization to an anisotropic conductor. In [3], an exact solution was obtained to the problem of the effective conductivity and the field distribution in a regular two-component system with a chessboard structure. It was demonstrated that relation (1) is satisfied in such a system for any value of the parameter $Z = (\sigma_1 - \sigma_2)/(\sigma_1 + \sigma_2)$, although this is achieved in a rather sophisticated way.

A perturbation theory with respect to a small deviation of the local conductivity from its mean value was considered in [4].

In the general case, the problem of the field distribution and the conductivity of a multicomponent system can be reduced to a system of integral equations for the density of charges arising along the boundaries of domains. For a two-component system, such a system of equations depends only on a single parameter Z.

Below, we present an efficient method that allows one to determine the distribution of charges and a field in a regular two-component system composed of regular triangles to a high degree of accuracy for arbitrary values of the parameter Z.

The Dykhne relation [1] will be applied to verify the accuracy of the approximation used.

2. CONDUCTIVITY OF A REGULAR TWO-COMPONENT SYSTEM WITH CELLS IN THE FORM OF REGULAR TRIANGLES

The two-component system under consideration consists of regular triangles (Fig. 1). The effective conductivity σ_{eff} of such a system is isotropic. Therefore, it suffices to determine a current for the orientation of the external electric field shown in Fig. 1. It is obvious from the symmetry considerations that there exist only two

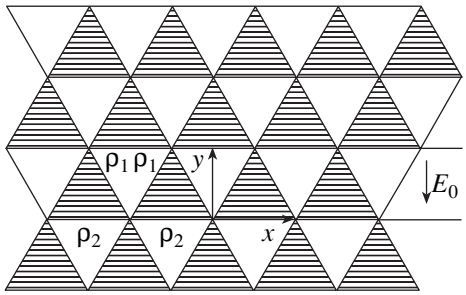

Fig. 1. Two-component system with cells in the form of regular triangles.

independent charge densities $\rho_{1,2}$ distributed along the edges of the cells in the structure under consideration. Inside each triangle, the equation

$$\Delta\varphi = 0 \tag{3}$$

holds, where φ is a scalar potential, which is everywhere continuous, and Δ is the Laplace operator. Equation (3) follows from the conservation law for current $\mathbf{j}$

$$\mathrm{div}\,\mathbf{j} = 0. \tag{4}$$

It follows from Eq. 3 that potential φ can be represented as

$$\varphi = E_0 y - 4\pi\int d^2 r_1 G(r - r_1)\rho(r_1), \tag{5}$$

where G is a two-dimensional Green's function,

$$G = \frac{1}{2\pi}\ln|r - r_1|. \tag{6}$$

The charge density ρ is distributed along the edges of triangles,

$$\rho(r) = \hat{\rho}\,\delta(\hat{y}), \tag{7}$$

where $\hat{y}$ is a local coordinate transverse to the boundary of a triangle. Henceforth, we will omit the sign $\hat{}$ over the charge density.

The following relations hold on the boundaries of triangles:

$$E_n^{(1)} - E_n^{(2)} = 4\pi\hat{\rho}, \quad \sigma_1 E_n^{(1)} = \sigma_2 E_n^{(2)}, \tag{8}$$

where $E = -\partial\varphi/\partial r$ is an electric field and $\mathbf{n}$ is a normal vector to the boundary of a triangle. From Eqs. (5) and (8), we obtain a closed system of equations for the charge densities $\tilde{\rho}_{1,2}$:

$$\frac{Z}{2\pi}\left\{\frac{1}{2} + \frac{2\pi}{\sqrt{3}}\int_0^1 dt\,(\tilde{\rho}_1(t) - \tilde{\rho}_2(t))\sum_{M=-\infty}^{\infty}\frac{\tan\left(\frac{\pi}{2}(t+M)\right)}{\sinh^2\left(\frac{\pi}{\sqrt{3}}\left(\frac{M}{2} - t_1 + \frac{t}{2}\right)\right) + \cosh^2\left(\frac{\pi}{\sqrt{3}}\left(\frac{M}{2} - t_1 + \frac{t}{2}\right)\right)\tan^2\left(\frac{\pi}{2}(M+t)\right)}\right\} = \tilde{\rho}_1(t_1),$$

$$\frac{Z}{2\pi}\left\{1 + \frac{2\pi}{\sqrt{3}}\int_0^1 dt\,\tilde{\rho}_1(t)\left[\sum_{M=-\infty}^{\infty}\frac{\tan\left(\frac{\pi}{2}(t+M)\right)}{\sinh^2\left(\frac{\pi}{\sqrt{3}}\left(\frac{M}{2} - t_1 + \frac{t}{2}\right)\right) + \cosh^2\left(\frac{\pi}{\sqrt{3}}\left(\frac{M}{2} - t_1 + \frac{t}{2}\right)\right)\tan^2\left(\frac{\pi}{2}(M+t)\right)}\right.\right. \tag{9}$$

$$\left.\left. + \sum_{M=-\infty}^{\infty}\frac{\tan\left(\frac{\pi}{2}(M+t)\right)}{\sinh^2\left(\frac{\pi}{\sqrt{3}}\left(\frac{M}{2} + t_1 + \frac{t}{2}\right)\right) + \cosh^2\left(\frac{\pi}{\sqrt{3}}\left(\frac{M}{2} + t_1 + \frac{t}{2}\right)\right)\tan^2\left(\frac{\pi}{2}(M+t)\right)}\right]\right\} = -\tilde{\rho}_2(t_1).$$

In (9), we have passed to the dimensionless variables

$$\hat{t} = a\tilde{t}, \quad \rho_{1,2} = E_0\tilde{\rho}_{1,2},$$

where $\hat{t}$ is the length along the edge measured from the corner point (Fig. 1) and a is the length of the triangle's edge. The effective conductivity σ_{eff} is expressed in terms of the function $\tilde{\rho}_2(t)$ by the simple relations

$$\sigma_{\mathrm{eff}} = -\frac{4\pi\sigma_1\sigma_2}{\sigma_1 - \sigma_2}\int_0^1 dt\tilde{\rho}_2(t),$$
$$\frac{\sigma_{\mathrm{eff}}}{\sqrt{\sigma_1\sigma_2}} = -\frac{2\pi\sqrt{1 - Z^2}}{Z}\int_0^1 dt\tilde{\rho}_2(t). \tag{10}$$

The examination of Eqs. (9) reveals that the functions $\tilde{\rho}_{1,2}$ satisfy the relations

$$\tilde{\rho}_2(t) = \tilde{\rho}_2(1-t), \quad \tilde{\rho}_1(t) = -\frac{\tilde{\rho}_2(t)}{2} + \rho_1^1(t), \qquad (11)$$

where the function ρ_1^1 changes its sign under the substitution of $1 - t$ for t:

$$\rho_1^1(t) = -\rho_1^1(1-t). \qquad (12)$$

It follows from the system of equations (9) that the functions $\tilde{\rho}_{1,2}(t)$ are doubly periodic analytic functions of the complex variable t with periods of $(1/2 \pm i\sqrt{3}/2)$. The points

$$t_{N,M} = \frac{1}{2}(N+M) + \frac{i\sqrt{3}}{2}(N-M)$$

are branching points of the functions $\tilde{\rho}_{1,2}$. In the neighborhood of the point $t = 0$, we have

$$\tilde{\rho}_2(t) = -\frac{\tilde{C}}{t^{2\kappa}}, \quad \rho_1^1(t) = \frac{\tilde{A}}{t^{2\kappa}}, \qquad (13)$$

where $\tilde{A}$, $\tilde{C}$, and κ are certain constants. From Eqs. (9), (11), and (13), we obtain the following system of equations for the coefficients $\tilde{A}$, $\tilde{C}$, and κ:

$$\begin{aligned} \frac{3}{2}Z\frac{\sin(\pi/6 - \pi\kappa/3)}{\cos(\pi\kappa)}\tilde{C} &= \tilde{A}, \\ 2Z\frac{\cos(\pi/6 - \pi\kappa/3)}{\sin(\pi\kappa)}\tilde{A} &= \tilde{C}. \end{aligned} \qquad (14)$$

The solvability condition for the system of equations (14) yields the following equation for the parameter κ:

$$3Z^2\frac{\sin(\pi/3 - 2\pi\kappa/3)}{\sin(2\pi\kappa)} = 1. \qquad (15)$$

Solving Eq. (15), we obtain an explicit expression for the parameter κ,

$$\kappa = \frac{1}{2} - \frac{3}{2\pi}\arctan\left(\sqrt{3\frac{1-Z^2}{1+3Z^2}}\right). \qquad (16)$$

In addition to the singularity (13), the functions $\tilde{\rho}_{2,1}$ have a singularity of the form

$$\tilde{\rho}_{1,2} \propto t^{2\tilde{\kappa}}, \quad \tilde{\kappa} > 0. \qquad (17)$$

The parameter $\tilde{\kappa}$ satisfies Eq. (15) under the replacement $\kappa \longrightarrow -\tilde{\kappa}$,

$$\frac{3Z^2\sin\left(\frac{2\pi}{3} - \frac{2\pi}{3}\tilde{\kappa}\right)}{\sin(2\pi\tilde{\kappa})} = -1, \qquad (18)$$

a solution to which is given by

$$\tilde{\kappa} = \frac{1}{2} + \kappa + \frac{3L}{2}, \quad L = 0, 1, 2, \ldots. \qquad (19)$$

The functions $\tilde{\rho}_{1,2}$ are generated by doubly periodic analytic functions whose periods $T_{1,2}$ are given by

$$T_1 = 2, \quad T_2 = Ke^{i\pi/3}, \qquad (20)$$

where K is a positive integer. The period $T_1 = 2$ is associated with the fact that the functions $\rho_{1,2}$ must assume the original value after a turn around the points (0, 1). This means that a meromorphic elliptic function, which is a basic one for constructing $\rho_{1,2}$, has an ordered arrangement of poles and zeros on the set $\{\tilde{K}e^{i\pi/3} + L\}$, where $\tilde{K}$ is fixed and $L = 0, \pm1, \pm2, \ldots$; i.e., for any value of L, only one pole and one zero of the same order can be located at the neighboring points $(L, L+1)$. For any value of K, there exist $2K$ meromorphic elliptic functions whose poles and zeros are ordered in the aforementioned sense. Among these functions, there exists a maximal set of $2K$ functions that are mutually transformed under the translations

$$t_{N,M} = \frac{1}{2}(N+M) + \frac{i\sqrt{3}}{2}(N-M).$$

Taking into account complex conjugation, we obtain equivalent sets of meromorphic functions for $K = 1, 2$ that are insufficient for satisfying conditions (14), (15), (17), (18). These functions are contained in the sets that arise for $K > 2$. An arbitrary meromorphic function with prescribed periods and location of poles and zeros is expressed in terms of the Jacobi theta function [5]. In our case, we have

$$\tau = 2, \quad \tau' = \frac{i\sqrt{3}}{2}K + \left(\frac{1}{2}K - 2L'\right),$$

where L' is an integer such that $|K'/2 - 2L'|$ is minimal:

$$\begin{aligned} \vartheta_1\left(\frac{t}{\tau}\right) = i\sum_{N=-\infty}^{\infty}(-1)^N \exp\left(\frac{i\pi}{\tau}\tau'\left(N - \frac{1}{2}\right)^2\right) \\ \times \exp\left\{\frac{2i\pi t}{\tau}\left(N - \frac{1}{2}\right)\right\}. \end{aligned} \qquad (21)$$

When $K = 1$ ($L' = 0$), there exists a single meromorphic elliptic function $\phi_1(t)$ that can be used for constructing the charge densities ρ_1^1 and ρ_2:

$$\phi_1(t) = \left(\frac{\sum_{N=1}^{\infty} \cos\left(\pi t\left(N-\frac{1}{2}\right)\right)\exp\left(-\frac{\pi\sqrt{3}}{4}\left(N-\frac{1}{2}\right)^2\right)\exp\left(\frac{i\pi}{4}N(N-1)\right)}{\sum_{N=1}^{\infty}(-1)^{N+1}\sin\left(\pi t\left(N-\frac{1}{2}\right)\right)\exp\left(-\frac{\pi\sqrt{3}}{4}\left(N-\frac{1}{2}\right)^2\right)\exp\left(\frac{i\pi}{4}N(N-1)\right)}\right)^2, \tag{22}$$

$$\phi_1(1-t) = \phi_1^{-1}(t), \quad \hat{\phi}_1(t) = \phi_1^{\kappa}(t), \quad \hat{\phi}_1(1-t) = \frac{1}{\hat{\phi}_1(t)}.$$

Consider the case of $K = 3$. Eight meromorphic functions are divided into two sets of functions that are invariant under the translations $t_{N,M}$. One of these sets consists of two functions, $\phi_1(t)$ and $\phi_1(1-t)$, which are defined in Eq. (22). The second set consists of six functions,

$$\{\phi_2(t),\ \phi_2^{-1}(t),\ \phi_2(t+e^{i\pi/3}),\ \phi_2^{-1}(t+e^{i\pi/3}),\ \phi_2(t+2e^{i\pi/3}),\ \phi_2^{-1}(t+2e^{i\pi/3})\}, \tag{23}$$

where

$$\phi_2(t) = \phi_1(t)\left(\frac{-e^{i\pi/2}\vartheta_1\left(\frac{e^{i\pi/3}-t}{\tau}\right)}{\vartheta_1\left(\frac{1+e^{i\pi/3}-t}{\tau}\right)}\right)^4,$$

$$\phi_2(t+e^{i\pi/3}) = \phi_1(t)\left(\frac{\vartheta_1(t/\tau)}{\vartheta_1\left(\frac{1-\tau}{\tau}\right)}\right)^4, \tag{24}$$

$$\phi_2(t+2e^{i\pi/3}) = \phi_1(t)\left(\frac{-e^{i\pi/2}\vartheta_1\left(\frac{2e^{i\pi/3}-t}{\tau}\right)}{\vartheta_1\left(\frac{1+2e^{i\pi/3}-t}{\tau}\right)}\right)^4.$$

In (24), the theta function is defined by expression (21):

$$\vartheta_1\left(\frac{t}{\tau}\right) = i\sum_{N=-\infty}^{\infty}(-1)^N\exp\left\{\frac{i3\pi}{2}e^{i\pi/3}\left(N-\frac{1}{2}\right)^2\right\} \times\exp\left\{i\pi t\left(N-\frac{1}{2}\right)\right\}. \tag{25}$$

Under the translations by the periods $\tau = 2$ and $\tau' = 3e^{i\pi/3}$, this theta function is transformed as follows:

$$\vartheta_1\left(\frac{t+\tau}{\tau}\right) = -\vartheta_1\left(\frac{t}{\tau}\right),$$
$$\vartheta_1\left(\frac{t+\tau'}{\tau}\right) = -\vartheta_1\left(\frac{t}{\tau}\right)\exp\left[-i\pi\left(t+\frac{3}{2}e^{i\pi/3}\right)\right]. \tag{26}$$

Let us introduce the functions $\hat{\phi}_2(t)$, $\hat{W}(t)$, and $\hat{W}_1(t)$ by the relations

$$\hat{\phi}_2(t) = \phi_2^{\kappa}(t), \quad \hat{\phi}_2(t+e^{i\pi/3}) = \phi_2^{\kappa}(t+e^{i\pi/3}),$$
$$\hat{\phi}_2(t+2e^{i\pi/3}) = \phi_2^{\kappa}(t+2e^{i\pi/3}),$$
$$\hat{W}(t) = \hat{\phi}_2(t)+\hat{\phi}_2(t+e^{i\pi/3})+\hat{\phi}_2(t+2e^{i\pi/3}),$$
$$\hat{W}_1(t) = \hat{\phi}_2^{-1}(t)+\hat{\phi}_2^{-1}(t+e^{i\pi/3})+\hat{\phi}_2^{-1}(t+2e^{i\pi/3}). \tag{27}$$

The functions $\hat{\phi}_1(t)$, $\hat{W}(t)$, and $\hat{W}_1(t)$ are basis functions for constructing the charge densities $\rho_{1,2}$. Retaining only these functions as the basis and taking into account the symmetry properties (11) and (12), we obtain

$$\rho_2(t) = -C_1\left[(\hat{\phi}_1(t)+\hat{\phi}_1^*(t))+\left(\frac{1}{\hat{\phi}_1(t)}+\frac{1}{\hat{\phi}_1^*(t)}\right)\right] + iC_2\left[(\hat{\phi}_1(t)-\hat{\phi}_1^*(t))+\left(\frac{1}{\hat{\phi}_1(t)}-\frac{1}{\hat{\phi}_1^*(t)}\right)\right] - C_3[(\hat{W}(t)+\hat{W}^*(t))+(\hat{W}_1(t)+\hat{W}_1^*(t))] + iC_4[(\hat{W}(t)-\hat{W}^*(t))+(\hat{W}_1(t)-\hat{W}_1^*(t))],$$
$$\rho_1^1(t) = A_1\left[(\hat{\phi}_1(t)+\hat{\phi}_1^*(t))-\left(\frac{1}{\hat{\phi}_1(t)}+\frac{1}{\hat{\phi}_1^*(t)}\right)\right] - iA_2\left[(\hat{\phi}_1(t)-\hat{\phi}_1^*(t))-\left(\frac{1}{\hat{\phi}_1(t)}-\frac{1}{\hat{\phi}_1^*(t)}\right)\right] \tag{28}$$

$$+ A_3[(\hat{W}(t) + \hat{W}^*(t)) - (\hat{W}_1(t) + \hat{W}_1^*(t))]$$

$$- iA_4[(\hat{W}(t) - \hat{W}^*(t)) - (\hat{W}_1(t) - \hat{W}_1^*(t))].$$

In formula (28), the asterisk denotes complex conjugation, and the coefficients C_{1-4} and A_{1-4} are certain constants that will be defined below.

Expressions (28) for the charge densities ρ_2 and ρ_1^1 exhibit required behavior at all points $t_{N,M}$ and possess the symmetry properties (11) and (12) under the substitution of $1 - t$ for t. Therefore, one may hope that, even if these functions do not provide an exact solution to Eqs. (9), they may serve as a good approximation to the exact solution uniformly throughout the range of variation of Z.

Now, let us pass to the calculation of the coefficients C_{1-4} and A_{1-4}. First of all, note that, in the neighborhood of the singularity $t^{2\kappa}$, the expansion is carried out in even powers of t. This means that the quantity L (see (19)) is equal to 1, and, hence, $\tilde{\kappa} = \kappa + 2$. The vanishing of the coefficients of $t^{2\kappa}$ and $t^{2\kappa+2}$ in the expressions for ρ_2 and ρ_1^1 yields four equations for the coefficients C_{1-4} and A_{1-4}. Two equations are derived from the solvability condition (14). Another equation can be obtained by integrating the first (or second) equation in (9) with respect to t_1 over the interval (0, 1). Finally, the last (eighth) equation is chosen in such a way that the functions $\rho_{1,2}$ defined by Eqs. (28) should provide the best approximation to the exact solution of the system of equations (9).

Let us introduce eight functions G_{1-4} and $\hat{F}_{1-4}$ of parameter κ by the following relations:

$$G_1 = \int_0^1 dt(\hat{\phi}_1(t) + \hat{\phi}_1^*(t)), \quad G_3 = -i\int_0^1 dt(\hat{\phi}_1(t) - \hat{\phi}_1^*(t)),$$
$$\hat{F}_1 = \int_0^1 dt(\hat{W}(t) + \hat{W}^*(t)), \quad \hat{F}_3 = -i\int_0^1 dt(\hat{W}(t) - \hat{W}^*(t)), \tag{29}$$

$$\begin{pmatrix} G_2 \\ G_4 \\ \hat{F}_2 \\ \hat{F}_4 \end{pmatrix} = \sum_M \int_0^1 dt_1 \int_0^1 dt \frac{\tan\left(\frac{\pi}{2}(t+M)\right)}{\sinh^2\left(\frac{\pi}{\sqrt{3}}\left(\frac{M}{2} - t_1 + \frac{t}{2}\right)\right) + \cosh^2\left(\frac{\pi}{\sqrt{3}}\left(\frac{M}{2} - t_1 + \frac{t}{2}\right)\right)\tan^2\left(\frac{\pi}{2}(M+t)\right)} \begin{pmatrix} \hat{\phi}_1(t) + \hat{\phi}_1^*(t) \\ -i(\hat{\phi}_1(t) - \hat{\phi}_1^*(t)) \\ \hat{W}(t) + \hat{W}^*(t) \\ -i(\hat{W}(t) - \hat{W}^*(t)) \end{pmatrix}.$$

Expression (29) for $G_{2,4}$ and $\hat{F}_{2,4}$ in (29) can be substantially simplified. Summing over M, we obtain

$$\begin{pmatrix} G_2 \\ G_4 \\ \hat{F}_2 \\ \hat{F}_4 \end{pmatrix} = 2\int_0^1 dt \int_0^\infty dt_1 \left(\frac{\tan\left(\frac{\pi t}{2}\right)}{\sinh^2\left(\frac{\pi t_1}{\sqrt{3}}\right) + \cosh^2\left(\frac{\pi t_1}{\sqrt{3}}\right)\tan^2\left(\frac{\pi t}{2}\right)} - \frac{\cot\left(\frac{\pi t}{2}\right)}{\sinh^2\left(\frac{\pi t_1}{\sqrt{3}}\right) + \cosh^2\left(\frac{\pi t_1}{\sqrt{3}}\right)\cot^2\left(\frac{\pi t}{2}\right)} \right)$$
$$\times \begin{pmatrix} \hat{\phi}_1(t) + \hat{\phi}_1^*(t) \\ -i(\hat{\phi}_1(t) - \hat{\phi}_1^*(t)) \\ \hat{W}(t) + \hat{W}^*(t) \\ -i(\hat{W}(t) - \hat{W}^*(t)) \end{pmatrix} = \sqrt{3}\int_0^1 dt(1-2t) \begin{pmatrix} \hat{\phi}_1(t) + \hat{\phi}_1^*(t) \\ -i(\hat{\phi}_1(t) - \hat{\phi}_1^*(t)) \\ \hat{W}(t) + \hat{W}^*(t) \\ -i(\hat{W}(t) - \hat{W}^*(t)) \end{pmatrix}. \tag{30}$$

Substituting expression (28) for the charge density ρ_2 into (10), we obtain the following expression for the effective conductivity in terms of the coefficients C_{1-4}:

$$\frac{\sigma_{\text{eff}}}{\sqrt{\sigma_1\sigma_2}} = \frac{4\pi}{Z}\sqrt{1-Z^2} \times [(C_1G_1 + C_2G_3) + (C_3\hat{F}_1 + C_4\hat{F}_3)]. \quad (31)$$

As we noted above, there exist seven natural equations for eight coefficients A_{1-4} and C_{1-4}. This system of seven equations defines a one-parameter family of functions $\rho_{1,2}$ (see (28)). Along with this family of functions, we also consider the family of functions $\rho_{1,2}^{(\text{it})}$ that represents the first iteration of the system of equations (9) with respect to the functions $\rho_{1,2}$ of zero-order approximation. As the norm S, we choose a functional of the form

$$S = \int_0^1 dt\{\left|\rho_2 - \rho_2^{(\text{it})}\right| + \left|\rho_1 - \rho_1^{(\text{it})}\right|\}. \quad (32)$$

The value of the free parameter is chosen from the minimum condition for the functional S:

$$\delta S = 0. \quad (33)$$

The final expression for the functions $\rho_{1,2}$ is independent of the choice of the free parameter.

To derive the other seven equations, we have to use the expansion of the functions $\hat{\phi}_{1,2}(t)$ in the domain $0 < t \ll 1$ up to the fourth-order terms. To facilitate the calculations, we will use the general properties of meromorphic elliptic functions. Suppose that ψ is an elliptic function that has one zero and one second-order pole in the parallelogram of periods and can be expanded as

$$\psi = \frac{a}{t^2} + b + ct^2 + \ldots \quad (34)$$

in the neighborhood of the pole. Then, the function $\psi(t)$ is a solution to the equation

$$\psi^3 - \frac{a}{4}(\psi')^2 - 3b\psi^2 - (5ac - 3b^2)\psi = 0. \quad (35)$$

In our case, the function $\psi(t)$ also satisfies the relation

$$\psi(1-t) = 1/\psi(t). \quad (36)$$

Formulas (35) and (36) also imply that, in this case, the coefficient c is given by

$$c = \frac{3b^2 - 1}{5a} \quad (37)$$

and, consequently, ψ satisfies the equation

$$\psi^3 - \frac{a}{4}(\psi')^2 - 3b\psi^2 + \psi = 0. \quad (38)$$

Equation (38) substantially facilitates the determination of the Taylor expansion coefficients of the function $\psi(t)$.

Now, let us consider the function $\phi_1(t)$. In the domain $t \ll 1$, we determine the first two terms in the Laurent series expansion of the function $\phi_1(t)$ from formula (22) and recover the third term by formula (37):

$$\phi_1(t) = \frac{R_1 e^{i\gamma_1}}{t^2}[1 + R_2 e^{i\gamma_2}t^2 + R_3 e^{i\gamma_3}t^4], \quad (39)$$

where

$$R_1 e^{i\gamma_1} = \frac{1}{\pi^2}\left(\frac{\sum_{N=1}^{\infty}\exp\left(-\frac{\pi\sqrt{3}}{4}\left(N-\frac{1}{2}\right)^2\right)\exp\left(\frac{i\pi}{4}N(N-1)\right)}{\sum_{N=1}^{\infty}(-1)^{N+1}\left(N-\frac{1}{2}\right)\exp\left(-\frac{\pi\sqrt{3}}{4}\left(N-\frac{1}{2}\right)^2\right)\exp\left(\frac{i\pi}{4}N(N-1)\right)}\right)^2,$$

$$R_2 e^{i\gamma_2} = -\pi^2\left[\frac{\sum_{N=1}^{\infty}\left(N-\frac{1}{2}\right)^2\exp\left(-\frac{\pi\sqrt{3}}{4}\left(N-\frac{1}{2}\right)^2\right)\exp\left(\frac{i\pi}{4}N(N-1)\right)}{\sum_{N=1}^{\infty}\exp\left(-\frac{\pi\sqrt{3}}{4}\left(N-\frac{1}{2}\right)^2\right)\exp\left(\frac{i\pi}{4}N(N-1)\right)}\right. \quad (40)$$

$$\left. -\frac{1}{3}\frac{\sum_{N=1}^{\infty}(-1)^{N+1}\left(N-\frac{1}{2}\right)^3\exp\left(-\frac{\pi\sqrt{3}}{4}\left(N-\frac{1}{2}\right)^2\right)\exp\left(\frac{i\pi}{4}N(N-1)\right)}{\sum_{N=1}^{\infty}(-1)^{N+1}\left(N-\frac{1}{2}\right)\exp\left(-\frac{\pi\sqrt{3}}{4}\left(N-\frac{1}{2}\right)^2\right)\exp\left(\frac{i\pi}{4}N(N-1)\right)}\right],$$

$$R_3 e^{i\gamma_3} = \frac{1}{5}[3R_2^2 e^{2i\gamma_2} - R_1^{-2}e^{-2i\gamma_1}].$$

Using the explicit expressions for the theta functions ($\tau = 2$, $\tau' = 3e^{i\pi/3}$) given in Appendix A, we find the first two terms in the Laurent series expansion of the function

$$\left(\vartheta_1\left(\frac{1-t}{\tau}\right)\Big/\vartheta_1\left(\frac{t}{\tau}\right)\right)^2.$$

As above, the third term is recovered by formula (37):

$$\left(\frac{\vartheta_1\left(\frac{1-t}{\tau}\right)}{\vartheta_1\left(\frac{t}{\tau}\right)}\right)^2 = \frac{D_1 e^{i\varphi_1}}{t^2}(1 + D_2 e^{i\varphi_2} t^2 + D_3 e^{i\varphi_3} t^4), \quad (41)$$

where

$$D_1 e^{i\varphi_1} = \frac{1}{\pi^2}\left(\frac{\sum_{N=1}^{\infty}\exp\left(-\frac{\pi 3\sqrt{3}}{4}\left(N-\frac{1}{2}\right)^2\right)\exp\left(\frac{i3\pi}{4}N(N-1)\right)}{\sum_{N=1}^{\infty}(-1)^{N+1}\left(N-\frac{1}{2}\right)\exp\left(-\frac{\pi 3\sqrt{3}}{4}\left(N-\frac{1}{2}\right)^2\right)\exp\left(\frac{i3\pi}{4}N(N-1)\right)}\right)^2, \quad (42)$$

$$D_2 e^{i\varphi_2} = -\pi^2\left[\frac{\sum_{N=1}^{\infty}\left(N-\frac{1}{2}\right)^2\exp\left(-\frac{\pi 3\sqrt{3}}{4}\left(N-\frac{1}{2}\right)^2\right)\exp\left(\frac{i3\pi}{4}N(N-1)\right)}{\sum_{N=1}^{\infty}\exp\left(-\frac{\pi 3\sqrt{3}}{4}\left(N-\frac{1}{2}\right)^2\right)\exp\left(\frac{i3\pi}{4}N(N-1)\right)}\right.$$

$$\left. -\frac{1}{3}\frac{\sum_{N=1}^{\infty}\left(N-\frac{1}{2}\right)^3\exp\left(-\frac{\pi 3\sqrt{3}}{4}\left(N-\frac{1}{2}\right)^2\right)\exp\left(\frac{i3\pi}{4}N(N-1)\right)}{\sum_{N=1}^{\infty}(-1)^{N+1}\left(N-\frac{1}{2}\right)\exp\left(-\frac{\pi 3\sqrt{3}}{4}\left(N-\frac{1}{2}\right)^2\right)\exp\left(\frac{i3\pi}{4}N(N-1)\right)}\right],$$

$$D_3 e^{i\varphi_3} = \frac{1}{5}[3D_2^2 e^{2i\varphi_2} - D_1^{-2} e^{-2i\varphi_1}].$$

There exists a simple relation between the elliptic functions on the right-hand side of (24), which directly follows from the transformation formulas (26):

$$\frac{\vartheta_1\left(\frac{e^{i\pi/3}+t}{\tau}\right)}{\vartheta_1\left(\frac{1+e^{i\pi/3}+t}{\tau}\right)} = \frac{\vartheta_1\left(\frac{2e^{i\pi/3}-t}{\tau}\right)}{\vartheta_1\left(\frac{1+2e^{i\pi/3}-t}{\tau}\right)}. \quad (43)$$

The elliptic functions $\phi_2(t)/\phi_1(t)$, $\phi_2(t + e^{i\pi/3})/\phi_1(t)$, and $\phi_2(t + e^{2i\pi/3})/\phi_1(t)$ on the right-hand side of (24) differ only by a shift in the argument. Therefore, all these functions satisfy the same equation whose coefficients a and b are defined by formula (41):

$$a = D_1 e^{i\varphi_1}, \quad b = D_1 D_2 e^{i(\varphi_1+\varphi_2)}. \quad (44)$$

Hence, to determine the Taylor expansion coefficients of the function $\phi_2(t)/\phi_1(t)$ equal to

$$\left(\frac{e^{-i\pi/2}\vartheta_1\left(\frac{e^{i\pi/3}-t}{\tau}\right)}{\vartheta_1\left(\frac{1+e^{i\pi/3}-t}{\tau}\right)}\right)^2 = \mathcal{F}_0 e^{i\chi_0} \quad (45)$$

$$\times(1 + \mathcal{F}_1 e^{i\chi_1} t + \mathcal{F}_2 e^{i\chi_2} t^2 + \mathcal{F}_3 e^{i\chi_3} t^3 + \mathcal{F}_4 e^{i\chi_4} t^4),$$

it suffices to determine its value at $t = 0$. This is done in Appendix A. The values of the other coefficients are obtained by Eq. (38):

$$\mathcal{F}_1 e^{i\chi_1} = -\frac{2}{\sqrt{a}}\sqrt{-3b + \mathcal{F}_0 e^{i\chi_0} + \frac{1}{\mathcal{F}_0}e^{-i\chi_0}},$$

$$\mathcal{F}_2 e^{i\chi_2} = \frac{1}{a}\left(-6b + 3\mathcal{F}_0 e^{i\chi_0} + \frac{1}{\mathcal{F}_0}e^{-i\chi_0}\right),$$

$$\mathcal{F}_3 e^{i\chi_3} = -\frac{4}{a\sqrt{a}} \times \sqrt{-3b + \mathcal{F}_0 e^{i\chi_0} + \frac{1}{\mathcal{F}_0} e^{-i\chi_0}}(-b + \mathcal{F}_0 e^{i\chi_0}),$$

$$\mathcal{F}_4 e^{i\chi_4} = \frac{1}{a^2} \times \left[3 + 6b^2 - 15\mathcal{F}_0 e^{i\chi_0} + 5\mathcal{F}_0^2 e^{i\chi_0} - \frac{b}{\mathcal{F}_0} e^{-i\chi_0}\right]. \quad (46)$$

The numerical values of the coefficients R_i, D_i, $\mathcal{F}_i$, γ_i, φ_i, and χ_i are given in Appendix A. Separating the term having a singularity $\sim t^{-2\kappa}$ from expressions (28) for ρ_1^1 and ρ_2, we obtain the following relations for the coefficients A_i and C_i from Eq. (14):

$$\begin{aligned} &A_1\cos(\kappa\gamma_1) + A_2\sin(\kappa\gamma_1) \\ &+ A_3\left[2\mathcal{F}_0^{2\kappa}\cos(\kappa(\gamma_1 + 2\chi_0)) - \left(\frac{D_1}{R_1}\right)^{2\kappa}\cos(\kappa(\gamma_1 - 2\varphi_1))\right] \\ &+ A_4\left[2\mathcal{F}_0^{2\kappa}\sin(\kappa(\gamma_1 + 2\chi_0)) + \left(\frac{D_1}{R_1}\right)^{2\kappa}\sin(\kappa(\gamma_1 - 2\varphi_1))\right] \\ &= \frac{3}{2}Z\frac{\sin\left(\frac{\pi}{6} - \frac{\pi\kappa}{3}\right)}{\cos(\pi\kappa)}\left\{C_1\cos(\kappa\gamma_1) + C_2\sin(\kappa\gamma_1)\right. \\ &+ C_3\left[2\mathcal{F}_0^{2\kappa}\cos(\kappa(\gamma_1 + 2\chi_0)) + \left(\frac{D_1}{R_1}\right)^{2\kappa}\cos(\kappa(\gamma_1 - 2\varphi_1))\right] \\ &+ C_4\left[2\mathcal{F}_0^{2\kappa}\sin(\kappa(\gamma_1 + 2\chi_0)) - \left(\frac{D_1}{R_1}\right)^{2\kappa}\sin(\kappa(\gamma_1 - 2\varphi_1))\right]\Bigg\}. \end{aligned} \quad (47)$$

Up to terms of the fourth order in t, we obtain the following expressions for the functions $\hat{\phi}_1^{-1}$ and $\hat{\phi}_2^{-1}$ from formulas (24), (39), (41), and (45):

$$\begin{aligned} \hat{\phi}_1^{-1}(t) &= \frac{t^{2\kappa}}{R_1^\kappa}e^{-i\kappa\gamma_1}\left[1 - \kappa t^2 R_2 e^{i\gamma_2} + t^4\left(-\kappa R_3 e^{i\gamma_3} + \frac{\kappa(\kappa+1)}{2}R_2^2 e^{2i\gamma_2}\right)\right], \\ \hat{\phi}_1(t + e^{i\pi/3}) &= \frac{t^{2\kappa}}{R_1^\kappa}\left(\frac{R_1}{D_1}\right)^{2\kappa}e^{i\kappa(\gamma_1 - 2\varphi_1)} \times [1 + t^2\mathcal{P}_1 e^{i\alpha_1} + t^4\mathcal{P}_2 e^{i\alpha_2}], \\ \frac{1}{\hat{\phi}_2(t)} + \frac{1}{\hat{\phi}_2(t + e^{i\pi/3})} &= 2\frac{t^{2\kappa}}{R_1^\kappa}\frac{e^{-i\kappa(\gamma_1 + 2\chi_0)}}{\mathcal{F}_0^{2\kappa}} \times [1 + t^2 Q_1 e^{i\beta_1} + t^4 Q_2 e^{i\beta_2}]. \end{aligned} \quad (48)$$

The expressions for the coefficients $\mathcal{P}_i$, Q_i, α_i, and β_i in terms of R_i $\mathcal{F}_i$, D_i, γ_i, and χ_i are given in Appendix B. Using expressions (A.8) and (A.9) for the charge densities $\rho_1^1(t)$ and $\rho_2(t)$, we obtain the remaining five equations for the coefficients A_i and C_i. The first four equations are obtained from the vanishing of the coefficients of $t^{2\kappa}$ and $t^{2\kappa+2}$ in the expressions for the charge densities ρ_1^1 and ρ_2, while the last equation follows from Eqs. (13) and (14):

$$\begin{aligned} &C_1\cos(\kappa\gamma_1) - C_2\sin(\kappa\gamma_1) \\ &+ C_3\left[\left(\frac{R_1}{D_1}\right)^{2\kappa}\cos(\kappa(\gamma_1 - 2\varphi_1)) + \frac{2}{\mathcal{F}_0^{2\kappa}}\cos(\kappa(\gamma_1 + 2\chi_0))\right] \\ &+ C_4\left[\left(\frac{R_1}{D_1}\right)^{2\kappa}\sin(\kappa(\gamma_1 - 2\varphi_1)) - \frac{2}{\mathcal{F}_0^{2\kappa}}\sin(\kappa(\gamma_1 + 2\chi_0))\right] = 0, \\ &-\kappa R_2 C_1\cos(\kappa\gamma_1 - \gamma_2) + \kappa R_2 C_2\sin(\kappa\gamma_1 - \gamma_2) \\ &+ C_3\left[\left(\frac{R_1}{D_1}\right)^{2\kappa}\mathcal{P}_1\cos(\kappa(\gamma_1 - 2\varphi_1) + \alpha_1) + \frac{2}{\mathcal{F}_0^{2\kappa}}Q_1\cos(\kappa(\gamma_1 + 2\chi_0) - \beta_1)\right] \\ &+ C_4\left[\left(\frac{R_1}{D_1}\right)^{2\kappa}\mathcal{P}_1\sin(\kappa(\gamma_1 - 2\varphi_1) + \alpha_1) - \frac{2}{\mathcal{F}_0^{2\kappa}}Q_1\sin(\kappa(\gamma_1 + 2\chi_0) - \beta_1)\right] = 0, \\ &-A_1\cos(\kappa\gamma_1) + A_2\sin(\kappa\gamma_1) \end{aligned}$$

$$+A_3\left[\left(\frac{R_1}{D_1}\right)^{2\kappa}\cos(\kappa(\gamma_1-2\varphi_1))\right.$$

$$\left.-\frac{2}{\mathscr{F}_0^{2\kappa}}\cos(\kappa(\gamma_1+2\chi_0))\right]$$

$$+A_4\left[\left(\frac{R_1}{D_1}\right)^{2\kappa}\sin(\kappa(\gamma_1-2\varphi_1))\right.$$

$$\left.+\frac{2}{\mathscr{F}_0^{2\kappa}}\sin(\kappa(\gamma_1+2\chi_0))\right]=0,$$

$$\kappa A_1R_2\cos(\kappa\gamma_1-\gamma_2)-\kappa R_2A_2\sin(\kappa\gamma_1-\gamma_2)$$

$$+A_3\left[\left(\frac{R_1}{D_1}\right)^{2\kappa}\mathscr{P}_1\cos(\kappa(\gamma_1-2\varphi)+\alpha_1)\right.\qquad(49)$$

$$\left.-\frac{2}{\mathscr{F}_0^{2\kappa}}Q_1\cos(\kappa(\gamma_1+2\chi_0)-\beta_1)\right]$$

$$+A_4\left[\left(\frac{R_1}{D_1}\right)^{2\kappa}\mathscr{P}_1\sin(\kappa(\gamma_1-2\varphi_1)+\alpha_1)\right.$$

$$\left.+\frac{2}{\mathscr{F}_0^{2\kappa}}Q_1\sin(\kappa(\gamma_1+2\chi_0)-\beta_1)\right]=0,$$

$$-A_1\left[-\kappa R_3\cos(\kappa\gamma_1-\gamma_3)+\frac{\kappa(\kappa+1)}{2}R_2^2\cos(\kappa\gamma_1-2\gamma_2)\right]$$

$$+A_2\left[-\kappa R_3\sin(\kappa\gamma_1-\gamma_3)+\frac{\kappa(\kappa+1)}{2}R_2^2\sin(\kappa\gamma_1-2\gamma_2)\right]$$

$$+A_3\left[\left(\frac{R_1}{D_1}\right)^{2\kappa}\mathscr{P}_2\cos(\kappa(\gamma_1-2\varphi_1)+\alpha_2)\right.$$

$$\left.-\frac{2}{\mathscr{F}_0^{2\kappa}}Q_2\cos(\kappa(\gamma_1+2\chi_0)-\beta_2)\right]$$

$$+A_4\left[\left(\frac{R_1}{D_1}\right)^{2\kappa}\mathscr{P}_2\sin(\kappa(\gamma_1-2\varphi_1)+\alpha_2)\right.$$

$$\left.+\frac{2}{\mathscr{F}_0^{2\kappa}}Q_2\sin(\kappa(\gamma_1+2\chi_0)-\beta_2)\right]$$

$$=\frac{3Z}{2}\frac{\sin\left(\frac{\pi}{6}-\frac{\pi\kappa}{3}\right)}{\cos(\pi\kappa)}\left\{C_1\left[-\kappa R_3\cos(\kappa\gamma_1-\gamma_3)\right.\right.$$

$$\left.+\frac{\kappa(\kappa+1)}{2}R_2^2\cos(\kappa\gamma_1-2\gamma_2)\right]$$

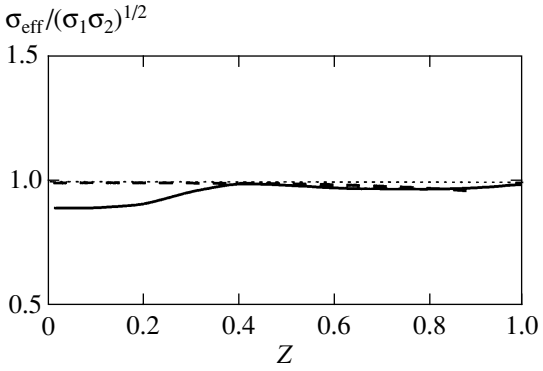

Fig. 2. The ratio $\sigma_{\text{eff}}/\sqrt{\sigma_1\sigma_2}$ as a function of parameter Z (solid curve) for the solution defined by (28) and (dashed curve) the result obtained by the first iteration of functions (28).

$$-C_2\left[-\kappa R_3\sin(\kappa\gamma_1-\gamma_3)+\frac{\kappa(\kappa+1)}{2}R_2^2\sin(\kappa\gamma_1-2\gamma_2)\right]$$

$$+\left[\left(\frac{R_1}{D_1}\right)^{2\kappa}\mathscr{P}_2\cos(\kappa(\gamma_1-2\varphi_1)+\alpha_2)\right.$$

$$\left.+\frac{2}{\mathscr{F}_0^{2\kappa}}Q_2\cos(\kappa(\gamma_1+2\chi_0)-\beta_2)\right]$$

$$+C_4\left[\left(\frac{R_1}{D_1}\right)^{2\kappa}\mathscr{P}_2\sin(\kappa(\gamma_1-2\varphi_1)+\alpha_2)\right.$$

$$\left.\left.-\frac{2}{\mathscr{F}_0^{2\kappa}}Q_2\sin(\kappa(\gamma_1+2\chi_0)-\beta_2)\right]\right\}.$$

The functions $\rho_{1,2}$ defined by Eqs. (28) do not represent an exact solution to system (9). Nevertheless, they provide a very good approximation to the exact solution for any value of the parameter Z. Figure 2 represents the ratio $\sigma_{\text{eff}}/\sqrt{\sigma_1\sigma_2}$ as a function of Z for the solution defined by formula (28) (solid curve). For the exact solution, this ratio is independent of Z and identically equal to unity. Using (28) as the zero-order approximation, we obtain its first iteration by the system of equations (9). The expression for $\sigma_{\text{eff}}/\sqrt{\sigma_1\sigma_2}$ obtained with the use of these functions is shown in Fig. 2; the dashed curve corresponds to the first iteration. Figures 3 and 4 represent the functions $\tilde{\rho}_{1,2}$ for the values $Z = 0.2, 0.4, 0.6, 0.8$ (solid curves) defined by formulas (28) (zero-order approximation) and (dashed curves) the results of the first iteration. We also present the values of the coefficients A_{1-4} and C_{1-4} at the points $Z = \{0.2, 0.4, 0.6, 0.8\}$.

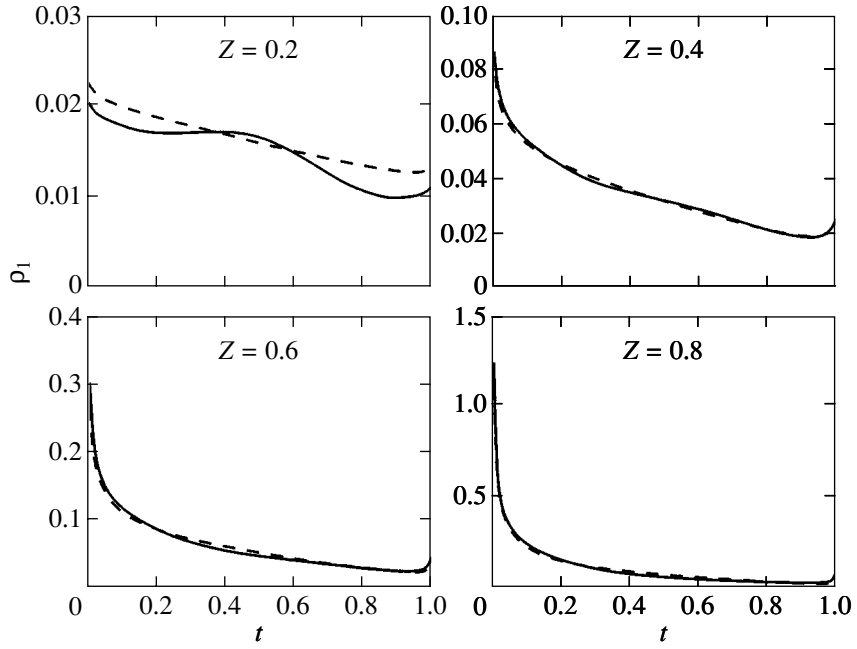

Fig. 3. Function $\tilde{\rho}_1$ for $Z = \{0.2, 0.4, 0.6, 0.8\}$ (solid curve) defined by formula (28) and (dashed curve) the result of the first iteration.

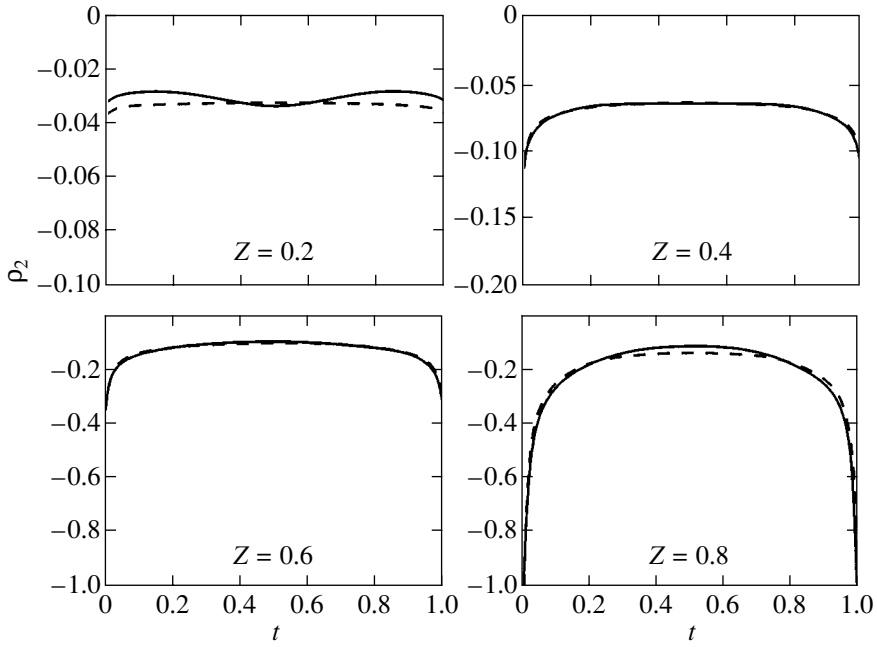

Fig. 4. Function $\tilde{\rho}_2$ for $Z = \{0.2, 0.4, 0.6, 0.8\}$ (solid curve) defined by formula (28) and (dashed curve) the result of the first iteration.

3. CONCLUSION

The conductivity and the distributions of charge, current density, and electric field are analyzed in a two-component system composed of regular triangles. An efficient method is proposed for investigating the properties of two-component systems that is based on the application of elliptic functions. This method admits a generalization to multicomponent systems.

The presence of corner points leads to a singular distribution of the charge density. Therefore, the conventional perturbation theory is inefficient. The method proposed in this paper (see also [3]) correctly takes into

Coefficients A_{1-4} and C_{1-4} at the points $Z = \{0.2, 0.4, 0.6, 0.8\}$

Z	A_1	A_2	A_3	A_4	C_1	C_2	C_3	C_4
0.2	544.796	−95.428	−544.756	95.545	−11368.274	−1673.776	3789.333	−663.774
0.4	70.423	−60.533	−70.353	60.661	−766.805	−289.381	255.505	−218.651
0.6	7.124	−13.678	−7.090	13.791	−49.934	−36.644	16.617	−32.006
0.8	0.964	−3.208	−0.943	3.305	−6.685	−8.223	2.220	−7.718

consideration all specific features arising in the charge-density distribution. The functions $\rho_{1,2}$ (see (28)) are double-periodic analytic functions of the variable t with the periods $(1/2 \pm i\sqrt{3}/2)$ associated with the structure of the system. The basis of doubly periodic functions used in this study can easily be extended. Nevertheless, the minimal basis used for constructing the functions $\rho_{1,2}$ allows one to determine the functions $\rho_{1,2}$ to a high degree of accuracy and provides a good first-order approximation for the iterative procedure.

ACKNOWLEDGMENTS

This work was supported by the CRDF (grant no. RP1-2251) and the Russian Foundation for Basic Research (project no. 00-02-17729a).

APPENDIX

Appendix A

Let us derive an explicit expression for the four theta functions used in Eq. (24). From formula (21), we obtain

$$\tau = 2, \quad \tau' = 3\exp\left(\frac{i\pi}{3}\right), \tag{A.1}$$

$$\vartheta_1\left(\frac{t}{\tau}\right)\Big/\exp\left(\frac{3i\pi}{16}\right) = 2\sum_{N=1}^{\infty}(-1)^{N+1}S_N \times \sin\left(\pi\left(N-\frac{1}{2}\right)t\right)[\cos T_N + i\sin T_N],$$

$$\vartheta_1\left(\frac{1-t}{\tau}\right)\Big/\exp\left(\frac{3i\pi}{16}\right) = 2\sum_{N=1}^{\infty}(-1)^{N+1}S_N \times \sin\left(\pi\left(N-\frac{1}{2}\right)(1-t)\right)[\cos T_N + i\sin T_N],$$

$$\vartheta_1\left(\frac{\exp\left(\frac{i\pi}{3}-t\right)}{\tau}\right)\Big/\exp\left(\frac{3i\pi}{16}\right)$$

$$= \sum_{N=1}^{\infty}(-1)^N S_N\left\{\left[\exp\left(\frac{\pi\sqrt{3}}{2}\left(N-\frac{1}{2}\right)\right)\times\sin\left(T_N-\pi\left(N-\frac{1}{2}\right)\left(\frac{1}{2}-t\right)\right)\right.\right.$$

$$-\exp\left(-\frac{\pi\sqrt{3}}{2}\left(N-\frac{1}{2}\right)\right)\times\sin\left(T_N+\pi\left(N-\frac{1}{2}\right)\left(\frac{1}{2}-t\right)\right)\Big]$$

$$-i\left[\exp\left(\frac{\pi\sqrt{3}}{2}\left(N-\frac{1}{2}\right)\right)\times\cos\left(T_N-\pi\left(N-\frac{1}{2}\right)\left(\frac{1}{2}-t\right)\right)\right.$$

$$\left.\left.-\exp\left(-\frac{\pi\sqrt{3}}{2}\left(N-\frac{1}{2}\right)\right)\times\cos\left(T_N+\pi\left(N-\frac{1}{2}\right)\left(\frac{1}{2}-t\right)\right)\right]\right\},$$

$$\vartheta_1\left(\frac{1+\exp\left(\frac{i\pi}{3}\right)-t}{\tau}\right)\Big/\exp\left(\frac{3i\pi}{16}\right)$$

$$= \sum_{N=1}^{\infty}(-1)^{N+1}S_N\left\{\left(\exp\frac{\pi\sqrt{3}}{2}\left(N-\frac{1}{2}\right)\right)\times\sin\left(T_N+\pi\left(N-\frac{1}{2}\right)\left(\frac{1}{2}+t\right)\right)\right.$$

$$\left.-\exp\left(-\frac{\pi\sqrt{3}}{2}\left(N-\frac{1}{2}\right)\right)\times\sin\left(T_N-\pi\left(N-\frac{1}{2}\right)\left(\frac{1}{2}+t\right)\right)\right]$$

$$- i\Big[\exp\Big(\frac{\pi\sqrt{3}}{2}\Big(N-\frac{1}{2}\Big)\Big)$$

$$\times\cos\Big(T_N+\pi\Big(N-\frac{1}{2}\Big)\Big(\frac{1}{2}+t\Big)\Big)$$

$$-\exp\Big(-\frac{\pi\sqrt{3}}{2}\Big(N-\frac{1}{2}\Big)\Big)$$

$$\times\cos\Big(T_N-\pi\Big(N-\frac{1}{2}\Big)\Big(\frac{1}{2}+t\Big)\Big)\Big]\Big\},$$

where

$$S_N = \exp\Big(-\frac{\pi 3\sqrt{3}}{4}\Big(N-\frac{1}{2}\Big)^2\Big),$$
$$T_N = \frac{3\pi}{4}N(N-1). \tag{A.2}$$

The numerical calculation yields the following values of the coefficients R_i, γ_i, D_i, φ_i (39) and (41) and $\mathcal{F}_0$, χ_0 (45):

$$\begin{aligned} R_1 &= 0.39153, \quad R_2 = 2.9492,\\ R_3 &= 6.5232, \quad \gamma_1 = 0.5236,\\ \gamma_2 &= -2.0944, \quad \gamma_3 = 2.0944,\\ D_1 &= 0.40591, \quad D_2 = 1.6449,\\ D_3 &= 0.40591, \quad \varphi_1 = -0.0022821,\\ \varphi_2 &= -3.1407, \quad \varphi_3 = -0.0068458,\\ \mathcal{F}_0 &= 1.017408, \quad \chi_0 = -0.26294. \end{aligned} \tag{A.3}$$

Substituting D_i and φ_i into Eq. (43), we obtain the coefficients a and b by which we determine the coefficients $\mathcal{F}_i$ and χ_i (i = 1, 2, 3, 4) (45):

$$\begin{aligned} \mathcal{F}_3 &= 6.229212, \quad \mathcal{F}_2 = 19.52981,\\ \mathcal{F}_3 &= 51.3458, \quad \mathcal{F}_4 = 129.1729,\\ \chi_1 &= \pi, \quad \chi_2 = -0.066447,\\ \chi_3 &= 2.9838, \quad \chi_4 = 0.23792. \end{aligned} \tag{A.4}$$

Appendix B

Up to terms of the fourth order in t, from Eqs. (24) and (40) we obtain

$$\hat{\phi}_2(t+e^{i\pi/3}) = \frac{t^{2\kappa}}{R_1^\kappa}\Big(\frac{R_1}{D_1}\Big)^{2\kappa}\exp(i\kappa(\gamma_1-2\varphi_1)) \tag{A.5}$$
$$\times[1+R_2e^{i\gamma_2}t^2+R_3e^{i\gamma_3}t^4]^\kappa(1+D_2e^{i\varphi_2}t^2+D_3e^{i\varphi_3}t^4)^{-2\kappa}.$$

Comparing expression (45) with (A.5) for $\hat{\phi}_2(t+e^{i\pi/3})$, we obtain the following values of the parameters $\mathcal{P}_i$ and α_i:

$$\begin{aligned} \mathcal{P}_1e^{i\alpha_1} &= \kappa[R_2e^{i\gamma_2}-2D_2e^{i\varphi_2}],\\ \mathcal{P}_2e^{i\alpha_2} &= \kappa\Big[R_3e^{i\gamma_3}-2D_3e^{i\gamma_3}+\frac{\kappa-1}{2}R_2^2e^{2i\gamma_2}\\ &\quad -2\kappa R_2D_2e^{i(\gamma_2+\varphi_2)}+(2\kappa+1)D_2^2e^{2i\varphi_2}\Big]. \end{aligned} \tag{A.6}$$

The coefficients Q_i and β_i are obtained in a similar way from Eqs. (24), (44), and (45):

$$\begin{aligned} Q_1e^{i\beta_1} &= \kappa[-R_2e^{i\gamma_2}-2\mathcal{F}_2e^{i\chi_2}+(2\kappa+1)\mathcal{F}_1^2e^{2i\chi_1}],\\ Q_2e^{i\beta_2} &= \kappa\Big\{-R_3e^{i\gamma_3}-2\mathcal{F}_4e^{i\chi_4}+(2\kappa+1)\mathcal{F}_2^2e^{2i\chi_2}\\ &\quad +2(2\kappa+1)\mathcal{F}_1\mathcal{F}_3e^{i(\chi_1+\chi_3)}\\ &\quad -2(\kappa+1)(2\kappa+1)\mathcal{F}_1^2\mathcal{F}_2e^{i(2\chi_1+\chi_2)}\\ &\quad +\frac{(\kappa+1)(2\kappa+1)(2\kappa+3)}{6}\mathcal{F}_1^4e^{4i\chi_1}+2\kappa R_2\mathcal{F}_2e^{i(\chi_2+\gamma_2)}\\ &\quad -\kappa(2\kappa+1)R_2\mathcal{F}_1^2e^{i(\gamma_2+2\chi_1)}+\frac{\kappa+1}{2}R_2^2e^{2i\gamma_2}\Big\}. \end{aligned} \tag{A.7}$$

Let us determine the term proportional to $t^{2\kappa}$ in the expressions for the charge densities ρ_2 and ρ_1^1. From Eqs. (28) and (45), we obtain

$$\begin{aligned} \rho_2(t) \longrightarrow \frac{2t^{2\kappa}}{R_1^\kappa}\Big\{ & C_1\Big[\cos(\kappa\gamma_1)-\kappa t^2R_2\cos(\kappa\gamma_1-\gamma_2)\\ &+t^4\kappa\Big(-R_3\cos(\kappa\gamma_1-\gamma_3)+\frac{\kappa+1}{2}R_2^2\cos(\kappa\gamma_1-2\gamma_2)\Big)\Big]\\ &-C_2\Big[\sin(\kappa\gamma_1)-\kappa t^2R_2\sin(\kappa\gamma_1-\gamma_2)\\ &+t^4\kappa\Big(-R_3\sin(\kappa\gamma_1-\gamma_3)+\frac{\kappa+1}{2}R_2^2\sin(\kappa\gamma_1-2\gamma_2)\Big)\Big]\\ &+C_3\Big[\Big(\frac{R_1}{D_1}\Big)^{2\kappa}(\cos((\kappa(\gamma_1-2\varphi_1))\\ &+t^2\mathcal{P}_1\cos(\kappa(\gamma_1-2\varphi_1)+\alpha_1))\\ &+t^4\mathcal{P}_2\cos(\kappa(\gamma_1-2\varphi_1)+\alpha_2))\\ &+\frac{2}{\mathcal{F}_0^{2\kappa}}(\cos(\kappa(\gamma_1+2\chi_0))\\ &+Q_1t^2\cos(\kappa(\gamma_1+2\chi_0)-\beta_1) \end{aligned} \tag{A.8}$$

$$+ t^4 Q_2 \cos(\kappa(\gamma_1 + 2\chi_0) - \beta_2))\Big]$$

$$+ C_4\Big[\Big(\frac{R_1}{D_1}\Big)^{2\kappa}(\sin(\kappa(\gamma_1 - 2\varphi_1))$$

$$+ t^2\mathcal{P}_1\sin(\kappa(\gamma_1 - 2\varphi_1) + \alpha_1)$$

$$+ t^4\mathcal{P}_2\sin(\kappa(\gamma_1 - 2\varphi_1) + \alpha_2))$$

$$- \frac{2}{\mathcal{F}_0^{2\kappa}}(\sin(\kappa(\gamma_1 + 2\chi_0))$$

$$+ t^2 Q_1\sin(\kappa(\gamma_1 + 2\chi_0) - \beta_1)$$

$$+ t^4 Q_2\sin(\kappa(\gamma_1 + 2\chi_0) - \beta_2))\Big]\Big\},$$

$$\rho_1^1(t) \longrightarrow \frac{2t^{2\kappa}}{R_1^{2\kappa}}\Big\{-A_1\Big[\cos(\kappa\gamma_1) - \kappa R_2 t^2\cos(\kappa\gamma_1 - \gamma_2)$$

$$+ t^4\kappa\Big(-R_3\cos(\kappa\gamma_1 - \gamma_3) + \frac{\kappa+1}{2}R_2^2\cos(\kappa\gamma_1 - 2\gamma_2)\Big)\Big]$$

$$+ A_2\Big[\sin(\kappa\gamma_1) - \kappa R_2 t^2\sin(\kappa\gamma_1 - \gamma_2)$$

$$+ t^4\kappa\Big(-R_3\sin(\kappa\gamma_1 - \gamma_3) + \frac{\kappa+1}{2}R_2^2\sin(\kappa\gamma_1 - 2\gamma_2)\Big)\Big]$$

$$+ A_3\Big[\Big(\frac{R_1}{D_1}\Big)^{2\kappa}(\cos(\kappa(\gamma_1 - 2\varphi_1))$$

$$+ \mathcal{P}_1 t^2\cos(\kappa(\gamma_1 - 2\varphi_1) + \alpha_1)$$

$$+ t^4\mathcal{P}_2\cos(\kappa(\gamma_1 - 2\varphi_1) + \alpha_2))$$

$$- \frac{2}{\mathcal{F}_0^2}(\cos(\kappa(\gamma_1 + 2\chi_0))$$

$$+ t^2 Q_1\cos(\kappa(\gamma_1 + 2\chi_0) - \beta_1)$$

$$+ t^4 Q_2\cos(\kappa(\gamma_1 + 2\chi_0) - \beta_2))\Big]$$

$$+ A_4\Big[\Big(\frac{R_1}{D_1}\Big)^{2\kappa}(\sin(\kappa(\gamma_1 - 2\varphi_1)$$

$$+ \mathcal{P}_1 t^2\sin(\kappa(\gamma_1 - 2\varphi_1) + \alpha_1)$$

$$+ \mathcal{P}_2 t^4\sin(\kappa(\gamma_1 - 2\varphi_1) + \alpha_2))$$

$$+ \frac{2}{\mathcal{F}_0^{2\kappa}}(\sin(\kappa(\gamma_1 + 2\chi_0))$$

$$+ Q_1 t^2\sin(\kappa(\gamma_1 + 2\chi_0) - \beta_1)$$

$$+ Q_2 t^4\sin(\kappa(\gamma_1 + 2\chi_0) - \beta_2))\Big]\Big\}. \quad \text{(A.9)}$$

Expressions (A.8) and (A.9) have been used for deriving Eqs. (46) for the coefficients A_i and C_i.

REFERENCES

1. A. M. Dykhne, Zh. Éksp. Teor. Fiz. **59**, 110 (1970) [Sov. Phys. JETP **32**, 63 (1971)].
2. V. G. Marikhin, Pis'ma Zh. Éksp. Teor. Fiz. **71**, 391 (2000) [JETP Lett. **71**, 271 (2000)].
3. Yu. N. Ovchinnikov and A. M. Dyugaev, Zh. Éksp. Teor. Fiz. **117**, 1013 (2000) [JETP **90**, 881 (2000)].
4. I. M. Khalatnikov and A. Yu. Kamenshchik, Zh. Éksp. Teor. Fiz. **118**, 1456 (2000) [JETP **91**, 1261 (2000)].
5. M. A. Lavrent'ev and B. V. Shabat, *Methods of the Theory of Functions of a Complex Variable* (Fizmatgiz, Moscow, 1958).

Translated by I. Nikitin

Journal of Experimental and Theoretical Physics, Vol. 94, No. 1, 2002, pp. 22–25.
Translated from Zhurnal Éksperimental'noĭ i Teoreticheskoĭ Fiziki, Vol. 121, No. 1, 2002, pp. 31–34.

NUCLEI, PARTICLES, AND THEIR INTERACTION

The Effect of Diffraction-Induced Friction

A. Yu. Lavrenov
Moscow State University, Vorob'evy gory, Moscow, 119899 Russia
e-mail: anton@solst.phys.msu.su
Received September 18, 2001

Abstract—The effect of radiative friction emerging during the transverse motion of a screen with a slit relative to the luminous flux is considered. It is shown that the effect is associated with the diffraction of light. Although this effect is weak, it must be taken into consideration in high-precision measurements like those for detecting gravity waves. The effect is analyzed for various types of slits and in the framework of various diffraction modes. © *2002 MAIK "Nauka/Interperiodica".*

1. INTRODUCTION

During the last several decades, considerable advances were made in the theory of physical measurements. The methods developed in this field have made it possible to study new physical phenomena mainly related to quantum physics and to carry out experiments (such as the detection of gravity waves) which were formerly impossible. The following example illustrates the complexity of such a problem: the detection of gravity waves involves the measurement of the displacement of one of the mirrors by a distance on the order of 10^{-16} cm [1]. In high-precision measurements, the effects which could be formerly disregarded due to their smallness must be taken into account. One of such effects is diffraction-induced friction, which was introduced during an analysis of the Heisenberg microscope [2], where it limits considerably the sensitivity of the measuring circuit. The essence of this effect can be described as follows. Let a photon beam be incident on a moving screen with a slit. As a result of diffraction from the slit and the Doppler effect, photons acquire an additional momentum transferred in the direction of motion of the slit. In accordance with the momentum conservation principle, an equal and opposite momentum is transferred to the screen, resulting in friction. This effect is close to the Robertson–Poynting light friction [3, 4] observed for an astronomical object as a consequence of the Maxwell electromagnetic theory.

In [2], only the main principles of this effect were formulated. Subsequent discussions proved that a more rigorous analysis of this effect is required. This article is devoted to a detailed description of this effect. In Section 2, the basic equation for the diffraction-induced frictional force is derived. An analysis of the effect for various types of slits is carried out in Section 3 for two models of diffraction, which provide different descriptions of the radiation intensity for large diffraction angles.

2. BASIC EQUATION

We choose a laboratory frame of reference which is fixed relative to an observer (the quantities related to this frame are primed). As a model, we take an ideal conductor in the form of a flat thin screen lying in the plane $z' = 0$ with a narrow long slit cut in it along the y' axis. The slit width amounts to several wavelengths of the incident light (see figure). In such a formulation of the problem, diffraction effects are independent of y' and the light intensity is reduced to the solution of a 2D diffraction problem. A plane phonon beam incident along the normal to the screen will be defined by frequency ω_0'. In order to register the momentum, we mentally arrange a series of photodetectors around the slit for measuring the energy of photons incident on them. It is well known that the momentum and energy of photons are connected through the relation $p = E/c$ (c is the velocity of light). Consequently, the total momentum transferred to the screen by the luminous flux is given by

$$dp_x = -\frac{1}{c}\int \sin\Theta dE, \qquad (1)$$

where Θ is the smallest angle formed with the normal to the screen and the integral is taken over an arbitrary surface bounding the slit. The energy dE of the luminous flux hitting a detector during the time interval dt in the solid angle $d\Omega$ visible from the side of the slit is determined by the intensity of the light wave passing through the slit, $I(\Theta, \omega) = I(\Theta)\delta(\omega - \omega_0)$, through the relation

$$dE = I(\Theta, \omega)S\cos\Theta dt d\omega d\Omega. \qquad (2)$$

Here, S is the area of the slit and $S\cos\Theta$ is the area of the slit visible from the detector side. It is convenient to

carry out a further analysis for the case when the detectors are arranged at a large distance behind the slit so that the slit can be regarded as a point source with a given angular distribution of intensities $I(\Theta)$. In this approximation, light waves from light sources distributed over the surface of the slit propagate in parallel to an arbitrarily chosen detector (as in the Huygens–Fresnel diffraction model).

Let us now assume that the slit moves at a velocity $V \ll c$. In this approximation, we will omit the terms of the order of V^2/c^2 in subsequent calculations. We seek the force acting on the screen and proportional to V. This simplifies the calculations since the terms containing $\sqrt{1 - v^2/c^2}$, as well as the relativistic change in the width of the slit and the detectors, are disregarded in the transformations of the wave vector upon a transition to another frame of reference.

In the laboratory frame of reference, a diffraction pattern varying with time is formed around the slit; for this reason, it is convenient to pass to a reference frame in which the slit is stationary. In this frame of reference, a wave is incident on the screen at a small angle $\beta \approx V/c$ and the field distribution will be characterized by the intensity $I(\Theta, \beta)$. The force acting on the screen is given by

$$F_x = \frac{dp_x}{dt} = -K\int I(\Theta, \beta)\cos\Theta(\sin\Theta + \beta)d\Theta. \quad (3)$$

Here, $K = S\Delta\phi/c$, $\Delta\phi$ being the angular size of the detectors along the y axis. The second term in the parentheses in the integrand is the initial value of the photon momentum which would be transferred to an absorbing screen without a slit:

$$F_x^{\text{initio}} = -\frac{\beta W}{c},$$

where

$$W = K\int I(\Theta, \beta)\cos\Theta d\Theta$$

is the power of diffracted light. Photons that do not participate in diffraction create no frictional force; for this reason, the effect is referred to as diffraction-induced friction. Let us consider the change in formula (3) upon a transition to the laboratory frame of reference.

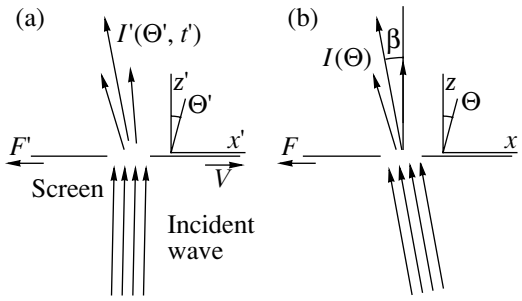

Schematic diagram of propagation of a light wave (a) in the laboratory frame of reference and (b) in a frame of reference where the slit is stationary.

In the laboratory frame, the photon frequency (energy) varies in different angular directions in accordance with the Doppler effect: $d\omega' = d\omega(1 + \beta\sin\Theta)$. Consequently, the force acting on the screen can be expressed through the angular distribution of intensity in a reference frame in which the slit is stationary as follows:

$$F_x' = -K\int I(\Theta, \beta)(\sin\Theta + \beta + \beta\sin^2\Theta)\cos\Theta d\Theta. \quad (4)$$

This expression includes only the force created by the wave passing through the slit and should be supplemented with the force created by the wave reflected from the surface of the screen (we consider the case of ideal reflection). According to [5], if we consider diffraction as radiation emitted from the screen edges, its intensity turns out to be the same in the half-planes in front of and behind the screen; consequently, the value of friction must be doubled:

$$F_x'^{\text{full}} = 2F_x'.$$

We will now analyze the coefficient of diffraction-induced friction (m is the mass of the screen),

$$\sigma = -\frac{F_x'^{\text{full}}}{mV} = \frac{W}{mc^2}\delta, \quad (5)$$

expressed in terms of an auxiliary coefficient δ which depends only on the intensity distribution of the diffraction pattern:

$$\delta = 2\frac{\int_{-\pi/2}^{\pi/2}\{I(\Theta, \beta)(1 + \sin^2\Theta) + I_\beta'(\Theta, \beta)\sin\Theta\}_{\beta = 0}\cos\Theta d\Theta}{\int_{-\pi/2}^{\pi/2} I(\Theta)\cos\Theta d\Theta}. \quad (6)$$

Since the diffraction-induced scattering of the wave is small, we can calculate the power of the diffracted wave behind the screen (the quantity in the denominator) confining ourselves to small diffraction angles; in this case, the dependence on β is insignificant.

In the next section, we will calculate the coefficient δ for two different types of slits in two models of diffraction.

3. FRICTION FOR DIFFERENT TYPES OF SLITS IN DIFFERENT DIFFRACTION MODELS

In order to determine the intensity of a light wave passing through the slit, we define the polarization of the vector field potential **A** along the y axis, $I \propto A_y^2$. This is essential since the choice of polarization affects the intensity distribution in some cases [5].

3.1. Fresnel Diffraction

Fresnel diffraction [3] is the simplest model of diffraction, in which the field at the point of observation is treated as a superposition of the fields created by point sources distributed over the surface of the slit (of width a). The intensity at a large distance from the slit, such that $a^2/\omega_0 r \ll 1$ (Fraunhofer approximation), is proportional to the Fourier transform of the transmission coefficient $T(x)$ of the slit:

$$I(\Theta, \beta) \propto \left| \int_{-\infty}^{\infty} T(x) e^{ikx(\sin\Theta + \beta)} dx \right|^2. \qquad (7)$$

It does not depend on the properties or thickness of the screen material.

Let us consider a slit with a Gaussian distribution of the transmission coefficient (as in the Heisenberg microscope [2]),

$$T(x) = e^{-x^2/2a^2}, \quad I \sim e^{-k_0^2 a^2(\sin\Theta + \beta)^2}, \quad k_0 = \frac{2\pi}{\omega_0}.$$

The field decreases rapidly and, hence, we can confine our analysis to small angles, setting $\sin\Theta \propto \Theta$. The coefficient

$$\delta \approx \frac{\sqrt{2}}{(k_0 a)^2} \qquad (8)$$

is proportional to the square of the diffraction angle.

A slit with sharp boundaries such that

$$T(x) = \begin{cases} 1, & -a \le x \le a \\ 0, & x < -a, \quad x > a \end{cases}$$

displays a different behavior. In this case, we have

$$I \propto \frac{\sin^2[k_0 a(\sin\Theta + \beta)]}{(\sin\Theta + \beta)^2}.$$

For a narrow slit ($k_0 a \ll 1$), we obtain $\delta = 2.7$. For a wide slit ($k_0 a \gg 1$), numerical calculations give the following dependence:

$$\delta = \frac{\xi_F}{k_0 a}, \qquad (9)$$

where the parameter $\xi_F(k_0 a)$ oscillates in the range of values from 0.6 to 1.9 with a period π.

3.2. Sommerfeld Diffraction

A more accurate expression for the intensity distribution can be obtained by representing the screen as an aggregate of infinitely thin wedges separated from one another by a distance a. For a perfectly conducting wedge, Sommerfeld solved the diffraction problem exactly [5]. The superposition with the solution for the second wedge leads to the following expression:

$$I \propto \frac{\sin^2[k_0 a(\sin\Theta + \beta)]}{\sin^2[(\Theta + \beta)/2]} + \frac{\cos^2[k_0 a(\sin\Theta + \beta)]}{\cos^2[(\Theta - \beta)/2]}.$$

For a narrow slit ($k_0 a \ll 1$), we obtain $\delta \approx 2$. For a wide slit, a numerical calculation leads to an expression similar to that in the Fresnel theory:

$$\delta = \frac{\xi_Z}{k_0 a}, \qquad (10)$$

where the parameter $\xi_Z(k_0 a)$ oscillates in the range from 2.1 to 2.2 with a period π. The discrepancy with the Fresnel theory is significant. This indicates that, while calculating the coefficient of diffraction-induced friction, one cannot confine the analysis to approximate models of diffraction.

A more accurate expression for intensity [5] in the case of a wide slit takes into account the effects of mutual diffraction at the screen edges, but contains corrections to ξ of the order of $(k_0 a)^{-1/2}$, which are insignificant for our analysis. For a narrow slit with $k_0 a \ll 1$, we have $I \propto \cos^2\Theta$. In this case, $\delta = 1.2$.

4. CONCLUSIONS

Let us consider a diffraction grating with a view of possible practical applications and for obtaining numerical estimates. The total intensity from several slits can be obtained by multiplying the intensity from one slit (calculated using a more accurate Sommerfeld theory) and the grating factor

$$\frac{\sin^2(N k_0 d \sin\Theta)}{\sin^2(k_0 d \sin\Theta)},$$

where d is the grating constant and N is the number of slits. A numerical analysis shows that for $N \gg 1$, the coefficient δ oscillates about the value of 2 and is virtually independent of d and N. The minimum value of $\delta \approx 0.1$ is attained for a slit width such that $k_0 a \approx 8.2$, while the maximum value of $\delta \approx 3.1$ is attained for $k_0 a \approx 11.2$. The amplitude of oscillations decreases monotonically upon an increase in $k_0 a$. Consequently, the average coefficient of diffraction-induced friction

$$\sigma \approx \frac{2W}{mc^2}$$

has a value that must be taken into account in high-precision measurements in an analysis of the motion of the diffraction grating in a luminous flux. For a screen of mass $m = 10^{-6}$ g and a laser of power $W = 1$ W creating a diffraction pattern, the coefficient of diffraction-induced friction $\sigma \sim 10^{-8}$ s^{-1}. It follows from this estimate that the inclusion of diffraction-induced friction becomes essential in an analysis of the motion of a diffraction grating in a luminous flux if the duration of high-precision measurements is several months or more.

ACKNOWLEDGMENTS

The author is grateful to S.P. Vyatchanin and K.A. Postnov, who contributed a lot to this publication.

REFERENCES

1. L. P. Grishchuk, V. M. Lipunov, K. A. Postnov, *et al.*, Usp. Fiz. Nauk **171**, 1 (2001).
2. S. P. Vyatchanin and A. Yu. Lavrenov, Phys. Lett. A **238**, 38 (1997).
3. J. H. Poynting, Philos. Trans. R. Soc. London, Ser. A **202**, 525 (1903).
4. H. P. Robertson, Mon. Not. R. Astron. Soc. **93**, 423 (1937).
5. H. Hönl, A. W. Maue, and K. Westpfahl, in *Handbuch der Physik*, Ed. by S. Flügge (Springer-Verlag, Berlin, 1961; Mir, Moscow, 1964), Vol. 25, Part 1, p. 218.

Translated by N. Wadhwa

Journal of Experimental and Theoretical Physics, Vol. 94, No. 1, 2002, pp. 26–36.
Translated from Zhurnal Éksperimental'noĭ i Teoreticheskoĭ Fiziki, Vol. 121, No. 1, 2002, pp. 35–46.

PLASMA, GASES

The Diffusion of Macroparticles and Criteria of Phase Transitions for Dust Structures in Weakly Ionized Plasma

O. S. Vaulina

Institute of High Energy Density, Institute of High Temperatures Scientific Association (IVTAN), Russian Academy of Sciences, Moscow, 127412 Russia

e-mail: idustpl@redline.ru

Received June 29, 2001

Abstract—The dynamics of charged particles is investigated under conditions close to those of experiments in a weakly ionized laboratory gas-discharge dust plasma. The existing phenomenological criteria of phase transitions for dust structures in such a plasma are treated, and new criteria are suggested. The parameters responsible for the order and scaling of dynamic processes in Yukawa dissipative systems are determined. The relation for the diffusion coefficient D of macroparticles in strongly correlated liquid structures is derived. © *2002 MAIK "Nauka/Interperiodica".*

1. INTRODUCTION

A dust plasma is a partially ionized gas containing micron-sized particles of condensed matter (dust). Dust particles in plasma may acquire electric charges and interact with one another. The combined effect of forces of interparticle interaction and dissipation processes may lead to the formation of steady-state dust structures (similar to liquid or solid), as well as to complex oscillatory or chaotic modes [1–10].

It is customary to assume that dust particles in a weakly ionized plasma interact with one another through the intermediary of a screened Coulomb potential (Yukawa potential),

$$\phi_D = \frac{eZ}{l}\exp\left(-\frac{l}{\lambda}\right), \quad (1)$$

where eZ is the dust particle charge, λ is the screening length, and l is the interparticle spacing. The properties of nonideal Yukawa systems are subjected to extensive numerical simulation studies [9–22]. The nonideality of dust plasma is usually characterized by the parameter Γ equal to the ratio of the potential energy of Coulomb interaction between neighboring particles to their kinetic temperature T,

$$\frac{(eZ)^2 n^{1/3}}{T}$$

(here, n is the dust concentration and T is measured in energy units). The numerical calculation results indicate that, at $\Gamma > 1$, the short-range order arises in the Coulomb system of particles, and the value of the critical nonideality parameter $\Gamma = \Gamma_c$ on the crystallization curve is close to 106 [16, 19–21]. The assumption of screened interaction given by Eq. (1) leads to an increase in the parameter Γ_c on the crystallization curve of dust systems. The phase diagram for Yukawa systems, obtained by way of generalization of the numerical simulation results [11–18], is given in Fig. 1. The simulation results demonstrate that the phase transitions in Yukawa systems are defined by two dimensionless parameters Γ and $\kappa = n^{-1/3}/\lambda$. However, the correlation $f(\Gamma, \kappa)$ relating these parameters to the quantity $\Gamma_c = \Gamma_c = f(\Gamma, \kappa)$ has not yet been obtained either for liquid–crystal phase transitions or for the transition between the body-centered cubic (bcc) lattice and face-centered cubic (fcc) structure. The authors of a number of publications restrict themselves to the introduction of linear approximations of the data of numerical simulation in different regions of the phase diagram [13, 15]. Such approximations result from the optimal mathematical fitting of the calculated points by the linear function and are not validated from the physical standpoint. The most successful of relevant papers [12] suggests the condition of constancy of the normalized value of the nonideality parameter as the criterion for melting of the bcc lattice,

$$\Gamma^* = (1 + \kappa + \kappa^2/2)\exp(-\kappa)\Gamma$$

($\Gamma_c^* \approx 106$). It has been demonstrated in [18] that the normalized value of Γ_c^* is almost independent of the ambient gas viscosity (friction coefficient of dust particles ν_{fr}). This fact is important because, in laboratory plasma-dust systems, the macroscopic particles find themselves in a viscous medium, where the dissipation due to collisions with gas atoms or molecules plays an important part.

The diffusion of macroparticles is the main transport process of mass transfer, which defines the energy loss (dissipation) in dust systems and their dynamic characteristics such as the phase state and the conditions of

wave propagation and of formation of dust instabilities. By using hydrodynamic approaches, one can obtain a successful description of the diffusion of macroparticles only in the case of short-range interactions. When the forces of interparticle interaction are not as small as in gases, the attempts at constructing a correct kinetic equation fail. The theory of diffusion in molecular liquid has been developing in two directions, one of which (more fundamental) leans upon the general principles of statistical physics. The other approach ("jump" theory) is based on analogies between liquid and solid and gives the following expression for the molecular diffusion coefficient [23]:

$$D_M = \frac{d^2}{6\tau_0}\exp\left(-\frac{W}{T}\right), \quad (2)$$

where d is the mean distance between particles, τ_0 is the characteristic time defining the frequency ν_0 of transitions of a particle from one "settled" state to another, and W is the energy barrier surmounted by the particle during those transitions. The exponential dependence of D_M on temperature T in molecular liquids is supported experimentally. A similar temperature dependence for the coefficient D of self-diffusion of macroparticles was found as a result of calculations for Yukawa dissipative systems [18]. The experimental verification of this result is hampered by the fact that a variation of any of the parameters of a plasma-dust system leads to a self-consistent variation of the remaining parameters defining the particle dynamics. The solution to this problem resides in determining simple functional dependences or approximations for the coefficients of self-diffusion of macroparticles in Yukawa systems, the search for which is an object of intensive investigations [22–28]. The value of diffusion coefficients for dissipative systems of macroparticles interacting with the screened potential given by Eq. (1) is of interest from the standpoint of both determining the dynamic characteristics of dust plasma and analyzing various kinetic processes in molecular biology, medicine, polymer chemistry, and so on [22–28]. Various approximations suggested at present for the coefficients of self-diffusion of macroparticles in Yukawa systems are based either on virial expansions for various thermodynamic functions such as effective viscosity η in the Einstein relation $D_0 = \eta T$ [25–27] or on analogies with critical phenomena in gases [22, 24]. In view of this, under certain conditions, the quantity D may be represented either by the sum of the first expansion terms,

$$D_0(1 + \zeta_0),$$

or as a power function of the form

$$\zeta_1 + \zeta_2(T/T_c - 1)^{\psi},$$

where T_c is the temperature at the melting point, and the parameters ζ_0, ζ_1, ζ_2, and ψ are determined for concrete

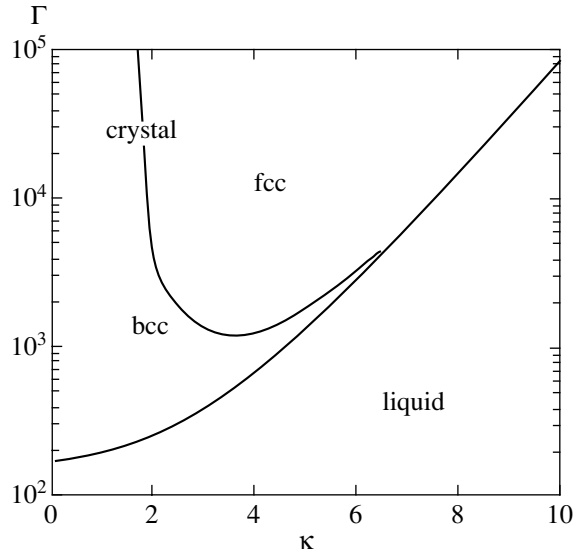

Fig. 1. The dependence of the Coulomb parameter Γ on κ on the phase curves, plotted by the results of different calculations [1–4].

conditions (n, eZ, κ, ν_{fr}) as a result of measurements or by numerical simulation.

I have investigated the criteria of various phase transitions and the processes of diffusion of interacting macroparticles in Yukawa dissipation systems with parameters close to the conditions of experiments in a weakly ionized laboratory gas-discharge dust plasma.

2. SIMULATION OF MACROPARTICLE DYNAMICS

A correct simulation of the motion of dust particles in a weakly ionized plasma calls for the use of the method of Brownian dynamics, which is based on the solution of a set of ordinary differential equations with the Langevin force $\mathbf{F}_{Br}$, allowing for random impacts by the surrounding gas molecules,

$$m_p\frac{d^2\mathbf{l}_k}{dt^2} = \sum_j F_{int}(l)\big|_{l=|\mathbf{l}_k-\mathbf{l}_j|}\frac{\mathbf{l}_k-\mathbf{l}_j}{|\mathbf{l}_k-\mathbf{l}_j|} - m_p\nu_{fr}\frac{d\mathbf{l}_k}{dt} + \mathbf{F}_{Br}, \quad (3)$$

where m_p is the particle mass, and the quantity

$$F_{int}(l) = -eZ\frac{\partial\phi_D}{\partial l}$$

describes the pair interparticle interaction in the system. For analyzing the macroparticle dynamics, three-dimensional equations of motion (3) were solved for periodic boundary conditions. The total number of particles in the system being simulated was $N_p = 125 \times 27$, where 125 is the number of independent particles

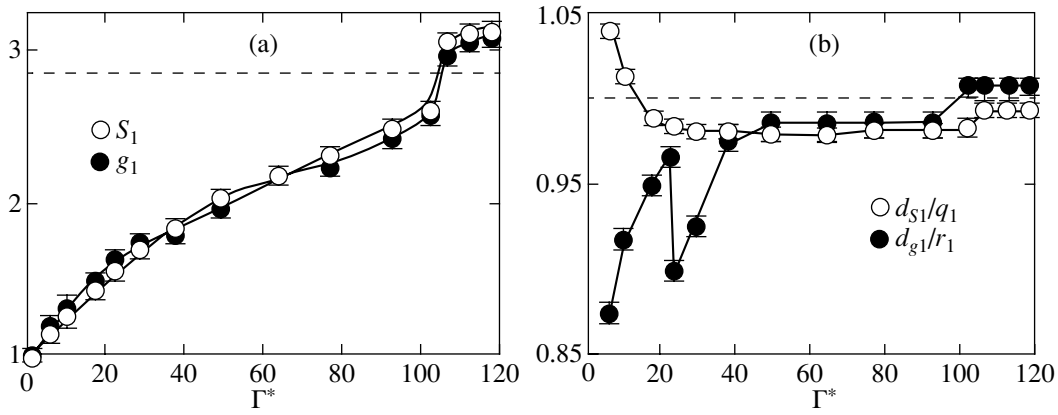

Fig. 2. (a) The first maxima of the structural factor S_1 and pair correlation function g_1 and (b) their relative positions d_{S1}/q_1 and d_{g1}/r_1 as functions of Γ* (the ranges of absolute deviations of the quantities for different cases of calculation are indicated: $\xi = 0.166$, 0.5; $\kappa = 2.4$, 4.8).

and 27 is the number of counting cells for the three-dimensional problem given by Eq. (3). The interaction potential was truncated at distances exceeding $4d$, where $d = n^{-1/3}$ is the mean interparticle spacing. The time step was selected to be

$$\Delta t = \min(1/\nu_{fr}, 1/\omega^*)/20,$$

where

$$\omega^* = eZ(n/m_p)^{1/2}(1 + \kappa + \kappa^2/2)^{1/2}\exp(-\kappa/2)$$

is the normalized dust frequency. The total count time varied from $2000/\nu_{fr}$ for $\nu_{fr} < \omega^*$ to $2000\nu_{fr}/\omega^{*2}$ for $\nu_{fr} > \omega^*$ and ranged from $2 \times 10^5 \Delta t$ to $2 \times 10^6 \Delta t$ for different parameters of the system. A more detailed description of the algorithm of the numerical experiment may be found in [18].

The coefficient of self-diffusion of macroparticles was treated as the quantity defining the dynamic behavior of a dust system,

$$D = \lim_{t\to\infty} D(t) = \frac{\langle\langle \mathbf{l}(t) - \mathbf{l}(0)\rangle_N^2\rangle_t}{6t}, \qquad (4)$$

where $\mathbf{l}(t)$ is the displacement of an individual particle, and $\langle\langle\rangle\rangle$ denotes averaging over the ensemble (N) and in time (t). The values of the diffusion coefficient D of dust particles were found for different values of the buffer gas pressure (ν_{fr}), the characteristic dust frequency ω^*, the dust temperature T, and the screening length λ ($\kappa = 2.4$, 4.8). The choice of the screening length for performing the calculations was governed by the condition necessary for correct simulation of the dynamics of Yukawa systems, i.e., the counting cell size $L \gg \lambda$ [11]. In our calculations,

$$L \approx 5n^{-1/3} > 12\text{–}24\lambda.$$

The correlation between the interparticle interaction and dissipation in the system was preassigned by the parameter

$$\xi = \frac{\omega^*}{\nu_{fr}} = \frac{eZ(n/m_p)^{1/2}(1 + \kappa + \kappa^2/2)^{1/2}\exp(-\kappa/2)}{\nu_{fr}}. \qquad (5)$$

The values of the latter parameter were selected proceeding from the results of analysis of experimental conditions in a gas-discharge plasma [1–10]. For the given conditions, the frequency of friction may be written in a free-molecular approximation [29],

$$\nu_{fr}[\text{s}] \approx C_V P[\text{Torr}]/(\rho[\text{g cm}^{-3}]r[\mu\text{m}]),$$

where r is the particle radius, ρ is the density of the material, P is the pressure, and C_V is some parameter defined by buffer gas neutrals (for example, $C_V \approx 840$ for argon and $C_V \approx 600$ for neon). The equilibrium charge of dust particles may be represented as [30]

$$Z \approx C_z r[\mu\text{m}]T_e[\text{eV}],$$

where T_e is the electron temperature, and $C_z \approx 2000$ for most experiments in inert gases. Then, for some averaged parameters ($\rho \approx 4$ g cm^{-3}, $T_e \approx 1.5$ eV, $C_V \approx 700$, $k \approx 2$), one can obtain the following estimate for the quantity defined by Eq. (5):

$$\xi \approx 10^{-3}(n[\text{cm}^{-3}]/r[\mu\text{m}])^{1/2}(P[\text{Torr}])^{-1}. \qquad (6)$$

From this, we derive the following range for particles of radius $r = 2.5$ μm (with their concentration n varying from 10^3 to 10^5 cm^{-3} and the gas pressure P varying from 1 to 0.01 Torr):

$$\xi = 0.02 \text{ to } 4.2.$$

In accordance with this range, the parameters of the system were varied in our numerical experiment (ξ = 0.055, 0.166, 0.5, 1.5, 4.5).

In order to analyze the formation of order in the systems being simulated, use was made of the pair correlation function $g(r)$ and structure factor $S(q)$. The dependence of the magnitude of the first maxima for these functions (q_1, S_1) and their positions ($r = d_{g1}$, $q = d_{S1}$) on the quantity Γ^* are given in Figs. 2a and 2b for different parameters of the system. An analysis of the results of these calculations reveals that the normalized parameter Γ^* fully defines the correlation of macroparticles (the emergence of both long-range and short-range orders in a dust system) and may be treated as the order parameter for a Yukawa dissipative system from $\Gamma^* < 1$ to the point of its crystallization. In the case of increasing parameter $\Gamma^* \longrightarrow \Gamma_c^*$, a body-centered crystal structure was formed. The position of the first maxima of the functions g_1 and S_1 for the crystal structure corresponded to a bcc lattice ($d_{g1} \approx r_1 = (3\sqrt{3}/4n)^{1/3}$, $d_{S1} \approx q_1 = 2\pi(\sqrt{2}\,n)^{1/3}$; see Fig. 2b) [31, 32].

The ratio of the diffusion coefficients D of charged particles to the diffusion coefficient $D_0 = T/n_{fr}m_p$ of noninteracting (Brownian) macroparticles for different values of κ and ξ is given in Fig. 3. One can see from this figure that the dynamics of highly nonideal systems ($\Gamma^* > 40$) is defined by two main parameters Γ^* and ξ, the latter of which may be treated as the scaling parameter for liquid dissipative systems.

3. DIFFUSION COEFFICIENT OF MACROPARTICLES IN STRONGLY CORRELATED LIQUID STRUCTURES

It should be recalled that the jump theory gives quite an adequate description for the diffusion coefficient D_M (2) of molecules in real liquids, and the diffusion coefficient D of macroparticles in highly nonideal Yukawa systems is exponentially dependent on the parameter Γ^* [18],

$$D \propto \exp(-c_1\Gamma^*/\Gamma_c^*).$$

As an illustration, Fig. 4 gives the dependence of D on Γ^* on a log scale. One can readily see that the $D(\Gamma^*)$ curves in the range of Γ^* from 102 to 50 are close to linear and exhibit identical slopes ($c_1 \approx$ const). We will take the value of the parameter Γ^* on the crystallization curve to correspond to that in the middle of the region of abrupt variation of the diffusion coefficient (Fig. 3), $\Gamma_c^* \sim 104.5$. Then, $c_1 \approx 3$ within $\pm 3\%$ for all parameters of the calculations of ξ and κ [18]. The jumps observed in Yukawa systems being simulated are illustrated in Fig. 5, which shows the difference in averaging the system over the ensemble,

$$\Delta_N = \sqrt{\frac{\langle \mathbf{l}(t) - \mathbf{l}(0)\rangle_N^2}{d^2}},$$

and over time,

$$\Delta_N^t = \sqrt{\frac{\langle\langle \mathbf{l}(t) - \mathbf{l}(0)\rangle_N^2\rangle_t}{d^2}},$$

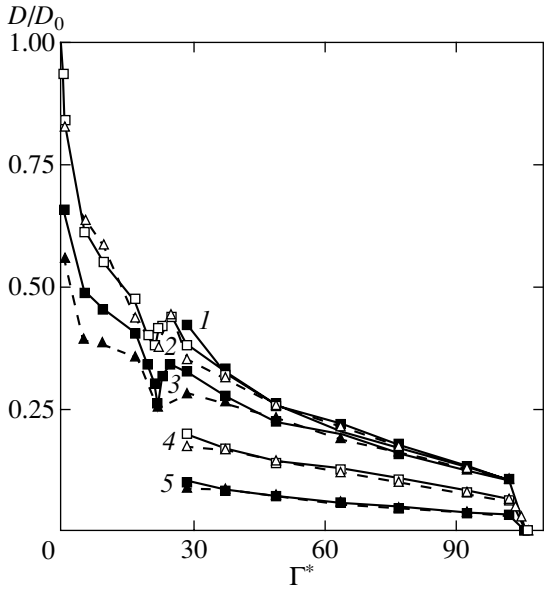

Fig. 3. The ratio of the coefficients D/D_0 as a function of the parameter Γ^* for different values of κ = 4.8 (triangles, broken curves) and 2.4 (squares, solid curves) and ξ = (*1*) 0.055, (*2*) 0.166, (*3*) 0.5, (*4*) 1.5, and (*5*) 4.5.

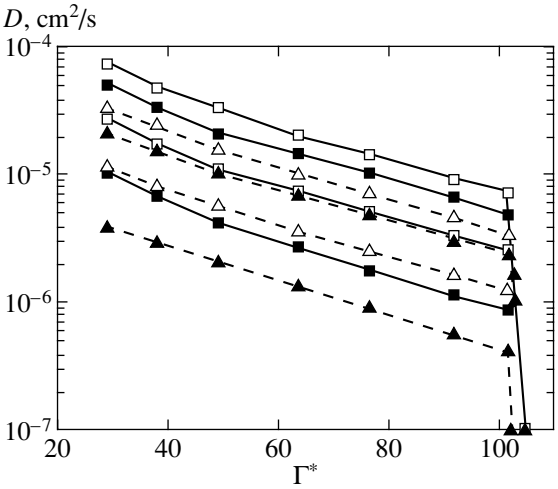

Fig. 4. The diffusion coefficient D as a function of the parameter Γ^* for κ = 2.4 (triangles) and 4.8 (squares).

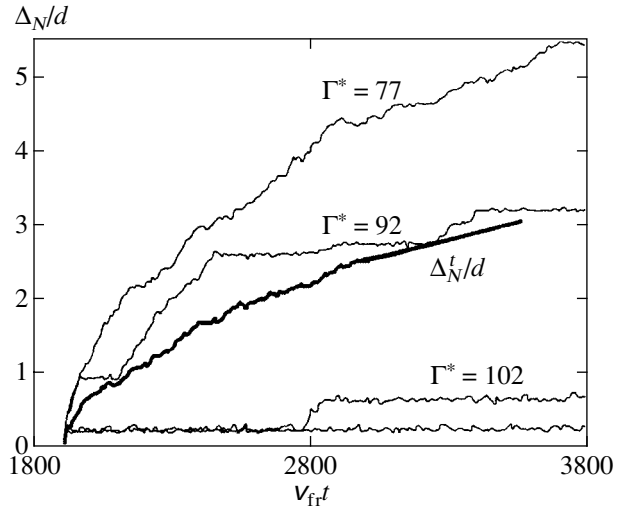

Fig. 5. The relative root-mean-square displacement Δ_N/d as a function of $\nu_{fr}t$ for an ensemble of dust particles with ξ = 0.5 and κ = 2.4. The solid curve indicates the case of averaging Δ_N in time (Δ_N^t) for Γ^* = 92.

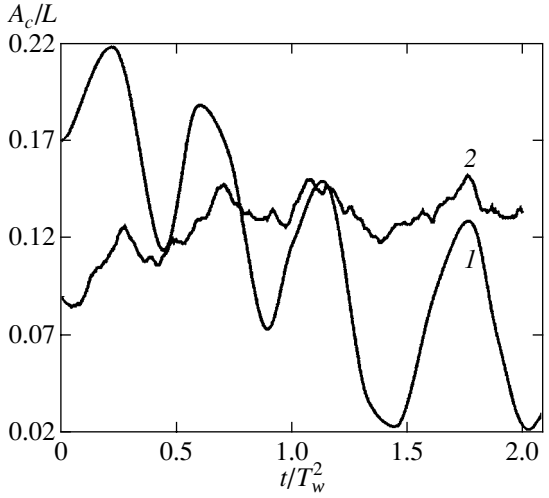

Fig. 6. The relative displacement of the center of mass A_c/L (L is the counting cell size) as a function of the ratio of time t to the vibrational period $T_w = 2\pi/w_f$, where $w_f = w^*/\sqrt{\pi}$, for the following values of parameters: (*1*) ξ = 1.5, Γ^* = 102, κ = 4.8; (*2*) ξ = 0.5, Γ^* = 92, κ = 2.4.

in the vicinity of the crystallization curve of the system. This difference disappears with decreasing parameter Γ^*, and the system being investigated becomes ergodic.

Therefore, the search for a simple empirical function for the value of the diffusion coefficient D of interacting particles may be based on the choice of a suitable value for the characteristic time τ_0 in relation (2). Assume that the characteristic frequency ν_0 of transition between neighboring settled states is defined by random collisions of particles with one another (at some characteristic frequency $\omega \approx c_2\omega^*$, where c_2 = const) and with molecules of ambient gas at the frequency ν_{fr}. We will further assume that the quantity $\tau_0 \approx 2/\nu_0$ may be written as

$$\tau_0 = \frac{2(\omega + \nu_{fr})}{\omega^2},$$

because the frequency ν_0 must tend to ω for $\xi \ll 1$ and to ω^2/ν_{fr} for $\xi \gg 1$ [33]. Then, the unknown coefficient c_2 may be determined by finding the best fit to the numerical results obtained by the method of Brownian dynamics. The procedure of minimization of the standard deviation between relation (2) and the numerical results in the range of Γ^* from 102.5 to 50 gives $c_2 \approx (\pi)^{-1/2}$. Then, with due regard for the resultant coefficients (c_1, c_2) and transformation

$$\Gamma^* = \frac{m_p(\omega^* d)^2}{T},$$

one can write the following expression for the diffusion coefficient:

$$D \approx \frac{T\Gamma^*}{12\pi(\pi^{-1/2}\omega^* + \nu_{fr})m_p}\exp\left(-3\frac{\Gamma^*}{\Gamma_c^*}\right). \qquad (7)$$

The error of approximation of the calculation results for the diffusion coefficient by formula (7) does not exceed 2.5% for Γ^* varying from 102.5 to 50. As Γ^* decreases to 40, the error increases to 7–13% and amounts to approximately 25–30% for Γ^* = 30.

Note that the characteristic frequency of collisions between macroparticles in liquid, $\omega_l = (\pi)^{-1/2}\omega^*$, may be obtained if one treats the force of interparticle interaction in a dust system,

$$F = (eZ)^2\exp(-l/Z)\frac{1 + l/\lambda}{l^2},$$

assuming that the electric fields from all particles, except for the nearest ones, are fully compensated [12]. Then, the quantity ω_l will be defined by the derivative dF/dl at point $l = d$ as

$$\omega_l^2 = 4n(eZ)^2\exp(-\kappa)\frac{1 + \kappa + \kappa^2/2}{4\pi}.$$

It is interesting that the vibration of particles at frequencies close to $\omega_l = (\pi)^{-1/2}\omega^*$ may be revealed in motions of a system even at a fairly high viscosity of gas, where ξ = 0.5 (Fig. 6). It was not the objective of our study to investigate the behavior of this vibration; however, it has been observed that such regular motions disappear with decreasing Γ^*.

A relation similar to Eq. (7) may be derived if one assumes the independence and randomness of collisions between charged macroparticles (ω) and between particles and neutrals of ambient gas (ν_{fr}), and also if

one assumes that, for the dust system being investigated, the Maxwell–Boltzmann distribution is valid. Then the dynamic processes in this system will be described by Langevin equations which, as a result of simple transformations [32], may be represented as a system of N_1 equations for mean-square displacements of particles in the "settled" state,

$$m_p\frac{d^2x_i^2}{dt^2} = -m_p\nu_{\rm fr}\frac{dx_i^2}{dt} - 2\omega_c^2x_i^2 + 2m_p\left(\frac{dx_i}{dt}\right)^2 + 2x_iF_{Br}, \quad (8a)$$

and N_2 equations which describe the motion of "free" dust particles,

$$m_p\frac{d^2x_j^2}{dt^2} = -m_p(\omega+\nu_{\rm fr})\frac{dx_j^2}{dt} + 2m_p\left(\frac{dx_j}{dt}\right)^2 + 2x_i(F_{Br}+F_\Sigma). \quad (8b)$$

Here,

$$F_\Sigma \approx \frac{1}{\sqrt{3}}\left|\sum_j F_{\rm int}(l)\big|_{l=|\mathbf{l}_k-\mathbf{l}_i|}\frac{\mathbf{l}_k-\mathbf{l}_j}{|\mathbf{l}_k-\mathbf{l}_j|}\right|$$

is the random force of impacts exerted by free dust particles ($j = 1 - N_2$), ω_c is the characteristic frequency of vibrations of particles, and x describes the particle displacement in the preferred direction. In view of the fact that only free particles diffuse, the solution of the set of equations (8a) and (8b) at $t \longrightarrow \infty$ gives the expression

$$D = \frac{\langle K_j\rangle N_2}{(\omega+\nu_{\rm fr})m_pN_p},$$

for the diffusion coefficient, where

$$\langle K_j\rangle = m_p\langle(dx_j/dt)^2\rangle, \quad N_p = N_1 + N_2.$$

In the case of $N_1 = 0$ and $\omega = 0$, this coefficient coincides with the diffusion coefficient of Brownian particles

$$D_0 = T/\nu_{\rm fr}m_p.$$

For the case of $N_1 \ll N_2 \approx N$, the law of conservation of energy in the set of equations (8a) and (8b) gives the following expression [23, 32]:

$$D \approx \frac{W}{(\omega+\nu_{\rm fr})m_p}\exp\left(-\frac{W}{T}\right), \quad (9)$$

where W is the energy characterizing the transition of particles from the settled to free state. Then, assuming that $W/T = c\Gamma^*$ (where c = const) and in view of the fact that the total energy of a settled particle at the crystallization point of the system being treated cannot exceed the energy of an ideal three-dimensional oscillator $E = 3T$, we find that the coefficient $c = 3/\Gamma_c^*$ and the diffusion coefficient is

$$D \approx \frac{3}{\Gamma_c^*}\frac{T\Gamma^*}{(\omega+\nu_{\rm fr})m_p}\exp\left(-3\frac{\Gamma^*}{\Gamma_c^*}\right). \quad (10)$$

This relation is similar to expression (7); therefore, the coefficients appearing in these expressions before the exponential must be close to one another. If one assumes that $\omega \approx \omega^*(\pi)^{-1/2}$, then the value of the nonideality parameter at the crystallization point may be derived from the simultaneous solution of Eqs. (7) and (10),

$$\Gamma_c^* = 36\pi \approx 110,$$

which agrees within approximately 5% with the value of 104.5 found by the jump of the diffusion coefficient.

In conclusion of this section, we will give two simple relations for the diffusion coefficient D in two limiting cases,

$$D \approx \begin{cases} \frac{d}{12}\sqrt{\frac{T\Gamma^*}{\pi m_p}}\exp\left(-3\frac{\Gamma^*}{\Gamma_c^*}\right), & \omega \gg \nu_{\rm fr}, \quad (11a) \\ D_0\frac{\Gamma^*}{12\pi}\exp\left(-3\frac{\Gamma^*}{\Gamma_c^*}\right), & \omega \ll \nu_{\rm fr}. \quad (11b) \end{cases}$$

These relations enable one to fairly easily determine the modified parameter Γ^* from the results of measurement of the mean interparticle spacing, the temperature, and the diffusion of particles in liquid systems and may be of use in the case of experimental analysis of particle parameters such as the charge and the screening length.

4. CRITERIA OF PHASE TRANSITIONS

4.1. The Melting of a Three-Dimensional Crystal

Different phenomenological criteria of crystallization of a system of interacting particles are known, which have found application in the physics of dust plasma. Best known is the Lindemann criterion [34], according to which the solid phase melts if the ratio of the root-mean-square displacement

$$\Delta_0 = \sqrt{\langle(\mathbf{l}-\mathbf{l}_0)^2\rangle}$$

of a particle from its position of equilibrium $\mathbf{l}_0$ to the mean interparticle spacing $d = n^{-1/3}$ reaches a value on the order of 0.15. Note that, in numerical experiments, one usually measures the displacement $\Delta = \sqrt{2}\,\Delta_0$ of a particle relative to the center of mass of the system, whence, in accordance with the criterion, the ratio Δ/d on the melting curve must be on the order of 0.21. For the majority of solids at the melting point, $\Delta/d \sim 0.2$–0.25 [35]. However, according to the results of numerical simulation performed by different researchers, this value varies from 0.16–19 in the case of melting of an

fcc lattice to 0.18–0.2 for bcc structures. For all cases discussed in my paper, the crystallization was observed at $\Delta/d \longrightarrow 0.19$–$0.2$ (Fig. 4). This fact may be due to the insufficient number N_p of particles in the systems being simulated, because $\Delta/d \longrightarrow 0.2$ with increasing N_p in the case of melting of lattices of both types [15].

Another known criterion suggested by Hansen defines the value of the first maximum S_1 for the liquid structural factor [36] as being less than 2.85 (this value likewise varies from 2.5 to 3.2 in different calculations). The variation of the value of S_1 from 2.65 to 3.1 during the transition of the system from the liquid to crystalline state was observed in my calculations as well (see Fig. 2a). A simple criterion of crystallization in terms of a binary correlation function is provided by the equality of the ratio between its minimal and maximal values to 0.2. Note that, for a system with a finite number of particles, the latter two criteria depend strongly on the procedure of determining the structural factor and the pair correlation function, respectively. In addition, the fluctuations of correlations between particles increase infinitely in the vicinity of the crystallization points of the system or of other phase transitions [37]. Therefore, the results of calculation of characteristics for a bounded dust system may prove to be incorrect on the phase curves.

The condition of constant value of the modified nonideality parameter Γ^* on the melting curve of the system may be treated as a simple criterion for the liquid–bcc structure phase transition. As was already mentioned above, the value of the parameter Γ^* on the curve between melting and crystallization of a structure may be defined as $\Gamma_c^* \approx 104.5$. This value corresponds to the middle of the range of $\Gamma^* = 102$–107, where the ratio of the coefficients D/D_0 decreases by more than two orders of magnitude (Fig. 3), and drastic variations occur in the values of the first maxima of the pair correlation function and structure factor (Fig. 2a). It should be emphasized that the value of $\Gamma_c^* \approx 104.5$ (±2%) is almost independent of the ambient gas viscosity; therefore, this criterion agrees with the results of calculation of the crystallization of Yukawa systems by the methods of molecular dynamics disregarding the particle friction [13–17]. The deviations of these calculation results from the value of $\Gamma_c^* \approx 104.5$ vary within ±5% [12] and may be associated with the differences in the numerical methods used in analyzing the system (the choice of different numbers of particles, integration step, and so on), as well as with the choice of the value of Γ either at the melting point or at the crystallization point of the system. Note that the obtained value of $\Gamma_c^* \approx 104.5$ (±2%) is consistent with the theoretical results of Slattery *et al.* [19], who give the value of 105 (±3%) for the nonideality parameter on the phase curve in Coulomb systems; this value agrees with the results of calculations within different criteria of liquid–crystal phase transitions (crystallization) [20] and crystal–liquid phase transitions (melting) [21].

A simple dynamic criterion of melting was obtained by Lowen *et al.* [38] for the conditions of colloidal solutions; this criterion defines the ratio of the diffusion coefficients of a dust particle D/D_0 on the line of liquid–crystal phase transition as a quantity whose value is close to 0.1. A reference to the inadequacy of this result, as applied to a gas-discharge dust plasma where the gas viscosity may not be high enough, was made in [12]. Indeed, one can use Eq. (11a) to derive $D/D_0 \approx 0.13$ for $\Gamma^* = \Gamma_c^* \approx 104.5$ at $\nu_{fr} \gg \omega$. With increasing ξ (decreasing ν_{fr}—see Fig. 3), the value of D/D_0 will decrease in inverse proportion to ν_{fr} at $\nu_{fr} \longrightarrow 0$, with the value of the coefficient D being in fact independent of the ambient gas viscosity according to Eq. (11b). Note further that, in view of the inferences made in the previous section, the ratio D/D_0 on the crystallization curve must depend on the lattice dimension.

A condition analogous to the Lindemann criterion may be obtained with due regard for the fact that the volume of thermal fluctuations

$$V_{tf} \sim 4\pi/3\Delta^3$$

for a bcc lattice must not exceed

$$(1 - \pi\sqrt{2}/8)V \approx 0.32V,$$

where

$$V = n^{-1} \approx \frac{4\pi}{3}a_{WS}^2,$$

and $a_{WS} = (4\pi n/3)^{-1/3}$ is the radius of the Wigner–Seitz cell. For a stable existence of an fcc structure, it is necessary that

$$V_{tf} < (1 - \pi\sqrt{2}/6)V \approx 0.26V$$

(see [27, 31]). We will allow for the possibility of counterdisplacement of particles and assume $\Delta = \sqrt{2}\,\Delta_0$ (where Δ denotes the most probable magnitude of displacement). From this, we derive that the value of Δ/d necessary for the destruction of a bcc structure must exceed 0.211 ($\Delta_0/d > 0.15$) and, within 7%, be equal to $\Delta \sim 0.198$ on the melting curve of an fcc lattice ($\Delta_0/d \approx 0.14$). This result is in excellent agreement with the results of Stevens and Robbins [15] and with all further estimates given in my paper (see table).

The values of the parameters Γ_c^* and Δ on the melting curve of crystal lattices enable one to estimate the characteristic oscillation frequency of particles ω in a dust crystal, the determination of which is treated in a number of theoretical papers [13, 22, 27]. For an ideal harmonic oscillator, we have

$$\Delta_0^2 = 3T/m_p\omega_c^2, \qquad (12)$$

where ω_c is the characteristic oscillation frequency. We express T in terms of ω^* and Γ^* to find

$$\omega_c = \omega^*(\Gamma^*\Delta_0^2/3d^2)^{-1/2}.$$

(Note that relation (12) is the solution to the set of equations (8a) and (8b) for the case of $N_1 = 0$.) We assume that $\Gamma^* = 104.5$ and $\Delta_0/d = 0.15$ to derive (with an accuracy of up to 1.5%), for the characteristic oscillation frequency $\omega_c = \omega_{bcc}$ of particles in the bcc lattice, the frequency whose value is twice that found for the liquid case,

$$\omega_{bcc}^2 \approx 4n_p(eZ)^2\exp(-\kappa)\frac{1+\kappa+\kappa^2/2}{\pi}.$$

An analogous value for ω_{bcc} may be obtained in a different manner if one assumes that the value of Δ on the melting curve of the crystal lattice must be close to that of the mean free path l_{liq} of a particle in the liquid phase, $l_{liq} \approx (6D\tau_0)^{1/2}$, where the characteristic time $\tau_0 = 2(\omega + \nu_{fr})/\omega^2$ was introduced previously. Note that the ratio l_{liq}/d on the crystallization curve for liquid indeed corresponds to a value of 0.2.

Based on the foregoing and in view of the fact that $\Delta_0/d \approx 0.14$, the characteristic oscillation frequency of particles in an fcc lattice could be estimated as

$$\omega_{fcc} \approx 0.15\omega_{bcc}/0.14.$$

Then, the value of Γ^* on the crystallization curve of lattices of both types would have remained constant, which is inconsistent with the results of numerical simulation (see Fig. 7). This is associated with the fact that, as κ increases, the effect of the nearest neighbors on the behavior of an individual particle decreases as compared with the effect of the remaining particles of the system. On the assumption of homogeneity, the summation of the forces of interparticle interaction from each particle within some constant quantity produces

$$F_\Sigma = \alpha^3 n_p(eZ)^2\exp(-l/\lambda)\lambda\{1 + l/\lambda - \alpha\},$$

where $\alpha = (4\pi/3)^{-1/3} \approx 1.612$. From this, for the frequency characteristic of an fcc structure, one can derive the expression

$$\omega_{fcc}^2 = 2\alpha^3 n_p(eZ)^2\exp(-\kappa)(\kappa - \alpha).$$

On assuming $\Delta_0/d \approx 0.14$ on the melting curve of an fcc lattice, one can find from Eq. (12) the critical parameter

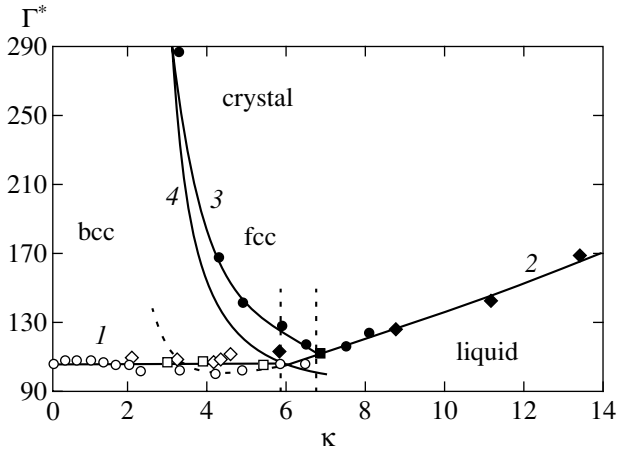

Fig. 7. The dependence of $\Gamma*$ on κ for different phase transitions: circles, [16]; squares, [15]; rhombs, [14] (the dark symbols correspond to the formation of an fcc lattice); (*1*) $\Gamma^* = 106$ (bcc ⟶ liquid); (*2*) fcc ⟶ liquid, Eq. (13); (*3*) bcc ⟶ fcc, Eq. (15); (*4*) fcc ⟶ bcc, Eq. (16).

The value δ_c of the ratio of the most probable displacement Δ to the mean interparticle spacing d, the value of the nonideality parameter $\Gamma_c = (eZ)^2n^{1/3}/T$ on the curve of different phase transitions in Yukawa systems, and the coefficients C_w for approximations $\omega_c^2 = C_w n(eZ)^2\exp(-\kappa)$ of the characteristic vibrational frequency ω_c of macroparticles in bcc and fcc lattices ($\alpha = (4\pi/3)^{-1/3}$, $\kappa = d/\lambda$)

Phase transition	$\delta_c = \Delta/d \equiv \sqrt{2}\Delta_0/d$	$\Gamma_c = C_p(K_n\exp(-\kappa))^{-1}$		C_w
		C_p	K_n	
bcc ⟶ liquid	$\frac{(1-\pi\sqrt{2}/8)^{1/3}}{2\alpha} \sim 0.211$	$\frac{6}{4\pi^{-1}\delta_c^2} \sim 106$	$1 + \kappa + \kappa^2/2$	$\frac{4}{\pi}\left(1+\kappa+\frac{\kappa^2}{2}\right)$
bcc ⟶ fcc	$\frac{(1-\pi\sqrt{2}/6)^{1/3}}{\sqrt{2}\alpha k}(\kappa-\alpha)$	$\frac{6}{4\pi^{-1}0.27^2} \sim 64$	$\frac{(1+\kappa+\kappa^2/2)(\kappa-\alpha)^2}{\kappa^2}$	
fcc ⟶ bcc	$\sim \frac{0.27(\kappa-\alpha)}{\kappa}$	$6/2\alpha^3 0.27^2 \sim 9.8$	$\frac{(\kappa-\alpha)^3}{\kappa^2}$	$2\alpha^3(\kappa-\alpha)$
fcc ⟶ liquid	$\frac{(1-\pi\sqrt{2}/6)^{1/3}}{2\alpha} \sim 0.198$	$6/2\alpha^3\delta_c^2 \sim 18.5$	$\kappa - \alpha$	

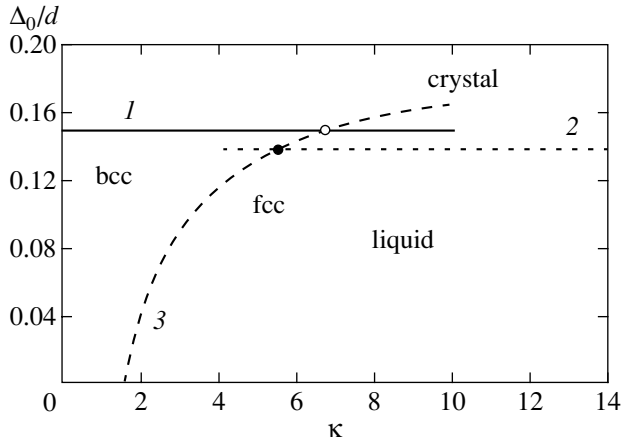

Fig. 8. The dependence of Δ_0/d on κ for different phase transitions: (*1*) bcc ⟶ liquid, (*2*) fcc ⟶ liquid, (*3*) bcc ⟶ fcc; hollow circles, κ = 5.8; filled circles, κ = 6.8.

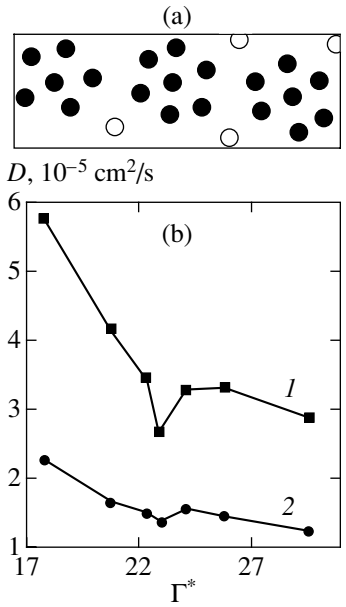

Fig. 9. (a) The condensation of dust clusters and (b) jumps of the diffusion coefficient D as functions of the parameter Γ* for κ = 2.4 and different values of the parameter ξ = (*1*) 0.5 and (*2*) 0.166.

Γ_c (see table) or the parameter Γ_c^* for the given phase transition,

$$\Gamma_c^* \approx 18.5(\kappa - \alpha)^{-1}(1 + \kappa + \kappa^2/2). \qquad (13)$$

The use of the normalized value of Γ_c^* as given by Eq. (13) enables one to illustrate the pattern of the fcc structure–liquid and bcc structure–liquid melting curves on a close (nonlog) scale (Fig. 7). The difference between the criterion given by Eq. (13) and the various results of simulation [14–16] of the fcc structure–liquid phase transition does not exceed 2% for κ > 6.8. In the range of values of κ from 5.8 to 6.8, the triple point of the system (bcc–fcc–liquid) is located; the behavior of the system in the vicinity of this point will be analyzed below, along with the analysis of the effect of the screening length λ in the processes of formation of an fcc lattice for κ < 6.8. To this, we will add that, in the range of values of κ from 3 to 7, the obtained frequency ω_{bcc} will correspond to $0.15\omega_{bcc}/0.14$ with an accuracy of ±5%, as is reflected in the results of calculations of the values of Γ_c^* (see Fig. 7).

4.2. Phase Transition between bcc and fcc Structures

The most complete data for the phase diagram of transition of a Yukawa system from a bcc to an fcc structure were given by Hamaguchi *et al.* [16] (see Figs. 1 and 7). The criterion for this transition may be found when it is considered that, in order to change the bcc symmetry of the lattice, it is necessary that the spacing between particles in the system exceed their screening length λ. It is only subject to this condition that the interparticle interaction will be close to the "rigid-sphere" interaction, when the formation of an fcc structure is possible. Then, with due regard for the mean volume of thermal fluctuations

$$V_{fr} < (1 - \pi/3\sqrt{2})V$$

and the possibility of counterdisplacement of particles (see Subsection 4.1), we will derive the following condition for the transition of the system from a bcc to an fcc structure:

$$2(1 - \pi/3\sqrt{2})^{-1/3}\Delta_0 < a_{WZ} - \lambda. \qquad (14)$$

The values of the ratio Δ_0/d for different phase transitions are given in the table and in Fig. 8, where one can see that the range of values of κ from 5.8 to 6.8 defines the region of triple phase transition (bcc structure–fcc structure–liquid).

Condition (14) may be transformed to the condition for the nonideality parameter Γ_c (see table) or for the modified parameter Γ* using relation (12),

$$\Delta_0^2 = \frac{3T}{m_p\omega_c^2} \equiv \frac{3\pi}{4\Gamma^*},$$

where, for a bcc lattice, we assume that

$$\omega_c^2 = 4n_p(eZ)^2\exp(-\kappa)\frac{1 + \kappa + \kappa^2/2}{\pi}.$$

We substitute the numerical values of the coefficients to derive

$$\Gamma^* \approx 64\kappa^2(\kappa - \alpha)^{-2}. \qquad (15)$$

The validity of condition (15) as a criterion for the bcc–fcc transition was verified for the data of Hamaguchi *et al.* [16]. The verification has revealed that the devia-

tion of the calculated values of Γ^* for the bcc–fcc transition from relation (15) is within ±2%. An illustration is given in Fig. 7 (curve *3*). In view of the fact that the possibility of reverse transition from an fcc to bcc structure will be defined by the frequency

$$\omega_{fcc}^2 = 2\alpha^3 n_p (eZ)^2 \exp(-\kappa)(\kappa - \alpha),$$

the relation

$$\Gamma^* \approx 9.8\kappa^2(\kappa - \alpha)^{-3}(1 + \kappa + \kappa^2/2) \qquad (16)$$

may be treated as a criterion for this transformation. Note that condition (16) depends on the correctness of approximation of the frequency ω_{fcc} and may be erroneous for small values of $\kappa \longrightarrow \alpha$. Nevertheless, the results of calculations by formulas (15) and (16) (curves *3* and *4* in Fig. 7) fully define the region of triple phase transition (κ = 5.8 to 6.8) and agree with the results obtained for the values of the ratio Δ_0/d (see Fig. 8). We will add that the difference in the position of the curves defined by formulas (15) and (16) is capable of explaining the inconsistencies between the results of numerical simulation by different researchers [14–16] in determining the location of the triple point.

4.3. Condensation of Macroparticles

We will dwell on the qualitative analysis of the results of observation of condensation of macroparticles (growth of dust clusters—see Fig. 9a), when the parameter Γ^* takes values of about 23.5. The formation of groups of individual macroparticles was reflected by the variation of the position of the maximum of the pair correlation function (Fig. 2b) and by the abrupt variation of the diffusion coefficient (see Figs. 3 and 9b). It should be recalled that, for $\Gamma^* < 40$, the system being simulated is no longer described by simple relations (7)–(11) derived within the jump theory for molecular liquids, and the scaling parameter ξ given by Eq. (5) is not suitable for analyzing the macroparticle dynamics.

One can assume that the observed phenomenon is a phase transition (of the second order) of the system from a strongly correlated liquid to a nonideal gas. Some unsoundness of this assumption is due to two reasons, one of which is that, in the critical region of $\Gamma^* \sim$ 23.5, the diffusion coefficient does not tend to zero. This fact may be associated with the above-mentioned finite size of the counting cell which hampers further growth of dust clusters. Similar effects were observed by Maekawa *et al.* [39]. The second reason is that, in the set of equations (3), the attractive forces between particles were not preassigned in an explicit form.

The observed phenomenon may be associated with the symmetry of the interparticle interaction potential (similarly to the Bose–Einstein condensation arising due to the symmetry of the wave function [35]). Then, the value of $\Gamma^* \approx 23.5$ must define conditions under which a system begins to exhibit properties that are due to the identity of its particles. Indeed, if we assume the mean free path $l_{liq} = (6D\tau_0)^{1/2}$ of a particle in the liquid phase to be equal to the Wigner–Seitz cell radius a_{WS}, we derive a value of about 26 for the critical parameter Γ^*, which agrees with $\Gamma^* \approx 23.5$ within the accuracy of applying formula (7) to the region of $\Gamma^* < 40$.

In conclusion, note that, unlike the Bose–Einstein condensation occurring in the momentum space, the condensation of dust particles is observed in the coordinate space, similarly to the phenomena of real phase transitions from gas to liquid. Therefore, it remains unclear whether or not the observed phenomenon is a phase transition. Nevertheless, it is quite apparent that the dynamic characteristics of the system being simulated change qualitatively at point $\Gamma^* \approx 23.5$ (Fig. 3).

5. CONCLUSION

The dynamics of charged particles has been investigated in a wide range of temperatures under conditions close to those of experiments in a weakly ionized laboratory dust plasma. The existing phenomenological criteria for different phase transitions have been treated and new criteria suggested (see table). The order parameter for Yukawa systems has been determined, as well as the parameter responsible for the scaling of dynamic processes in a dissipative system of strongly interacting macroparticles. The relation for the diffusion coefficient D of dust particles in liquid structures has been derived. These results may be used for passive (nonpenetrative) diagnostics of the dynamic characteristics of liquid dust structures and for analysis of parameters of the system such as the nonideality parameter, the screening length, and the macroparticle charge.

ACKNOWLEDGMENTS

This study was supported in part by the Russian Foundation for Basic Research (projects nos. 01-02-16658 and 00-02-17520) and by CRDF (project no. RP2-2250).

REFERENCES

1. J. H. Chu and L. I, Phys. Rev. Lett. **72**, 4009 (1994).
2. H. Thomas, G. E. Morfill, V. Demmel, *et al.*, Phys. Rev. Lett. **73**, 652 (1994).
3. A. Melzer, T. Trottenberg, and A. Piel, Phys. Lett. A **191**, 301 (1994).
4. V. E. Fortov, A. P. Nefedov, V. M. Torchinskiĭ, *et al.*, Pis'ma Zh. Éksp. Teor. Fiz. **64**, 86 (1996) [JETP Lett. **64**, 92 (1996)].
5. A. M. Lipaev, V. I. Molotkov, A. P. Nefedov, *et al.*, Zh. Éksp. Teor. Fiz. **112**, 2030 (1997) [JETP **85**, 1110 (1997)].
6. D. A. Low, W. H. Steel, B. M. Annaratone, *et al.*, Phys. Rev. Lett. **80**, 4189 (1998).
7. G. Morfill, H. Thomas, U. Konopka, *et al.*, Phys. Rev. Lett. **83**, 1598 (1999).

8. S. Nunomura, T. Misawa, N. Ohno, and S. Takamura, Phys. Rev. Lett. **83**, 1970 (1999).
9. O. Vaulina, S. Khrapak, A. Nefedov, *et al.*, Phys. Rev. E **60**, 5959 (1999).
10. O. S. Vaulina, A. P. Nefedov, O. F. Petrov, *et al.*, Zh. Éksp. Teor. Fiz. **115**, 2067 (1999) [JETP **88**, 1130 (1999)].
11. R. T. Farouki and S. Hamaguchi, Appl. Phys. Lett. **61**, 2973 (1992).
12. O. S. Vaulina and S. A. Khrapak, Zh. Éksp. Teor. Fiz. **117**, 326 (2000) [JETP **90**, 287 (2000)].
13. M. O. Robbins, K. Kremer, and G. S. Grest, J. Chem. Phys. **88**, 3286 (1988).
14. E. J. Meijer and D. Frenkel, J. Chem. Phys. **94**, 2269 (1991).
15. M. J. Stevens and M. O. Robbins, J. Chem. Phys. **98**, 2319 (1993).
16. S. Hamaguchi, R. T. Farouki, and D. H. E. Dubin, Phys. Rev. E **56**, 4671 (1997).
17. H. Totsuji, T. Kishimoto, Y. Inoue, *et al.*, Phys. Lett. A **221**, 215 (1996).
18. O. S. Vaulina and S. A. Khrapak, Zh. Éksp. Teor. Fiz. **119**, 264 (2001) [JETP **92**, 228 (2001)].
19. W. L. Slattery, G. D. Doollen, and H. E. DeWitt, Phys. Rev. A **21**, 2087 (1980).
20. E. L. Plolloc and J. P. Hansen, Phys. Rev. A **8**, 3110 (1973).
21. H. M. van Horn, Phys. Lett. A **28**, 707 (1969).
22. H. Ohta and S. Hamaguchi, Phys. Plasmas **7**, 4506 (2000).
23. Ya. I. Frenkel, *Kinetic Theory of Liquids* (Leningrad, 1975).
24. G. L. Swinney, in *Photon Correlation and Light Beating Spectroscopy*, Ed. by H. Z. Cummins and E. R. Pike (Plenum, New York, 1974; Mir, Moscow, 1978), p. 332.
25. H. Z. Cummins, in *Photon Correlation and Light Beating Spectroscopy*, Ed. by H. Z. Cummins and E. R. Pike (Plenum, New York, 1974; Mir, Moscow, 1978), p. 287.
26. P. N. Pusey, in *Photon Correlation and Light Beating Spectroscopy*, Ed. by H. Z. Cummins and E. R. Pike (Plenum, New York, 1974; Mir, Moscow, 1978), p. 387.
27. J. M. A. Hofman, Y. J. H. Clercx, and P. P. J. Schram, Phys. Rev. E **62**, 8212 (2000).
28. A. A. Ovchinnikov, S. F. Timashev, and A. A. Belyĭ, *Kinetics of Diffusion-Controlled Chemical Processes* (Khimiya, Moscow, 1986).
29. I. T. Yakubov and A. G. Khrapak, Sov. Technol. Rev. B., Therm. Phys. **2**, 269 (1989).
30. J. Goree, Plasma Sources Sci. Technol. **3**, 400 (1994).
31. O. S. Vaulina, O. F. Petrov, and M. V. Taranin, Fiz. Plazmy **25**, 311 (1999) [Plasma Phys. Rep. **25**, 281 (1999)].
32. D. V. Sivukhin, in *Course of General Physics* (Nauka, Moscow, 1979), Vol. 2, p. 509.
33. V. E. Fortov, A. P. Nefedov, O. S. Vaulina, *et al.*, Zh. Éksp. Teor. Fiz. **114**, 2004 (1998) [JETP **87**, 1087 (1998)].
34. F. A. Lindemann, Z. Phys. **11**, 609 (1910).
35. *Physical Encyclopedia* (Bol'shaya Rossiĭskaya Éntsiklopediya, Moscow, 1998), Vol. 1, pp. 574, 219, 366.
36. J. P. Hansen and L. Verlet, Phys. Rev. **184**, 151 (1969).
37. H. E. Stanley, *Introduction to Phase Transitions and Critical Phenomena* (Clarendon, Oxford, 1971; Mir, Moscow, 1973).
38. H. Lowen, T. Palberg, and R. Simon, Phys. Rev. Lett. **70**, 1557 (1993).
39. T. Maekawa, K. Ishii, and S. Masuda, J. Jpn. Soc. Microgravity Appl. **15**, 130 (1998).

Translated by H. Bronstein

Journal of Experimental and Theoretical Physics, Vol. 94, No. 1, 2002, pp. 37–45.
Translated from Zhurnal Éksperimental'noĭ i Teoreticheskoĭ Fiziki, Vol. 121, No. 1, 2002, pp. 47–56.

PLASMA, GASES

Nonlinear Spectral Properties of Stimulated Brillouin Scattering in Plasma

K. Yu. Vagin[a], I. V. Kuzora[a], K. N. Ovchinnikov[a], V. P. Silin[a, *], S. A. Uryupin[a], C. J. McKinstrie[c], and M. V. Kozlov[b]

[a]*Lebedev Physical Institute, Russian Academy of Sciences, Leninskiĭ pr. 53, Moscow, 117991 Russia*
[b] *Rochester University, Rochester, USA*
[c]*Lucent Technologies, Holmdel, USA*
**e-mail: silin@sci.lebedev.ru*
Received July 9, 2001

Abstract—New phenomena in which the stimulated Brillouin scattering (SBS) changes the number and magnitude of frequency shifts in a plasma upon a nonlinear increase in the pumping field intensity are discovered. It is found that the SBS becomes forbidden and then allowed again (upon a subsequent increase in the pumping intensity). *© 2002 MAIK "Nauka/Interperiodica".*

The stimulated Brillouin scattering (SBS) may be accompanied by a strong nonlinear effect of variation of the scattered radiation spectrum if it involves strongly attenuating low-frequency excitations. This meets the requirement that the field of scattered radiation (pumping field) be strong enough to overcome dissipation determining the strong damping of low-frequency excitations. In this sense, the SBS itself is a strong nonlinear effect. Since the damping of the low-frequency excitations we are interested in is comparable with their frequency, the spectrum of excitations participating in scattering changes as compared to the spectrum of such strongly damped excitations in the absence of a pumping field even at the SBS instability threshold. In the superthreshold region, this effect is manifested in a dependence of the SBS spectrum on the pumping field intensity. The possibility of the effect under consideration will be demonstrated for a plasma with two species of ions for which peculiar nonlinear properties of the scattered radiation spectrum are observed.

The properties of collective excitations of collisionless plasmas with two species of ions have been attracted the attention of researchers for a long time [1–6]. Such collective excitations may be manifested in the SBS in a peculiar way [7–10]. In the latter case, collective excitations in the plasma are usually associated with ion-sound waves. The properties of such waves change in a certain way under the action of the scattering pumping field. This enables us to speak of the decay of a pumping wave into a scattered wave and a sound SBS quasimode. In the simplest case of weak damping of ordinary ion-sound waves in a plasma, the main difference between the sound SBS quasimodes and ordinary waves is that the quasimodes do not attenuate beyond the parametric instability threshold. However, the situation changes radically when the damping of ordinary ion-sound waves is significant and when their damping decrement is not very small as compared to their frequency. Indeed, at the SBS threshold, the damping of ion-sound waves must be suppressed by the pumping field. For strongly damped ion-sound waves, the intensity of the pumping field is so high that it results in a considerable difference between the frequencies of the threshold SBS quasimodes and of the ordinary ion-sound waves. Since the spectrum of SBS quasimodes is acoustic ($\omega = kV$), the velocity V of the quasimodes differs considerably from the ordinary velocities of sound for fast and slow ion-sound waves (see below) which may take place in a plasma with two species of ions in zero electromagnetic pumping field [1–6].

In [10], distinctive dependences of the velocity of the threshold SBS quasimodes on the impurity concentrations and the parameter characterizing the deviation from isothermal equilibrium (i.e., the ratio of the electron and ion temperatures) were established for a hydrogen plasma. It was shown in [10], among other things, that, for the same value of this parameter, three different SBS quasimodes with different thresholds can be excited. It was also established that for the same threshold, two different quasimodes with different frequencies can be excited in an unusual way, which corresponds to SBS with two different frequencies shifts existing simultaneously [10]. It should be emphasized in this connection that such a nonlinear variation of the velocity of ion sound under the action of a pumping field takes place for not very strong pumping fields. This is observed when the ratio of the energy of oscillations of an electron in the pumping field to its thermal energy is equal in order of magnitude to the small ratio of the frequency of electron–ion collisions to the pumping field frequency. This noticeably distinguishes the nonlinear effect under investigation from the variation

of the velocity of ion sound under the action of a strong pumping field in the case when the energy of oscillations of an electron is higher than its thermal energy [11].

In this communication, we consider some nonlinear properties of the SBS quasimodes under the conditions when the parametric instability threshold is surpassed. It has been found that the velocity of sound for the SBS quasimodes changes nonlinearly upon an increase in the pumping intensity in the superthreshold region. We will demonstrate that the SBS quasimodes may disappear upon an increase in the pumping intensity and that the SBS might be forbidden and then allowed again upon a subsequent increase in the pumping field.

We assume that the pumping field is linearly polarized:

$$\mathbf{E}(\mathbf{r}, t) = \frac{\mathbf{E}_0}{2}\exp(i\mathbf{k}_0\cdot\mathbf{r} - i\omega_0 t) + \text{c.c.}, \quad (1)$$

where $\omega_0^2 = \omega_{Le}^2 + k_0^2c^2$, $\omega_{Le}^2 = 4\pi e^2N_e/m_e$. For the amplitude of the electron oscillation speed in the pumping field, we have $\mathbf{v}_E = e\mathbf{E}_0/m_e\omega_0$. The electromagnetic field of the scattered wave has the frequency $\omega_s = \omega_0 - \omega$ and the wave vector $\mathbf{k}_s = \mathbf{k}_0 - \mathbf{k}$, where ω and $\mathbf{k}$ are the frequency and the wave vector of quasimodes, respectively. Following [12, 13], we will describe the SBS by using the dispersion equation

$$\frac{1}{\delta\varepsilon_e(\omega, k)} + \frac{1}{\delta\varepsilon_i(\omega, k)} = \frac{k^2|(\mathbf{k}-\mathbf{k}_0)\times\mathbf{v}_E|^2}{4(\mathbf{k}-\mathbf{k}_0)^2D_-}, \quad (2)$$

where

$$D_- = -(\omega - i\gamma_{ei} - \omega_0)^2 + c^2(\mathbf{k}-\mathbf{k}_0)^2 + \omega_{Le}^2 \quad (3)$$

is the dispersion function of the scattered field and $\gamma_{ei} = -\omega_{Le}^2\nu_{ei}/2\omega^2$, ν_{ei} being the frequency of electron–ion collisions. In Eq. (2), we have

$$\delta\varepsilon_i(\omega, k) = \sum_\alpha \delta\varepsilon_\alpha(\omega, k),$$

where summation is carried out over all the species of ions. We assume in Eq. (2) that $|\delta\varepsilon_i| \gg 1$ and $v_E^2 \ll \omega\omega_0 r_{De}^2$, which corresponds to the ion-sound spectrum of the SBS quasimodes.

Analyzing the SBS evolution in time, we assume in Eq. (2) that $\omega \longrightarrow \omega + i\gamma$, where $\gamma \ll \omega$. Considering that the condition $c^2(2\mathbf{k}\cdot\mathbf{k}_0 - k^2) = 2\omega\omega_0 - \omega^2$ is satisfied, we obtain $D_- = 2i\omega_0(\gamma - \gamma_{ei})$. In this case, Eq. (2) leads to the following two equations:

$$a(\omega, k) = \gamma\frac{\partial}{\partial\omega}b(\omega, k), \quad (4)$$

$$0 = b(\omega, k) + \gamma\frac{\partial}{\partial\omega}a(\omega, k) + \frac{k^2|(\mathbf{k}-\mathbf{k}_0)\times\mathbf{v}_E|^2}{8\omega_0(\gamma-\gamma_{ei})k_0^2}, \quad (5)$$

where

$$a(\omega, k) = \text{Re}\left\{\frac{1}{\delta\varepsilon_e(\omega, k)} + \frac{1}{\delta\varepsilon_i(\omega, k)}\right\}$$

$$b(\omega, k) = \text{Im}\left\{\frac{1}{\delta\varepsilon_e(\omega, k)} + \frac{1}{\delta\varepsilon_i(\omega, k)}\right\}.$$

These equations define the increment of the SBS excitation buildup and the quasimode spectrum. In the approximation of the Maxwellian distribution of particles in a plasma containing two species of ions, we assume that the ion temperatures are equal ($T_1 = T_2 = T_i$) and use the notation $X = T_e/T_i$ for their ratio. We assume that the sound velocity of quasimodes is smaller than the thermal velocity $v_{Te} = \sqrt{\kappa T_e/m_e}$ of electrons. For the thermal velocities of various species of ions, we assume that $\sqrt{\kappa T_i/m_1} = v_{T1} > v_{T2} = \sqrt{\kappa T_i/m_2}$ and also use the notation $z = V/v_{T1}$. Then, Eqs. (4) and (5) can be written in the form

$$X + \Phi_1(z) = -\frac{\gamma}{kv_{T1}}X\frac{\partial\Psi(X, Z)}{\partial z}, \quad (6)$$

$$I\frac{\gamma_{ei}}{\gamma_{ei}-\gamma} + \frac{\gamma}{kv_{T1}}\frac{1}{X}\frac{d\Phi_1(z)}{dz} = \Psi(X, z). \quad (7)$$

In these equations, the following notation has been used:

$$I = \frac{\omega_0}{\nu_{ei}}\frac{|(\mathbf{k}-\mathbf{k}_0)\times\mathbf{v}_E|^2}{4k_0^2v_{Te}^2}, \quad (8)$$

$$\Psi(X, z) = \sqrt{\frac{\pi}{2X}\frac{m_e}{m_1}}z + \frac{\Phi_2(z)}{X}.$$

$$\Phi_1(z) = F_1(z)[F_1^2(z) + F_2^2(z)]^{-1},$$

$$\Phi_2(z) = F_2(z)[F_1^2(z) + F_2^2(z)]^{-1},$$

$$F_1(z) = \xi_1\left[1 - \sqrt{2}zF\left(\frac{z}{\sqrt{2}}\right)\right] + \xi_2\left[1 - \sqrt{2}zuF\left(\frac{zu}{\sqrt{2}}\right)\right],$$

$$F_2(z) = \sqrt{\frac{\pi}{2}}z\left\{\xi_1\exp\left(-\frac{z^2}{2}\right) + \xi_2u\exp\left(-\frac{u^2z^2}{2}\right)\right\},$$

$$\xi_1 = Z_1\left(1 + \frac{Z_2N_2}{Z_1N_1}\right)^{-1}, \quad \xi_2 = Z_2\left(1 + \frac{Z_1N_1}{Z_2N_2}\right)^{-1}.$$

Here, Z_α is the degree of ionization, N_α is the number density of ions of species α, $u = \sqrt{m_2/m_1}$, and

$$F(x) = e^{-x^2}\int_0^x e^{t^2}dt$$

is Dawson's integral [14].

We will demonstrate the peculiar consequences of Eqs. (6) and (7) describing the nonlinear dependence of the SBS quasimode spectrum on the pumping intensity for the $Xe_y^{+40}H_{1-y}^+$ plasma (see Figs. 1–7 below). We will analyze the case when Xe ions play the role of an impurity ($y \equiv N_2/(N_1 + N_2) \ll 1$).

Figure 1 shows the curves characterizing the velocity $z_{th}(X)$ of sound SBS quasimodes at the instability threshold and the excitation threshold $I_{th}(X) \equiv \Psi(X, z_{th}(X))$ for such quasimodes as functions of the parameter X describing the deviation from isothermal equilibrium. Taking into account the definition (8) of quantity I and the radiation flux density $q = cE_0^2/8\pi$, we can conclude that the threshold value $I_{th}(X)$ corresponds to a relatively small value of flux density. In particular, for the backward SBS, when $\mathbf{k} = 2\mathbf{k}_0$, we have

$$q_{th} \equiv \frac{c}{8\pi}(E_0^2)_{th} = \frac{c}{8\pi}\frac{\nu_{ei}}{\omega_0}\frac{m_e^2\omega_0^2 v_{Te}^2}{e^2} I_{th}(X)$$

$$= I_{th}(X) \times 2.7 \times 10^{15} \left[\frac{W}{cm^2}\right]\frac{\nu_{ei}}{\omega_0}\frac{T_e}{\lambda^2}\,[keV]\,[\mu m].$$

Here, T_e is the electron temperature in kiloelectronvolts, and λ is the wavelength of the pumping field in micrometers. Solid curves correspond to the Xe concentration $y = 0.01$, while dashed curves correspond to a higher concentration $y = 0.06$. In both cases, three branches of SBS quasimodes are present for $X_{min}(y) < X < X_{max}(y)$. For $y = 0.01$, we have $X_{max}^{(1)} \approx 1.60$, while $y = 0.06$ corresponds to $X_{min}^{(2)} \approx 2.14$ and $X_{max}^{(2)} \approx 2.44$. In the case when $y = 0.01$, the region of the three quasimode branches is not bounded from below; i.e., $X_{min}^{(1)} = 0$. An even more important property in the case of the lower concentration is the existence of a self-intersection point on the threshold curve in Fig. 1b, which is not observed for the higher concentration.

Let us first consider the case of the lower concentration $y = 0.01$, described by the solid curves in Fig. 1. The upper solid curve in Fig. 1a in this case is a nonlinear continuation to the region of small deviations from the isothermal equilibrium velocity of the fast quasimode, which corresponds to the velocity $V = r_{De}\sqrt{\omega_{L1}^2 + \omega_{L2}^2}$ of ordinary fast sound for $X \gg 1$. The two lower solid curves are separated by a considerable distance from the curve corresponding to the fast wave and can be regarded as the result of spectral splitting for a slow ion-sound wave.

We will attribute the lowermost solid curve in Fig. 1a to the velocity z_s, which will be referred to as the slow wave velocity, while the upper of the two solid curves will be attributed to the velocity z_i referred to as the intermediate velocity. For $X = X_{max}^{(1)}$, the two lower

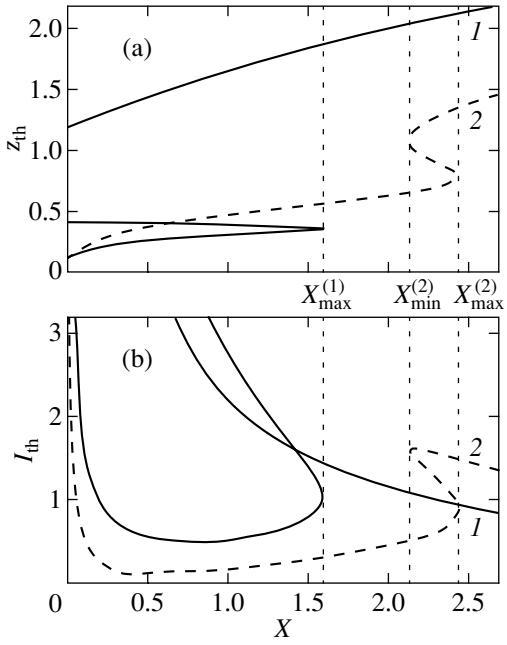

Fig. 1. Dependence (a) of the velocity $z_{th}(X)$ of sound SBS quasimodes at the instability threshold and (b) of the excitation threshold $I_{th}(X)$ for such quasimodes in a $Xe_y^{+40}H_{1-y}^+$ plasma on the parameter X for the Xe concentration values $y = 0.01$ (curves *1*) and $y = 0.06$ (curves *2*).

branches of the SBS quasimodes converge. The properties of these two comparatively slow quasimodes, whose velocities differ considerably from the velocity of the fast wave under investigation, can be explained qualitatively on the basis of the above-mentioned concept concerning the nonlinear splitting of the ordinary mode of slow ion sound. We will demonstrate this using an analytic corollary which can be derived from Eq. (6) under the assumption that the velocities of the SBS quasimodes are smaller than v_{T1}, on the one hand, and greater than v_{T2}, on the other hand. The latter relation corresponds to the conditions of realization of slow ion-sound waves in zero pumping field. Under our conditions, we obtain from Eq. (6)

$$z^2 = \frac{\xi_2}{u^2}\left[\xi_1 + \frac{1}{2X\left[1 + \frac{\gamma}{kv_{T1}}\frac{\partial\Psi}{\partial z}\right]}\right.$$

$$\left. \pm \sqrt{\frac{1}{\left\{2X\left[1 + \frac{\gamma}{kv_{T1}}\frac{\partial\Psi}{\partial z}\right]\right\}^2} - F_2^2(z)}\right]^{-1}. \quad (9)$$

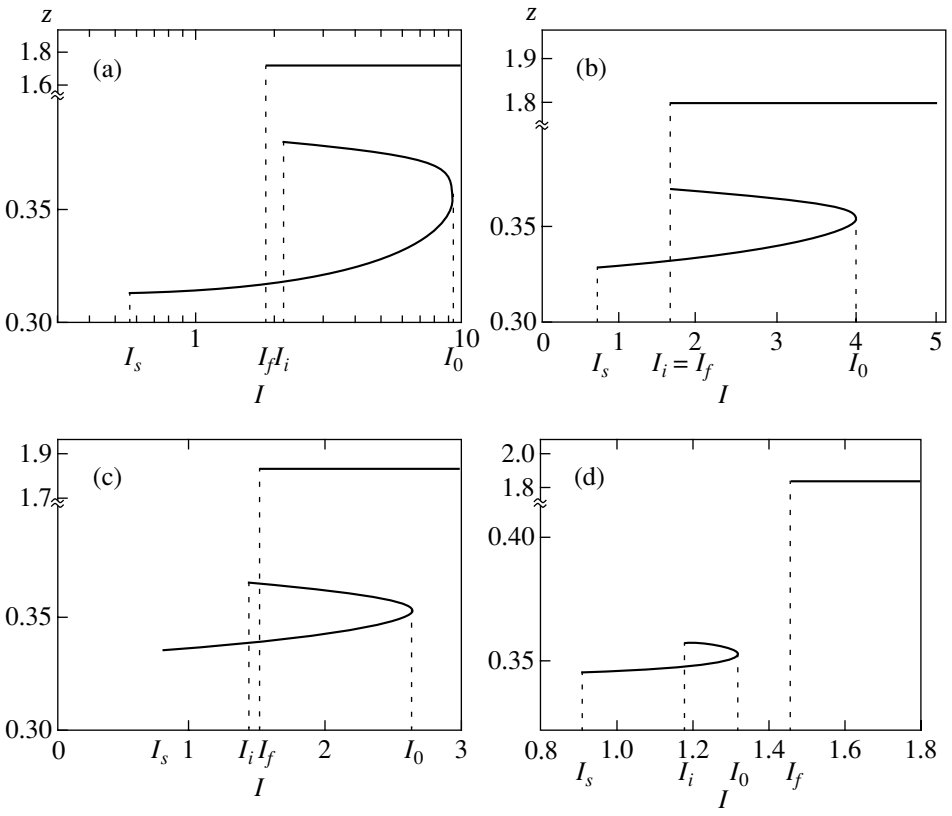

Fig. 2. Dependence of the velocity $z(I)$ of the SBS quasimodes excited in a $Xe_y^{+40}H_{1-y}^+$ plasma on the pumping intensity I for $y = 0.01$ and the following values of the parameter X: 1.20 (a), ≈1.43 (b), 1.50 (c), and 1.58 (d).

The plus sign in this formula corresponds to the smaller value of velocity, i.e., to the lower branch of the nonlinear dependence $z_s(I)$ on the dimensionless pumping intensity I and to a smaller value of the instability threshold I_s. The minus sign corresponds to a larger value of the sound velocity $z_i(I)$ of the SBS quasimode and to a higher value of the instability threshold I_i. After the attainment of the excitation threshold for a quasimode with velocity $z_i(I)$, the two branches converge upon a further increase in the pumping intensity. Accordingly, the intensity value I_0, which is determined, in accordance with Eq. (9), by the condition

$$1 = \left[2X\left(1 + \frac{\gamma}{k v_{T1}}\frac{\partial \Psi}{\partial z}\right)\right]^2 F_2^2(z),$$

corresponds to nonlinear convergence of the two branches $z_s(I)$ and $z_i(I)$. Thus, the lower branch $z_s(I)$ lies between the points $I_s \le I \le I_0$, while the upper branch $z_i(I)$ lies between the points $I_i \le I \le I_0$.

Let us compare the qualitative corollaries of formula (9) with the nonlinear dependences presented in Fig. 2 and corresponding to the solutions of Eqs. (6) and (7) for different values of X. The fast ion-sound SBS quasimode z_f is excited at the threshold I_f. This quasimode corresponds to $z > z_i$. In this case, two patterns of development of the SBS instability are possible. Figure 2a illustrates the situation when $I_s < I_f < I_i$. For $I_s < I < I_f$, this case corresponds to an SBS spectrum with a single frequency corresponding to the slow quasimode. For $I_f < I < I_i$, we have an SBS spectrum with two frequency shifts corresponding to one slow and one fast quasimode. As the pumping intensity increases, the quasimode z_i is excited, and we deal with an SBS spectrum with three frequency shifts. A further increase in the pumping intensity again leads to the case with two frequency shifts in the scattered radiation in the vicinity of $I = I_0$, since the branches z_s and z_i coincide. The results presented in Fig. 2a show that the sound velocity of two slower quasimodes near $I = I_0$ is a strongly nonlinear function of the pumping intensity, which also follows, by the way, from formula (9). For $I > I_0$, an SBS instability with the conventional shift in the scattered radiation spectrum by a frequency of the fast quasimode takes place (see Fig. 2a). Figure 2b illustrates the situation when a fast quasimode is excited at the same threshold as for the excitation of the intermediate quasimode z_i. This is observed for $X \approx 1.43$. For a large excess over the threshold value in the interval $I_i = I_f < I < I_0$, the SBS spectrum of the scattered wave field is characterized by

three frequency shifts. Finally, for $I > I_0$, the conventional situation of a single frequency shift of the scattered field takes place. In the case corresponding to the Xe concentration $y = 0.01$ and illustrated in Fig. 2c, we have $X = 1.5$. Here, the excitation of a slow quasimode for a comparatively low threshold in the interval $I_s \le I < I_i$ leads to only one frequency shift of scattered radiation by the frequency of the slow wave. Then, an intermediate wave is excited at $I = I_i$, and, accordingly, two frequency shifts are possible in the SBS spectrum in the interval $I_i \le I < I_f$. After this, a fast quasimode is excited at $I = I_f$, leading to three frequency shifts in the SBS spectrum. Finally, for $I > I_0$, only one frequency shift takes place in the scattered radiation spectrum. Figure 2d illustrates a peculiar nonlinear SBS effect, when an increase in the pumping intensity first leads to the excitation of the z_s branch; i.e., the SBS with a single frequency shift is realized. Then, the z_i branch is excited, while the fast z_f branch is still under the superthreshold conditions. This corresponds to the SBS with two frequency shifts. After this, in accordance with Fig. 2d, two slow branches z_s and z_i merge into one at $I = I_0$ owing to their strong nonlinear interaction. It turns out, however, that the excitation threshold for the fast quasimode has not been reached yet. Consequently, an increase in the excess intensity over the threshold value to $I_0 < I < I_f$ imposes a nonlinear prohibition which is removed for $I > I_f$. In other words, Fig. 2d illustrates the effect of nonlinear prohibition followed by nonlinear permission of SBS. This effect is strongly nonlinear in analogy with the strongly nonlinear dependence of the sound velocity of slow quasimodes on the pumping intensity in the vicinity of $I = I_0$ (see Figs. 2a, 2b, and 2c).

Figure 3 presents the curves characterizing the time increment of the SBS instability for the cases corresponding to Figs. 2c (solid curve) and 2d (dashed curve). The straight lines in Fig. 3 correspond to a fast wave with velocity v_f from Figs. 2c and 2d, according to which such a velocity is virtually independent of the pumping intensity, i.e., corresponds to the pattern (in the pumping intensity range presented in the figures) similar to that emerging in the linear theory of excitation spectra. In turn, the straight lines in Fig. 3 characterize the linear functional dependence of the SBS instability increments corresponding to the fast quasimode on the pumping intensity. Such a functional dependence is typical of the conventional linear theory of stimulated scattering. The nonlinear curves in the left part of Fig. 3 describe the dependence of the increment of the parametric instability associated with the excitation of a split slow SBS quasimode; this corresponds to the velocities $v_s(I)$ and $v_i(I)$ in Figs. 2c and 2d, which are nonlinear functions of the pumping intensity. These curves located in the left part of Fig. 3 and characterizing the increments of slow quasimodes differ qualitatively from the linear dependence of the increment of fast quasimodes on the pumping intensity. Vertical

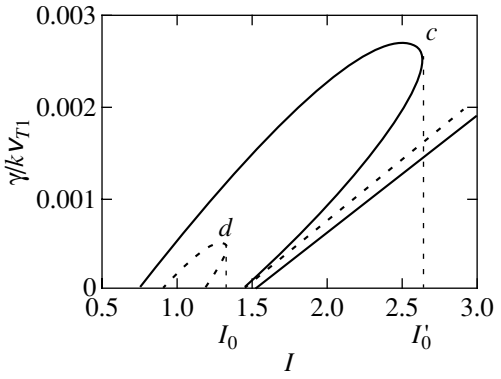

Fig. 3. Dependence of the time increment $\gamma(I)$ of the SBS instability on the pumping intensity I for the same plasma parameters as in Figs. 2c and 2d.

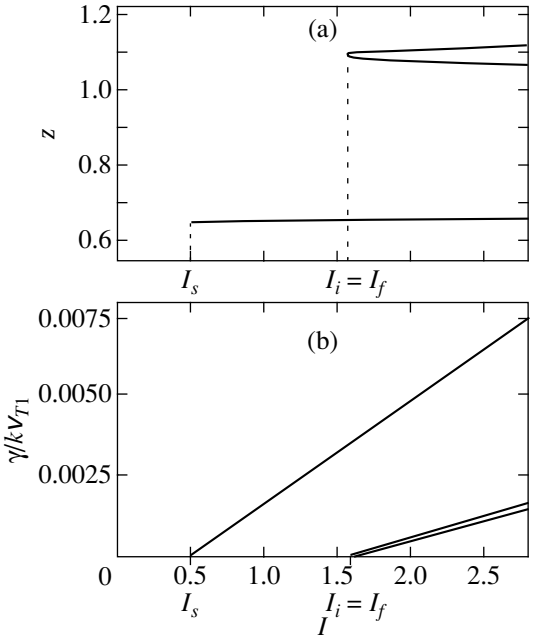

Fig. 4. Dependence of the velocity $z(I)$ and the time increment $\gamma(I)$ of the excited SBS quasimodes on the pumping intensity I for the concentration $y = 0.06$ and the parameter $X \equiv X_{\min}^{(2)} \approx 2.14$.

dashed lines in Fig. 3 correspond to the maximum values of the pumping intensity for which the splitting of slow waves still exists (to be more precise, terminates). It should be emphasized that the maximum value of the increment of the split SBS quasimode is attained before the convergence and is realized for the slow wave.

Let us now demonstrate the nonlinear spectral properties of the SBS, which are observed when the value of X is close to $X_{\min}(y) \neq 0$. This case corresponds to curves *2* in Figs. 1a and 1b obtained for $y = 0.06$. Curve *2* in Fig. 1b corresponding to the SBS threshold has no point of self-intersection. Figure 4 shows the dependences of the velocity $z(I)$ of quasimodes and the time

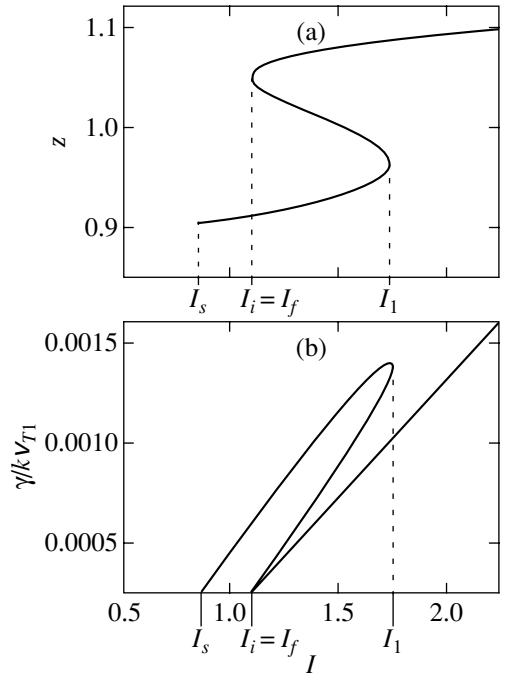

Fig. 5. Dependence of the velocity $z(I)$ and the time increment $\gamma(I)$ of the excited SBS quasimodes on the pumping intensity I for the concentration $y = 0.075$ and the parameter $X \equiv X_{\min} \approx 2.78$.

increment $\gamma(I)/kv_{T1}$ of the SBS instability on the intensity I of the pumping field, corresponding to the solution of the system of equations (6) and (7) for the value of the parameter $X = X_{\min}^{(2)}$. For $I = I_s$, a slow quasimode with velocity $z_s(I)$ exhibiting a weak dependence on the pumping field intensity is excited, and only one frequency shift of scattered radiation is observed on the interval $I_s \le I < I_i = I_f$ (see Fig. 4a). This quasimode corresponds to a linearly increasing time increment in the range of relatively small values of I under investigation (see Fig. 4b). For $I = I_i = I_f$, the second frequency shift emerges in the scattered radiation spectrum, which corresponds to the excitation of intermediate and fast quasimodes with identical frequencies $z_i(I_i = I_f) = z_f(I_i = I_f)$ considerably exceeding the sound velocity z_s of the slow quasimode. The nonlinear effect of pumping on fast quasimodes is manifested most strongly precisely in the vicinity of $I_i = I_f$. A further increase in the pumping intensity leads to nonlinear splitting of the conventional fast mode of ion sound, which attenuates relatively strongly for the value of the parameter X under investigation, into two quasimodes with close velocities: a fast quasimode with the highest velocity of sound $z_f(I)$ and an intermediate quasimode with a lower value of velocity $z_i(I)$. The nonlinear effect of pumping on the velocity of split waves is insignificant, although it is just the nonlinear effect of the pumping field which causes the splitting of fast quasimodes. Such a behavior of the velocities z_i and z_f is similar to a certain extent to the nonlinear splitting of a slow wave (see Fig. 2). Thus, for $I > I_i = I_f$, the scattered radiation spectrum contains three frequency shifts corresponding to $z_s(I)$, $z_i(I)$, and $z_f(I)$. It can be seen from Fig. 4b that, in the range of relatively small values of I under investigation, two split quasimodes correspond to virtually coinciding time increments of SBS instability which are smaller in absolute value than the increment for the slow quasimode. Figure 4b shows that the nonlinear effect of pumping on the increment of quasimodes is even weaker than the effect produced on their velocity.

It was proved in the discussion of Fig. 4 that the qualitative peculiarity of the scattered radiation spectrum for values of the plasma parameter X close to $X_{\min}$ lies in the nonlinear splitting of exactly the fast mode of ion sound into two quasimodes, while, for values of X close to $X_{\max}$, it is the slow mode of ion sound that splits nonlinearly (see Figs. 2a–2d). Let us now consider the situation when, in contrast to the cases depicted in Figs. 2 and 4a, the nonlinear behavior of the velocity of quasimodes cannot be reduced to splitting of slow or fast waves. Figure 5a demonstrates a nonlinear dependence of the sound velocities of all three SBS quasimodes on I, which is realized in the range of small values of pumping intensity I for a $Xe_y^{+40}H_{1-y}^{+}$ plasma for values of concentration y slightly smaller than $y_0 = 0.0765$. According to [10], y_0 corresponds to the highest value of the concentration of the heavy impurity ions Xe^{+40} for which the region of three values of the threshold curves $z_{\text{th}}(X)$ and $I_{\text{th}}(X)$ still exists. For $y = 0.075 < y_0$, the behavior of the threshold velocity $z_{\text{th}}(X)$ and the SBS threshold $I_{\text{th}}(X)$ is qualitatively similar to that illustrated by curves *2* in Figs. 1a and 1b, but the boundary values $X_{\min} \approx 2.78$ and $X_{\max} \approx 2.79$ of the parameter X differ insignificantly in this case. It can be seen from Fig. 5a that, for $I = I_s$, a slow quasimode with the sound velocity $z_s(I)$ is excited and there exists only one frequency shift in scattered radiation corresponding to this quasimode in the interval $I_s \le I < I_i = I_f$. For $I = I_i = I_f$, a faster intermediate and a fast quasimode with coinciding frequencies $z_i = z_f$ are excited. As the pumping intensity increases further in the interval $I_i = I_f < I < I_1$, the scattered radiation spectrum acquires all three frequency shifts. It can be seen from Fig. 5b that, in the interval of pumping intensities $I_i = I_f < I < I_1$ in which all the three quasimodes exist, their time increments are of the same order of magnitude. In this case, the slow quasimode with velocity $z_s(I)$ is enhanced most effectively. The intermediate mode $z_i(I)$ increases less effectively, while the fast quasimode $z_f(I)$ has the smallest increment. With a further increase in the pumping field for $I > I_1$, scattered radiation again displays only one frequency shift associated with the excitation of quasimode $z_f(I)$. Figure 5 shows the pumping intensities for which the nonlinear effect of pumping is manifested

most clearly. In the vicinity of $I_i = I_f$, both velocities and increments corresponding to the split fast and intermediate quasimodes experience a strong nonlinear effect of pumping. In the vicinity of I_1, the pumping field produces a considerable nonlinear effect on the same quantities corresponding to the split slow and intermediate quasimodes. Outside the above-indicated ranges of I, the nonlinear effect of pumping on the sound velocities of quasimodes is preserved (the slow quasimode increases for $I_s \le I < I_1$, the intermediate quasimode for $I_i < I < I_1$, and the fast quasimode for $I_f < I$), and the increment of the increases of the corresponding quasimodes in time is a linear function of the pumping intensity. It should be emphasized that, for the concentration $y = 0.075$ in question, which is close to the boundary concentration y_0, the velocities of all three quasimodes differ insignificantly. However, the relation between the slow, intermediate, and fast quasimodes described above is characterized by a strong nonlinear dependence on the pumping intensity I. This property distinguishes the situation considered above from the cases discussed earlier ($y = 0.01$ and X is close to X_{max} or $y = 0.06$ and X is close to X_{min}), when one of the three branches (fast in the first case and, accordingly, slow in the second case) weakly depends on the pumping field intensity and can be described in the framework of the linear theory of stimulated scattering.

In conclusion, we consider another peculiar case of a nonlinear effect of pumping on the SBS spectrum, which is manifested for parameters X close to X_{min}. This case has no analogues among those considered earlier and supplements the qualitative variety of manifestations of nonlinear spectral properties of SBS. It was mentioned earlier that curve *1* in Fig. 1b, which determines the threshold value of the pumping intensity $I_{th}(X)$ for $y = 0.01$, displays self-intersection as a result of which the threshold of the fast quasimode turns out to be lower than the threshold for the intermediate quasimode for parameters X smaller than that corresponding to the self-intersection point (see Fig. 2a). However, for concentration $y = 0.01$, the three-valued region of the threshold curve is not bounded from below in the parameter X; i.e., $X_{min}^{(1)} = 0$. It was shown in [10] that the threshold curves $I_{th}(X)$ for a $Xe_y^{+40}H_{1-y}^{+}$ plasma in the concentration range $0.024 < y < 0.037$ exhibit self-intersection, and the lower boundary of the three-valued region of $X_{min}(y)$ differs from zero, so that the fast and intermediate branches of the threshold curve $I_{th}(X)$ form a loop closed for $X_{min} \neq 0$ to the left of the self-intersection point. Figure 6 shows on a magnified scale a segment of the $I_{th}(X)$ curve containing a self-intersection point and the loop formed in this case. Here, $X_{min}^{(3)} = 0.714$. It should be emphasized that, in the loop region, the threshold of the fast quasimode I_f (lower part of the loop) is lower than the threshold for the intermediate quasimode I_i (upper part of the loop) only slightly. For this reason, the values of the pumping intensity corresponding to the excitation of these two quasimodes virtually coincide in Fig. 7a, which presents the nonlinear pattern of variation of the SBS

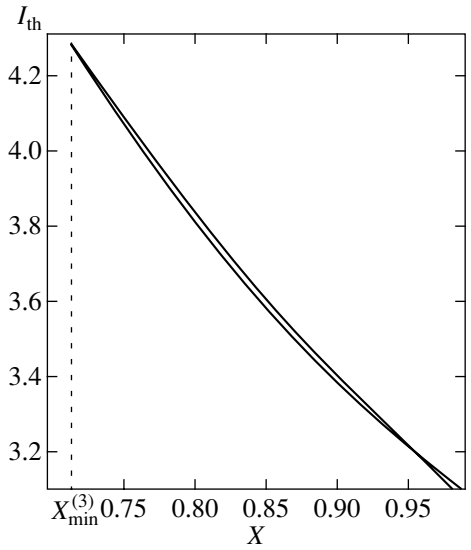

Fig. 6. Segment of the threshold curve I_{th} containing the neighborhood of the self-intersection point and the closed loop formed in this case for the concentration $y = 0.035$ on a magnified scale.

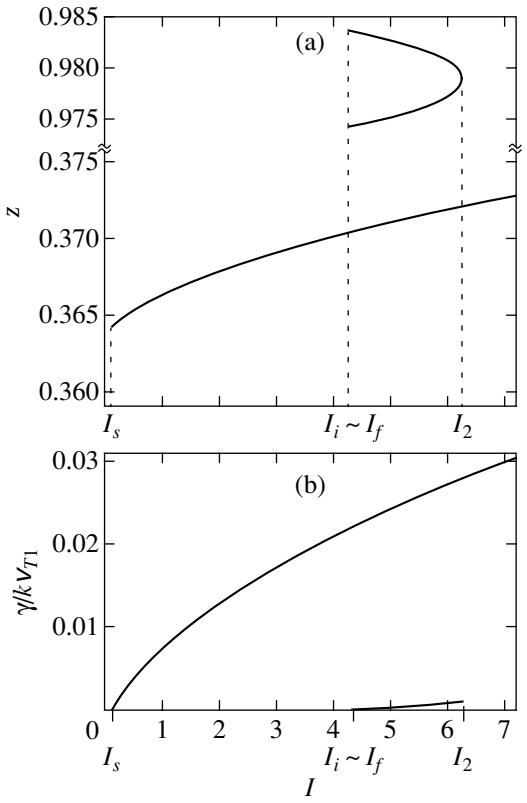

Fig. 7. Dependence of the velocity $z(I)$ and the time increment $\gamma(I)$ of the excited SBS quasimodes on the pumping intensity I for the concentration $y = 0.035$ and the parameter $X = 0.714$.

quasimode spectrum upon an increase in the pumping intensity for the parameter $X = 0.7142$, which exceeds the value of $X_{\min}^{(3)}$ only slightly. In can be seen from Fig. 7a that even for a low pumping intensity I_s, the slow quasimode $z_s(I)$ is excited. In contrast to the case presented in Fig. 4 for the concentration $y = 0.06$, when the nonlinear effect of pumping on the spectrum and increment of the slow quasimode is weak, Fig. 7 shows that the velocity $z_s(I)$ of the slow quasimode and the appreciable time increment of its buildup exhibit a strong nonlinear increase with the pumping intensity I. Such a nonlinear effect of pumping is due to the extremely low excitation threshold I_s for the slow SBS quasimode, which may correspond to a considerable excess over the SBS threshold associated with the excitation of this quasimode even in the range of relatively small values of pumping intensity I under investigation. As the pumping intensity increases further, a fast and an intermediate quasimode are exited successively for $I = I_f \approx I_i$, and the SBS spectrum acquires three different frequency shifts for a pumping intensity $I > I_i$. It should be noted that for $I > I_i$, close values of velocities $z_i(I)$ and $z_f(I)$ considerably exceed $z_s(I)$, which again corresponds to nonlinear splitting of a conventional strongly damped ion-sound wave into two (fast and intermediate) quasimodes. As the pumping intensity increases still further, the fast and intermediate branches converge. In the vicinity of $I = I_2$, the nonlinear effect of pumping on the velocities of the intermediate and fast quasimodes is manifested most strongly and leads to their merging, so that only one slow quasimode is excited for $I > I_2$. Such a manifestation of the nonlinear effect of pumping on the velocities of fast and intermediate quasimodes, which rules out their excitation upon an increase in the pumping intensity, resembles to a certain extent the manifestation of the nonlinear effect of pumping on the SBS quasimode spectrum in the case presented in Fig. 2, where an increase in the pumping intensity led first to the nonlinear merging and then to the prohibition on the excitation of the slow and intermediate SBS quasimodes. On the other hand, the nonlinear convergence and subsequent disappearance of faster nonlinearly split quasimodes upon an increase in the pumping intensity for values of X slightly exceeding $X_{\min}$ are qualitatively different manifestations of the nonlinear effect of pumping on the spectrum and increment of the SBS quasimodes in the case characterized by the threshold curve $I_{\text{th}}(X)$ with a loop and a self-intersection point as compared to the case of the threshold curve without self-intersection considered above for values of X close to $X_{\min}$ (see curve *2* in Fig. 1b), when an increase in the pumping intensity leads to the opposite result, viz., nonlinear splitting of the indicated quasimodes with a subsequent increase in the difference between their velocities (see Fig. 4a). Since the threshold for the slow SBS quasimode I_s is lower than the thresholds of the intermediate and fast quasimodes ($I_f \approx I_i$) by almost 1.5 orders of magnitude, the time increments of the latter quasimodes turn out to be much smaller than the increment for the slow quasimode (Fig. 7b). It can also be seen that the increments of the intermediate and fast quasimodes virtually coincide and are linear functions of the pumping intensity for values of I not very close to I_2. The relative smallness of the time increments of the fast and intermediate quasimodes as compared to the increment of the slow quasimode indicates that SBS is mainly determined by the slow quasimode. On the other hand, the value of pumping intensity I_2 for which the splitting of the fast sound wave terminates turns out to be quite sensitive to small variations of the plasma parameter X. The value of I_2 increases by almost an order of magnitude upon an increase in the value of X by just one percent. For such a small increase in the parameter X for $I > I_i$, we arrive at the pattern corresponding to the existence of one slow and two faster quasimodes with close velocities z_i and z_f exhibiting a weak dependence on I.

Summarizing the results of our analysis, it is appropriate to note that the nonlinearity of the SBS quasimode spectrum caused by a relatively weak pumping field is manifested most strongly exactly in the vicinity of the boundaries $X_{\min}(y)$ and $X_{\max}(y)$ of the three-valued region on the threshold curves depicted in Fig. 1.

Thus, the idea that the frequency of low-frequency excitations whose damping decrement is not small as compared to their frequency may change nonlinearly under the effect of the pumping field in the case of the SBS involving such excitations has been implemented in this article. The SBS spectra for a nearly isothermal completely ionized plasma with two species of ions clearly display a nonlinear variation. It is shown that under certain conditions determined by the properties of plasma, different numbers of SBS quasimodes with different numbers of frequency shifts in scattered radiation can be manifested depending on the pumping intensity, the frequency shifts themselves being determined by the pumping intensity. The phenomenon of nonlinear prohibition and subsequent permission of the SBS is also ascertained. It is manifested in that the parametric instability appearing after overcoming a certain threshold becomes forbidden upon a further increase in the pumping intensity. The SBS becomes possible only as a result of a subsequent increase in the pumping intensity and overcoming another SBS threshold. All these facts indicate, in particular, the variety of nonlinear optical properties of plasmas with a complex composition.

ACKNOWLEDGMENTS

This work was partly financed by the CRDF (grant no. RP1-2268), the Russian Foundation for Basic Research (project no. 99-02-18075), and the Federal Program Supporting Leading Scientific Schools (project no. 00-15-96720).

REFERENCES

1. I. Alexeff, W. D. Jones, and D. Montgomery, Phys. Rev. Lett. **19**, 422 (1967).
2. A. Hirose, I. Alexeff, and W. D. Jones, Phys. Fluids **13**, 1290 (1970).
3. B. D. Fried, R. B. White, and T. K. Samec, Phys. Fluids **14**, 2388 (1971).
4. L. L. Pasechnik and V. F. Semenyuk, Zh. Tekh. Fiz. **43**, 1071 (1973) [Sov. Phys. Tech. Phys. **18**, 676 (1973)].
5. I. M. A. Gledhill and M. A. Hellberg, J. Plasma Phys. **36**, 75 (1986).
6. J. C. Fernandez, J. A. Cobble, B. H. Faiber, *et al.*, Phys. Rev. E **53**, 2747 (1996).
7. H. X. Vu, J. M. Wallace, and B. Bezzerides, Phys. Plasmas **1**, 3542 (1994).
8. E. A. Williams, R. L. Berger, R. P. Drake, *et al.*, Phys. Plasmas **2**, 129 (1995).
9. H. X. Vu, J. M. Wallace, and B. Bezzerides, Phys. Plasmas **2**, 1682 (1995).
10. I. V. Kuzora, M. V. Kozlov, C. J. McKinstrie, *et al.*, Phys. Lett. A **284**, 194 (2001).
11. Yu. M. Aliev and V. P. Silin, Zh. Éksp. Teor. Fiz. **48**, 901 (1965) [Sov. Phys. JETP **21**, 601 (1965)].
12. L. M. Gorbunov, Zh. Éksp. Teor. Fiz. **55**, 2298 (1968) [Sov. Phys. JETP **28**, 1220 (1969)].
13. V. P. Silin, in *Parametric Effect of High-Power Radiation on Plasma* (Nauka, Moscow, 1973), p. 140.
14. *Handbook of Mathematical Functions*, Ed. by M. Abramowitz and I. A. Stegun (National Bureau of Standards, Washington, 1964; Nauka, Moscow, 1979).

Translated by N. Wadhwa

Journal of Experimental and Theoretical Physics, Vol. 94, No. 1, 2002, pp. 46–59.
Translated from Zhurnal Éksperimental'noĭ i Teoreticheskoĭ Fiziki, Vol. 121, No. 1, 2002, pp. 57–72.

PLASMA, GASES

The Effect of Spatial Dispersion and Boundaries of a Medium on Resonance Radiation Transfer

A. N. Starostin* and M. A. Chesnokov

State Scientific Center Troitsk Institute for Innovation and Thermonuclear Studies (TRINITI), Troitsk, Moscow oblast, 142190 Russia

**e-mail: a.starostin@relcom.ru*

Received July 30, 2001

Abstract—An integral equation is derived for the spectral density of excited atoms using optically dense bounded dispersion media as an example. It is found that the inclusion of the thermal motion of atoms and of the effects due to the existence of a boundary brings about a nonlocal correlation between the concentration of excited particles and the intensity of electromagnetic field in the medium. It is demonstrated that, when the spatial dispersion of permittivity and the boundary effects are disregarded, the obtained result transforms to the well-known Biberman–Holstein equation. The problem on the spectral intensity of radiation of a heated half-space is also investigated. *© 2002 MAIK "Nauka/Interperiodica".*

1. INTRODUCTION

One of the most important characteristics defining the resonance radiation transfer in a medium is the spectral density of excited atoms $N(\mathbf{r}, \mathbf{v}, \omega, t)$. In the semiclassical limit, this density is defined as the number of atoms capable of emitting a photon with the frequency ω located at the moment of time t at point $\mathbf{r}$ and having the velocity $\mathbf{v}$ [1–3].

In fairly dense media, conditions may be realized under which the frequency of irregularity of the phase of excited atom in broadening collisions, γ_{coll}, will be high compared with the probability γ_R of spontaneous transitions (i.e., $\gamma_{\text{coll}} \gg \gamma_R$). In this case, the correlation of the frequencies of absorbed and emitted photons disappears; i.e., the atom "forgets" about the frequency exhibited by the absorbed photon and emits a photon with a probability proportional to the spectral line profile. This mode is referred to as "complete frequency redistribution" (CFR). In the case of a resonance mechanism of broadening [4], associated with the transfer of excitation from one atom to another, we have, for γ_{coll},

$$\gamma_{\text{coll}} = N\pi\frac{d_{12}^2}{\hbar},$$

where N is the particle density in the ground state, and d_{12} is the matrix element of dipole moment for resonance transition. In what follows, the subscript 1 will indicate the ground state of an atom, and the subscript 2, the excited state. For the probability of spontaneous radiation γ_R, we have [3]

$$\gamma_R = \frac{4}{3}\frac{\omega^3 d_{12}^2}{hc^3},$$

where c is the velocity of light, and ω is the resonance photon frequency. Therefore, the condition $\gamma_{\text{coll}} \gg \gamma_R$ will be valid for such a gas density N that

$$\frac{N\lambda^3}{32\pi} \gg 1. \quad (1)$$

For sodium atoms, condition (1) for the resonance line of atomic vapor implies that $N \geq 3 \times 10^{13}$ cm^{-3}. If, in this case, the correlation $\gamma_{\text{coll}} > kv_T$ is valid (where kv_T is the Doppler line width $k = 2\pi/\lambda$, and v_T is the atomic thermal velocity), then, as is shown in [6], the photon free path $l_\omega \sim 1/k_\omega$ (k_ω is the absorption coefficient in the line) for such a gas density becomes comparable with the wavelength, and the description of radiation transfer in terms of photons becomes invalid. In this case, the theory must take into account the effect of the dielectric properties of the medium on the resonance wave propagation. For sodium atoms, the condition $\gamma_{\text{coll}} > kv_T$ becomes valid at $N > 10^{17}$ cm^{-3}.

We will restrict ourselves to the treatment of the case of not too high an atom density, when the medium is "transparent," i.e., the resonance photon free path is long compared with the wavelength, but the condition for the mode of complete frequency redistribution (1) is valid. In the case of a transparent medium, a kinetic equation of standard form may be written for the spectral radiation intensity, which is a particular case of the Dyson equation for the Green's photon function, written in a quasiclassical approximation.

The resonance radiation transfer in the CFR mode was studied in detail by Biberman [7] and Holstein [8]. They have demonstrated that, in the case of complete frequency redistribution, the spectral density of excited

particles may be represented as

$$N_2(\omega) = \int N_2(\omega, \mathbf{v})d\mathbf{v} = N_2 a(\omega), \quad (2)$$

where $a(\omega)$ is the spectral line profile, and N_2 is the total population of higher state (in the general case, it is nonequilibrium). This correlation, which is valid for the case of moderate detuning from resonance, $\Delta = \omega - \omega_0 \ll T$ (T is the temperature of broadening particles, and ω_0 is the resonant transition frequency), implies that the probability of emission of a quantum of frequency ω does not depend on the absorbed photon frequency and is proportional to the spectral line profile. This assumption is valid when frequent collisions with broadening particles bring about a random walk of an excited atom within the line profile and make the atom forget the excitation history (i.e., in the case of complete redistribution in particles). Note that the purely radiative mechanism of broadening does not cause the frequency redistribution of emitted photons, which is important from the standpoint of radiation transfer in optically dense media, when the main fraction of energy is transferred in the spectral line wings (in the line wings, the Voigt line profile exhibits the Lorentz asymptotic behavior).

In addition, an integral equation (Biberman–Holstein equation) for total density of excited atoms $N_2(\mathbf{r})$ was obtained in the CFR limit, describing the nonlocal transfer of excitation due to resonance radiation,

$$\nu N_2(\mathbf{r}) = Q(\mathbf{r}) + \int d\mathbf{r}' K(\mathbf{r}, \mathbf{r}') N_2(\mathbf{r}'). \quad (3)$$

Here, $\nu = \gamma_R + \gamma_T$ is the total rate of depopulation of the excited level due to spontaneous decay and inelastic collisions, and $Q(\mathbf{r})$ is the rate of collisional population of the excited level (for example, by an electron impact). In the case of a homogeneous medium, the kernel of integral equation (3) has the form

$$K(\mathbf{r}, \mathbf{r}) = \gamma_R \times \int d\omega \frac{k_\omega a_\omega}{4\pi|\mathbf{r} - \mathbf{r}'|^2} \exp(-k_\omega|\mathbf{r} - \mathbf{r}'|). \quad (4)$$

The physical meaning of Eq. (3) consists in that the density of excited atoms at point $\mathbf{r}$ decaying at the rate ν is formed owing to inelastic collisions $Q(\mathbf{r})$ and resonance radiation emitted by excited atoms (located at point $\mathbf{r}'$) at the rate $\gamma_R a_\omega$ in the frequency range of ω, $\omega + d\omega$. When this radiation arrives at point $\mathbf{r}$, it is attenuated proportionally to the factor

$$\frac{\exp(-k_\omega|\mathbf{r} - \mathbf{r}'|)}{4\pi|\mathbf{r} - \mathbf{r}'|^2}$$

and is absorbed at this point with the probability proportional to the value of the absorption coefficient k_ω. In optically dense media, when $k_{\omega_0} R \gg 1$ (R is the characteristic size of the system), the contribution made by the frequency range in the vicinity of the line center $\Delta = \omega - \omega_0 \ll \Gamma$ is exponentially small, and the main contribution to the integral in Eq. (4) is made by the line wings, i.e., $\Delta \gg \Gamma$.

Note that Eq. (3) was first written from purely heuristic considerations. In addition, Eq. (3) was written disregarding the effects caused by the existence of the boundary and by the thermal motion of atoms of the medium (i.e., the spatial dispersion of permittivity). As will be demonstrated below, the thermal motion of atoms and the presence of the boundary result in a nonlocal pattern of the response of the medium to the electromagnetic field in bounded systems. It is the objective of our study to derive a generalized Biberman–Holstein equation that would include these effects. It will be found that the spectral density of excited particles satisfies an equation of the form of (3) with the generalized kernel $\tilde{K}$ dependent on the dielectric properties of the medium. It will be further demonstrated that, if the spatial dispersion and the presence of the boundary are ignored, the kernel $\tilde{K}$ transforms to Eq. (4).

In addition, we treat the problems on the radiation emitted by a heated half-space and on the transmission of resonance waves through a medium. The expressions for the Green's photon functions may be found directly from the solution of the appropriate kinetic equation in the external and internal regions and subsequent joining at the interface. The explicit form of the coefficient of reflection of electromagnetic waves from a resonant medium will be found. Note that this problem was previously studied by Wood [9] and Veklenko and Tkachuk [10]. We will also derive the expression for the reflection coefficient, which includes explicitly the spatial dispersion and, thereby, generalizes the known Fresnel–Wood result [9]. In addition, explicit expressions have been derived for the spectral radiation intensity in a medium, which is due to incident resonance waves and spontaneous photon sources. In what follows, we will demonstrate that the function of a bulk source of spontaneous radiation ε_ω is proportional to the spectral density N_2 of excited atoms. Therefore, given the depth dependence of N_2, the obtained results enable one to fully describe the transmission of incident radiation through a medium, as well as the emission of radiation by a heated half-space into vacuum.

2. KINETIC EQUATION FOR SPECTRAL DENSITY OF EXCITED ATOMS

We will treat a semi-infinite, homogeneous and isotropic medium consisting of two-level nondegenerate systems. Thereby, various effects associated with the polarization of radiation will be ignored. The xy plane will be selected as the interface, and the z axis will be directed into the bulk of the medium.

The traditional mechanism enabling one to derive an equation for the spectral density $N(\mathbf{r}, \mathbf{v}, \omega, t)$ of excited atoms is the mechanism of the kinetic Green's func-

tions. Note, however, that, in what follows, we will deal only with the projections of the atomic Green's function $G_{ij}^{\alpha\beta}$ $(i, j = 1, 2)$ onto the ground and excited states. For example, for G_{ij}^{-+}, we have

$$iG_{ij}^{\alpha\beta}(x, x') = -\int \varphi_i^*(\xi)\langle \hat{\Psi}^+(x'\xi')\hat{\Psi}(x\xi)\rangle \varphi_j(\xi')d\xi d\xi'.$$

Here, $x = \{t, \mathbf{r}\}$ is the 4-coordinate of the atomic center of gravity, and ξ denotes the variables characterizing the motion of atomic electrons. The operator $\hat{\Psi}$ is the Heisenberg field operator of atomic particles (for definiteness, we will assume that $\hat{\Psi}$ satisfies the Fermi statistics), and φ_i $(i = 1, 2)$ is a set of atomic functions. The subscripts α and β have, in accordance with the Keldysh technique [11], the values of + or –. Note that, in the absence of coherent pumping, the nondiagonal elements of $G_{ij}^{\alpha\beta}$ $(i \neq j)$ are zero.

We will assume a fairly slow variation of all quantities in space and time, which will enable us to impart to theory the form of kinetic equations for the populations of atomic states and spectral intensities. Following is the correlation, in a semiclassical approximation, between the spectral density $N(\mathbf{r}, \mathbf{v}, \omega, t)$ of excited particles and the kinetic Green's function G_{22}^{-+} of excited particles:

$$N(\mathbf{r}, \mathbf{v}, \omega, t) = -\int G_{22}^{-+}(\mathbf{r}_1, t_1, \mathbf{r}_2, t_2) \times \exp(i\omega_p\tau - i\mathbf{k}\cdot\boldsymbol{\rho})d\tau d\boldsymbol{\rho}, \quad (5)$$

$$\tau = t_1 - t_2, \quad \boldsymbol{\rho} = \mathbf{r}_1 - \mathbf{r}_2, \quad \mathbf{r} = \frac{\mathbf{r}_1 + \mathbf{r}_2}{2}, \quad t = \frac{t_1 + t_2}{2}.$$

The wave vector $\mathbf{k}$ is related to the velocity $\mathbf{v}$ of an atomic particle by the relation $\mathbf{v} = \hbar\mathbf{k}/M$, where M is the atomic mass. Note that the quantity $N_2(\mathbf{r}, \mathbf{v}, \omega_p, t)$ has no physical meaning because of the uncertainty principle and, generally speaking, may be negative. Only the moments of spectral density have a physical meaning. The Green's function G_{22}^{-+} is the solution of the corresponding kinetic equation representing a particular case of the Dyson equation. Therefore, the derivation of the expression for the spectral density of excited atoms reduces to finding the Green's function G_{22}^{-+} of excited particles, i.e., to the solution of the corresponding kinetic equation. We will solve this equation under the following assumptions: the atomic gas is nondegenerate—i.e., we ignore the terms of the order of $N\lambda_T^3$ $(\lambda_T = \sqrt{2\pi\hbar^2/MT}$ is the thermal de Broglie atomic wavelength) compared with unity; the interaction between photons and atoms of the medium is described in the dipole approximation; detuning of frequencies from resonance is small, i.e.,

$$\Delta = \omega - \omega_0 \ll \omega_0, \quad \omega_0 = \omega_2 - \omega_1.$$

In addition to the atomic Green's functions, we will use the correlation functions of electromagnetic field $D_{ik}^{\alpha\beta}$ determined in terms of the Heisenberg operators of the vector potential $\hat{A}_i$. For example, for the kinetic Green's photon function D_{ik}^{-+}, we have (assuming the calibration with the scalar potential $\varphi = 0$)

$$iD_{ik}^{-+}(x, x') = \langle \hat{A}_k(x')\hat{A}_i(x)\rangle,$$

$$iD_{0i}^{-+} = iD_{i0}^{-+} = 0, \quad i, k = 1, 2, 3.$$

The retarded $D^R(G^R)$ and advanced $D^A(G^A)$ Green's functions are expressed in terms of the $D^{--}(G^{--})$, $D^{++}(G^{++})$, and previously introduced $D^{-+}(G^{-+})$ functions as follows:

$$D^R = D^{--} - D^{-+}, \quad D^A = D^{-+} - D^{++}.$$

As was already indicated, finding the spectral density N_2 of atoms in the excited state reduces to solving the appropriate equation for the kinetic Green's function of excited particles G_{22}^{-+}, which is a particular case of the Dyson equation. We change over in this equation to Fourier components with respect to time and coordinate differences and take into account the definition (cf. Eq. (5))

$$G_{22}^{-+}(z_1, z_2, \mathbf{k}_\perp, \omega_p, t) = \int d\tau d\boldsymbol{\rho}_\perp \exp(i\omega_p\tau - i\mathbf{k}_\perp\cdot\boldsymbol{\rho}_\perp)G_{22}^{-+}(\mathbf{r}_1, t_1, \mathbf{r}_2, t_2),$$

$$\tau = t_1 - t_2, \quad \boldsymbol{\rho}_\perp = \mathbf{r}_{1\perp} - \mathbf{r}_{2\perp}, \quad t = \frac{t_1 + t_2}{2}$$

(the subscript $\perp$ indicates the direction perpendicular to the z axis) to derive, for a half-space,

$$\left[-i\hbar\frac{\partial}{\partial t} - \frac{\hbar^2}{2M}\left(\frac{d^2}{dz_1^2} - \frac{d^2}{dz_2^2}\right)\right]G_{22}^{-+}(z_1, z_2, t) = -\int_0^\infty dz_3\{\Sigma_{22}^{--}(z_1, z_3, t)G_{22}^{-+}(z_3, z_2, t) + \Sigma_{22}^{-+}(z_3, z_2, t)G_{22}^{-+}(z_1, z_3, t) + \Sigma_{22}^{-+}(z_1, z_3, t)G_{22}^{++}(z_3, z_2, t) + \Sigma_{22}^{--}(z_3, z_2, t)G_{22}^{--}(z_1, z_3, t)\}. \quad (6)$$

Here and in what follows, in order to simplify the notation, we will not indicate explicitly the arguments $\mathbf{k}_\perp$ and ω_p. In deriving Eq. (6), we have ignored the retardation effects, which is justified when the radiation intensity varies in time rather slowly. The mass opera-

tors $\Sigma_{22}^{\alpha\beta}$ describe the interaction of excited particles with resonance photons and broadening particles (for example, electrons), with the following correlation being valid in the limit of low atomic density:

$$\Sigma_{22}^{-+} \ll \Sigma_{22}^{+-}, \Sigma_{22}^{--}, \Sigma_{22}^{++}.$$

The last two terms on the right-hand side of Eq. (6) correspond to the incoming term associated with the absorption of resonance photons by atoms in the ground state, as well as with transitions to the excited level under the effect of collisions. Analogously, the first two terms describe the depopulation of the excited level due to spontaneous and induced emission or collisions.

We will seek a steady-state solution to Eq. (6) in the CFR mode; i.e., we will assume the frequency of elastic collisions (leading to a random walk of excited atoms along the line profile) γ_{coll} to be higher than the frequencies of spontaneous radiative transitions γ_R and of inelastic collision transitions γ_T. In this case, from the equality to zero of the elastic collision integral, $\text{St}^{\text{elastic}} = 0$, we derive that $G_{22}^{-+}(G_{22}^{+-})$ may be represented in the form [12]

$$\begin{aligned} G_{22}^{+-}(\omega, \mathbf{k}) &= (G_{22}^R - G_{22}^A)(1 - \tilde{N}_2(\omega, \mathbf{k})) \\ &= 2\pi i a_2(\varepsilon_{\mathbf{p}})(1 - \tilde{N}_2(\omega, \mathbf{k})), \\ G_{22}^{-+}(\omega, \mathbf{k}) &= -(G_{22}^R - G_{22}^A)\tilde{N}_2(\omega, \mathbf{k}) \\ &= 2\pi i a_2(\varepsilon_p)\tilde{N}_2(\omega, \mathbf{k}). \end{aligned} \tag{7}$$

Here,

$$\varepsilon_{\mathbf{p}} = \omega - \omega_2 - E(\mathbf{k}) + \mu, \quad E(\mathbf{k}) = \frac{\mathbf{k}^2}{2M}$$

is the energy of translational motion of an atomic particle; μ is the chemical potential; and $a_2(\varepsilon_p)$ is the Lorentz profile of excited state,

$$a_2(\varepsilon_p) = \frac{\gamma_2}{2\pi}\left(\varepsilon_p^2 + \frac{\gamma_2^2}{4}\right)^{-1}.$$

The quantity $\tilde{N}_2(\omega, \mathbf{k})$ in the case of degenerate gas and moderately broad lines; i.e., $\gamma_2 \leqslant T$ (we assume that the broadening particles are described by the Fermi distribution with the absolute temperature T), is written as

$$\tilde{N}_2(\omega, \mathbf{k}) = \tilde{N}_2 \lambda_T^3 \exp\left(-\frac{\varepsilon_p + E(\mathbf{k})}{T}\right). \tag{8}$$

Here, λ_T is the de Broglie wavelength of a particle, and $\tilde{N}_2$ is the effective nonequilibrium population of higher state defined in the general case by radiative and collision-induced (inelastic) transitions between the ground and excited levels. Therefore, the kinetic equations for the concentration of excited particles in the CFR limit will now be formulated in terms of the quantities $\tilde{N}_2$. Expressions (7) and (8) represent a generalization of the inferences made in the traditional theory of transfer to the case of broad spectral lines and enable one, in the case of thermodynamic equilibrium, to derive a correct expression for spectral intensity [12]. At equilibrium, the "populations" $\tilde{N}_i$ ($i = 1, 2$) obey the Boltzmann equations. We substitute expressions (7) and (8) into the equation for spectral radiation intensity to arrive (in contrast to the traditional theory) at the correct Planck formula for photon occupation numbers. Note further that, in the case of very narrow lines, i.e., for $\gamma_2 \ll T$, we can ignore ε_p in the exponent; in this case, the "populations" $\tilde{N}_i$ coincide with the true populations obtained by integration of (7) with respect to frequency and momenta.

We will first solve Eq. (6) in view of relations (7) and (8). We will treat in more detail the absorption by atoms of resonance photons from the ground state. For this purpose, we will first write the last term on the right-hand side of Eq. (6) in the explicit form

$$\begin{aligned} \text{St}_1^+ = i\left(\frac{j}{c}\right)_i \left(\frac{j}{c}\right)_k \int_0^\infty dz_3 \frac{d\omega}{2\pi}\frac{d\mathbf{q}_\perp}{2\pi} G_{22}^R(z_1, z_3, \mathbf{k}_\perp, \omega_p) \\ \times D_{ik}^{-+}(z_3, z_2, \mathbf{q}_\perp, \omega, t) G_{11}^{(0)-+}(z_3, z_2, \mathbf{k}_\perp - \mathbf{q}_\perp, \omega_p - \omega). \end{aligned} \tag{9}$$

In deriving Eq. (9), use was made of the correlation $G^{--} \approx G^R$, valid in the case of a low atom density. In addition, we ignored the broadening of the ground atomic state and used the Green's function of unperturbed atoms as G_{11}^{-+}. The function G_{22}^R is the higher level retarded Green's function, and j_k is the kth projection of matrix element of the current density operator between states 2 and 1 (summation is implied by the subscripts i and k). The function G_{22}^R satisfies the corresponding Dyson equation with the mass operator Σ_{22}^R, which we solve to derive

$$\begin{aligned} G_{22}^R(z, z', \mathbf{k}_\perp, \omega_p) &= \frac{1}{\hbar} \\ &\times \sum_k \frac{\psi_k(z)\psi_k^*(z')}{\omega_p - \omega_2 - E_k + \mu + i\gamma_2/2}. \end{aligned} \tag{10}$$

In deriving Eq. (10), we used the relation

$$\Sigma_{22}^R = \frac{1}{2}(\Sigma_{22}^{--} - \Sigma_{22}^{++}) - \frac{1}{2}(\Sigma_{22}^{+-} - \Sigma_{22}^{-+}),$$

where the first term characterizes the level shift due to interaction with resonance photons and broadening particles, and the second term characterizes the finite width of the excited level. In Eq. (10), the functions $\psi_k(z) \propto \sin(kz)$ are the eigenfunctions of the Laplacian,

which describe the translational motion of an atom in the region of $z > 0$;

$$E_k = \frac{\hbar k^2}{2M} + \frac{\hbar \mathbf{k}_\perp^2}{2M}$$

denotes the respective eigenvalues of energy; and ω_2 is the frequency renormalized in view of the shift. The quantity

$$\gamma_2 \approx -2\mathrm{Im}\Sigma_{22}^R \approx \Sigma_{22}^{+-}$$

is the total width of the excited level, which, in the general case, is due to collisions and spontaneous decay. In the purely radiative mode, $\gamma_2 = A$, where A is the probability of the spontaneous $2 \longrightarrow 1$ transition (Einstein coefficient). For the Green's function $G_{11}^{(0)-+}$, it follows immediately from the definition that

$$G_{11}^{(0)-+}(z, z', \mathbf{k}_\perp, \omega_p) = 2\pi i \sum_k \psi_k(z)\psi_k^*(z') \times \delta(\omega_p - \omega_1 - E_k + \mu) N_1(k, \mathbf{k}_\perp), \quad (11)$$

where $N_1(k, \mathbf{k}_\perp)$ are the occupation numbers of atoms in the ground state by the quantum numbers k and $\mathbf{k}_\perp$. We substitute Eqs. (10) and (11) into (9) and take into account the smallness of the photon wave vector compared with the particle wave vector to derive the following expression for the incoming term St_1^+:

$$\mathrm{St}_1^+ = -2\pi\left(\frac{j}{c}\right)_i\left(\frac{j}{c}\right)\int_0^\infty dz_3 \int \frac{d\omega d\mathbf{q}_\perp}{(2\pi)^4} \times \frac{D_{ik}^{-+}(z_3, z, \mathbf{q}_\perp, \omega, t)}{\varepsilon_p + i\gamma_2/2} \frac{N_1(k, \mathbf{k}_\perp)}{|\nu_z|} \times \left\{\cos\left[\frac{\Delta}{\nu_z}(z + z_3)\right] + \cos\left[\frac{\Delta}{\nu_z}(z - z_3)\right]\right\}, \quad (12)$$

where

$$\Delta = \varepsilon_p - \omega + \omega_0 + \mathbf{q}_\perp \mathbf{v}_\perp, \quad \varepsilon_p = \omega_p - \omega_2 + E_k + \mu, \quad \nu_z = \frac{k}{M}, \quad \mathbf{v}_\perp = \frac{\mathbf{k}_\perp}{M}. \quad (13)$$

In deriving Eq. (12), averaging was performed over rapidly oscillating functions of the type $\exp(ip(z_1 + z_2))$. One can analogously derive an expression for the third term in the right-hand part of Eq. (6). On adding this third term to Eq. (12), we will derive the final expression for the incoming term describing the photoabsorption from the ground state,

$$\mathrm{St}^+ = 2\pi i a_2(\varepsilon_p)\left(\frac{j}{c}\right)_i\left(\frac{j}{c}\right)_k\int_0^\infty dz_3 \frac{d\omega d\mathbf{q}_\perp}{(2\pi)^3} \times D_{ik}^{-+}(z_3, z, \mathbf{q}_\perp, \omega, t)\frac{N_1(k, \mathbf{k}_\perp)}{|\nu_z|} \times \left\{\cos\left[\frac{\Delta}{\nu_z}(z + z_3)\right] + \cos\left[\frac{\Delta}{\nu_z}(z - z_3)\right]\right\}. \quad (14)$$

Expression (14) describes the nonlocal absorption of radiation in the vicinity of the half-space boundary. As follows from Eq. (14), the characteristic scale of nonlocality of the kernel is $L \sim \nu_z/\Delta$. Away from the boundary, at a distance much longer than L, we can ignore the nonlocality and extend the integration for z_3 to the entire axis from $-\infty$ to $+\infty$, with the kernel being of the order of $\delta(z - z_3)$.

Turning back to Eq. (6), we will treat the terms defining the depopulation of the excited level due to radiative decay. Disregarding the induced radiation, the decay term may be written as

$$\mathrm{St}^- = -\hbar A N_2(z, k, \mathbf{k}_\perp, \omega_p), \quad (15)$$

where A is the probability of the spontaneous $2 \longrightarrow 1$ transition. We substitute Eqs. (14) and (15) into Eq. (6) to derive the kinetic equation for the spectral density N_2 of atoms in the upper state,

$$\left(\frac{\partial}{\partial t} + \nu_z\frac{\partial}{\partial z}\right)N_2(z, \omega_p) = -AN_2 + 2\pi i a_2(\varepsilon_p)\left(\frac{j}{c}\right)_i\left(\frac{j}{c}\right)_k \times N_1\int_0^\infty dz_3 \int \frac{d\omega d\mathbf{q}_\perp}{(2\pi)^3} D_{ik}^{-+}(z_3, z, \mathbf{q}_\perp, \omega, t)\frac{f(k, \mathbf{k}_\perp)}{|\nu_z|} \times \left\{\cos\left[\frac{\Delta}{\nu_z}(z + z_3)\right] + \cos\left[\frac{\Delta}{\nu_z}(z - z_3)\right]\right\}. \quad (16)$$

Here, N_1 is the total number of atoms on the lower level; $f(k, \mathbf{k}_\perp)$ is the distribution function of atoms in the ground state over the quantum numbers k and $\mathbf{k}_\perp$, i.e., $N_1(k, \mathbf{k}_\perp) = N_1 f(k, \mathbf{k}_\perp)$; and $\nu_z = k/M$ is the z projection of the atomic velocity. In performing numerical calculations, we will use the Maxwell distribution function as the distribution function $f(\mathbf{k})$.

In the steady-state case, the general solution of Eq. (16) may be written in the form

$$N_2(z, \omega_p) = \exp\left(-\frac{Az}{\nu_z}\right) \times \left\{\bar{N}_2(z_0) + \int_{z_0}^z \frac{dz'}{\nu_z}\exp\frac{Az'}{\nu_z}\mathrm{St}^+\right\}, \quad (17)$$

where St^+ is the integral of collisions with photons (14), and the quantities $z_0 = z_0(\nu_z)$ and $\bar{N}_2(z_0)$ must be determined from the boundary conditions. We will first treat the atoms with $\nu_z < 0$, i.e., the atoms moving towards the interface. We assume that $z_0 = \infty$ and that $N_2(z) \longrightarrow 0$ at $z \longrightarrow \infty$ to derive from Eq. (17)

$$N_2(z, \nu_z < 0, \omega_p) = -\int_z^\infty \frac{dz'}{\nu_z}\exp\left(-\frac{A}{\nu_z}(z-z')\right)St^+. \quad (18)$$

We will now derive the expression for the atom density N_2 with $\nu_z > 0$, i.e., for the atoms moving into the bulk of the medium. For this purpose, we will designate the fraction of mirror collisions of atomic particles with the interface by η; accordingly, the quantity $1 - \eta$ will give the fraction of diffuse collisions. We assume $z_0 = 0$ and, in view of Eqs. (17) and (18), find

$$N_2(z, \nu_z > 0, \omega_p) = \eta\int_0^\infty \exp\left(-\frac{A}{\nu_z}(z+z')\right)\frac{St^+}{\nu_z}dz' + \int_0^z \exp\left(-\frac{A}{\nu_z}(z-z')\right)\frac{St^+}{\nu_z}dz'. \quad (19)$$

We will dwell on the case of purely specular collisions, $\eta = 1$. Here, the following correlation is valid on the interface $z = 0$:

$$N_2(z = 0, \nu_z < 0, \omega_p) = N_2(z = 0, \nu_z > 0, \omega_p). \quad (20)$$

It follows from Eq. (20) that atoms with velocities $\nu_z > 0$ may be regarded as atoms that passed through the plane $z = 0$ from the region $z < 0$. Owing to a certain symmetry arising as a result of specular collisions, the problem actually reduces to finding the spectral density of excited particles in the entire space provided the following correlations are valid:

$$D^{-+}(z, z') = D^{-+}(-z, z'), \quad N_2(z < 0) = N_2(z > 0). \quad (21)$$

Proceeding from Eqs. (18) and (19) in view of (21), the respective expression for the total concentration

$$N_2(z, \omega_p) = \int N_2(z, k, \mathbf{k}_\perp)dk d\mathbf{k}_\perp$$

of atoms in the upper state will be written as

$$N_2(z, \omega_p) = 2\pi i N_1\left(\frac{j}{c}\right)_i\left(\frac{j}{c}\right)_k a_2(\varepsilon_p)\int_0^\infty dz_3\int\frac{d\omega d\mathbf{q}_\perp}{(2\pi)^3} \times \int_{-\infty}^\infty dz' D_{ik}^{-+}(z_3, z', \mathbf{q}_\perp, \omega)K(z_3, z'|z), \quad (22)$$

where

$$K(z_3, z'|z) = \int_0^\infty \frac{d\nu_z}{\nu_z}\exp\left(-\frac{A}{\nu_z}|z-z'|\right)\int d\mathbf{v}_\perp\frac{f(\nu_z, \mathbf{v}_\perp)}{\nu_z} \times\left\{\cos\left[\frac{\Delta}{\nu_z}(z'+z_3)\right] + \cos\left[\frac{\Delta}{\nu_z}(z'-z_3)\right]\right\}. \quad (23)$$

As was already mentioned, the kernel K of the integral contains the description of the effects of nonlocal absorption of radiation in the vicinity of the interface (i.e., at $z \lesssim L = \nu_z/\Delta$), which are due to the absorption, by atoms at point z, of the radiation emitted by atoms at some other point z_3. In addition, this kernel takes into account various effects associated with the thermal motion of atoms, i.e., the specular reflections of particles from the plane $z = 0$ and the transfer of excitations by the moving atoms. In the case of thermal transfer of excitations, the atom that absorbed a photon at point z' may then emit this photon at another point z with the probability proportional to the factor $\exp(-A|z - z'|/\nu_z)$. Analogously, the excited atoms reflected from the interface also make an additional contribution to the excited particle concentration N_2 at depth z. Therefore, the inclusion of the thermal motion of atoms may bring about an increase in the effective number of excited atoms in the medium. In the case when the thermal velocity of particles is fairly low and the upper level is short-lived, the thermal effects become insignificant (except for the narrow region in the vicinity of the boundary, where the reflected atoms must be taken into account). In this limit, the kernel K is simplified considerably and takes the form

$$K(z_3, z'|z) = \delta(z'-z)\int d\mathbf{v}\frac{f(\mathbf{v})}{|\nu_z|} \times\left\{\cos\left[\frac{\Delta}{\nu_z}(z+z_3)\right] + \cos\left[\frac{\Delta}{\nu_z}(z-z_3)\right]\right\}. \quad (24)$$

It is important to note that, in media with the permittivity $|\varepsilon - 1| \sim 1$, the reflection of electromagnetic waves from the interface takes on significance; this results in an additional contribution to the intensity of radiation in the material, thereby causing an increase in the population of the upper level.

We have treated the case of purely specular reflections of atoms from the interface $z = 0$. The problem may be reduced to that on finding the spectral density in the entire space. Under conditions when diffuse reflections cannot be ignored, one must use other methods for solving Eqs. (18) and (19) for the region $z > 0$. Given D_{ik}^{-+}, formulas (22) and (23) fully define the dependence of the spectral density $N_2(z, \omega_p)$ of excited particles on the depth z. However, D_{ik}^{-+}, in turn, depends on $N_2(z, \omega_p)$; i.e., Eq. (22) is essentially an inte-

gral equation for spectral density. Therefore, in order to close the set of equations, one must solve the equation for the photon function D_{ik}^{-+}.

3. THE RADIATION TRANSFER IN THE CASE OF SEMI-INFINITE MEDIUM AND THE RADIATION OF HEATED HALF-SPACE

In order to derive a closed equation for the spectral density N_2 of excited atoms, one must find the kinetic Green's photon function D_{ik}^{-+} (see [22]). It follows immediately from the definition that the quantity D_{ik}^{-+} is a second-rank tensor. Determining all of the components of this tensor reduces to solving the set of equations for D_{ik}^{-+}, derived from the appropriate Dyson equation [13]. In the general case, the solution of this set of equations involves very cumbersome computations and cannot be reduced to a set of algebraic equations, because we treat a semi-infinite medium (and it is necessary to apply methods of solving sets of integro-differential equations on a half-line). It is only when the spatial dispersion is ignored that this system is simplified and allows an analytical solution.

In this study, we are interested in the case when the spatial dispersion is significant. Therefore, for procedural purposes, we will not investigate the polarization properties of the function D_{ik}^{-+} and will confine ourselves to the treatment of the model problem, assuming that

$$D_{ik}^{\alpha\beta} = D^{\alpha\beta}\delta_{ik}.$$

We will assume a scalar form of the photon function D_{ik}^{-+} and will treat only one component of the polarization of radiation.

For convenience, we will represent D_{ik}^{-+} as the sum

$$D^{-+} = D_{\mathrm{sp}}^{-+} + D_{\mathrm{in}}^{-+},$$

where the first term corresponds to spontaneous photon sources, and the second term, to the radiation incident on the medium from vacuum. We will first investigate the part of the Green's function that is associated with incident radiation, D_{in}^{-+}. The Dyson equation for this function will be written in the form (the vector $\mathbf{q}_\perp$ will be directed along the y axis)

$$\left[\frac{d^2}{dz^2} + \frac{\omega^2}{c^2} - q_\perp^2\right] D_{\mathrm{in}}^{-+}(z, z') = 4\pi\hbar \int_0^\infty \Pi^R(z, z_2) D_{\mathrm{in}}^{-+}(z_2, z')\, dz_2, \quad z, z' > 0, \tag{25}$$

$$\left[\frac{d^2}{dz^2} + \frac{\omega^2}{c^2} - q_\perp^2\right] D_{\mathrm{in}}^{-+}(z, z') = 0, \quad z < 0, \quad z' > 0, \tag{26}$$

$$\left[\frac{d^2}{dz'^2} + \frac{\omega^2}{c^2} - q_\perp^2\right] D_{\mathrm{in}}^{-+}(z, z') = 4\pi\hbar \int_0^\infty D_{\mathrm{in}}^{-+}(z, z_1) \Pi^A(z_1, z')\, dz_1, \quad z, z' > 0, \tag{27}$$

$$\left[\frac{d^2}{dz'^2} + \frac{\omega^2}{c^2} - q_\perp^2\right] D_{\mathrm{in}}^{-+}(z, z') = 0, \quad z > 0, \quad z' < 0. \tag{28}$$

We will assume that the collisions of particles with the interface are purely specular. In this case, we use the even extension to the negative semiaxis $z < 0$ to derive, from Eq. (25),

$$D_{\mathrm{in}}^{-+}(z, z') = \int_{-\infty}^{\infty} \frac{dk}{2\pi} e^{ikz} \frac{2D_{\mathrm{in}}'^{-+}(+0, z')}{\frac{\omega^2}{c^2}\varepsilon(\omega, k, q_\perp) - k^2 - q_\perp^2}. \tag{29}$$

Here, the prime indicates a derivative with respect to the first argument (with respect to z). The quantity $\varepsilon(\omega, k, q_\perp)$ is the permittivity of the medium, expressed in terms of the polarization operator Π^R,

$$\varepsilon(\omega, k, q_\perp) = 1 - \frac{4\pi}{3\hbar} d^2 \left[\tilde{N}_1 - \tilde{N}_2 \exp\left(-\frac{\omega - \omega_0}{T}\right)\right] \times \int d\mathbf{v} \frac{f(\mathbf{v})}{\Delta - k v_z - \mathbf{q}_\perp \mathbf{v}_\perp + i\gamma_2/2}. \tag{30}$$

Here, $\tilde{N}_1$ and $\tilde{N}_2$ denote the effective population of the upper and lower states, respectively (see Eqs. (7) and (8)). Generally speaking, ε is a function of both the frequency ω and the photon wave vector $\mathbf{k}$ and describes the temporal and spatial dispersion of permittivity, respectively. As was already mentioned, the following condition may be valid in the case of a fairly high atom density:

$$\gamma_2 = \gamma_{\mathrm{sp}} + \gamma_{\mathrm{coll}} > \Delta\omega_D,$$

where $\Delta\omega_D$ is the Doppler width, γ_{sp} is the radiation line width, and $\gamma_{\mathrm{coll}} \sim N$ is the collisional line width (proportional to the density of broadening particles). For such media, the dependence of permittivity on k and $\mathbf{q}_\perp$ becomes unimportant. In this study, we are interested in the case of rather rarefied media, when the above-identified condition is invalid, and the spatial dispersion of permittivity proves to be significant (in application to sodium atoms, this means $N < 10^{17}$ cm^{-3}).

The Green's function derivative D'^{-+}_{in} may be found from the joining of solutions obtained in the regions $z < 0$ and $z > 0$ on the interface $z = 0$. For this purpose, we will first treat the case $z < 0$, $z' > 0$. From Eq. (26), we find

$$D^{-+}_{\text{in}}(z, z') = A(e^{ik_z^0 z} + re^{-ik_z^0 z})c(z'),$$
$$k_z^0 = \sqrt{\frac{\omega^2}{c^2} - q_\perp^2}. \tag{31}$$

Here, A is the incident wave amplitude, r is the coefficient of reflection from the boundary, k_z^0 is the projection of the wave vector of incident wave onto the z axis (in the case of normal incidence, $k_z^0 = \omega/c$), and $c(z')$ is some function of z' which may be determined by treating Eq. (27). From the condition of continuity of the electric and magnetic field intensities on the boundary, we can derive the boundary conditions for D^{-+}_{in},

$$D^{-+}_{\text{in}}(+0, z') = D^{-+}_{\text{in}}(-0, z'),$$
$$D'^{-+}_{\text{in}}(+0, z') = D'^{-+}_{\text{in}}(-0, z'). \tag{32}$$

We find from Eqs. (29) and (31) in view of boundary conditions (32)

$$D^{-+}_{\text{in}}(z, z') = 2ik_z^0 A(1 - r)c(z')$$
$$\times \int_{-\infty}^{\infty} \frac{dk}{2\pi} \frac{e^{ikz}}{\frac{\omega^2}{c^2}\varepsilon(\omega, k, q_\perp) - k^2 - q_\perp^2}. \tag{33}$$

One can see that the function $D^{-+}_{\text{in}}(z, z')$ may be written in the form of the product of two functions dependent on only one of the coordinates,

$$D^{-+}_{\text{in}}(z, z') = \varphi(z)c(z').$$

In order to determine $c(z')$, we will turn to Eq. (27). We will use the even extension to the negative semiaxis $z' < 0$ to derive the following correlation for the function $c(z')$:

$$c(z') = \int_{-\infty}^{\infty} \frac{dk}{2\pi} e^{ikz'} \frac{2c'(+0)}{\frac{\omega^2}{c^2}\varepsilon^*(\omega, k, q_\perp) - q_\perp^2 - k^2}. \tag{34}$$

In deriving Eq. (34), use was made of the inequality $\Pi^A = (\Pi^R)^*$. The derivative $c'(+0)$ may be found from the boundary conditions (32). Indeed, from the definition of the photon function D^{-+}_{in} and from Eq. (31), we derive

$$c'(+0) = -A^* ik_z^0(1 - r^*).$$

On substituting Eq. (34) into (33), we arrive at the final expression for the Green's photon function $D^{-+}_{\text{in}}(z, z')$ corresponding to resonance waves incident on the medium,

$$D^{-+}_{\text{in}}(z, z') = \frac{4|A|^2(k_z^0)^2}{\pi^2|1 + \mu|^2}$$
$$\times \int_{-\infty}^{\infty} dk d\xi \frac{\exp(ikz + i\xi z')}{\left[\frac{\omega^2}{c^2}\varepsilon - q_\perp^2 - k^2\right]\left[\frac{\omega^2}{c^2}\varepsilon^* - q_\perp^2 - \xi^2\right]}, \tag{35}$$

where

$$\mu = \frac{1 + r}{1 - r} = \frac{ik_z^0}{\pi} \int_{-\infty}^{\infty} \frac{dk}{\frac{\omega^2}{c^2}\varepsilon - k^2 - q_\perp^2}. \tag{36}$$

It follows from Eq. (35) that the Green's function D^{-+}_{in} is proportional to the square of the amplitude of a wave incident on the medium, i.e., to the incoming flow. Note that the quantity D^{-+}_{ik}, in turn, is associated with the radiation flux (Poynting vector) in the medium. In the case of a transparent medium (i.e., a medium in which $\varepsilon' = \text{Re}\varepsilon \longrightarrow 1$ and $\varepsilon'' = \text{Im}\varepsilon \longrightarrow 0$), the Poynting vector component will be written as

$$S_z^{\text{in}} = \frac{1}{4\pi}\text{Re}\int_0^{\infty} \frac{\omega d\omega}{\pi} \frac{d\mathbf{q}_\perp}{(2\pi)^2} \frac{\partial}{\partial z} D^{-+}_{\text{in}}(z, z', \mathbf{q}_\perp, \omega)\Big|_{z' = z}. \tag{37}$$

Here, the quantity S_z^{in} defines the radiation flux at depth z, which is associated with incident resonance waves. Therefore, relation (35) is in fact a generalization of the known Fresnel formula to the case of a medium with spatial dispersion of permittivity. Note that, as was demonstrated by Schuurmans [14], in media with spatial dispersion and a boundary, one must take into account the thermal transfer of excitation and the reflection of atoms from the walls. These effects result in the disturbance of local correlation between the electromagnetic radiation intensity and the populations of atomic levels at some depth z; as was demonstrated in [14], the decay of electromagnetic waves in the medium proceeds by other than an exponential law. The radiation transfer in this case, generally speaking, cannot be described in terms of the complex refractive index; therefore, the existing theory of transfer must be generalized.

When the effects of nonlocality are ignored, it becomes possible to use the complex refractive index for describing the radiation transfer through the medium. Indeed, on ignoring the spatial dispersion in Eqs. (35) and (36) and assuming that $\mathbf{q}_\perp = 0$ (i.e., treating the normal incidence), we arrive at the conventional

Fresnel formula [15] relating the intensities of the incident, reflected, and transmitted waves on the interface,

$$D_{\text{in}}^{-+}(z, z') = 4|A|^2 \frac{|\mu|^2}{|1+\mu|^2} e^{i\bar{k}z - i\bar{k}z'},$$

where

$$\mu = \frac{k_z^0}{\bar{k}}, \quad \bar{k} = \sqrt{\frac{\omega^2}{c^2}\varepsilon} \approx \sqrt{\varepsilon'}\frac{\omega}{c} + \frac{i}{2}\frac{\omega}{c}\frac{\varepsilon''}{\sqrt{\varepsilon'}}.$$

The wave vector $\bar{k}$ defines the propagation of radiation in the medium. In nonabsorbing media, $\bar{k} = \omega n/c$ is a real quantity (here, $n = n(\omega) = \sqrt{\varepsilon'}$ is the refractive index of the medium). The quantity $\mu = 1/\sqrt{\varepsilon'}$, i.e., is inversely proportional to the refractive index. For an absorbing medium, the wave vector $\bar{k}$ becomes complex. The imaginary part of $\bar{k}$, proportional to the imaginary part of permittivity ε'', is responsible for the absorption of an incident wave by the medium atoms ($\varepsilon'' > 0$ at $\omega > 0$). In this case, the field decay in the material proceeds by an exponential law.

We have treated the part of the kinetic Green's function D^{-+} that corresponds to incident radiation. We will now dwell on the Green's function D_{sp}^{-+} associated with spontaneous emission of photons by the medium atoms. This function may be found from the corresponding Dyson equation,

$$D_{\text{sp}}^{-+}(z_3, z, \mathbf{q}_\perp, \omega) = -\int_0^\infty D^R(z_3, z_1, \mathbf{q}_\perp, \omega) \times \Pi^{-+}(z_1, z_2, \mathbf{q}_\perp, \omega) D^A(z_2, z, \mathbf{q}_\perp, \omega) dz_1 dz_2. \quad (38)$$

Here, Π^{-+} is the polarization operator describing the interaction between the photon field and atoms, and D^R and D^A are the retarded and advanced Green's photon functions, respectively. It follows from the definition of the retarded and advanced photon functions that

$$D^A(z_2, z, \mathbf{q}_\perp, \omega) = D^{R*}(z, z_2, \mathbf{q}_\perp, \omega). \quad (39)$$

Therefore, in order to find D_{sp}^{-+}, we must calculate only the retarded function D^R by solving the corresponding Dyson equation with the polarization operator Π^R,

$$\left[\frac{d^2}{dz^2} + \frac{\omega^2}{c^2} - q_\perp^2\right] D^R(z, z') = 4\pi\hbar\delta(z - z') + 4\pi\hbar \int_0^\infty \Pi^R(z, z_2) D^R(z_2, z') dz_2. \quad (40)$$

We proceed as in the case of the function D_{in}^{-+} (i.e., use the even extension to the negative semiaxis $z < 0$) to find, from Eq. (40),

$$D^R(z, z') = \int_{-\infty}^\infty \frac{dk}{2\pi} e^{ikz} \frac{2D'^R(+0, z') + 8\pi\hbar\cos(kz')}{\frac{\omega^2}{c^2}\varepsilon - k^2 - q_\perp^2}. \quad (41)$$

The derivative $D'^R(+0, z')$ may also be obtained from the joining of solutions obtained in the regions $z < 0$ and $z > 0$, on the interface at $z = 0$. In view of the definition of the retarded Green's function D^R and kinetic Green's function D^{-+}, we have, from Eq. (31),

$$D^R(z, z') = (e^{-ik_z^0 z} + re^{ik_z^0 z}) s(z'), \quad z < 0, \quad z' > 0. \quad (42)$$

Similarly to the function $c(z')$ in Eq. (31), the function $s(z')$ may be found from the solution of the corresponding Dyson equation for the variable z'. Proceeding from Eqs. (41), (42), and (34) and the boundary conditions for D^R, we arrive at the final expression for the retarded Green's photon function,

$$D^R(z, z', q_\perp, \omega) = \int_{-\infty}^\infty \frac{dk}{2\pi} e^{ikz} \Psi_{\omega q k}(z'), \quad (43)$$

$$\Psi_{\omega q k}(z') = \frac{1}{\frac{\omega^2}{c^2}\varepsilon - k^2 - q_\perp^2} \times \left\{ 8\pi\hbar\cos(kz') - \frac{4i\hbar k_z^0}{\mu} \int_{-\infty}^\infty dk' \frac{\cos(k'z')}{\frac{\omega^2}{c^2}\varepsilon - k'^2 - q_\perp^2} \right\}. \quad (44)$$

Note that the integrals over k appearing in formulas (34)–(36), (41), and (44) do not reduce to the contribution of residues of integrands, because $\varepsilon(\omega, k, q_\perp)$ has discontinuities in the k plane. It is with this fact that the effect of selective narrowing of reflection for Doppler-broadened lines [14] is formally associated.

We will turn back to Eq. (23) and treat in more detail the polarization operator Π^{-+} defining the intensity of spontaneous sources in the medium. In the case of resonance, the contribution by the vertex functions to Π^{-+} becomes insignificant, and the one-loop approximation may be used,

$$\Pi^{-+}(z, z', \mathbf{q}_\perp, \omega > 0) = i\frac{(j/c)^2}{3} \int \frac{d\omega_p d\mathbf{k}_\perp}{(2\pi)^3} \times G_{11}^{+-}(z', z, \mathbf{k}_\perp - \mathbf{q}_\perp, \omega_p - \omega) G_{22}^{-+}(z, z', \mathbf{k}_\perp, \omega_p). \quad (45)$$

One can see that the polarization operator Π^{-+} is proportional to the density of excited particles and contains

the description of the effects of nonlocality (in the absence of nonlocality, $\Pi^{-+} \propto \delta(z - z')$. In deriving Eq. (45), we ignored the decay effects, which is true in the case of a fairly slow variation of the concentration of excited particles with time.

According to Eqs. (7) and (8), the Green's function of excited particles G_{22}^{-+} has the form

$$G_{22}^{-+}(z, \mathbf{k}_\perp, \omega) = iN_2(z, k, \mathbf{k}_\perp, \varepsilon_p) = i\tilde{N}_2(z, k, \mathbf{k}_\perp, \varepsilon_p)a_2(\varepsilon_p),$$

where $\tilde{N}_2(z, k, \mathbf{k}_\perp, \varepsilon_p)$ is the effective population of the excited level (see Eq. (8)). We assume that $\tilde{N}_2(z, k, \mathbf{k}_\perp, \varepsilon_p)$ varies little over distances on the order of the thermal de Broglie wavelength of a particle, λ_T. Then, we derive from Eq. (7) that the Green's function G_{22}^{-+} of excited particles may be written as

$$G_{22}^{-+}(z, z', k, \mathbf{k}_\perp, \omega) = i\tilde{N}_2(z', \omega) \times \sum_k \frac{\gamma_2}{2\pi} \frac{\psi_k(z)\psi_k(z')}{\varepsilon_p^2 + \gamma_2^2/4} f(k, \mathbf{k}_\perp). \quad (46)$$

Here,

$$\tilde{N}_2(z', \omega) = \int \tilde{N}_2(z', k, \mathbf{k}_\perp, \omega)\frac{d\mathbf{k}}{(2\pi)^3}$$

is the integral density of excited particles and $f(k, \mathbf{k}_\perp)$ is the function of distribution of atoms in the ground state over the quantum numbers k and $\mathbf{k}_\perp$. We substitute Eq. (45) into (46) and ignore the broadening of the ground state of an atom (i.e., use the appropriate function for an unperturbed atom instead of the Green's function G_{11}^{+-} to find the explicit form of the polarization operator Π^{-+}

$$\Pi^{-+}(z, z', \mathbf{q}_\perp, \omega) = i\frac{(j/c)^2}{3} \times \int d\varepsilon_p a_2(\varepsilon_p)K(z, z')\tilde{N}_2(z')\exp\left(-\frac{\omega - \omega_0}{T}\right). \quad (47)$$

Here, $\tilde{N}_2(z')$ is the total effective population of the upper level (see Eq. (8)), and the factor $\exp(-(\omega - \omega_0)/T)$ is necessary for generalizing the theory to the case of broad spectral lines $\gamma_2 \gtrsim T$. The function $K(z, z')$ has the form

$$K(z, z') = \int \frac{d\mathbf{p}}{(2\pi)^3}\frac{f(\mathbf{p})}{|v_z|} \times \left\{\cos\left[\frac{\Delta}{v_z}(z + z')\right] + \cos\left[\frac{\Delta}{v_z}(z - z')\right]\right\}, \quad (48)$$

where

$$f(\mathbf{p}) = \lambda_T^3 \exp\left(-\frac{E(\mathbf{p})}{T}\right)$$

is the function of distribution of atoms over the quantum numbers $\mathbf{p}$. When the boundary effects are ignored, the kernel $K(z, z'|z_3)$ appearing on the right-hand side of the equation for spectral density (22) changes to $K(z, z')$ from Eq. (47). So, we substitute Eqs. (47), (43), and (39) into (38) to obtain the explicit form of the Green's photon function D_{sp}^{-+} corresponding to spontaneous photon sources in the medium,

$$D_{sp}^{-+}(z, z') = -i\frac{(j/c)^2}{3\hbar}\int_0^\infty dz_1 \tilde{N}_2(z_1)D^R(z, z_1) \times \Phi_{\omega q}(z', z_1)\exp\left(-\frac{\omega - \omega_0}{T}\right), \quad (49)$$

where

$$\Phi_{\omega q}(z', z_1) = \int_{-\infty}^{\infty}\frac{d\xi}{2\pi}\frac{\cos(\xi z')}{\frac{\omega^2}{c^2}\varepsilon^* - q_\perp^2 - \xi^2}\left\{8\pi\hbar\varphi(\omega, \xi, q_\perp) \times \cos(\xi z_1) + \frac{4i\hbar k_z^0}{\mu^*}\int_{-\infty}^{\infty} d\theta \frac{\varphi(\omega, \theta, q)\cos(\theta z_1)}{\frac{\omega^2}{c^2}\varepsilon^* - q_\perp^2 - \xi}\right\}, \quad (50)$$

$$\varphi(\omega, k, q_\perp) = \int d\varepsilon_p a_2(\varepsilon_p)\int \frac{d\mathbf{p}}{(2\hbar)^3}\lambda_T^3 \times \exp\left(-\frac{E(\mathbf{p})}{T}\right)\delta(kv_z - \Delta). \quad (51)$$

The φ function from Eq. (51) is a Voigt line profile including both the homogeneous broadening due to spontaneous decay and collisions with broadening particles and the inhomogeneous Doppler broadening. We have obtained parts of the kinetic Green's photon function corresponding to incident flow (see Eq. (35)) and to emitted photons (see Eq. (49)). On summing both these contributions, one can find the total radiation flux in the medium. In fact, the solution to the equation of resonance radiation transfer has been found. Given the spectral density, these results describe fully the propagation of resonance radiation in the material, as well as the spectral intensity of radiation of a heated semi-infinite medium. We will study in more detail the problem on radiation of a heated half-space in the case when the medium is in thermodynamic equilibrium. In this case, the effective populations $\tilde{N}_2$ and $\tilde{N}_1$ are independent

of coordinates and satisfy the Boltzmann relations. In addition, the relation

$$n(\omega) = \frac{\tilde{N}_2 \exp\left(-\frac{\omega-\omega_0}{T}\right)}{\tilde{N}_1 - \tilde{N}_2 \exp\left(-\frac{\omega-\omega_0}{T}\right)} = \frac{1}{\exp\left(\frac{\omega}{T}\right)-1} \quad (52)$$

is valid, where $n(\omega)$ denotes the Planck (equilibrium) occupation numbers of photons. We substitute Eq. (43) into (49) in view of (52) to derive the expression for the spectral Poynting vector on the interface for an equilibrium medium,

$$S_{z\omega}\big|_{z=0} = -\frac{\hbar\omega^3}{4\pi^2 c^2} n(\omega) \int_0^1 dx\, x(1-R),$$
$$R = \frac{(\mathrm{Im}\mu)^2}{|\mu|^2}. \quad (53)$$

Relation (53) defines the spectral distribution of the intensity of radiation emitted by a heated half-space and is, in fact, Kirchhoff's law reflecting the energy balance on the interface. The quantity R denotes the energy coefficient of reflection of electromagnetic waves from the interface. The first term in Eq. (53) describes the radiation flux incident on the boundary from the medium, and the second term corresponds to photons reflected from the boundary. It follows from Eq. (53) that the reflection of waves from the boundary becomes significant for fairly dense media, i.e., media with a refractive index appreciably different from unity ($|\varepsilon' - 1| \sim 1$).

Assuming $R = 0$, we will obtain from Eq. (53) half the Planck flux. This is due to the fact that we have treated only one of two possible directions of polarization of the electromagnetic field.

4. GENERALIZED BIBERMAN–HOLSTEIN EQUATION

As was already mentioned, the problem on propagation of incident radiation in a medium and the problem on radiation of a heated half-space reduce to finding the spectral density of excited atoms. We will demonstrate that the spectral density satisfies the integral equation (Biberman–Holstein equation). For this purpose, we will treat the case where no incident radiation is present, assuming $D_{\mathrm{in}}^{-+} = 0$. In this case, the radiation flux in the medium will be caused by spontaneous sources alone; i.e., $D^{-+} = D_{\mathrm{sp}}^{-+}$.

For simplicity, we will assume the case of narrow spectral lines. Then, the effective populations $\tilde{N}_i$ coincide with the true populations of atomic states. We substitute Eq. (49) into (22) to derive the integral equation for $N_2(z)$, the total concentration of excited particles at depth z,

$$N_2(z) = Q(z) + \frac{2N_1}{3\hbar}\left(\frac{j}{c}\right)^4 \mathrm{Re}\int_0^\infty d\omega \int \frac{d\mathbf{q}_\perp}{(2\pi)^2} \times \int_0^\infty dz_1 \bar{K}_{\omega q}(z, z_1) N_2(z_1), \quad (54)$$

$$\bar{K}_{\omega q}(z, z_1) = \int_{-\infty}^{\infty} dz' \int_0^\infty dz_3 \times D^R_{\omega q}(z_3, z_1)\Phi_{\omega q}(z_1, z')K_{\omega q}(z_3, z'|z). \quad (55)$$

We introduced here the quantity $Q(z)$ characterizing the rate of incoherent pumping to an excited level due to recombination or inelastic collisions. In addition, the presence of a boundary leads to the emergence of an additional contribution to the concentration of excited particles due to atomic particles reflected from the boundary of the medium, as well as to the effective increase in the field intensity in the medium with due regard for the electromagnetic waves reflected from the boundary. The function $K_{\omega q}(z_3, z'|z)$ is defined by expression (23).

Equation (54) describes the nonlocal radiation transfer in the medium due to resonance radiation and is, in fact, a generalization of the well-known Biberman–Holstein equation including the spatial dispersion of permittivity and the presence of a boundary. The solution of this equation helps us find an exact solution to the problem on the transfer of resonance waves through the medium. In what follows, we will demonstrate that, if the spatial dispersion and boundary effects are ignored, the obtained result transforms to the Biberman equation.

We will treat the simplest case, when the excited level is short-lived and the particle velocity is not too high. Then the kernel $K(z, z_1|z')$ is simplified appreciably and takes the form of Eq. (24) everywhere except for a narrow region at the boundary with a width on the order of the thermal de Broglie wavelength. In this case, the respective expression for the total kernel $\bar{K}(z, z')$ (see Eq. (55)) may be written as

$$\bar{K}(z, z_1) = \left\{A(z - z_1) - \frac{1}{2}A(z)\frac{B(z_1)}{B(0)}\right\} \times \left\{A^*(z_1 - z) - \frac{1}{2}A^*(z_1)\frac{B^*(z)}{B^*(0)}\right\}, \quad (56)$$

where

$$A(z) = 8\pi\hbar\int_{-\infty}^{\infty}\frac{dk}{\frac{\omega^2}{c^2}\varepsilon - k^2 - q_\perp^2}\varphi(\omega, k, q_\perp)\cos(kz),$$
$$B(z) = \int_{-\infty}^{\infty}\frac{dk}{\frac{\omega^2}{c^2}\varepsilon - k^2 - q_\perp^2}\cos(kz), \quad (57)$$

and the quantities ε and φ are defined by relations (30) and (51), respectively.

In the case when the spatial dispersion is insignificant (for example, at a fairly high atom density), one can ignore the wave vector dependence of permittivity (with the same accuracy, we can assume that the function φ depends on frequency alone). In view of Eqs. (56) and (57), the integral equation (54) is written as

$$N_2(\omega) = Q_2(z) + \text{const}\int_0^\infty d\omega a_2^2(\omega)\int_0^\infty dz_1 N_2(z_1)$$
$$\times\int_1^\infty\frac{dt}{t}\left\{\exp(-k_\omega t|z-z_1|) + \frac{1}{4}\exp[-k_\omega t(z+z_1)]\right.$$
$$-\operatorname{Re}\exp\left[-i\frac{\omega\sqrt{\varepsilon'}}{tc}(|z+z_1| - |z-z_1|)\right.$$
$$\left.\left.-\frac{k_\omega t}{2}(|z+z_1| + |z-z_1|)\right]\right\}. \quad (58)$$

Here, $a_2(\omega)$ is the spectral line profile and

$$k_\omega = \frac{\omega\varepsilon''}{c\sqrt{\varepsilon'}}$$

is the absorption coefficient of resonance radiation at frequency ω.

The first term in the braces from Eq. (58) corresponds to the classical expression for the kernel in the Biberman–Holstein theory. It defines the absorption of a resonance photon emitted by an excited atom at point z_1.

In deriving Eq. (58), we ignored the thermal transfer of excitations. Therefore, the last two terms define the effect of the boundary of the medium on the concentration of excited atoms. The second term in the braces describes the additional contribution to the population of an excited level due to waves reflected from the surface of the medium. One can see in Eq. (58) that, at depth z, these waves are attenuated in proportion to the factor $\exp(-k_\omega tz)$. Accordingly, the third term characterizes the interference of resonance waves reflected from the boundary and waves emitted by excited atoms at point z_1. Note that, when we ignore the effect of the boundary on the concentration of excited particles, we directly derive from Eq. (58) the Biberman–Holstein equation,

$$N_2(z) = Q_2(z) + \text{const}\int_0^\infty d\omega a_2^2(\omega)$$
$$\times\int_0^\infty dz_1 N_2(z_1)\int_1^\infty\frac{dt}{t}\exp(-k_\omega t|z-z_1|). \quad (59)$$

5. NUMERICAL CALCULATION RESULTS

In order to illustrate the above theory, numerical calculations were performed using the resonance line of sodium atom as an example: the transition $3S_{1/2}$–$3P_{3/2}$ (λ = 5889.95 Å). The probability of spontaneous emission for this line is (see, for example, [16]) $A = 6.25 \times 10^7$ s^{-1}. The collisional width in the case being treated is associated with the resonance mechanism of excitation transfer and is $\gamma_{\text{coll}} = 4.78 \times 10^{-7}N$, where N [cm^{-3}] is the concentration of sodium atoms, and γ_{coll} is given in s^{-1}. The temperature dependence of the concentration N of sodium vapor was determined using the data of Nesmeyanov [17]. The collisional width exceeds the radiation width starting from the values of the concentration $N \approx 10^{14}$ cm^{-3} (at temperatures $T > 550$ K). The total homogeneous width associated with radiative decay and collisions exceeds the inhomogeneous Doppler width starting from the values of the temperature $T \approx 750$ K.

We have previously obtained the explicit form of the integral equation for the concentration of excited particles,

$$N_2(z) = Q(z) + \text{const}\operatorname{Re}\int_0^\infty d\omega$$
$$\times\int\frac{d\mathbf{q}_\perp}{(2\pi)^2}\int_0^\infty dz_1\bar{K}_{\omega q}(z, z_1)N_2(z_1).$$

In the general case, the equation kernel $\bar{K}(z, z_1)$ is defined by relation (55). Here, we will restrict ourselves to treating a simpler kernel, when $\bar{K}(z, z_1)$ is defined by relations (56) and (57). Therefore, we will ignore the contribution by the particles reflected from the medium boundary to the population of the upper level at a depth greater than the thermal de Broglie wavelength.

We will investigate the spectral dependence of the total kernel $\bar{K}(z, z_1)$ (for simplicity, we assume that $\mathbf{q}_\perp = 0$), which has the form

$$\bar{K}(z, z_1) = \left\{A(z-z_1) - \frac{1}{2}A(z)\frac{B(z_1)}{B(0)}\right\}$$
$$\times\left\{A^*(z_1-z) - \frac{1}{2}A^*(z_1)\frac{B^*(z)}{B^*(0)}\right\}, \quad (60)$$

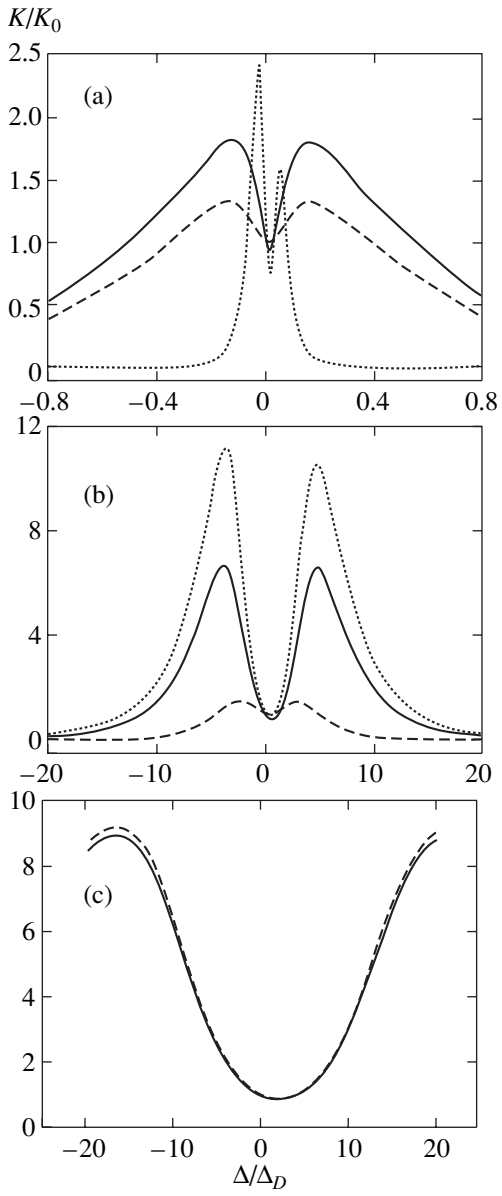

Fig. 1. The integral equation kernel $\bar{K}_\omega(z, z')$ as a function of detuning of frequency from resonance, $\Delta = \omega - \omega_0$, for the values of depth $z = 0$ and $z' = 10\lambda$. The solid curve indicates the calculation by formula (60) in view of spatial dispersion and effects of the boundaries, the dashed curve indicates the calculation by Biberman's formula (59) in view of spatial dispersion, and the dotted curve indicates the calculation by Biberman's formula (59) disregarding spatial dispersion. Each curve is normalized to the respective quantity K_0 (the value of the kernel $\bar{K}_\omega$ at $\omega = \omega_0$); plotted on the abscissa is the ratio of frequency detuning to the Doppler width $\Delta_D = \omega_0 v_T/c$; $T = 600$ (a), 800 (b), and 900 K (c).

where A and B are defined by expressions (57) with $\mathbf{q}_\perp = 0$. We will further consider the pattern of variation of the spectral composition of the kernel in view of spatial dispersion. For this purpose, one must compare the results obtained using the suggested theory with the results obtained using the Biberman–Holstein theory.

We will assume that the density of excited particles is low, $N_2 \ll N_1 \sim N$ (N is the total number of particles). In this case, the expression for the permittivity of a resonant medium will be written as (it is assumed that the lines are rather narrow compared with the temperature of the broadening particles, so that the effective populations coincide with total populations of atomic levels)

$$\varepsilon(\omega, k, q_\perp) = 1 - \frac{4\pi}{3\hbar} d^2 N \int d\mathbf{v} \frac{f(\mathbf{v})}{\Delta - k v_z - \mathbf{q}_\perp \mathbf{v}_\perp + i\gamma_2/2}.$$

It is most natural to select the Maxwell distribution function as the atomic velocity distribution function $f(\mathbf{v})$.

Given in Fig. 1 is the spectral dependences of the function $\bar{K}_\omega$ obtained for different temperatures (the quantity K_0 is the respective value at the line center). We treat the temperature $T = 600$, 800, and 900 K, at which the quantity g (the homogeneous-to-Doppler width ratio $\omega_0 v_T/c$) assumes the values of 0.06, 5.37, and 23.8, respectively.

Note that the case of most interest is that when the distance between the emitting and absorbing atoms becomes longer than or on the order of the resonance photon free path (this is possible in the case of optically dense media). For this purpose, we will treat the case of $z = 0$ and $z' = 10\lambda$ ($\lambda = 2\pi c/\omega_0$ is the resonance photon wavelength). It follows from the figure that the main contribution is made in this case by the line tails, i.e., by the high values of detuning $\Delta \gg \gamma$ (in the case of very high values of detuning, the asymptotic form change to the Lorentz asymptotic form). This is reflective of the fact that, in optically dense media, the main fraction of energy is transferred in the line wings, and the energy transfer at the line center may be ignored (the effect of trapping of resonance radiation).

At a fairly low temperature ($T = 600$ K), the Doppler width exceeds considerably the homogeneous width. In this case, the main contribution to the spectral line broadening is made by Doppler broadening; therefore, the spatial dispersion of permittivity must be taken into account. Figure 1a gives the spectral dependence of the kernel $\bar{K}_\omega$ at temperature $T = 600$ K ($g = 0.06$). One can see from the figure that, when the thermal motion of atoms is ignored, the Biberman curve has a characteristic form of a doublet with a minimum at the line center. The width of the peaks and of the dip at the line center is defined by the homogeneous width at a given temperature. As a result of inclusion of spatial dispersion in the Biberman kernel, this dependence ceases to be so pronounced due to the Doppler "smearing" of the peaks. The peak width comes to be on the order of the Doppler width. The results obtained using the foregoing theory (solid curve) demonstrate that the inclusion of the boundary leads to a narrowing of the Doppler-broadened curve. The line profile contains an additional contribution with a width on the order of the homogeneous

width (one can see in the figure that the width of the dip at the center is on the order of the homogeneous width). Schuurmans [14] demonstrated that this contribution is due to the spatial dispersion of permittivity (caused by the thermal motion of atoms) and exists at $g \lesssim 1$. From the mathematical standpoint, this means that, as a result of spatial dispersion, the integrand in Eqs. (56) and (57) has, in addition to poles, lines of discontinuity which must be included in the integration in the complex plane k. According to Schuurmans [14], it is the integrals along the discontinuity line that give the narrow additional contribution to the spectral dependence of the kernel. Therefore, the integrals given by Eqs. (56) and (57), generally speaking, cannot be simply reduced to residues of the integrand. Note further that the results obtained using the theory referred to above and the Biberman theory start to agree only in very distant wings of the spectral line. In the case of high values of detuning, $\Delta \gg \max(\Delta_D, \gamma)$, we have $\varepsilon' \longrightarrow 1$, $\varepsilon'' \longrightarrow 0$; i.e., the dielectric properties of the medium in the case of high values of detuning become unimportant, and the results obtained in view of the dispersion agree with those obtained disregarding the dispersion.

As the temperature increases, the homogeneous line width increases due to the increase in the broadening collision frequency. At temperature T = 800 K, the homogeneous width is on the order of the Doppler width, and one must take the spatial dispersion into account. Figure 1b gives the spectral dependence of the kernel $\bar{K}_\omega$ at temperature T = 800 K (g = 5.37). As in the case with T = 600 K, it follows from the curve given in this figure that the inclusion of the boundaries and of the spatial dispersion brings about a narrowing of the Doppler-broadened profile. At the same time, one can see in the figure that the depth of the dip at the line center is defined by the homogeneous width (at a given temperature).

Figure 1c gives the dependence of $\bar{K}_\omega$ obtained at temperature T = 900 K. One can see in the figure that the results obtained using the theory treated by us and the Biberman–Holstein theory agree in almost the entire range of values of detuning Δ. Indeed, at high temperatures (T = 900 K), the homogeneous width exceeds considerably the Doppler width, and the spatial dispersion of permittivity may be ignored. Therefore, the results obtained using the present theory and the Biberman–Holstein theory must coincide. This is supported by the dependences given above.

6. CONCLUSION

We have derived integral equations for the concentration of excited atoms, which generalize the well-known Biberman–Holstein equations to the case where the spatial dispersion and the importance of the medium boundaries are taken into account. An example of a half-space is used to demonstrate that the kernel of the integral equation is defined by the retarded and advanced Green's functions for photons, which allow for the dielectric properties of the resonance medium and for the reflection of radiation from the half-space boundary. Numerical calculations have been performed of the spectral part of the kernel of the integral equation for the concentration of excited particles at different temperatures using sodium vapor as an example and allowing for all of the above-identified effects. It has been demonstrated that, in the temperature range of $T \lesssim$ 800 K, the effects of the type of narrowing of Doppler profiles upon reflection from the interface produce an appreciable influence on the dependence of the spectral component of the kernel differing from the respective expression in the classical Biberman–Holstein equation.

ACKNOWLEDGMENTS

We are grateful to Yu.K. Zemtsov for assistance in performing numerical calculations. This study was supported in part by the Russian Foundation for Basic Research (project no. 99-0218176) and by the grant for support of scientific schools (no. 00-15-96539).

REFERENCES

1. D. Mihalas, *Stellar Atmospheres* (Freeman, San Francisco, 1978; Mir, Moscow, 1982), Vols. 1, 2.
2. V. V. Sobolev, *Course of Theoretical Astrophysics* (Nauka, Moscow, 1985).
3. V. V. Ivanov, *Radiation Transfer and Spectra of Celestial Bodies* (Nauka, Moscow, 1969).
4. I. I. Sobelman, L. A. Vainshtein, and E. A. Yukov, *Excitation of Atoms and Broadening of Spectral Lines* (Nauka, Moscow, 1979; Springer-Verlag, Berlin, 1981).
5. I. I. Sobel'man, *Introduction to the Theory of Atomic Spectra* (Nauka, Moscow, 1973).
6. Yu. K. Zemtsov, A. Yu. Sechin, and A. N. Starostin, Zh. Éksp. Teor. Fiz. **110**, 1654 (1996) [JETP **83**, 909 (1996)].
7. L. M. Biberman, Zh. Éksp. Teor. Fiz. **17**, 416 (1947).
8. T. Holstein, Phys. Rev. **72**, 1212 (1947).
9. R. W. Wood, Philos. Mag. **18**, 187 (1909).
10. B. A. Veklenko and G. B. Tkachuk, Opt. Spektrosk. **38**, 1132 (1975) [Opt. Spectrosc. **38**, 653 (1975)].
11. L. V. Keldysh, Zh. Éksp. Teor. Fiz. **47**, 1515 (1964) [Sov. Phys. JETP **20**, 1018 (1964)].
12. Yu. K. Zemtsov and A. N. Starostin, Zh. Éksp. Teor. Fiz. **103**, 345 (1993) [JETP **76**, 186 (1993)].
13. L. D. Landau and E. M. Lifshitz, *Physical Kinetics* (Gostekhizdat, Moscow, 1957).
14. M. F. H. Schuurmans, J. Phys. (Paris) **37**, 469 (1976).
15. L. D. Landau and E. M. Lifshitz, *Electrodynamics of Continuous Media* (Gostekhizdat, Moscow, 1957; Pergamon, Oxford, 1960).
16. A. A. Radtsig and B. M. Smirnov, *Handbook of Atomic and Molecular Physics* (Atomizdat, Moscow, 1980).
17. An. N. Nesmeyanov, *Vapor Pressure of Chemical Elements* (Akad. Nauk SSSR, Moscow, 1961).

Translated by H. Bronstein

Journal of Experimental and Theoretical Physics, Vol. 94, No. 1, 2002, pp. 60–72.
From Zhurnal Éksperimental'noĭ i Teoreticheskoĭ Fiziki, Vol. 121, No. 1, 2002, pp. 73–87.

PLASMA, GASES

The Generation of Fast Particles in Plasmas Created by Laser Pulses with Different Wavelengths¶

F. B. Rosmej[1], D. H. H. Hoffmann[1], W. Süß[1], A. E. Stepanov[2], Yu. A. Satov[2], Yu. B. Smakovskii[2], V. K. Roerich[2], S. V. Khomenko[2], K. N. Makarov[2], A. N. Starostin[2], A. Ya. Faenov[3], I. Yu. Skobelev[3,*], A. I. Magunov[3], M. Geißel[4], P. Pirzadeh[4], W. Seelig[4], T. A. Pikuz[5], R. Bock[6], T. Letardi[7], F. Flora[7], S. Bollanti[7], P. Di Lazzaro[7], A. Reale[8], A. Scafati[8], G. Tomassetti[8], T. Auguste[9], P. d'Oliveira[9], S. Hulin[9], P. Monot[9], and B. Yu. Sharkov[10]

[1]*Technische Universität Darmstadt, Institut für Kernphysik, Abt. Strahlen- und Kernphysik, D-64289, Darmstadt, Germany*
[2]*Troitsk Institute of Innovative and Thermonuclear Research (TRINITI), Moscow, 142092 Russia*
[3]*Multicharged Ions Spectra Data Center of VNIIFTRI, Mendeleevo, Moscow oblast, 141570 Russia*
[4]*Technische Universität Darmstadt, Institut für Angewandte Physik, D-64289, Darmstadt, Germany*
[5]*Bauman Moscow State Technical University, Moscow, 107005 Russia*
[6]*Gesellschaft für Schwerionenforschung, Plasmaphysics, D-64291, Darmstadt, Germany*
[7]*Dipartimento Innovazione, CR ENEA, Frascati, Italy*
[8]*Dipartimento di Fisica e INFM, INFN g.e. LNGS, Università de L'Aquila, 67010, L'Aquila, Italy*
[9]*Centre d'Etudes de Saclay, DSM/DRECAM/SPAM, Bât 52291191, Gif-sur-Yvette, Cédex, France*
[10]*Institute of Theoretical and Experimental Physics, Moscow, 117257 Russia*
**e-mail: skobelev@orc.ru*

Received July 30, 2001

Abstract—By means of spatially resolved high-resolution X-ray spectroscopy, we have investigated the generation of fast ions at various laser installations with different flux densities and laser wavelengths. It is demonstrated that the fast ion generation in laser-produced plasma can be achieved for a very low level of the averaged laser intensity on the target. The time-of-flight mass spectrometry ion diagnostics and X-ray spectrographs give very close results for the energy distribution of the thermal ion component. For higher energies, however, we found significant differences: the spatially resolved high-resolution spectrographs expose the presence of suprathermal ions, while the time-of-flight method does not. Suprathermal ion energies E_{ion} plotted as a function of the $q\lambda^2$ parameter show a large scatter far above the experimental errors. The cause of these large scatters is attributed to a strong nonuniformity of the laser intensity distribution in the focal spot. The analysis by means of hydrodynamics and spectral simulations show that the X-ray emission spectrum is a complex convolution from different parts of the plasma with strongly different electron density and temperature. It is shown that the highly resolved Li-like satellite spectrum near He_α contains significant distortions even for very low hot electron fractions. Non-Maxwellian spectroscopy allows determination of both the hot electron fraction and the bulk electron temperature. © *2002 MAIK "Nauka/Interperiodica".*

1. INTRODUCTION

The interaction of intense laser radiation with matter leads to the creation of plasma in which the absorbed energy is not completely thermalized. This gives rise to the familiar phenomena of fast ion emission, whose understanding is important for both laser fusion and development of fast ion sources [1–3].

Until now, the main part of the experimental information on the fast ion production in laser plasmas was obtained with the help of mass spectrometry methods (see, e.g., review [4] and the special issue [5]). These methods are based on the direct observation of ions over large distances, usually performed by charged particle detectors (e.g., Faraday detector) several meters away from the place of plasma creation. In this case, the results strongly depend on the recombination processes that occur during the plasma expansion to large distances. Thus, although these methods are suitable to investigate laser-produced plasmas as possible sources of multicharged fast ions for some practical applications, they have serious limitations for studies of the fast ion production mechanisms inside the laser-produced plasma. More suitable for this purpose are indirect spectroscopic methods—the observation of photons emitted by fast ions rather than the direct observation of fast ions. At present, such spectroscopic methods are not widely used for the investigations of fast ions. There are only several papers where these methods have been used in nanosecond [6–8] and femtosecond [9, 10] laser-produced plasmas.

¶This article was submitted by the authors in English.

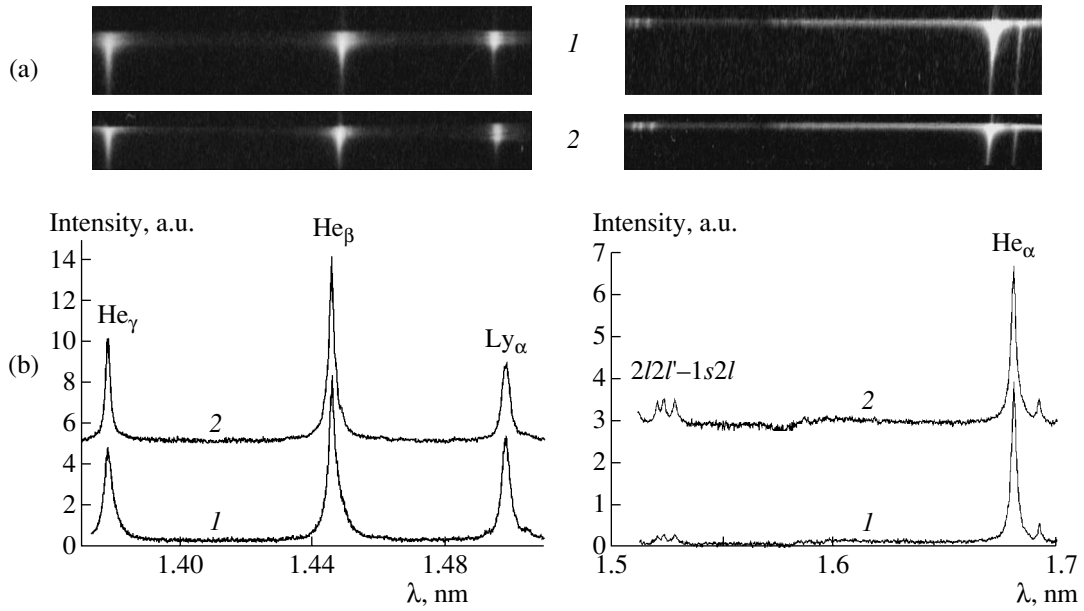

Fig. 1. The X-ray images of fluorine (a) and densitograms (b) obtained from the teflon plasma radiation for different observation directions: (*1*) parallel to the target surface, (*2*) at the angle $\phi_b = 45°$ to the target surface ($\phi_{las} = 0$). The XeCl laser pulse parameters are $\lambda_{las} = 0.308$ μm, $\tau_{las} = 12$ ns, $E_{las} = 2$ J, $q = 6 \times 10^{12}$ W/cm^2, and $q\lambda_{las}^2 = 6 \times 10^{11}$ W μm^2/cm^2.

In this paper, we present results for the fast ion production in plasmas created by nanosecond laser pulses with different wavelengths (0.308, 0.8, 1.06, and 10.6 μm). The results of X-ray spectroscopic methods show that the parameter $q\lambda_{las}^2$ (where q is the laser flux density and λ_{las} is the laser wavelength) is important for the processes of fast ion generation, but it does not completely determine these processes. It is also shown that, using laser radiation with the wavelength ~1 μm, it is possible to generate multicharged ions with MeV energy (so-called MeV ions) even for moderate values of laser flux density at about 10^{13} W/cm^2.

2. EXPERIMENTAL SETUP

The experimental investigations were carried out at four different research centers: GSI-Darmstadt and the Technical University of Darmstadt (Germany), Frascati (Italy), Saclay (France), and TRINITI (Russia). At GSI, the experiments were carried out at the nhelix-laser installation (nanosecond high-energy laser for heavy-ion experiments). nhelix is a Nd-glass/Nd-YAG laser ($\lambda_{las} = 1.06$ μm) with a pulse duration of 15 ns and energy up to 100 J. The present experiments, however, were performed with an energy of 17 J. The laser radiation is focused with a plane-convex lens (diameter 100 mm, focal length $f = 130$ mm) onto a solid teflon target (CF_2). With a spot size of about 500 μm, we obtain a flux density of about 10^{12} W/cm^2 onto the target and an extremely extended plasma source where the radiation emission of the He-like ions extends up to 1.5 cm [8]. In order to obtain different laser fluxes onto the target, the distance between the lens and the target was changed.

In the Saclay laser center, the experiments were performed with the UHI10, a Ti:sapphire laser with $\lambda = 0.8$ μm It was designed to generate 10-TW ultrashort pulses with a 10-Hz repetition rate. In the experiments reported here, the oscillator was switched off and the amplified pulse was provided by a regenerative amplifier used as a free-running Q-switched nanosecond oscillator. The pulse had a nearly Gaussian temporal profile with the full width at half maximum equal to 8 ns. The available energy in the experimental chamber was between 0.6 and 0.8 J. The 80-mm-diameter p-polarized laser beam was focused with an f/2.35 off-axis parabolic mirror onto a CF_2 target with the incidence angle $\phi_{las} = 45°$ (Fig. 1). The $1/e^2$ focal spot radius was between 10 to 20 μm, giving a flux density of about 5×10^{13} W/cm^2.

The excimer laser HERCULES used in Frascati is a discharge pumped XeCl system ($\lambda_{las} = 0.308$ μm) designed and built by ENEA, INN FIS Department of Frascati [11]. The capacitor bank of HERCULES is directly connected to the laser electrodes. Just before the rising voltage reaches the self-breakdown level, an X-ray pulse is injected into the Ne-based XeCl gas mixture providing an avalanche process. This phototriggering technique allows circumventing the typical problem of reliable switching in the main discharge circuit. In this way, HERCULES can be easily operated in the repetition rate mode without limitations because of

both the high charge transfer (~30 mC) and the high current rate (~10^{11} A/s). In the present experiments, we used an injected PBUR (positive branch unstable resonator) configuration, which means that HERCULES was used as a laser amplifier amplifying the beam generated by a commercial laser (Spectra Physics) with a 10-ns pulse duration. The energy thus obtained was 2 J per pulse with a 10-Hz repetition rate. The laser beam was focused by a triplet lens (with the *f* number $F = 3$) to a spot with a diameter of 50–80 μm onto a plane solid target, giving an intensity of about 6×10^{12} W/cm^2.

In TRINITI, the experiments were carried out using the TIR-1 facility, which was thoroughly described in [12]. The TIR-1 scheme can be used to generate CO_2 laser pulses with stable parameters and duration that can be varied in the range from 2 to 30 ns. Gas-phase saturable absorbers eliminated the feedback between the target under study and the laser system. The wave front of the radiation was shaped by spatial filters and matched irises. The output beam with a diameter of 200 mm had a divergence close to the diffraction limit. The laser system characteristics ensured good repeatability and optimization of the laser pulse parameters from the start. In the experiments described below, the laser source was a single-mode CO_2 oscillator built around the amplifier module of the TIR-1 facility with an active volume of ~17 liters. The radiation was produced in an unstable resonator having a length of 2.7 m and amplification equal to ~3. The energy of the output beam with a diameter of 150 mm was about 60 J, and the laser pulse duration was 20 ns. The laser radiation is focused with a lens (with the focal length $f = 600$ mm) onto a solid magnesium target with a spot diameter of about 500 μm. In this case, the laser flux density was about 10^{12} W/cm^2. In order to obtain different laser fluxes onto the target, the distance between the lens and the target was varied.

In all experiments, soft X-ray radiation was simultaneously recorded by two spectrographs with spherically bent mica crystals. The angle between the target normal and the laser beam was ϕ_{las}, and the angle between the target surface and the central ray of the second (*b*) spectrograph was ϕ_b. The curvature radii of the crystals were 150 and 100 mm. Both spectrographs were installed in the FSSR-2D scheme [13, 14]. This allowed observing spectra with spectral resolution $\lambda/\delta\lambda = 3000$–$5000$ and spatial resolution $\delta x = 25$–45 μm. In the TRINITI experiments, we simultaneously used both X-ray spectroscopy and traditional mass spectrometry (described in detail in [12]) diagnostics.

The experiments at GSI, Frascati, and Saclay were performed with flat solid teflon targets. In these cases, spectrographs were tuned to the spectral region of 13.7–17 Å containing the resonance line Ly_α of H-like F IX and the lines He_α, He_β, and He_γ of He-like F VIII. In the TRINITI experiments, flat solid magnesium targets were used. In this case, we observed (in the second order of crystal reflection) the spectral regions of 9.0–9.5 and 7.8–8.6 Å, which contain the Ly_α line of Mg XII and the He_α and He_β lines of Mg XI. Examples of the spectrograms and densitograms obtained are presented in Figs. 1 and 2.

3. RESULTS AND DISCUSSION

The main idea to use X-ray spectroscopy for the observation of fast ions is as follows. Suppose that a plasma expansion occurs predominantly in the direction normal to the target surface (the *z* axis). The observed emission spectra then depend on the angle between the direction of observation and the *z* axis because of the Doppler effect. Using several spectrographs simultaneously, it is possible to derive the direction of the predominant plasma expansion and its velocity distribution from the observed spectra. For example, if the plasma is cylindrically symmetric (the usual case for the interaction of a laser pulse with a flat target), the use of two spectrographs already provides the necessary information. In this case, spectrograph (*a*) observes the plasma in the direction perpendicular to the *z* axis and the line profiles are expected to be essentially symmetric. The width of the lines (apart from the random walk characterized by the ion temperature T_i) is determined by the transverse component $V_{x,y}$ of the plasma expansion velocity,

$$\frac{\Delta\lambda(a)}{\lambda} \approx \frac{V_{x,y}}{c}. \tag{1}$$

For the second spectrograph (*b*), the situation is different: the plasma motion is not symmetric, because the plasma moves only in the positive *z* direction. The spectral line is then shifted to shorter wavelengths by

$$\Delta\lambda = \lambda_0 \frac{V_z}{c} \sin\phi_b. \tag{2}$$

Because different ions can have different expansion velocities, the observed spectra show corresponding wings on the blue side of all spectral lines. The line profile is strongly asymmetric. Using the relation

$$I\left(\lambda_0 + \lambda_0 \frac{V_z}{c} \sin\varphi_b\right) \propto N(V_z), \tag{3}$$

it is possible to determine the number $N(V_z)$ of fast ions for a given velocity, i.e., the velocity distribution. We note that usually $V_z \gg V_{x,y}$, and consequently, the asymmetry observed by spectrograph (*b*) must be much more pronounced than the broadening observed by spectrograph (*a*). Exceptions from the symmetrical line shape for spectrograph (*a*) can be caused by radiation transport effects in transverse differentially moving (*x*-, *y*-direction) plasmas. Differential plasma motion results in a relative shift of the emission and absorption profiles, and the emission profiles are asymmetric [2].

The first X-ray spectroscopic observations of fast ions in a laser-produced plasma from solid targets were

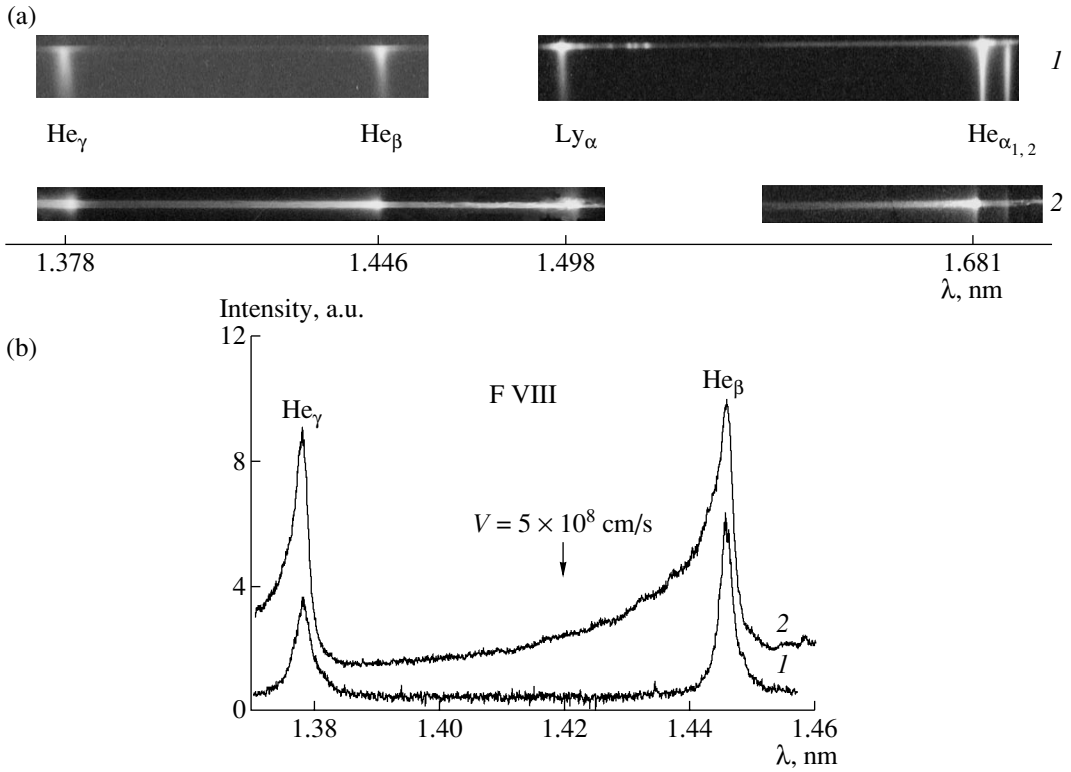

Fig. 2. The X-ray images of fluorine (a) and densitograms (b) obtained from the teflon plasma radiation for different observation directions: (*1*) parallel to the target surface, (*2*) at the angle $\phi_b = 90°$ to the target surface ($\phi_{las} = 45°$). The Ti:sapphire laser pulse parameters are $\lambda_{las} = 0.8$ μm, $\tau_{las} = 8$ ns, $E_{las} = 0.7$ J, $q = 5 \times 10^{13}$ W/cm^2, and $q\lambda_{las}^2 = 3 \times 10^{13}$ W μm^2/cm^2.

made many years ago [6, 7]. The spectral distribution of Doppler-shifted radiation from fast He-like ions was detected using flat or cylindrically bent crystal spectrographs. This technique has the serious drawback of spatial integration (we note that, although the introduction of slits in principle also provides a spatial resolution with flat crystals, the intensity drops considerably and the signal-to-noise ratio becomes insufficient for a detailed analysis of spectra). However, the use of focusing spectrographs with spherically bent crystals allows obtaining a high spatial resolution while maintaining high luminosity. The high spectral and spatial resolution, as well as the high luminosity, allows measurements for low intensity sources (and less intense lines, which are extremely important for diagnostic purposes) with higher spectral line densities.

The spectrograms shown in Figs. 1 and 2 were obtained using the various laser facilities described above. Figure 1 presents the plasma production by a relatively low-intensity and short-wavelength laser pulse. Figure 1a shows the images, and Fig. 1b shows the corresponding traces (spectra). The lines from highly charged fluorine detected by the spectrometer aligned perpendicularly to the plasma expansion axis, i.e., along the target surface (images *1* in Fig. 1a), exhibit a symmetrical shape. The width of the He_α and He_β lines are approximately equal to each other, indicating that Stark broadening does not dominate in the line wings. Images *2* in Fig. 1a correspond to aligning the spectrograph at the angle $\phi_b = 45°$ to the target surface. More details are seen from the spectra obtained by tracing the corresponding images (Fig. 1b, spectra *1* and *2*). The width of the lines is determined by the Doppler broadening due to the expansion at thermal velocities and by the plasma optical thickness.

In contrast, the results obtained for the teflon plasma using the GSI and Saclay laser facilities (see, e.g., Fig. 2) show that the line shape detected in the direction at 55° to the target surface exhibits a strong asymmetry in the blue wings (e.g., for each line He_α, He_β, He_γ, Ly_α). This asymmetry occurs because of the expansion dynamics and corresponds to large Doppler shifts (which cannot be explained by thermal expansion) and manifests the existence of a considerable amount of fast ions. The arrow near the curve in Fig. 2b shows the value of the Doppler shift that corresponds to a relative velocity of 5×10^8 cm/s. We note that, although the laser wavelengths and pulse durations were rather similar, the pulse energies and focusing conditions were quite different.

Similar results were obtained for a Mg plasma produced by a long-wavelength CO_2-laser pulse for the

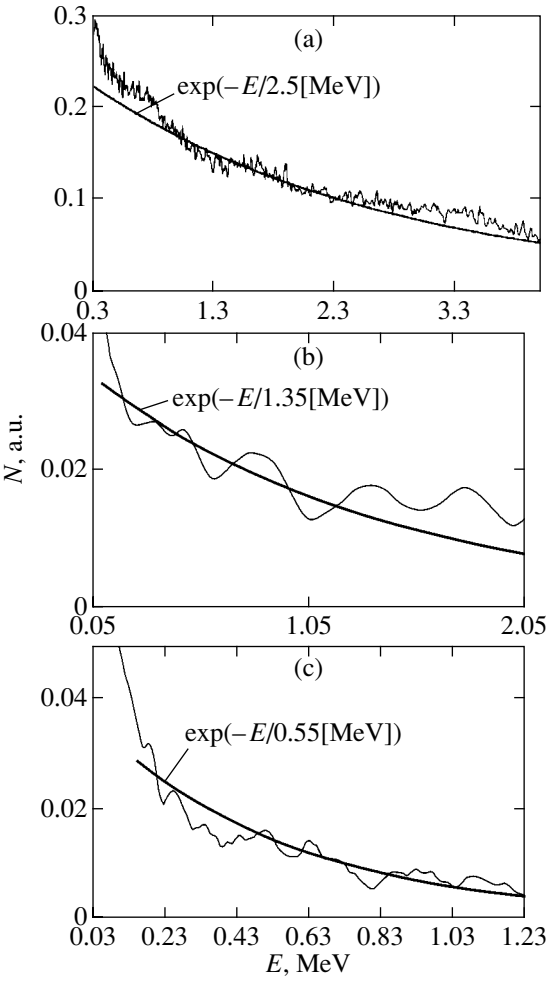

Fig. 3. Ion energy distributions derived from the relative intensities in the blue wings of the spectral lines of He_α of F VIII and He_α of Mg XI. The smooth lines represent the Maxwell distribution fits: (a) Saclay experiment, (b) GSI experiment, (c) TRINITI experiment.

observation angle $\phi_b = 45°$. In this case, the line asymmetry is pronounced for the optically thick resonance line ($He_{\alpha 1}$) and for the spectrally resolved optically thin intercombination line ($He_{\alpha 2}$).

The extraction of the average energy of fast ions from the measured spectra is based on the analysis of the blue wings of the spectral lines. Because the motion of ions is directed towards the spectrograph, the radiation emitted by fast ions must not pass through dense absorbing plasma regions. We now estimate possible absorption effects. The frequency-dependent optical thickness is given by

$$\tau_{ji}(\omega) = \int_0^L \frac{1}{4}\lambda_{ji}^2 \frac{g_j}{g_i} A_{ji} n_i \varphi_{ji}(\omega) dx, \qquad (4)$$

where λ_{ji} is the wavelength for the transition $j \longrightarrow i$, g_j and g_i are the statistical weights of the upper/lower states, A_{ji} is the spontaneous transition probability, n_i is the absorbing ground state, ϕ_{ij} is the line profile, and L is the relevant plasma size. The line center optical thickness τ_0 can be estimated from

$$\tau_{0,ji} \approx 1.25 \times 10^{-10} \lambda_{ji}^3[\mathrm{m}] A_{ji} \frac{\lambda}{\Delta\lambda} n_i[\mathrm{cm}^{-3}] L_{\mathrm{eff}}[\mu\mathrm{m}], \quad (5)$$

where $\lambda/\Delta\lambda$ is the relative line width. For a Doppler profile, the relative line width is given by

$$\frac{\Delta\lambda}{\lambda} = 7.69 \times 10^{-5} \sqrt{\frac{kT_i[\mathrm{eV}]}{M[\mathrm{amu}]}}. \qquad (6)$$

For $n_e = 10^{21}$ cm^{-3} (the critical density of the Nd-glass laser), $kT_i = 200$ eV, $M = 24$, and $L_{\mathrm{eff}} = 100$ μm, we obtain $\tau_0 \approx 40$ for the He-like resonance line $He_{\alpha 1}$ of Mg ($A = 1.95 \times 10^{13}$ s^{-1}) and $\tau_0 \approx 0.1$ for the intercombination line $He_{\alpha 2}$ ($A = 3.40 \times 10^{10}$ s^{-1}). The optical thickness of the intercombination line can therefore be neglected even in the line center, and for the resonance line, the optical thickness is negligible about one FWHM from the line center. Therefore, the spectral dependence of the intensities is directly related to the ion velocity distribution function.

Figure 3 shows the relative intensity in the blue wings of the He_β line of fluorine versus the Doppler shift measured in terms of the ion energy (directed motion). The smooth lines represent Maxwell distribution fits (with the temperature determined by the angle to the abscissa axis in logarithmic plots). The results show that the experimental uncertainty is sufficiently small to determine the average energy values for the fast ions. It should be noted that the difference between the Saclay (Fig. 3a) and GSI (Fig. 3b) results can be caused by two factors. The first is the higher laser flux density for the UHI10 facility. The second factor can be related to a resonance absorption of the *p*-polarized laser pulse [15–17] occurring when the angle $\phi_{\mathrm{las}} \neq 0$. Figure 3c shows the results for the TIR-1 CO_2-laser installation.

Figure 4a presents the velocity distribution of He-like ions measured in the TRINITI experiment (CO_2 Laser) by a mass spectrometer. Figure 4b shows the mass spectroscopic measurements together with the line spectroscopic results obtained from the He-like Mg lines. The low-velocity part is obtained from the optically thin He-like intercombination line

$$\mathrm{He}_{\alpha 2} = 1s2p\,^3P_1 \longrightarrow 1s^2\,^1S_0 + h\nu,$$

whereas the high-velocity part originates from the He-like resonance line

$$\mathrm{He}_{\alpha 1} = 1s2p\,^1P_1 \longrightarrow 1s^2\,^1S_0 + h\nu.$$

It can be seen that, for velocities below 1.4×10^8 cm/s (with 1.4×10^8 cm/s corresponding to an energy of 245 keV for Mg ions), the agreement is very good;

however, only the line spectroscopic measurements access the higher velocity region.

Figure 5 presents the fast ion average energy per nucleon as a function of the parameter $q\lambda_{las}^2$ as was proposed in [4]. In Fig. 5, we compare the measurements carried out for flat targets and ns-laser pulses [6, 7, 18–25]; we note, however, that the measurements indicated with filled squares were obtained for 35 ps-pulses [15, 17]. The results of the present mass spectrometry measurements (open triangles in Fig. 5) are also shown. The various results show a large scattering (by orders of magnitude) of the data for both the X-ray observations and the mass spectroscopy measurements. This indicates that the parameter $q\lambda_{las}^2$ may not be the only important parameter in the description of the fast ion generation.

We note that the mass-spectrometry and X-ray spectroscopy methods deal with different registration areas. In the first method, the ions are detected in a region far from the laser pulse and the interaction zone, while, in the second method, the interaction region involves various processes related to the formation of spontaneous X-ray radiation. One can therefore expect a more complicated scaling behavior of the average energy with the laser pulse parameters than that presented in [4]. At the same time, direct measurements from the interaction region provide more information for the understanding of the fast ion generation mechanisms.

4. SIMULATION TECHNIQUES

To reveal the physical phenomena responsible for different features of the measured X-ray spectra, we performed numerical simulations using two computer codes. The first is the one-dimensional GIDRA-1 code for the simulation of plasma hydrodynamics and population kinetics. Although real plasma movement is evidently not one-dimensional, this approach allows a good estimate of the average plasma parameters to be obtained. The numerical model is described in detail in [26]. Plasma hydrodynamics is described in the one-fluid two-temperature approximation. The model includes electron heat conduction with heat flux limitation, electron–ion temperature relaxation, and heating by laser light taken into account semiempirically. The electron energy balance equation also includes terms corresponding to the ionization and excitation of plasma ions and to the energy loss due to the plasma radiation. The energy losses due to the radiation in spectral lines and in the continuum are self-consistently taken into account along with the hydrodynamics and population kinetics. The interaction of laser light with plasma is modeled in the geometrical optics approximation by the ray-tracing technique. The ideal gas equation of state was used to couple the system of equations.

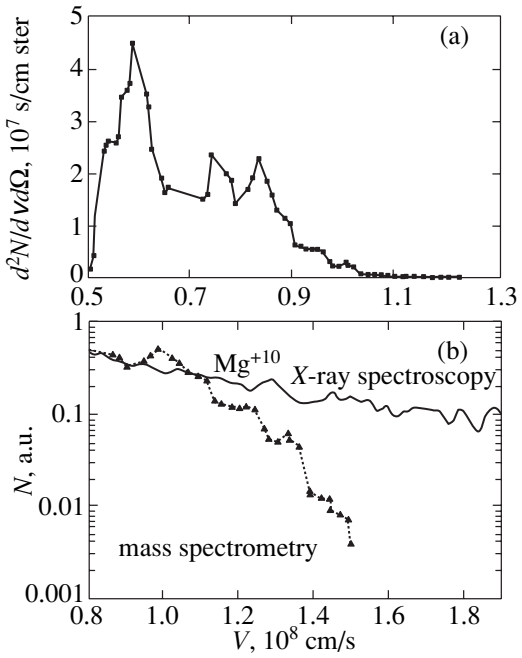

Fig. 4. (a) Mass spectroscopic measurements of the He-like Mg ion velocity distribution in CO_2-laser-produced plasmas; (b) comparison of the Mg XI ion velocity distribution in the CO_2 laser plasma derived from the X-ray spectroscopy (solid line) and mass spectrometry (dotted line with symbols) methods.

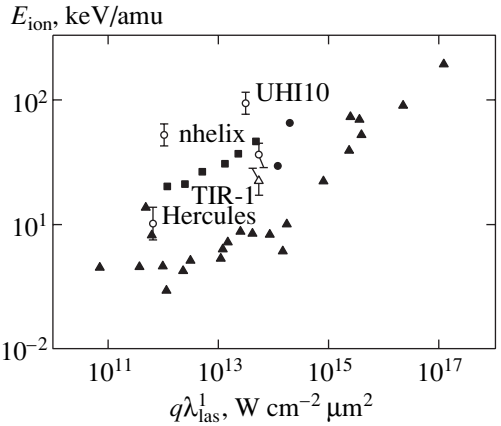

Fig. 5. The average fast ion energy E_{ion} [keV/amu] vs. $q\lambda_{las}^2$. Open symbols are the results obtained in the present work: circles are the X-ray spectroscopy measurements; the triangle is the mass spectrometry measurement. The filled circle is the X-ray spectroscopic result from [6], filled triangles denote the data in [15–24], and filled squares are the results in [15, 17].

The total number of atomic and ionic states for Mg used in the simulation was 77. The atomic model equations were solved self-consistently along with the hydrodynamics equations, which also allowed correct treatment of the transient effects in population kinetics. Temperature-dependent rates are calculated under the

assumption that the temperature distribution of electron energies obtained from hydrodynamics is given by the Maxwell distribution function. The effect of the line radiation re-absorption was described within the photon escape probability approach. The values of escape probabilities were calculated in the Sobolev approximation [27]. The drawback of the GIDRA-1 code for the purpose of X-ray spectra analysis is that doubly excited states are absent in the atomic model, and no satellite lines are therefore present in the generated spectrum.

On the other hand, another code package exploited in the course of the present work, MARIA [28], solves multilevel multi-ion stage atomic model equations with two important features: the correct account for a large number of doubly excited levels and a non-Maxwellian electron energy distribution function. MARIA solves the completely transient set of nonlinear population kinetics equations

$$\frac{dn_j}{dt} = -n_j \sum_{k=1}^{N} W_{jk} + \sum_{i=1}^{N} n_i W_{ij}, \tag{7}$$

where n_j are the population densities, N is the maximum number (dynamic) of levels (ground, singly excited, and multiexcited states of various ion stages), and the W matrix contains all the collision radiative processes and radiation transport effects. If a matrix element physically does not exist, its value is zero. More details related to the applications to spectra interpretation are described elsewhere [2, 28–31].

We have confined ourselves to the representation of non-Maxwellian distribution functions with the lowest possible number of temperature parameters T that allowed a reasonable description of the experimental spectra to be achieved. This was checked by means of three T parameters and a monoenergetic beam by changing the respective relative fractions and energies. The non-Maxwellian electron distribution function can then be characterized by the hot electron fraction

$$f_{\text{hot}} = \frac{n_{\text{hot}}}{n_{\text{cold}} + n_{\text{hot}}}. \tag{8}$$

The non-Maxwellian rate coefficients are given by

$$\langle V\sigma \rangle = (1 - f_{\text{hot}})\langle V\sigma, T_{\text{cold}}\rangle + f_{\text{hot}}\langle V\sigma, T_{\text{hot}}\rangle, \tag{9}$$

where the brackets indicate the integration of the cross section with the distribution function (assumed to be Maxwellian with the parameter T),

$$\langle V\sigma, T\rangle = \int_{E_0}^{\infty} \sigma(E)V(E)F(E)dE, \tag{10}$$

where

$$F(E) = \frac{2}{\sqrt{\pi}}\sqrt{E}\frac{\exp(-E/kT)}{(kT)^{3/2}}. \tag{11}$$

For three-body recombination, the corresponding expression is more complicated because it then becomes necessary to simultaneously introduce two distribution functions and the double differential ionization cross section

$$\langle V\sigma^{Tr}\rangle = (1 - f_{\text{hot}})^2\langle V_1V_1\sigma^{Tr}\rangle + f_{\text{hot}}^2\langle V_2V_2\sigma^{Tr}\rangle + 2f_{\text{hot}}(1 - f_{\text{hot}})\langle V_1V_2\sigma^{Tr}\rangle, \tag{12}$$

where

$$\langle V_kV_l\sigma_{ji}^{Tr}\rangle = \frac{\pi^2\hbar^3}{m_e^2}\frac{g_i}{g_j}\int_0^{\infty} dE_k \times \int_0^{\infty} dE_l \frac{E}{\sqrt{E_kE_l}}\sigma_{ij}^{I}(E, E_k)F(E_k)F(E_l). \tag{13}$$

If $k = l$, the integral in Eq. (13) can be reduced to an integral involving the usual ionization cross section $\sigma^I(E)$ (physically, this is equivalent to the application of the detailed balance principle). For $k \neq l$ the integrals are calculated numerically using the double differential ionization cross section $\sigma_{ij}^{I}(E, E_k)$.

Because we use the MARIA code to generate the detailed X-ray spectra for a given plasma density, temperature, and electron distribution function, we first investigated the validity of this approach. The two important features of laser plasma are the strong nonuniformity of plasma parameters and the essentially transient ionization and recombination processes occurring when plasma flows from the cold nearly solid-state density region through the hot critical zone to the rare and rather cold "corona." We restrict our treatment to one-dimensional effects (however, spherical geometry was chosen).

One type of simulation was made for a Nd laser at the irradiation conditions corresponding to the experiments at the nhelix-laser facility at GSI. The target was assumed to be solid magnesium. The pulse shape was Gaussian with a FWHM of 15 ns, and the peak of the pulse was shifted by 7.5 ns from the start of the simulation (therefore, the simulation time $t = 7.5$ ns corresponds to the peak of laser power). The peak power density of a pulse with a Gaussian temporal shape irradiating a solid target was set as $P_{\text{las}} = 10^{12}$ W/cm^2, $\lambda = 1.06$ μm. The initial radius of the target was set to $R_0 = 750$ μm.

Figure 6 presents the results of this simulation for a (Lagrangian) plasma particle that passes the point where T_e reaches the maximum at the time of the laser power peak. Figure 6a shows the relative abundances of Li-like and He-like Mg as a function of time for a Lagrangian particle. It is clearly seen that Li-like ions are present only for a few nanoseconds. Thereafter, the He-like ion population becomes dominant very soon. After the electron density becomes several times

smaller than the critical density, the ionization state of the plasma becomes "frozen" because the characteristic recombination time is much longer than the characteristic time of rarefaction. For the same Lagrangian particle, we also calculated the relative abundances obtained under the assumption that all populations are in a steady state. The steady-state He-like ion population becomes significantly different from the transient one only after 15 ns when the laser pulse is already over. Figure 6b shows the evolution of the electron density N_e and the electron temperature T_e. In Fig. 6c, the radiation power loss per unit volume is plotted for the resonance line of He-like Mg ions. The peak of the radiation power loss occurs slightly earlier than the peak of the electron temperature. This is because the electron density is rapidly decreasing.

Another type of GIDRA-1 simulation corresponds to irradiation conditions at the TIR-1 laser facility at TRINITI. The initial radius was set to $R_0 = 200$ μm. The optical system of the TIR-1 laser was designed to provide a power density close to 10^{14} W/cm^2. However, it turned out to be impossible to obtain high-quality spectra because of film overexposure (probably caused by fast electrons hitting the crystal and resulting in X-ray radiation from the mica surface). To avoid this effect, the target was displaced from the optimal focus position. This led to a smaller laser power density and significantly decreased the amount of fast electrons. In accordance with estimates, the peak intensity in the simulation was set to $P_0 = 2 \times 10^{12}$ W/cm^2. The pulse shape was Gaussian with the full width at half maximum equal to 26 ns, and the peak of the pulse was shifted by 13 ns from the start of the simulation. Simulations were performed in spherical geometry, providing a qualitatively correct distribution of plasma parameters even for the one-beam illumination geometry of a plane target (provided the initial diameter of the target in the simulation is about 1.5–2 times larger than the focal spot size). The initial radius of the spherical target for the simulation was 400 μm, while the focal spot size in the experiment was estimated to be 400–600 μm.

Simulation data are shown in Fig. 7. Because the peak of the electron temperature is higher than it was in the Nd-glass laser simulation, stationary populations deviate from the transient values at the temperature peak moments. The strongest effect is observed for the H-like ions: the relative abundance is less than 1% in the transient simulation, but two orders of magnitude larger in the steady-state simulation. The intensity peak of the He-like resonance line occurs before the temperature peaks (deviations of stationary populations from the transient ones are small). Based on these results, we expect that X-ray spectra produced by the MARIA code are reasonably accurate for the plasma regions close to the target surface.

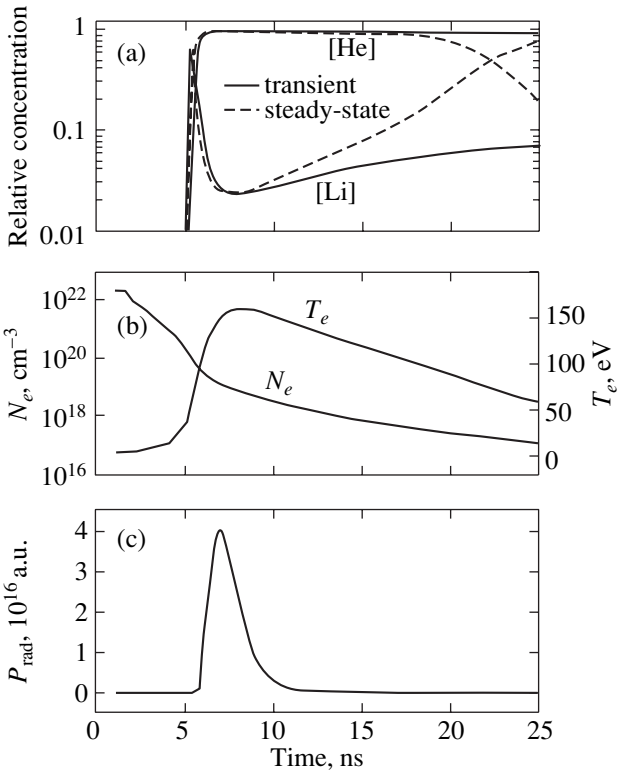

Fig. 6. Hydrosimulation for Nd-glass laser (GSI), $P_{las} = 10^{12}$ W/cm^2, $\lambda = 1.06$ μm, the initial target radius $R_0 = 750$ μm, the full Gaussian width $\tau = 15$ ns. Shown are the relative ion abundances (a), temperature and density (b), and radiation output of the He-like resonance line (c).

5. INVESTIGATION OF HOT ELECTRONS

Theoretical models [4, 15, 17] relate the generation of fast ions to the appearance of hot electrons. Although various mechanisms are under discussion (e.g., [4, 15, 17, 32, 33]), a satisfactory understanding is still missing. In this situation, the experimental investigation of fast ions and hot electrons inside the plasma volume where the laser energy is absorbed is mandatory for the understanding and benchmarking of theoretical models. X-ray spectroscopy set up with a high spectral and spatial resolution proves to be an excellent tool for these purposes. Moreover, the development of models for the interpretation of non-Maxwellian emission spectra have shown that the radiation from autoionizing states (the so-called dielectronic satellite spectra) plays a significant role [8, 28–30, 34–40]. However, the registration of these important satellite transitions requires very high luminosity spectrographs. Spherically bent mica crystals [13, 14] have been proved to simultaneously satisfy all the requirements that are necessary in practical applications: high spectral resolution ($\lambda/\delta\lambda \approx 5.000$), high spatial resolution ($\delta x \approx 10$ μm), high luminosity, and a sufficiently large spectral interval for the registration of various line emissions.

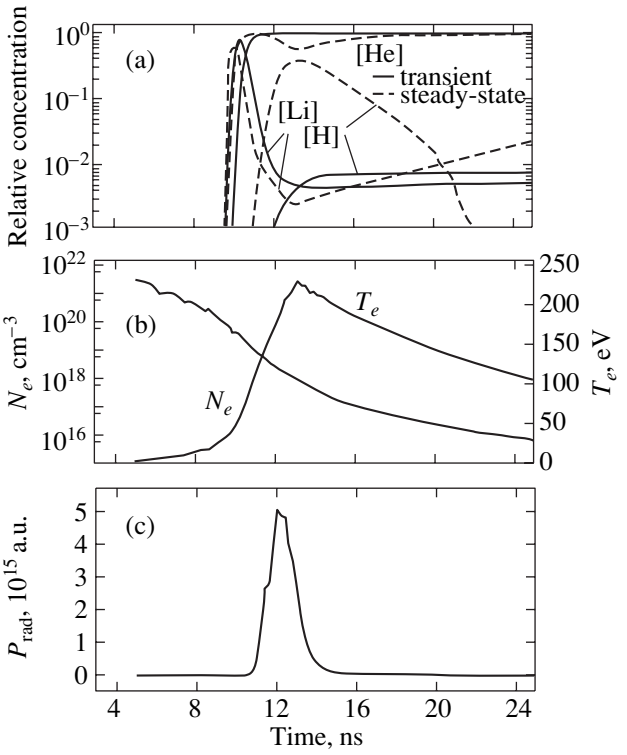

Fig. 7. Hydrosimulation for CO_2 laser (TRINITI), $P_{las} = 6 \times 10^{12}$ W/cm^2, $\lambda = 10.6$ μm, the initial target radius $R_0 = 200$ μm, the full Gaussian width $\tau = 26$ ns. Shown are the relative ion abundances (a), temperature and density (b), and radiation output of the He-like resonance line (c).

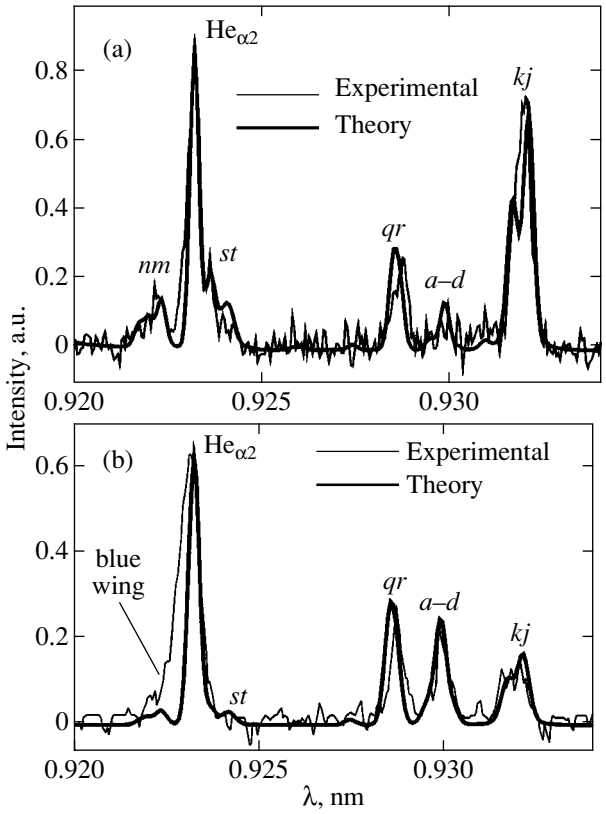

Fig. 8. (a) Experimental spectrum from the ns-nhelix laser at GSI. A good match between the theory (thick curve) and the experiment (thin curve) is obtained for the plasma parameters $kT_e = 200$ eV, $n_e = 2 \times 10^{20}$ cm^{-3}, $L_{eff} = 500$ μm; (b) experimental spectrum from He- and Li-like Mg ions obtained from the TRINITI CO_2 laser at 320 μm from the central spot. A good agreement could only be obtained assuming a non-Maxwellian energy distribution function. The simulation parameters are $kT_{cold} = 60$ eV, $n_e = 1 \times 10^{19}$ cm^{-3}, $kT_{hot} = 1$ keV, $f_{hot} = 4 \times 10^{-7}$, and $L_{eff} = 50$ μm.

Figure 8a shows the spectral interval from the He-like intercombination line up to the Li-like *kj* satellites (see, e.g., [41] for the satellite designation) from the nhelix-Nd-glass/YAG-laser at GSI. The spectrum corresponds to a distance of about 1.9 mm from the center of the laser spot. For these areas, the laser flux density is much lower than for the central spot, and we do not expect a considerable amount of hot electrons and fast ions. This spectrum is therefore suitable to experimentally cross-checking the spectra simulations of multiexcited ions under well-defined conditions. The theoretical modeling (thick line in Fig. 8a) fits the experiment in all spectral details with the following parameters: the electron temperature $kT_e = 200$ eV, the electron density $n_e = 2 \times 10^{20}$ cm^{-3}, and the photon path length $L_{eff} = 500$ μm. The essential point here consists in the simultaneous match of the intercombination line $He_{\alpha 2}$, the *qr*, *a-d*, and *jk* satellites that strongly depend on non-Maxwellian electrons because of their different excitation channels and excitation mechanisms [8, 28, 36]. It can be clearly seen that a good modeling is obtained without the introduction of hot electrons (we note that the slight discrepancies in wavelengths are not caused by inaccurate atomic data but rather by a nonlinear experimental wavelength scale). It is also worth paying attention to the good interpretation near the intercombination line $He_{\alpha 2}$, first, we note that no blue wings are observed, and second, we also obtained a good agreement of the satellite structure near the positions indicated with "nm" and "st." In fact, the corresponding intensities are caused by the emission not only from the Li-like $1s2l2l'$ satellites nm/st but also from higher order satellites originating from the $1s2l2nl'$ configurations. Extended atomic data calculations and subsequent spectra simulations have shown that these higher order satellites accumulate not only near the He-like resonance line $He_{\alpha 1}$, but also near the He-like intercombination line $He_{\alpha 2}$ [30].

An entirely different situation is realized for CO_2-laser-produced plasmas. Figure 8b shows the emission spectrum obtained from the TRINITI installation. Numerous parameter variations showed that the experimental situation could not be fitted by simulations with a Maxwellian electron energy distribution function. We have also investigated highly transient

phenomena that in principle could lead to enhanced *qr*-satellite emission due to an ionization abundance, which is lacking beyond the electron temperature. However, taking the transient numerical data for a Lagrangian cell from gas-dynamical calculations (see Fig. 7), we find that, in the early stage of plasma development (corresponding to spectra near the target surface to which we confine our present discussion), these effects are small. The main reason for this is the high electron density in the first few nanoseconds after the target ablation driving the confinement parameter ($n_e\tau$) to large values. The detailed non-Maxwellian investigation of the data with the MARIA simulations showed that $T_{\rm cold}$ is rather low, about 60 eV, while the temperature of hot electrons $T_{\rm hot}$ is about 1 keV (or higher). The reasons are as follows. Usually the hot electron component not only increases inner-shell excitation rates (and therefore raises the corresponding lines, e.g., the *qr* satellites), but also drives the ionic population to higher charge states through increased ionization rates. In quasi-stationary plasmas with the confinement parameters

$$n_e\tau \geq 10^{12}\ \text{cm}^{-3}\ \text{s}, \qquad (14)$$

the increased inner-shell excitation rates and depleted charge states can partly cancel. However, if the bulk electron temperature is very low, we meet with an entirely different regime: the hot electrons are not able to shift the ionic charge states to significantly higher values, and increased inner-shell excitation rates are directly visible through the increased emission of the corresponding lines. In this regime, the spectroscopic diagnostic is extremely sensitive to the hot electron fraction and the low values of $f_{\rm hot}$ about 10^{-6} lead to significant changes in the spectral distribution. This is shown in Fig. 9 for the intercombination line $He_{\alpha 2}$ and *qr* and *kj* satellites. Two important observations can be made from this figure: first, the critical value of $kT_{\rm cold}$, where the influence of the hot electrons starts to be essential, is different for different lines (see arrows); second, the "bumps" for curves (*b*) are also very different. In particular, the bump for the *qr* satellites at $kT_{\rm cold} \approx 50$ eV is so strongly pronounced that it even leads to a local maximum (the increased inner-shell excitation rates strongly dominate over the shifted balance—see the discussion above). Therefore, the *qr* satellites rise in intensity relative to the other emission lines. The different threshold values (in particular, those for the *kj* satellites) have the following origin: the dielectronic capture energy and the excitation energy for the intercombination line are different. The small bump for the *kj* satellites results from the dielectronic recombination caused by the distribution function with the parameter $kT_{\rm hot}$. These overall characteristics are caused by the excitation from different channels through different mechanisms: the inner-shell excitation for the *qr* satellites, collisional excitation from the He-like ground state for the intercombination line, and dielectronic capture into the He-like ground state for the *kj* satellites. Precisely these different channels make the selected emission lines suitable for the hot electron investigation.

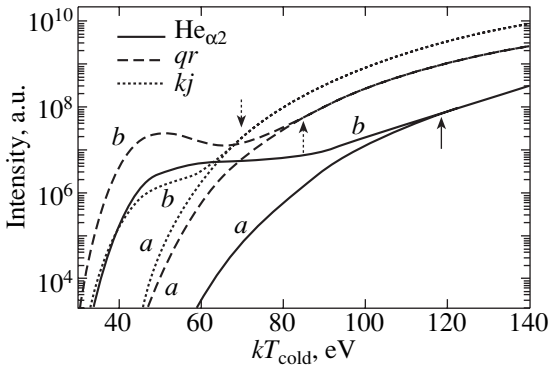

Fig. 9. Intensities of the He-like intercombination line $He_{\alpha 2}$ and the Li-like satellites *qr* and *jk* for different values of $T_{\rm cold}$ and different fractions of hot electrons: $n_e = 10^{21}$ cm^{-3}, $kT_{\rm hot} = 2$ keV. The arrows indicate the different threshold values of $kT_{\rm cold}$ for the strong onset of the hot electron influence on the line emission; $f = 0$ (*a*), 10^{-5} (*b*).

Figure 8b also shows the theoretical fitting of the experimental spectrum. The theoretical spectrum was obtained for $kT_{\rm cold} = 60$ eV, $n_e = 10^{19}$ cm^{-3}, $kT_{\rm hot} = 1$ keV, $f_{\rm hot} = 4 \times 10^{-7}$, and $L_{\rm eff} = 500$ μm. It should be noted that it was impossible to describe the relative structure of satellite lines without introducing hot electrons. On the other hand, it is impossible to explain the blue wing of the $He_{\alpha 2}$ line without the introduction of fast ions. The relative structure of satellite intensities is not very sensitive to the hot electron energy if $T_{\rm hot}$ is comparable to or larger than the threshold value (because the rate coefficients are mainly inversely proportional to the square root of $T_{\rm hot}$ and do not show a strong exponential dependence). Therefore, $T_{\rm hot}$ may be significantly higher.

We next consider spatial nonuniformity of the plasmas. In Fig. 10, we present the spatial distribution of plasma parameters (at the time of the peak laser intensity) from the simulation of the CO_2-laser-produced plasma. Figure 10a shows the electron density as a function of radius together with the population densities of Li-like and He-like Mg. It is easily seen that Li-like ions are present only in a rather narrow spatial region of about 20 μm, while the He-like Mg ions occupy an order-of-magnitude wider region. Figure 10b shows the distribution of the electron temperature and Fig. 10c presents the distribution of the radiation power density (per unit volume) for the He-like resonance (*R*) and intercombination (*I*) lines. Two things are important to emphasize. First, resonance and intercombination lines of He-like magnesium have a peak of the radiation power at an electron density much higher than critical. This explains the rather large X-ray emission

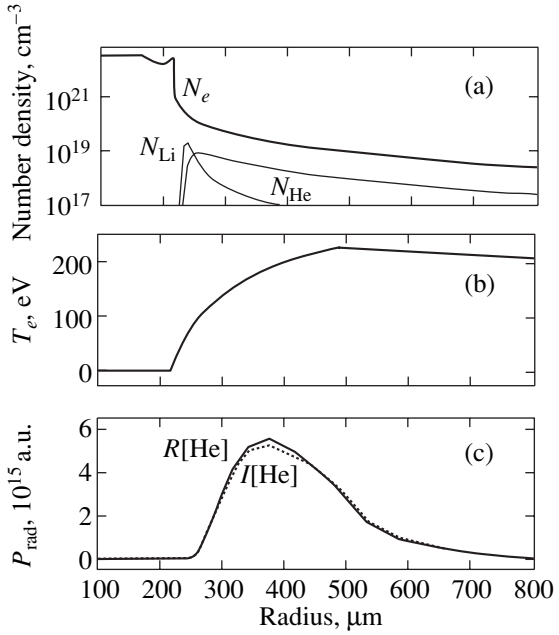

Fig. 10. The calculated distribution of plasma parameters for a spherically symmetric target irradiated by a CO_2 laser pulse: (a) electron density (N_e) and number densities of Li-like and He-like magnesium (N_{Li} and N_{He}, respectively) along the radius; (b) the electron temperature T_e; and (c) the radiation power density of the resonance and intercombination lines of He-like magnesium (R[He] and I[He], respectively).

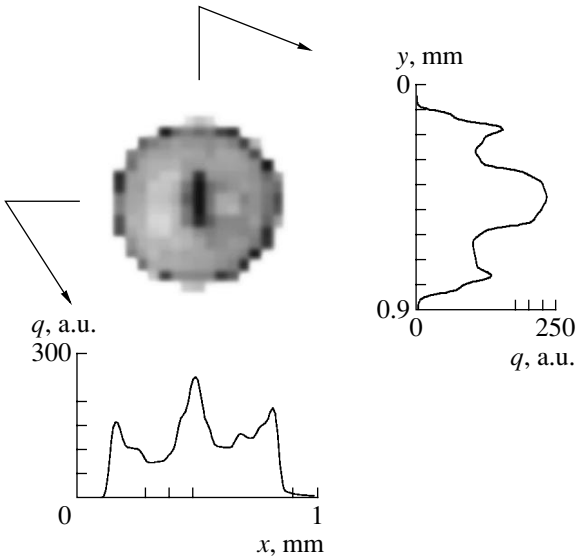

Fig. 11. The measured laser intensity distribution in the focal spot at the nhelix laser facility.

intensity fixed in experiments. Second, the electron temperature at the point where the peak of these two lines occurs is about 200 eV, which is significantly higher than the temperature at the point where the peak of Li-like Mg is situated (60 eV). From these results, we conclude that the emission of the He-like resonance line and associated satellite lines originate from two distinct regions in which both the temperature and electron density are quite different. The fact that the resonance line and the satellites are radiated from different spatial regions is valid for lower and higher laser radiation intensities (we performed simulations in the range of intensities $P_0 = 5 \times 10^{11}$–1×10^{14} W/cm^2) as well as for plasma parameters corresponding to the peak of the Li-like ion abundance. The peak of the He-like resonance line is found to be very conservative against changes of the laser power density.

The presence of blue wings at the He-like resonance and intercombination lines and the absence of this feature on satellites also indicate that satellites are radiated from narrow regions where the velocity does not change significantly. On the other hand, the resonance line is radiated from a rather wide region where the plasma is strongly accelerated.

Taking the plasma nonuniformity into account, we treat the effective electron temperature obtained by comparing the intensities of both He-like and Li-like transitions as, probably, strongly underestimated in comparison to the peak electron temperature. Because we revealed that the He-like resonance line is insensitive to the density fraction of hot electrons (for $f \le 10^{-5}$ at least) at electron temperatures above $T_e = 120$ eV, the value of f obtained by the spectrum fitting is probably also underestimated. Nevertheless, the sensitivity of the method to the density of hot electrons is surprisingly high.

6. NONUNIFORM LASER INTENSITY DISTRIBUTION WITHIN THE FOCAL SPOT

One of the important features of our experiments was a strong nonuniformity of the laser intensity distribution within the focal spot at the nhelix and TIR-1 lasers. At the nhelix laser facility, this distribution was measured. Results presented in Fig. 11 demonstrate the complex structure of the laser intensity distribution.

Under the conditions of experiments at the TIR-1 laser facility, the intensity pattern was also not uniform (due to the shifts of targets away from the optimal focus). The two-dimensional laser intensity distribution was obtained from numerical simulation performed with the FOCUS code for the real experimental geometry. FOCUS is a two-dimensional diffraction code for the calculation of light intensity distribution in complex optical schemes that can include an arbitrary number of apertures of arbitrary shape and plane or spherical mirrors. The concentric gap appears due to the shadow of the target and the support pivot placed into the converging light beam. Diffraction of the laser beam on the target introduces additional peaks. In our view, these quite nonuniform intensity distribution patterns provoke filamentation of laser light, which leads to the creation of locally overheated regions. This effect in the CO_2-laser-

produced plasma was, probably, first reported in [42], where the filamentation effect was observed above an incident intensity of $\sim 2 \times 10^{12}$ W/cm^2, a value significantly lower than that in our experiments at TIR-1. At the same time, our pinhole images produced by several subsequent shots (from four to ten) clearly demonstrate several "plasma jets" (see arrows in Fig. 12), which, would be averaged on the film in the case of stochastic filamentation. The example of an X-ray pinhole image is shown in Fig. 12. This qualitatively proves the presumed correlation of the laser intensity nonuniformity and the appearance of laser light filamentation, which, as a consequence, leads to an "easier" generation of fast ions and electrons. This might be a way to control the fast particle production, but in the present work, we did not aim at any optimizations.

Our experiments demonstrate that the generation of fast electrons and ions can be achieved at very low levels of laser intensity compared to that reached at femtosecond lasers [43, 44] ($q\lambda^2 > 10^{18}$ W μm^2/cm^2). As Fig. 5 indicates, fast ion energy shows no clear correlation with the $q\lambda^2$ parameter. This is in line with the observation of the fast ion generation in the CO_2-laser-produced plasma, which was significantly less efficient than when we studied plasmas created by lasers in the visible wavelength range (while one would expect the opposite due to much lower critical electron density).

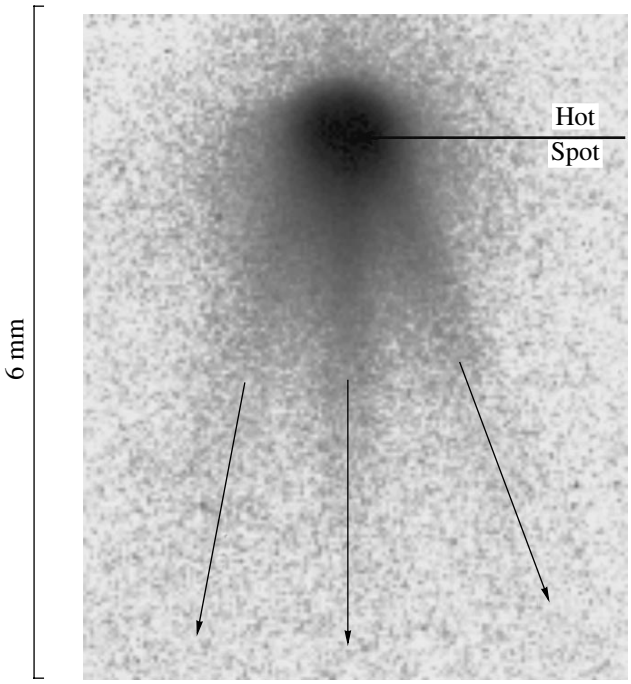

Fig. 12. The X-ray pinhole image of Mg plasmas produced by CO_2 TIR-1 laser at 6×10^{12} W/cm^2 (average over ten shots). Three plasma jets (see arrows) originate from the hot spot.

7. CONCLUSIONS

We have studied the fast ion and hot electron production at various different laser installations at GSI-Darmstadt (Germany), Saclay (France), Frascati (Italy), and TRINITI (Russia) for Nd-glass, Ti-sapphire, XeCl, and CO_2 lasers by means of high-resolution X-ray spectroscopic methods and ion time-of-flight measurements. The spectroscopic approach provides information about the plasma particles even inside the plasma volume. Experimentally further advantageous is the fact that the analysis is based on a unique footing, namely, on the investigation of a highly resolved spectral interval containing numerous X-ray line transitions of target ions from states with various charges.

Fast ion distributions have been characterized through Doppler-shifted line wings of spatially resolved X-ray spectra originating from highly charged target ions inside the plasma volume. For laser intensities $q\lambda^2 < 10^{14}$ W μm^2/cm^2, a large scattering (by orders of magnitude) of fast ion energies has been obtained. These observations are presumably caused by inhomogeneous intensity distributions over the laser spot, which have been identified with measurements and two-dimensional diffraction calculations. These scatters might be advantageous for a simple creation of MeV-energy ions with sufficiently low laser intensities: in fact, MeV-energy ions for relatively low intensities $q\lambda^2 < 10^{13}$ W μm^2/cm^2 have been observed.

MHD and non-Maxwellian spectroscopy have been used to characterize plasmas containing non-Maxwellian particles. Methods were developed to determine the electron bulk temperature and the hot electron fraction with a sensitivity down to about 10^{-5} (compared to the electron bulk). These methods are based on the detailed analysis of the spectral distribution of the radiation emission of multiexcited target ions near the target surface.

ACKNOWLEDGMENTS

This work was partly supported by INTAS (project no. 97-2090).

REFERENCES

1. *PHELIX, Petawatt High-Energy Laser for Heavy-Ion Experiments*, GSI-98-10, Report (1998).
2. F. B. Rosmej, U. N. Funk, M. Geißel, *et al.*, J. Quant. Spectrosc. Radiat. Transf. **65**, 477 (2000).
3. J. Lindl, Phys. Plasmas **2**, 3934 (1995).
4. S. J. Gitomer, R. D. Jones, F. Begay, *et al.*, Phys. Fluids **29**, 2679 (1986).
5. Laser Part. Beams **24** (3) (1996).
6. V. A. Boiko, O. N. Krokhin, S. A. Pikuz, *et al.*, Fiz. Plazmy **1**, 309 (1975) [Sov. J. Plasma Phys. **1**, 165 (1975)].

7. N. G. Basov, S. V. Bobashev, K. Gotz, *et al.*, Pis'ma Zh. Éksp. Teor. Fiz. **36**, 229 (1982) [JETP Lett. **36**, 281 (1982)].
8. F. B. Rosmej, D. H. H. Hoffmann, W. Süß, *et al.*, Pis'ma Zh. Éksp. Teor. Fiz. **70**, 262 (1999) [JETP Lett. **70**, 270 (1999)].
9. S. Dobosz, M. Schmidt, M. Perdrix, *et al.*, Pis'ma Zh. Éksp. Teor. Fiz. **68**, 454 (1998) [JETP Lett. **68**, 485 (1998)].
10. A. G. Zhidkov, A. Sasaki, T. Tajima, *et al.*, Phys. Rev. E **60**, 3273 (1999).
11. S. Bollanti, P. Di Lazarro, F. Flora, *et al.*, Phys. Scr. **51**, 326 (1995).
12. V. Yu. Baranov, K. N. Makarov, V. C. Roerich, *et al.*, Laser Part. Beams **14**, 347 (1996).
13. I. Yu. Skobelev, A. Ya. Faenov, B. A. Bryunetkin, *et al.*, Zh. Éksp. Teor. Fiz. **108**, 1263 (1995) [JETP **81**, 692 (1995)].
14. B. K. F. Young, A. L. Osterheld, D. F. Price, *et al.*, Rev. Sci. Instrum. **69**, 4049 (1998).
15. P. Wägli and T. P. Donaldson, Phys. Rev. Lett. **40**, 875 (1978).
16. M. Schnürer, M. P. Kalashnikov, P. Nickles, *et al.*, Phys. Plasmas **2**, 3106 (1995).
17. P. Wägli, T. P. Donaldson, and P. Lädrach, Appl. Phys. Lett. **32**, 638 (1978).
18. B. C. Boland, F. E. Irons, and R. W. P. McWhirter, J. Phys. B **1**, 1180 (1968).
19. C. Fauquignon and F. Floux, Phys. Fluids **13**, 386 (1970).
20. M. Waki, T. Yamanaka, H. Kang, *et al.*, Jpn. J. Appl. Phys. **11**, 420 (1972).
21. Los Alamos Sci. Lab. Rep., No. LA-UR 76-2242 (1976).
22. K. Dick and H. Pepin, Opt. Commun. **13**, 289 (1975).
23. C. Yamanaka, T. Yamanaka, T. Sasaki, and J. Mizui, Phys. Rev. Lett. **32**, 1038 (1974).
24. E. Fabre, C. Garban, C. Popovics, *et al.*, in *Proceedings of the Conference on Plasma Physics and Controlled Nuclear Fusion Research* (IAEA, Vienna, 1975), Vol. II, p. 597.
25. H. Pepin, B. Grek, F. Rhealt, and D. Nagel, J. Appl. Phys. **48**, 3312 (1977).
26. A. E. Stepanov, A. N. Starostin, V. C. Roerich, *et al.*, J. Quant. Spectrosc. Radiat. Transf. **58**, 937 (1997).
27. G. B. Rybicki and D. G. Hummer, Astrophys. J. **274**, 380 (1983).
28. F. B. Rosmej, J. Phys. B **30**, L819 (1997).
29. F. B. Rosmej, A. Ya. Faenov, T. A. Pikuz, *et al.*, Pis'ma Zh. Éksp. Teor. Fiz. **65**, 679 (1997) [JETP Lett. **65**, 708 (1997)].
30. F. B. Rosmej, A. Ya. Faenov, T. A. Pikuz, *et al.*, J. Quant. Spectrosc. Radiat. Transf. **58**, 859 (1997).
31. F. B. Rosmej, D. Reiter, V. S. Lisitsa, *et al.*, Plasma Phys. Controlled Fusion **41**, 191 (1999).
32. D. W. Forslund and J. U. Blackbill, Phys. Rev. Lett. **48**, 1614 (1982).
33. N. E. Andreev, Yu. A. Zakharenkov, N. N. Zorev, *et al.*, Zh. Éksp. Teor. Fiz. **70**, 547 (1976) [Sov. Phys. JETP **43**, 283 (1976)].
34. A. S. Shlyaptseva, A. M. Urnov, and A. V. Vinogradov, Preprint No. 193, FIAN (Lebedev Institute of Physics, Academy of Sciences of USSR, Moscow, 1981).
35. M. K. Inal and J. Dubau, J. Phys. B **22**, 3329 (1989).
36. F. B. Rosmej, J. Quant. Spectrosc. Radiat. Transf. **51**, 319 (1994).
37. F. B. Rosmej and O. N. Rosmej, AIP Conf. Proc. **299**, 560 (1994).
38. F. B. Rosmej, J. Phys. B **28**, L747 (1995).
39. J. Abdallah, Jr., A. Ya. Faenov, D. Hammer, *et al.*, Phys. Scr. **53**, 705 (1996).
40. J. P. Matte, J. C. Kieffer, S. Ethier, and M. Chaker, Phys. Rev. Lett. **53**, 1461 (1994).
41. A. H. Gabriel, Mon. Not. R. Astron. Soc. **160**, 99 (1972).
42. T. P. Donaldson and I. J. Spalding, Phys. Rev. Lett. **36**, 467 (1976).
43. P. Gibbon and E. Forster, Plasma Phys. Controlled Fusion **38**, 759 (1996).
44. A. G. Zhidkov, A. Sasaki, T. Tajima, *et al.*, Phys. Rev. E **60**, 3273 (1999).

Journal of Experimental and Theoretical Physics, Vol. 94, No. 1, 2002, pp. 73–83.
Translated from Zhurnal Éksperimental'noĭ i Teoreticheskoĭ Fiziki, Vol. 121, No. 1, 2002, pp. 88–101.

PLASMA, GASES

On the Interaction of Femtosecond Laser Pulses with Cluster Targets

I. Yu. Skobelev[a, *], A. Ya. Faenov[a], A. I. Magunov[a], T. A. Pikuz[a], A. S. Boldarev[b], V. A. Gasilov[b], J. Abdallach, Jr.[c], G. C. Junkel-Vives[c], T. Auguste[d], P. d'Oliveira[d], S. Hulin[d], P. Monot[d], F. Blasco[e], F. Dorchies[e], T. Caillaud[e], C. Bonte[e], C. Stenz[e], F. Salin[e], and B. Yu. Sharkov[f]

[a]*Center of Data on Spectra of Multiply Charged Ions, All-Russia Research Institute of Physicotechnical and Radio Engineering Measurements, Mendeleevo, Moscow oblast, 141570 Russia*

[b]*Institute for Mathematical Modeling, Russian Academy of Sciences, Russia*

[c]*Los Alamos National Laboratory, P. P. Box 1663, Los Alamos, New Mexico 87545, USA*

[d]*CEA, Centre D'Etudes de Saclay, DSM/DRECAM, Service des Photons Atomes et Molecules, 91191 Gif-sur-Yvette, France*

[e]*CELIA, Universite Bordeaux, 33405 Talence, France*

[f]*Institute of Theoretical and Experimental Physics, Russian Academy of Sciences, Moscow, 117259 Russia*

**e-mail: skobelev@orc.ru*

Received July 30, 2001

Abstract—The heating of clusters by femtosecond laser pulses is studied theoretically and experimentally. Both the formation of a cluster target and the results of experimental studies of the cluster plasma by the methods of X-ray emission spectroscopy are considered. A numerical model of cluster formation in a supersonic gas jet is proposed. It is shown that detailed studies of two-phase gas-dynamic processes in a nozzle forming the jet give the spatial distributions of all parameters required for the correct calculation of the cluster heating by short laser pulses. Calculations of nozzles of different configurations show that in a number of cases an almost homogeneous cluster target can be formed, whereas in other cases the distributions of parameters prove to be not only inhomogeneous but also even nonmonotonic. A simple physical model of the plasma production by a femtosecond laser pulse and a picosecond prepulse is proposed. It is shown that a comparison of X-ray spectra with detailed calculations of the ion kinetics makes it possible to determine the main parameters of the plasma being produced. © *2002 MAIK "Nauka/Interperiodica".*

1. INTRODUCTION

Studies of the interaction of high-power ultrashort (femtosecond) laser pulses with solid-state and gas targets have become especially important in the recent years. On the one hand, such studies yield information on the fundamental properties of matter under extreme conditions (see, for example, [1–12]), and, on the other hand, they allow one to use new approaches for solving a number of applied problems, such as the initiation of nuclear reactions, the acceleration of heavy particles, and the creation of a bright X-ray emission source for medical, biological, and lithographic studies (see, for example, [1, 2, 11, 13]).

It is obvious that the properties of the plasma produced by an ultrashort laser pulse should depend first of all on the aggregate state of the target material. Using, for example, solid-state or cluster targets, an ultrahigh-density hot plasma with a temperature of several hundred electronvolts can be produced. Because of the high density of the plasma, its ionization occurs mainly due to electron–ion collisions. For example, the authors of papers [9, 14, 15] produced multiply charged Ar XVII and Kr XXVII ions by irradiating cluster targets by ultrashort laser pulses with the power density q_{las} = 10^{17}–10^{18} W/cm^2. The production of such ions due to tunnel ionization would be possible only at much greater (by several orders of magnitude) intensities of laser pulses.

In the opposite case of low-density gas targets, the efficiency of target heating by laser pulses is substantially lower, and the temperature of a comparatively low-density plasma being produced will be only several tens of electronvolts (see, for example, [16]). In this case, the ionization state of the plasma will be determined by multiphoton or tunnel ionization.

However, as the first experiments with solid targets have shown, there exists another very important parameter determining the nature of the interaction of ultrashort laser pulses with matter, namely, the contrast of the laser pulse, i.e., the ratio of the laser radiation power at the maximum of the femtosecond pulse to the prepulse power. In particular, it was found that the ultrahigh-density plasma could be formed only using pulses with a very high contrast (~10^{10}), when the heating radiation flux density in the prepulse is insufficient for producing a preplasma and the main-pulse energy is absorbed directly in a solid (see, for example, [17–21]).

The character of the interaction of a femtosecond pulse with cluster targets should depend on its contrast even in a greater extent than for solid targets. Recall that cluster targets represent the gas containing clusters, i.e., large conglomerates of atoms or molecules, which are produced during the escape of cooled gas through a high-pressure nozzle. The size L_{cl} of clusters and the number N_{cl} of particles in them are determined by the gas being used and by the values of its parameters (temperature, density), as well as by the nozzle construction, and achieve $L_{cl} \approx 100$–1000 Å and $N_{cl} \approx 10^4$–10^6 atom/cluster, the density of particles in the cluster being comparable with the density of a solid (see, for example, reviews [1, 22]). In this case, the situation proves to be even more complicated than in the case of solid targets, and two new parameters, the laser prepulse duration $\tau_{prepulse}$ and the cluster size, acquire a crucial role in the interaction physics. Indeed, if the intensity of the femtosecond pulse is high enough (experiments are usually performed at the radiation flux density $q_{las} \approx 10^{17}$–10^{18} W/cm^2), then, even for sufficiently high contrasts of about 10^4–10^5 (which are typical for femtosecond lasers), the flux density in the prepulse is 10^{13}–10^{14} W/cm^2 and is quite sufficient for the destruction of the cluster and the production of the preplasma with the electron temperature T_e of the order of 100–300 eV. Due to the expansion of such cluster plasma for the time

$$\tau_{expansion} \sim L_{cl}\left(\frac{m_i}{Z_n k T_e}\right)^{1/2} (10^{23}/N_{cr})^{1/3} \qquad (1)$$

(where Z_n, and m_i are the charge and mass of the ion and N_{cr} is the critical density for the heating laser), its electron density becomes smaller than the critical one [1]. This means that, if the prepulse duration satisfies the condition

$$\tau_{prepulse} \gg \tau_{expansion}, \qquad (2)$$

then the main femtosecond pulse will interact not with clusters but with the low-density plasma, and the character of the interaction will be in fact the same as upon heating of gas targets (a weak absorption of laser radiation and the almost complete absence of collision ionization).

It follows from (1) that, for typical values $kT_e \sim 100$ eV, $N_{cr} \sim 10^{21}$ cm^{-3}, and $L_{cl} \sim 100$–1000 Å, $\tau_{expansion}$ has a value on the order of 1–10 ps, and condition (2) was fulfilled with a large margin in earlier experiments with the nanosecond prepulse [1]. In paper [15], the case of a comparatively short prepulse with $\tau_{prepulse} \approx \tau_{expansion}$ has been studied for the first time, when density regions efficiently absorbing the main pulse remain in the cluster preplasma after the prepulse termination.

It is rather difficult to control the laser prepulse duration under real experimental conditions. For this reason, different cases of the interaction of femtosecond pulses with clusters can be much more easily realized by varying the average size L_{cl} of the cluster or changing the laser contrast, which in fact determines the preplasma temperature T_e. In any case, to construct an adequate model of the interaction of a laser pulse with clusters, one should know the initial state of the target, i.e., at least the average size of clusters in the gas flow and the distance between them. In papers devoted to the study of the interaction of laser radiation with clusters, the main attention was paid, as a rule, to the behavior of clusters irradiated by laser pulses, whereas the process of cluster formation itself was not investigated. The parameters of clusters were commonly estimated using the empirical theory developed by Hagena [23–25] and special experiments related to Rayleigh scattering [1]. Such approaches do not involve a detailed consideration of processes proceeding in the gas flow, and, therefore, they permit only qualitative estimates of the conditions of cluster formation and rather rough estimates of the average size of clusters and of their concentration. The parameters obtained in this way are related to the gas flow as a whole, whereas information on their spatial and time distributions cannot be obtained. At the same time, such information is necessary both for the solution of the fundamental problem of numerical simulation of laser heating of cluster targets and for some possible practical applications (for example, the building of an X-ray laser), which require the production of a sufficiently homogeneous plasma of a large extension along one of the spatial coordinates. Such data can be obtained by simulating gas-dynamic processes proceeding in a gas jet.

In this paper, we consider the process of formation of a cluster target and the results of experimental studies of the cluster plasma by the methods of X-ray emission spectroscopy, which have given so far the main information on the interaction of ultrashort laser pulses not only with clusters but also with solid targets and low-density gas targets. We also propose simple models for calculating the emission spectrum of the plasma for different heating conditions.

In Section 2, we consider a numerical model of cluster formation in a supersonic gas jet. It is shown that detailed studies of two-phase dynamic processes in a nozzle forming the jet allow one to obtain spatial distributions of all the parameters of clusters, which are required for the correct calculation of cluster heating by short laser pulses. The calculations performed for nozzles of different configuration show that in a number of cases an almost homogeneous cluster target can be produced, whereas in other cases the distributions of parameters prove to be not only inhomogeneous but also even nonmonotonic.

In Section 3, we consider the physical model of plasma production in the regime $\tau_{prepulse} \sim \tau_{expansion}$. It is shown that a comparison of X-ray spectra with detailed calculations of the ion kinetics makes it possible to

determine the main parameters of the plasma being produced.

2. NUMERICAL SIMULATION OF THE PROCESS OF CLUSTER FORMATION IN GAS JETS

The methods that have been used so far for estimating parameters of a cluster jet (semiempirical Hagena theory [23–25] and measurements of Rayleigh scattering of weakened laser radiation [1]) give qualitative estimates of the average size and concentration of clusters. The parameters obtained in this way are related to the gas flow as a whole, whereas information on their spatial and time distributions is absent. The data on the spatial structure of a cluster target can be obtained only from a detailed study of gas-dynamic and thermodynamic processes proceeding in gas jets and in nozzles where the jets are formed. Numerical experiments can be efficiently used for studying nozzle flows.

Note that, whereas gas-dynamic equations give, as a rule, the flow pattern that agrees well with the experiment, models of kinetic phase transitions (formation of clusters) are often not so accurate. Therefore, a comparison of experimental and calculated data for such parameters as the concentration of clusters and their average size is also useful from the point of view of the development and study of phase transition models.

2.1. Mathematical Model of a Gas Jet with Formation of Clusters

The methods for calculating supersonic gas flows in nozzles are described in detail, for example, in [26]. One of the simplest models is the gas-dynamic equations

$$\frac{\partial \rho}{\partial t} + \mathrm{div}(\rho \mathbf{v}) = 0, \tag{3}$$

$$\frac{\partial \rho \mathbf{v}}{\partial t} + \mathrm{div}(\rho \mathbf{v} \times \mathbf{v}) = -\mathrm{grad} P, \tag{4}$$

$$\frac{\partial}{\partial t}\left(\rho e + \frac{\rho \mathbf{v}^2}{2}\right) + \mathrm{div}\left(\rho \mathbf{v}\left(e + \frac{\mathbf{v}^2}{2}\right)\right) = -\mathrm{div}(P\mathbf{v}), \tag{5}$$

$$P = P(\rho, \varepsilon) \tag{6}$$

with the boundary conditions of "the absence of flow"

$$\mathbf{v} \cdot \mathbf{n} = 0$$

through the nozzle walls and

$$e + \frac{P}{\rho} + \frac{\mathbf{v}^2}{2} = e_0 + \frac{P_0}{\rho_0}, \quad S(P, \rho) = S(P_0, \rho_0)$$

at the input surface. Here, ρ, $\mathbf{v}$, e, and P are the gas density, velocity, specific internal energy, and pressure; e_0, P_0, and ρ_0 are the values of gas parameters in a vessel from which the gas is delivered to the nozzle; and S is entropy.

Although this model neglects cluster formation, it can be useful for studying the jet structure (jumps, etc.), which can play a key role in the formation of the spatial distribution of clusters. Below, we will consider an example of such calculations. In addition, this model can be used as a starting point for the construction of more complicated models that take into account the formation of clusters.

The formation of clusters can be treated as condensation of the supercooled gas. Although, in principle, there exist flow regimes in which solid clusters are formed (for example, such clusters are observed in carbon-dioxide jets because carbon dioxide has an extremely high pressure at the triple point compared to other gases used), in this paper we restrict ourselves to the consideration of the liquid-phase formation. Therefore, the terms a "cluster" and a "drop" become identical. Because the gas blown into a nozzle does not contain condensation centers (ions, solid particles, etc.), density fluctuations play the role of condensation nuclei (spontaneous condensation).

Spontaneous condensation occurs in vapor turbines for appropriate parameters, and it has been investigated in detail in many papers (see [26–29] and references therein). The general picture of the nozzle flow with spontaneous condensation was obtained using calculations and experimental methods. Because the gas is expanded adiabatically in the nozzle flow, it saturates in some section when the gas parameters at the nozzle entrance are chosen appropriately. However, because condensation nuclei are absent, the isoentropic expansion continues for some time and the gas becomes supercooled. As the gas supercooling rises, the efficiency of nucleus formation increases due to density fluctuations, and at some point, where the number of condensation centers becomes large enough, finely divided moisture precipitates abruptly (condensation jump occurs). The gas parameters become close to those of the saturation line. Therefore, there exists only a rather thin layer where drops are formed. Downstream, only the growth of the drops occurs, the gas expanding virtually along the saturation line.

The most general approach to the simulation of flows with spontaneous condensation is based on the introduction of the distribution function $f(r, \mathbf{x}, t)$ of drops over their radii and the addition of the kinetic equation

$$\frac{\partial f}{\partial t} + \mathrm{div}(\mathbf{v} f) + \frac{\partial}{\partial r}\left(f \frac{dr}{dt}\right) = I_\Sigma \tag{7}$$

(where dr/dt is the growth rate of drops and I_Σ is the number of newly produced drops) to the system of equations (3)–(5). It is assumed that the drops are so small that they are immobile relative to the gas. Because the curved surface of a small drop provides an additional pressure $2\sigma/r$ (σ is the surface tension coefficient and r is the drop radius), thereby decreasing the work required for extracting a molecule from a drop, a

small drop can be in equilibrium or evaporate even being surrounded by the supercooled gas. Therefore, for the specified parameters of the supercooled gas, there exists the critical radius r_* at which the drop is in equilibrium with the gas. Drops with $r < r_*$ are evaporated and disappear, and only the drops with the radius $r > r_*$ can grow.

Thus, a condensation nucleus capable of a further growth can appear only when the fluctuation occurs resulting in the appearance of a drop of radius $r > r_*$. We calculated the frequency of such fluctuations by the Frenkel–Zel'dovich formula

$$I = \frac{1}{\rho_l}\sqrt{\frac{2\sigma\mu}{\pi N_A}}\left(\frac{P}{kT}\right)^2 \exp\left(\frac{4\pi\sigma r_*^2}{3k_BT}\right), \quad (8)$$

where ρ_l is the liquid-phase density, μ is the molar mass, N_A is Avogadro's number, and k_B is the Boltzmann constant. This formula may give large errors for small critical radii because it uses macroscopic values of temperature, drop radius, and surface tension coefficient, which become meaningless for clusters consisting of several tens or hundreds of molecules. There are other approaches for calculating the rate of nucleus formation (see, for example, [28]).

Because the probability of the drop appearance due to fluctuations strongly (exponentially) decreases with increasing the drop radius, whereas drops of radii $r < r_*$ are evaporated and disappear and, hence, can be neglected, we can assume that the drops being formed have a radius that is close to the critical one, and $I_\Sigma = I\delta(r - r_*)$.

The detailed calculations of the number of molecules leaving a drop and precipitated on it give the expressions for the critical radius

$$r_* = \frac{2\sigma}{\rho_l RT\ln(P/P_s)}$$

of the drop (where $P_s = P_s(T)$ is the saturation pressure at temperature T) and for the growth rate

$$\frac{dr}{dt} = \frac{P}{\rho_l\sqrt{2\pi RT}}\left(1 - \frac{P_s(T_l)}{P}\sqrt{\frac{T}{T_l}}\right)$$

for the drops that already exist (the Hertz–Knudsen formula). To further derive the equations of the model, it is necessary that dr/dt be independent of r. For this purpose, it is assumed that the temperature T_l of a drop is equal to the saturation temperature $T_s(P)$ at a given pressure (this assumption is generally invalid for small drops). As a result, we have

$$\frac{dr}{dt} = \frac{P}{\rho_l\sqrt{2\pi RT}}\left(1 - \sqrt{\frac{T}{T_s(P)}}\right).$$

To eliminate the additional independent variable r in equation (7), we introduce, following [30, 27], the moments of the distribution function

$$\rho\Omega_n(\mathbf{x}, t)\int_0^\infty f(r, \mathbf{x}, t)r^n dr, \quad n = 0, 1, 2, \ldots.$$

By multiplying (7) by r^n and integrating over r from 0 to ∞, we obtain the equations for the moments

$$\frac{\partial\rho\Omega_0}{\partial t} + \mathrm{div}(\rho\Omega_0\mathbf{v}) = I, \quad (9)$$

$$\frac{\partial\rho\Omega_n}{\partial t} + \mathrm{div}(\rho\Omega_n\mathbf{v}) = Ir_*^n + \rho n\Omega_{n-1}\frac{dr}{dt}, \quad n = 1, \ldots, \quad (10)$$

under the condition that dr/dt is independent of r. Because the third moment is related to the degree of dryness β of the gas phase in the mixture,

$$\beta = 1 - \frac{4}{3}\pi\rho_l\Omega_3,$$

the system of equations (9), (10) for $n = 0, \ldots 3$, together with equations (3)–(5) and the equation of state for the two-phase medium

$$P = P(\rho, e, \beta), \quad T = T(P, \rho, \beta),$$

becomes closed.

2.2. Results of Calculations

The models described above were applied to the nozzles used in our experiments. We considered the Laval nozzle and a conic nozzle through which argon was blown with the initial parameters P_0 = 20–60 bar and T_0 = 293 K. The results of calculations presented below are related to some instant of time when the flow was virtually steady-state.

The results of calculations performed for the Laval nozzle (P_0 = 40 bar) by neglecting cluster formation show that there exists a rather complicated system of oblique pressure shocks in the cylindrical part of the nozzle, their formation being determined exclusively by geometrical factors (poor profile of the nozzle wall). The reflection of the first oblique shock (in the left one-third of the cylindrical part of the nozzle) from the axis occurs in the Mach regime (reflections of shocks are described in detail in [31]), resulting in the formation of a direct pressure shock (the so-called Mach leg). The intensity of this shock is quite large because the pressure drop in the shock is approximately threefold, whereas the theoretically possible value is

$$\frac{\gamma + 1}{\gamma - 1} = 4$$

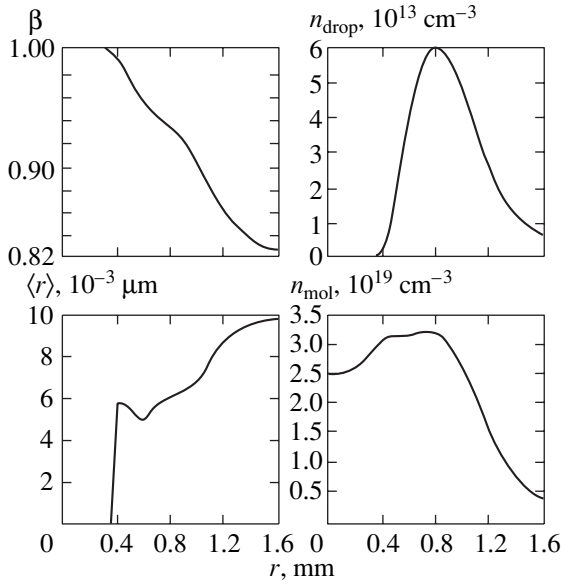

Fig. 1. Distributions of the gas jet parameters at a distance of 1.5 mm from the Laval nozzle edge.

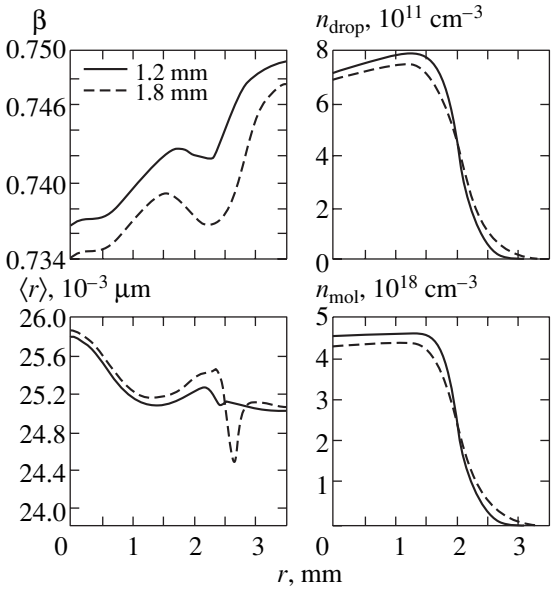

Fig. 2. Distributions of the gas jet parameters at distances of 1.2 and 1.8 mm from the conic nozzle edge.

(γ is the adiabatic index), and the Mach number decreases from 9 to 0.3. All this strongly decreases the nozzle efficiency because the Mach number at the nozzle exit becomes equal to 3–4 instead of its theoretical value M = 5, which can be obtained for the given expansion.

For this reason, it is natural to expect that the flow will also be substantially inhomogeneous when the cluster formation is taken into account, the driest gas escaping near the flow axis because this gas has passed through a strong pressure shock. In addition, the total number of clusters in such a nozzle can be lower than expected. The results of calculations for the same nozzle taking the cluster formation into account confirm this conclusion. In this case, the region of dry gas, beginning from the Mach leg and extending downstream to the nozzle, is indeed observed.

Figures 1 and 2 show the distributions of parameters calculated behind the nozzle edge for a pressure of 40 bar for the Laval and conic nozzles. The dependences on the distance from the jet axis are presented for the following quantities: the degree dryness β, the concentration of drops n_{drop}, the average drop radius $\langle r \rangle$, and the average concentration of atoms n_{mol}. One can see from these figures that the distribution of all the parameters for the conic nozzle is much more homogeneous than for the Laval nozzle. For the conic nozzle, the parameters only weakly change over the entire jet cross section (up to r = 2 mm), whereas, in the case of the Laval nozzle, there exists a region of completely dry gas at the jet center, while clusters exist only at the periphery.

3. CLUSTER HEATING IN THE $\tau_{prepulse} \sim \tau_{expansion}$ REGIME

As mentioned above, the physics of interaction of short laser pulses is substantially determined by the relation between times $\tau_{prepulse}$ and $\tau_{expansion}$. Among the three possible cases, the case $\tau_{prepulse} \gg \tau_{expansion}$, when the main femtosecond pulse almost does not interact with clusters and the relatively low-temperature plasma is produced only by the prepulse, is of the least interest. In the other two cases, the femtosecond pulse efficiently interacts with matter, producing high-energy electrons in the plasma, and the degree of plasma ionization drastically increases compared to that in the first case. However, the details of the interaction and the plasma parameters produced in these cases strongly differ from each other and should be considered separately. At present, the case $\tau_{prepulse} \sim \tau_{expansion}$ is the most interesting because it is very difficult to obtain the condition $\tau_{prepulse} \ll \tau_{expansion}$ in experiments and such experiments are scarce so far. Here, we will consider the physical model of the plasma production in the $\tau_{prepulse} \sim \tau_{expansion}$ regime and will demonstrate the possibility of application of X-ray spectroscopy for its diagnostics. The dependences of the plasma parameters on the laser contrast, the pulse duration, and the cluster size require separate detailed studies.

The experimental studies were performed using a 800-nm 10-TW Ti : Al_2O_3 sapphire crystal laser of the UHI10 type (Saclay, France). The laser beam was focused on a cluster target by an off-axis parabolic mirror, the laser beam diameter in the focal plane being approximately 25 μm. The main laser pulse had a dura-

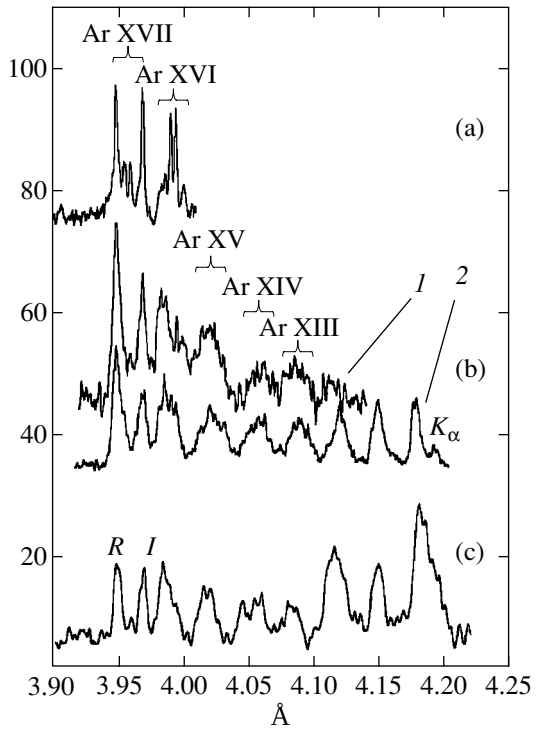

Fig. 3. Emission spectra of the argon plasma produced on different plasma setups: (a) nanosecond laser plasma [35]; (b) femtosecond laser plasma [(*1*) this paper, (*2*) [37]); (c) plasma focus [36].

tion of 60 fs and an energy of about 0.6 J, providing the power density on the target of about 10^{18} W/cm^2. The laser prepulse duration was about 1 ps. Because the contrast was approximately 10^5, the power density in the prepulse was of the order of 10^{13} W/cm^2.

The argon cluster target was produced upon adiabatic expansion of the gas in vacuum through a pulsed conic high-pressure nozzle (the input and output diameters of the nozzle were 1 and 8 mm, respectively, and its length was 20 mm).

The plasma diagnostics was performed by the X-ray spectroscopy methods. Two X-ray spectrographs with spherical mica crystals (the radius of curvature was 150 mm) were arranged in the FSPR-2D scheme [32–34] and were tuned to the spectral ranges of 3.9–4.2 Å and 3.35–3.45 Å containing the He_α and He_β lines of the He-like Ar XVII ion. In some experiments, one the spectrographs was tuned to the range of 3.72–3.82 Å containing the resonance Ly_α line of the H-like Ar XVIII ion; however, we failed to detect this line. Note that, upon observation of the 3.9–4.2 Å range in the fourth order of reflection from the crystal, the shorter wavelength He_γ line from the fifth reflection order was also present in the spectrogram.

Figure 3 shows the spectrum obtained in the 3.9–4.2 Å range. For comparison, analogous spectra are also presented which were obtained earlier upon heating an argon target by a nanosecond laser pulse [35] on the "plasma focus" setup [36] and by a less powerful femtosecond laser [37]. One can clearly see from this figure that the emission spectra of the femtosecond laser plasma (Fig. 3b) and of the "plasma focus" (Fig. 3c) are quite similar and drastically differ from the emission spectrum of the nanosecond laser plasma (Fig. 3a). First, in the cases shown in Figs. 3b and 3c, intense satellite structures are observed, which are related to the transitions in many-electron argon ions (Be-, B-, and C-like), whereas, in the case shown in Fig. 3a, only the lines of He- and Li-like ions are observed. Second, the intensities of "collision" Li-like *q*, *r*, and *a–d* satellites in the femtosecond plasma, as in the plasma focus, exceed those of the "dielectron" satellites *k*, *j*, whereas in the nanosecond plasma the situation is opposite.

Both these differences can be easily explained by assuming that the ionization state of the plasma corresponds to the electron temperature on the order of 100–200 eV and the spectra are excited by high-energy electrons (with energies on the order of 5–10 keV). In the case of the plasma focus, where the plasma temperature is indeed comparatively low and fast-electron beams are present, such an assumption seems quite reasonable, and it was used in [36] to explain the experimental results. Below, we will show that, when the condition $\tau_{\text{prepulse}} \leq \tau_{\text{expansion}}$ is fulfilled, a similar situation can also take place in the femtosecond cluster plasma.

3.1. Model of the Plasma Dynamics

Consider the interaction of an intense femtosecond laser pulse with argon clusters. Because the laser pulse contrast in the experiments described above was about 10^5, the power density of the prepulse (~10^{12}–10^{13} W/cm^2) was sufficient for the destruction of clusters and production of the preplasma with the electron temperature of several hundred electronvolts. The spatial distributions of the electron density and temperature in the preplasma are formed during the dispersion of heated clusters. Because the ionization processes occurred in the clusters that had initially the density of a solid, the time of collision ionization did not exceed 1 ps for all argon ions with the number of bound electrons $m > 2$. This means that the produced preplasma should contain the He-, Li-, Be-, B-like, etc., argon ions at concentrations corresponding to the equilibrium distribution. Note that the H-like Ar XVIII ions are not produced in fact in the preplasma, because the ionization rate for the $1s^2$ shell by 100- to 200-eV electrons is several orders of magnitude lower than the ionization rate for the $1s^22l$ shell.

The main femtosecond pulse will interact with the inhomogeneous preplasma and its energy will be predominantly absorbed in the preplasma regions where the electron density exceeds the critical density. As a result, the plasma temperature in a small volume (within some characteristic distance r_{hot}) abruptly increases up to several thousand electronvolts, whereas

the plasma temperature in other regions remains low. Therefore, during the action of the main pulse, hot points will appear in the plasma. The distance r_{cold} between these points is approximately equal to the distance between clusters in the gas jet, and the distance r_{hot} is of the order of magnitude of the initial cluster size. It is important that the ionization state of the plasma remains virtually unchanged during plasma heating by the main femtosecond pulse because of its short duration.

After the main-pulse termination, hot electrons appear in the plasma, whose relative amount is approximately

$$(r_{hot}/r_{cold})^3 \sim 10^{-8}–10^{-6},$$

and their temperature reaches 5–10 keV (see, for example, calculations in papers [22, 38]). The thermalization time of these electrons is a few tens of picoseconds even in a plasma with the critical density equal to 10^{21} cm^{-3}, while their mean free path exceeds the distance between clusters. This means that after the termination of the femtosecond pulse, hot electrons will also be present in cold regions of the plasma produced by the laser prepulse. Therefore, after the main-pulse termination, the plasma will have, first, low-density (N_{cold}) regions with low electron temperature (T_{cold}) containing a small amount of hot (T_{hot}) electrons and, second, higher density regions (with $N_e \sim N_{cr}$) in which the fraction of hot electrons will be much higher. It is important that the ionization state of the plasma will be almost the same in all regions and will correspond to the electron temperature T_{cold}.

Even the simplified model of the plasma dynamics described above is rather complicated. The emission spectra of the plasma can be calculated using even a simpler model, which is based on the above considerations and takes into account the basic features of the interaction of the laser pulse with clusters, but uses very simple temporal and spatial distributions of plasma parameters. Namely, we will consider three stages of the plasma evolution.

(a) The preplasma stage. The plasma contains dense regions of size r_{hot} with the electron density $N_{cr} = 10^{21}$ cm^{-3}. The distance between the dense regions is r_{cold}, and the electron density outside the dense regions is $N_{cold} = 10^{20}$ cm^{-3}. The temperature of all plasma is T_{cold}. The ionization state of the plasma is stationary and corresponds to the temperature T_{cold}. The duration of this stage is $\tau_1 \sim 1$ ps.

(b) Heating by the main pulse. The temperature of the dense regions increases to T_{hot}. The temperature of the low-density plasma regions and the ionization state of all plasma do not change. The duration of this stage is $\tau_{las} \ll \tau_1$.

(c) The decay stage. Hot electrons generated in dense regions at the stage (b) are distributed over the entire plasma. The plasma parameters in the dense regions do not change ($N_e = 10^{21}$ cm^{-3}, $T_e = T_{hot}$). Outside dense regions, the plasma density is 10^{20} cm^{-3}, the temperature is T_{cold}, and a small amount of hot electrons $(r_{hot}/r_{cold})^3 \times 10^{20}$ cm^{-3} have the temperature T_{hot}. The duration of this stage is $\tau_2 \sim \tau_1 \gg \tau_{las}$.

We used these space–time distributions of the plasma parameters for simulating its emission spectra. Note that the calculated spectra depend not only on the plasma density and temperature but also on the parameters $\tau = \tau_1/\tau_2$ and $\beta = (r_{hot}/r_{cold})^3$. The exact values of these parameters are unknown. Simple estimates can give only the order of magnitude of these parameters:

$$\tau \sim 1, \quad \beta \sim 10^{-8}–10^{-6}.$$

The final values of τ and β were chosen by comparing the model and experimental spectra.

3.2. Kinetic Calculations

We solved the system of stationary radiative-collision kinetic equations for a homogeneous plasma with different values of plasma parameters. Multiply charged argon ions with the total number of bound electrons $m = 1$, 2, 3, and 4 were considered. We studied the atomic configurations of the H-, He-, Li-, and Be-like ions with principal quantum numbers $n < 6$, including autoionization states (25 H-like levels, 59 He-like levels, 334 Li-like levels, and 1188 Be-like levels). The rates of collision processes were calculated using the model energy distribution of electrons [39, 40], which included a hot electronic component. A relatively large thermalization time for hot electrons allowed us to treat them as an electron beam with a Gaussian distribution centered at the energy E_0. In calculations, we used the value $E_0 = 5$ keV. The relative amount of hot electrons (the quantity f in Figs. 4 and 5) was varied from 0 (single-temperature plasma) to 5×10^{-5}. The emission spectra of the plasma were calculated in the spectral regions of 3.93–4.04 Å and 3.3–3.5 Å, which were observed in our experiments.

Figure 4 shows the dependence of the emission spectra of the argon plasma on its density. One can see that the increase in the electron density up to 10^{22} cm^{-3} in the single-temperature plasma ($f = 0$) does not change significantly the emission spectrum in the region of the He_α line and its satellites.

Figure 5 demonstrates the dependence of the emission spectrum on the electron temperature. One can see that for $f = 0$ the spectrum is much more sensitive to the temperature than to the plasma density. One can also see that the influence of hot electrons on satellite transitions drastically decreases with increasing temperature.

It follows from these results that, when hot electrons are absent ($f = 0$), the intensities of the Li-like satellites

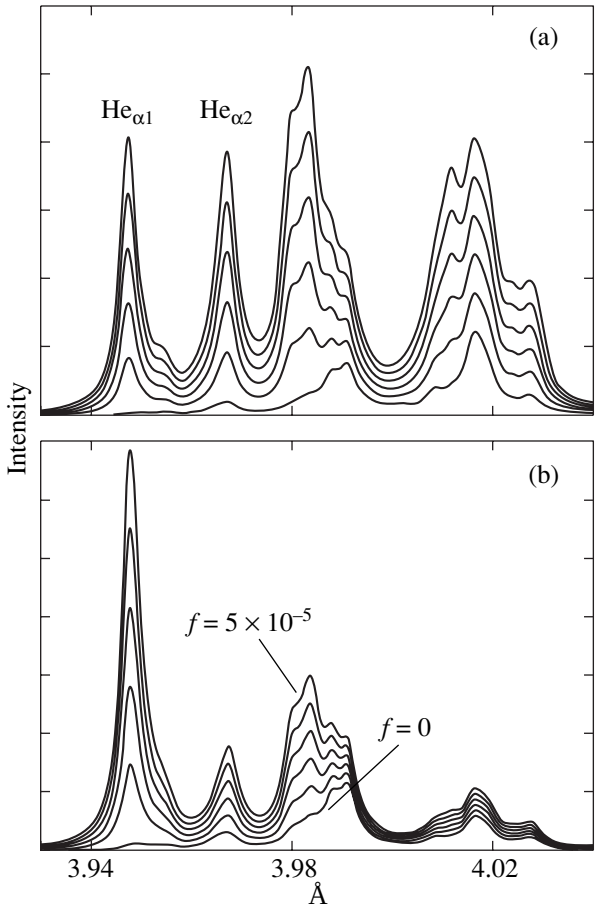

Fig. 4. Emission spectra of the argon plasma with the electron temperature $T_e = 190$ eV, the electron density $N_e = 10^{20}$ (a) and 10^{22} cm^{-3} (b), and different fractions of fast electrons $f = 0$, 10^{-5}, 2×10^{-5}, 3×10^{-5}, 4×10^{-5}, and 5×10^{-5} in the spectral range 3.9–4.2 Å.

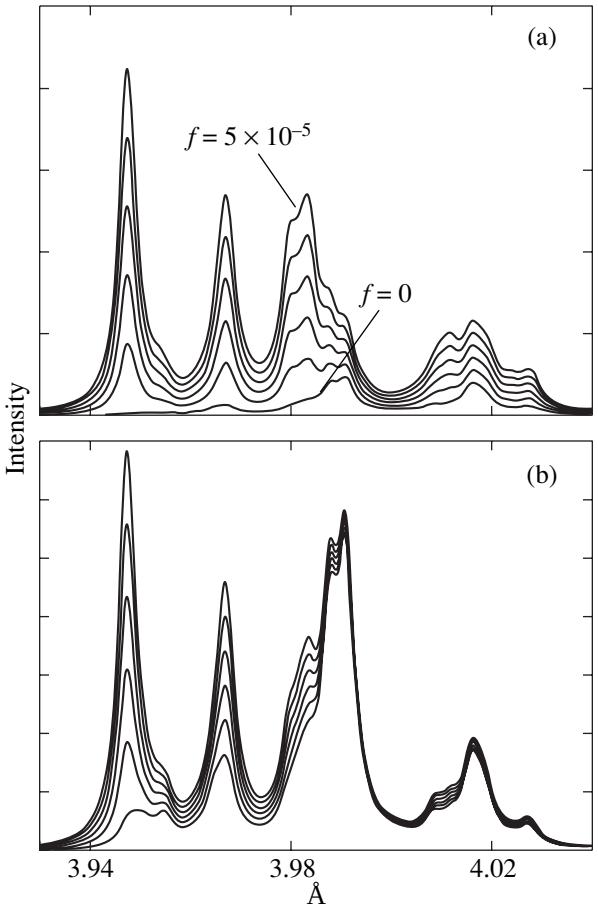

Fig. 5. Emission spectra of the argon plasma with the electron density $N_e = 10^{21}$ cm^{-3}, the electron temperatures $T_e =$ 180 (a) and 220 eV (b), and different fractions of fast electrons $f = 0$, 10^{-5}, 2×10^{-5}, 3×10^{-5}, 4×10^{-5}, and 5×10^{-5} in the spectral region 3.9–4.2 Å.

k and *j* are much greater than those of satellites *q*, *r*, *a*–*d*. The predominance of collision satellites *q*, *r*, *a*–*d* in the emission spectra at moderate plasma densities can be explained only by the presence of hot electrons (in general, a similar structure of the intensity of Li-satellites can be observed in a single-temperature ultrahigh-density plasma with $N_e > 10^{23}$ cm^{-3}, but such an assumption explains neither the intensity of satellites of other ions nor the intensity of the intercombination line).

3.3. Comparison of the Results of Calculation with the Experimental Spectrum

We used the above kinetic calculations for simulating the emission spectra of the plasma observed in our experiments. Because the experimental data were not time-resolved and the plasma was inhomogeneous, it was necessary to calculate the spectra for all regions of the plasma and then to sum the results obtained for all instants of time. The spatial and temporal properties of the plasma were simulated using simple dependences described above. We used the value $T_{\text{cold}} = 190$ eV and $T_{\text{hot}} = 5$ keV.

The results presented in Fig. 6 show that our model describes the experimental spectra well when the parameters

$$\tau = \tau_1/\tau_2 = 1, \quad \beta = (r_{\text{hot}}/r_{\text{cold}})^3 = 4 \times 10^{-7}$$

are used. A small difference between the experimental and theoretical spectra is caused by the presence of the He_γ line of Ar XVIII ($\lambda = 3.1996$ Å) in the experimental spectrum, which is related to the five-order reflection and was not taken into account in calculations in the spectral range from 3.93 to 4.04 Å.

The theoretical spectrum shown in Fig. 6 is a sum of the spectra emitted from different plasma regions at different instants of time. It is interesting to understand what stage of the plasma evolution gives the main contribution to its total emission. Our calculations showed

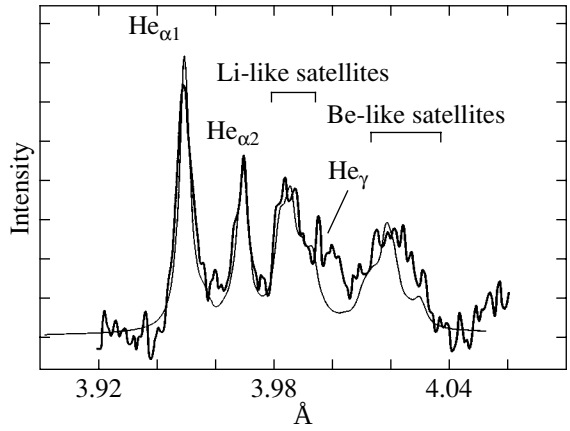

Fig. 6. Comparison of the emission spectrum of the femtosecond argon-cluster plasma (solid curve) with the model spectrum (thin curve) in the spectral region containing the He_{α} line of the Ar XVII ion. The theoretical spectra are calculated for $N_e = 10^{21}$ cm^{-3}, $T_{cold} = 190$ eV, and $T_{hot} = 5$ keV.

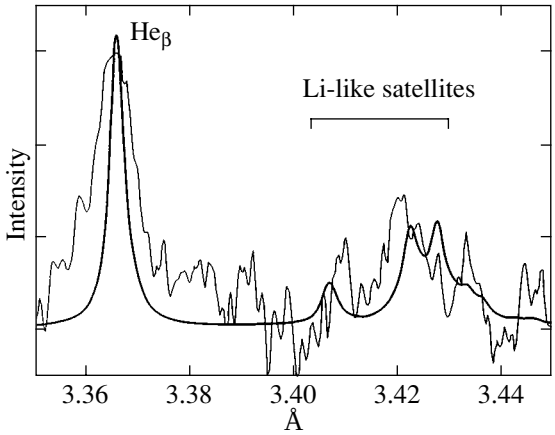

Fig. 7. Comparison of the emission spectrum of the femtosecond argon-cluster plasma (thin curve) with the model spectrum (solid curve) in the spectral region containing the He_{β} line of the Ar XVII ion. The theoretical spectra are calculated for $N_e = 10^{21}$ cm^{-3}, $T_{cold} = 190$ eV, and $T_{hot} = 5$ keV.

that the plasma emission is predominantly related to the stage c. The preplasma stage proves to be important only for the Be-like satellites and Li-like "dielectronic" satellites *k*, *j*. It also follows from the calculations that almost all emission of the He-like and Li-like ions at the stage c is caused by the most dense plasma regions, while the low-density plasma makes a noticeable contribution only to the intensities of the Be-like lines and to the *k* and *j* transitions in the Li-like ion.

We used the above model with the same values of the plasma parameters for calculating the mission spectrum in the range of 3.35–3.45 Å, where the He_{β} line of Ar XVII is located. Figure 7 demonstrates good agreement with the experimental spectrum in this spectral region as well.

Our model shows that only a very small amount of the H-like Ar XVIII ions can be produced during heating of clusters under our experimental conditions. This conclusion is also confirmed by the fact that we have failed to observe the Ly_{α} line of the H-like Ar XVIII ion.

Note that a single-temperature stationary kinetic model is not valid for the case of heating of clusters by femtosecond laser pulses, and attempts to use it for diagnostics of such plasma can lead to absolutely incorrect results. For example, the single-temperature model gives the best agreement with the emission spectrum observed in the region of 3.92–4.00 Å ($He_{\alpha 1,2}$ lines and Li satellites) for $N_e = 10^{21}$ cm^{-3} and $T_e = 550$ eV. However, the agreement between this model and the experimental data is very poor, and the emission spectrum in the region of the He_{β} line calculated for the same parameters drastically differs from the experimental spectrum.

Good agreement between the theoretical and experimental spectra proves the presence of hot electrons in the cluster plasma produced by the intense femtosecond laser pulse. In general, a comparison of experimental and model spectra allows one to measure the average energy of hot electrons. However, the dependence of the spectrum on the energy of hot electrons is expressed in terms of the parameter

$$(r_{hot}/r_{cold})^3 \exp(-E_{exc}/T_{hot})/T_{hot}^{1/2},$$

and to measure T_{hot}, one should measure independently the ratio $(r_{hot}/r_{cold})^3$, which gives the relative amount of hot electrons. Unfortunately, we could not measure this quantity in our experiments.

Thus, we have shown that the interaction of a high-intensity femtosecond laser pulse, having a picosecond prepulse, with argon clusters can be used for producing a bright X-ray source. At first glance, it may seem that our result contradicts the conclusion made in paper [1]. However, the prepulse duration in experiments [1] was several nanoseconds. The clusters were completely destroyed in this time, and no regions with the critical density remained in the plasma by the main-pulse arrival. Under such conditions, the femtosecond pulse was not absorbed in fact, the plasma was not heated, and, hence, no X-ray emission was observed. This completely agrees with the above conclusion about the inefficiency of the plasma production in the $\tau_{prepulse} \gg \tau_{expansion}$ regime. Our experiments corresponded to the condition $\tau_{prepulse} \sim \tau_{expansion}$. In this case, the prepulse duration is too long for the production of a homogeneous low-density nonabsorbing plasma.

The laser–cluster interaction in the $\tau_{prepulse} \sim \tau_{expansion}$ regime provides the production of the plasma

whose ionization state is determined by the prepulse properties, while its temperature (or, more exactly, the characteristic energy) of hot electrons is determined by the main-pulse intensity. This means that, by varying the ratio between the intensities of the main pulse and prepulse, one can rather easily control the degree of the nonstationary state of the plasma.

Such a plasma is of interest first of all for the problems of atomic spectroscopy, because it allows the study of the ion levels that are efficiently populated upon collisions or ionization of the inner shells of many-electron highly charged ions. On the other hand, the plasma with such properties can also find some practical applications, for example, in the development of X-ray lasers operating at the transitions in the Ne- and Ni-like ions, because the conditions that are optimal for producing the high population inversion are easily realized (see, for example, [41–44]).

4. CONCLUSIONS

We have considered two scopes of the problems that are relevant to heating of clusters by ultrashort laser pulses. First, we described a numerical model of the cluster formation in a supersonic gas jet and showed that detailed studies of two-phase gas-dynamic processes in the nozzle forming the jet allow one to obtain the spatial distributions of all parameters required for the correct calculation of the cluster heating by short laser pulses. The calculations performed for nozzles of different configurations showed that in some cases a virtually homogeneous cluster target can be formed, whereas, in other cases, the distributions prove to be not only inhomogeneous but even also nonmonotonic. Second, we considered the physical model of the plasma production in the $\tau_{prepulse} \sim \tau_{expansion}$ regime and showed that a comparison of the X-ray emission spectra with the detailed calculations of the ion kinetics allows one to determine the basic parameters of the plasma being produced. The dependences of the plasma parameters on the laser contrast, the pulse duration, and the cluster size require separate studies.

ACKNOWLEDGMENTS

This work was partly supported by the Energy Department of USA, the Fond Europeen de Development Economique Regional et Conseil Regional D'Aquitaine (France), and by the NATO grant PST.CLG.977637. A.Ya.F and T.A.P. thank CRDF for the grant owing to which this work was presented at international conferences.

REFERENCES

1. T. Ditmire, T. Donnelly, A. M. Rubenchik, *et al.*, Phys. Rev. A **53**, 3379 (1996).
2. T. Ditmire, J. Zweiback, V. P. Yanovsky, *et al.*, Nature **398**, 490 (1999).
3. A. McPherson, B. D. Tompson, A. B. Borisov, *et al.*, Nature **370**, 631 (1994).
4. T. Ditmire, R. A. Smith, J. W. G. Smith, and M. H. R. Hutchinson, Phys. Rev. Lett. **78**, 3121 (1997).
5. Y. L. Shao *et al.*, Phys. Rev. Lett. **77**, 3343 (1996).
6. T. Ditmire, J. W. G. Tisch, E. Springate, *et al.*, Nature **386**, 54 (1997).
7. T. Ditmire, J. W. G. Tisch, E. Springate, *et al.*, Phys. Rev. Lett. **78**, 2732 (1997).
8. E. M. Snyder, S. A. Buzza, and A. W. Castleman, Phys. Rev. Lett. **77**, 3347 (1996).
9. M. Tarasov, D. Golubev, V. Shumeiko, *et al.*, Pis'ma Zh. Éksp. Teor. Fiz. **68**, 426 (1998) [JETP Lett. **68**, 454 (1998)].
10. S. Dobosz, M. Schmidt, M. Pedrix, *et al.*, Zh. Éksp. Teor. Fiz. **115**, 2051 (1999) [JETP **88**, 1122 (1999)].
11. J. Zweiback, R. A. Smith, T. E. Cowan, *et al.*, Phys. Rev. Lett. **84**, 2634 (2000).
12. E. Parra, T. Alexeev, J. Fan, *et al.*, Phys. Rev. E **62**, R5931 (2000).
13. P. Gibbon and E. Forster, Plasma Phys. Controlled Fusion **38**, 769 (1996).
14. C. Stenz, V. Bagnoud, F. Blasco, *et al.*, Kvantovaya Élektron. (Moscow) **30**, 721 (2000).
15. T. Auguste, P. D'Oliveĭra, S. Hulin, *et al.*, Pis'ma Zh. Éksp. Teor. Fiz. **72**, 54 (2000) [JETP Lett. **72**, 38 (2000)].
16. N. E. Andreev, M. V. Chegotov, M. E. Veĭsman, *et al.*, Pis'ma Zh. Éksp. Teor. Fiz. **68**, 566 (1998) [JETP Lett. **68**, 592 (1998)].
17. A. Ya. Faenov, J. Abdallah, Jr., R. E. H. Clark, *et al.*, Proc. SPIE **3157**, 10 (1997).
18. A. M. Urnov, J. Dubau, A. Ya. Faenov, *et al.*, Pis'ma Zh. Éksp. Teor. Fiz. **67**, 513 (1998) [JETP Lett. **67**, 489 (1998)].
19. A. Ya. Faenov, A. I. Magunov, T. A. Pikuz, *et al.*, Phys. Scr. T **T80**, 536 (1999).
20. A. Maksimchuk, M. Nantel, G. Ma, *et al.*, J. Quant. Spectrosc. Radiat. Transf. **65**, 367 (2000).
21. F. B. Rosmej, U. N. Funk, M. Gessel, *et al.*, J. Quant. Spectrosc. Radiat. Transf. **65**, 477 (2000).
22. R. A. Smith, J. W. G. Tisch, T. Ditmire, *et al.*, Phys. Scr. T **T80**, 35 (1999).
23. O. F. Hagena and W. Obert, J. Chem. Phys. **56**, 1793 (1972).
24. O. F. Hagena, Surf. Sci. **106**, 101 (1981).
25. O. F. Hagena, Rev. Sci. Instrum. **63**, 2374 (1992).
26. U. G. Pirumov and G. S. Roslyakov, *Gas Dynamics of Nozzles* (Nauka, Moscow, 1990).
27. G. A. Saltanov, *Nonequilibrium and Nonstationary Processes in Gas Dynamics* (Nauka, Moscow, 1979).
28. L. E. Sternin, *Foundations of Gas Dynaimcs of Two-Phase Flows in Nozzles* (Mashinostroenie, Moscow, 1974).
29. M. E. Deĭch and G. A. Filippov, *Gas Dynamics of Two-Phase Media* (Énergoizdat, Moscow, 1981).
30. R. A. Tkalenko, Izv. Akad. Nauk SSSR, Mekh. Zhidk. Gaza, No. 6 (1972).

31. R. Courant and K. O. Friedrichs, *Supersonic Flow and Shock Waves* (Interscience, New York, 1948; Inostrannaya Literatura, Moscow, 1950).
32. I. Yu. Skobelev, A. Ya. Faenov, B. A. Bryunetkin, *et al.*, Zh. Éksp. Teor. Fiz. **108**, 1263 (1995) [JETP **81**, 692 (1995)].
33. T. A. Pikuz, A. Ya. Faenov, S. A. Pikuz, *et al.*, J. X-Ray Sci. Technol. **5**, 323 (1995).
34. B. K. F. Young, A. L. Osterheld, D. F. Price, *et al.*, Rev. Sci. Instrum. **69**, 4049 (1998).
35. V. M. Dyakin, I. Yu. Skobelev, A. Ya. Faenov, *et al.*, Kvantovaya Élektron. (Moscow) **24**, 709 (1997) [J. Quant. Electron. **27**, 691 (1997)].
36. E. Biemont, P. Quinet, A. Ya. Faenov, *et al.*, Phys. Scr. **61**, 555 (2000).
37. G. C. Junkel-Vives, J. Abdallah, Jr., F. Blasco, *et al.*, Phys. Rev. A **64**, 021201 (2001).
38. T. Ditmire, P. K. Patel, R. A. Smith, *et al.*, J. Phys. B **31**, 2825 (1998).
39. J. Abdallah, Jr., R. E. H. Clark, A. Ya. Faenov, *et al.*, J. Quant. Spectrosc. Radiat. Transf. **62**, 85 (1999).
40. J. Abdallah, Jr., A. Ya. Faenov, T. A. Pikuz, *et al.*, J. Quant. Spectrosc. Radiat. Transf. **62**, 1 (1999).
41. P. V. Nickles, V. N. Shlyaptsev, M. Kalachnikov, *et al.*, Phys. Rev. Lett. **78**, 2748 (1997).
42. J. Dunn, A. L. Osterheld, V. N. Shlyaptsev, *et al.*, in *Proceedings of the 11th APS Topical Conference on Atomic Processes in Plasmas*, Ed. by E. Oks and M. S. Pindzola (American Institute of Physics, New York, 1998), AIP Conf. Proc. **443**, 106 (1998).
43. J. Dunn, A. L. Osterheld, V. N. Shlyaptsev, *et al.*, in *Proceedings of the 6th International Conference on X-ray Lasers, Kyoto, Japan, 1998*, Ed. by Y. Kato, H. Takuma, and H. Daido (Institute of Physics, Bristol, 1998), Inst. Phys. Conf. Ser. **159**, 51 (1998).
44. J. Dunn, A. L. Osterheld, R. Shepherd, *et al.*, Phys. Rev. Lett. **80**, 2825 (1998).

Translated by M. Sapozhnikov

Journal of Experimental and Theoretical Physics, Vol. 94, No. 1, 2002, pp. 8–11.
Translated from Zhurnal Éksperimental'noĭ i Teoreticheskoĭ Fiziki, Vol. 121, No. 1, 2002, pp. 14–18.

NUCLEI, PARTICLES, AND THEIR INTERACTION

Randomly Layered Active Medium as a Broadband Amplifier

K. Yu. Bliokh

Institute of Radioastronomy, National Academy of Sciences of Ukraine, Krasnoznamennaya ul. 4, Kharkov, 61002 Ukraine
e-mail: kostya@bliokh.kharkiv.com

Received May 31, 2001

Abstract—A flat-layered active medium in which two types of layers with different refractive indices alternate is considered. The thickness of a layer is assumed to be random and large as compared to the wavelength of propagating radiation. A wave propagating along the normal to the layers in such a medium is exponentially enhanced over lengths of the order of many layer thicknesses. In contrast to the familiar case of a periodic flat-layered active medium, waves with any (not necessarily definite resonant) frequency are amplified identically in a wide frequency range. By way of an example, convective instability of space-charge waves in a flow of charged particles moving through a randomly layered medium is considered. The predicted effect can be regarded as an analogue of Anderson's localization, when increasing solutions rather than exponentially decreasing ones are selected in view of the activity of the medium. © *2002 MAIK "Nauka/Interperiodica".*

1. INTRODUCTION

The equation of a linear oscillator with a varying eigenfrequency is a basic model for many physical problems. These can be mechanical oscillators or electromagnetic oscillatory circuits with parameters varying in time, or quantum particles in an external potential, or linear waves propagating in an inhomogeneous medium. The behavior of the solutions of equations for a linear oscillator was studied in detail from the physical and mathematical points of view for various typical dependences of its eigenfrequency on an independent variable. The same mathematical result may correspond to different physical phenomena depending on the physical system for which the oscillator equation is a model. For this reason and also because of the difference in the scientific language in different branches of physics, a result obtained in some field may be unclaimed in another field.

It so happened that the obvious similarity between Anderson's localization (a quantum-mechanical particle in a random potential) and the parametric instability of an oscillator with random variations of the eigenfrequency has been noted only recently [1], although the pioneering work of Anderson [2] was published in 1958. It is clear now that the time-independent Schrödinger equation in the former case is precisely the equation of a harmonic oscillator and that the quantity equal to the particle energy minus the potential plays the role of the square of the eigenfrequency. The equation for an oscillator with random variations of the eigenfrequency has two (exponentially increasing and exponentially attenuating) solutions. The only difference is that Anderson's localization problem is formulated in the form of a boundary-value problem, while parametric instability is described by the initial value Cauchy problem. In the former case, the exponentially increasing solution is discarded since it does not satisfy the boundary conditions (the wave function must be bounded), while in the latter case, on the contrary, the exponentially small attenuating solution is disregarded as compared to the increasing solution. However, from the mathematical point of view, we are obviously dealing with manifestations of the same effect.

We consider here the propagation of an electromagnetic wave in a flat-layered active medium composed of two types of alternating layers with random thicknesses. This system can be described by the equation of an oscillator with random eigenfrequency jumps (see figure). A similar problem was considered earlier [3, 4] for an analogous optically passive medium. As a result, the effect of an exponentially attenuating wave propagating to the bulk of such a medium (i.e., the reflection of a wave incident on such a medium) was discovered and a similarity with Anderson's localization was noted. In this problem, no exponentially increasing solutions are observed since these solutions do not obey the energy conservation principle (the medium is passive). A similar (from the mathematical point of view) problem was considered in [5] for an oscillator with an analogous parametric action. In [5], we studied the parametric instability of the system and analyzed the exponentially increasing solutions. However, the formulas for the damping increment [3, 4] and the instability increment [5] derived in different ways proved to be identical, which means that, in these publications, two different solutions of the same linear equation were dealt with.

In the present work, we combine the ideas developed in [3, 4] and in [5]. Indeed, if the medium is active, the exponentially increasing solutions can exist (the wave can receive energy from the medium). Various media with beams may serve as examples of active

media. Problems with periodic inhomogeneities in such media were considered by many authors (see [6–9] and the references cited therein), and the existence of increasing solutions corresponding to attenuating solutions in the case of a passive medium was confirmed. In periodically heterogeneous media, the exponentially increasing solutions correspond to parametric resonances of an oscillator; for this reason, only waves with certain frequencies for which resonance conditions are satisfied will increase in a periodic layered active medium. A distinguishing feature of a layered active medium with random thicknesses is that it amplifies waves with a wide frequency range and the gain in this range depends only on the relative refractive indices and average thickness of the layer. If the ratios of the refractive indices for different layers are independent of frequency, incident waves are amplified identically irrespective of their frequency. Thus, such a medium can be used as a wideband amplifier or generator.

2. GENERAL MODEL

Let us consider the equation of a classical harmonic oscillator,

$$f'' + w^2(\zeta) f = 0, \tag{1}$$

where primes denote the derivative with respect to an independent variable ζ. The energy of the system can be written in the form

$$E = \frac{1}{2}(f'^2 + w^2 f^2). \tag{2}$$

The solution of Eq. (1) for a constant frequency is the function

$$f = a\cos(w\zeta + \varphi), \tag{3}$$

where a and φ are the amplitude and phase of the solution, respectively, defined by the initial conditions of the problem. Substituting expression (3) into (2), we obtain

$$E = \frac{1}{2}a^2 w^2. \tag{4}$$

Let the function $w(\zeta)$ have the form presented in the figure. On the segments where the value of w is constant, the solutions are defined by formula (3) with corresponding values of a and φ. At instantaneous jumps, solutions of the form (3) can be joined using the continuity conditions for f and f'. In this case, the change in energy (2) as a result of the jump from $w = w_0$ to $w = w_1$ is given by

$$E - E_0 = \frac{f^2}{2}(w_1^2 - w_0^2), \tag{5}$$

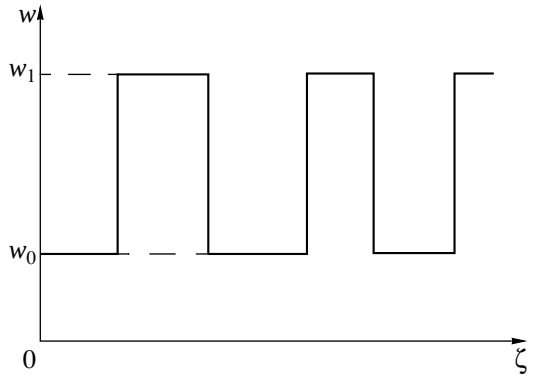

Dependence of the eigenfrequency w on the independent variable ζ in the oscillator equation describing waves in a randomly layered media. Segments with $w = w_0$ and $w = w_1$ correspond to different types of the layers.

where E_0 is the value of energy before the jump. Using formulas (3) and (4), we can write expression (5) in the form

$$E = E_0\left(1 + \frac{w_1^2 - w_0^2}{w_0^2}\cos^2\varphi_0\right), \tag{6}$$

where φ_0 is the value of the phase of the solution at the instant of jump in w. The change in energy as a result of the reverse jump from w_1 to w_0 can be written similarly.

Using expression (6) and considering that the energy of the system does not change for a constant value of w, we obtain the following expression for the oscillator energy after $2N$ jumps:

$$E_N = E_0\prod_{i=1}^{N}\left(1 + \frac{w_1^2 - w_0^2}{w_0^2}\cos^2\varphi_i\right) \times\left(1 + \frac{w_0^2 - w_1^2}{w_1^2}\cos^2\varphi_i'\right), \tag{7}$$

where φ_i and φ_i' are the phases of solutions (3) at the instants of jumps in w from w_0 to w_1 and back, respectively. The value of energy (7) strongly depends on the phases of the solution at the instants of jumps. If, however, we consider an ensemble of systems with random phases or the same system with random jumps in a parameter over a long interval of time, we can carry out averaging over phases. (The phases of solutions can be regarded as random at instants of jumps if the typical spread in the intervals between jumps is larger than or of the order of the characteristic period of oscillations w^{-1} (strong-disorder approximation [3]).)

It will be proved below that the energy increases exponentially with N; for this reason, the energy loga-

rithm must be averaged over phases. After the averaging of expression (7) over φ_i and φ_i', we obtain

$$\left\langle \ln\frac{E_N}{E_0}\right\rangle = 2N\ln\frac{(w_0+w_1)^2}{4w_0w_1}, \tag{8}$$

where we have used the fact that

$$\langle \ln(1+\alpha\cos^2 x)\rangle \equiv \frac{1}{2\pi}$$
$$\times\int_0^{2\pi}\ln(1+\alpha\cos^2 x)dx = 2\ln\frac{1+\sqrt{1+\alpha}}{2}.$$

It can be seen from relation (8) that the energy logarithm averaged over phases increases linearly with N. Thus, the energy increases approximately exponentially on intervals much larger than the separation between the jumps:

$$E \approx E_0\exp(\lambda t\zeta).$$

The increment λ is defined as

$$\lambda = \frac{2}{T}\ln\frac{(w_0+w_1)^2}{4w_0w_1} > 0, \tag{9}$$

where $T = \zeta/N$ is the average period of a cycle of variation from $w = w_0$ to $w = w_1$ and back. Apart from T, increment λ depends only on the ratio w_1/w_0. In the case of waves in a layered medium, this ratio is determined by the ratio of refractive indices of the layers.

Among other things, formula (9) describes the attenuation of waves in a randomly layered passive medium. In this case, the quantity λ is the damping decrement or the inverse localization length. The value of this quantity was determined using other methods in [3, 4]. The above derivation of formula (9) is in line with the idea formulated in [5]. An analysis of this formula, the fields of its application, and the results of numerical simulations can be found in the above-mentioned publications.

3. EXAMPLE

Let us consider space-charge waves in a flow of charged particles propagating in a layered medium. A periodic layered medium and the instability of space-charge waves in such a medium were investigated in [7, 9]. The initial system of equations is formed by Maxwell's equations, the continuity equation, and the equation of motion linearized over small perturbations of the electric field of the space charge, velocity, and number density of particles:

$$\frac{\partial D}{\partial x} = 4\pi en,$$
$$\frac{\partial n}{\partial t} + \frac{\partial}{\partial x}(n_0 v + n v_0) = 0, \tag{10}$$
$$\frac{\partial v}{\partial t} + v_0\frac{\partial v}{\partial x} = \frac{e}{m}E.$$

Here, x is the coordinate perpendicular to the layers, along which the particles move (we consider the 1D case); n_0 and v_0 are the unperturbed constant values of the number density and the velocity of particles, respectively; n and v are their varying perturbations; e and m are the charge and mass of a particle, respectively; E is the electric field strength; and $D = \varepsilon(x)E$ is the electric induction. The permittivity $\varepsilon(x)$ is constant and real-valued in each layer and is a function similar to that depicted in the figure with permittivity values ε_0 and ε_1 in alternating layers. In a homogeneous medium, space-charge waves are characterized by the dispersion

$$k = \pm\frac{\omega_p}{v_0\sqrt{\varepsilon}} + \frac{\omega}{v_0}, \tag{11}$$

where ω and k are the frequency and the wave number of a wave, respectively, and

$$\omega_p = \sqrt{\frac{4\pi n_0 e^2}{m}}$$

is the plasma frequency of particles in the beam.

Taking into account the fact that the problem under investigation is homogeneous in time and the wave number contains the constant term ω/v_0, we will seek the solutions of Eqs. (10) in the form

$$q(x,t) = \tilde{q}(x)\exp\left[i\left(\frac{\omega}{v_0}x - \omega t\right)\right],$$

where $q(x, t)$ is any of the variables under investigation. As a result, system (10) can be reduced to the following equation:

$$\tilde{D}'' + \frac{\omega_p^2}{\varepsilon(x)v_0^2}\tilde{D} = 0. \tag{12}$$

The quantities $\tilde{D}$ and $\tilde{n} \sim \tilde{D}'$ must be continuous when a wave intersects the boundary between two layers [7]. Obviously, Eq. (12) is completely analogous to Eq. (1) considered above. Consequently (cf. relation (9)), the solutions to Eq. (12) with a wavelength smaller than or of the order of indeterminacy in the layer thickness

exhibit an exponential increase (or damping) with the increment

$$\lambda = \frac{1}{L}\ln\frac{(\sqrt{\varepsilon_0}+\sqrt{\varepsilon_1})^2}{4\sqrt{\varepsilon_0\varepsilon_1}} > 0, \qquad (13)$$

where L is the average period of the layered system (the ratio of its thickness to the number of pairs of the layers) and expressions (9) and (13) differ by a factor of two since the energy is proportional to the square of the solution amplitude. The quantity λ is independent of the wave frequency ω and the beam current; it contains only the parameters of the layered medium.

In order to find out whether the emergence of the effective eigenvalue (13) characterizes the instability or the attenuation of the wave, we return to the initial variables. Then, the effective wave number of the oscillations under investigation can be written in the form

$$k_{\text{eff}} = \pm i\lambda + \frac{\omega}{v_0} + \chi(\varepsilon, \omega_p, v_0), \qquad (14)$$

where χ is a certain real function whose explicit form is insignificant. Let us now use the well-known Briggs criterion [10, 11] according to which the oscillations are enhanced if the quantity $\mathrm{Im}\,k(\omega)$ changes its sign upon a variation of $\mathrm{Im}\,\omega$ from $+\infty$ to 0. The wave number (14) with $\mathrm{Im}\,k_{\text{eff}} = -i\lambda$ (for $\mathrm{Im}\,\omega = 0$) satisfies this condition due to the presence of the term ω/v_0 responsible for the transport of oscillations by the flow of particles. It is precisely the kinetic energy of this motion that ensures the activity of the system under investigation, as in other cases of beam instabilities.

4. CONCLUSIONS

We have considered a layered structure with random thicknesses of alternating layers of two types and the propagation of linear waves in this medium along the normal to the layers. The mathematical model of such a system is the equation of an oscillator with random eigenfrequency jumps between two preset values. This system has an effective eigenvalue with a nonzero real part on the scale of many layers. This eigenvalue corresponds to attenuating solutions in the case of a passive medium [3, 4] or in the problem of Anderson's localization of a quantum particle [2] and to increasing solutions in the case of a parametric action on a mechanical system [5] or for an active layered medium.

The latter case was considered in this paper. It is shown that a randomly layered active medium can be used as a wideband amplifier due to the fact that the increment of the buildup of the waves is independent of their frequency. The characteristic wavelengths in this case must be smaller than the characteristic spread in the thicknesses of the layers. In the example of the instability of a space-charge wave considered above, this leads to the condition

$$\frac{\sqrt{\varepsilon}v_0}{\omega_p} < \delta L,$$

where $\delta L \le L$ is the characteristic deviation of the thickness of a layer from the average value for one type of layer. In the opposite case, we must use the weak-disorder approximation leading to a different frequency dependence of the gain [3]. The situation corresponding to the weak-disorder approximation and a transition to a periodic passive layered medium were also considered in [12].

In view of the mathematical identity of the problem for the above examples of passive and active media, the results obtained from an analysis of the localization constant for passive media can be extended to the properties of the instability increment in the corresponding cases of active media.

ACKNOWLEDGMENTS

This work was partly financed by the INTAS (grant no. 00-002292).

REFERENCES

1. L. Tessieri and F. M. Izrailev, Phys. Rev. E **62**, 3, 3090 (2000).
2. P. W. Anderson, Phys. Rev. **109**, 1492 (1958).
3. V. Baluni and J. Willemsen, Phys. Rev. A **31**, 3358 (1985).
4. M. V. Berry and S. Klein, Eur. J. Phys. **18**, 222 (1997).
5. K. Yu. Bliokh and O. V. Usatenko, Izv. Vyssh. Uchebn. Zaved., Prikl. Nelineĭnaya Din. **9** (2), 92 (2001).
6. Ya. B. Fainberg and P. V. Bliokh, Zh. Tekh. Fiz. **26**, 530 (1956).
7. V. M. Yakovenko, Solid State Commun. **39**, 847 (1981).
8. K. Yu. Bliokh, Radiofiz. Radioastron. **3**, 231 (1998).
9. F. G. Bass, A. A. Bulgakov, and A. P. Tetervov, *High-Frequency Properties of Semiconductors with Superlattices* (Nauka, Moscow, 1989).
10. E. M. Lifshitz and L. P. Pitaevskiĭ, *Physical Kinetics* (Nauka, Moscow, 1979; Pergamon, Oxford, 1981), Para. 63.
11. A. I. Akhiezer and R. V. Polovin, Usp. Fiz. Nauk **104**, 185 (1971) [Sov. Phys. Usp. **14**, 278 (1971)].
12. E. V. Zamyatin, Candidate's Dissertation in Physics and Mathematics (RIAN, Kharkov, 1989).

Translated by N. Wadhwa

Journal of Experimental and Theoretical Physics, Vol. 94, No. 1, 2002, pp. 84–93.
Translated from Zhurnal Éksperimental'noĭ i Teoreticheskoĭ Fiziki, Vol. 121, No. 1, 2002, pp. 102–112.

SOLIDS
Structure

Disorientation Kinetics of the B_{80}^4 Centers in Single Crystal Silicon

A. S. Kaminskii

Institute of Radio Engineering and Electronics, Russian Academy of Sciences, Moscow, 101999 Russia
e-mail: kam@mail.cplire.ru

Received June 8, 2001

Abstract—Using exciton spectroscopy methods, it was established that B_{80}^4 centers can be oriented under uniaxial compression conditions not only in the [111] axis direction, but in the $[\bar{1}11]$ and $[1\bar{1}1]$ directions as well. Disorientation of the B_{80}^4 centers was studied in detail, a kinetic equation adequately describing this process is presented, and an expression for the characteristic reorientation time as a function of the temperature was obtained. It was found that the reorientation rate obeys the Arrhenius law with an activation energy of about 1.54 eV. The experimental results are explained proceeding from a hypothesis that the B_{80}^4 center is identical to a ring hexavacancy. A mechanism of the B_{80}^4 center (hexavacancy) reorientation is proposed within the framework of this model, according to which the hexavacancies are thermally excited into the first metastable state and then pass to a ring state with different orientation. Involving the spatial displacement of hexavacancies during reorientation, this process has to be accompanied by the Brownian motion of the hexavacancies. A correlation was found between the direction of orientation of the B_{80}^4 centers (hexavacancies) and the relative change in the $\langle 110 \rangle$ bond length under uniaxial compression conditions. This result is interpreted in terms of the hexavacancy geometry. © *2002 MAIK "Nauka/Interperiodica".*

1. INTRODUCTION

This paper continues the previous communication [1], in which preliminary results on the disorientation kinetics of B_{80}^4 centers were reported and experimental evidence was presented that allowed the B_{80}^4 centers to be identified with ring hexavacancies (V_6).[1] The results were naturally explained by assuming that hexavacancies may possesses several metastable states. Each ring hexavacancy represents a cavity appearing upon the removal of six silicon atoms from the vertices of a chair-shaped hexagon possessing a third-order axis parallel to the [111] crystallographic axis.

The previous investigations of B_{80}^4 centers [2–4] showed that these defects (i) appear upon annealing pure silicon single crystals containing a large number of vacancies, (ii) behave as isoelectron quasi-acceptors with an electron-attracting potential depending on the deformation tensor, (iii) belong to the trigonal system, and (iv) possess a not less than C_{3v} point symmetry. In particular, it was shown that excitons bound on the B_{80}^4 centers are of a triplet–singlet type [4] and a Hamiltonian describing all properties of such excitons was constructed. Recently, it was established [5] that the B_{80}^4 centers can be oriented by uniaxially compressing a sample in one of the $\langle 111 \rangle$ directions.

Below, we describe in detail the process of disorientation of the B_{80}^4 centers and present new data to confirm that these centers represent hexavacancies.

2. EXPERIMENTAL

The samples with dimensions $17 \times 1.25 \times 1.25$ mm, having the shape of bars terminated with tetragonal pyramids oriented in the [111] or $[1\bar{1}0]$ directions (see Figs. 1 and 2 below), were cut from a pure silicon single crystal irradiated with neutrons with a Cd number of ~50 to a total dose of 10^{17} cm^{-2}. Here, the directions with negative indexes indicate the orientation of samples cut from an ingot grown in the [111] direction.

The samples were uniaxially compressed at temperatures in the interval from 150 to 500°C. For this purpose, a sample was mounted between stainless steel plunger dies with 0.5-mm-deep 120° cone-shaped wells. During compression, the wells acquired the

[1] Unless otherwise is stated, we employ the notation adopted in [1, 3].

shape of terminal pyramids (for each succeeding test, the cone-shaped wells have to be restored). In order to eliminate the buildup of shear stresses (capable of destroying the sample), a steel ball was placed between the plunger and a rod transferring the applied load.

In order to create the B_{80}^4 centers oriented either along the [111] axis or in the $[\bar{1}11]$ or $[1\bar{1}1]$ directions, the crystal samples uniaxially compressed in the [111] or $[1\bar{1}0]$ directions, respectively, can be annealed for 30 min at 375°C. However, a more convenient procedure consists in creating unoriented centers (by annealing the initial samples at 375°C without applied load) and their subsequent orientation. The latter is achieved by annealing the samples for 30 min at a temperature of about 250°C and a pressure of 0.25 GPa. It was found that the total number of centers remains virtually unchanged in the course of orientation and disorientation processes. This circumstance allows the samples to be multiply reused and facilitates interpretation of the results.

The samples were immersed in liquid helium and excited by radiation from an Ar laser with a power of up to 200 mW. Special measures were taken to maintain the samples at a constant temperature during each experiment. This is related to the fact that the ratio of intensities of the recombination emission lines strongly depends on the temperature [3]. The recombination emission spectra were studied with the aid of an SDL-1 spectrometer equipped with a cooled photomultiplier operating in the photon count mode. The spectra were analyzed at a resolution of about 200 μeV.

It must be noted that, since the recombination emission of the samples containing oriented centers is polarized, the spectrum becomes significantly distorted upon passage through the optical tract. Previously [1], these distortions were eliminated by recording the spectra of two components of the recombination emission with mutually perpendicular polarizations, followed by summing these components multiplied by the corresponding correction factors. In this study, the results were corrected by means of a correction parameter r introduced into the calculation relationships. The parameter was experimentally determined as the ratio of the transmission coefficients of the recombination emission components polarized perpendicular and parallel to the sample axis. This method provides for a better accuracy and simplifies the experimental procedure. Special checks showed that the two methods of correction yield virtually identical results.

3. MODEL CALCULATIONS

As demonstrated previously [1, 5], the I_1/I_2 value representing the ratio of intensities of the $X_{80}^4(J_1)$ and $X_{72}^4(J_2)$ lines in the recombination emission spectrum of excitons bound on the B_{80}^4 centers depends on the relation between concentrations n_1, n_2, n_3, and n_4 of the centers oriented in various ⟨111⟩ directions. If the centers are initially oriented (i.e., the major axes are aligned in certain selected directions), the thermal motion of the lattice gives rise to a disorientation process leveling the number of centers oriented in various directions. As a result, the quantity I_1/I_2 also exhibits a change. In order to determine the I_1/I_2 ratio as a function of time, we will first study the time variation of the concentrations n_1, n_2, n_3, and n_4 representing the centers of types 1–4 with the major axes oriented in the [111], $[\bar{1}11]$, $[\bar{1}\bar{1}1]$, and $[1\bar{1}1]$ directions, respectively. Then, we will relate the concentrations n_i to intensities of the $X_{80}^4(J_1)$ and $X_{72}^4(J_2)$ lines. Assuming that (i) the total concentration of the B_{80}^4 centers remains unchanged in the course of disorientation and (ii) the probability of a change in the orientation of a given center does not depend on the initial and final directions, the kinetic equations describing variation of the n_i values can be written in the following form [1]:

$$\begin{aligned}
\frac{dn_1}{dt} &= -\frac{3n_1}{\tau} + \frac{n_2}{\tau} + \frac{n_3}{\tau} + \frac{n_4}{\tau},\\
\frac{dn_2}{dt} &= \frac{n_1}{\tau} - \frac{3n_2}{\tau} + \frac{n_3}{\tau} + \frac{n_4}{\tau},\\
\frac{dn_3}{dt} &= \frac{n_1}{\tau} + \frac{n_2}{\tau} - \frac{3n_3}{\tau} + \frac{n_4}{\tau},\\
\frac{dn_4}{dt} &= \frac{n_1}{\tau} + \frac{n_2}{\tau} + \frac{n_3}{\tau} - \frac{3n_4}{\tau},
\end{aligned} \tag{1}$$

where $\tau = \tau_{ij} = \tau_{ji}$ is the characteristic time for reorientation of a center from ith to jth direction, $-3n_i/\tau$ is the rate of decrease in the concentration n_i, and n_k/τ is the rate of increase in the concentration n_i ($i \neq k$). The sum of Eqs. (1) yields $dn/dt = 0$, which is equivalent to the assumption concerning conservation of the total number of centers in the course of disorientation.

Introducing the "vector" $\mathbf{n} = \{n_1, n_2, n_3, n_4\}$ with the sum of components representing the total concentration n, we can write Eqs. (1) in matrix form as

$$\frac{d\mathbf{n}}{dt} = A\mathbf{n}, \quad A = \frac{1}{\tau}(M - 4I), \tag{2}$$

where M is the fourth-order matrix with all elements equal to unity and I is the unity matrix of the fourth order. Note that Eqs. (1) cannot be used to describe the process of orientation, since the uniaxial compression renders the centers oriented in various directions unequivalent ($\tau_{ij} \neq \tau_{ji}$).

For an initial distribution of centers at $t = 0$ described by the vector $\mathbf{n}(0)$, a solution to the above

Table 1. The ratio I_1/I_2 of the intensities of X_{80}^4 and X_{72}^4 lines calculated with an allowance for distortions caused by differential transmission of the parallel and perpendicular components of the recombination emission for the disorientation processes $\{1\} \longrightarrow \{2, 3, 4\}$ ($x = n_2/n_1$) and $\{2, 4\} \longrightarrow \{1, 3\}$ ($x = n_1/n_2$)

Sample orientation	**k**	$\mathbf{e}_\perp$	I_1/I_2 for $x = 0$*	I_1/I_2 for $x = 1$	I_1/I_2
[111]	$[11\bar{2}]/\sqrt{6}$	$[1\bar{1}0]/\sqrt{2}$	wr	$2w$	$w\dfrac{3r + (8 + 5r)x}{3 + (1 + 4r)x}$
$[1\bar{1}0]$	$[\bar{1}\bar{1}2]/\sqrt{6}$	$[111]/\sqrt{3}$	$wr\dfrac{3 + 8r}{6 + r}$	$2w$	$w\dfrac{(3 + 8r) + (9 + 4r)x}{(6 + r) + 5rx}$
$[1\bar{1}0]$	$[111]/\sqrt{3}$	$[11\bar{2}]/\sqrt{6}$	$wr\dfrac{3 + 7r}{6 + 2r}$	$2w$	$w\dfrac{(3 + 7r) + (9 + 5r)x}{(6 + 2r) + 4rx}$

Note: **k** and $\mathbf{e}_\perp$ are the wavevector and the polarization vector of the recombination emission; the quantity $1/r$ gives the factor by which the spectrometer sensitivity to the perpendicular component is smaller than that to the parallel component (determined from experiment); For the reverse processes $\{2, 3, 4\} \longrightarrow \{1\}$ and $\{1, 3\} \longrightarrow \{2, 4\}$, the quantity x should be replaced by $1/x$. * Expressions for $x = 0$ refer to direct processes only.

matrix equation can be presented in the following form [6]:

$$\mathbf{n}(t) = G\mathbf{n}(0) = e^{At}\mathbf{n}(0), \quad (3)$$

where G is the operator of evolution of the vector $\mathbf{n}(t)$. Using a spectral matrix theorem [6], the matrix G can be expressed as

$$G = gI_4 + \frac{(1-g)M}{4},$$

where $g = \exp(-4t/\tau)$. Thus, once the initial distribution of orientations of the centers is known, the time variation of this distribution is described by relationship (3). Let us consider two particular cases corresponding to the experimental results obtained in this study.

1. When a sample is annealed with a deforming load applied along the [111] direction, the centers can orient either in the same [111] direction or along the $[\bar{1}11]$, $[\bar{1}\bar{1}1]$, and $[1\bar{1}1]$ axes. In the former case, the initial state of orientation is conveniently described as

$$\mathbf{n}(0) = \{1 - 3p, p, p, p\}n,$$

where $p = n_2/n = n_3/n = n_4/n \le 1/4$. Upon calculating $\mathbf{n}(t) = G\mathbf{n}(0)$ and determining the n_2/n_1 ratio for $\mathbf{n}(t)$, we can describe the $\{1\} \longrightarrow \{2, 3, 4\}$ disorientation process by the function

$$x(t) = \frac{n_2}{n_1} = \frac{1 - g(1-4p)}{1 + 3g(1-4p)}, \quad x(0) = \frac{p}{1-3p}. \quad (4)$$

Below, we will denote by x the ratio of a smaller concentration n_i to a greater quantity and by p the ratio of a smaller quantity n_i to the total concentration n.

By the same token, the "reverse" process $\{2, 3, 4\} \longrightarrow \{1\}$ beginning from the initial state

$$\mathbf{n}(0) = \{p, (1-p)/3, (1-p)/3, (1-p)/3\}n$$

(with $p = n_1/n \le 1/4$) is described by the function

$$x(t) = \frac{n_1}{n_2} = \frac{3 - 3g(1-4p)}{3 + g(1-4p)}, \quad x(0) = \frac{3p}{1-p}. \quad (5)$$

2. When the deforming load during annealing is applied in the $[1\bar{1}0]$ direction, the centers can align either in the $[\bar{1}11]$ and $[1\bar{1}1]$ directions or along the [111] and $[\bar{1}\bar{1}1]$ axes. In the former case, the initial state of orientation is conveniently described as

$$\mathbf{n}(0) = \left\{p, \frac{1}{2} - p, p, \frac{1}{2} - p\right\}n,$$

where $p = n_1/n$. Upon calculating $\mathbf{n}(t) = G\mathbf{n}(0)$ and determining the n_1/n_2 ratio for $\mathbf{n}(t)$, we can describe the $\{2, 4\} \longrightarrow \{1, 3\}$ disorientation process by the function

$$x(t) = \frac{n_1}{n_2} = \frac{1 - g(1-4p)}{1 + g(1-4p)}, \quad x(0) = \frac{2p}{1-2p}. \quad (6)$$

For the "reverse" process $\{1, 3\} \longrightarrow \{2, 4\}$ beginning from the initial state

$$\mathbf{n}(0) = \left\{\frac{1}{2} - p, p, \frac{1}{2} - p, p\right\}n,$$

(with $p = n_1/n \le 1/4$) we obtain

$$x(t) = \frac{n_2}{n_1} = \frac{1 - g(1-4p)}{1 + g(1-4p)}, \quad x(0) = \frac{2p}{1-2p}. \quad (7)$$

Now, we can describe the time variation of the ratio of intensities I_1/I_2 of the X_{80}^4 and X_{72}^4 lines in the recombination emission spectrum of excitons bound on the B_{80}^4 centers. This can be done using the expressions for

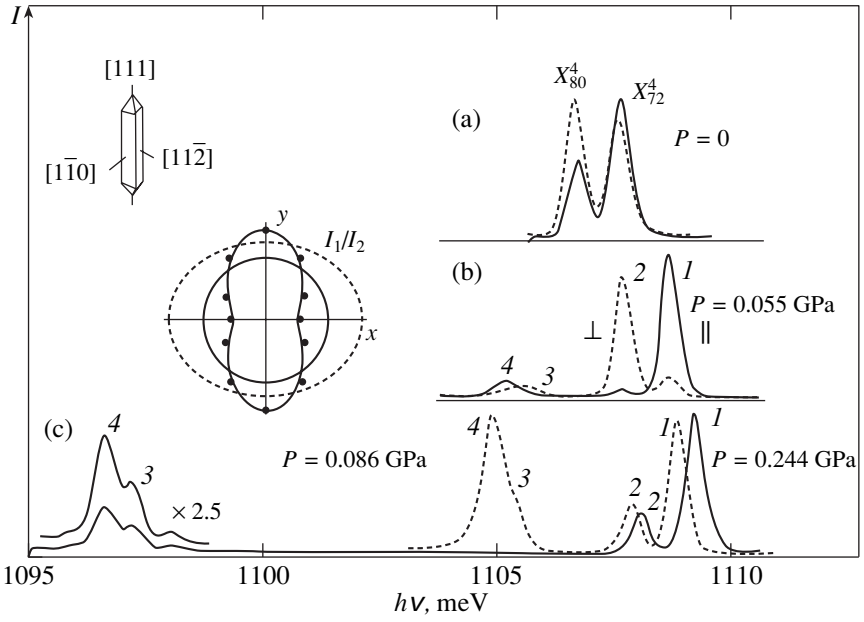

Fig. 1. Recombination emission spectra of excitons bound on the B^4_{80} centers in single crystal silicon samples cut along the [111] axis (measured at $T = 4.2$ K): (a) the spectra of samples with unoriented (dashed curve) and [111]-oriented (solid curve) centers at a pressure of $P = 0$; (b) emission line components polarized perpendicularly (dashed curve) and parallel (solid curve) to the axis of a sample with [111]-oriented centers at $P = 0.055$ GPa; (c) the spectra of a sample with unoriented centers measured at $P = 0.086$ (dashed curve) and 0.244 GPa (solid curve). The insets show the sample configuration and the plots of I_1/I_2 versus angle β of the sample rotation around the $[11\bar{2}]$ axis: (points) experiment; (sold curves) calculation by formula (A.3) for the $\{1\} \longrightarrow \{2, 3, 4\}$ process and a unit circle; (dashed curve) calculation for the $\{2, 3, 4\} \longrightarrow \{1\}$ process.

intensities of the components of the X^4_{80} and X^4_{72} emission lines polarized parallel and perpendicular to the sample axis (see Tables 3 and 4 in the Appendix). For example, the I_1/I_2 ratio for the emission in the $[11\bar{2}]$ direction from a sample oriented in the [111] direction is obtained by setting $\varphi = 0$ in Table 4, adding intensities of the parallel and perpendicular components (the latter have to be multiplied by the experimentally determined correction coefficient r for the perpendicular components of X^4_{80} and X^4_{72} lines), and taking the required ratio. The I_1/I_2 ratios determined in this way for the experimental situations studied are presented in Table 1.

An expression for the I_1/I_2 ratio as a function of the time of annealing at a constant temperature T is obtained by substituting the corresponding functions $x(t)$ from Eqs. (4)–(7) into the formulas for I_1/I_2 in Table 1, in which the parameter w is determined experimentally for $x \longrightarrow 1$ or $t \longrightarrow \infty$.

4. RESULTS AND DISCUSSION

First, it will be demonstrated that the centers under consideration can be effectively oriented both in the [111] direction and along the $[\bar{1}11]$ and $[1\bar{1}1]$ axes. Figure 1 shows the spectra of recombination emission of excitons bound on the B^4_{80} centers measured for the samples cut in the [111] direction. The samples were mounted parallel to the spectrometer slit so as to analyze the light emitted in the $[11\bar{2}]$ direction. The dashed curve in Fig. 1a represents the spectrum of a sample containing B^4_{80} centers in an unoriented state, while the solid curve shows the spectrum of the same sample annealed in a compressed state. As can be seen, the ratio of intensities I_1/I_2 of the X^4_{80} and X^4_{72} lines decreased from 1.15 to 0.55 ($I_1/I_2 < 2w$, see Table 1), which indicates that the B^4_{80} centers are oriented to a considerable extent.[2] Let us consider distribution of the B^4_{80} centers in these samples with respect to orientations. Upon compression in the [111] direction, the centers divide into two groups, {1} and {2, 3, 4}, which is manifested in the recombination emission spectrum as the orientation-related splitting of lines. Evidently, the intensity of lines representing each group is proportional to the number of centers belonging to this group.

Figure 1b shows components of the recombination emission spectrum corresponding to the parallel and perpendicular polarizations in a sample compressed in

[2] As demonstrated below, these spectra can be used for reconstructing the initial orientation distribution $\mathbf{n}(0)$.

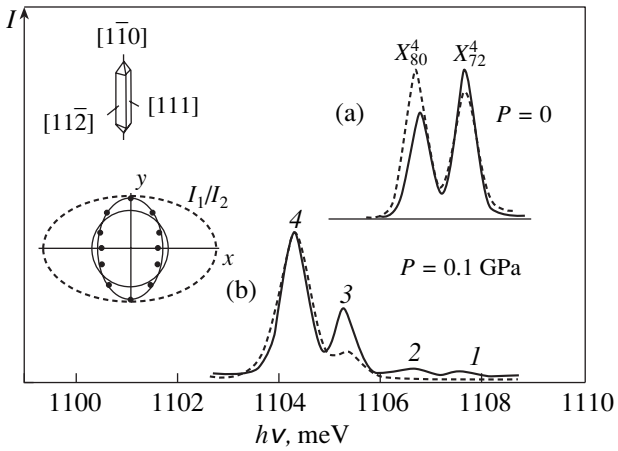

Fig. 2. Recombination emission spectra of excitons bound on the B^4_{80} centers in single crystal silicon samples cut along the $[1\bar{1}0]$ axis (measured at $T = 4.2$ K) in the samples containing unoriented (dashed curve) and $[\bar{1}11]$- and $[1\bar{1}1]$-oriented (solid curve) centers at a pressure of $P = 0$ (a) and 0.1 GPa (b). The insets show the sample configuration and the plots of I_1/I_2 versus angle β of the sample rotation around the [111] axis: (points) experiment; (solid curves) calculation by formula (A.4) for the $\{2, 4\} \longrightarrow \{1, 3\}$ process and a unit circle; (dashed curve) calculation for the $\{1, 3\} \longrightarrow \{2, 4\}$ process.

the [111] direction and, hence, containing the B^4_{80} centers in an oriented state. The spectra display two clearly distinguished groups of lines with the components denoted by *1*, *2* and *3*, *4*. The same groups of lines are well pronounced in the uniaxially compressed samples containing the B^4_{80} centers in an unoriented state. As the pressure varies, the spectral positions of the lines change in an independent manner. By comparing the amplitudes of lines belonging to each group observed at small pressures, we may note that the orientation process transforms these centers into a group represented by the components *1*, *2* in Figs. 1b and 1c. Finally, comparing the experimental data on the polarizations of components *1* and *2* (Fig. 1b) to the calculated relative intensities (Appendix, Table 4), we conclude that the B^4_{80} centers in the case under consideration are oriented in the [111] direction.

The same result can be obtained in a more exquisite manner. For this purpose, we can express the I_1/I_2 ratio as a function of the angle of rotation β around the $[11\bar{2}]$ direction (**k** direction) for a sample containing the B^4_{80} centers in the oriented state and compare this expression to a dependence calculated by formula (A.3) presented in the Appendix. This dependence was determined and depicted by black circles on the inset in Fig. 1 (where solid curves show a dependence calculated for the centers oriented in the [111] direction and a unit circle that allows the I_1/I_2 ratio to be readily determined for an arbitrary rotation angle). As can be seen, the experimental data fit the calculated curve well. At the same time, the dashed curves, corresponding to the case of centers oriented in the $[\bar{1}11]$, $[\bar{1}\bar{1}1]$, and $[1\bar{1}1]$ directions, qualitatively differ from the experimental pattern.

Here, it is necessary to refine the essence of the method proposed for determining the orientation of the B^4_{80} centers. The spectrometer used in the experiment is nonideal (in our case, $r \approx 0.37$) and transmits the component polarized perpendicularly to the entrance slit differently (worse by a factor of about 2.7) as compared to the component polarized parallel to the slit. In other words, the optical tract of the spectrometer contains an implicit "effective polarizer" that is responsible for the observed dependence of I_1/I_2 on β. Upon going from the direct ($\{1\} \longrightarrow \{2, 3, 4\}$) to reverse ($\{2, 3, 4\} \longrightarrow \{1\}$) process, positions of the emitting centers relative to the "effective polarizer" (modeling the differential polarization effect introduced by the optical tract) exhibit a change leading to a qualitatively different I_1/I_2 versus β relationship. In the ideal spectrometer ($r = 1$), these angular dependences can be obtained only by introducing a polarizer into the optical tract. This effect is well consistent with expressions (A.3) and (A.4) derived in the Appendix for the I_1/I_2 versus β relationship. As can be seen from these expressions, the angular dependence vanishes for $r = 1$.

Now let us proceed to the samples cut in the $[1\bar{1}0]$ direction. The emission was measured in the [111] direction. Figure 2 shows the spectra of the recombination emission of excitons bound on the B^4_{80} centers measured in this case. The dashed curve in Fig. 2a represents the spectrum of a sample containing B^4_{80} centers in an orientation-disordered state, while the solid curve shows the spectrum of the same sample annealed in a compressed state. As can be seen, the ratio of intensities I_1/I_2 of the X^4_{80} and X^4_{72} lines decreased from 1.15 to 0.71 ($I_1/I_2 < 2w$, see Table 1), which indicates that the B^4_{80} centers are oriented to a considerable extent either in the $[\bar{1}11]$ and $[1\bar{1}1]$ directions or along the [111] and $[\bar{1}\bar{1}1]$ axes.

An attempt at distinguishing between the two possibilities is illustrated in Fig. 2b, where the dashed and solid curves show the spectra of samples with unoriented centers and with the centers oriented by annealing under uniaxial compression in the $[1\bar{1}0]$ direction. The spectra display two clearly pronounced groups of lines (with the components denoted by *1*, *2* and *3*, *4*) and show the intensity redistribution between these groups, reflecting an increase in the number of centers

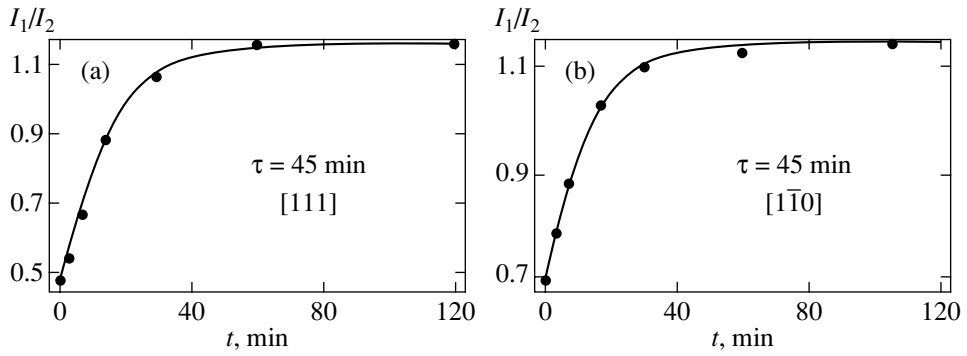

Fig. 3. Experimental (black circles) and theoretical (solid curves) plots of the ratio of intensities I_1/I_2 of the X^4_{80} (J_1) and X^4_{72} (J_2) emission lines versus the time of annealing (T = 217.5°C) for the samples cut in the directions (a) [111] (calculation parameters w = 0.575; r = 0.357; p = 0.1) and (b) [1$\bar{1}$0] (w = 0.575; r = 0.357; p = 0.11).

belonging to one group at the expense of a decrease in another group. However, it was impossible to judge with confidence on the dominating group ({1, 3} versus {2, 4}), which is probably explained by a strong mixing of exciton states in the samples deformed in this mode.

In order to solve the problem, the experimental dependence of I_1/I_2 on the angle β of sample rotation around the [111] direction was measured for a sample containing the B^4_{80} centers in the oriented state. These experimental data are depicted by black circles on the inset in Fig. 2, where the solid curves show the same dependence calculated for the centers oriented in the [$\bar{1}$11] and [1$\bar{1}$1] directions and a unit circle. As can be seen, the experimental points fit the calculated curve well. If the centers were oriented in the [111] and [$\bar{1}\bar{1}$1] directions, the points would fit the dashed curve. Thus, the disorientation kinetics should be studied in terms of relationships (4) and (6).

Returning to Figs. 1a and 2a, let us consider how these data can be used to determine the initial orientation distribution **n**(0). Upon determining I_1/I_2 from these data, these values should be substituted into the corresponding expressions presented in Table 1. The resulting equations are used to find x(0). Finally, relationships (4) and (6) for x(0) can be used to determine p representing the ratio of the smaller group concentration to the total concentration of the centers studied.

Now let us consider the kinetics of disorientation of the B^4_{80} centers. The main parameter in Eq. (2) describing this process is the characteristic reorientation time τ(T). At a given temperature T, the reorientation time was determined by comparing the experimental curve of I_1/I_2 versus annealing time t to the calculated dependence obtained by substituting x(t) from (4) and (6) into the expressions for I_1/I_2 presented in Table 1. Figures 3a and 3b show typical plots of the I_1/I_2 ratio versus annealing time at T = 217.5°C for two different orientations of the B^4_{80} centers, measured in the course of the {1} ⟶ {2, 3, 4} and {2, 4} ⟶ {1, 3} disorientation processes, respectively. The spectra of the initial and final states of these processes are given in Figs. 1a and 2a. It must be noted that these different processes lead to the same reorientation time. This result confirms validity of the assumptions made in deriving Eq. (1).

The mechanism of reorientation of the B^4_{80} centers was explained based on the experimental τ(T) depen-

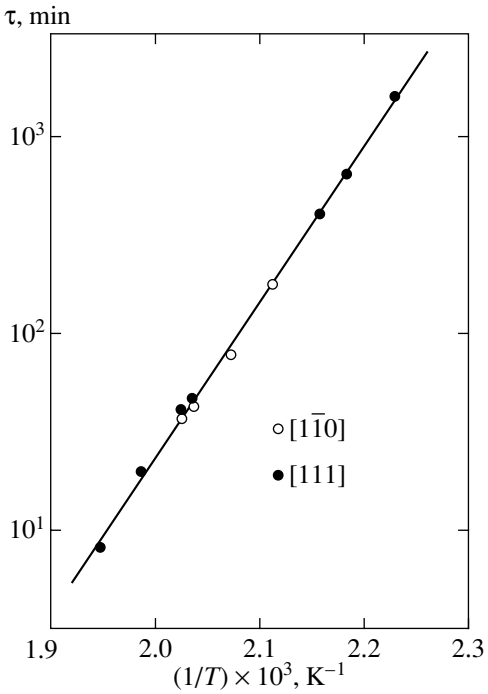

Fig. 4. The plot of reorientation time τ versus annealing temperature T for different reorientation processes: (black circles) {1} ⟶ {2, 3, 4} in [111]-cut samples; (open circles) {2, 4} ⟶ {1, 3} in [1$\bar{1}$0]-cut samples.

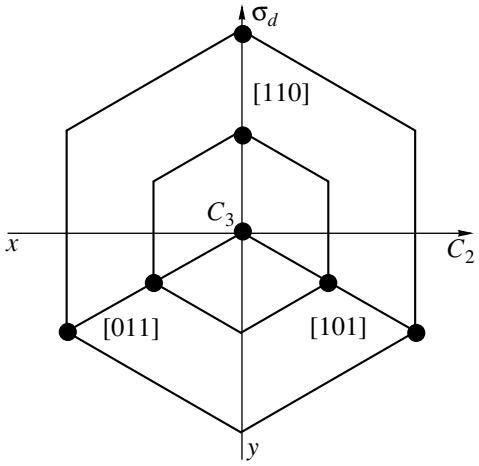

Fig. 5. The schematic diagram of bonds in a hexavacancy viewed along the [111] direction showing silicon atoms (black circles), double bonds (thick solid lines), the second-order rotation axis C_2 perpendicular to the principal axis C_3 of the hexavacancy, and the mirror reflection plane σ_d containing the principal axis (hexagons are drawn so as to indicate the hexavacancy symmetry).

dence. The reorientation time was determined from the curves analogous to those presented in Fig. 3, measured in the temperature range from 175 to 240°C. The resulting τ versus T curve is depicted in Fig. 4. The statistical processing of these data yielded an exponent [7]

$$\frac{1}{\tau} = a\exp\left(-\frac{E}{kT}\right), \quad (8)$$

where $E = 1.5462 \pm 0.03$ eV and $a = (1.7197 \pm 1) \times 10^{14}$ min^{-1}. In other words, the rate of reorientation of the B_{80}^4 centers obeys the Arrhenius law with an activation energy of 1.54 eV.

In order to interpret the obtained results, we assume as previously [1] that the B_{80}^4 centers are identical to ring hexavacancies (V_6). Then, the mechanism of reorientation of the B_{80}^4 centers can naturally be explained by the fact that such hexavacancies may possesses several metastable states. A ring hexavacancy, which is most stable among the vacancy centers, represents a combination of six vacancies (or, e.g., three divacancies), belongs to the point symmetry group D_{3d}, and contains a completely closed bond system [8]. A special feature of V_6 is the ability of occurrence in several metastable states. The first of these is characterized by a binding energy about 0.87 eV smaller than that of stable V_6, while the other metastable states are lower by more than 3.5 eV. Taking into account [8] that the activation energy for reorientation of the B_{80}^4 centers is close both to the energy of divacancy breakage ($V_2 \longrightarrow V_1 + V_1$) equal to 1.69 eV and to the energy required for a transition to the first metastable state (about 0.87 eV), we may consider the reorientation process as proceeding by the following scheme. A thermally excited hexavacancy V_6 passes into the first metastable state and then returns back to the previous state but with a different orientation [1]. It should be noted that the process of V_6 reorientation involves the displacement of hexavacancies and, hence, has to be accompanied by their Brownian motion in the crystal.

In conclusion, let us establish a correlation between the direction of sample compression and the orientation of the B_{80}^4 centers proceeding from the hypothesis of B_{80}^4 and V_6 identity and taking into account the geometry of hexavacancies (determined by the ⟨110⟩ bonds). It can be shown that the hexavacancies tend to orient in the directions for which the ⟨110⟩ bond lengths decrease to a greater extent under uniaxial loading conditions. In other words, the directions of predominant V_6 orientation are determined by the hexavacancy geometry. Evidently, hexavacancies occurring in a deformation field and oriented in unequivalent directions will change their shapes and bond lengths differently and, hence, the binding energies. This is just what accounts for the appearance of preferred orientation directions.

Figure 5 shows a schematic diagram of bonds in the V_6 hexavacancy viewed along the [111] crystallographic axis. The invisible bonds (situated beneath the figure plane) are determined by applying the S_6 operation (mirror rotation relative to the [111] axis perpendicular to this plane) to the visible bonds. The ⟨110⟩ bonds are selected by being strongly stretched as compared to the normal silicon–silicon bonds. The V_6 hexavacancy structure contains a total of six double bonds of the ⟨110⟩ type: each of the three ⟨110⟩ bonds depicted in Fig. 5 corresponds to a parallel bond situated under the figure plane). Therefore, the number of unequivalent double ⟨110⟩ bonds is three.

Now, let us assume that a change in the length of these initially stretched bonds determines the major contribution to variation of the hexavacancy formation energy. Moreover, we will suggest that a change in the hexavacancy formation energy is proportional to the average relative change in length of the three bonds. The average values of bond length for hexavacancies oriented in various directions for a given uniaxial compression direction are listed in Table 2. As can be seen from these data for the samples compressed in both [111] and $[1\bar{1}0]$ directions, a maximum change in the average ⟨110⟩ bond length is observed in the directions of orientation of the B_{80}^4 centers (indicated by an asterisk in Table 2) for the samples annealed under uniaxial compression conditions. For example, in a sample compressed along the [111] axis, this is the [111] direction corresponding to the {1} ⟶ {2, 3, 4} disorientation

Table 2. Average relative variations of the ⟨110⟩ bond lengths for hexavacancies oriented along the [111], [$\bar{1}$ 11], [$\bar{1}$ $\bar{1}$ 1], and [$\bar{1}$ 11] axes in silicon single crystal samples compressed in the [111], [1$\bar{1}$ 0], and [001] directions

Uniaxial compression direction	V_6 orientation direction	
	[111]	[$\bar{1}$ $\bar{1}$ 1]
P [111]	$-P(S_{11} + 2S_{12} + S_{44}/2)/3 = -0.322 \times 10^{-11}\ P*$	$-P(S_{11} + 2S_{12} - S_{44}/2)/3 = -0.043 \times 10^{-11}\ P$
P [1$\bar{1}$ 0]	$-P(S_{11} + 2S_{12} - S_{44}/4)/3 = -0.087 \times 10^{-11}\ P$	$-P(S_{11} + 2S_{12} - S_{44}/4)/3 = -0.087 \times 10^{-11}\ P$
P [001]	$-P(S_{11} + 2S_{12})/3 = -0.113 \times 10^{-11}\ P*$	$-P(S_{11} + 2S_{12})/3 = -0.113 \times 10^{-11}\ P*$
Uniaxial compression direction	V_6 orientation direction	
	[$\bar{1}$ 11]	[1$\bar{1}$ 1]
P [111]	$-P(S_{11} + 2S_{12} - S_{44}/2)/3 = -0.043 \times 10^{-11}\ P$	$-P(S_{11} + 2S_{12} - S_{44}/2)/3 = -0.043 \times 10^{-11}\ P$
P [1$\bar{1}$ 0]	$-P(S_{11} + 2S_{12} + S_{44}/4)/3 = -0.218 \times 10^{-11}\ P*$	$-P(S_{11} + 2S_{12} + S_{44}/4)/3 = -0.218 \times 10^{-11}\ P*$
P [001]	$-P(S_{11} + 2S_{12})/3 = -0.113 \times 10^{-11}\ P*$	$-P(S_{11} + 2S_{12})/3 = -0.113 \times 10^{-11}\ P*$

Note: For silicon, $S_{11} = 0.768 \times 10^{-11}$ m^2/N; $S_{12} = -0.214 \times 10^{-11}$ m^2/N; $S_{44} = 1.256 \times 10^{-11}$ m^2/N; $P > 0$.

process; in a sample compressed along the [1$\bar{1}$0] axis, these are the [$\bar{1}$11] and [1$\bar{1}$1] directions corresponding to the {2, 4} ⟶ {1, 3} disorientation process. As can be seen from Table 2, the average relative changes in the bond lengths for hexavacancies oriented in other directions are much smaller. Apparently, this coincidence is due to a characteristic geometry of the ring hexavacancies. Thus, it is possible that a change in the energy of hexavacancies in the deformation field is related to a change in the ⟨110⟩ bond length.

5. CONCLUSION

It should be recalled that the hexavacancies were predicted theoretically. The original method employed in this study has provided experimental evidence that the B_{80}^4 point center can be identified with a hexavacancy. The obtained results well agree with the data reported recently by Hourahine *et al.* [10] suggesting B_{80}^4 centers to be the most appropriate candidate for the role of hexavacancies in silicon. However, the hypothesis that the B_{80}^4 center is identical to the hexavacancy needs further justification. It should be noted that a series of hexavacancy-based hydrogen-containing centers was predicted in [10], which must possess interesting properties. Therefore the research in this direction can be expected to yield valuable results.

ACKNOWLEDGMENTS

The author is grateful to V.I. Rogovoĭ for the neutron irradiation and orientation of samples and to A.A. Mishukova for her active participation in the experiment.

This study was supported by the Russian Foundation for Basic Research (project no. 99-02-16652) and by the Program of Support for the Leading Scientific Schools (project no. 00-15-96663).

APPENDIX

All axes and planes in the crystallographic coordinate system are determined in terms of the Müller indexes. The B_{80}^4 centers belong to a trigonal system and are characterized by a point symmetry of not less than C_{3v} (C_{3v} is a subgroup of the hexavacancy D_{3d} group [11]). The third-order principal axis of the B_{80}^4 center is directed in one of the four ⟨111⟩ directions. Let a coordinate system *x*, *y*, *z* related to a B_{80}^4 center oriented in the [111] direction possess a basis set

$$[1\bar{1}0]/\sqrt{2}, \quad [11\bar{2}]/\sqrt{6}, \quad [111]/\sqrt{3},$$

while the basis sets for the B_{80}^4 centers oriented in the [$\bar{1}$11], [$\bar{1}\bar{1}$1], and [1$\bar{1}$1] directions are obtained by rotating the above basis set around the [001] axis by $\pi/2$, π, and $3\pi/2$, respectively. For a hexavacancy, the *x* axis coincides with the C_2 symmetry axis, the *y* axis is perpendicular to the principal axis and belongs to the σ_d reflection plane, and the *z* axis (the main axis of the B_{80}^4 center) coincides with the principal axis of the hexavacancy (Fig. 5). In calculating the relative probabilities of the optical decay of excitons bound on the B_{80}^4 cen-

Table 3. Relative intensities of various components of the X_{80}^4 and X_{72}^4 emission lines for the B_{80}^4 centers oriented along the equivalent directions [111], $[\bar{1}\,\bar{1}\,1]$ and $[\bar{1}\,11]$, $[1\,\bar{1}\,1]$ in a $[1\bar{1}\,0]$-cut sample

Emission line	Set of equivalent centers $n_1 = n_3$, $n_2 = n_4$	$I_\parallel$	$I_\perp$
$X_{80}^4\,(J_1)$	n_1, n_3	$18n_1$	$[9 + u(\varphi)]n_1$
	n_2, n_4	$6n_2$	$[15 - u(\varphi)]n_2$
$X_{72}^4\,(J_2)$	n_1, n_3	0	$[9 - u(\varphi)]n_1$
	n_2, n_4	$12n_2$	$[3 + u(\varphi)]n_2$
$\mathbf{e}_\perp$	$[\cos\varphi + \sqrt{2}\sin\varphi,\ \cos\varphi + \sqrt{2}\sin\varphi,\ -2\cos\varphi + \sqrt{2}\sin\varphi]/\sqrt{6}$		
$\mathbf{k}$	$[\sqrt{2}\cos\varphi - \sin\varphi,\ \sqrt{2}\cos\varphi - \sin\varphi,\ \sqrt{2}\cos\varphi + 2\sin\varphi]/\sqrt{6}$		

Note: $\mathbf{k}$ and $\mathbf{e}_\perp$ are the wavevector and polarization vector of the recombination emission, respectively; $u(\varphi) = \cos 2\varphi - 2\sqrt{2}\sin 2\varphi$; φ is the angle of emission measured from the [111] axis in the plane perpendicular to the sample orientation axis $[1\bar{1}\,0]$.

ters from a singlet (X_{80}^4 line) and doublet (X_{72}^4 line) states, it will be assumed that the electric dipole moments corresponding to these transitions are directed along the *z* or *x* and *y* axes.

The relative intensities of the X_{80}^4 and X_{72}^4 line components of the recombination emission from a sample with an arbitrary distribution of orientations $\mathbf{n} = \{n_1, n_2, n_3, n_4\}$ of the B_{80}^4 centers were calculated using the expressions

$$I_1 \propto \sum_{\substack{k=1 \\ l=x,y}}^{4} (\mathbf{e}\cdot\mathbf{d}_{k,l})^2 n_k m_k,$$
$$I_2 \propto \sum_{k=1}^{4} (\mathbf{e}\cdot\mathbf{d}_{k,z})^2 n_k m_k, \qquad \text{(A.1)}$$

where $\mathbf{e}$ is the vector of polarization of the recombination emission; $m_k = 0$ or 1 plays the role of a mask separating the recombination emission from equivalent centers; and $\mathbf{d}_{k,l}$ and $\mathbf{d}_{k,z}$ are the vectors of electric dipole moments corresponding to the X_{80}^4 and X_{72}^4 emission lines:

$$\mathbf{d}_{1,x} = [1\bar{1}0]/\sqrt{2}, \quad \mathbf{d}_{1,y} = [11\bar{2}]/\sqrt{6},$$
$$\mathbf{d}_{2,x} = [110]/\sqrt{2}, \quad \mathbf{d}_{2,y} = [\bar{1}1\bar{2}]/\sqrt{6},$$
$$\mathbf{d}_{3,x} = [\bar{1}10]/\sqrt{2}, \quad \mathbf{d}_{3,y} = [\bar{1}\bar{1}\bar{2}]/\sqrt{6},$$
$$\mathbf{d}_{4,x} = [\bar{1}\bar{1}0]/\sqrt{2}, \quad \mathbf{d}_{4,y} = [1\bar{1}\bar{2}]/\sqrt{6}, \qquad \text{(A.2)}$$
$$\mathbf{d}_{1,z} = [111]/\sqrt{3}, \quad \mathbf{d}_{2,z} = [\bar{1}11]/\sqrt{3},$$
$$\mathbf{d}_{3,z} = [\bar{1}\bar{1}1]/\sqrt{3}, \quad \mathbf{d}_{4,z} = [1\bar{1}1]/\sqrt{3}.$$

An analysis of the two cases considered in this study led to the following results.

1. The centers oriented predominantly in the $[\bar{1}11]$ and $[1\bar{1}1]$ directions in the samples cut along the $[1\bar{1}0]$ axis. To calculate the relative intensities of various components of the recombination emission in the direction $\mathbf{k}$, polarized parallel ($\mathbf{e}_\parallel = [1\bar{1}0]/\sqrt{2}$) or perpendicular ($\mathbf{e}_\perp$) to the sample axis $[1\bar{1}0]$, the polarization ($\mathbf{e}_\parallel$ or $\mathbf{e}_\perp$) vector and the mask (separating the centers with preset polarization) were substituted into expressions (A.1), after which the sums were taken using expressions for the electric dipole moments. The results are summarized in Table 3.

2. The centers oriented predominantly in the [111] directions in the samples cut along the [111] axis. The relative intensities of various components of the recombination emission in the direction $\mathbf{k}$, polarized parallel ($\mathbf{e}_\parallel = [111]/\sqrt{3}$) or perpendicular ($\mathbf{e}_\perp$) to the sample axis [111], were calculated by a procedure analogous to that used in the first case. The results are summarized in Table 4.

Now let us express the ratio of intensities I_1/I_2 of the X_{80}^4 and X_{72}^4 lines as a function of the angle of rotation β around the recombination emission direction (i.e., around the $\mathbf{k}$ vector). For the samples cut along the [111] axis, containing the B_{80}^4 centers oriented in the [111] direction, and rotated around the $[11\bar{2}]$ axis, this expression is as follows:

$$\frac{I_1}{I_2} = \frac{w[(1+r)(3+13x) - 3(r-1)(x-1)\cos 2\beta]}{(1+r)(3+5x) + 3(r-1)(x-1)\cos 2\beta}. \qquad \text{(A.3)}$$

Table 4. Relative intensities of various components of the X_{80}^4 and X_{72}^4 emission lines for the B_{80}^4 centers oriented along the equivalent directions [111] or $[\bar{1}\,11]$, $[\bar{1}\,\bar{1}\,1]$, $[1\,\bar{1}\,1]$ in a [111]-cut sample

Emission line	Set of equivalent centers n_1, $n_2 = n_3 = n_4$	$I_\parallel$	$I_\perp$
X_{80}^4 (J_1)	n_1	0	$3n_1$
	n_2, n_3, n_4	$8n_2$	$5n_2$
X_{72}^4 (J_2)	n_1	$3n_1$	0
	n_2, n_3, n_4	n_2	$4n_2$
$\mathbf{e}_\perp$	$[\sqrt{3}\cos\varphi + \sin\varphi, -\sqrt{3}\cos\varphi + \sin\varphi, -2\sin\varphi]/\sqrt{6}$		
$\mathbf{k}$	$[\cos\varphi - \sqrt{3}\sin\varphi, \cos\varphi + \sqrt{3}\sin\varphi, -2\cos\varphi]/\sqrt{6}$		

Note: $\mathbf{k}$ and $\mathbf{e}_\perp$ are the wavevector and polarization vector of the recombination emission, respectively; φ is the angle of emission measured from the $[11\bar{2}]$ axis in the plane perpendicular to the sample orientation axis [111].

For the samples cut along the $[1\bar{1}0]$ axis, containing the B_{80}^4 centers oriented in the $[\bar{1}11]$ and $[1\bar{1}1]$ direction, and rotated around the [111] axis, the corresponding expression is

$$\frac{I_1}{I_2} = \frac{w[(1+r)(5+7x) - 2(r-1)(x-1)\cos 2\beta]}{2(1+r)(2+x) + (r-1)(x-1)\cos 2\beta}, \quad \text{(A.4)}$$

where the angle β is measured from the initial position of the sample axis.

For the B_{80}^4 centers oriented along the $[\bar{1}11]$, $[\bar{1}\bar{1}1]$, $[1\bar{1}1]$ or [111], $[\bar{1}\bar{1}1]$ directions, the angular dependences of I_1/I_2 are obtained by substituting $1/x$ for x in expressions (A.3) and (A.4), respectively.

REFERENCES

1. A. S. Kaminskii, Pis'ma Zh. Éksp. Teor. Fiz. **73**, 33 (2001) [JETP Lett. **73**, 28 (2001)].
2. A. S. Kaminskii, B. M. Leĭferov, and A. N. Safonov, Fiz. Tverd. Tela (Leningrad) **29**, 961 (1987) [Sov. Phys. Solid State **29**, 551 (1987)].
3. A. S. Kaminskii, A. N. Safonov, and É. V. Lavrov, Fiz. Tverd. Tela (Leningrad) **33**, 859 (1991) [Sov. Phys. Solid State **33**, 488 (1991)].
4. A. S. Kaminskii and É. V. Lavrov, Zh. Éksp. Teor. Fiz. **108**, 1081 (1995) [JETP **81**, 595 (1995)].
5. A. S. Kaminskii and E. V. Lavrov, Solid State Commun. **108**, 751 (1998).
6. F. R. Gantmacher, *The Theory of Matrices* (Fizmatgiz, Moscow, 1967, 3rd ed.; Chelsea, New York, 1959).
7. G. D. Watkins and J. W. Corbett, Phys. Rev. **121**, 1001 (1961).
8. J. L. Hastings, S. K. Estreicher, and P. A. Fedders, Phys. Rev. B **56**, 10215 (1997).
9. L. D. Landau and E. M. Lifshitz, *Course of Theoretical Physics*, Vol. 7: *Theory of Elasticity* (Nauka, Moscow, 1965; Pergamon, New York, 1986).
10. B. Hourahine, R. Jones, A. N. Safonov, *et al.*, Phys. Rev. B **61**, 12594 (2000).
11. G. F. Koster, J. O. Dimmok, R. G. Wheelert, *et al.*, in *Properties of the Thirty-Two Point Groups* (MIT Press, Cambridge, 1963), p. 58.

Translated by P. Pozdeev

Journal of Experimental and Theoretical Physics, Vol. 94, No. 1, 2002, pp. 94–107.
Translated from Zhurnal Éksperimental'noĭ i Teoreticheskoĭ Fiziki, Vol. 121, No. 1, 2002, pp. 113–128.

SOLIDS
Structure

Structural Transitions in Silicon Induced by a Femtosecond Laser Pulse: The Role of an Electron–Hole Plasma and Phonon–Phonon Anharmonicity

S. I. Kudryashov* and V. I. Emel'yanov**

International Teaching and Research Laser Center, Moscow State University, Moscow, 119899 Russia
**e-mail: sergeikudryashov@chat.ru; sergeikudryashov@hotmail.com*
***e-mail: emel@em.msk.ru*

Received June 25, 2001

Abstract—It is shown by the methods of time-resolved self-reflection and linear reflection that irradiation of a silicon target by a 100-fs laser pulse induces successive structural transitions of the target material to new crystal and liquid metal phases, which can occur during the laser pulse or 0.1–10^3 ps after the pulse termination, depending on the excitation conditions. The thresholds of these structural transitions are determined, and "'soft" phonon modes involved in them are identified, which represent "hot" short-wavelength LA modes. The dynamics of the structural transitions in silicon in the time interval from 0.1 to 10^3 ps is described using the model of instability of phonon modes caused by an electron–hole plasma and intra- and intermode phonon–phonon anharmonic interactions © *2002 MAIK "Nauka/Interperiodica".*

1. INTRODUCTION

Beginning from the early 1980s, when the first experimental observations were reported [1, 2] on the "nonthermal" plasma-induced disordering and melting of semiconductors exposed to intense femtosecond pulses, which were predicted earlier in papers [3–6], many experimental and theoretical studies were performed in this field (see references in [7–10]). Because of the high rates of linear and nonlinear optical generation of free carriers, femtosecond lasers can produce a dense electron–hole (e–h) plasma in semiconductors with the density $N_e > 10^{22}$ cm^{-3}. The formation of such a dense e–h plasma in a semiconductor results in a variety of electronic effects such as Auger recombination and collision ionization [11, 12], a transport of charge carriers from the excited region to the material volume [1, 9], and a decrease in the band gap caused by many-body interactions in the plasma and by screening of the ion core [13]. The interaction of free carriers with a crystal lattice results in a change in the lattice state—excitation and "softening" of some acoustic or optical phonon modes [3–6, 14–22]. The destabilization of one or several such modes causes a phase (vibronic) transition through a "soft" mode, which is accompanied by a change in the crystal structure of the material. Such ultrafast structural transitions have been theoretically predicted and described in papers [3–6, 18–22] and have been observed experimentally (with a delay of a few hundred femtoseconds after a pump pulse termination) upon transformations to a metal liquid phase (in Si [1, 8], GaAs [8], InSb [23]) and in a new crystal phase (in amorphous $Ge_{0.04}Sb_{0.96}$ [24]). Nevertheless, the mechanisms of these structural transitions are not conclusively established. In particular, at present the nature of the soft mode is treated differently in different papers. Thus, the authors of papers [3–6] believe that soft modes represent transverse acoustic TA modes near the boundary of the Brillouin zone, whereas in papers [19, 18] the soft modes are treated as longitudinal optical LO modes at the center of the Brillouin zone or their combinations, respectively.

Along with the vibronic mechanism of plasma-induced (nonthermal) ultrafast structural transitions in semiconductors, which are phase transitions of the second kind, an alternative thermal model of structural transformation at a subpicosecond time scale was proposed in a number of papers [18, 20–22] for semiconductors (Si, GaAs, and graphite). In particular, it was shown [18] that ultrafast structural transitions with a subpicosecond (longer than 100 fs) delay can be explained by ultrafast transfer of the kinetic energy to the crystal lattice, which exceeds the melting enthalpy of the material, and by excitation due to anharmonic interactions of the continuum of phonon modes, resulting in the phase transition of the first kind. Unfortunately, no experiments have been performed so far that would allow the measurement of the temperature (population of phonon modes) of new structural phases at the subpicosecond scale, in particular, the temperature of the liquid phase. Nevertheless, one can assume that both factors—the lattice heating and excitation of the e–h plasma—favor the structural transformations [5, 6]; and in the general case, the development of these processes, as phase transitions of the first or second

kind (thermal or nonthermal mechanism), will be determined not only by the excess over the thermodynamic threshold of the structural transition (melting enthalpy or the threshold density of the plasma, respectively) but also by the transition kinetics.

It is known that thermal phase transitions of the first kind, being activation processes, originate on the seeds of a new phase, which appear, as a rule, on the surface of the initial phase, and propagate in its volume at a velocity that does not exceed the speed of sound, even in the presence of strong heating [25]. Conversely, plasma-induced nonthermal structural transformations, being transitions of the second kind (without activation), occur in any region of the initial phase where the threshold density N_c of the plasma for the soft mode instability is surpassed. These transitions proceed at the time scale of the order of the oscillation period $T = 2\pi/\omega_0(q)$ of the corresponding soft phonon mode with the initial frequency $\omega_0(q)$ ($T \sim 10^{-13}$ s). They have a "volume" character, and the growth rate of the new phase is determined only by the spatial distribution of the plasma density N_e (controlling parameter), whose local value ($N_e \geq N_c$ determines the frequency of the unstable (soft) mode [3–6, 19],

$$\omega^2(q) = \omega_0^2(q)(N_e/N_c - 1), \quad (1)$$

and the transition duration $t(N_e)$,

$$t(N_e) = \frac{T}{\sqrt{N_e/N_c - 1}}. \quad (2)$$

It follows from expression (2) that, for plasma-induced structural transformations, both the "critical" slowing down [26] near the instability threshold ($N_e \approx N_c$) of the soft mode can occur, which is inherent in phase transitions of the second kind (slowing down to 10–15 ps was experimentally observed in [27]), and the transition time can become shorter than the characteristic oscillation period of the unperturbed soft mode when its instability threshold is strongly surpassed ($N_e \gg N_c$). In the case of critical slowing down of a transition of the second kind, the thermal and nonthermal mechanisms began to compete with each other (due to phonon–phonon relaxation occurring at the time scale of 10^{-12}–10^{-11} s, and it can be difficult to establish the nature of the structural transformation. Conversely, when the instability threshold for the soft mode is strongly surpassed $N_e \gg N_c$), the transition time can be comparable with the oscillation period of the mode ($t \leq 10^{-13}$ s), which unambiguously indicates the nonthermal nature of the effect. The possibility of the plasma-induced change in the symmetry of the GaAs lattice during a 100-fs laser pulse was noted in SHG experiments [8, 28, 29]; however, as far as we know, no systematic studies of the dependence of the structural transition duration on the controlling parameter (the e–h plasma density, and the energy density or the laser pump radiation intensity in the experiment) have yet been performed for different semiconductors (in [27], such a dependence was obtained for GaAs for times longer than 0.3 ps, but the dependence was not interpreted and its parameters were not determined). At the same time, the parameters of this dependence are of considerable interest. Thus, the characteristic transition time T, which is determined by the frequency $\omega_0(q)$ of the soft mode allows one to explain the microscopic mechanism of the structural transformation, while the threshold of the e–h plasma density for the infinitely slow development of the soft mode characterizes a real thermodynamic instability threshold, which is of interest for theoretical studies of plasma-induced phenomena in semiconductors.

In this paper, we used the methods of ellipsometry (self-reflection of pump pulses for *s* and *p* polarizations) and of linear reflection of the second-harmonic probe radiation ($2\hbar\omega = 3.12$ V) for time-resolved studies of structural transformations in silicon samples induced by 100-fs fundamental-harmonic laser pulses ($\hbar\omega = 1.56$ eV). The ellipsometric data processed with the time resolution "within" a laser pump pulse by the method proposed in the paper revealed three successive discrete red shifts of both linear absorption bands of silicon ("collapse" of the band gap E_g along the corresponding direction of the Brillouin zone) during the pump pulse. In each case, a new metastable crystal state of matter appeared and the process terminated by melting of the excited surface layer at the blue wing of the E_2 band. Analysis of the dynamics of linear reflection of the second harmonic by the method of optical microscopy confirmed the presence of discrete red shifts and the successive formation of three new structural states. The model of instability of phonon modes caused by the e–h plasma and phonon–phonon anharmonicity proposed in the paper is used to describe the dependence of the duration of structural transitions on the experimental controlling parameter—the effective (absorbed) laser pump energy density. The thresholds of these transformations are determined, the involved soft phonon modes are identified (nonequilibrium, or "hot" short-wavelength LA modes), the mechanism of generation of these modes from long-wavelength LO modes is established, and the contributions of diffusion and recombination to the dynamics of the e–h plasma are estimated.

2. EXPERIMENTAL

The studies were performed using a standard Ti:Al_2O_3 sapphire crystal femtosecond laser setup at the Institute of Laser and Plasma Physics, University of Essen (Germany). The basic components of the setup, a Kerr lens master oscillator and a regenerative and a multipass amplifier, are described in papers [30, 31]. The laser emitted 794-nm (the fundamental harmonic), 100-fs (FWHM) pulses with a normal power distribution, an energy of up to 1.5 mJ (TEM_{00} mode), and a

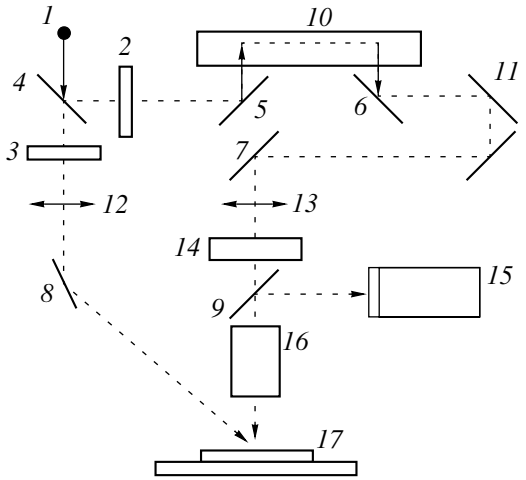

Fig. 1. Schematic of the optical microscopy setup: (*1*) input laser radiation; (*2*, *3*) electromechanical shutters; (*4*–*9*) beam-splitters and dielectric mirrors; (*10*) optical delay line; (*11*) broadband retroreflector; (*12*, *13*) focusing lenses; (*14*) nonlinear PBBO crystal (frequency doubler); (*15)* CCD camera with a fundamental-harmonic cutoff filter; (*16*) objective; (*17*) target on a dual-axis translation stage with step motors.

pulse repetition rate of 10 Hz. The relative amplitudes of the precursor and accompanying parasitic pulses were less than 7%.

An input laser beam was split in the experimental setup (Fig. 1) into the pump and probe beams with the energy ratio 3 : 1. The pump beam was polarized (*s* or *p* polarization), and its pulse energy was measured with a calibrated photodiode. Then, the beam was focused with a lens with the focal length 50 cm and was directed on the target surface at an angle of 45°. The distribution of the pump energy density on the target was described by a Gaussian with parameters $\sigma_x \approx 70$ μm and $\sigma_y \approx 40$ μm. The targets were undoped silicon Si(100) plates, which were mounted on a dual-axis translation stage which was translated from pulse to pulse using step motors. The energy of the reflected pump beam with *s* and *p* polarizations was measured with a pyroelectric detector.

The probe beam passed through an optical delay line and was focused, passing through a nonlinear crystal to produce the second harmonic (the fundamental harmonic was rejected with a narrowband filter), on a circular diaphragm of diameter 100–150 μm, which was used for eliminating long-wavelength inhomogeneities of the transverse distribution of the radiation energy. Then, the second-harmonic radiation was focused through the objective of an optical microscope near the target surface (for normal incidence) so that the spot from the low-intensity probe beam (second harmonic) on the target surface would be 3–6 times greater than that from the pump beam (fundamental harmonic). The probe beam specularly reflected from the target was directed back through the objective and a beam splitter to a synchronized CCD camera equipped with a filter rejecting the fundamental harmonic. The parameters of the probe channel allowed us to study the dynamics of reflectivity of the excited area of the target with a spatial resolution of about 2 μm and a time resolution of about 100 fs (time-resolved optical microscopy [32]).

The data on optical probing of excited silicon were processed by normalizing the images of a sample, which were obtained in the reflected light of the normally incident probe pulse for different delays t_d with respect to the center of the pump pulse, to the image of an unexcited sample. After calibration, these images represented the two-dimensional spatial distribution of the reflectivity $R_1^{2\omega}$ of the sample, which was symmetrical with respect to the center of the pump radiation spot. The vertical cross sections of normalized images passing through the center of the pump radiation spot on the sample surface, after the transformation of spatial coordinates, characterize the dependence of $R_1^{2\omega}$ on the energy density for different values of t_d.

3. EXPERIMENTAL RESULTS AND DISCUSSION

We studied the dependence of the self-reflection coefficient for pump radiation in silicon samples (for both polarizations of the fundamental harmonic) on the incident energy and the dynamics of linear reflection of the probing second harmonic at the fixed maximum energy density of *p*-polarized pump radiation.

3.1. Linear Self-Reflection of Pump Laser (Fundamental Harmonic) Pulses

We processed the experimental dependences of the self-reflection coefficients R_s^ω and R_p^ω of samples on the pump pulse energy obtained for both polarizations using the iteration procedure, which eliminated the averaging of the coefficients because of the spatial inhomogeneity of the energy density *F* in the light spot of the TEM_{00} mode on the target. The processing procedure was based on the consideration of the relative contribution from circular parts of the light spot, which differed in the local energy density *F*, to the integrated reflection. The resulting dependences of R_{1s}^ω and R_{1p}^ω on the effective (absorbed) pump energy density $F_{\text{eff}} = (1 - R_{1s,\,1p}^\omega)F$ integrated over the pulse are presented in Fig. 2a. Such a representation allows one to compare the parts of the curves for R_{1s}^ω and R_{1p}^ω in Fig. 2 that correspond to the identical excitation conditions. The corresponding dependences $F_{\text{eff}}(F)$ for pump radiation at both polarizations are monotonic and do not contain a plateau or any special features.

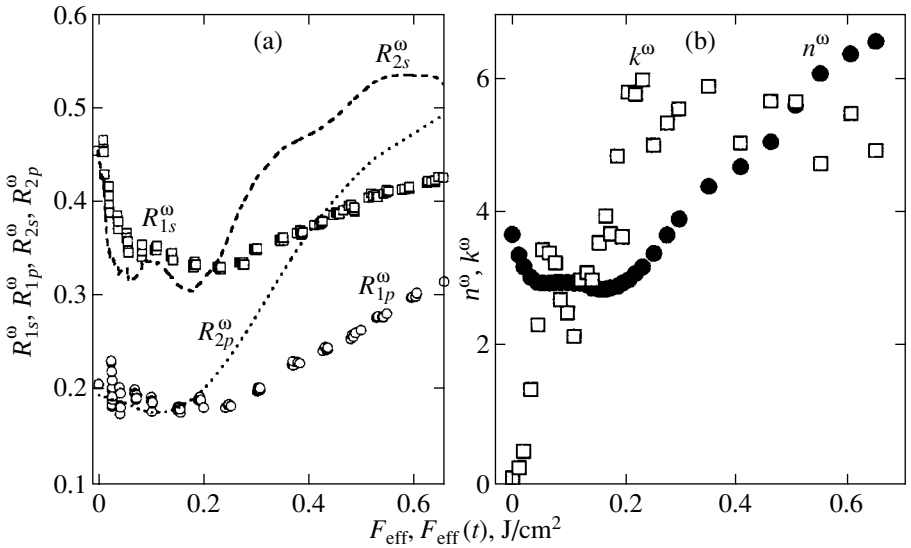

Fig. 2. Dependences of (a) self-reflection coefficients for excited silicon for *s*- and *p*-polarized pump radiation (fundamental harmonic) (dependences of R^{ω}_{1s} and R^{ω}_{1p} on F_{eff} and R^{ω}_{2s} and R^{ω}_{2p} on $F_{\text{eff}}(t)$) and (b) the real n^{ω} and imaginary k^{ω} parts of the refractive index of excited silicon on $F_{\text{eff}}(t)$.

Because of the self-action effect of laser radiation [8, 28], which is manifested in a continuous variation of the optical parameters of the semiconductor during the laser pulse, the dependences of R^{ω}_{1s} and R^{ω}_{1p} on F_{eff} are time-averaged within the laser pulse duration. For this reason, these curves were additionally processed graphically (time-transformed) using the expressions [33]

$$R_1(F_{\text{eff}}) = \int_{F_{\text{eff1}}}^{F_{\text{eff2}}} R_2(F')\,dF' \Big/ \int_{F_{\text{eff1}}}^{F_{\text{eff2}}} dF', \qquad (3)$$

$$R_2(F_{\text{eff}}) = R_1(F_{\text{eff}}) + \frac{dR_2(F_{\text{eff}})}{dF_{\text{eff}}} F_{\text{eff}}, \qquad (4)$$

where R^{ω}_{2s} and R^{ω}_{2p} (Fig. 2a) are "true" values of the reflection coefficient of silicon for the instantaneous quantity $F_{\text{eff}}(t)$ representing the integral of the radiation intensity for the time t during the laser pulse, and the values F_{eff1} and F_{eff2} determine the integration range in which the above transformation is valid. Note that the transformation of the dependence of R^{ω}_{1s} and R^{ω}_{1p} on F_{eff} according to expressions (3) and (4) assumes that excitation of the material is nonstationary, when diffusion and recombination contributions can be neglected in the kinetic equation for the e–h plasma density. The first contribution can be neglected when $\alpha l_{\text{dif}} \ll 1$, where $l_{\text{dif}} \sim 10$ nm is the diffusion length in the plasma during the pump pulse (100 fs) and α^{-1} is the skin depth for the excited semiconductor. As will be shown below, the recombination contribution also can be neglected in the range of pump energy densities under study according to the results of papers [1, 13], which demonstrated saturation of the rate of Auger recombination at e–h plasma densities above $N_e \approx (3\text{–}5) \times 10^{21}$ cm^{-3} caused by a strong screening of the e–h interaction potential.

The dependences $R^{\omega}_{2s}(F_{\text{eff}}(t))$ and $R^{\omega}_{1p}(F_{\text{eff}}(t))$ in Fig. 2a have two distinct minima at 0.03–0.10 J/cm^2 and 0.11–0.21 J/cm^2 in the region of small $F_{\text{eff}}(t) \leq 0.15$ J/cm^2 and rapidly increase at $F_{\text{eff}}(t) \geq 0.21$ J/cm^2; for the *p*-polarized pump radiation, both minima are present but they are not resolved. The presence of one minimum and a subsequent increase in the linear reflection with increasing F was observed earlier in semiconductors and was explained by the attainment of the plasma reflection edge [1, 9]. However, the two resolved minima that we observed for the dependences $R^{\omega}_{2s}(F_{\text{eff}}(t))$ and $R^{\omega}_{1p}(F_{\text{eff}}(t))$ allow us to propose a new interpretation of these features. For this purpose, we calculated the optical constants n^{ω} and k^{ω} for excited silicon for different values of $F_{\text{eff}}(t)$ (Fig. 2b) by Fresnel formulas using these dependences. The calculations were performed by selecting pairs of the values of n^{ω} and k^{ω} that provided the minimum discrepancy between calculated and experimental values of R^{ω}_{2s} and R^{ω}_{2p}.

According to the dependences $n^{\omega}(F_{\text{eff}}(t))$ and $k^{\omega}(F_{\text{eff}}(t))$ obtained, the two minima of curves $R^{\omega}_{2s}(F_{\text{eff}}(t))$ and $R^{\omega}_{2p}(F_{\text{eff}}(t))$ correspond to two intense linear absorption bands of silicon at $F_{\text{eff}}(t) \approx 0.08$ and 0.16 J/cm^2 in the absence of strong two-photon absorp-

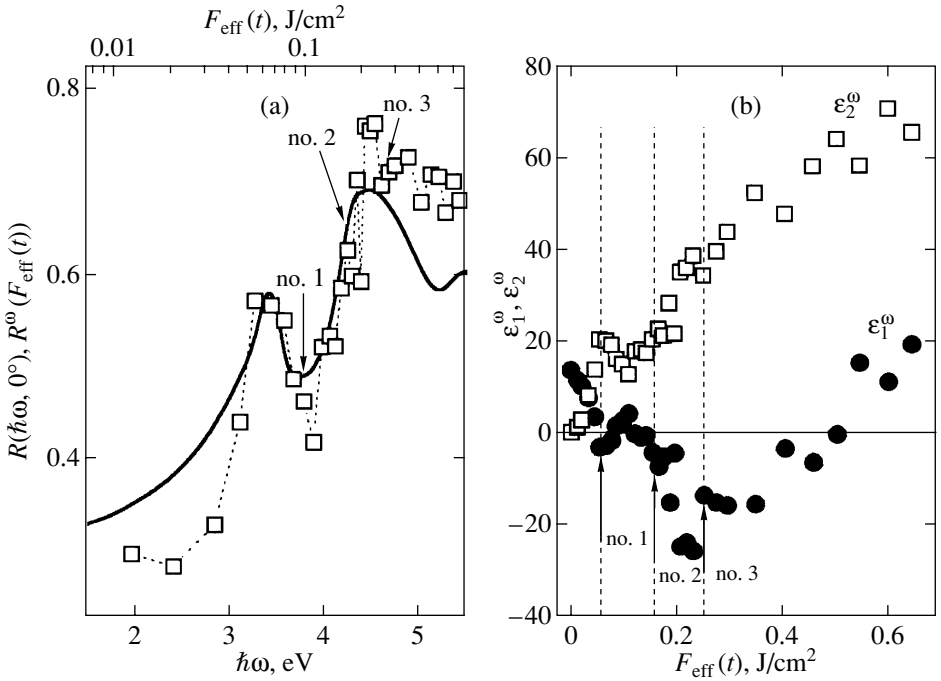

Fig. 3. (a) Dependence of $R^{\omega}(F_{eff}(t), 0°)$ for excited silicon (open squares and dashed curve) plotted using the corresponding values of $n^{\omega}(F_{eff}(t))$ and $k^{\omega}(F_{eff}(t))$ (Fig. 2b) and the spectral dependence $R^{\omega}(\hbar\omega, 0°)$ for Si^0 (solid curve, the values of $n(\hbar\omega)$ and $k(\hbar\omega)$ taken from [34]). (b) Dependences of the real ε_1^{ω} and imaginary ε_2^{ω} parts of the dielectric constant of excited silicon on $F_{eff}(t)$.

tion and free-carrier absorption, which are weaker than the residual absorption between the peaks in the curve $k^{\omega}(F_{eff}(t))$ (Fig. 2b). The position and amplitude of the first maximum in the curve $k^{\omega}(F_{eff}(t))$ in Fig. 2b agree well with the data from paper [34]; however, the region of the second maxima was not studied in [34].

Taking into account the red shift of the linear absorption band of semiconductors in a high-density e–h plasma caused by the band gap collapse [27], we can assume that we detected both interband transition bands E_1 and E_2 of silicon during the 100-fs pump pulse, which lie at 3.4 and 4.3 eV, respectively, in unexcited silicon (Si^0) [35]. Recall that this effect was earlier observed only in GaAs and only for long delays $t_d \geq 0.3$ ps [27], although a weak decrease in the process duration with increasing F was noted. Good agreement between the dependence $R^{\omega}(F_{eff}(t), 0°)$ for the normal incidence in Fig. 3a, which was plotted using the corresponding values of n^{ω} and k^{ω} for an excited sample (Fig. 2b), and the spectral dependence $R(\hbar\omega, 0°)$ for Si^0 (the values of $n(\hbar\omega)$ and $k(\hbar\omega)$ were taken from [35]) qualitatively confirms the hypothesis of the red shift for both linear absorption bands of silicon.

The successive plasma-induced band gap collapses along different crystallographic axes in silicon is probably caused by the renormalization of the band structure of silicon due to the change in its crystal structure upon vibronic phase transitions rather than by the electronic effects such as multiparticle interactions in the e–h plasma and screening of its ion composition [13]. Indeed, at present the effect of band gap collapse along a certain direction in the Brillouin zone, which causes the red shift of the interband absorption band, was observed not only in semiconductors but also in metals having the interband absorption [36, 37], and its vibronic nature is reliably established. Therefore, the red shift of the absorption bands E_1 and E_2 of Si^0 that we observed during the pump pulse can be explained by the successive (with increasing input energy) structural vibronic transitions to metastable and, as follows from the preservation of the band structure upon the red shift of the absorption band, crystal phases nos. 1 and 2. According to the band theory, metastable phases nos. 1 and 2 will be semimetal and metal, respectively, and their specific features are indeed observed in the dependence of the real part of the dielectric constant $\varepsilon_1^{\omega}(F_{eff}(t))$ (nos. 1 and 2 in Fig. 3b), which allows us to estimate the red shift for the corresponding vibronic transitions as $\hbar\omega_1 \approx 3.8$ eV and $\hbar\omega_2 \approx 4.2$–4.3 eV (arrows 1 and 2 in Fig. 3a). Phases nos. 1 and 2 can be probably assigned to the phases of Si-III with the body-centered cubic (bcc) lattice and of tetragonal Si II [38]. Note that such a sequence of the formation of semimetal and metal phases upon irradiation of semiconductors by ultrashort laser pulses was predicted in [39].

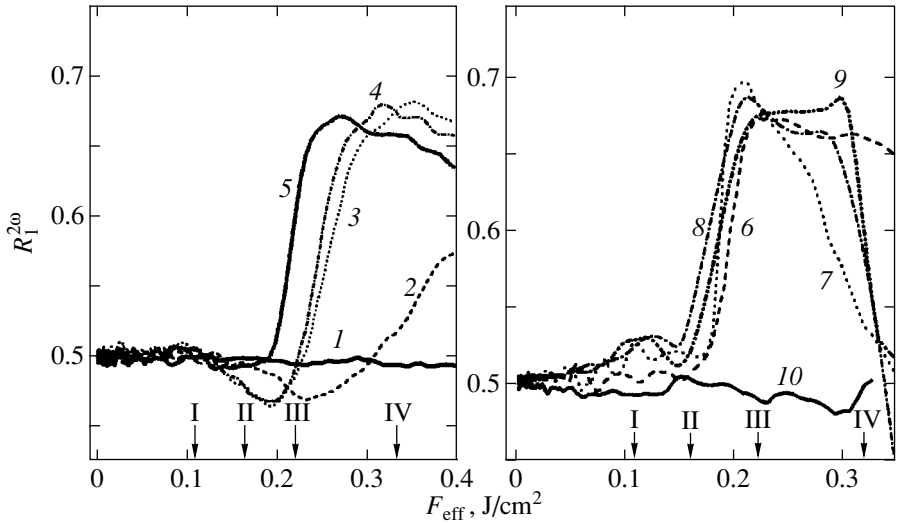

Fig. 4. Dependences of $R_1^{2\omega}(F_{\text{eff}})$ for different delays t_d of a second-harmonic probe pulse for τ_d (ps) = –0.1 (*1*), 0.1 (*2*), 0.3 (*3*), 0.4 (*4*), 0.8 (*5*), 1 (*6*), 10 (*7*), 100 (*8*), 800 (*9*), and τ_d = 10 s (conditionally, $t_d = 10^5$ ps, curve *10*). The arrows I–IV indicate the characteristic parts of the excited region of a sample.

The dependences $n^{\omega}(F_{\text{eff}}(t))$ and $k^{\omega}(F_{\text{eff}}(t))$ in Fig. 2b also demonstrate for the first time the plasma-induced ultrafast melting of the material [metal phase *l*'-Si (no. 3) in Fig. 3] during the 100-fs pump laser pulse above the threshold $F_{\text{eff}}(t) \approx 0.25$ J/cm^2 which corresponds to the monotonic increase of the curves $R_{2s}^{\omega}(F_{\text{eff}}(t))$ and $R_{2p}^{\omega}(F_{\text{eff}}(t))$ (Fig. 2a) after the preceding abrupt jump. The melting is experimentally confirmed by the agreement between the values of $n^{\omega}(F_{\text{eff}}(t)) \approx 3.7 \pm 0.4$ and $k^{\omega}(F_{\text{eff}}(t)) \approx 5.3 \pm 0.5$ for $F_{\text{eff}}(t) \geq 0.25$ J/cm^2 and the optical constant for the equilibrium liquid phase of *l*-Si [n(1.5 eV) = 3.3 and k(1.5 eV) = 5.7 [40]]. In addition, near $F_{\text{eff}}(t) \approx 0.25$ J/cm^2, the reduced plasma density $N_e/M_{\text{opt}} \approx (2.0 \pm 0.3) \times 10^{23}$ cm^{-3} in the material (where M_{opt} is the optical electron mass) calculated using the Drude model with the above values of n^{ω}(0.25 J/cm^2) and k^{ω}(0.25 J/cm^2) becomes equal to the maximum concentration of valence electrons $N_e^0 \approx 2 \times 10^{23}$ cm^{-3} in crystal silicon at room temperature under the assumption that for each atom there are four conduction electrons and the initial density of the material is preserved. Therefore, $M_{\text{opt}} = 1.0 \pm 0.2$, which is generally typical for structureless conducting media (metal liquid, plasma) and solid univalent metals, i.e., in this case, for the liquid *l*'-Si phase. Estimated by the data of Fig. 3a (arrow no. 3), the red shift corresponding to the material melting amounts to $\hbar\omega_3 \approx 4.7$ eV.

Therefore, the experimental study of self-reflection of the fundamental harmonic in silicon during the pump pulse revealed the successive transformations of two metastable crystal states and the liquid phase of silicon upon three vibronic transitions manifested in three successive red shifts of the absorption spectrum of Si^0. The dynamics of these structural transitions was studied with a time resolution of about 100 fs in experiments with the linear reflection $R_1^{2\omega}$ of the probe second harmonic (by the method of optical microscopy). The results of these experiments are presented in the next section (Fig. 4).

3.2. Dynamics of Linear Reflection of Probe (Second Harmonic) Laser Pulses

Unlike the experiments on self-reflection of the fundamental harmonic pump radiation from the silicon surface, in which the oblique incidence of radiation favors the observation of structural transformations even in relatively thin layers, the probing depth in experiments on linear reflection of the normally incident second-harmonic probe beam can be substantially greater than the depth of structural modification of the material, which requires the consideration of thin-film effects (Fig. 5).

According to the results of [27], the red shift of the linear interband absorption spectrum accompanying structural transitions in semiconductors can also be observed at other frequencies of the probe radiation; i.e., upon probing by the second harmonic radiation, the red shift of the spectrum of Si^0 should take place, beginning from $\hbar\omega \geq 3.1$ eV. In this case, the relatively stable (metastable) nature of the emerging new phases will be manifested in the quasi-stationary behavior of $R_1^{2\omega}$, whereas, in the case of continuous deformation of the material, the corresponding red shift of the linear

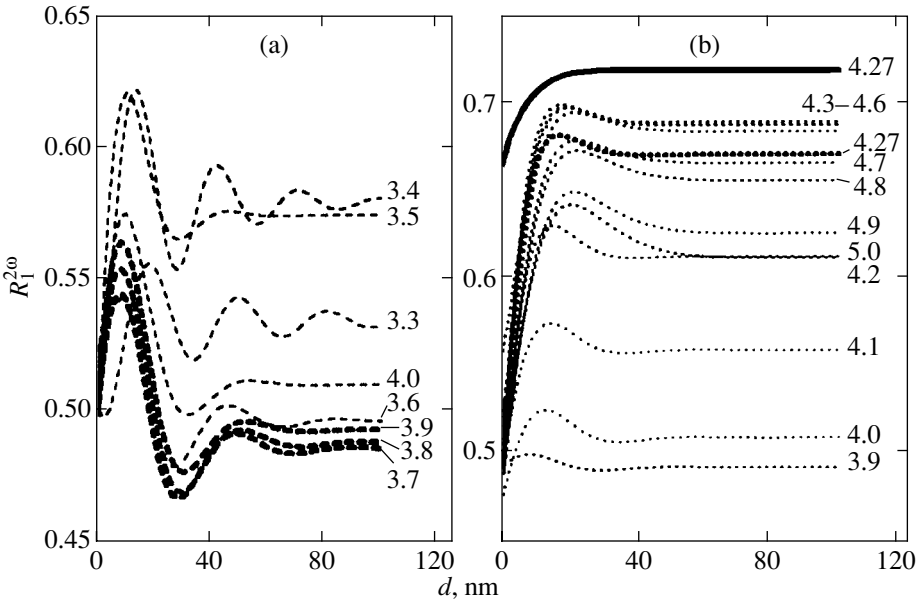

Fig. 5. Dependences of $R_1^{2\omega}$ on the thickness d (a) for a film located on the surface of the optically thick phase of Si^0 {n(3.18 eV) = 5.8, k(3.18 eV) = 0.7 [34]} with different optical constants within the linear absorption E_1 band of silicon (dashed curves, the figures at the curves are photon energies); and (b) for a film located on the surface of the optically thick phase no. 1 {n(3.8 eV) = 4.7, k(3.8 eV) = 2.1 [34]} with different optical constant within the linear absorption E_2 band (point curves, the figures at the curves are photon energies). The solid curve shows the dependence of $R_1^{2\omega}$ on the thickness of the l-Si melt film {n(3.1 eV) = 1.8 ± 0.2, k(3.1 eV) = 4.2 ± 0.2 [39]} on the surface of phase no. 2 {n(4.27 eV) = 3.7, k(4.27 eV) = 4.6 [34]}.

absorption spectrum will be manifested in a monotonic dependence of $R_1^{2\omega}$ on time. Indeed, the analysis of the reflectivity of the excited silicon sample (Fig. 4) shows that the specific features in curves $R_1^{2\omega}(F_{\text{eff}})$—the decay, rise, and plateau—can be assigned not only to the features of the absorption spectrum of Si^0 but also to the same discrete red shifts of this spectrum as in experiments on self-reflection of the fundamental harmonic, i.e., to the new phases of the material mentioned above. Figure 6 shows the time dependences of $R_1^{2\omega}$ for several characteristic cases corresponding to certain parts of excited silicon (I–IV in Fig. 4) for F_{eff} = 0.11, 0.18, 0.22, and 0.31 J/cm^2.

Thus, the decrease in $R_1^{2\omega}$ in the region $F_{\text{eff}} \geq$ 0.11 J/cm^2 in the time interval t_d = 0.1–0.4 ps (Fig. 4a) can be assigned to the "bleaching" of the sample surface layer caused by the formation of a surface phase with $n^\omega(F_{\text{eff}}) < n$(3.1 eV, Si^0) = 5.5 and $n^\omega(F_{\text{eff}}) > k^\omega(F_{\text{eff}})$, whose thickness increases with increasing F_{eff}. According to the dependences $R^\omega(F_{\text{eff}}(t), 0°)$ and $R(\hbar\omega, 0°)$ (Fig. 3a), the bleaching effect takes place for $3.6 \leq \hbar\omega \leq 3.9$ eV. More exactly, as follows from the value $R_1^{2\omega} \approx 0.47 \pm 0.01$ for the optically thick layer of this phase, which is indicated by arrow II in Fig. 4a, this effect is observed for $n(3.8 \pm 0.1 \text{ eV}) = 4.7 \pm 0.2$ and $k(3.8 \pm 0.1 \text{ eV}) = 2.1 \pm 0.3$ for the photon $\hbar\omega_1 = 3.8 \pm 0.1$ eV (Fig. 5a) at the minimum of $R^\omega(F_{\text{eff}}(t), 0°)$ and $R(\hbar\omega, 0°)$ in the blue wing of the E_1 band (no. 1 in Fig. 3a), i.e., for hypothetical semimetal phase no. 1. Note that the alternative interpretation of the minimum of $R_1^{2\omega}$ as a plasma reflection edge [1, 9] contradicts the decrease in this quantity to $R_1^{2\omega} \approx 0.47 \pm 0.01$ which was observed after the pump pulse termination for delays t_d = 0.1–0.4 ps, whereas the plasma component in the optical constants of excited silicon should be maximum by the pump pulse end (at $t_d \approx 0.1$ ps).

In region I (Fig. 4), at times t_d = 0.2–0.8 ps, the value $R_1^{2\omega} \approx 0.49 \pm 0.01$ is reached (curve *1* in Fig. 6a), which characterizes the optically thin layer of phase no. 1 (the curve for $\hbar\omega = 3.8 \pm 0.1$ eV in Fig. 5a). The further dynamics of the material in this region is determined by the increase in $R_1^{2\omega}$ for the time $t_d \approx 10$ ps to the stationary value of 0.52 ± 0.01, which does not change up to $t_d \approx 3$ ns, the spatial region of the increasing $R_1^{2\omega}$ being coincident with the preceding bleaching region. Therefore, taking into account that $t_d \sim 10$ ps is the characteristic time of the absorbed energy transfer to a phonon subsystem due to the electron–phonon interaction and

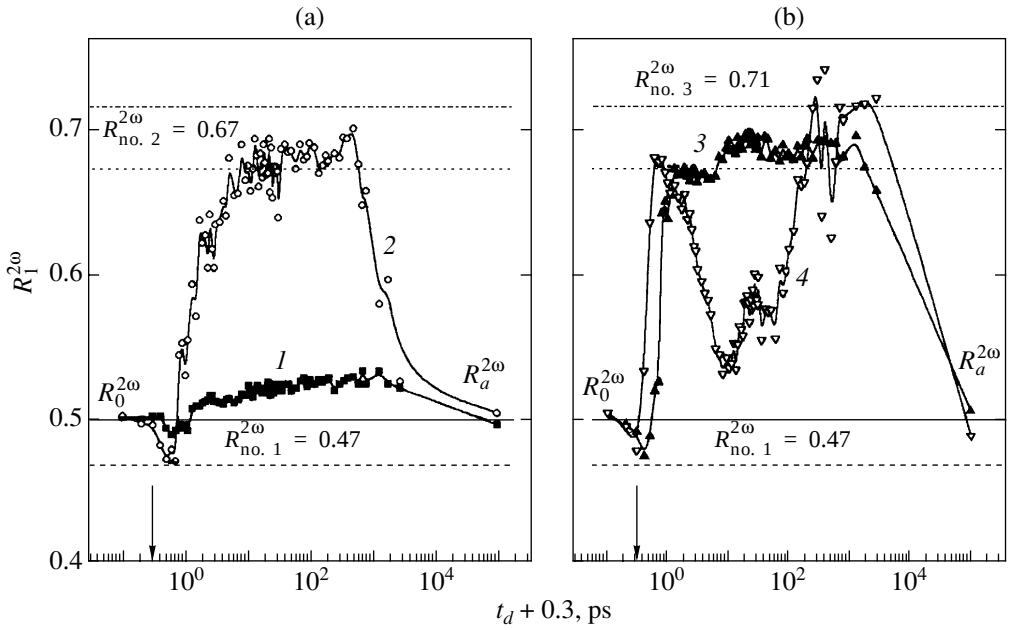

Fig. 6. Time dependences of $R_1^{2\omega}$ for the values of F_{eff} corresponding to regions I–IV in Fig. 4: (a) 0.11 (*1*) and 0.16 J/cm^2 (*2*); (b) 0.22 (*3*) and 0.31 J/cm^2 (*4*). The horizontal straight lines correspond to the stationary values of $R_1^{2\omega}$ for phases nos. 1–3: $R_{\text{no. 1}}^{2\omega} \approx 0.47$, $R_{\text{no. 2}}^{2\omega} \approx 0.67$, and $R_{\text{no. 3}}^{2\omega} \approx 0.71$; $R_0^{2\omega}$ is the initial reflection level, $R_a^{2\omega}$ is the reflectivity of the amorphous phase ring around the crater. The arrow shows the pump-pulse center.

Auger recombination [1, 7, 13], as well as due to phonon–phonon and acoustic relaxation in the skin layer of thickness up to 50 nm probed by the second harmonic, the increase in $R_1^{2\omega}$ can be explained by a further red shift of the linear absorption spectrum of Si^0, approximately to $\hbar\omega \approx 4.0$ eV, caused by the thermal expansion (deformation) of the layer of phase no. 1, assuming that phonon modes are thermalized for 10 ps (in the general case, they can be characterized by the effective temperature T^*). Taking into account the above red shift of the absorption spectrum by 0.2 eV, which is described by the temperature dependence of the band gap of Si^0 for direct interband transitions [41], the maximum temperature in the layer was estimated as $T^* \approx 700$ K. This value reasonably agrees with the estimate $T^* \approx 1 \times 10^3$ K, which was obtained for $F_{\text{eff}}(t) \approx 0.11$ J/cm^2 by calculating (using the dependence $k^\omega(F_{\text{eff}}(t))$, Fig. 2b) the volume energy density (of about 3.6×10^5 J/mol) absorbed during the pump pulse in the skin layer of thickness $\alpha^{-1} \approx 3 \times 10^{-6}$ cm and due to the ambipolar diffusion of the e–h plasma (the diffusion coefficient $D \sim 10^2$ cm^2/s) distributed in a layer of thickness 10^{-5}–10^{-4} cm during the plasma lifetime of the order of 10 ps. Finally, after the target cooling within a few tens of seconds (conditionally, at $t_d = 10^5$ s), the initial level of $R_1^{2\omega}$ ($R_0^{2\omega} \approx 0.50$ at room temperature) is virtually restored, which can indicate the reversibility of the transition to phase no. 1.

The increase in $R_1^{2\omega}$ to 0.68 ± 0.01 and its stationary value 0.67 ± 0.01 observed for $F_{\text{eff}} \geq 0.18$ J/cm^2 for times $t_d = 0.1$–1 ps (Fig. 4) agree well, according to the data in Fig. 5b, with the formation of the reflecting surface layer with the coefficients $n^\omega(F_{\text{eff}})$ and $k^\omega(F_{\text{eff}})$ corresponding to $n(\hbar\omega) = 3.7 \pm 0.2$ and $k(\hbar\omega) = 4.6 \pm 0.2$ for Si^0 for the photon $\hbar\omega_2 = 4.27 \pm 0.05$ eV in the red wing of the E_2 band (arrow no. 2 in Fig. 3a). The appearance of this layer under different excitation conditions of the sample in different time intervals (Fig. 6) indicates that a new phase no. 2 is formed. Note that the assignment of $\hbar\omega_2$ to the red wing of the E_2 band rather than to the blue wing ($\hbar\omega \approx 4.7$ eV) follows from a comparison of the values of $\hbar\omega_2$ in experiments with the fundamental and second harmonics, as well as from the absence of the characteristic reflection maximum of $R(\hbar\omega, 0°) \approx 0.69$ for $\hbar\omega \approx 4.5$ eV in curves $R_1^{2\omega}$ (Figs. 4 and 6) for $F_{\text{eff}} \approx 0.18$ J/cm^2

In the region II ($F_{\text{eff}} = 0.18$ J/cm^2) (Fig. 4) at $t_d < 0.4$ ps, the matter passes through phase no. 1 (curve *2* in Fig. 6a), whose optical layer ($R_{\text{no. 1}}^{2\omega} \approx 0.47 \pm 0.01$) is formed at the pump pulse end ($t_d \approx 0.1$ ps). Then, $R_1^{2\omega}$ increases to 0.63 for 2 ps and continues to rise slowly

up to the stationary value of 0.67 ± 0.01 (t_d = 5–30 ps), which corresponds to the formation of the optically thick layer of phase no. 2. It is obvious that the development of phase no. 2 at t_d = 0.4–5 ps (Fig. 6a) occurs during the Auger recombination of the e–h plasma and is probably stimulated by the intra- and (or) intermode phonon–phonon anharmonicity. At times t_d = 40–100 ps, $R_1^{2\omega}$ increases to the characteristic value $R(\hbar\omega, 0°) \approx 0.69$ (Fig. 3a, $\hbar\omega \approx 4.5$ eV) and then somewhat decreases to $R_1^{2\omega} = 0.67 \pm 0.01$, in accordance with the data presented in Fig. 3a, which can be treated as a whole as a further quasi-thermal red shift of the absorption spectrum of Si^0 to $\hbar\omega \approx 4.7$ eV. In this case, the subsequent increase in $R_1^{2\omega}$ above 0.69 at t_d = 200–500 ps is probably caused by material melting. The decrease in $R_1^{2\omega}$ beginning with $t_d \approx 500$ ps is caused by sample cooling due to thermal conductivity, which virtually terminates at $t_d \geq 3$ ns. Finally (at $t_d = 10^5$ ps), the value $R_1^{2\omega} = R_a^{2\omega} \approx 0.51 \pm 0.01$ somewhat exceeds the initial value $R_0^{2\omega} \approx 0.50$ due to the formation of the reflecting amorphous surface *a*-Si layer [42]; the corresponding circle with a higher reflection coefficient was indeed observed around the crater on the target images, which were obtained within a few tens of seconds after irradiation by the pump pulse. The appearance of the amorphous phase confirms the formation of the melt film on the surface of phase no. 2. A rapid cooling of the film can be caused by the potentially high thermal conductivity of the metal phase no. 2, which plays the role of a substrate. Therefore, in accordance with the results obtained in [36, 37], we can assume that the last red shift (up to $\hbar\omega \approx 4.7$ eV) caused by the quasi-thermal deformation of crystal phase no. 2, i.e., by the next vibronic transition, corresponds to a virtually complete disappearance of the band structure for the state lying near the band gap and, hence, to material melting.

Curves *3* and *4* in Fig. 6b, which correspond to regions III and IV in Fig. 4 (F_{eff} = 0.22 and 0.31 J/cm^2), also confirm the formation of the optically thick layer of phase no. 2 ($R_{\text{no. 1}}^{2\omega} \approx 0.67$) at $t_d \approx 0.3$–1 ps (Fig. 6b). The transition to this phase through intermediate phase no. 1 ($R_{\text{no. 1}}^{2\omega} \approx 0.47 \pm 0.01$) begins already at the center of the pump pulse (at $t_d \approx 0$). Under these conditions, because the input energy greatly exceeds the formation threshold of phase no. 2, the phase is strongly heated due to Auger recombination and electron–phonon relaxation at $t_d \sim 10$ ps, and the next red shift occurs to $\hbar\omega_3 \approx 4.7$ eV. This shift is manifested in a monotonic increase in $R_1^{2\omega}$ up to 0.69 ± 0.01 at times t_d = 7–40 ps followed by its decrease to 0.67 ± 0.01; then, as for curve *2*, the value of $R_1^{2\omega}$ increases due to melting (curve *3* in Fig. 6b). Curve *4* in Fig. 6b behaves similarly and characterizes the dynamics of the state of the matter in region IV ($F_{\text{eff}} = 0.31$ J/cm$^2 \leq F_{\text{abl}}$, where F_{abl} is the ablation energy), i.e., at the external edge of the emerging crater (Fig. 4b). Although in the latter case the vibronic transition and melting in phase no. 2 are masked at times t_d = 2–200 ps by the thermal expansion of the melt and ablation of the material, the termination of ablation and cooling of the melt due to thermal conductivity restore after 250–300 ps the reflection of the material at the level corresponding to the value of $R_1^{2\omega}$ for the optically thick phase of the *l*-Si melt ($R_{\text{no. 3}}^{2\omega} \approx 0.71 \pm 0.01$) with the temperature near the melting point, as follows from the value of $R_1^{2\omega}$ calculated using the optical constants for *l*-Si [n(3.1 eV) = 1.8 ± 0.2, k(3.1 eV) = 4.2 ± 0.2] from paper [40]. Note that, in experiments on self-reflection of the fundamental harmonic, the material melting (phase no. 3 of *l*'-Si) is observed on the surface of phase no. 2 already during the pump pulse (Fig. 3), which, together with the data for the second harmonic, indicates the combined effect of the e–h plasma and phonon-phonon anharmonicity on the melting dynamics of silicon.

3.3. Description of the Dynamics of Structural Transitions in Silicon

Using curves $R_1^{2\omega}(F_{\text{eff}})$ for different delays t_d (Fig. 4), we determined thresholds F_{eff} for the appearance of specific features in the curves corresponding to the initiation of phases nos. 1 and 2. The dependences of the delay time t_d for the formation of these phases on F_{eff} (Fig. 7a) with the asymptotic values of thresholds F_1 and F_2 of structural transitions, in accordance with analogous experimental dependences for GaAs [27], have the functional form of inverse proportionality [like expression (2)], which is quite expected according to the theory of plasma-induced structural transitions [3–6, 19]. Nevertheless, unlike [27], we observed the asymptotic behavior of the dependences $t_d(F_{\text{eff}})$ up to times $t_d \approx 10^3$ ps at which the e–h plasma no longer affects the dynamics of the corresponding structural transitions, and it seems that another controlling parameter, the effective temperature T^* caused by the intermode phonon anharmonicity, plays a key role. In the intermediate range from 1 to 10 ps, structural transitions to phases nos. 1 and 2 obviously occur under a combined action of parameters N_e and T^*.

By processing the curves in Fig. 7a, it is reasonable to choose the quantity F_{eff} as a controlling parameter for the structural transitions, by describing dependences $t_{di}(F_{\text{eff}})$ [taking expression (2) into account] in the phenomenological form

$$t_{di}(F_{ni}) = T_i F_{ni}^{\gamma i}, \tag{5}$$

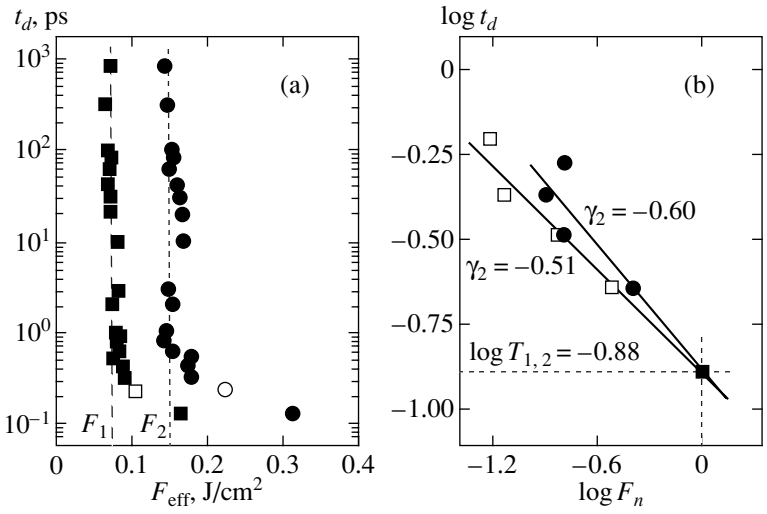

Fig. 7. (a) Dependences of the duration t_d of the $Si^0 \longrightarrow$ no. 1 and no. 1 $\longrightarrow$ no. 2 vibronic transitions on F_{eff} (F_1 and F_2 are asymptotic thresholds, and open symbols are thresholds of the corresponding transitions occurring during the pump pulse upon fundamental-harmonic probing); (b) subpicosecond part of the above dependences plotted in double logarithmic coordinates $\log t_d$–$\log F_n$, where $F_{ni} = F_{\text{eff}}/F_i$, $i = 1, 2$.

which follows in this case from the condition of vanishing of the frequency $\nu(q)$ of the corresponding soft mode under the action of parameters N_e and T^*:

$$\nu^2(q) = \nu_0^2(q)\left(1 - \frac{N_e}{N_c} - \frac{T^*}{T_c}\right), \qquad (6)$$

where $T_i = \nu_{0i}^{-1}(q)$ is the characteristic time of the ith transition ($i = 1, 2$ for phases nos. 1 and 2) and the oscillation period of the corresponding soft mode; $F_{ni} = F_{\text{eff}}/F_i - 1$ is the reduced energy density; γ_i is the exponent taking into account the root dependence of t_{di} on real controlling parameters N_e and T^* [expression of type (2)] and the dependence of these parameters on F_{eff}; and N_c and T_c are the critical density of the e–h plasma and the temperature of the structural transition, respectively. We processed the subpicosecond part of the curves in Fig. 7a, which was plotted in double logarithmic coordinates $\log t_d$–$\log F_n$ (Fig. 7b). In this part, the contribution from N_e dominates over that from T^*, which simplifies the form of the power dependence in (5). In addition, in this part of the curve, the scatter of data is minimal, in accordance with the inverse-proportionality character of experimental curves $t_d(F_{\text{eff}})$.

The method proposed by us for processing dependences $t_d(F_{\text{eff}})$ gives for the asymptotic thresholds of transitions to phases nos. 1 and 2 $F_1 \approx 0.08$ J/cm^2 and $F_2 \approx 0.15$ J/cm^2 the close values of the characteristic transition time $T_1 = 0.13 \pm 0.02$ ps and $T_2 = 0.14 \pm 0.03$ ps (frequencies $\nu_{01}(q) = 7.8 \pm 1.0$ THz and $\nu_{02}(q) = 7.4 \pm 1.5$ THz, respectively). Both dependences $\log(t_d)$–$\log(F_n)$ in Fig. 7b have the slope γ_i of about −0.5 (–0.51 ± 0.05 and −0.60 ± 0.11), which suggests that the dependence $N_e(F_{\text{eff}})$ is linear at $t_d \le 1$ ps, as was assumed earlier upon transformation of the dependences $R_{1s}^{\omega}(F_{\text{eff}})$ and $R_{1p}^{\omega}(F_{\text{eff}})$ according to expressions (3) and (4) neglecting Auger recombination and diffusion in the kinetic equation for the dynamics of the e–h plasma during the pump pulse (about 100 ps). Note that the linearity of the dependence $N_e(F_{\text{eff}})$ in the subpicosecond time interval is provided only when the rate of Auger recombination is low. If this recombination was dominant, it would give $\gamma_i \approx -0.17$ because this process involves three particles. However, according to papers [1, 13], this process does not occur. Therefore, the subpicosecond dynamics of the e–h plasma is mainly determined by ambipolar diffusion [1], which is consistent with the linear dependence of $N_e(F_{\text{eff}})$.

The found frequencies $\nu_{01}(q) = 7.8 \pm 1.0$ THz and $\nu_{02}(q) = 7.4 \pm 1.5$ THz of soft modes involved in vibronic transitions to phases nos. 1 and 2 correspond, within the experimental error, to the half frequency of the *LO* mode near the center of the Brillouin zone of silicon $\nu_{LO}(0) \approx 15.5$ THz) [41], which is predominantly excited due to the electron–phonon interaction in the conduction band. The above relation between the frequencies indicates the possibility of appearance of nonequilibrium short-wavelength *LA* modes due to fast (within 100 fs) symmetric decay of a long-wavelength *LO* phonon into two *LA* phonons with identical energies and oppositely directed quasi-momenta having the same magnitude (Fig. 8), corresponding to the known

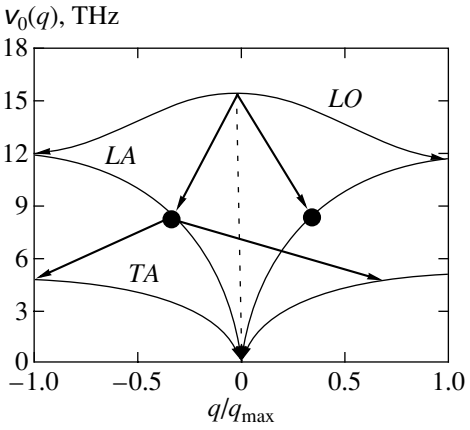

Fig. 8. Schematic diagram of the decay of high-energy long-wavelength longitudinal optical (*LO*) phonons upon relaxation of hot carriers in silicon with emission of longitudinal (*LA*) and transverse (*TA*) acoustic phonons.

scheme of phonon–phonon relaxation [43]. The time dependence of the normalized differential reflection

$$r_1^{2\omega} = \frac{R_1^{2\omega} - \langle R_1^{2\omega} \rangle}{R_1^{2\omega}}$$

(where $\langle R_1^{2\omega} \rangle$ are the time-averaged value of $R_1^{2\omega}$) observed in the subpicosecond range of t_d at comparatively low values of F_{eff} = 1–6 mJ/cm^2 (Fig. 9a) shows that the quantity $R_1^{2\omega}$ is modulated probably due to Raman scattering of probe radiation in the weakly excited material [44] resulting in the appearance of a number of nonequilibrium modes (Fig. 9b), including the mode with $\nu \approx 8$ THz. Note, however, that due to time-averaging of the value of $R_1^{2\omega}$ over the duration of the second-harmonic pump pulse (about 100 fs), the power of components in the high-frequency part of the spectrum (10–15 THz) is underestimated in this experiment. (Fig. 9b).

It follows from the data presented in Fig. 7 that the initial long-wavelength *LO* mode remains stable upon exceeding the instability threshold for "weaker" *LA* modes and is not directly involved in the vibronic transition. In contrast, hot *LA* modes are destabilized probably due to a combined action of the e–h plasma and intramode phonon–phonon anharmonicity at short times (phonon–phonon relaxation times), and predominantly of the intermode phonon–phonon anharmonicity at times of the order of a few tens and hundreds of picoseconds. The destabilization of short-wavelength hot *LA* modes along axes Λ, Σ, and Δ of the phonon spectrum corresponds to the band gap collapse in the crystal over three corresponding directions of the Brillouin zone, resulting in three discrete red shifts of both linear absorption bands E_1 and E_2 of crystalline silicon. The preservation of the band and phonon spectra in excited silicon during successive transitions to phases nos. 1 and 2 and to the melt unambiguously indicates the crystalline nature of intermediates phases nos. 1 and 2. Note that these phase transitions of the second kind are related to the destabilization of short-wavelength *LA* modes and occur due to the formation of a spatial compression–rarefaction grating in the excited surface layer of silicon. New phases appearing in compression regions will probably be analogous to known high-

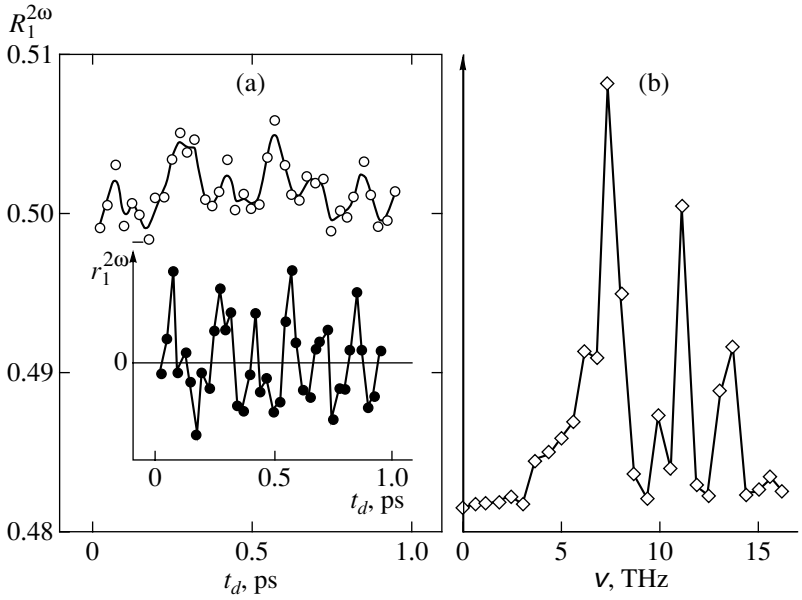

Fig. 9. (a) Time dependence of $R_1^{2\omega}$ in the subpicosecond range for $F_{\text{eff}} \approx 1$ mJ/cm^2 (inset shows $r_1^{2\omega}$ for the same conditions) and (b) the power spectrum for Raman-active modes of silicon under the same conditions.

pressure phases (Si-II and Si-III), which are formed upon hydrostatic compression due to phase transitions of the first kind. Along with this, at times t_d that are shorter than the characteristic time of acoustic relaxation $\tau_a \sim 10$ ps, the compression-rarefaction grating represents a set of nuclei of a new phase (a stage of the premelting type), which is transformed at $t_d \geq \tau_a$ to a continuous phase, which grows inside the sample.

The mechanism of vibronic transitions in silicon proposed in this paper is substantially different from known mechanisms [3–6, 18, 19]. First, based on our experimental data, we assume that soft modes are short-wavelength nonequilibrium modes *LA* modes rather than short-wavelength TA modes [3–6, 18] or long-wavelength *LO* modes [19]. The possibility of the appearance of such hot short-wavelength modes is confirmed by the results of our experimental studies and studies performed in [43]. Second, we established here for the first time the role of the intra- and intermode phonon–phonon anharmonicity for vibronic transitions (in addition to the known plasma-induced instability [3–6, 18, 19]), which favors structural transformations over tens and hundreds of picoseconds, i.e., for times that are substantially longer than the lifetime of the high-density e–h plasma in semiconductors.

Indeed, we can consider the softening of the frequency of nonequilibrium *LA* phonons taking into account the intra- and intermode anharmonicity (along with the plasma contribution) by using the equation for the Fourier amplitude u_q of the *LA* mode in the form

$$\frac{\partial^2 u_q}{\partial t^2} + \omega_0^2(q)\left(1 - \frac{N_e}{N_c}\right)u_q = u_q \sum_{q_1} \beta_{q_1} u_{q+q_1}^2, \qquad (7)$$

where $\omega_0(q) = 2\pi\nu_0(q)$, β_{q_1} is the constant of interaction between the q mode and the $q + q_1$ mode whose Fourier amplitude is u_{q+q_1}, and the term with $\beta_0 \equiv \beta_{q_1 = 0}$ takes the intramode anharmonicity into account. It is obvious that the intramode anharmonicity of the *LA* mode under study is substantial at the time scale of decay (10^{-11}–10^{-10} s) of nonequilibrium *LA* phonons into pairs of transverse *TA* phonons (with lower frequencies), when, owing to a large amplitude of *LA* vibrations, their frequency decreases. Further, at the time scale of thermalization of the absorbed energy, the softening of *LA* phonons is maintained by excitation of all the acoustic modes due to the intermode anharmonicity. We can assume that the contribution summed over the spectrum to the renormalization of the frequency of *LA* phonons with the wave vector q on the right-hand side of expression (7) will be virtually constant at all stages of phonon–phonon relaxation. This assumption allows us to introduce the characteristic of the level of laser excitation of an acoustic subsystem of a semiconductor—the effective nonequilibrium temperature T^*, which was already mentioned—as

$$\sum_{q_1} \beta_{q_1} u_{q+q_1}^2 \approx AT^*, \qquad (8)$$

where A is a constant determining the value of the critical temperature $T_c = \omega^2(q)/A$ in expression (6). As a result, the destabilization of the q mode of nonequilibrium *LA* phonons, which is initiated at short times by the contribution from the e–h plasma (the parameter N_e), is continuously sustained and even develops at longer times due to anharmonic interactions of the q mode with strongly excited acoustic vibrations of the lattice (the parameter T*). Thus, the above model explains the asymptotic time divergence of thresholds for vibronic transitions to phases nos. 1 and 2 to their "thermodynamic" limits F_1 and F_2 (Fig. 7a), which are related, similarly to the critical slowing down of phase transitions of the second kind, to the corresponding critical temperatures T_{ci}.

Unfortunately, we failed to separate the effect of melting of silicon against the background of the reflecting phase no. 2 and to study its dynamics in subpicosecond second-harmonic experiments. Nevertheless, as follows from the data presented in Figs. 2, 3, and 7, the melting dynamics is qualitatively similar to the dynamics of the vibronic transitions $Si^0 \longrightarrow$ no. 1 and no. 1 $\longrightarrow$ no. 2: both the ultrafast (during the pump pulse) and relatively slow ($t_d \approx 1$–10^3 ps) melting occur caused by the e–h plasma and different types of phonon–phonon anharmonicity. The ultrafast melting occurs at the blue wing of the E_2 band (Fig. 3a). Recall that, at the red wing, the contribution from interband transitions along the Δ axis is dominant (the destabilization of the corresponding phonon mode is probably related to the formation of phase no. 2), whereas, at the blue wing, the main contribution comes from transitions along the Σ axis [41]. Taking into account that the band gap for valence σ electrons, which is maximal along the axes X, Δ, and Σ, is similar to the splitting of the energy states in molecules (HOMO–LUMO gap), which is related to the energy of a covalence bond, we can assume that the bonding of atoms along these directions predominantly determines the stability of a silicon crystal. For this reason, at the blue wing of the E_2 band a complete destabilization of a crystal lattice (melting, i.e., the formation of the *l*'-Si phase) should occur, as shown above, via the vibronic mechanism, which is typical for phases nos. 1 and 2. Indeed, the lower estimate of the frequency of the mode whose destabilization causes melting of the material by the pump-pulse end ($t_d \leq 0.2$ ps) for $F_{\text{eff}}(t) \geq 0.25$ J/cm^2 and the minimum value of the asymptotic melting threshold $F_3 \geq F_2 \approx 0.15$ J/cm^2 gives, according to expression (5), the value $\nu_{03} \geq 6.6$ THz (the characteristic melting time $\nu_3 \leq 0.16$ ps), which is comparable with $\nu_{01}(q)$ and $\nu_{02}(q)$, confirming indirectly the vibronic nature of silicon melting in our experiments.

4. CONCLUSIONS

We have observed for the first time by the method of ellipsometry three consecutive discrete red shifts of both linear absorption bands of an undoped silicon crystal during a 100-fs pump fundamental-harmonic laser pulse accompanied by silicon melting. Time-resolved probing of the sample by second-harmonic radiation showed that the shifts occur at a large time scale (0.1–10^3 ps). We explained these results by the consecutive appearance of three long-lived (0.1–10^3 ps) metastable states of silicon, which are characterized by certain emergence thresholds and correspond to certain discrete red shifts of the absorption spectrum of silicon. The dependence of the duration of transitions to these states on the effective energy density showed that these transitions have a vibronic nature (soft short-wavelength *LA* modes of the phonon spectrum along the corresponding crystallographic directions) and are related to structural transformations in silicon, the appearing semimetal (no. 1) and first metal (no. 2) phases being crystalline, whereas the second metal phase (no. 3) is a melt. We determined the microscopic mechanism of formation of the soft modes and proposed the model describing the role of the electron–hole plasma and of the intra- and intermode phonon-phonon anharmonicity in vibronic transitions proceeding in silicon at the time scale 0.1–10^3 ps.

ACKNOWLEDGMENTS

The authors thank D. von der Linde, K. Sokolowski-Tinten, and V. V. Temnov for their help in the organization of experiments and useful discussion. This work was partially supported by DAAD (Germany) (the 1999–2000 scholarship for S. I. K.)

REFERENCES

1. C. V. Shank, R. Yen, and C. Hirliman, Phys. Rev. Lett. **50**, 454 (1983).
2. C. V. Shank, R. Yen, and C. Hirliman, Phys. Rev. Lett. **51**, 900 (1983).
3. V. Heine and J. A. van Vechten, Phys. Rev. B **13**, 1622 (1976).
4. R. Biswas and V. Ambegoakar, Phys. Rev. B **26**, 1980 (1982).
5. J. Bok, Phys. Lett. A **84**, 448 (1981).
6. M. Combescot and J. Bok, Phys. Rev. Lett. **48**, 1413 (1982).
7. S. A. Akhmanov, N. I. Koroteev, and I. L. Shumay, in *Laser Science and Technology*, Vol. 2: *Nonlinear Optical Diagnostics of Laser-Excited Semiconductor Surfaces* (Harwood Academic Publ., New York, 1989).
8. K. Sokolowski-Tinten, J. Bialkowski, and D. von der Linde, Phys. Rev. B **51**, 14186 (1995).
9. K. Sokolowski-Tinten and D. von der Linde, Phys. Rev. B **61**, 2643 (2000).
10. J. P. Callan, A. M.-T. Kim, L. Huang, *et al.*, Chem. Phys. **251**, 167 (2000).
11. E. J. Yoffa, Phys. Rev. B **21**, 2415 (1980).
12. P. P. Pronko, P. A. VanRompay, C. Horvath, *et al.*, Phys. Rev. B **58**, 2387 (1998).
13. D. H. Kim, H. Ehrenreich, and E. Runge, Solid State Commun. **89**, 119 (1994).
14. G. C. Cho, W. Kütt, and H. Kurz, Phys. Rev. Lett. **65**, 764 (1990).
15. T. Pfeifer, W. Kütt, H. Kurz, *et al.*, Phys. Rev. Lett. **69**, 3248 (1992).
16. H. J. Zeiger, J. Vidal, T. K. Cheng, *et al.*, Phys. Rev. B **45**, 768 (1992).
17. S. Hunsche and H. Kurz, Appl. Phys. A **A65**, 221 (1997).
18. P. Stampfli and K. H. Bennemann, Phys. Rev. B **42**, 7163 (1994).
19. V. I. Emel'yanov and D. V. Babak, Fiz. Tverd. Tela (St. Petersburg) **41**, 1462 (1999) [Phys. Solid State **41**, 1338 (1999)].
20. P. L. Silvestrelli, A. Alavi, M. Parrinello, *et al.*, Phys. Rev. Lett. **77**, 3149 (1996).
21. J. S. Graves and R. E. Allen, Phys. Rev. B **58**, 13627 (1998).
22. A. Gambirasio, M. Bernasconi, and L. Colombo, Phys. Rev. B **61**, 8233 (2000).
23. I. L. Shumay and U. Höfer, Phys. Rev. B **53**, 15878 (1996).
24. K. Sokolowski-Tinten, J. Solis, J. Bialkowski, *et al.*, Phys. Rev. Lett. **81**, 3679 (1998).
25. F. Spaepen and D. Turnbull, in *Laser Processing of Semiconductors*, Ed. by J. M. Poate and J. W. Mayer (Academic, New York, 1982), p. 15.
26. E. M. Lifshitz and L. P. Pitaevskiĭ, *Course of Theoretical Physics*, Vol. 10: *Physical Kinetics* (Nauka, Moscow, 1979; Pergamon, Oxford, 1981), Chap. 2.
27. E. N. Glezer, Y. Siegal, L. Huang, *et al.*, Phys. Rev. B **51**, 6959 (1995).
28. S. V. Govorkov, V. I. Emel'yanov, and I. L. Shumay, Laser Phys. **2**, 77 (1992).
29. E. N. Glezer, Y. Siegal, L. Huang, *et al.*, Phys. Rev. B **51**, 9589 (1995).
30. *Femtosecond Laser Pulses: Principles and Experiments*, Ed. by C. Rulliere (Springer-Verlag, Berlin, 1998).
31. P. G. Kryukov, Kvantovaya Élektron. (Moscow) **31**, 95 (2001).
32. K. Sokolowski-Tinten, J. Bialkowski, M. Boing, *et al.*, Phys. Rev. B **58**, 11805 (1998).
33. S. I. Kudryashov and V. I. Emel'yanov, Pis'ma Zh. Éksp. Teor. Fiz. **73**, 263 (2001) [JETP Lett. **73**, 228 (2001)].
34. D. H. Reitze, T. R. Zhang, Wm. M. Wood, *et al.*, J. Opt. Soc. Am. B **7**, 84 (1990).
35. *Handbook of Optical Constants of Solids*, Ed. by E. D. Palik (Academic, Orlando, 1985).
36. C. Guo, G. Rodriguez, A. Lobad, *et al.*, Phys. Rev. Lett. **84**, 4493 (2000).
37. C. Guo and A. J. Taylor, Phys. Rev. B **62**, 5382 (2000).

38. E. Yu. Tonkov, *High Pressure Phase Transformations: a Handbook* (Metallurgiya, Moscow, 1988; Gordon and Breach, Philadelphia, 1992).
39. Yu. V. Kopaev, V. V. Menyaĭlenko, and S. N. Molotkov, Fiz. Tverd. Tela (Leningrad) **27**, 3288 (1985) [Sov. Phys. Solid State **27**, 1979 (1985)].
40. K. M. Shvarev, B. A. Baum, and N. V. Gel'd, Fiz. Tverd. Tela (Leningrad) **16**, 3246 (1974) [Sov. Phys. Solid State **16**, 2111 (1974)].
41. *Landolt-Börnstein: Numerical Data and Functional Relationships in Science and Technology, New Series* (Springer-Verlag, Berlin, 1982), Group III, Vol. 17a.
42. J. M. Liu, R. Yen, H. Kurz, *et al.*, Appl. Phys. Lett. **39**, 755 (1981).
43. R. Orbach, IEEE Trans. Sonics Ultrason. SU-14, 140 (1967).
44. O. V. Misochko, Zh. Éksp. Teor. Fiz. **119**, 285 (2001) [JETP **92**, 246 (2001)].

Translated by M. Sapozhnikov